THANH-DINH NGUYEN

METAL OXIDE, MIXED OXIDE, AND HYBRID METAL@OXIDE NANOCRYSTALS: SIZE- AND SHAPE-CONTROLLED SYNTHESIS AND CATALYTIC APPLICATIONS

Thèse présentée
à la Faculté des études supérieures et postdoctorales de l'Université Laval
dans le cadre du programme de doctorat en génie chimique
pour l'obtention du grade de **Philosophiae Doctor (Ph.D.)**

DÉPARTEMENT DE GÉNIE CHIMIQUE

FACULTÉ DES SCIENCES ET DE GÉNIE, UNIVERSITÉ LAVAL

QUÉBEC, CANADA

2011

Résumé

Le contrôle de la taille et de la morphologie de nanocristaux d'oxydes métalliques simples, d'oxydes mixtes et d'oxydes métalliques hybrides est un sujet de grand intérêt. La dépendance de leur propriétés physio-chimiques avec leurs taille et morphologies, génèrent une variété de leur applications dans plusieurs domaines. Cependant, le dévellopement des nanocristaux en controllant la taille, la forme, l'assemblage et l'homogénéité de la composition chimique pour l'optimisation de propriété spécifiques demandent la combinaison de nombreux parametres de synthèse.

Les trois différentes approches ont été développées dans le cadre de la thèse pour la synthèse d'une variété de nouveaux nanomatériaux d'oxydes simples, d'oxydes mixtes et d'oxydes métalliques hybrides dont la taille et la forme ont été bien controllées. Ces méthodes ont été nommées comme des méthodes solvo-hydrothermiques assistées par des molécules structurantes à l'état monophasique (eau ou eau/éthanol) et à l'état biphasique (eau-toluène). Nos approches de synthèse ont permi de préparer des nanocristaux des oxydes de métaux de transition (V, Cr, Mn, Co, Ni, In), et des terres rares (Sm, Ce, La, Gd, Er, Ti, Y, Zr), ainsi que des oxydes métalliques mixtes (tungstate, orthovanadate, molybdate). Ces nanomatériaux sont sous forme colloïdale mono-dispersée qui présente une cristallinité élevée. La taille et la forme de tels nanocristaux peuvent facilement être contrôlées par une simple variation des paramètres de synthèse telle que la concentration de précurseurs, la nature de la molécule structurante, la température et le temps de réaction. A large variété de techniques a été utilisée pour la caracterisation de ces nanomatériaux telles que TEM/HRTEM, SEM, SAED, EDS, XRD, XPS, FTIR, TGA-DTA, UV-vis, photoluminescence, BET. Les propriétés catalytiques de ces matériaux ont aussi été étudiées.

Dans ce travail, le contrôle de la cinétique de croissance des nucléides ainsi que le mécanisme gouvernant la forme qui conduit à la taille et la morphologie finale du nanocrystal ont été proposé. L'effet de la taille et de la forme des nanoparticules d'oxyde métallique hybrides sur les propriétés catalytiques pour la réaction d'oxydation du CO et la photo-dégradation du bleue de méthylène a été aussi étudié. Car les catalyseurs existant

actuellement à base de métaux nobles sont très couteux et en plus très sensibles à l'empoisonnement par le gas H_2S ou les émissions polluantes de SO_x. L'activité catalytique des nanocristaux d'oxydes métallique hybrides Cu@CeO_2 de formes cubiques dans l'oxydation de CO et de Ag@TiO_2 de formes de ceinture dans la photo dégradation du bleue de méthylène ont montré la dépendance de la taille et la forme des nanocristaux avec leur propriétés catalytiques.

Abstract

The ability to finely control the size and shape of metal oxide, mixed metal oxide, hybrid metal/oxide nanocrystals has become an area of great interest, as many of their physical and chemical properties are highly dependent on morphology, and the more technological applications will be possible for their use. Large-scale synthesis of such high-quality nanocrystals is the first and key step to this area of science. A tremendous effort has recently been spent in attempt to control these novel properties through manipulation of size, shape, structure, and composition. Flexibly nanocrystal size/shape control for both monodisperse single and multiple-oxide nanomaterial systems, however, remains largely empirical and still presents a great challenge. In this dissertation, new synthetic approaches have been developed and described for the synthetic design of a series of colloidal monodisperse metal oxide, mixed metal oxide, hybrid metal-oxide nanocrystals with controlled size and shape. These materials were generally characterized using TEM/HRTEM, SEM, SAED, EDS, XRD, XPS, FTIR, TGA-DTA, UV-vis, photoluminescence, BET techniques. Effect of the size and shape of these obtained hybrid metal-oxide nanocrystals on the catalytic properties is illustrated.

We have developed three different new surfactant-assistant pathways for the large-scale synthesis of three types of nanomaterials including metal oxide, mixed metal oxide, hybrid noble-metal-oxide colloidal monodisperse nanocrystals. Namely, the solvo-hydrothermal surfactant-assisted methods in one-phase (water or water/ethanol) and two-phase (water-toluene) systems were used for the synthesis of metal oxide (transition metal-V, Cr, Mn, Co, Ni, In and rare earth-Sm, Ce, La, Gd, Er, Ti, Y, Zr) and mixed metal oxide (tungstate, orthovanadate, molybdate). The seed-media growth with the assistant of bifunctional surfactant was used for the synthesis of hybrid noble metal@oxide (Ag@TiO_2, (Cu or Ag)@CeO_2, Au/tungstate, Ag/molybdate, etc.) nanocrystals. A significant feature of our synthetic approaches was pointed out that most resulting nanocrystal products are monodisperse, high crystallinity, uniform shape, and narrow distribution. The size and shape of such nanocrystals can be controlled easily by simple tuning the reaction parameters such as the concentration of precursors and surfactants, the nature of surfactant,

the temperature and time of synthetic reaction. The prepared nanocrystals with the functional surface were used as the building blocks for the self-assembly into hierarchical mesocrystal microspheres. The effective ways how to control the growth kinetics of the nuclei and the shape-guiding mechanisms leading to the manipulation of morphology of final products were proposed. Our current approaches have several conveniences including used nontoxic and inexpensive reagents (most using inorganic metal salts as starting precursors instead of expensive and toxic metallic alkoxides or organometallics), relatively mild conditions, high-yield, and large-scale production; in some causes, water or ethanol was used as environmentally benign reaction solvent.

Catalytic activity and selectivity are governed by the nature of the catalyst surface, making shaped nanocrystals ideal substrates for understanding the influence of surface structure on heterogeneous catalysis at the nanoscale. Finally, this work was concentrated on demonstration of heterogeneous catalytic activity of hybrid metal-oxide nanomaterials ($Cu@CeO_2$, $Ag@TiO_2$) as a typical example. We synthesized the high-crystalline titanium oxide and cerium oxide nanocrystals with control over their shape and surface chemistry in high yield via the aqueous surfactant-assist method. The novel hybrid metal-oxide nanocrystals were produced by the depositing noble metal ion (Cu, Ag, Au) precursors on the pre-synthesized oxide seeds via seed-mediated growth. The catalytic activity of these metal-oxide nanohybrids of $Cu@CeO_2$ nanocubes for CO oxidation conversion and $Ag@TiO_2$ nanobelts for Methylene Blue photodegradation with size/shape-dependent properties were verified.

Preface

This Ph.D. thesis was built in the form of a collection of scientific papers, which at the time of the thesis submission, were mostly published or submitted for publication. The first author for these papers is the submitter of this Ph.D. thesis.

The thesis is divided into nine chapters. After a general introduction to the emerging field of nanomaterials, the objectives of the research were elaborated in Chapter 1. The literature review which is related to the subject of the dissertation was reviewed in Chapter 2. This chapter is fully reviewed highlighting the category following the types of metal oxide, mixed metal oxide, hybrid metal-oxide nanocrystals and catalytic activity of nanomaterials over CO conversion and photocatalysis that were recently published. Important development in the synthesis and characterization of nanoscale oxide materials that have contributed to this chapter are presented. Chapter 3 describes the kinetics of nucleation and growth process as well as mechanism of Oriented Attachment of colloidal nanocrystals during wet-chemistry synthesis. Chapter 4 describes the way to control the size/shape and self-assembly of nanocrystals. Chapter 5 describes the experimental synthetic procedures, characterization techniques, and apparatus that were employed for performing this Ph.D. work.

Chapter 6 reports size- and shape-controlled synthesis and characterization of metal oxide nanocrystals in one-phase and two-phase systems. Accordingly, different general two-phase (water-toluene) approaches have been developed for the synthesis of two classes of monodisperse colloidal metal oxide nanomaterials including rare earth and transition metal oxide nanocrystals. These routes are simple and inexpensive, using metal salts instead of organometallic compounds, with mild reaction conditions, easily controlled size and shape, and multigram-scale products. In these two-phase systems, *tert*-butylamine (nucleophile agent) and ethanol (reducing agent) are the key factors for the formation of rare earth oxides of Y, Ce, Sm, Gd, La, Er and transition metal oxides of Cr, Mn, Co, Ni nanocrystals, respectively. Different sizes and shapes of monodisperse nanoparticles such as spherical, cubic, peanut, rod, and hexagonal nanocrystals were obtained, depending on the nature of metal precursors, monomeric precursor concentration, type of precursors, and reaction time. This paper was published in *Journal of Physical Chemistry C* **2009**, *113*, 11204-11214. Through novel two-phase route, the monodisperse samaria nanocrystals with controlled shape obtained in very high yield using commercial bulk Sm_2O_3 powders as a starting source. Controlled self-assembly of Sm_2O_3 nanoparticles into nanorods was controlled by reaction temperature. Furthermore, the width of nanorods can be controlled by the length of capping alkyl chain agents (e.g., oleic acid, myristic acid, decanoic acid). This paper was published in *Journal of Physical Chemistry C* **2008**, *112*, 15226-15235. A new "one-phase" solvo-hydrothermal method had been developed for the synthesis of uniform vanadium oxide nanocrystals with various sizes and shapes in aliphatic amine/toluene/water using prepared V(V) diperoxo alkylammonium complexes. The XRD and XPS results revealed that the as-made vanadium oxide products exhibited the monoclinic rutile VO_2 structure, which was however converted to the orthorhombic $V_2O_{4.6}$ structure after calcination in air. This paper was published in *Langmuir* **2009**, *25*, 5322-5332. Using one-phase "water/ethanol" system, shape- and size-controlled synthesis of monoclinic ErOOH and cubic Er_2O_3 from micro- to nano-structures and their upconversion luminescence shape via the solvo-hydrothermal reaction of erbium nitrate in water/ethanol/decanoic acid media. This paper was published in *ACSNano* **2010**, *4*, 2263-2273.

Chapter 7 reports size- and shape-controlled synthesis and characterization of colloidal mixed metal oxide nanocrystals in one-phase and two-phase systems. A new solvothermal "one-phase" approach has been developed for the synthesis of monodisperse and well-crystallized tetragonal-phase rare earth orthovanadate ($REVO_4$, RE = Sm and Ce) nanocrystals with different morphologies from the reaction of $RE(OA)_3$ and $VO_4(TOA)_3$ complexes in toluene in the presence of surfactant (oleylamine or oleic acid). The XPS results study on the oxidation states of the metals on the mixed oxide nanocrystal surface revealed that that only one oxidation state of samarium, cerium, and vanadium for each metal (e.g., Sm^{3+}, Ce^{3+}, V^{5+}) was stable on the particle surface, while the existence of two oxidation states of these metals is observed (e.g., Sm^{3+}/Sm^{2+}, Ce^{4+}/Ce^{3+}, V^{5+}/V^{4+}) in the corresponding single metal oxide nanocrystals. These papers were published in *Journal of*

Physical Chemistry C **2009**, *113*, 18584-18595 and *Langmuir* **2009**, *25*, 11142-11148. Using water as reaction solvent and amino acid biomolecules as capping agent, shape-controlled synthesis of single-crystalline $MnWO_4$ nanoparticles and spontaneous assembly of polypeptide-stabilized mesocrystal microspheres were performed via the hydrothermal reaction of $Mn(NO_3)_2$ and Na_2WO_4 precursors in amino acid/water medium. This paper was published in *CrystEngComm* **2011**, *13*, 1450-1460. Undoped and cerium doped $LaCO_3OH$ annular-shaped nanoarchitectures with high specific surface area were fabricated via the thermolysis of $Ce_xLa_{1-x}(oleate)_3$ (x = 0-20 mol%) complexes in a toluene-water system containing *tert*-butylamine/oleylamine. Concentration- and oxidation state-dependent photoluminescences of cerium dopant in nanostructured $LaCO_3OH$ annular-shaped architectures were proposed. This paper was published in *Inorg. Chem.* **2011**, *50*, 1309-1320.

Chapter 8 reports the controllable synthesis of hybrid metal-oxide nanocrystals and their catalytic applications. Well-shaped and single-crystalline CeO_2 nanocubes and ~120 nm edge length were synthesized via the hydrothermal reaction of cerium nitrates in a basic environment in the presence of bifunctional hexamethylenediamine ligand. The surfaces of ceria possessed a hydrophilic character because of the use of the bifunctional diamine capping agents. The novel hybrid metal-ceria nanocrystals were produced by the deposition of noble metal ion (Cu, Ag) precursors on the pre-synthesized ceria seeds via seed-mediated growth. The formation of the metal-oxide nanohybrids consisted of the adsorption of positively charged noble metal precursors on the negatively charged surfaced ligand-capped oxide nanocrystals and then the reduction of noble metal ions into metallic particles by $NaBH_4$ reducing agent. The hybrid Cu@{100}-faceted CeO_2 catalyst demonstrated a much higher catalytic activity for CO oxidation than the pure CeO_2 catalyst. This paper was submitted to *Advanced Materials* **2011**. A general procedure to synthesize highly crystalline metal oxide (Ti, Zr, Ce, Y, In) and mixed oxide (metal tungstates, vanadates, molybdates) nanocrystals in aqueous medium in the presence of 6-aminohexanoic acid. As a bifunctional ligand, the role of capping 6-aminohexanoic acid is to capture metal ion by its interaction with -COOH group, which favors for the formation of highly dispersed metal on the oxide surface during the synthesis. Hence, the hybrid metal/oxide nanocrystals were synthesized via the decoration of noble metal precursors on obtained AHA-capped seeds. The photocatalytic activity of Ag@TiO_2 nanobelts as a typical hybrid sample for Methylene Blue degradation was studied. This paper was published in *Nanoscale* **2011**, *3*, 1861-1873.

Finally, Chapter 9 completes the thesis by summarizing general conclusions and recommendations for future work.

Acknowledgements

No work such as this can be done alone, and as such there are many people who deserve thanks for both getting to this point and keeping me going. First and foremost, I would like to express my wholehearted gratitude to my thesis supervisor, Professor Trong-On Do, for his deepest guidance, persistence, enlightening instructions, and support in the joyful but challenging journey of my Ph.D. study. I am grateful for his enthusiasm and insight about science which kept inspiring me to think deeply and logically about scientific phenonmena. His valuable suggestions on my research and paper writing for the completion of the whole thesis are greatly appreciated. I am very fortunate to have the opportunity to study and work with him, and in fact without his trust and vision, none of this could have been.

I would also like to thank the members of my scientific committee for their helpful suggestions and feedback during the preparation of this thesis.

I am very gratefully for the friendship and generous help from all my colleagues in professor Do's lab in performing my thesis work: Dr. Bousselham Echchahed, Mr. Driss Mrabet, Mr. Vuong Thanh-Gia, Mr. Cao Thang-Dinh, Mr. Pham Minh-Hao, Mr. Robenson Cherizol, Mr. Innocents Alain Ikouba, Ms. Thi Thuy-Duong Vu, Ms. Nguyen Phuong-Trinh, Ms. Maissa Bouguerra. Especially Dr. Bousselham Echchahed helped me translate the abstract of thesis into French and Driss Mrabet Ph.D. candidate helped me to test the catalytic activity of hybrid nanocatalysts for carbon monoxide oxidation conversion.

Special gratitude must be given to all the professors, staff and graduate students of the Department of Chemical Engineering from Laval University for their great assistance and cooperation.

I am also grateful to the Natural Science and Engineering Research Council of Canada (NSERC) and Laval University for financial support.

Most important of all, I would like to thank my big family for their love, continued support, encouragement, and assistance throughout the academic years. I would like to

specially thank my wife, Minh-Chau TranNgoc, with all my love, for her endless love, valuable perspective, patience, and sound criticism throughout the last years of graduate school. Thanks to my son, Kelvin Nguyen Thanh, for being proud and encouraging me along way and making sure I never gave up.

Last, but certainly not least, thanks are extended to my close Vietnamese friends in Laval University for their friendship, encouragement, and support.

DEDICATION

To my grandmother-in-law, mother, father, mother-in-law, sisters, sister-in-laws, young brothers, brother-in-laws, nephews, and nieces.

To my wife, Minh-Chau TranNgoc and my son, "Little elephant" Kelvin Nguyen Thanh.

I love you!

Table of Contents

Index of Tables

Index of Figures

Index of Schemes

Chapter 1 Introduction

1.1. General Background

The field of nanomaterials has become an ever-growing discipline of science of the entire world. Even those who do not know what it represents mathematically are invariably aware that it refers to something "very small". One of the earliest records, Ancient Greeks and Romans used PdS nanoparticles to permanently the black-to-grey color of hair in middle ages (~2000 years ago). About 1000 years later, gold nanoparticles were used as a pigment of ruby-colored stained glass windows at Cathedral of Notre Dame or Lycurgus glass cup at British Museum. The different-sized gold nanoparticles scattered light producing bright red and purple colors (Moores and Goettmann 2006). An understanding of the science behind these materials started with Michael Faraday's research in the mid 19th century, who prepared gold sols and characterized their nanoscale optical properties, arising from the confinement of the surface Plasmon (Moores and Goettmann 2006). These first studies revealed that certain physical and chemical properties of colloids were different from the bulk. However, the nanomaterials generated an ever-increasing interest since with the development of high resolution transmission electron microscopy in the 20th century. The ability to synthesize the nanoparticles of desired size in a controlled shape and finally the advent of a broad range of different nanomaterial systems that have come up in the last few decades. The colloidal nanocrystals have proven exciting opportunities for discovering new phenomena in an emerging research area of science and followed by a technological revolution in diverse useful applications.

A nanocrystal or nanoparticle (not fully crystalline) is defined as a particle with size in range of 1 to 100 nm (10^2 to 10^7 atoms) from one to three dimensions, which exhibit the unique physiochemical properties due to the quantum size effect that cannot be anticipated from bulk counterparts. Strictly speaking, the name of "nanocrystal" is only used for crystalline nanoparticle, and is a more general term which can refer to both crystalline and non-crystalline nanoparticles. Accordingly, their particle size is intermediate between molecule and bulk solid size (Rao, Müller and Cheetham 2005, Sorensen 2009, Schmid 2005). Nanocrystals can be formed in a variety of shapes including dot, sphere, cube, rod, triangle, hexagon and many others. In this size range, they possess a large surface area per unit volume, a very large percentage of atoms in the surface. As a result, their unexpected properties can be obtained as compared to the properties of both individual atoms/molecules and bulk counterpart of the same chemical composition.

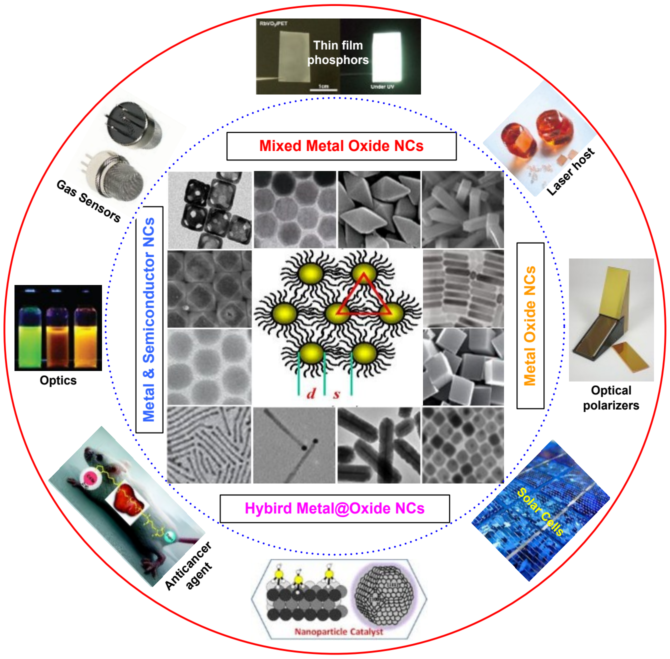

Figure 1.1. Representative shapes of inorganic nanocrystals developed to date. These kinds of nanocrystals utilized as key building blocks for the fabrication of novel nano-systems for catalytic, electronic, and biomedical technologies.

Nanostructured metal oxide and mixed oxide materials have been the focus of intense research to chemists and materials scientists in various fields for both unique properties and technological applications (Seshadri 2005, Burda et al. 2005, Mao et al. 2007, Yin and Alivisatos 2005). Metal oxides including the transition metals and rare earths, display a very wide variety of complex structures and interesting electronic and magnetic properties associated with the changes in electronic structure and bonding and in the presence of ordered defect complexes or extended defects. The nanostructured mixed oxides can greatly generate new synergetic properties and improve the overall application performance, that is not available from single metal oxide species, due to the appropriate combination of individual oxide components (Redl et al. 2003). The size- and shape-dependent properties of nanomaterials raising expectations for a better performance are generally a consequence of large suface area and effective percentage of active surface atoms (Alivisatos 1996). The precise controlled synthesis of the size, shape, chemical composition, crystal structure, and surface chemistry of nanomaterials allows one to observe their unique properties, which have become one of the most challenging issues faced by nanomaterial researchers. The properties of nanocrystals are drastically altered in the shape and size change, making nanocrystals ideal candidates for many applications in catalysis, energy storages, optoelectronics, sensing, magnetic resonance imaging, biomedicine, ect (Shopsowitz et al. 2010, Kinge, Crego-Calama and Reinhoudt 2008, Ying 2000, Na, Song and Hyeon 2009, Jun, Choi and Cheon 2006). A general picture in Figure 1-1 is schematically for the features and new phenomena of the nanoscale materials.

The unexpected properties of the nanocrystals can tune by changing in the dimension and designing the shape (Rao et al. 2005). Due to the materials at the nanoscale, low coordination number, surfaced edge, and corner atoms are usually chemically reactive, catalytically active and polarizable surface, contributing to their high chemical potential. For example, the high surface area is of particular importance regarding heterogeneous catalytic materials, because of the importance of molecular interactions with the catalyst (Abbet and Heiz 2005). Furthermore, the particle size not only affects the surface area of nanoparticles, but also their new properties can be arisen because of the quantum-size effect (e.g., electron confinement and surface effect) (Kroes et al. 2002, Kamat et al. 2010).

Nanostructured metal oxide, mixed oxide, hybrid metal-oxide materials have been the focus of intense research by chemists and materials scientists in various fields due to both their unique properties and technological applications (Seshadri 2005, Burda et al. 2005, Mao et al. 2007, Yin and Alivisatos 2005). Metal oxides including the transition metals and rare earths, display a wide variety of complex structures and interesting electronic and magnetic properties associated with the changes in electronic structure and bonding and in the presence of ordered defect complexes or extended defects. The nanostructured mixed oxides can greatly generate new synergetic properties and improve the overall application performance, that is not available from single metal oxide species, due to the appropriate combination of individual oxide components (Redl et al. 2003).

Furthermore, the size- and shape-dependent properties of nanomaterials raising expectations for a better performance generally are a consequence of quantum confinement within the particle (Alivisatos 1996). The precise controlled synthesis of the size, shape, chemical composition, crystal structure, and surface chemistry of nanomaterials allows to obtain their unique properties, which have become one of the most challenging issues faced by nanomaterial researchers. The properties of nanocrystals are drastically altered in the shape and size change, making nanocrystals ideal candidates for many applications in catalysis, energy storages, optoelectronics, sensing, magnetic resonance imaging, biomedicine and so forth (Shopsowitz et al. 2010, Kinge et al. 2008, Ying 2000, Na et al. 2009, Jun et al. 2006).

Due to the properties of colloidal metal oxide, mixed oxide, hybrid metal-oxide structures at the nanoscale depending on their size and shape, it is a great challenge to develop a "synthetic methodology" of nanocrystals that is as precise as that used to make building units. This allows scientists to study how these synthesis parameters impart to the unique collective properties of monodisperse nanocrystals. Two strategies are generally pursued to synthesize the nanomaterials: "top-down" approach, using physical methods involving the fractionating of bulk materials, and "bottom-up" employing chemical approaches, including the growth of nanomaterials from atomic-scale components (Schmid 2005). The advantage of the physical "top-down" method is the production of a large quantity of nanocrystals, whereas the synthesis of uniform-sized nanocrystals and their size control is very difficult to achieve using this route. On the other hand, the "bottom-up" approach can easily and efficiently create large quantities of nanomaterials, beginning with molecules or atoms through chemical nucleation and growth process in bulk solution. The use of atoms or molecules as building blocks has the advantage that highly advanced synthetic methodologies provide control over crystallite size and shape with a precision well beyond that of top-down lithography (Park et al. 2007). As a result, bottom-up assembly of well-defined nanoscale building blocks into nanocrystals with controlled size and shape represents a powerful tool to fabricate novel multi-component materials and devices (Nagarajan 2008). In order to control the crystal growth, the capping agents are often used to decrease the surface energies of crystals. The surfactants bind selectively to the different crystallographic faces, so that shape of nanocrytals can be controlled by the nonselective or selective surfactants (Cushing, Kolesnichenko and O'Connor 2004). The use of surfactant molecules result in oxide nanocrystals comprising an inorganic core coated with a layer of organic surfactant molecules. This organic capping provides electronic and chemical passivation of the surface dangling bonds, prevents uncontrolled growth and agglomeration of the nanoparticles, and permits chemical manipulations of the nanoparticles similarly to large molecules having their solubility and reactivity determined by the nature of the surface ligands. The most commonly used ones in colloidal syntheses include alkyl-thiols, long chain amines, carboxylic and phosphonic acids, phosphine oxides, phosphine, phosphates, phosphonates.

Understanding growth behavior and morphology evolution is crucial for efficient synthesis and good control of inorganic nanocrystals. In the bottom-up syntheses, for the growth process of nuclei, the behavior was described by the classical Ostwald ripening mechanism, in which the growth of larger particles at the expense of smaller ones driven by surface energy reduction. This phenomenon was extensively used to explain the formation of thermodynamically stable nanocrystals with nearly spherical morphologies. For the controlled self-assembly of nanoparticles into well-defined anisotropic nanostructures, organic capping reagents usually play critical roles in reducing the activity of the nanocrystal surface to promote or tune the ordered self-assembly (Kinge et al. 2008, Sellinger et al. 1998, MalenfantPatrick et al. 2007, Yin and Alivisatos 2005). An oriented attachment mechanism could offer as an additional tool to design advanced materials with anisotropic properties and could be used for the synthesis of more complex crystalline one-dimensional structures. In addition, the sterically diffusive kinetics and selective binding or nonbinding of surfactant molecules to different faces of the growing nanocrystal can also control the product’s morphology due to the possibility of breaking the limitations of crystal growth dynamically. In some cases, the formation of the intrinsic anisotropic nanocrystals is found to be a highly kinetics-driven process, which occurs far away from the thermodynamic equilibrium, and must be overdriven by high precursor monomer concentrations.

In addition, the surface modification of the surfactant-capped nanocrystals with various shapes allows them to readily form two- and three-dimensional superstructures composed of single component or binary component nanocrystals by varying the reaction conditions such as nature and concentration of surfactants, precursors, solvent, reaction temperature and time. Assembling nanocrystals into highly ordered 1-, 2-, 3-D colloidal crystals and architectures requires monodisperse nanocrystals with uniform morphological distributions and capping agents usually play critical roles in reducing the activity of the nanocrystal building blocks to promote or tune the ordered self-assembly. For realising versatile functions, assembly of nanocrystals in regular patterns on surfaces and at interfaces generates new nanostructures, which have unforeseen collective and intrinsic physical properties (Bigioni et al. 2006, Zhang et al. 2006). In this dissertation, the basic growth concepts of nanoparticle building blocks and their self-assemblies will be presented. The motivation for this work will also be given.

The reaction medium is crucial in the solution-based approaches. To date, inorganic nanocrystals obtained from solution-based methods that mainly used the organic reagent as synthesis solvent such as toluene, diphenyl ether, oleic acid/oleylamine, etc. In organic solvent systems, expensive and toxic organometallic precursors and organic solvents are often not compatible with biomedical applications. Water, as an environmentally friendly solvent with the most abundant resources, and most metal nitrates and chloride salts were used as starting materials can overcome these barriers. Furthermore, due to the high solubility of metal salt precursors in aqueous media, the aqueous-based routes can be used for the synthesis of pure products in high yield. The development of the general synthetic strategies to produce the size- and shape-controlled metal oxide, mixed oxide, hybrid metal-oxide nanocrystals in terms of cost effectiveness, environmentally benign reagents, mild synthesis conditions, and potential for large-scale production are needed among the important research topics of the advanced materials chemistry.

This thesis has focused on an original solution-based method to synthesize a variety of the metal oxide, mixed oxide, hybrid metal-oxide nanocrystals. We provide our synthetic approaches and a brief account of our own results to prepare various kinds of metal oxide, mixed oxide, hybrid metal-oxide nanomaterials according to their compositions. The numerous adaptations to the synthetic procedures and the formation mechanisms will be proposed to control the size and shape with their unique dependent properties. The main advantages of this synthetic strategy are the use of inexpensive stable salts and commercial bulk metal oxide powders as starting materials instead of expensive, toxic metal alkoxides, and could be readily scaled up to gram-grade production of the nanoparticles. By carefully modifying synthetic parameters such as precursor monomer concentration, nature of surfactants, solvent composition, reaction temperature and time, we could manipulate the shape and size of these nanocrystals. Further applications of such nanoparticles in heterocatalysis will be studied.

1.2. Objectives and Scope of the Dissertation

The present Ph.D. work has been undertaken with the aim of studying the development of new simple approaches for the large-scale synthesis of uniform metal oxide, mixed metal oxide, hybrid metal-oxide nanocrystals with controlled size and shape and their catalytic applications for carbon monoxide oxidation conversion and photodegradation of Methylene Blue.

As mentioned above, nanomaterials exhibit unique physiochemical properties because of their large surface area and high percentage of active surface atoms that cannot be anticipated from bulk counterparts. Monodisperse metal oxide, mixed metal oxide, hybrid metal-oxide nanomaterials have currently emerged as key materials and have attracted much attention to chemists and materials scientists in numerous astonishing possibilities for applications such as catalysts, magnetic and optical devices, solar cells, biomedicines, ect. Studies on such nanocrystals, including synthesis, characterization of the structural, physiochemical properties, and practical applications, represent a fundamental cornerstone of nanoscience and nanotechnology. Development of new simple synthetic approaches for nanocrystal shape control for both single- and multiple-material systems, however, still presents a major challenge.

In this dissertation, new methods have been exploited to synthesize three classes of nanomaterials including metal oxide, mixed metal oxide, hybrid metal-oxide nanocrystals with controlled size and shape and their catalytic applications as following present:

- Developing the solvo-hydrothermal "one-phase" and "two-phase" approaches for size- and shape-controlled synthesis and characterization of a variety of uniform metal oxide nanocrystals.

- Developing the solvo-hydrothermal "one-phase" and "two-phase" approaches for size- and shape-controlled synthesis and characterization of a variety of uniform mixed metal oxide nanocrystals.

- Developing the hydrothermal "seed-mediated growth" approach in the assistance of bifunctional surfactant for size- and shape-controlled synthesis and characterization of a variety of novel hybrid metal-oxide nanocrystals.

- The catalytic activities of carbon monoxide oxidation conversion and Methylene Blue photodegradation over hybrid metal-oxide nanocatalysts with size- and shape-dependent properties were tested.

References

Abbet, S. & U. Heiz. 2005. *Nanocatalysis*. Wiley-VCH Verlag GmbH & Co. KGaA.

Alivisatos, A. P. (1996) Semiconductor Clusters, Nanocrystals, and Quantum Dots. *Science,* 271**,** 933-937.

Bigioni, T. P., X.-M. Lin, T. T. Nguyen, E. I. Corwin, T. A. Witten & H. M. Jaeger (2006) Kinetically driven self assembly of highly ordered nanoparticle monolayers. *Nat Mater,* 5**,** 265-270.

Burda, C., X. Chen, R. Narayanan & M. A. El-Sayed (2005) Chemistry and Properties of Nanocrystals of Different Shapes. *Chemical Reviews,* 105**,** 1025-1102.

Cushing, B. L., V. L. Kolesnichenko & C. J. O'Connor (2004) Recent Advances in the Liquid-Phase Syntheses of Inorganic Nanoparticles. *Chemical Reviews,* 104**,** 3893-3946.

Jun, Y.-w., J.-s. Choi & J. Cheon (2006) Shape Control of Semiconductor and Metal Oxide Nanocrystals through Nonhydrolytic Colloidal Routes. *Angewandte Chemie International Edition,* 45**,** 3414-3439.

Kamat, P. V., K. Tvrdy, D. R. Baker & J. G. Radich (2010) Beyond Photovoltaics: Semiconductor Nanoarchitectures for Liquid-Junction Solar Cells. *Chemical Reviews,* 110**,** 6664-6688.

Kinge, S., M. Crego-Calama & D. N. Reinhoudt (2008) Self-Assembling Nanoparticles at Surfaces and Interfaces. *ChemPhysChem,* 9**,** 20-42.

Kroes, G.-J., A. Gross, E.-J. Baerends, M. Scheffler & D. A. McCormack (2002) Quantum Theory of Dissociative Chemisorption on Metal Surfaces. *Accounts of Chemical Research,* 35**,** 193-200.

MalenfantPatrick, R. L., J. Wan, S. T. Taylor & M. Manoharan (2007) Self-assembly of an organic-inorganic block copolymer for nano-ordered ceramics. *Nat Nano,* 2**,** 43-46.

Mao, Y., T.-J. Park, F. Zhang, H. Zhou & S. S. Wong (2007) Environmentally Friendly Methodologies of Nanostructure Synthesis. *Small,* 3**,** 1122-1139.

Moores, A. & F. Goettmann (2006) The plasmon band in noble metal nanoparticles: an introduction to theory and applications. *New Journal of Chemistry,* 30**,** 1121-1132.

Na, H. B., I. C. Song & T. Hyeon (2009) Inorganic Nanoparticles for MRI Contrast Agents. *Advanced Materials,* 21**,** 2133-2148.

Nagarajan, R. 2008. Nanoparticles: Building Blocks for Nanotechnology. In *Nanoparticles: Synthesis, Stabilization, Passivation, and Functionalization*, 2-14. American Chemical Society.

Park, J., J. Joo, S. G. Kwon, Y. Jang & T. Hyeon (2007) Synthesis of Monodisperse Spherical Nanocrystals. *Angewandte Chemie International Edition,* 46**,** 4630-4660.

Rao, C. N. R., A. Müller & A. K. Cheetham. 2005. *Nanomaterials – An Introduction*. Wiley-VCH Verlag GmbH & Co. KGaA.

Redl, F. X., K. S. Cho, C. B. Murray & S. O'Brien (2003) Three-dimensional binary superlattices of magnetic nanocrystals and semiconductor quantum dots. *Nature,* 423**,** 968-971.

Schmid, G. 2005. *General Introduction*. Wiley-VCH Verlag GmbH & Co. KGaA.

Sellinger, A., P. M. Weiss, A. Nguyen, Y. Lu, R. A. Assink, W. Gong & C. J. Brinker (1998) Continuous self-assembly of organic-inorganic nanocomposite coatings that mimic nacre. *Nature,* 394**,** 256-260.

Seshadri, R. 2005. *Oxide Nanoparticles*. Wiley-VCH Verlag GmbH & Co. KGaA.

Shopsowitz, K. E., H. Qi, W. Y. Hamad & M. J. MacLachlan (2010) Free-standing mesoporous silica films with tunable chiral nematic structures. *Nature,* 468**,** 422-425.

Sorensen, C. M. 2009. *Particles as Molecules*. John Wiley & Sons, Inc.

Yin, Y. & A. P. Alivisatos (2005) Colloidal nanocrystal synthesis and the organic-inorganic interface. *Nature,* 437**,** 664-670.

Ying, J. Y. (2000) Nanostructural tailoring: Opportunities for molecular engineering in catalysis. *AIChE Journal,* 46**,** 1902-1906.

Zhang, H., E. W. Edwards, D. Wang & H. Mohwald (2006) Directing the self-assembly of nanocrystals beyond colloidal crystallization. *Physical Chemistry Chemical Physics,* 8**,** 3288-3299.

Chapter 2 Literature Review

In this chapter, general background on the synthesis and characterization of metal oxide, mixed metal oxide, hybrid metal-oxide nanocrystals with controlled size and shape will be presented. Size- and shape-dependent properties of such nanocrystals will be discussed. Subsequently, the catalytic activity of nanomaterials for CO oxidation and organic-contaminant photodegradation will be introduced.

2.1. Size- and Shape-Dependent Properties of Nanocrystals

Size effects constitute a fascinating aspect of nanomaterials. As the size of a crystal decreases to the nanometer regime, the associated properties are increasingly governed by considerations such as the surface-area-to-volume ratio and energy quantization. Quantum confinement is a widely used terminology in the study of nanocrystals. Size quantization refers to changes in the energy-level structures of materials as the building unit size drops below a certain size. This size, which can be identified with the Bohr diameter of the material, can vary from almost 100 nm to a single nanometer or even less. The electronic structure is altered from the continuous electronic bands to discrete or quantized electronic levels leading to the size-dependent properties. Further since the properties of nanocrystals follow from the confinement of the electrons to the physical dimensions of the nanocrystals, it would be interesting to vary the shape of the nanocrystals, study on the effect of confinement of electrons in such artificial shapes, and follow by optimizing the physiochemical properties.

The effects of reducing size are very different for nanomaterials with localized electrons where defects are the most significant contributor to the evolution of structural, thermodynamic, electronic, spectroscopic, electromagnetic and chemical features of these finite systems. Figure 2-1b shows the effective percentage of surface atoms as a function of particle diameter, in which a percentage of surface atoms strongly increases as the particle size decreases . Because of the number of atoms at the surface and the limited number of atoms within the lattice, such atoms are considered to be defect site relative to coordinatively unsaturated ions that affect on the surface chemistry and bonding of nanoparticles. Some early reports illustrated the size-dependent property, whereby the solutions of synthesized Au clusters possess optical properties similar to those of the sols. This behavior originated from the self-assembly of metallic Au_n nanoclusters with shells of atoms in a cubic close packed arrangement in enhanced stability (so-called cluster compounds). The magic numbers 13, 55, 147, 309, 561 correspond to the closure of 1, 2, 3, 4 5 shells respectively, as shown in Figure 2-1a . This former includes the appearance of new features in the electronic structure of nanoscale materials with the high surface area-to-volume ratio. On the other hand, the electronic structures of metal and semiconductor nanocrystals differ from those of bulk materials and isolated atoms were also shown in Figure 2-1c (Jun et al. 2006).

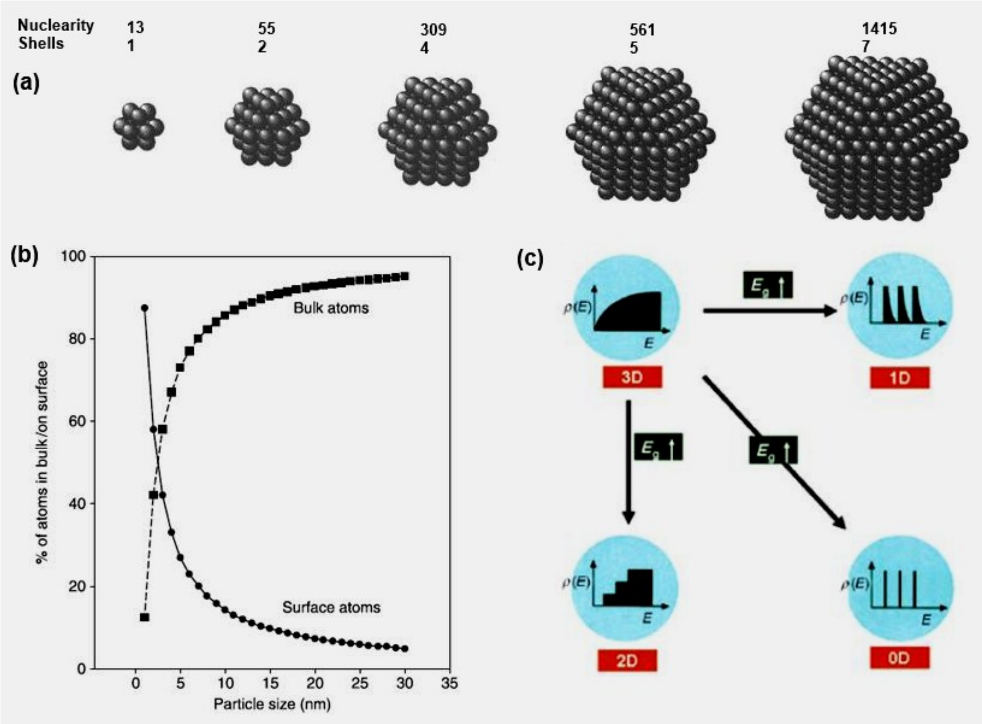

Figure 2.1. (a) Metal nanocrystals in closed-shell configurations with magic number of atoms (Martin et al. 1991, Sorensen 2009); (b) Calculated surface to bulk atomic ratio (Klabunde et al. 1996); (c) Shape evolution of nanocrystals and the shape-dependent properties (Jun et al. 2006).

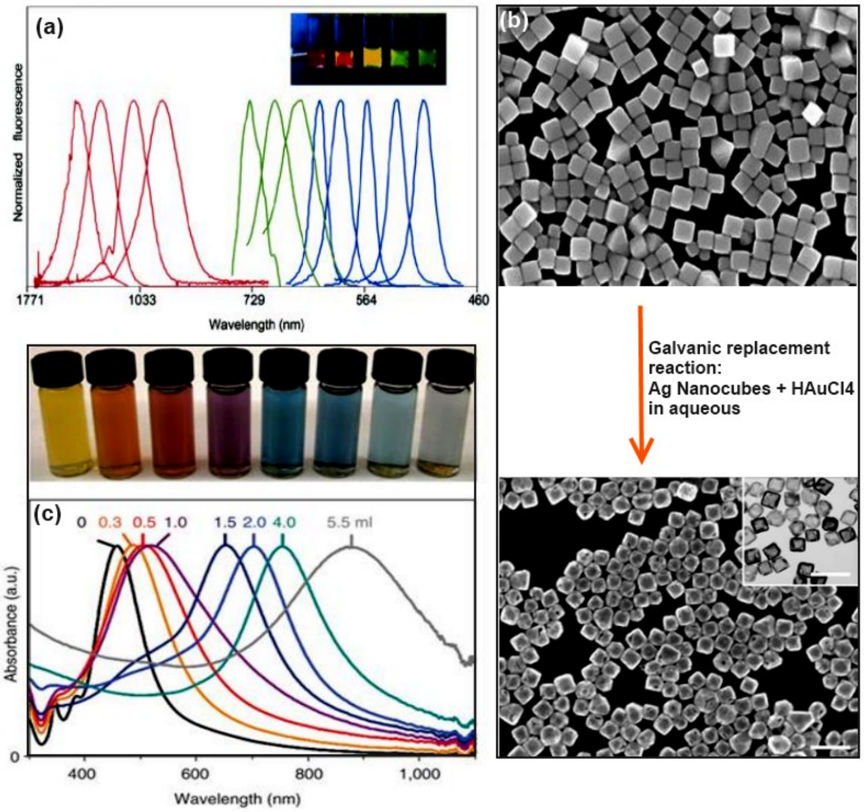

Figure 2.2. Optical property of nanocrystals. Size-dependent emission spectra (a) can be tuned from red to blue by decreasing the size of sub-10 nm InAs, InP, CdSe semiconductor quantum dots, inset of colloidal solutions quantum dots illuminated with ultraviolet radiation (Bruchez et al. 1998); (b) Au nanocages prepared by galvanic replacement reaction between Ag nanocubes and $HAuCl_4$ aqueous solution; (c) the surface Plasmon resonance peak of Au nanocages is tunable through the visible and near-IR regions with increasing displacement, inset of colloidal solutions of the corresponding Au nanocages (Skrabalak et al. 2007).

To date, many of the exciting size-dependent properties of inorganic nanomaterials arise as compared to their microcrystalline counterparts. For example, optical properties such as surface plasmon resonance and surface-enhanced Raman scattering (SERS) observed for Au and Ag nanoparticles are very sensitive to the particle size and/or surface area. Au becomes paramagnetic at room temperature and ferromagnetic at temperatures around 3K when the particle size is on the order of 2 nm. For nanostructured semiconductor materials, quantum confinement effects often lead to several interesting and intriguing phenomena. As the size of the semiconductor nanocrystals (quantum dots) decreases relative to the characteristic excition radius, confinement becomes more pronounced resulting in an overall increase in the energy gap which varies as $\sim 1/r^2$, where r is the nanocrystal radius. Opening of the energy gap manifest itself very clearly as a blue shift in the photoluminescence spectrum (Figure 2-2a) (Bruchez et al. 1998). The narrow, tunable, symmetric emission spectrum along with the broad continuous excitation profile make these semiconductor nanocrystals particularly attractive candidates for fluorescent biological labels, with respect to traditional fluorophores.

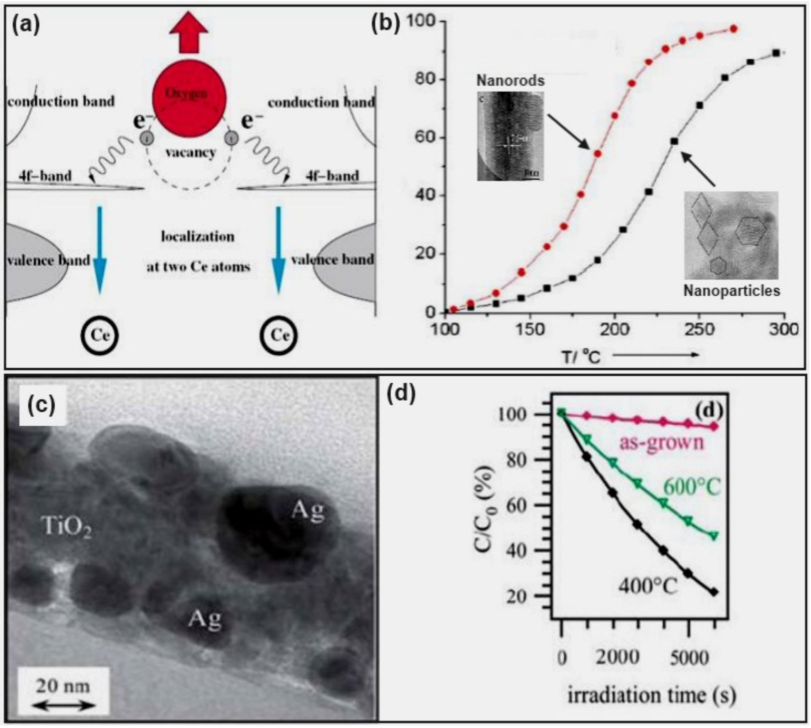

Figure 2.3. (a) The process of oxygen-vacancy formation in ceria, in which an oxygen atom moves away from its lattice position leaving behind two electrons, which localize on two cerium atoms, turning Ce^{4+} into Ce^{3+} (Skorodumova et al. 2002); (b) Percentage conversion versus temperature plots for the oxidation of CO over CeO_2 nanoparticles and CeO_2 nanorods (Zhou et al. 2005); (c) Ag@TiO_2 nanorods and (d) photobleaching of Plasmocorinth B aqueous solutions by Ag@TiO_2 nanorods at different calcinations (Armelao et al. 2009).

There has been much attention in controlling the shape of nanomaterials owing to their intriguing shape-dependent optical properties, and it has become a topic of fundamental importance in nanocrystal research. For instance, the colors of Ag nanocrystal colloids were tunable by controlling the various shapes of single nanocrystals. The various shapes of Ag nanocrystals exhibited the corresponding different maximum absorption of scattering spectra due to the different distribution of active atoms on the corners/edges of the Ag nanocrystal surface. The number of resonances depends on the number of ways, in which the electron density can be polarized and is determined by the shape of the nanoparticles. Sharp tips and edges in nanoparticles are regions of high electric field that greatly enhance the effects; nanoprisms of gold and silver have been investigated in detail owing to this aspect. Similarly, it has been found that the Raman signal is increased many orders of magnitude when Ag with sharp corners is used as a substrate due to the intense electric field generated by the localized surface plasmon resonance. For even more complex nanocrystals such as the Au nanocages produced by galvanic displacement of Ag nanocubes by Xia et al., shape can be used to precisely tune the surface plasmon response to span the visible and near-IR regions of the spectrum, as shown in Figure 2-2b,c (Skrabalak et al. 2007).

Chemical reactivity is also strongly dependent on both the size and shape of nanocrystals. With the continuing decrease in size, the ratio of surface-area-to-volume increases dramatically as shape imparts its own influence on the structure of the surface. An understanding of the different surface structures and how they affect the dynamics of adsorbates on nanoscale materials may allow for the development of highly selective catalysts through precise tuning of nanocrystal morphology. The crystallographic orientation of the planar terrace surfaces, the number of step edges and kink sites associated with corners and edges, as well as the high surface area, all play a significant role in catalytic activity. Daroczi et al. (Guczi et al. 2003) had revealed the size effect of Au nanoparticles that demonstrated correlation between Au nanoparticle size, electron structure, and catalytic activity. The valence band density of states of gold nanoparticles changed with decreasing particle size and brought about the enhancement of activity. The Pt nanocrystals with exposed {111}-facets was found to be several times more active than the Pt {110} facets for aromatization reactions while Pt nanoparticles covered by high-index planes show much higher catalytic activity for electrooxidation reactions compared to those bound by low-index planes (Tian et al. 2007). The reversible CeO_2-Ce_2O_3 reduction transition associated with oxygen-vacancy formation and migration is shown to be directly coupled with the quantum process of electron localization, as shown in Figure 2-3a. This behavior make ceria materials to be an excellent candidate for CO oxidation due to their high oxygen storage capacity (Skorodumova et al. 2002). Li et al.(Zhou et al. 2005) demonstrated that the CeO_2 nanorods were more active than CeO_2 nanoparticles for CO oxidation (Figure 2-3b). The instability associated with the high reactivity and high interfacial area promotes undesired interfacial reactions in several nanohybrids. The catalytic performances of such hybrid materials were significantly influenced by metal-oxide interactions (Costi, Saunders and Banin 2010). In 1987, Haruta et al.(Zeng and Sun 2008) were the first to report the surprising catalytic activities of nanosized Au clusters deposited on oxide supports for low-temperature CO oxidation. Stanger et al.(Armelao et al. 2009) illustrated that the Ag/TiO_2 nanohybirds exhibited the photocatalytic activity enhancement with respect to pure TiO_2 (Figure 2-3c,d). As seen from the examples above, a reduction in particle size affect and shape control could affect almost all possible properties of a material and may lead to completely new and fundamental phenomena not seen in the bulk. Consequently, over the past few years there has been intense investigation into the synthetic control of nanocrystal morphology. We will discuss some of the methods that have been developed, particularly with regard to metal oxides, mixed oxide, hybrid metal-oxides, for which shape has a clear impact on their optical, magnetic, and catalytic properties.

References

Armelao, L., D. Barreca, G. Bottaro, A. Gasparotto, C. Maccato, E. Tondello, O. I. Lebedev, S. Turner, G. Van Tendeloo, C. Sada & U. L. Štangar (2009) Rational Design of Ag/TiO_2 Nanosystems by a Combined RF-Sputtering/Sol-Gel Approach. *ChemPhysChem,* 10, 3249-3259.

Bruchez, M., M. Moronne, P. Gin, S. Weiss & A. P. Alivisatos (1998) Semiconductor Nanocrystals as Fluorescent Biological Labels. *Science,* 281, 2013-2016.

Burda, C., X. Chen, R. Narayanan & M. A. El-Sayed (2005) Chemistry and Properties of Nanocrystals of Different Shapes. *Chemical Reviews,* 105, 1025-1102.

Chen, C., D. Chen, X. Jiao & S. Chen (2007) In2O3 Nanocrystals with a Tunable Size in the Range of 4−10 nm: One-Step Synthesis, Characterization, and Optical Properties. *The Journal of Physical Chemistry C,* 111**,** 18039-18043.

Costi, R., A. E. Saunders & U. Banin (2010) Colloidal Hybrid Nanostructures: A New Type of Functional Materials. *Angewandte Chemie International Edition,* 49**,** 4878-4897.

Guczi, L., G. Petö, A. Beck, K. Frey, O. Geszti, G. Molnár & C. Daróczi (2003) Gold Nanoparticles Deposited on SiO_2/Si(100): Correlation between Size, Electron Structure, and Activity in CO Oxidation. *Journal of the American Chemical Society,* 125**,** 4332-4337.

Jun, Y.-w., J.-s. Choi & J. Cheon (2006) Shape Control of Semiconductor and Metal Oxide Nanocrystals through Nonhydrolytic Colloidal Routes. *Angewandte Chemie International Edition,* 45**,** 3414-3439.

Klabunde, K. J., J. Stark, O. Koper, C. Mohs, D. G. Park, S. Decker, Y. Jiang, I. Lagadic & D. Zhang (1996) Nanocrystals as Stoichiometric Reagents with Unique Surface Chemistry. *The Journal of Physical Chemistry,* 100**,** 12142-12153.

Martin, T. P., T. Bergmann, H. Goehlich & T. Lange (1991) Shell structure of clusters. *The Journal of Physical Chemistry,* 95**,** 6421-6429.

Skorodumova, N. V., S. I. Simak, B. I. Lundqvist, I. A. Abrikosov & B. Johansson (2002) Quantum Origin of the Oxygen Storage Capability of Ceria. *Physical Review Letters,* 89**,** 166601.

Skrabalak, S. E., L. Au, X. Li & Y. Xia (2007) Facile synthesis of Ag nanocubes and Au nanocages. *Nat. Protocols,* 2**,** 2182-2190.

Sorensen, C. M. 2009. *Particles as Molecules*. John Wiley & Sons, Inc.

Tian, N., Z.-Y. Zhou, S.-G. Sun, Y. Ding & Z. L. Wang (2007) Synthesis of Tetrahexahedral Platinum Nanocrystals with High-Index Facets and High Electro-Oxidation Activity. *Science,* 316**,** 732-735.

Zeng, H. & S. Sun (2008) Syntheses, Properties, and Potential Applications of Multicomponent Magnetic Nanoparticles. *Advanced Functional Materials,* 18**,** 391-400.

Zhou, K., X. Wang, X. Sun, Q. Peng & Y. Li (2005) Enhanced catalytic activity of ceria nanorods from well-defined reactive crystal planes. *Journal of Catalysis,* 229**,** 206-212.

2.2. Metal Oxide Nanocrystals

2.2.1. Introduction

Within the broad family of functional materials, metal oxides play a very important role in many scientific and technological areas . For decades they have been extensively investigated for their physiochemical properties and useful applications by solid-state chemists. Oxides including the transition metals and rare earths, display a very wide variety of complex structures and interesting properties. These metal elements are able to form a large diversity of oxide compounds, giving the inspiration for designing new materials. The crystal structures are often fabricate by the formation of the metal-oxygen bonds to produce simple rock salt or complex oxide with varying nearly ionic to covalent or metallic. The oxidic materials exhibit fascinating electronic and magnetic properties associating with the changes in electronic structure and bonding . Additionally, metal oxides having multivalent oxidation states have attracted much attention among specialists because they often exhibit superior catalytic reaction performance .

2.2.2. Types of metal oxide nanocrystals

2.2.2.1. Transition metal oxides

Transition metal oxides generally show ordered defect complexes or extended defects instead of isolated point defects (Rawls 1981). They also occur as shear structures or infinitely adaptive structures. Some structure types such as rock salt, spinel, rutile, cuprite, fluorite, and corundum type structures, play an important role in the identification of their complex structures (Corpuz and Richards 2010). A variety of transition metal oxides exhibits transformations from one crystal structure to another as the temperature or pressure is varied. The phase transformations of their crystal structure often undergo the changes of the atomic, electronic or spin configuration. Transition metal oxides include both localized and itinerant *d*-electron behavior (Thiel 1998). Typical examples of transition metal monoxides are MnO, CoO, and NiO, processing the rock salt structure. The cation *d* orbitals in the rock salt structure would be splitted into t_{2g} and e_g sets by the octahedral crystal field of the anions. While in transition metal monoxide, TiO and NiO ($3d^2$ and $3d^8$), the *d* levels would be partially filled; hence the simple band theory predicts them to be metallic. The prediction is true in the case of TiO and to some extent in the case of VO. Stoichiometric MnO, CoO, NiO are, however, all good insulators showing antiferromagnetism. The insulating nature of FeO can be understood by assuming that the t_{2g} subband is completely filled for the $3d^6$ configuration, but the insulating nature of MnO, CoO, NiO cannot be understood in terms of simple band theory (Baerends Evert, Gritsenko Oleg and van Leeuwen 1996).

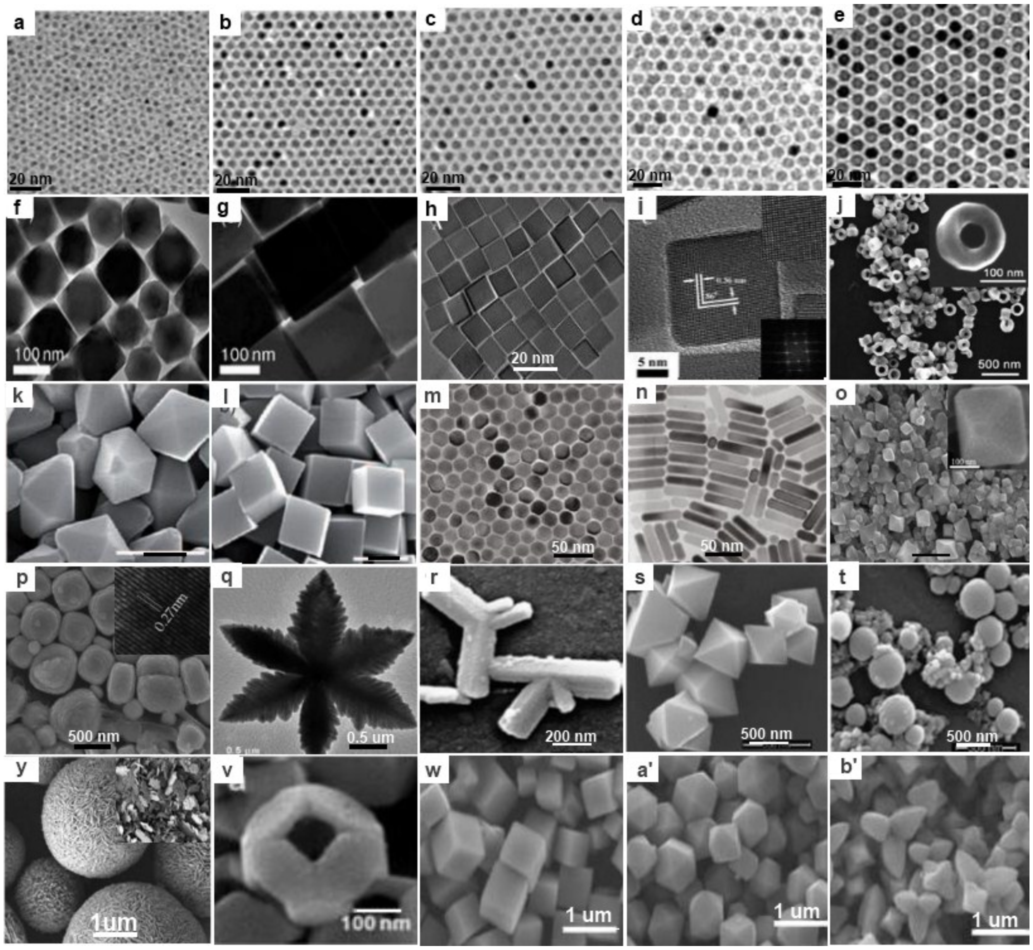

Figure 2.4. Gallery of representative TEM/HRTEM/SEM images of synthesized transition-metal oxide nanocrystals. Monodisperse iron oxide nanospheres with controlled particle sizes of (a) 6 nm, (b) 8 nm, (c) 10 nm, (d) 11 nm, (e) 13 nm(Park et al. 2005); (f) mixture of truncated cubic and truncated octahedral nanocrystals and (g) truncated nanocubes of Fe_3O_4 species (Park et al. 2005); (h,i) pseudocubic iron oxide nanocrystals, inset FFT pattern (Wang and Gao 2009); (j) single-crystalline α-Fe_2O_3 nanorings (Jia et al. 2008); single-crystalline iron oxide nanocrystals with (k) tetrakaidecahedron and (l) oblique parallelepiped shapes (Wang et al. 2010a); Mn_3O_4 nanocrystals with (m) spherical and (n) rod shapes and (o) $LiMn_2O_4$ nanocrystals (Wang et al. 2010c); (p) nest-like SnO nanostructures (Ning et al. 2009); (q) α-Fe_2O_3 nanosnowflakes, (r) Mn_2O_3 triangular nanorods, (s) CoO octahedral nanostructures, and (t) Cr_2O_3 nanospheres (Polshettiwar, Baruwati and Varma 2009); (y) hollow Cu_2O microspheres (Zhang et al. 2007a); (v) Cu_2O

hierarchical hollow microspheres; single-crystalline Cu_2O nanocrystals with (w) cubic, (a') truncated cubic, (b') extended hexapod shapes (Kuo and Huang 2008).

Transition metal oxide nanocrystals are particularly useful in various applications in magnetic field (Mahmoudi et al. 2010). The synthesis of well-defined magnetic nanocrystals is an important issue, because magnetic properties change drastically with particle size. Representative TEM/HRTEM//SEM examples of a variety of transition metal oxide nanocrystals are shown in Figure 2-4. The hot injection and heat-up processes are generally carried out in hot surfactant solutions and have been widely used to synthesize uniform nanocrystals. Iron carbonyl, acetate, acetylacetonate, carboxylate, and chloride are some of the commonly used precursors for making monodisperse iron oxide nanocrystals. For example, the thermal decomposition of $Fe(CO)_5$ in octyl ether in the presence of oleic acid or lauric acid resulted in the formation of essentially amorphous iron particles (Hyeon et al. 2001). Spherical α-Fe_2O_3 nanocrystals could also be directly generated with size ranging from 4 to 16 nm by introducing an oxidation agent, trimethylamine *N*-oxide or $(CH_3)_3NO$, into the reaction solution. Hyeon et al.(Park et al. 2005) revealed that monodisperse iron nanoparticles with different sizes of 4, 8, 11 nm were prepared by changing the molar $Fe(CO)_5$:oleic acid ratio from 1:1 to 1:2 and 1:3. In a next step, these seed nanocrystals were reacted with iron oleate solutions of defined concentrations, resulting in monodisperse iron nanocrystals that transform into iron oxide nanoparticles of 6, 7, 8, 9, 10, 11, 12, 13 nm on exposure to air (Figure 2-5a-e). Cheon et al.(Cheon et al. 2004) had achieved the thermal decomposition of $Fe(CO)_5$ in *o*-dichlorobenzene/dodecylamine to yield α-Fe_2O_3 nanocrystals with controlled different shapes, including diamonds (40%), triangle plates (30%), and spheres (30%). Zeng et al.(Sun and Zeng 2002) reported the synthesis of monodisperse magnetite nanoparticles from iron(III) acetylacetonate, $Fe(acac)_3$, using a high-temperature reaction. In this approach, 4 nm magnetite nanoparticles were formed by refluxing a reaction mixture composed of $Fe(acac)_3$, diphenyl ether, 1,2-hexadecanediol, oleic acid, and oleylamine. A seeded growth process was also demonstrated for generating large nanoparticles. By controlling the ratio of seed relative to the precursor, nanoparticles up to 16 nm in diameter were obtained. Using different precursors, including $Fe(acac)_3$, iron acetate, O'Brien et al.(Redl et al. 2004) had explored the thermal decomposition of iron pentacarbonyl in trioctylamine or octyl ether in the presence of oxidants such as pyridine *N*-oxide and trimethyl *N*-oxide hydrate to wüstite Fe_xO ($0.84 < x < 0.95$) nanocrystals.

Some recent progresses for the controlled synthesis of high-quality transition metal oxide nanocrystals were achieved. The representative examples of iron oxide nanocrystals are illustrated. Gao et al.(Wang and Gao 2009) reported the morphology-controlled synthesis and magnetic property of pseudocubic iron oxide nanoparticles using the mixture of iron(III) chloride/sodium oleate/oleic acid/ethanol. Lu et al.(Wang et al. 2010a) synthesized the single-crystalline iron oxide nanocrystals with tetrakaidecahedron and oblique parallelepiped shapes and high-index facets exposed in high yields through the solvothermal reaction of a mixture of $K_3[Fe(CN)_6]$, N_2H_4, sodium carboxymethyl cellulose at 160 ^{o}C for 6 h. Magnetic properties of these two kinds of nanocrystals displayed shape-dependent magnetic behaviors. Raabe et al.(Jia et al. 2008) presented a novel approach for synthesizing single-crystalline α-Fe_2O_3 nanorings with outer diameters of 150-170 nm, inner diameters of 70-100 nm, and heights of 80-120 nm, employing a double anion-assisted hydrothermal treatment of the aqueous solution of $FeCl_3$, $NH_4H_2PO_4$, Na_2SO_4 at 220 °C for 48 h. Gao et al.(Wang and Gao 2009) have prepared α-Fe_2O_3 nanoparticles enclosed by six (Burda et al.) of planes, in which the uniformity of morphology should be further improved. Yan et al.(Jia et al. 2005a) reported on the synthesis of single-crystalline α-Fe_2O_3 nanotubes through a coordination assisted dissolution process involving the selective adsorption of phosphate ions on hematite. Zeng et al.(Xu and Zeng 2004) synthesized Co_3O_4 nanocubes smaller than 10 nm and their superstructures by adding capping agent Tween-85 into their reaction system.

Considerable effort has been devoted to the development of alternative energy storage/conversion devices with high power and energy densities because of the up-coming depletion of fossil fuels. Recent progress has been devoted to synthesis and electrochemical applications for oxide nanomaterials. For example, the solvothermal reaction of $Mn(NO_3)_2$/oleylamine/dodecanol recently flourished by Li et al.(Wang et al. 2010c) was a successful way for shape control of highly monodisperse Mn_3O_4 nanocrystals with dot, rod, wire shapes. Moreover, the as-prepared hydrophobic spherical or elongated nanoparticles were used as building blocks to be rationally assembled into three-dimensional (3D) Mn_3O_4 colloidal spheres with a facile ultrasonication route. The as-prepared colloidal spheres were chemically converted to $LiMn_2O_4$ nanomaterials in a simple solid-state reaction. Such materials showed distinct electrochemical performance, mainly depending on their crystallinity and particle size. Dai et al.(Wang et al. 2010d) reported a two-step solution-phase method for growing Mn_3O_4 nanoparticles on graphene oxide to form a Mn_3O_4-reduced graphene oxide hybrid material. The grown of Mn_3O_4 nanoparticles on graphene oxide sheets includes two steps: (i) hydrolysis of $Mn(CH_3COO)_2$ in a graphene oxide suspension with a 10:1 *N*,*N*-dimethylformamide (DMF)/H_2O mixed solvent at 80 °C, (ii) distribution of well-crystallized Mn_3O_4 nanoparticles on graphene oxide sheets by transferring the above reaction solution to deionized water and treated in hydrothermal conditions at 180 °C for 10 h. The gas-liquid interfacial route was used to synthesize water-soluble Fe_3O_4 nanoparticles in iron nitrate, ethylene glycol (EG) and ammonia solution. The Fe_3O_4 nanoparticles could be incorporated into a carbon matrix under the hydrothermal method and such materials exhibited excellent anode materials for high-performance Li^+-ion batteries (Cui et al. 2009b). The vanadium pentoxide (V_2O_5) has been attracting much attention in low-cost energy battery because it can serve as the anode in Li ion battery design or as the cathode material in rechargeable Li ion batteries.

2.2.2.2. Rare earth oxides

The chemically similar fourteen elements in the bottom of periodic table ranging in atomic number from 57 to 71 are known as the lanthanoids that have in common an open 4*f* shell. The lanthanides are sometimes referred to as the “rare earths” which originates from the isolation of these elements early in their discovery (Greinacher 1981). The lanthanide ions are trivalent and their physiochemical properties principally originate from the trivalent ions which are important rather than those of the neutral atoms. A series of lanthanide thus possesses many similar chemical and physical properties to the other members of the lanthanoid group. It is noted that lanthanum should be considered a member of the lanthanide family as it lacks *f*-electrons (LeROY and Holmberg 1963). The

Group III transition metals Sc and Y are also frequently included in discussions about the lanthanides due to having many similar properties to the lanthanide family of elements. The electron configuration of the lanthanides range from [Xe] $6s^2 5d^1$ for lanthanum (La) to [Xe] $6s^2 4f^{14} 5d^1$ for lutetium (Lu). The 4f orbitals lie well inside the electronic shell and are well protected from external influences by the filled $6s$ and $5p$ orbitals. Although the trend is observed from the atomic radii, it is best shown by the radii of the trivalent cations. A consequence of the lanthanide contraction is that holmium (Ho^{3+}) is the same size as the much lighter Y^{3+} with corresponding similar properties. The majority of the optical properties of the lanthanide ions can also be attributed to the shielded nature of the $4f$ orbitals (Moeller 1967).

Recently, high-quality rare-earth nanocrystals have drawn great attention because of their unique physical and chemical properties and potential applications in the fields of catalysis, luminescence devices, optical transmission, biochemical probes, medical diagnostics, and so forth (Shen, Sun and Yan 2008, Zhang et al. 2010a). The different synthetic routes have been developed to a number of size- and shape-controlled dispersible rare earth oxide nanocrystals. Representative TEM//HRTEM/SEM examples of a variety of rare earth oxide nanocrystals are shown in Figure 2-5. Yan et al.(Si et al. 2005) synthesized the single-crystalline and monodisperse cubic rare-earth (RE = La to Lu, Y) oxide nanocrystals with plate and disk shapes via a nonhydrolytic approach in oleic acid/oleylamine/1-octadecene using various rare-earth complexes, including acetylacetonate, benzoylacetonate, and acetate, as the precursors. The selective adsorption of coordinating oleic acid ligands onto specific crystal planes of cubic RE_2O_3 nanocrystals made them adopt a plate shape with the confined growth of facets and/or a disk shape with the confined growth of facets. The as-prepared high-quality luminescent Y_2O_3:Eu ultrathin nanodisks displayed strong surface-dependent, highly pure red emissions that were due to selective incorporation of Eu^{3+} ions in the surface of the nanodisks (Si et al. 2006). The hydrolysis of metal nitrates in octadecylamine to generate the rare earth (Ce) and transition (Ni, Zn, Co) oxide nanocrystals was achieved by Li et al.(Wang et al. 2008a). Subsequently, calcination was carried out to remove the surfactants to produce mesoporous metal oxides by surfactant-assisted self-assembly process, which showed large pores, thermally stable pore mesostructures, and potential applications in catalysis and lithium-ion batteries. By thermolysis of rare-earth benzoylacetonate complexes in oleic acid/oleylamine, Xu et al.(Zhang et al. 2007d) synthesized the Y_2O_3:Tb nanorods were obtained by self-assembly of long-chain alkyl amine-capped nanocrystals prepared from thermolysis of yttrium-oleate complexes.

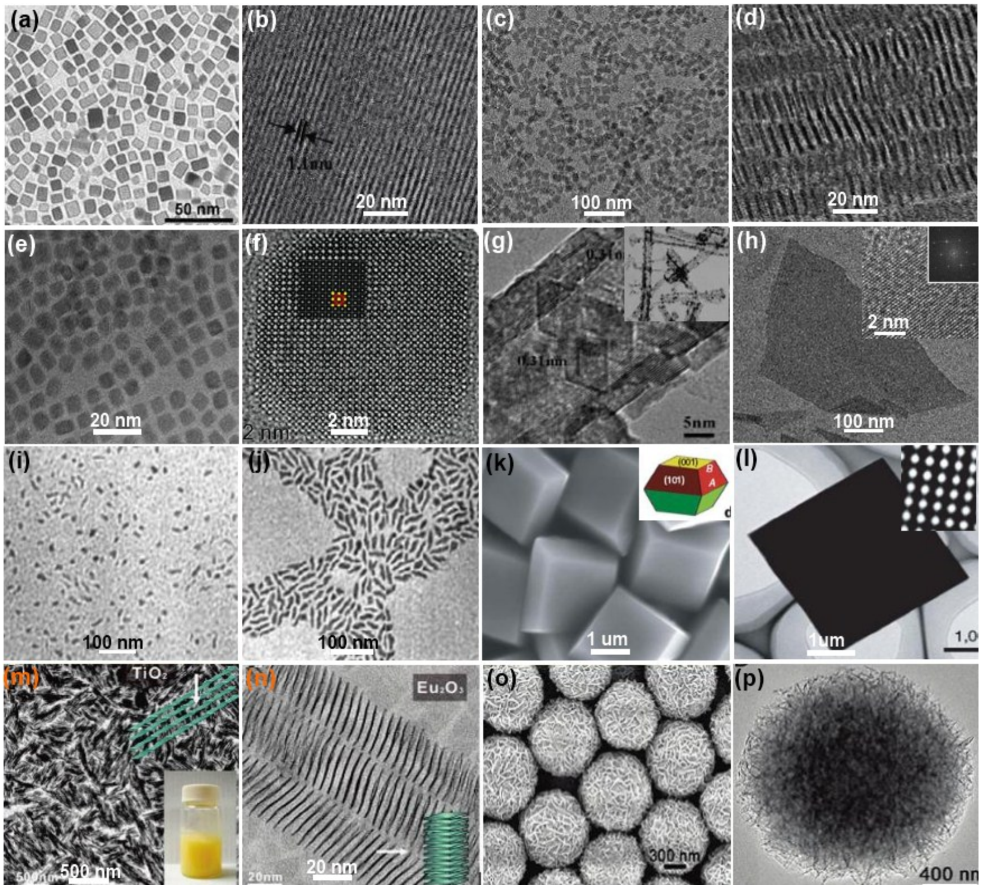

Figure 2.5. Gallery of representative TEM/HRTEM/SEM images of transition-metal oxide nanocrystals: (a) CeO_2 nanocubes (Wang et al. 2008a); Sm_2O_3 with (b) wire, (c) square, (d) plate shapes (Yu et al. 2006); (e,f) CeO_2 nanocubes (Yang and Gao 2006); (g) CeO_2 nanotubes (Zhou, Yang and Yang 2007); (h) CeO_2 nanosheets (Yu, Lim and Xia 2010); (i,j) ZrO_2 nanorices (Zhao et al. 2006); (k,l) single-crystalline truncated TiO_2 nanocrystals (Yang et al. 2008); (m) TiO_2 rod-shaped superstructures, inset of an image of the as-prepared gel-like product; (n) Eu_2O_3 nanodisks (Huo et al. 2009); (o,p) TiO_2 microspheres (Chen et al. 2010a).

Gao et al.(Yang and Gao 2006) reported the shape- and size-controlled synthesis of uniform CeO_2 nanocubes by reaction of cerium nitrate aqueous solution and *tert*-butylamine in toluene/oleic acid at 180 °C via a solvo-hydrothermal two-phase process. Adschiri et al.(Zhang et al. 2007b) modified this reaction system for the synthesis of CeO_2 nanocubes using cerium hydroxide precursors under supercritical water conditions. The product shape could be controlled by tuning the interaction of organic molecules with various crystallographic planes of fluorite cubic ceria. The morphology and displayed crystallite plane of CeO_2 nanocrystals could be controlled by the length of dicarboxylic acids (Taguchi et al. 2009). The ceria nanocrystals with spherical, wire, and tadpole shapes were controllably fabricated via a nonhydrolytic sol-gel process using oleic acid and oleylamine as cosurfactant (Yu et al. 2005b). Very recently, Si et al.(Du et al. 2007b) synthesized ceria nanocrystals via an alcohothermal process at 180 °C in ethanol, using alkylamine as the base and polyvinylpyrrolidone as the stabilizer, and furthermore, the ceria nanocrystals were self-organized into chainlike and dendritic nanostructures by oriented attachment. Xia el al.(Yu et al. 2010) recently synthesized the CeO_2 nanosheets with lateral dimensions up to 4 μm and thickness of ~2.2 nm by the heating of the aqueous cerium nitrate solution in the presence of 6-aminohexanoic acid ligand. Yan et al.(Zhou et al. 2008) reported a rapid thermolysis of $(NH_4)_2Ce(NO_3)_6$ in oleic acid/oleylamine to generate the CeO_2 nanoflowers from the aggregation of tiny particle by a unique 3D oriented-attachment mechanism due to a well-maintained balance of the nucleation and growth stages. The CO catalytic performance of CeO_2 nanocatalysts with different shapes were illustrated. For CO conversion to CO_2 from 200 to 400 ^{o}C, the activity of the catalysts followed the trend of nanoflowers > nanopolyhedra > nanocubes, in good agreement with the order of the specific surface areas. This result indicated that the flower-shaped catalyst with higher specific surface area could provide more active sites for CO conversion.

Pure ZrO_2 can exist in three polymorphs at atmospheric pressure, e.g., monoclinic (*m*, between room temperature and 1170 °C), tetragonal (*t*, between 1170 and 2370 °C), and cubic (*c*, between 2370 and 2706 °C) phases (Srinivasan et al. 1993, Rashad and Baioumy 2008). Tang et al.(Tang et al. 2008) reported one-step controllable synthesis for ultrafine ZrO_2 nanocrystals via a two-phase interface hydrolysis reaction under hydrothermal conditions. The coexisting *m*- and *t*-ZrO_2 nanocrystals can be found under this condition. Zhao et al.(Zhao et al. 2006) reported the mixed *m*- and *t*-ZrO_2 nanocrystals synthesized via a two-phase approach. Lin et al.(Lin, Zhang and Lin 2007) reported the mixed *m*- and *t*-ZrO_2 nanocrystals synthesized via the pechini-type sol-gel process. Becker et al.(Becker et al. 2008, Zheng et al. 2009) reported mixed *m*- and *t*-ZrO_2 nanocrystals synthesized in near- and supercritical water and supercritical isopropyl alcohol. The phase stability of nanocrystalline ZrO_2 depends upon the size, e.g., the critical size is 10 nm. The tetragonal ZrO_2 and monoclinic ZrO_2 can coexist between 11 and 30 nm, while pure monoclinic ZrO_2 is stable with the size above approximately 30 nm. Becker et al.(Bremholm, Becker-Christensen and Iversen 2009) regarded that the critical particle size stems from the difference in the surface energy of the two ZrO_2 polymorphs, with *t*-ZrO_2 being lowest. The structure of nanomaterials surfaces contributes significantly to the energetic character of nanomaterials. The nonhydrolytic sol-gel reaction between zirconium(IV) isopropoxide and zirconium(IV) chloride at 340 °C to generate large quantities of highly monodisperse tetragonal zirconia nanocrystals (~4 nm) were performed by Hyeon et al.(Joo et al. 2003).

In this dissertation, we have studied on the synthesis and characterization of a series of colloidal transition-metal (V, Cr, Co, Mn, Ni, In) and rare earth (La, Ce, Y, Zr, Ti, Sm, Gd, Er) oxide nanocrystals. The different size and shape of these metal oxide nanocrystals could be controlled by simple adjusting of the synthesis conditions.

References

Baerends Evert, J., V. Gritsenko Oleg & R. van Leeuwen. 1996. Effective One-Electron Potential in the Molecular Orbital Theory. In *Chemical Applications of Density-Functional Theory*, 20-41. American Chemical Society.

Becker, J., P. Hald, M. Bremholm, J. S. Pedersen, J. Chevallier, S. B. Iversen & B. B. Iversen (2008) Critical Size of Crystalline ZrO_2 Nanoparticles Synthesized in Near- and Supercritical Water and Supercritical Isopropyl Alcohol. *ACS Nano,* 2**,** 1058-1068.

Bremholm, M., J. Becker-Christensen & B. B. Iversen (2009) High-Pressure, High-Temperature Formation of Phase-Pure Monoclinic Zirconia Nanocrystals Studied by Time-Resolved in situ Synchrotron X-Ray Diffraction. *Advanced Materials,* 21**,** 3572-3575.

Burda, C., X. Chen, R. Narayanan & M. A. El-Sayed (2005) Chemistry and Properties of Nanocrystals of Different Shapes. *Chemical Reviews,* 105**,** 1025-1102.

Chen, J. S., Y. L. Tan, C. M. Li, Y. L. Cheah, D. Luan, S. Madhavi, F. Y. C. Boey, L. A. Archer & X. W. Lou (2010) Constructing Hierarchical Spheres from Large Ultrathin Anatase TiO_2 Nanosheets with Nearly 100% Exposed (001) Facets for Fast Reversible Lithium Storage. *Journal of the American Chemical Society,* 132**,** 6124-6130.

Cheon, J., N.-J. Kang, S.-M. Lee, J.-H. Lee, J.-H. Yoon & S. J. Oh (2004) Shape Evolution of Single-Crystalline Iron Oxide Nanocrystals. *Journal of the American Chemical Society,* 126**,** 1950-1951.

Corpuz, A. & R. Richards. 2010. Chemistry of Rocksalt-Structured (111) Metal Oxides. In *Nanoscale Materials in Chemistry: Environmental Applications*, 51-76. American Chemical Society.

Cui, Z.-M., L.-Y. Jiang, W.-G. Song & Y.-G. Guo (2009) High-Yield Gas−Liquid Interfacial Synthesis of Highly Dispersed Fe_3O_4 Nanocrystals and Their Application in Lithium-Ion Batteries. *Chemistry of Materials,* 21**,** 1162-1166.

Du, N., H. Zhang, B. Chen, X. Ma & D. Yang (2007) Ligand-free Self-Assembly of Ceria Nanocrystals into Nanorods by Oriented Attachment at Low Temperature. *The Journal of Physical Chemistry C,* 111**,** 12677-12680.

Greinacher, E. 1981. History of Rare Earth Applications, Rare Earth Market Today. In *Industrial Applications of Rare Earth Elements*, 3-17. AMERICAN CHEMICAL SOCIETY.

Huo, Z., C.-K. Tsung, W. Huang, M. Fardy, R. Yan, X. Zhang, Y. Li & P. Yang (2009) Self-Organized Ultrathin Oxide Nanocrystals. *Nano Letters,* 9**,** 1260-1264.

Hyeon, T., S. S. Lee, J. Park, Y. Chung & H. B. Na (2001) Synthesis of Highly Crystalline and Monodisperse Maghemite Nanocrystallites without a Size-Selection Process. *Journal of the American Chemical Society,* 123**,** 12798-12801.

Jia, C.-J., L.-D. Sun, F. Luo, X.-D. Han, L. J. Heyderman, Z.-G. Yan, C.-H. Yan, K. Zheng, Z. Zhang, M. Takano, N. Hayashi, M. Eltschka, M. Kläui, U. Rüdiger, T. Kasama, L. Cervera-Gontard, R. E. Dunin-Borkowski, G. Tzvetkov & J. r. Raabe (2008) Large-Scale Synthesis of Single-Crystalline Iron Oxide Magnetic Nanorings. *Journal of the American Chemical Society,* 130**,** 16968-16977.

Jia, C.-J., L.-D. Sun, Z.-G. Yan, L.-P. You, F. Luo, X.-D. Han, Y.-C. Pang, Z. Zhang & C.-H. Yan (2005) Single-Crystalline Iron Oxide Nanotubes. *Angewandte Chemie International Edition,* 44**,** 4328-4333.

Joo, J., T. Yu, Y. W. Kim, H. M. Park, F. Wu, J. Z. Zhang & T. Hyeon (2003) Multigram Scale Synthesis and Characterization of Monodisperse Tetragonal Zirconia Nanocrystals. *Journal of the American Chemical Society,* 125**,** 6553-6557.

Kuo, C.-H. & M. H. Huang (2008) Facile Synthesis of Cu2O Nanocrystals with Systematic Shape Evolution from Cubic to Octahedral Structures. *The Journal of Physical Chemistry C,* 112**,** 18355-18360.

LeROY, E. & B. O. Holmberg. 1963. Ordered Phases and Nonstoichiometry in the Rare Earth Oxide System. In *Nonstoichiometric Compounds*, 46-57. AMERICAN CHEMICAL SOCIETY.

Lin, C., C. Zhang & J. Lin (2007) Phase Transformation and Photoluminescence Properties of Nanocrystalline ZrO_2 Powders Prepared via the Pechini-type Sol−Gel Process. *The Journal of Physical Chemistry C,* 111**,** 3300-3307.

Mahmoudi, M., H. Hosseinkhani, M. Hosseinkhani, S. Boutry, A. Simchi, W. S. Journeay, K. Subramani & S. Laurent (2010) Magnetic Resonance Imaging Tracking of Stem Cells in Vivo Using Iron Oxide Nanoparticles as a Tool for the Advancement of Clinical Regenerative Medicine. *Chemical Reviews***,** null-null.

Moeller, T. 1967. Coordination Chemistry of the Lanthanide Elements? One Hundred Years of Development and Understanding. In *Werner Centennial*, 306-317. AMERICAN CHEMICAL SOCIETY.

Ning, J., T. Jiang, K. Men, Q. Dai, D. Li, Y. Wei, B. Liu, G. Chen, B. Zou & G. Zou (2009) Syntheses, Characterizations, and Applications in Lithium Ion Batteries of Hierarchical SnO Nanocrystals. *The Journal of Physical Chemistry C,* 113**,** 14140-14144.

Park, J., E. Lee, N.-M. Hwang, M. Kang, S. C. Kim, Y. Hwang, J.-G. Park, H.-J. Noh, J.-Y. Kim, J.-H. Park & T. Hyeon (2005) One-Nanometer-Scale Size-Controlled Synthesis of Monodisperse Magnetic Iron Oxide Nanoparticles. *Angewandte Chemie,* 117**,** 2932-2937.

Polshettiwar, V., B. Baruwati & R. S. Varma (2009) Self-Assembly of Metal Oxides into Three-Dimensional Nanostructures: Synthesis and Application in Catalysis. *ACS Nano,* 3**,** 728-736.

Rashad, M. M. & H. M. Baioumy (2008) Effect of thermal treatment on the crystal structure and morphology of zirconia nanopowders produced by three different routes. *Journal of Materials Processing Technology,* 195**,** 178-185.

Rawls, R. (1981) Inorganic chemistry. *Chemical & Engineering News,* 59**,** 42-43.

Redl, F. X., C. T. Black, G. C. Papaefthymiou, R. L. Sandstrom, M. Yin, H. Zeng, C. B. Murray & S. P. O'Brien (2004) Magnetic, Electronic, and Structural Characterization of Nonstoichiometric Iron Oxides at the Nanoscale. *Journal of the American Chemical Society,* 126**,** 14583-14599.

Shen, J., L.-D. Sun & C.-H. Yan (2008) Luminescent rare earth nanomaterials for bioprobe applications. *Dalton Transactions***,** 5687-5697.

Si, R., Y.-W. Zhang, L.-P. You & C.-H. Yan (2005) Rare-Earth Oxide Nanopolyhedra, Nanoplates, and Nanodisks. *Angewandte Chemie International Edition,* 44**,** 3256-3260.

Si, R., Y.-W. Zhang, H.-P. Zhou, L.-D. Sun & C.-H. Yan (2006) Controlled-Synthesis, Self-Assembly Behavior, and Surface-Dependent Optical Properties of High-Quality Rare-Earth Oxide Nanocrystals. *Chemistry of Materials,* 19**,** 18-27.

Srinivasan, R., C. R. Hubbard, O. B. Cavin & B. H. Davis (1993) Factors determining the crystal phases of zirconia powders: a new outlook. *Chemistry of Materials,* 5**,** 27-31.

Sun, S. & H. Zeng (2002) Size-Controlled Synthesis of Magnetite Nanoparticles. *Journal of the American Chemical Society,* 124**,** 8204-8205.

Taguchi, M., S. Takami, T. Naka & T. Adschiri (2009) Growth Mechanism and Surface Chemical Characteristics of Dicarboxylic Acid-Modified CeO_2 Nanocrystals Produced in Supercritical Water: Tailor-Made Water-Soluble CeO_2 Nanocrystals. *Crystal Growth & Design,* 9**,** 5297-5303.

Tang, K., J. Zhang, W. Yan, Z. Li, Y. Wang, W. Yang, Z. Xie, T. Sun & H. Fuchs (2008) One-Step Controllable Synthesis for High-Quality Ultrafine Metal Oxide Semiconductor Nanocrystals via a Separated Two-Phase Hydrolysis Reaction. *Journal of the American Chemical Society,* 130**,** 2676-2680.

Thiel, W. 1998. Thermochemistry from Semiempirical Molecular Orbital Theory. In *Computational Thermochemistry*, 142-161. American Chemical Society.

Wang, C., H. Yin, S. Dai & S. Sun (2010a) A General Approach to Noble Metal–Metal Oxide Dumbbell Nanoparticles and Their Catalytic Application for CO Oxidation. *Chemistry of Materials,* 22**,** 3277-3282.

Wang, C., H. Zhang, F. Li & L. Zhu (2010b) Degradation and Mineralization of Bisphenol A by Mesoporous Bi_2WO_6 under Simulated Solar Light Irradiation. *Environmental Science & Technology,* 44**,** 6843-6848.

Wang, D.-S., T. Xie, Q. Peng, S.-Y. Zhang, J. Chen & Y.-D. Li (2008) Direct Thermal Decomposition of Metal Nitrates in Octadecylamine to Metal Oxide Nanocrystals. *Chemistry – A European Journal,* 14**,** 2507-2513.

Wang, H., L.-F. Cui, Y. Yang, H. Sanchez Casalongue, J. T. Robinson, Y. Liang, Y. Cui & H. Dai (2010c) Mn_3O_4–Graphene Hybrid as a High-Capacity Anode Material for Lithium Ion Batteries. *Journal of the American Chemical Society,* 132**,** 13978-13980.

Wang, L. & L. Gao (2009) Morphology-Controlled Synthesis and Magnetic Property of Pseudocubic Iron Oxide Nanoparticles. *The Journal of Physical Chemistry C,* 113**,** 15914-15920.

Xu, R. & H. C. Zeng (2004) Self-Generation of Tiered Surfactant Superstructures for One-Pot Synthesis of Co_3O_4 Nanocubes and Their Close- and Non-Close-Packed Organizations. *Langmuir,* 20**,** 9780-9790.

Yang, H. G., C. H. Sun, S. Z. Qiao, J. Zou, G. Liu, S. C. Smith, H. M. Cheng & G. Q. Lu (2008) Anatase TiO_2 single crystals with a large percentage of reactive facets. *Nature,* 453**,** 638-641.

Yang, S. & L. Gao (2006) Controlled Synthesis and Self-Assembly of CeO_2 Nanocubes. *Journal of the American Chemical Society,* 128**,** 9330-9331.

Yu, T., J. Joo, Y. I. Park & T. Hyeon (2005) Large-Scale Nonhydrolytic Sol–Gel Synthesis of Uniform-Sized Ceria Nanocrystals with Spherical, Wire, and Tadpole Shapes. *Angewandte Chemie,* 117**,** 7577-7580.

Yu, T., B. Lim & Y. Xia (2010) Aqueous-Phase Synthesis of Single-Crystal Ceria Nanosheets. *Angewandte Chemie International Edition,* 49**,** 4484-4487.

Zhang, C., L. Sun, Y. Zhang & C. Yan (2010) Rare earth upconversion nanophosphors: synthesis, functionalization and application as biolabels and energy transfer donors. *Journal of Rare Earths,* 28**,** 807-819.

Zhang, H., Q. Zhu, Y. Zhang, Y. Wang, L. Zhao & B. Yu (2007a) One-Pot Synthesis and Hierarchical Assembly of Hollow Cu_2O Microspheres with Nanocrystals-Composed Porous Multishell and Their Gas-Sensing Properties. *Advanced Functional Materials,* 17**,** 2766-2771.

Zhang, J., S. Ohara, M. Umetsu, T. Naka, Y. Hatakeyama & T. Adschiri (2007b) Colloidal Ceria Nanocrystals: A Tailor-Made Crystal Morphology in Supercritical Water. *Advanced Materials,* 19**,** 203-206.

Zhang, Y., J. Guo, T. White, T. T. Y. Tan & R. Xu (2007c) Y_2O_3:Tb Nanocrystals Self-Assembly into Nanorods by Oriented Attachment Mechanism. *The Journal of Physical Chemistry C,* 111**,** 7893-7897.

Zhao, N., D. Pan, W. Nie & X. Ji (2006) Two-Phase Synthesis of Shape-Controlled Colloidal Zirconia Nanocrystals and Their Characterization. *Journal of the American Chemical Society,* 128**,** 10118-10124.

Zheng, H., K. Liu, H. Cao & X. Zhang (2009) l-Lysine-Assisted Synthesis of ZrO_2 Nanocrystals and Their Application in Photocatalysis. *The Journal of Physical Chemistry C,* 113**,** 18259-18263.

Zhou, H.-P., Y.-W. Zhang, H.-X. Mai, X. Sun, Q. Liu, W.-G. Song & C.-H. Yan (2008) Spontaneous Organization of Uniform CeO_2 Nanoflowers by 3D Oriented Attachment in Hot Surfactant Solutions Monitored with an In Situ Electrical Conductance Technique. *Chemistry – A European Journal,* 14**,** 3380-3390.

Zhou, K., Z. Yang & S. Yang (2007) Highly Reducible CeO_2 Nanotubes. *Chemistry of Materials,* 19**,** 1215-1217.

2.3. Mixed Metal Oxide Nanocrystals

2.3.1. Introduction

Over the past decades, nanostructured mixed metal oxide materials have been the focus of intense research to chemists and material scientists because of their important applications in catalysis, magnetic and optical devices, microelectronic circuits, biomedicines, ect (Mao, Park and Wong 2005). They are generally the result of high temperature synthesis and consist exclusively of metal cations and oxygen anions. With respect to single-metal oxides, the chemical behavior of mixed-metal oxides can be different as a consequence of several following factors. The appropriate combination of different individual components in a nanoscale mixed oxide system can produce new materials with structural or electronic synergetic properties that can lead to superior catalytic activity or high selectivity (Wachs 2005). In some situations, the cations in a mixed-metal oxide system can work in a cooperative way catalyzing different steps of a chemical process. At a structural level, a dopant can introduce stress into the lattice of an oxide host, inducing in this way the formation of defects that have a high chemical activity. The lattice of the oxide host can impose on the dopant element non-typical coordination modes with a subsequent perturbation in the dopant chemical properties (Norris, Efros and Erwin 2008). Finally, metal $\leftrightarrow$ metal or metal $\leftrightarrow$ oxygen $\leftrightarrow$ metal interactions in mixed metal oxides can give a rise to electronic states not seen in single-metal oxides (Fu and Wagner 2007). These interactions directly effect on the electronic and chemical properties of mixed-metal oxides. In the following section, we presented the types of colloidal mixed metal oxide nanocrystals recently synthesized by various surfactant-assisted methods. The examples for the discussion of each synthetic pathway and corresponding formation mechanism as well as the structural and physiochemical properties and practical applications of shape-controlled nanomaterials are described briefly.

2.3.2. Types of mixed metal oxides

2.3.2.1. Metal vanadate, tungstate, molybdate compounds

Three typical types of mixed oxide materials, namely vanadate, tungstate, molybdate, have attracted much attention in the past decades due to their potential applications in various fields. For example, the metal tungstates are good photocatalysts for the degradation of organic compounds under UV light irradiation in order to purify wastewater from households and industries (Zhang et al. 2007b); rare earth molybdates are promising candidate in laser hosts and up-conversion lasing applications (Stevens et al. 1991). Rare earth vanadates are an active and selective catalysts for many organic reactions including oxidative dehydrogenation of alkanes/olefins (Downing et al. 1996). The metal vanadate/molybdate/tungstate nanocrystals are generally synthesized by wet chemical template or template free-assisted routes such as modified coprecipitation, reverse micelles, solvo-hydrothermal process, which are based on the liquid coprecipitation reaction between the metal nitrate or chloride and vanadate/molybdate/tungstate (Mao et al. 2005, Buissette et al. 2006, Feng et al. 2010). The reaction parameters, such as the pH values in the initial solution, precursor sources, capping agents, were responsible for crystal phase and shape of final products.

Representative TEM/SEM examples of a variety of metal orthovanadate nanocrystals can be found in Figure 2-6. The general synthetic routes have often been devoted to vanadate nanomaterials with remakably luminescence properties. For example, Li group (Liu and Li 2007) had developed a general oleic acid-assisted hydrothermal method for the synthesis of a series of colloidal rare earth orthovanadate nanocrystals through the hydrothermal reaction of metal nitrate, NaOH, NH_4VO_3, oleic acid, ethanol/water mixture. The morphologies of all products were mainly square sheetlike shape with average diameters of ~20-40 nm (Figure 2-6a). The products were formed by capping of oleic acid to Ln^{3+} first, then oleic acid attached rare earth ion (Ln^{3+}) reacted with VO_4^{3-} to form $LnVO_4$ nuclei at the water-oleic acid interface. This was followed by crystal growth until the nanocrystals were big enough to fall to the bottom of the vessel. Further Eu^{3+}-doped $LnVO_4$ nanocrystals emitted intense red light. The author also used this route to synthesize colloidal uniform rare earth floride nanocrystals (Li, Peng and Li 2009, Wang et al. 2006).

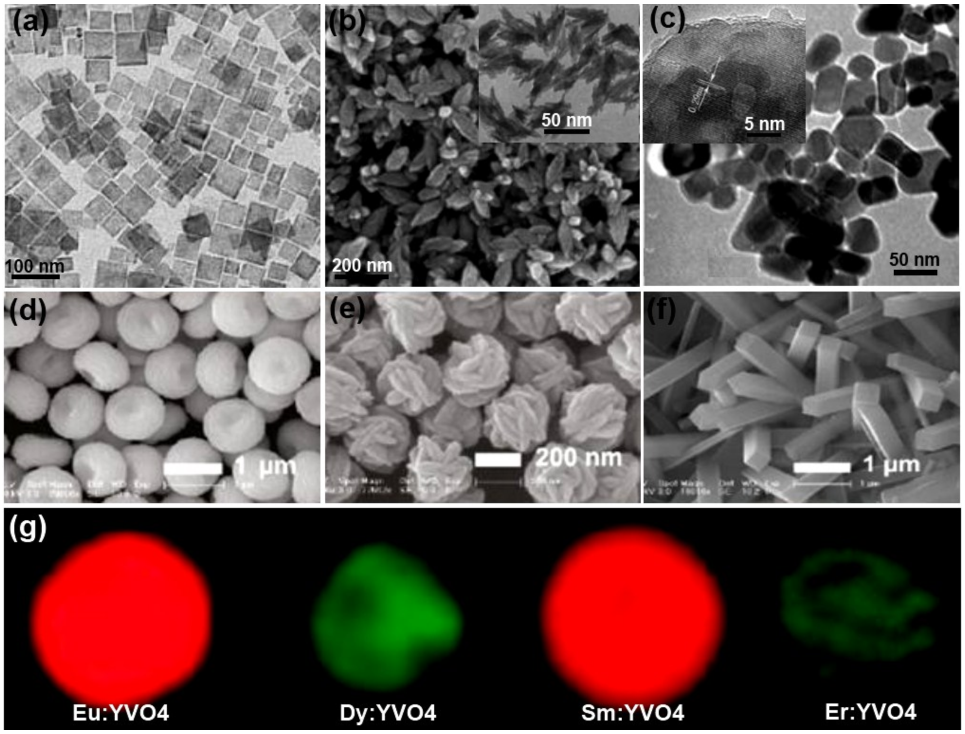

Figure 2.6. Gallery of representative TEM/HRTEM/SEM images illustrating examples of rare earth orthovanadate nanocrystals: (a) $LaVO_4$ nanosquares (Liu and Li 2007); (b) $LaVO_4$ spindle-shaped nanocrystals (Yu et al. 2008); (c) YVO_4:Er^{3+} tetragonal-like nanocrystals (Sun et al. 2006b); YVO_4 microcrystals with different shapes: (d) doughnut;

(e) flower; (f) cuboid rod; and (g) the insets are the luminescence photographs of the doped YVO_4 samples (Xu et al. 2010b).

An another general ultrasonic irradiation route for the lanthanide orthovanadate $LnVO_4$ (Ln = La-Lu) nanocrystals from the aqueous solution of $Ln(NO_3)_3$ and NH_4VO_3 without any surfactant were also reported by Lin et al. (Yu et al. 2008). The resultant $LnVO_4$ nanocrystals had spindle-like shape with the equatorial diameter of 30-70 nm and the length of 100-200 nm, which were the aggregates of small particles of 10-20 nm (Figure 2-6b). Furthermore, the Eu^{3+} and Dy^{3+}-doped $LnVO_4$ (Ln = La, Gd, Lu) samples showed the characteristic dominant emissions of Eu^{3+} at 613 nm and Dy^{3+} at 572 nm, respectively, as a result of an energy transfer from VO_4^{3-} to Eu^{3+} or Dy^{3+}. The author also synthesized and studied the luminescence properties of Ln^{3+} (Ln = Eu, Dy, Sm, Er)-doped YVO_4 nanocrystals via the trisodium citrate-assisted hydrothermal process (Figure 2-6d-g) (Xu et al. 2010b). Haase et al.(Sun et al. 2006b) also demonstrated an increase of visible emission intensity of Er^{3+}-doped YVO_4 nanocrystals resulting of photoadsorption and energy transfer of Er^{3+} ions to the host YVO_4 (Figure 2-7c).

Representative TEM/SEM examples of a variety of metal tungstate and molybdate nanocrystals are shown in Figure 2-7. The $MnWO_4$ materials would represent a typical class of tungstates with highly structure-sensitive multifunctionalities like humidity sensors or simultaneous coexistence of ferroelectricity, ferromagnetism, and ferroelasticity (Heyer and et al. 2006, Dellwo, Keller and Meyer 1997). $MnWO_4$ structures had been synthesized to show several morphologies such as flower-like clusters (Figure 2-7a,b), nanowires, nanoplates, and nanorods (Zhang et al. 2007a, Zhou et al. 2008b, Thongtem, Wannapop and Thongtem 2009, Chen et al. 2003, Zhou et al. 2008a). Additionally, kinetic control of $MnWO_4$ nanoparticle grown for tailored structural properties were studied by Li et al.(Tong et al. 2010). To extend on these tungstates, Wong et al.(Zhang et al. 2008) developed a room-temperature template-directed method for the synthesis of single-crystalline alkaline-earth-metal tungstate AWO_4 (A = Ca, Sr, Ba) nanorods with unique optoelectronic properties. The 2D self-organization of $BaWO_4$ nanorods at the water-air interface was performed on the basis of a Langmuir-Blodgett technique (Kim et al. 2001). By using the catanionic reversed micelle templating method, single-crystalline $BaWO_4$ nanorods with high-aspect-ratio were produced (Shi et al. 2003b). The penniform $BaWO_4$ nanostructures could be generated in reverse micellar system containing double-hydrophilic block copolymers (Shi et al. 2003a). Also using a microemulsion with solvothermal association, the $SrWO_4$ nanorods measuring 100 nm in diameter and 500-1500 nm in length were yielded (Sun et al. 2006a). Yu et al.(Zhang et al. 2007c) used the refluxing method to fabricate the uniform core-shell heterostructured $ZnWO_4$@MWO_4 (M = Mn, Fe) nanorods with optical and antiferromagnetic characters (Figure 2-7c,d). The directed crystallization of the MWO_4 nuclei happened on the backbone of $ZnWO_4$ nanorods without surfactant. The formation of the hybrid $ZnWO_4$@MWO_4 (M = Mn, Fe) nanorods was on the basis of the oriented aggregation. The shell thickness of MWO_4 could be tuned by changing the molar ratio of these raw materials.

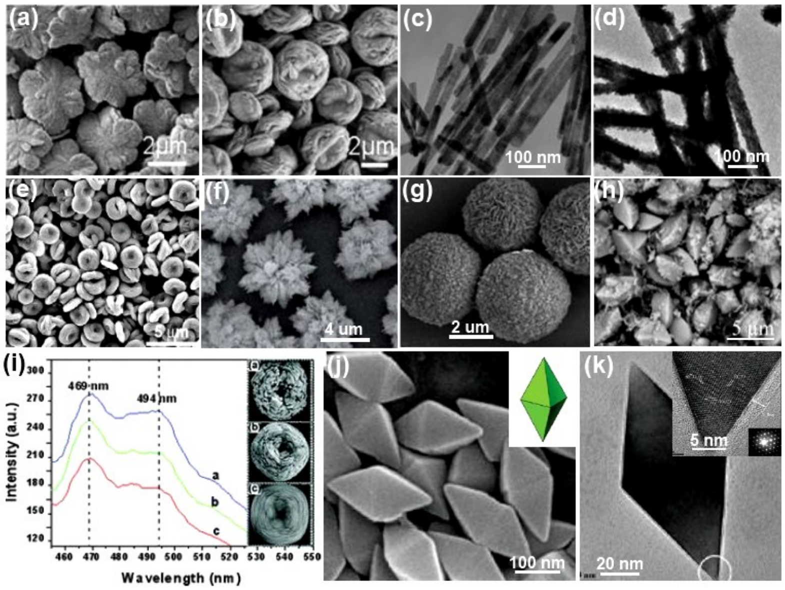

Figure 2.7. Gallery of representative TEM/HRTEM/SEM images illustrating examples of metal stungstate and molybdate nanocrystals: $FeWO_4$ nanocrystals of (a) platelike and (b) cookielike shapes (Zhou et al. 2008b); (c) $ZnWO_4$ nanorods and (d) hybrid $FeWO_4$@$ZnWO_4$ nanorods (Zhang et al. 2007c); (e) $CaMoO_4$ doughnut microstructures (Wang et al. 2009); hierarchical $La_2(MoO_4)_3$ microstructures with (f) flower and (g) sphere shape (Xu et al. 2010a); (h) $NaGd_{0.95}Yb_{0.05}(WO_4)_2$ microcrystals (Esteban-Betegón, Zaldo

and Cascales 2010); (i) photoluminescence spectra of $CaMoO_4$ nanoerythrocyte samples at different aging times: (a) 12 h, (b) 6 h, (c) 30 min (Luo et al. 2010); (j,k) $NaLa(MoO_4)_2$ tetragonal bipyramid-shaped nanocrystals (Bu et al. 2009).

The synthesis of metal molybdate nanomaterials has received great attention due to their interesting physical characteristics such as luminescence, reflectivity, and thermal properties. For example, the shape- and size-controlled synthesis of self-assemblied $CaMoO_4$ hierarchical doughnut-shaped microstructures were achieved by the reaction of Ca^{2+} and $Mo_7O_{24}^{6-}$ in the presence of sodium dodecyl sulfate surfactant at room temperature (Figure 2-7e) (Wang et al. 2009). $CaMoO_4$ flower-like mesocrystals were synthesized by a microemulsion-mediated route (Gong et al. 2006). The tetragonal scheelite-phase $CaMoO_4$ hierarchical erythrocyte-like nanostructures were synthesized in high-yield by the solvothermal reaction between Ca^{2+} and MoO_4^{2-} ions in a *N*,*N*-dimethylacetamide-H_2O system (Luo et al. 2010). Single uniform $CaMoO_4$ erythrocytes with quite rough surface had a diameter ranging from 4 to 5 mm and a thickness of about 1.5 mm that were made up of 15 nm nanoplatelets. The formation of erythrocyte-like $CaMoO_4$ hierarchical nanostructures might result from the crystal growth mechanism "oriented attachment" in terms of Ostwald ripening. The morphology, crystallization degree, configuration of the $CaMoO_4$ products all had effects on their luminescence properties. Recently, Xu et al.(Xu et al. 2010a) fabricated various self-assembled three-dimensional hierarchical architectures of $La_2(MoO_4)_3$ nanocrystals and studied the growth mechanisms, luminescence properties and adsorption activities (Figure 2-7f,g).

2.3.2.2. Rare earth doped lanthanum compounds

Rare-earth compounds have been an attractive subject due to their unique optical, magnetic, and catalytic properties (Buissette et al. 2006). The doped lanthanide nanomaterials improve reaction performance because of the presence of defects and oxygen vacancies in the lattice structures (Wang et al. 2010). These compounds have been widely used in various fields, such as high-performance luminescent devices, high-quality phosphors, up-conversion materials, catalysts, and so on. This behavior originates from their unique intra 4f transition with less influence by ligand field resulting in sharp emissions, due to shielding 4f orbitals by outer 5s and 5p orbitals. Representative TEM/SEM examples of a variety of lanthanum oxycarbonates nanostructures can be found in Figure 2-8.

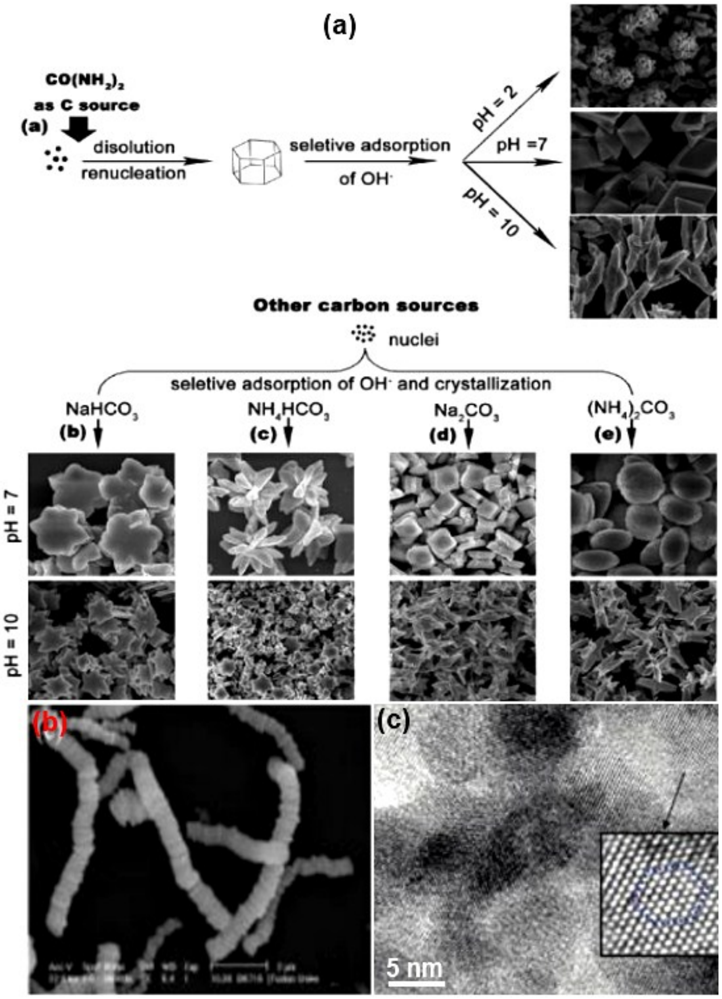

Figure 2.8. Gallery of representative SEM/HRTEM images of rare earth doped lanthanum compound nanocrystals: (a) schematic illustration for the formation process of $LaCO_3OH$ microcrystals with various morphologies using different carbon sources (Guerrero-Martínez, Pérez-Juste and Liz-Marzán 2010); (b) self-assemblied $La(OH)CO_3$ nanodisks (Xie et al. 2009); (c) nanostructured ceria-lanthana solid-solution (Dinh et al. 2009).

Remarkably, lanthanum oxycarbonates ($LaCO_3OH$) with hexagonal structure are suitable for the host materials of phosphors because they have a high chemical stability against both water and carbon dioxide. Recently, nanostructured undoped and doped lanthanide compounds and their derived mixed oxides have been synthesized. Xie et al.(Xie et al. 2009) fabricated the 1D layer-by-layer hexagonal-phased La(OH)CO_3 hierarchical nanomaterials with a diameter of ~700 nm and lengths in the range of 6-8 µm from the self-assembly of the single La(OH)CO_3 nanoplates via the hydrothermal reaction of bulk La_2O_3 powders with NH_2CH_2COOH molecules (Figure 2-8b). Under the thermal procedure, the obtained 1D La(OH)CO_3 nanostructures could be converted to porous $La(OH)_3$ and La_2O_3 nanorods. The La(OH)CO_3 was first transformed into La_2O_3 through calcination at 900 ^{o}C and then further change into hexagonal-phased $La(OH)_3$ by a hydrolysis process. The dopant ion obviously plays a crucial role in modifying the interesting optical properties of the produced mixed oxides.

The orthorhombic-phase Eu^{3+}/Tb^{3+} doped La_2OCO_3/La_2O_3 nano/microcrystals with multiform morphologies were synthesized via a homogeneous precipitation (Guerrero-Martínez et al. 2010). The multiform $LaCO_3OH$ products such as flakes, flowers, rhombuses, two-double hexagrams, sandwichlike spindles, peach-nucleus-shaped nanocrystals obtained by changes of the carbon sources [$CO(NH_2)_2$, Na_2CO_3, $NaHCO_3$, $(NH_4)_2CO_3$, and NH_4HCO_3], NH_4^+, Na^+ ions, and pH values of the initial solution (Figure 2-8a). $LaCO_3OH$ was easily converted to $La_2O_2CO_3$ and La_2O_3 with the initial morphologies under annealing at suitable temperatures. Reddy et al.(Dinh et al. 2009) synthesized the novel nanocrystalline $Ce_{1-x}La_xO_{2-\delta}$ (x = 0.2) solid solutions via a modified coprecipitation (Figure 2-9c). The mixed $Ce_{1-x}La_xO_{2-\delta}$ nanocomposites well matched with the standard fluorite type cubic phase of CeO_2. Variation in the lattice parameter of CeO_2 was ascribed to the partial substitution of Ce^{4+} with La^{3+}. The incorporation of La^{3+} into CeO_2 lattice led to the lattice expansion in unit cell volume because the ionic radius of La^{3+} (0.11 nm) is larger than Ce^{4+} (0.097 nm). The two oxidation states (Ce^{3+} and Ce^{4+}) coexisted in the segregation of La^{3+} in the $Ce_{1-x}La_xO_{2-\delta}$ structure. These $Ce_{1-x}La_xO_{2-\delta}$ catalysts were evaluated for OSC and CO oxidation activity. The nanosized Ce-La solid solution exhibited superior catalytic performance and thermal stability in comparison to heterostructured Ce-Zr solid solution. The excellent catalytic activity of the $Ce_{1-x}La_xO_{2-\delta}$ samples originated from the features of structure, redox behavior, bulk oxygen mobility.

In this dissertation, we have studied the synthesis and characterization of a variety of mixed metal oxide nanocrystals including rare earth orthovanadate, transition-metal tungstate, nanostructured $Ce_xLa_{1-x}CO_3OH$ solid solution and their derived oxides. The different size and shape of these mixed oxide nanocrystals were produced by simple adjusting of the synthesis conditions.

References

Bu, W., Z. Chen, F. Chen & J. Shi (2009) Oleic Acid/Oleylamine Cooperative-Controlled Crystallization Mechanism for Monodisperse Tetragonal Bipyramid $NaLa(MoO_4)_2$ Nanocrystals. *The Journal of Physical Chemistry C,* 113, 12176-12185.

Buissette, V., D. Giaume, T. Gacoin & J.-P. Boilot (2006) Aqueous routes to lanthanide-doped oxide nanophosphors. *Journal of Materials Chemistry,* 16, 529-539.

Chen, S.-J., X.-T. Chen, Z. Xue, J.-H. Zhou, J. Li, J.-M. Hong & X.-Z. You (2003) Morphology control of MnWO4 nanocrystals by a solvothermal route. *Journal of Materials Chemistry,* 13, 1132-1135.

Dellwo, U., P. Keller & J. U. Meyer (1997) Fabrication and analysis of a thick-film humidity sensor based on $MnWO_4$. *Sensors and Actuators A: Physical,* 61, 298-302.

Downing, E., L. Hesselink, J. Ralston & R. Macfarlane (1996) A Three-Color, Solid-State, Three-Dimensional Display. *Science,* 273, 1185-1189.

Esteban-Betegón, F. t., C. Zaldo & C. n. Cascales (2010) Hydrothermal Yb^{3+}-Doped $NaGd(WO_4)_2$ Nano- and Micrometer-Sized Crystals with Preserved Photoluminescence Properties. *Chemistry of Materials,* 22, 2315-2324.

Feng, W., L.-D. Sun, Y.-W. Zhang & C.-H. Yan (2010) Synthesis and assembly of rare earth nanostructures directed by the principle of coordination chemistry in solution-based process. *Coordination Chemistry Reviews,* 254, 1038-1053.

Fu, Q. & T. Wagner (2007) Interaction of nanostructured metal overlayers with oxide surfaces. *Surface Science Reports,* 62, 431-498.

Gong, Q., X. Qian, X. Ma & Z. Zhu (2006) Large-Scale Fabrication of Novel Hierarchical 3D $CaMoO_4$ and $SrMoO_4$ Mesocrystals via a Microemulsion-Mediated Route. *Crystal Growth & Design,* 6, 1821-1825.

Guerrero-Martínez, A., J. Pérez-Juste & L. M. Liz-Marzán (2010) Recent Progress on Silica Coating of Nanoparticles and Related Nanomaterials. *Advanced Materials,* 22, 1182-1195.

Heyer, O. & et al. (2006) A new multiferroic material: $MnWO_4$. *Journal of Physics: Condensed Matter,* 18, L471.

Kim, F., S. Kwan, J. Akana & P. Yang (2001) Langmuir−Blodgett Nanorod Assembly. *Journal of the American Chemical Society,* 123, 4360-4361.

Li, P., Q. Peng & Y. Li (2009) Dual-Mode Luminescent Colloidal Spheres from Monodisperse Rare-Earth Fluoride Nanocrystals. *Advanced Materials,* 21, 1945-1948.

Liu, J. & Y. Li (2007) General synthesis of colloidal rare earth orthovanadate nanocrystals. *Journal of Materials Chemistry,* 17, 1797-1803.

Luo, Y.-S., X.-J. Dai, W.-D. Zhang, Y. Yang, C. Q. Sun & S.-Y. Fu (2010) Controllable synthesis and luminescent properties of novel erythrocyte-like $CaMoO_4$ hierarchical nanostructures via a simple surfactant-free hydrothermal route. *Dalton Transactions,* 39**,** 2226-2231.

Mao, Y., T.-J. Park & S. S. Wong (2005) Synthesis of classes of ternary metal oxide nanostructures. *Chemical Communications***,** 5721-5735.

Norris, D. J., A. L. Efros & S. C. Erwin (2008) Doped Nanocrystals. *Science,* 319**,** 1776-1779.

Shi, H., L. Qi, J. Ma & H. Cheng (2003a) Polymer-Directed Synthesis of Penniform $BaWO_4$ Nanostructures in Reverse Micelles. *Journal of the American Chemical Society,* 125**,** 3450-3451.

Shi, H., L. Qi, J. Ma, H. Cheng & B. Zhu (2003b) Synthesis of Hierarchical Superstructures Consisting of $BaCrO_4$ Nanobelts in Catanionic Reverse Micelles. *Advanced Materials,* 15**,** 1647-1651.

Stevens, S. B., C. A. Morrison, T. H. Allik, A. L. Rheingold & B. S. Haggerty (1991) $NaLa(MoO_4)_2$ as a laser host material. *Physical Review B,* 43**,** 7386.

Sun, L., Q. Guo, X. Wu, S. Luo, W. Pan, K. Huang, J. Lu, L. Ren, M. Cao & C. Hu (2006a) Synthesis and Photoluminescent Properties of Strontium Tungstate Nanostructures. *The Journal of Physical Chemistry C,* 111**,** 532-537.

Sun, Y., H. Liu, X. Wang, X. Kong & H. Zhang (2006b) Optical Spectroscopy and Visible Upconversion Studies of YVO_4:Er^{3+} Nanocrystals Synthesized by a Hydrothermal Process. *Chemistry of Materials,* 18**,** 2726-2732.

Thongtem, S., S. Wannapop & T. Thongtem (2009) Characterization of $MnWO_4$ with flower-like clusters produced using spray pyrolysis. *Transactions of Nonferrous Metals Society of China,* 19**,** s100-s104.

Tong, W., L. Li, W. Hu, T. Yan, X. Guan & G. Li (2010) Kinetic Control of $MnWO_4$ Nanoparticles for Tailored Structural Properties. *The Journal of Physical Chemistry C,* 114**,** 15298-15305.

Wachs, I. E. (2005) Recent conceptual advances in the catalysis science of mixed metal oxide catalytic materials. *Catalysis Today,* 100**,** 79-94.

Wang, F., Y. Han, C. S. Lim, Y. Lu, J. Wang, J. Xu, H. Chen, C. Zhang, M. Hong & X. Liu (2010) Simultaneous phase and size control of upconversion nanocrystals through lanthanide doping. *Nature,* 463**,** 1061-1065.

Wang, W., Y. Hu, J. Goebl, Z. Lu, L. Zhen & Y. Yin (2009) Shape- and Size-Controlled Synthesis of Calcium Molybdate Doughnut-Shaped Microstructures. *The Journal of Physical Chemistry C,* 113**,** 16414-16423.

Wang, X., J. Zhuang, Q. Peng & Y. Li (2006) Hydrothermal Synthesis of Rare-Earth Fluoride Nanocrystals. *Inorganic Chemistry,* 45**,** 6661-6665.

Xie, J., Q. Wu, D. Zhang & Y. Ding (2009) Biomolecular-Induced Synthesis of Self-Assembled Hierarchical La(OH)CO3 One-Dimensional Nanostructures and Its Morphology-Held Conversion toward La_2O_3 and $La(OH)_3$. *Crystal Growth & Design,* 9**,** 3889-3897.

Xu, L., C. Lu, Z. Zhang, X. Yang & W. Hou (2010a) Various self-assembled three-dimensional hierarchical architectures of $La_2(MoO_4)_3$: controlled synthesis, growth mechanisms, luminescence properties and adsorption activities. *Nanoscale,* 2**,** 995-1005.

Xu, Z., X. Kang, C. Li, Z. Hou, C. Zhang, D. Yang, G. Li & J. Lin (2010b) Ln^{3+} (Ln = Eu, Dy, Sm, and Er) Ion-Doped YVO_4 Nano/Microcrystals with Multiform Morphologies: Hydrothermal Synthesis, Growing Mechanism, and Luminescent Properties. *Inorganic Chemistry,* 49, 6706-6715.

Yu, C., M. Yu, C. Li, C. Zhang, P. Yang & J. Lin (2008) Spindle-like Lanthanide Orthovanadate Nanoparticles: Facile Synthesis by Ultrasonic Irradiation, Characterization, and Luminescent Properties. *Crystal Growth & Design,* 9, 783-791.

Zhang, F., M. Y. Sfeir, J. A. Misewich & S. S. Wong (2008) Room-Temperature Preparation, Characterization, and Photoluminescence Measurements of Solid Solutions of Various Compositionally-Defined Single-Crystalline Alkaline-Earth-Metal Tungstate Nanorods. *Chemistry of Materials,* 20, 5500-5512.

Zhang, L., C. Lu, Y. Wang & Y. Cheng (2007a) Hydrothermal synthesis and characterization of $MnWO_4$ nanoplates and their ionic conductivity. *Materials Chemistry and Physics,* 103, 433-436.

Zhang, L., W. Wang, L. Zhou & H. Xu (2007b) Bi_2WO_6 Nano- and Microstructures: Shape Control and Associated Visible-Light-Driven Photocatalytic Activities. *Small,* 3, 1618-1625.

Zhang, Q., X. Chen, Y. Zhou, G. Zhang & S.-H. Yu (2007c) Synthesis of $ZnWO_4$@MWO_4 (M = Mn, Fe) Core−Shell Nanorods with Optical and Antiferromagnetic Property by Oriented Attachment Mechanism. *The Journal of Physical Chemistry C,* 111, 3927-3933.

Zhou, H., Y. Yiu, M. C. Aronson & S. S. Wong (2008a) Ambient template synthesis of multiferroic $MnWO_4$ nanowires and nanowire arrays. *Journal of Solid State Chemistry,* 181, 1539-1545.

Zhou, Y.-X., Q. Zhang, J.-Y. Gong & S.-H. Yu (2008b) Surfactant-Assisted Hydrothermal Synthesis and Magnetic Properties of Urchin-like $MnWO_4$ Microspheres. *The Journal of Physical Chemistry C,* 112, 13383-13389.

2.4. Hybrid Inorganic Nanocrystals

2.4.1. Introduction

In past decades, hybrid inorganic nanomaterials have attracted considerable research attention because an hybrid system that combines two or more different single-nanocomponents can usually provide new collective properties, which are not available from the corresponding individual components (Costi, Saunders and Banin 2010). They not only possess the multi-functionalities but also illustrate novel properties arising from the particle-particle interactions (Barreca, Gasparotto and Tondello 2011, Buso et al. 2008). It is well-known that metal particle deposited on the nanocrystal surface act as sinks for transferring the electron from support surface to reagents to perform the oxidation/redox processes (Subramanian, Wolf and Kamat 2003). The charge distribution between metal and support thus plays an important role in improving the catalytic activity (Chen and Goodman 2006). As a result, such hybrid nanomaterials have highlighted the featured properties for the various potential applications in catalysts, optical devices, solar energy conversions, magnetic resonance imaging agents, chemical sensors (Gao, Gu and Xu 2009, Na, Song and Hyeon 2009) that go beyond those of the individual component.

In the following sections, we will critically review recent progress made in the development of colloidal strategies for the tailored synthesis of new nanohybrids of metal-oxide and metal-semiconductor species with a topologically controlled distribution of their chemical composition, extending from core@shell to dumbbell geometries. The mechanisms by which heterostructures can be accessed in nonequivalent configurations will be systematically illustrated and discussed for a high selection of material associations within the frame of general seeded-growth methods to heteroepitaxial deposition in solution media. The main properties and technological advantages offered by such generations of complex nanomaterials will also be briefly highlighted.

2.4.2 Types of hybrid inorganic compounds

2.4.2.1. Metal@oxides

Recent research seems to indicate that small Au particles/clusters deposited on iron oxide supports for the formation of the junction structure (Au-Fe_3O_4), are the active agents due to the Au particle polarization towards the support at the interface. Representative TEM and HRTEM examples of these Au-Fe_3O_4 core-shell and dumbbell-shaped nanohybrids can be found in Figure 2-9, 2-10, 2-11. Sun et al.(Yu et al. 2005) synthesized dumbbell-like Au-Fe_3O_4 nanohybrids via thermal decomposition of $Fe(CO)_5$ on (Chen et al.)-surfaced Au particles and subsequent oxidation in 1-octadecene solvent. TEM/HRTEM images of these Au-Fe_3O_4 core-shell and dumbbell-shaped nanohybrids are shown in Figure 2-10. The sizes (~2-8 nm) of Au particles was controlled either by tailoring the molar ratio of $HAuCl_4$ to oleylamine or by controlling the temperature at which the $HAuCl_4$ solution was injected.

The sizes (~4-20 nm) of the Fe_3O_4 particles were tuned by adjusting $Fe(CO)_5$/Au ratio. TEM/HRTEM results revealed that the dumbbell-shaped structure was yielded by growing the (Chen et al.) faceted-Fe_3O_4 onto the (Chen et al.)-faceted Au. The oxidation of metallic Fe particles to Fe_3O_4 particles can be achieved, giving Au-Fe_3O_4 nanoparticles upon exposure to air (Xu et al. 2008).

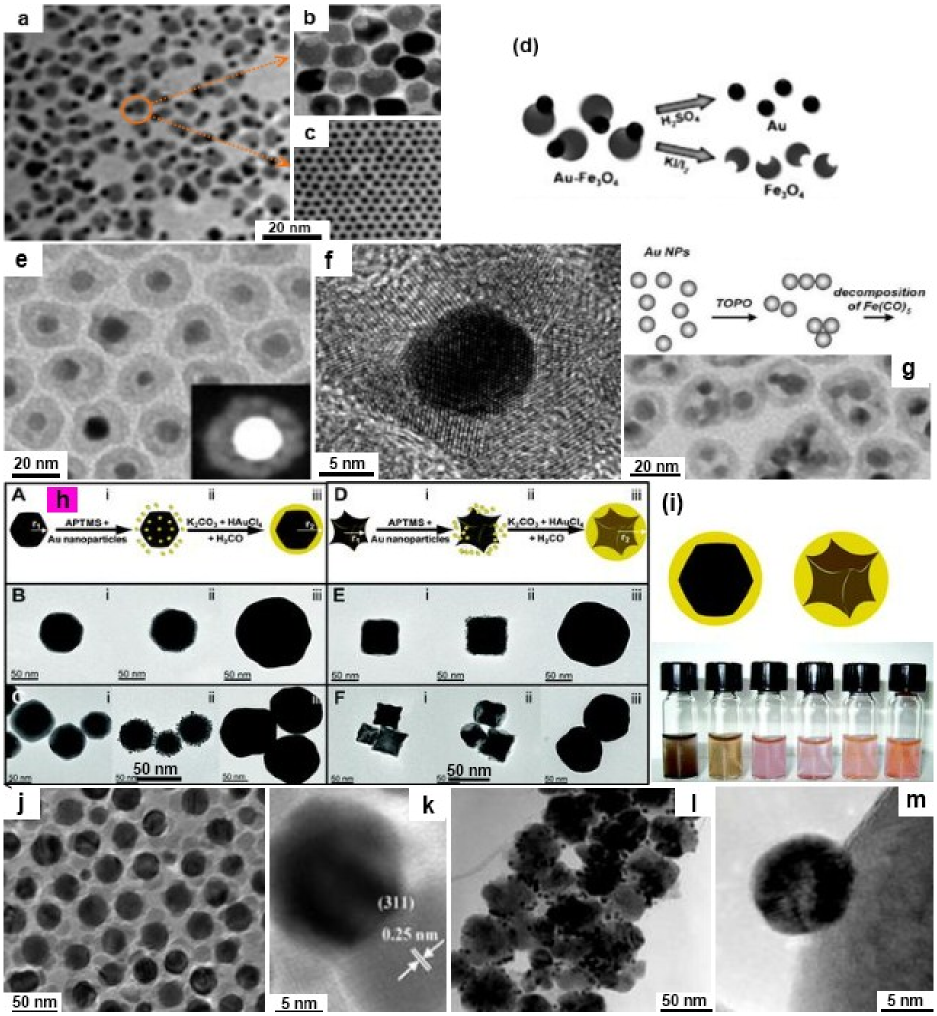

Figure 2.9. Gallery of representative TEM/HRTEM images illustrating examples of dumbbell and core@shell nanohybrids made of metal and semiconductor associations. Etching of (a) Au-Fe_3O_4 nanohybrids for the preparation of (b) Au particles and (c) dented Fe_3O_4 particles, (d) illustrated scheme of the etching process (Lee et al. 2010c); (e,f) Hollow gold-iron oxide core-shell nanohybrids, (g) formed hollow nanohybrids with multiple gold cores and corresponding scheme demonstrating the possible synthesis

mechanism (Shevchenko et al. 2008); (h,i) Magnetic-plasmonic core-shell nanohybrids of Au coated iron oxide with various shapes (Levin et al. 2009); (j,k) Au-Fe_3O_4 nanohybrids synthesized by thermal decomposition of mixtures of transition metal-oleate complexes and metal-oleylamine complexes (Choi et al. 2008); (l,m) Au-Fe_3O_4 nanohybrids formed from the functionalized cysteine-linked Fe_3O_4 nanocrystals and Au (Bao et al. 2007).

Single-component Au and Fe_3O_4 nanoparticles were formed from Au-Fe_3O_4 nanohybrids by etching of Au-Fe_3O_4 species by etching Fe_3O_4 away from the Au-Fe_3O_4 nanohybrids on carbon catalyst in diluted H_2SO_4 solution, and by a two-phase etching of Au from Au-Fe_3O_4 nanohybrids using KI/I_2 solution, respectively, as shown in Figure 2-9a-d. The H_2O_2 reduction was studied using these single-component and Au-Fe_3O_4 hybrid samples as catalysts. It is found that the enhanced activity of Au-Fe_3O_4 arose from the interaction of the Au-Fe_3O_4 interface, where the Fe_3O_4 nanoparticle surface became more active. Using oleylamine as a mild reducing and capping agent at low temperature, the Au-Fe_3O_4 dumbbell nanohybrids were produced by depositing Au on the Fe_3O_4 nanoparticles in a chloroform solution (Xu, Hou and Sun 2007). After the synthesis, the Au-Fe_3O_4 nanohybrids were transferred from the organic environment to water with CTAB and sodium citrate. The water-soluble nanohybrids were served as seeds for the formation of Au-Fe_3O_4 nanoparticles with thicker Au coatings by adding more $HAuCl_4$ under reductive conditions. Further using Au-Fe_3O_4 as seeds, Ag/Au-Fe_3O_4 nanodumbbells also obtained by adding $AgNO_3$ to the reaction solution under the same synthetic condition. Figure 2-9e-g shows that the hollow Au-Fe_3O_4 core-shell nanohybrids were synthesized from the deposition of an iron shell around the gold core and then oxidized the metallic iron shell to form a hollow iron oxide shell on the basis of Kirkendall mechanism (Shevchenko et al. 2008). The capping oleylamine and oleic acid ligands at the surface of the preformed gold seeds could affect the ability of iron to deposit on the seed's surface.

The deposition of iron precursors onto gold particles depends on the different oleylamine/oleic acid molar ratios (Figure 2-9e,f,g). At 1:1 oleylamine:oleic acid molar ratio, the thinnest oxide shell (~2 nm) around the gold nanoparticles was formed. The irregular iron oxide shells with polycrystalline and connecting some places with the gold core were produced in the presence of oleylamine without oleic acid. The iron nucleation and growth were to be slowed in the increase of the oleic acid concentration due to the formation of stable iron-oleate complex in the high-temperature reaction solution. The grown of the Au shell layer on the Fe_3O_4 nanocrystals was depicted in Figure 2-9h,i. The synthetic procedure illustrated that the surface of iron oxide nanocrystals was functionalized with the amine-terminated linker molecule which allowed small Au nanodots to attach and grow further onto the nanocrystal surface for the formation of Au-Fe_3O_4 core-shells. Hyeon et al.(Choi et al. 2008) reported a general route to synthesize numerous metal@oxide hetero-structures with diverse shapes via the thermal decomposition of mixtures of transition metal (Fe, Mn)-oleate complexes and metal (Au, Ag, Pt, Ni)-oleylamine complexes in organic solvent in the present of oleylamine surfactant (Figure 2-9j,k).

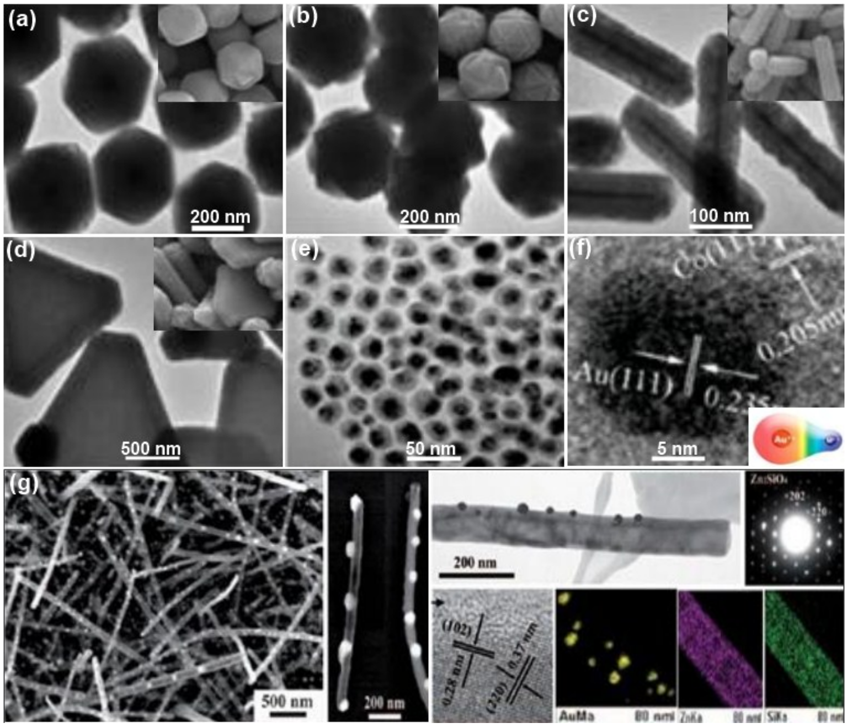

Figure 2.10. Gallery of representative TEM/HRTEM/SEM images illustrating examples of dumbbell and core@shell nanohybrids made of metal and oxide associations: Au-Cu_2O core-shell nanohybrids with (a) cuboctahedral, (b) truncated stellated icosahedra, (c) rod, (d) truncated triangular shapes (Kuo, Hua and Huang 2009); (e,f) Au-Co core-shell

nanohybrids (Wang and Li 2010); (g) one-dimensional Au/Zn_2SiO_4 nanohybrids formed by annealing solid ZnO-Au-SiO_2 nanowires (Yang et al. 2010).

Li et al.(Bao et al. 2007) expressed that the cysteine-linked Fe_3O_4 nanoparticles were carried out by the formation of amide bonds between the surface amino groups of the pre-synthesized Fe_3O_4 nanoparticles and the carboxylic groups of cysteine biomolecules. The Fe_3O_4 nanoparticles were then functionalized by thiol groups of alkylthiol ligand. The Au particles were prepared in aqueous media through the reduction of $HAuCl_4$ by $NaBH_4$. The bifunctional Au-Fe_3O_4 nanohybrids prepared from the conjugation of Au particles to thiol-modified Fe_3O_4 nanoparticles by the strong interaction between Au and thiol group under ultrasonic conditions. These results are shown in Figure 2-9l,m. Such materials showed that not only maintain excellent magnetic properties and highly efficient separation of the targeted protein obtained, but also the as-separated protein also maintained catalytic activity. The biomolecule lysine-assisted route could be expended to fabricate the diverse noble-metal (Au, Pt, Ag, Pt/Au)/Fe_2O_3 hybrid nanoparticles (Zhang et al. 2010). Lysine contains both amino and carboxylic groups that plays dual roles as both linker and capping agents in attaching metals onto Fe_2O_3 nanosupports. The hybrid sensors witnessed the significantly improved sensor performances in terms of high sensitivity and good reproducibility in comparison with pristine Fe_2O_3. Furthermore, bimetallic alloys were also considered an active site to deposit on the nanosupports of the enhanced reactive activity.

The nanocrystal-directed growth of Au-Cu_2O core-shells with precise shape control and highly symmetrical shell morphologies using Au nanoplates, nanorods, octahedra as the structure-directing cores for the overgrowth of Cu_2O shells were achieved by preparing a mixture of $CuCl_2$, sodium dodecyl sulfate surfactant, Au particles, NaOH, $NH_2OH.HCl$ aqueous solution (Kuo et al. 2009). TEM/HRTEM results in Figure 2-10a-d revealed that the Au particles located at the center of the heterostructures. The six {100}-faceted cuboctahedral Cu_2O shell strongly attached on the octahedral Au core, indicating that the shell growth were guided by the shape of the Au core. The electronic properties of Cu_2O might be modified by the inclusion of gold cores. Consequently, the electrical conductivity of the Au-Cu_2O hybrid nanocubes showed the significantly better conductivity as compared to single Cu_2O sample. The Pd@CeO_2 core-shell nanohybrids, as an active catalyst for CO oxidation, water-gas shift, and methanol steam reforming reaction, were synthesized by Fornasiero et al.(Cargnello et al. 2009) through adding the THF solution of MUA-Pd nanoparticles to the THF solution of cerium(IV)tetrakis(decyloxide), followed by the addition of a THF solution of dodecanoic acid. The hydrolysis of cerium(IV) alkoxide in the Pd-Ce solution was carried out by slowly adding H_2O in THF for the formation of core-shells.

A variety of oxide materials has been enwrapped within a SiO_2 shell and were then used to transfer such nanomaterials to biological environments for specific cell targeting/sorting or MRI imaging purposes (Guerrero-Martínez, Pérez-Juste and Liz-Marzán 2010). The 15 nm SiO_2 layer on the Au-ZnO nanowires by atomic layer deposition to generate a hybrid Au@Zn_2SiO_4 nanowires (Yang et al. 2010). From the SEM/TEM observations in Figure 2-10g, the formed ZnO-Au-SiO_2 sandwich nanostructure based on a controllable interfacial solid-solid reaction and Kirkendall effect. The 1D nanotubes were completely hollow or composed of discontinuous long tubular sections. An one-pot wet-chemical route to the Au-based hybrid magnetic nanostructures, including Au-Co core-shell nanocrystals with a core diameter of ~10 nm and a shell thickness of ~5 nm and Au-Ni spindly nanostructures with ~10 nm of tip size and ~15 nm of tail diameter have been developed by Li et al. (Wang and Li 2010). Accordingly, these hybrid nanocrystals were yielded by the solvothermal reaction of $HAuCl_4$ and transition metal nitrate ($Co(NO_3)_2 \cdot 6H_2O$ or $Ni(NO_3)_2 \cdot 6H_2O$) were used as starting materials and octadecylamine as surfactant and solvent. As seen in Figure 2-10e,f, for the Au-Co core-shell nanohybrids, the measured lattice spacings of 0.235 nm for the core and 0.205 nm for the shell correspond to cubic Au{111} and cubic Co{111} facets. For Au-Ni spindly nanostructures, clear lattice fringes with interplanar distances of 0.203 nm in both the tip and tail.

2.4.2.2. Metal@semiconductors

The hybrid metal-semiconductor nanocrystals have attracted a great deal of attention due to their optic and photocatalytic applications (Banin 2007). Figure 2-11 shows representative TEM/SEM/HRTEM images of some examples of such metal-semiconductor hybrid nanomaterials, which have been synthesized by direct heterogeneous nucleation and growth of the metal precursors onto preformed seeds. The difference in reactivity between the facets at the tips and at the sides of the CdS or CdSe nanoparticles has been documented. It was suggested that the anisotropic reactivity of the {001} tips of seeded CdSe/CdS nanorods resulted in the grown of metallic Au particles on only tips of the rod (Figure 2-11a,b,c) (Mokari et al. 2004). The facets at the fast-growing end, which is further from the CdSe core, tend to be sulfur-rich, while the facets at the end closer to the CdSe core tend to be cadmium-rich. The strong Au-S interaction indicated that Au deposition first occurred primarily on the facets at the end further from the CdSe core, followed by the deposition on the facets at the end closer to the CdSe core. Precise control over the deposition of Au at specific locations on the anisotropic CdS core-shell nanorods would not only be critical for directed assembly, but should also have the dramatic influence on the optical properties of the rods.

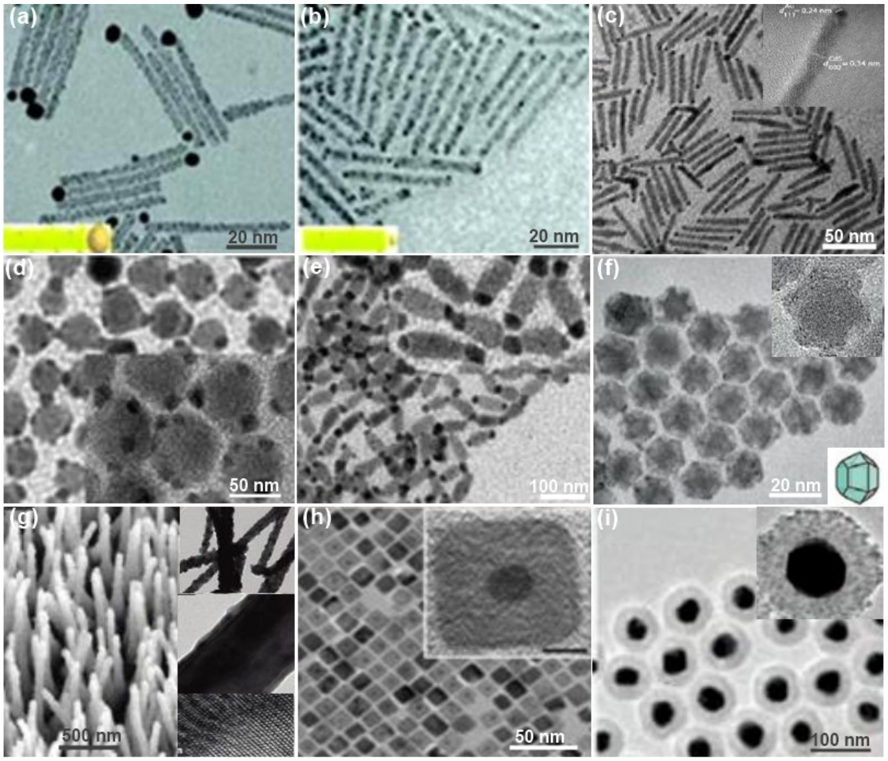

Figure 2.11. Gallery of representative TEM/HRTEM/SEM images illustrating examples of dumbbell and core@shell nanohybrids made of metal and oxide associations. Au growth on

CdS nanorods for 1 h: (a) dark at 313 K, (b) 473 nm laser irradiation at 313 K, (c) dark at 273 K (Mokari et al. 2004); CdSe-seeded CdS nanorods with varying degrees of Au deposition at (d) one end and (e) both ends of nanorod (Meyns et al. 2010); (f) Ru-Cu_2S hybrid nanocages (Macdonald et al. 2010); (g) ZnO-CdSSe nanorod grown on the Ti substrate (Myung et al. 2010); (h) hybrid FePt-PbS nanocubes (Lee et al. 2010b); (i) hybrid Au-SiO_2-CdSe quantum dots particle (Liu and Guyot-Sionnest 2006).

Dumbbell-shaped nanostructures from each PbSe sphere and CdSe rod were also synthesized by Manna et al.(Kudera et al. 2005). Significant modification of optical spectra was observed for the dumbbell-shaped nanostructures compared to those of either the initial CdSe nanorods or PbSe nanospheres. Moreover, Klinke et al.(Meyns et al. 2010) synthesized Au-CdSe rod- and pyramid-shaped nanohybrids via the growth and reductive transformation of a gold shell around pyramidal CdSe nanocrystals in the presence of chlorine under either electron beam irradiation or addition of a strong reducing agent during synthesis. The size of deposited gold nanodots can be tuned from 1.4 to 3.9 nm by varying the synthesis conditions including the ligands or the shape of the CdSe nanocrystals. The shape rod and pyramid were thermodynamically favored for the size-controlled growth of Au precursors on the corners/edges and tips of the CdSe nanocrystals through the suitable choice of metal precursor and surface ligand concentration (Figure 2-11d,e). The pyramid structure provided relatively sharp angles which were highly reactive sites for the nucleation of gold particles. The effect of the degree of mismatch between the crystal lattices of the two components have also been studied by Shim et al.(Kwon and Shim 2005) who examined the growth of different metal sulfides onto spherical Fe_2O_3 nanocrystals.

Chan et al.(Chakrabortty et al. 2010) used ambient light conditions similar to the Banin’s group to achieve the well-controlled deposition of Au on seeded CdSe/CdS nanohybrids by varying the additional Au precursor concentration (Menagen et al. 2009). The reactivity difference between the facets at the tips and sides of the nanorods caused the change of Au-decorated morphologies by adjusting the Au precursors concentration. Figure 2-11d,e show TEM/HRTEM images of the resultant CdSe-seeded CdS nanohybrids with Au deposited at distinct locations on their surface. The trend of selective Au growth at one tip, both tips, and throughout the nanorod with increasing concentrations of additional Au precursor was found. The attachment of Au particle into the nanorods at the exclusive tips showed non-epitaxial growth at the apex of the CdS shell. A similar procedure was also achieved to Ag_2S-CdSe/CdS hybrid nanorod heterostructures in which the Ag_2S particles located exclusively at the tips of the rods. Further the deposition of Au and Ag precursors on the seeded CdSe/CdS nanorods for the construction of Au-Ag@CdSe/CdS dumbbell structure.

Very recently, the Banin's group fabricated the cage-shaped Ru@Cu_2S nanohybrids via adding the Ru(acac)$_3$ solution to a suspension of the pre-synthesized Cu_2S nanoparticles in octadecylamine at 210 ^oC (Macdonald et al. 2010). As seen in the TEM image in Figure 2-11f, the resultant Ru@Cu_2S nanohybrids exhibited curious patterns of dark and light regions. HRTEM results revealed that the core of the nanohybrids was single crystalline and the protruding features suggested a frame structure around the core that was reminiscent of those seen of Au nanocages. The unique cage formation could be due to capping thiol-passivating ligands on the well-defined facets of the Cu_2S particles leading to blocking growth of these facets. Cage-shaped Ru@Cu_2S nanohybrids with remarkable synergistic properties were considered an excellent electro-catalyst towards H_2O_2 sensing that were two orders of magnitude higher than the bare Cu_2S electrode. The high redox catalytic activity could be due to the synergy of the two powerful concepts of unique cage shape and material combination. The hybrid materials composing of multicomponents have also been fabricated and designed recently. Park et al.(Myung et al. 2010) had fabricated vertically aligned ZnO-CdSSe core-shell nanoarrays with a controlled composition and shell thickness via the chemical vapor deposition on the pre-synthesized ZnO nanowire arrays (Figure 2-11g).

Colloidal FePt@PbS and FePt@PbSe heterogeneous nanostructures with effective optical, magnetic, electrical, magnetotransport properties were synthesized by combining a ferromagnetic FePt nanocrystals with either the quantum-confined PbS or PbSe semiconductors in form of core-shells or nanodumbbells through seed-mediated growth (Figure 2-11h) (Lee et al. 2010b). The products were formed by the injection of bis(trimethylsilyl) sulfide into the reaction mixture containing monodisperse FePt nanocrystals, oleic acid, Pb-oleate complex dissolved in 1-octadecene at 120-150 °C for 5-10 min. The shape of products was controlled by the reaction temperature and the capping ligands on the surface of FePt seeds. Hybrid PbSe/CdSe/CdS nanocrystals with two distinct geometries: core/shell/shells and tetrapods were synthesized and demonstrated the efficient emission in the IR with exceptionally long exciton lifetimes. These materials would be attracted for a variety of applications from lasing to photocatalysis and photovoltaics (Lee et al. 2010a). Well-defined hybrid Au/SiO_2/CdSe nanostructures comprising a gold core overcoated with a silica shell, following by a dense monolayer of colloidal CdSe quantum dots were formed through a multistep procedure.

In this dissertation, our work has focused on the synthesis and characterization of a series of hybrid nanocrystals of metal@oxide (Cu@CeO_2, Ag@Y_2O_3, Ag@In_2O_3), metal@semiconductor (Ag@TiO_2), metal@mixed oxide (Au@$MnWO_4$, Au@$CoWO_4$, Ag@$MnWO_4$, Ag@$CoWO_4$). The work on the catalytic activity of the nanohybrids for CO oxidation and Methylene Blue photodegradation will be limited to Cu@CeO_2 and Ag@TiO_2 nanocrystals as respresentative samples.

References

Banin, U. (2007) Nanocrystals: Tiny seeds make a big difference. *Nat Mater,* 6, 625-626.

Bao, J., W. Chen, T. Liu, Y. Zhu, P. Jin, L. Wang, J. Liu, Y. Wei & Y. Li (2007) Bifunctional Au-Fe_3O_4 Nanoparticles for Protein Separation. *ACS Nano,* 1, 293-298.

Barreca, D., A. Gasparotto & E. Tondello (2011) Metal/oxide interfaces in inorganic nanosystems: what's going on and what's next? *Journal of Materials Chemistry*.

Buso, D., M. Post, C. Cantalini, P. Mulvaney & A. Martucci (2008) Gold Nanoparticle-Doped TiO_2 Semiconductor Thin Films: Gas Sensing Properties. *Advanced Functional Materials,* 18, 3843-3849.

Cargnello, M., N. L. Wieder, T. Montini, R. J. Gorte & P. Fornasiero (2009) Synthesis of Dispersible Pd@CeO_2 Core−Shell Nanostructures by Self-Assembly. *Journal of the American Chemical Society,* 132, 1402-1409.

Chakrabortty, S., J. A. Yang, Y. M. Tan, N. Mishra & Y. Chan (2010) Asymmetric Dumbbells from Selective Deposition of Metals on Seeded Semiconductor Nanorods. *Angewandte Chemie International Edition,* 49, 2888-2892.

Chen, C., D. Chen, X. Jiao & S. Chen (2007) In_2O_3 Nanocrystals with a Tunable Size in the Range of 4−10 nm: One-Step Synthesis, Characterization, and Optical Properties. *The Journal of Physical Chemistry C,* 111, 18039-18043.

Chen, M. & D. W. Goodman (2006) Catalytically Active Gold: From Nanoparticles to Ultrathin Films. *Accounts of Chemical Research,* 39, 739-746.

Choi, S.-H., H. B. Na, Y. I. Park, K. An, S. G. Kwon, Y. Jang, M.-h. Park, J. Moon, J. S. Son, I. C. Song, W. K. Moon & T. Hyeon (2008) Simple and Generalized Synthesis of Oxide−Metal Heterostructured Nanoparticles and their Applications in Multimodal Biomedical Probes. *Journal of the American Chemical Society,* 130, 15573-15580.

Costi, R., A. E. Saunders & U. Banin (2010) Colloidal Hybrid Nanostructures: A New Type of Functional Materials. *Angewandte Chemie International Edition,* 49, 4878-4897.

Gao, J., H. Gu & B. Xu (2009) Multifunctional Magnetic Nanoparticles: Design, Synthesis, and Biomedical Applications. *Accounts of Chemical Research,* 42, 1097-1107.

Guerrero-Martínez, A., J. Pérez-Juste & L. M. Liz-Marzán (2010) Recent Progress on Silica Coating of Nanoparticles and Related Nanomaterials. *Advanced Materials,* 22, 1182-1195.

Kudera, S., L. Carbone, M. F. Casula, R. Cingolani, A. Falqui, E. Snoeck, W. J. Parak & L. Manna (2005) Selective Growth of PbSe on One or Both Tips of Colloidal Semiconductor Nanorods. *Nano Letters,* 5, 445-449.

Kuo, C.-H., T.-E. Hua & M. H. Huang (2009) Au Nanocrystal-Directed Growth of Au−Cu_2O Core−Shell Heterostructures with Precise Morphological Control. *Journal of the American Chemical Society,* 131, 17871-17878.

Kwon, K.-W. & M. Shim (2005) γ-Fe_2O_3/II−VI Sulfide Nanocrystal Heterojunctions. *Journal of the American Chemical Society,* 127, 10269-10275.

Lee, D. C., I. n. Robel, J. M. Pietryga & V. I. Klimov (2010a) Infrared-Active Heterostructured Nanocrystals with Ultralong Carrier Lifetimes. *Journal of the American Chemical Society,* 132, 9960-9962.

Lee, J.-S., M. I. Bodnarchuk, E. V. Shevchenko & D. V. Talapin (2010b) "Magnet-in-the-Semiconductor" FePt−PbS and FePt−PbSe Nanostructures: Magnetic Properties, Charge Transport, and Magnetoresistance. *Journal of the American Chemical Society,* 132, 6382-6391.

Lee, Y., M. A. Garcia, N. A. Frey Huls & S. Sun (2010c) Synthetic Tuning of the Catalytic Properties of Au-Fe_3O_4 Nanoparticles. *Angewandte Chemie International Edition,* 49, 1271-1274.

Levin, C. S., C. Hofmann, T. A. Ali, A. T. Kelly, E. Morosan, P. Nordlander, K. H. Whitmire & N. J. Halas (2009) Magnetic−Plasmonic Core−Shell Nanoparticles. *ACS Nano,* 3, 1379-1388.

Liu, M. & P. Guyot-Sionnest (2006) Preparation and optical properties of silver chalcogenide coated gold nanorods. *Journal of Materials Chemistry,* 16, 3942-3945.

Macdonald, J. E., M. Bar Sadan, L. Houben, I. Popov & U. Banin (2010) Hybrid nanoscale inorganic cages. *Nat Mater,* 9, 810-815.

Menagen, G., J. E. Macdonald, Y. Shemesh, I. Popov & U. Banin (2009) Au Growth on Semiconductor Nanorods: Photoinduced versus Thermal Growth Mechanisms. *Journal of the American Chemical Society,* 131, 17406-17411.

Meyns, M., N. G. Bastus, Y. Cai, A. Kornowski, B. H. Juarez, H. Weller & C. Klinke (2010) Growth and reductive transformation of a gold shell around pyramidal cadmium selenide nanocrystals. *Journal of Materials Chemistry,* 20, 10602-10605.

Mokari, T., E. Rothenberg, I. Popov, R. Costi & U. Banin (2004) Selective Growth of Metal Tips onto Semiconductor Quantum Rods and Tetrapods. *Science,* 304**,** 1787-1790.

Myung, Y., D. M. Jang, T. K. Sung, Y. J. Sohn, G. B. Jung, Y. J. Cho, H. S. Kim & J. Park (2010) Composition-Tuned ZnO−CdSSe Core−Shell Nanowire Arrays. *ACS Nano,* 4**,** 3789-3800.

Na, H. B., I. C. Song & T. Hyeon (2009) Inorganic Nanoparticles for MRI Contrast Agents. *Advanced Materials,* 21**,** 2133-2148.

Shevchenko, E. V., M. I. Bodnarchuk, M. V. Kovalenko, D. V. Talapin, R. K. Smith, S. Aloni, W. Heiss & A. P. Alivisatos (2008) Gold/Iron Oxide Core/Hollow-Shell Nanoparticles. *Advanced Materials,* 20**,** 4323-4329.

Subramanian, V., E. E. Wolf & P. V. Kamat (2003) Green Emission to Probe Photoinduced Charging Events in ZnO−Au Nanoparticles. Charge Distribution and Fermi-Level Equilibration†. *The Journal of Physical Chemistry B,* 107**,** 7479-7485.

Wang, D. & Y. Li (2010) One-Pot Protocol for Au-Based Hybrid Magnetic Nanostructures via a Noble-Metal-Induced Reduction Process. *Journal of the American Chemical Society,* 132**,** 6280-6281.

Xu, C., J. Xie, D. Ho, C. Wang, N. Kohler, E. G. Walsh, J. R. Morgan, Y. E. Chin & S. Sun (2008) Au–Fe_3O_4 Dumbbell Nanoparticles as Dual-Functional Probes. *Angewandte Chemie International Edition,* 47**,** 173-176.

Xu, Z., Y. Hou & S. Sun (2007) Magnetic Core/Shell Fe_3O_4/Au and Fe_3O_4/Au/Ag Nanoparticles with Tunable Plasmonic Properties. *Journal of the American Chemical Society,* 129**,** 8698-8699.

Yang, Y., R. B. Yang, H. J. Fan, R. Scholz, Z. Huang, A. Berger, Y. Qin, M. Knez & U. Gösele (2010) Diffusion-Facilitated Fabrication of Gold-Decorated Zn_2SiO_4 Nanotubes by a One-Step Solid-State Reaction. *Angewandte Chemie,* 122**,** 1484-1488.

Yu, H., M. Chen, P. M. Rice, S. X. Wang, R. L. White & S. Sun (2005) Dumbbell-like Bifunctional Au–Fe_3O_4 Nanoparticles. *Nano Letters,* 5**,** 379-382.

Zhang, J., X. Liu, X. Guo, S. Wu & S. Wang (2010) A General Approach to Fabricate Diverse Noble-Metal (Au, Pt, Ag, Pt/Au)/Fe_2O_3 Hybrid Nanomaterials. *Chemistry – A European Journal,* 16**,** 8108-8116.

2.5. Applications of Metal Oxide, Mixed Oxide, Hybrid Metal@Oxide Nanocatalysts

2.5.1. Carbon monoxide (CO) oxidation

2.5.1.1. Introduction

The oxidation of carbon monoxide is one of the pivotal reactions in heterogeneous catalysis, owing to its application in indoor air cleaning and toxic pollutant treatment from automobile exhaust (Creighton J and White J 1982). Nanocrystals of metal, metal oxide, mixed oxide, hybrid metal-oxide species have widely used for heterogeneous catalysts for low-temperature CO oxidation reactions because of their high surface-to-volume ratios and high surface energies (Peden Charles 1992, Rethwisch and Dumesic 1988). The high surface area of nanocatalyst would yield a number of defect sites that are coordinatively unsaturated ions or surface atoms arising from planes, edges, corners, anion/cation vacancies, and electron excess centers (Leong and Vittal 2010). Such defect sites are often attributed as the active sites for many useful and interesting catalytic reactions.

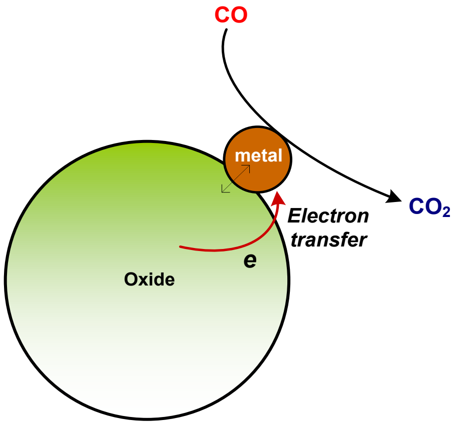

Figure 2.12. A schematic representation of reaction mechanism for the CO oxidation on hybrid metal@oxide nanocatalysts.

Hybrid noble-metal@oxide nanostructures as novel active catalyst with positional and shape control of the components have been viewed as excellent candidates for low-temperature CO oxidation. Figure 2-12 shows a possible model for illustrating reaction mechanism for CO oxidation on the hybrid metal-oxide nanocatalysts. In order to gain high catalytic activity, small-sized metal particles have generally to well-disperse on oxide support with exposed high-energy facets (El-Sayed 2001, Tisdale et al. 2010). Deciphering the hybrid structures attributes of these metal-oxide interfaces have been proposed to originate from one or more of three contributions: (i) presence of low coordinative metal sites; (ii) charge transfer between the metal and support. Recent approaches have utilized oxide nanocrystals as a support for the dispersion of noble-metal particles. In general, two main routes have typically been used for the controlled growth of metal-oxide nanohybrids:

(i) light-induced growth of the metal onto the pre-synthesized oxide semiconductor nanocrystals and (ii) reduced solution reaction of metal salt on the functionalized-oxide nanocrystals (Carbone and Cozzoli 2010). In the following section, we presented the catalytic CO oxidation activity of colloidal metal oxide, mixed oxide, and hybrid metal@oxide nanocrystals with various shapes and components recently synthesized by various surfactant-assisted methods.

2.5.1.2. Types of nanocatalysts

2.5.1.2.1. Single metal oxides

Figure 2-13 shows the shape-dependent catalytic properties for CO oxidation over single metal oxide nanocatalysts. The specific catalytic performance for CO oxidation of nanocatalysts is very close to the exposed reactive crystal faces and the presence of more oxygen vacancies. For example, ceria nanocrystals have high oxygen-storage capability and act as an important component in three-way catalytic converters to clean up automotive exhausts (Figure 2-13a). Accordingly, a direct relationship between the concentration of the oxygen vacancy and the reactivity of CeO_2 nanorods with different defect densities was revealed by Li et al.(Liu et al. 2009). Li et al.(Zhou et al. 2005) also demonstrated the CO oxidation activity of CeO_2 nanorods was more active than CeO_2 nanoparticles (Figure 2-13b,c).

The surface of nanocrystalline ceria plays a fundamental role in enhancing the catalytic activity of CeO_2 catalyst and particularly the pattern of oxygen vacancies originated by the redox processes involving the Ce^{4+}/Ce^{3+} pair allows effective O_2 adsorption and activation for CO oxidation (Min and Friend 2007, Carrettin et al. 2004). To elevate catalytic activity, it is desirable to prepare ceria samples with a high surface area. So far, ceria nanocrystals with diverse shapes have been synthesized. Yan et al.(Zhou et al. 2008) verified that the CO oxidation activity of CeO_2 nanocatalysts with different shapes followed the trend of nanoflowers > nanopolyhedra > nanocubes, in which the catalyst with higher specific surface area could provide more active sites for CO conversion (Figure 2-13d-f). Shen et al.(Cui et al. 2009) suggested that the CeO_2 nanospheres made up of numerous four-square flakes with more reactive facets exposed had better catalytic activity than the CeO_2 nanoparticles. A higher conversion was measured in the presence of CeO_2 hollow nanocubes compared to that of CeO_2 powders. The interconnected hollow structure in hollow nanocube-shaped nanocatalysts enabled better contact with the gas molecule owing to the existence of interior spaces and penetrable shell (Chen et al. 2008).

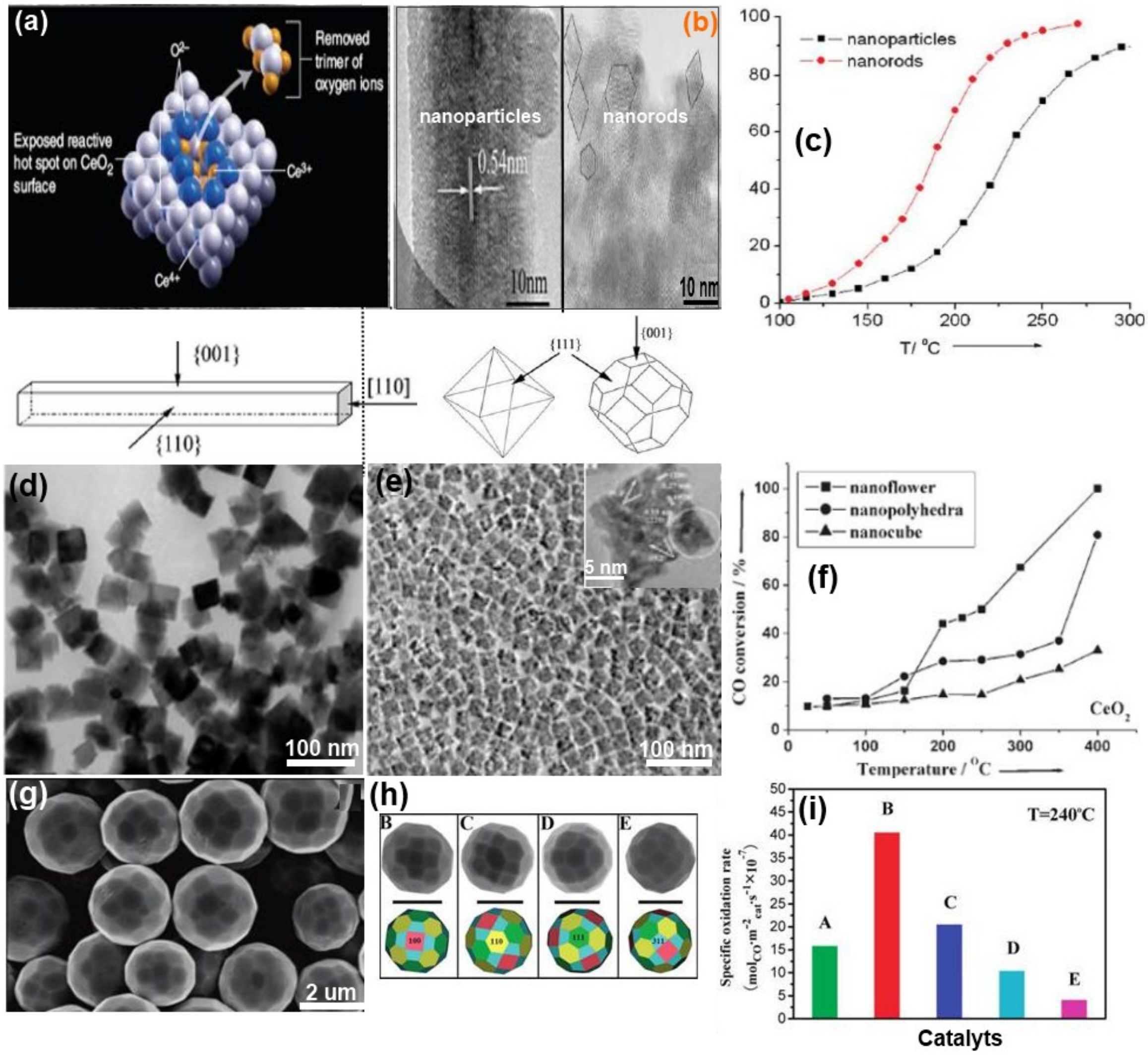

Figure 2.13. The shape-dependent catalytic properties for CO oxidation over single metal oxide nanocatalysts: (a) defected structure of ceria (Liu et al. 2009); (b) CeO_2 nanoparticles, (c) CeO_2 nanorods, (c) CO oxidation catalytic activity of corresponding crystalline CeO_2 particle and rod shapes (Zhou et al. 2005); (d) CeO_2 nanocubes, (e) CeO_2 nanoflowers, (f) CO conversion versus reaction temperature over corresponding ceria

nanopolyhedron, nanocube, nanoflower catalysts (Zhou et al. 2008); (g,h) polyhedral 50-facet Cu_2O microcrystals and (i) oxidation rates of CO over Cu_2O microcrystals (A), (B) polyhedral 50-facet, (C) rhombic dodecahedral, (D) octahedral, and (E) cubic shapes (Leng et al. 2010).

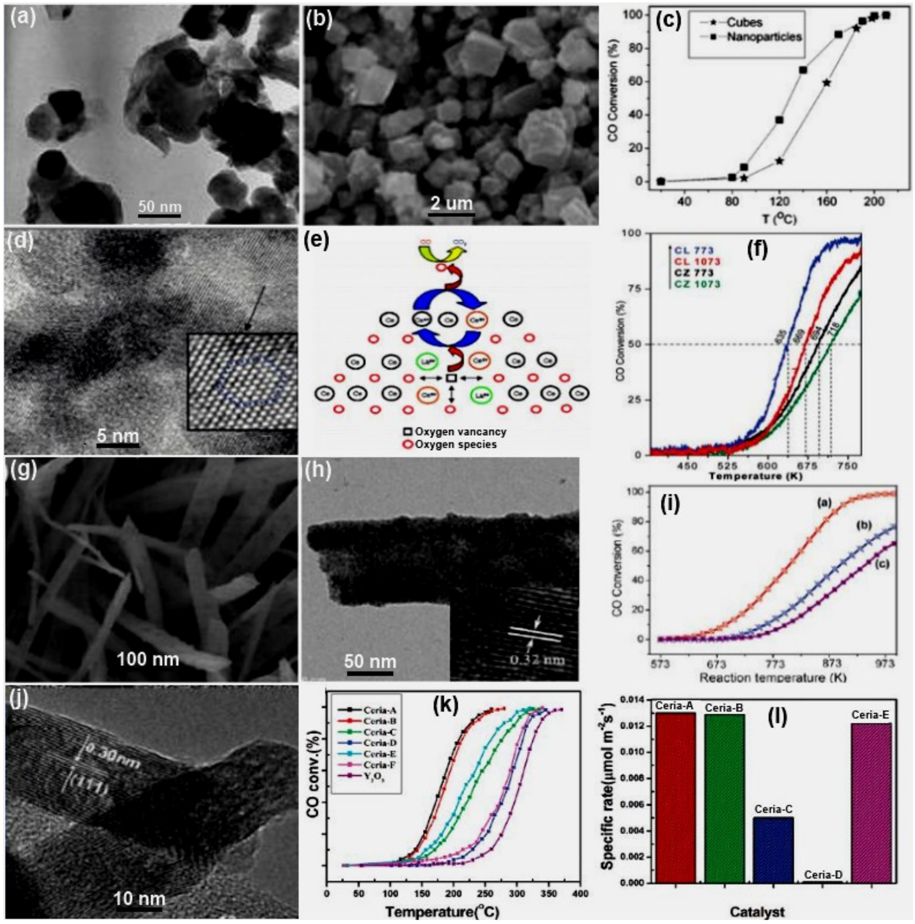

Figure 2.14. CO oxidation catalytic activity over mixed oxide nanocrystals: $La_{0.5}Sr_{0.5}MnO_3$ nanocrystals with (a) particle, (b) cubic shapes, (c) conversion of CO over $La_{0.5}Sr_{0.5}MnO_3$ nanoparticles and nanocubes (Liang et al. 2007); (d) nanostructured $Ce_xLa_{1-x}CO_3OH$ solid-solution, (e) simulated $Ce_xLa_{1-x}CO_3OH$ structure, (f) CO oxidation catalytic activity of $Ce_xLa_{1-x}CO_3OH$ catalysts with varying the cerium dopant components (Dinh et al. 2009); (g,h) $Ce_{1-x}Tb_xO_2$ nanobelts and (i) conversion of CO over $Ce_{1-x}Tb_xO_2$ nanocatalysts with belt, sheet, particle shapes (Li et al. 2009); (j) solid solution $Ce_{1-x}Y_xO_{2-x/2}$ nanorods, (k)

percentage conversion versus temperature plots for the oxidation of the samples, (l) graph showing the specific rate for CO oxidation of the FCC solid solution (Yang et al. 2010).

Other authors had obtained CeO_2 nanotubes with improved catalytic behavior in the oxidation of CO with respect to conventional ceria powders. The CeO_2 nanotubes with the outer diameter of ~200 nm and the length of 30-40 μm showed the catalytic activity in CO oxidation, at 200 °C, around 400 times higher than bulk CeO_2 powders (González-Rovira et al. 2009). This highly improved catalytic performance must be due to the fact that the nanotubes were made of randomly oriented assembling 1-3 nm size particles. The Co_3O_4 nanorods having preferentially expose reactive {110} facets were extremely active for low-temperature CO oxidation compared to the conventional Co_3O_4 nanoparticles with a few exposed active sites only, clearly demonstrating a shape-dependent effect (Xie and Shen 2009). The 10 nm x 200-300 nm Co_3O_4 nanorods were obtained by calcination of the nanorod-shaped cobalt hydroxycarbonate precursors that showed a much better catalytic activity for CO oxidation than the Co_3O_4 nanospheres, confirming the concept of shape-dependent nanocatalysis (Xie et al. 2010). Cuprous oxide (Cu_2O), also known as cuprite, has a cubic crystal structure in which oxygen atoms form a body-centered cubic lattice while copper atoms form a face-centered cubic lattice. Polyhedral 50-facet Cu_2O microcrystals partially enclosed by high-index {311} facets were synthesized and studied on the CO oxidation activity (Leng et al. 2010). For comparison, the rhombic dodecahedral-, octahedral-, cubic-shaped Cu_2O microcrystals were tested under the same conditions as shown in Figure 2-13g-i. These results clearly revealed that the CO oxidation over Cu_2O microcrystals exhibits morphology-dependent catalytic activity. The highest specific catalytic rate over a polyhedral 50-facet Cu_2O microcrystal might be attributed to the presence of high-index {311} facets on their surfaces.

2.5.1.2.2. Mixed metal oxides

In nanostructured mixed metal oxide catalysts, the high density of lattice oxygen is among the most important factors that contribute to their catalytic reactivity for oxidation reactions in heterogeneous catalysis (Mao, Park and Wong 2005, Fröba and Reller 1999). Multiple oxidation states, multiple phases, more oxygen vacancy, thermal stabilization at nanoscale could cause mainly to enhance the catalytic reactivity. Figure 2-14 shows the CO oxidation catalytic activity over many types of mixed oxide nanocrystals. The $La_{0.5}Sr_{0.5}MnO_3$ nanoparticle catalyst showed a higher activity than the cube catalyst for CO oxidation at a lower temperature (Figure 2-14a,b,c). While the catalytic activity of the cubes significantly increased at higher temperature, the complete conversion temperatures for CO were both the same at 210 °C. The proposed catalytic mechanism of CO oxidation over $La_{0.5}Sr_{0.5}MnO_3$ cubes states that the adsorbed CO was oxidized by the lattice oxygen. The chemisorbed oxygen over $La_{0.5}Sr_{0.5}MnO_3$ nanocubes was then transformed into the lattice oxygen by MnO6 octahedra to replace the consumed lattice oxygen. The catalytic performances of $La_{0.5}Sr_{0.5}MnO_3$ cubes and nanoparticles were mainly predominated by Jahn-Teller distortion of the catalysts (Liang et al. 2007). Thrimurthulu et al.(Dinh et al. 2009) revealed that the nanosized $Ce_{1-x}La_xO_{2-\delta}$ solid solution exhibited superior catalytic performance for CO oxidation in comparison to heterostructured Ce-Zr solid solution that were originated from their high oxygen storage capacity (Figure 2-14d,e,f).

Hammer et al.(Wang and Hammer 2007) proposed that, under operation conditions, a nanoscale Au oxide might be formed at the metal/oxide interface at the perimeter of Au nanoparticles, within which oxygen was responsible for low-temperature CO oxidation. A general observation of the structure-activity relationship in low-temperature CO oxidation catalyzed by supported Au nanoparticles was the size-dependent activity. By far, the experimental results demonstrated that active structures of gold in supported Au catalysts for low-temperature CO oxidation could only be acquired by reducing the particle size of supported Au nanoparticles to around 5 nm or smaller. The only exception came from an $Au/TiO_x/Mo$ model catalyst in which the extended Au film with a bilayer structure exhibited an exceptionally high activity in low-temperature CO oxidation (Chen and Goodman 2004). Arurault et al.(Li et al. 2009) synthesized $Ce_{1-x}TbO_x$ solid solution with belt, sheet, particle shapes and they demonstrated that $Ce_{1-x}TbO_x$ nanobelts were most active for the CO conversion reaction compared with $Ce_{1-x}TbO_x$ nanobelts and nanosheets. The high catalytic activity of $Ce_{1-x}TbO_x$ nanobelts can be attributed to the special nanostructures with high OSC. Zhou et al.(Yang et al. 2010) found that the amounts of the dopant (Y^{3+}) determined the concentration, type, and distribution of oxygen vacancies, which in turn influenced the reducibility and catalytic activity of the $Ce_{1-x}Y_xO_{2-x/2}$ ($0 \leq x \leq 1$) solid solution (Figure 2-14j,k,l).

2.5.1.2.3. Hybrid metal@oxides

The hybrid metal-oxide nanocrystals often exhibit an enhanced catalytic activity that raise from the particle-particle interaction. Therefore, different aspects have been studied in order to explain such extraordinary catalytic behavior, including the nature of noble metal active sites, the influence of support, the preparation method, the preparation conditions, the metal particle size and oxidation state, and the catalyst pretreatment method. El-Shall et al.(Glaspell, Fuoco and El-Shall 2005) reported a remarkable enhancement of the catalytic CO oxidation activity at low temperature, and directly correlated with the change in the morphology of the supported catalyst and the efficient dispersion of the small-sized active noble metal (Au, Pd) particles on the oxide (CeO_2, CuO, ZnO) supports. Cao et al.(Huang et al. 2009) demonstrated that the surface structure or the morphology of ceria markedly affects the dispersion and reducibility of Au/CeO_2 catalysts. Most of the cited studies attribute the activity of ceria-supported Au to a direct interaction between the metal and the support. The extent of such interaction, related to the gold particle size and to the support morphology, would affect the electronic state of the CeO_2 substrate. On the other hand, Petrov et al.(Andreeva et al. 2007) suggested that the high activity of gold/ceria catalysts is due to the enhanced electron transfer between defective ceria and partially charged gold particles via oxygen vacancies, with formation of a complex between partially charged gold clusters and the support, so that the oxidation reaction proceeds at the interface between small gold clusters in an intimate contact with ceria. Catalytic activities of CeO_2 nanorods and gold nanoparticles on the CeO_2 nanorods as a function of reaction temperature are shown in Figure 2-15a-e.

It is noted that the CO conversion increases with increasing reaction temperature for all samples. An 81% CO conversion was achieved at 220 °C for Au/CeO_2 nanorods as catalyst, while only 20-22% CO conversion was obtained at the same temperature for pure CeO_2 nanorods and nanoparticles as catalyst. The catalytic activity of Au/CeO_2 nanorods and Au/CeO_2 nanoparticles was much higher than that of pure CeO_2 nanorods and nanoparticles. There could be a synergistic interaction between gold particles and CeO_2 nanorods (Huang et al. 2005, Min and Friend 2007). Corma et al.(Guzman, Carrettin and Corma 2005) found the CeO_2 and rare earth oxide nanocrystals can significantly increase the catalytic activity of dispersed Au nanoparticles for CO oxidation. The decoration of Au nanoparticles on stable CeO_2 nanorods could efficiently prevent Au nanoparticles from the agglomeration. Recently, Venezia et al.(Venezia et al. 2005) found that the reactive oxygen on the surface of nanocrystalline CeO_2 and the strong interaction between cationic gold and ceria might determine the high activity for CO conversion. The smaller CeO_2 nanoparticles might supply more active sites and contributed to the strong interaction between gold and nanocrystalline CeO_2. Therefore, the catalytic activity of Au/CeO_2 nanoparticles was better as compared to that of Au/CeO_2 nanorods.

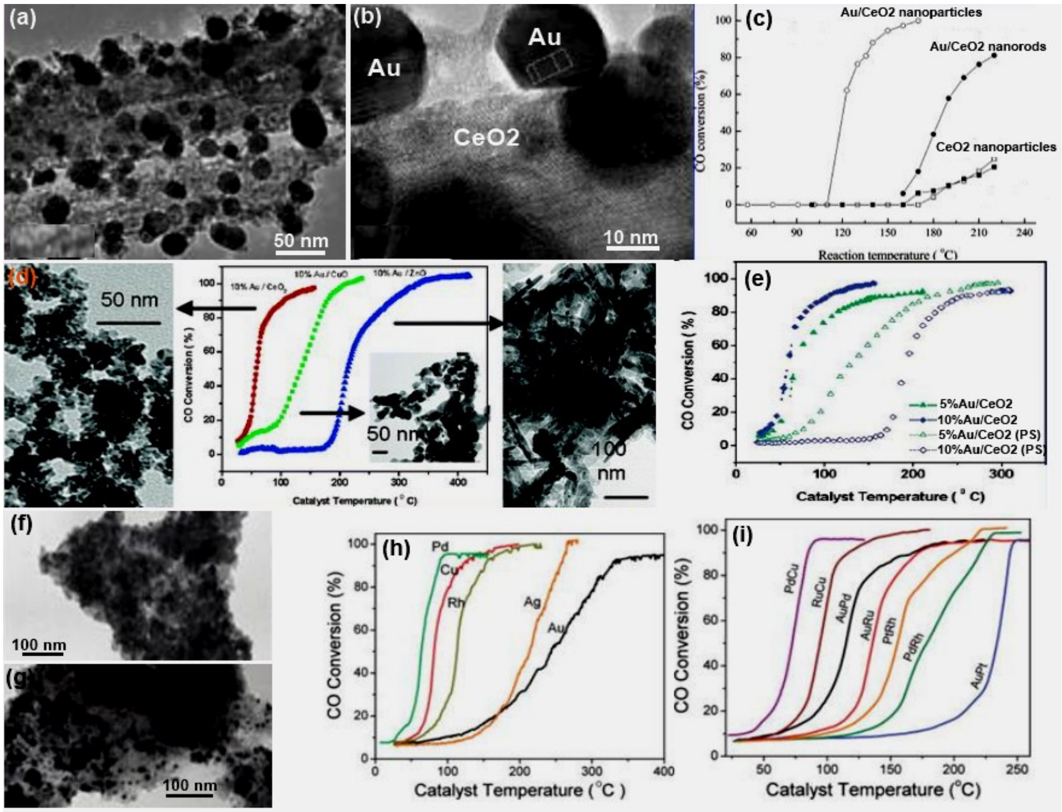

Figure 2.15. CO oxidation catalytic activity over hybrid metal-oxide nanocrystals: (a,b) Au/CeO_2 nanorods, (c) Conversion of CO over Au/CeO_2 nanorods, Au/CeO_2 nanoparticles, CeO_2 nanoparticles (Huang et al. 2009); (d) Conversion of CO over 10%Au/CeO_2 (red line), 10%Au/CuO (green line), 10% Au/ZnO (blue line) nanocatalysts and (e) coversion of

CO over Au/CeO_2 nanocatalysts with different Au components (Glaspell et al. 2005); (f) Pd/CeO_2, (g) Cu/CeO_2, (h) CO oxidationon different metal/CeO_2 nanoparticles, (i) CO oxidation on different bimetallic nanoalloys supported on CeO_2 nanoparticles (Abdelsayed et al. 2009).

Ambient-temperature CO oxidation activity of Pd/CeO_2 was found to increase by more than 20 times after thermal aging at 900 ^oC in air (Figure 2-15f). Although the aging resulted in a significant sintering accompanied by a 92% loss of surface area from 92 to 7 $m^2.g^{-1}$, Pd metal dispersion was preserved at a high degree. Owing to the formation of Pd-O-Ce bonding at the PdO/CeO_2 interface, 1-2 nm-sized Pd oxide species were highly dispersed into the surface structure of CeO_2 that would provide active sites for CO adsorption and following reactions with oxygen near room temperature (Hinokuma et al. 2010). Boronin et al.(Boronin et al. 2009) reported that ambient temperature activity to CO oxidation could be achieved by Pd highly dispersed on CeO_2, which consists of the surface interaction phase ($Pd_xCeO_{2-\delta}$) and very small Pd metal clusters (<1 nm). The catalytic activity of a variety of the selected bimetallic nanoalloys (5 wt.%) supported on CeO_2 nanoparticles prepared by the microwave irradiation method was reported by Alghamdi et al (Abdelsayed et al. 2009). As shown in Figure 2-15i, the highest activity was observed for the nanoalloys according to the order CuPd > CuRh > AuPd > AuRh > PtRh > PdRh > AuPt. Both the CuPd and CuRh supported nanoalloys showed promising results as efficient CO oxidation catalysts with 50% conversions at 74 and 95 ^oC, respectively. The highest conversions for these catalysts were 94% and 96% observed at 86 ^oC and 158 ^oC, respectively. The authors also declared that by alloying Pd into Au, the catalytic activity of Au for CO oxidation can be enhanced.

Catalysts based on combinations between copper and ceria constitute a more interesting alternative from an economical point of view. It is generally agreed that optimum catalytic properties for CO oxidation over copper oxide@ceria catalysts are achieved (Gamarra et al. 2007). Inverse CeO_2/CuO nanocatalysts were used as an alternative to classical direct configurations for preferential oxidation of CO in hydrogen-rich stream. The inverse CeO_2/CuO catalyst displayed the high CO oxidation activity as compared to the classical reference catalyst ($Cu_{0.2}Ce_{0.8}O_2$). The active sites for the CO oxidation reaction were related to interfacial Cu^+ species generated through a reductive process upon interaction with the CO oxidation reactant mixture (Hornés et al. 2009). The $Ce_{1-x}Eu_xO_{2-x/2}$ system presented a high number of surface oxygen vacancies, especially when the amount of dopant was around 10% (w/w). The resultant solid showed the enhanced catalytic properties for the CO oxidation reaction (Hernández et al. 2009).

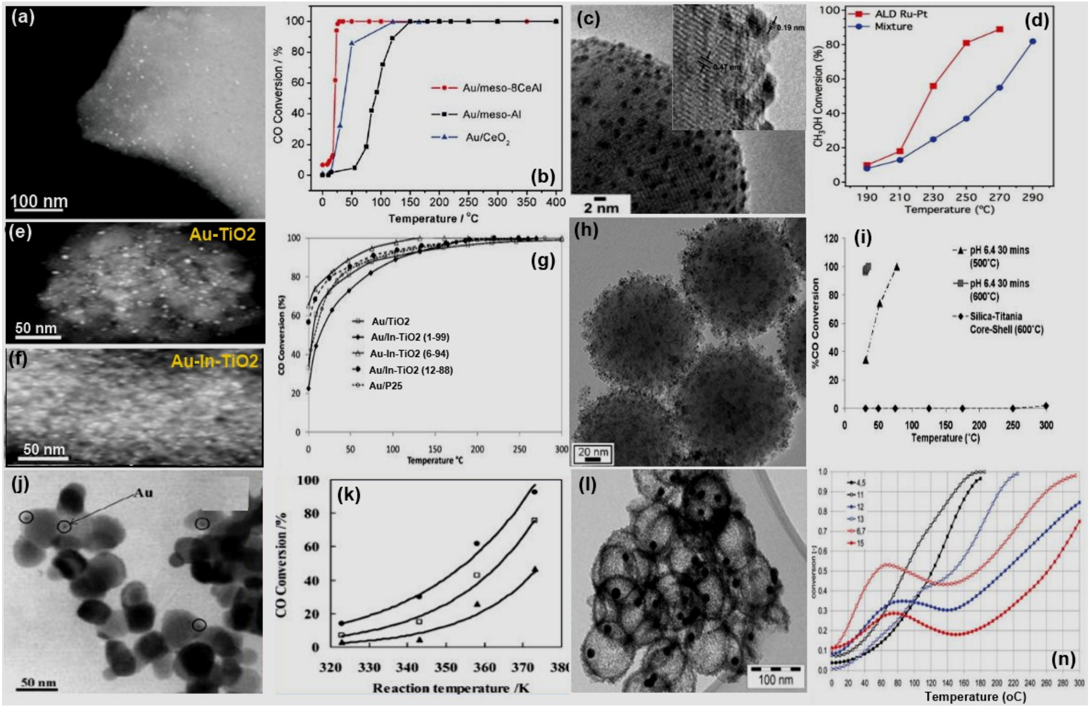

Figure 2.16. CO oxidation catalytic activity over hybrid metal-oxide nanocrystals: (a) Au/Ce-Al oxide mesoporous materials, (b) CO conversion over Au/meso-CeAl (red line), Au/meso-Al (black line), Au/CeO_2 (blue line) at 30 °C (Yuan et al. 2010b); (c) bimetallic Ru-Pt particles doped on alumina sphere, (d) Methanol decomposition over the Ru-Pt bimetallic catalyst (red line) and the physical mixture of Ru + Pt monometallic (blue line) catalysts (Christensen et al. 2010); (e) Au/TiO_2, (f) Au/In-TiO_2, (g) CO oxidation on the Au/In-TiO_2 catalysts and Au/Degussa (P25) reference (Rodríguez-González et al. 2009); (h) Au nanocrystals deposited on silica-titania pebbles and (i) CO conversion of bare silica-titania pebbles, pH = 6.4 gold catalysts without dilution by alumina (Lim et al. 2009); (j) Au/ZrO_2 nanocrystals and (k) catalytic activity of Au/ZrO_2 nanocatalysts (Zhang, Wang

and Xu 2005); (l) Au@ZrO_2 yolk-shell nanocatalysts and (n) CO conversion over Au@ZrO_2 yolk-shells (Pandey et al. 2010).

Yan et al.(Yuan et al. 2010a) achieved the deposition of 7 nm-sized Au nanoparticles on the mesoporous CeO_2-Al_2O_3 nanosupports prepared by the homogeneously dispersed 8 mol% ceria nanocatalyst with the size of 3-4 nm stabilized with ordered mesoporous alumina, for the CO oxidation activity in comparison with pure mesoporous alumina and pure ceria nanoparticles. The evolution of the CO conversion as a function of temperature is presented in Figure 2-16a,b. The sample 1 wt% Au/mesoporous Al_2O_3 gives 100% CO conversion at 150 ^{o}C, while 1 wt% Au/CeO_2 gave a higher activity with 100% conversion at 120 ^{o}C. The 8 wt.% Au/mesoporous Ce-Al oxide catalysts exhibited excellent catalytic activity with 100% conversion occurring at 26 ^{o}C, which was much better than the above two catalysts. This could be attributed to the strong synergistic interaction between the noble metal Au and CeO_2 and the nature of the mesosupport in determining the metallic Au catalysts' activity. Elam et al.(Christensen et al. 2010) synthesized the bimetallic Ru-Pt particles doped on alumina sphere via atomic layer deposition Figure 2-16c). Bimetallic nanoparticles exhibit an enhanced methanol conversion compared to pure Pt and Ru catalysts with similar loading (Figure 2-16d). Gomez et al.(Rodríguez-González et al. 2009) reported that the Au/In-TiO_2 catalysts were more stable than the Au/TiO_2 parent catalyst, resulting the Au/In-TiO_2 catalysts (6 and 12 wt % of In) were more active than the Au/TiO_2 parent catalyst for CO oxidation (Figure 2-16e,f,g).

Influence of synthesis parameters, such as selection of support, reaction pH, aging time, and heat treatment, of the synthesis of Au-decorated silica-titania core-shell on the CO oxidation activity, as shown in Figure 2-16h,i (Lim et al. 2009). Namely, highly dispersed gold over the 600 ^{o}C core-shell supports was obtained at pH 6.4-8.0 with an aging time of 30 min. The 3 nm active metallic gold could be obtained conveniently after mild heat treatment (<200 ^{o}C), but from 300 to 400 ^{o}C, agglomerates (6-20 nm) appear that are less active toward CO catalytic oxidation. The optimized material was synthesized at pH 6.4, displayed high loading and good dispersion of small-sized gold, and achieved

100% CO conversion at 35 ^{o}C. The catalytic activity of Au nanoparticles in Au/ZrO$_2$ for CO oxidation could be greatly improved by reducing the particle size of zirconia nanoparticles (Figure 2-16j,k). The continuous reduction of the ZrO$_2$ nanoparticles was attributed to Au-oxide contact boundaries and due to the presence of a larger number of oxygen vacancies at the surfaces of smaller ZrO$_2$ nanoparticles (Zhang et al. 2005). Besides defects have probably the most significant influence on the catalytic properties. The surface termination of dislocations and stacking faults in small 5 nm Au particles in the microstructure of Au-ZrO$_2$ yolk-shell catalysts act as active centers in CO oxidation (Figure 2-16l,n) (Pandey et al. 2010).

In this dissertation, we have studied on the catalytic activity for CO oxidation that will be limited to Cu@CeO$_2$ nanocrystals as a respresentative sample. The size-dependent catalytic activity can be controlled by tuning the particle size of deposited metallic Cu nanodots.

References

Abdelsayed, V., A. Aljarash, M. S. El-Shall, Z. A. Al Othman & A. H. Alghamdi (2009) Microwave Synthesis of Bimetallic Nanoalloys and CO Oxidation on Ceria-Supported Nanoalloys. *Chemistry of Materials,* 21**,** 2825-2834.

Andreeva, D., I. Ivanov, L. Ilieva, J. Sobczak, G. Avdeev & K. Petrov (2007) Gold based catalysts on ceria and ceria-alumina for WGS reaction (WGS Gold catalysts). *Topics in Catalysis,* 44**,** 173-182.

Boronin, A. I., E. M. Slavinskaya, I. G. Danilova, R. V. Gulyaev, Y. I. Amosov, P. A. Kuznetsov, I. A. Polukhina, S. V. Koscheev, V. I. Zaikovskii & A. S. Noskov (2009) Investigation of palladium interaction with cerium oxide and its state in catalysts for low-temperature CO oxidation. *Catalysis Today,* 144**,** 201-211.

Carbone, L. & P. D. Cozzoli (2010) Colloidal heterostructured nanocrystals: Synthesis and growth mechanisms. *Nano Today,* 5**,** 449-493.

Carrettin, S., P. Concepción, A. Corma, J. M. López Nieto & V. F. Puntes (2004) Nanocrystalline CeO$_2$ Increases the Activity of Au for CO Oxidation by Two Orders of Magnitude. *Angewandte Chemie International Edition,* 43**,** 2538-2540.

Chen, G., C. Xu, X. Song, S. Xu, Y. Ding & S. Sun (2008) Template-free Synthesis of Single-Crystalline-like CeO2 Hollow Nanocubes. *Crystal Growth & Design,* 8**,** 4449-4453.

Chen, M. S. & D. W. Goodman (2004) The Structure of Catalytically Active Gold on Titania. *Science,* 306**,** 252-255.

Christensen, S. T., H. Feng, J. L. Libera, N. Guo, J. T. Miller, P. C. Stair & J. W. Elam (2010) Supported Ru−Pt Bimetallic Nanoparticle Catalysts Prepared by Atomic Layer Deposition. *Nano Letters,* 10**,** 3047-3051.

Creighton J, R. & M. White J. 1982. Transient Low-Pressure Studies of Catalytic Carbon Monoxide Oxidation. In *Catalysis Under Transient Conditions*, 33-58. AMERICAN CHEMICAL SOCIETY.

Cui, R., W. Lu, L. Zhang, B. Yue & S. Shen (2009) Template-Free Synthesis and Self-Assembly of CeO_2 Nanospheres Fabricated with Foursquare Nanoflakes. *The Journal of Physical Chemistry C,* 113**,** 21520-21525.

Dinh, C.-T., T.-D. Nguyen, F. Kleitz & T.-O. Do (2009) Shape-Controlled Synthesis of Highly Crystalline Titania Nanocrystals. *ACS Nano,* 3**,** 3737-3743.

El-Sayed, M. A. (2001) Some Interesting Properties of Metals Confined in Time and Nanometer Space of Different Shapes. *Accounts of Chemical Research,* 34**,** 257-264.

Fröba, M. & A. Reller (1999) Synthesis and reactivity of functional metal oxides in nanoscopic systems. *Progress in Solid State Chemistry,* 27**,** 1-27.

Gamarra, D., C. Belver, M. Fernández-García & A. Martínez-Arias (2007) Selective CO Oxidation in Excess H_2 over Copper−Ceria Catalysts: Identification of Active Entities/Species. *Journal of the American Chemical Society,* 129**,** 12064-12065.

Glaspell, G., L. Fuoco & M. S. El-Shall (2005) Microwave Synthesis of Supported Au and Pd Nanoparticle Catalysts for CO Oxidation. *The Journal of Physical Chemistry B,* 109**,** 17350-17355.

González-Rovira, L., J. M. Sánchez-Amaya, M. López-Haro, E. del Rio, A. B. Hungría, P. Midgley, J. J. Calvino, S. n. Bernal & F. J. Botana (2009) Single-Step Process To Prepare CeO_2 Nanotubes with Improved Catalytic Activity. *Nano Letters,* 9**,** 1395-1400.

Guzman, J., S. Carrettin & A. Corma (2005) Spectroscopic Evidence for the Supply of Reactive Oxygen during CO Oxidation Catalyzed by Gold Supported on Nanocrystalline CeO_2. *Journal of the American Chemical Society,* 127**,** 3286-3287.

Hernández, W. Y., M. A. Centeno, F. Romero-Sarria & J. A. Odriozola (2009) Synthesis and Characterization of $Ce_{1-x}EuxO_{2-x/2}$ Mixed Oxides and Their Catalytic Activities for CO Oxidation. *The Journal of Physical Chemistry C,* 113**,** 5629-5635.

Hinokuma, S., H. Fujii, M. Okamoto, K. Ikeue & M. Machida (2010) Metallic Pd Nanoparticles Formed by Pd−O−Ce Interaction: A Reason for Sintering-Induced Activation for CO Oxidation. *Chemistry of Materials,* 22**,** 6183-6190.

Hornés, A., A. B. Hungría, P. Bera, A. L. p. Cámara, M. Fernández-García, A. Martínez-Arias, L. Barrio, M. Estrella, G. Zhou, J. J. Fonseca, J. C. Hanson & J. A. Rodriguez (2009) Inverse CeO_2/CuO Catalyst As an Alternative to Classical Direct Configurations for Preferential Oxidation of CO in Hydrogen-Rich Stream. *Journal of the American Chemical Society,* 132**,** 34-35.

Huang, P. X., F. Wu, B. L. Zhu, X. P. Gao, H. Y. Zhu, T. Y. Yan, W. P. Huang, S. H. Wu & D. Y. Song (2005) CeO_2 Nanorods and Gold Nanocrystals Supported on CeO_2 Nanorods as Catalyst. *The Journal of Physical Chemistry B,* 109**,** 19169-19174.

Huang, X.-S., H. Sun, L.-C. Wang, Y.-M. Liu, K.-N. Fan & Y. Cao (2009) Morphology effects of nanoscale ceria on the activity of Au/CeO_2 catalysts for low-temperature CO oxidation. *Applied Catalysis B: Environmental,* 90**,** 224-232.

Leng, M., M. Liu, Y. Zhang, Z. Wang, C. Yu, X. Yang, H. Zhang & C. Wang (2010) Polyhedral 50-Facet Cu_2O Microcrystals Partially Enclosed by {311} High-Index

Planes: Synthesis and Enhanced Catalytic CO Oxidation Activity. *Journal of the American Chemical Society,* 132, 17084-17087.

Leong, W. L. & J. J. Vittal (2010) One-Dimensional Coordination Polymers: Complexity and Diversity in Structures, Properties, and Applications. *Chemical Reviews,* 111, 688-764.

Li, G.-R., D.-L. Qu, Z.-L. Wang, C.-Y. Su, Y.-X. Tong & L. Arurault (2009) Ceria-terbia solid solution nanobelts with high catalytic activities for CO oxidation. *Chemical Communications*, 7557-7559.

Liang, S., F. Teng, G. Bulgan & Y. Zhu (2007) Effect of Jahn−Teller Distortion in $La_{0.5}Sr_{0.5}MnO_3$ Cubes and Nanoparticles on the Catalytic Oxidation of CO and CH4. *The Journal of Physical Chemistry C,* 111, 16742-16749.

Lim, S. H., N. Phonthammachai, Z. Zhong, J. Teo & T. J. White (2009) Robust Gold-Decorated Silica−Titania Pebbles for Low-Temperature CO Catalytic Oxidation. *Langmuir,* 25, 9480-9486.

Liu, X., K. Zhou, L. Wang, B. Wang & Y. Li (2009) Oxygen Vacancy Clusters Promoting Reducibility and Activity of Ceria Nanorods. *Journal of the American Chemical Society,* 131, 3140-3141.

Mao, Y., T.-J. Park & S. S. Wong (2005) Synthesis of classes of ternary metal oxide nanostructures. *Chemical Communications*, 5721-5735.

Min, B. K. & C. M. Friend (2007) Heterogeneous Gold-Based Catalysis for Green Chemistry: Low-Temperature CO Oxidation and Propene Oxidation. *Chemical Reviews,* 107, 2709-2724.

Pandey, A. D., R. Güttel, M. Leoni, F. Schüth & C. Weidenthaler (2010) Influence of the Microstructure of Gold−Zirconia Yolk−Shell Catalysts on the CO Oxidation Activity. *The Journal of Physical Chemistry C,* 114, 19386-19394.

Peden Charles, H. F. 1992. Carbon Monoxide Oxidation on Model Single-Crystal Catalysts. In *Surface Science of Catalysis*, 143-159. American Chemical Society.

Rethwisch, D. G. & J. A. Dumesic. 1988. Adsorptive and Catalytic Properties of Carbon Monoxide and Carbon Dioxide Over Supported Metal Oxides. In *Catalytic Activation of Carbon Dioxide*, 102-122. American Chemical Society.

Rodríguez-González, V., R. Zanella, L. A. Calzada & R. Gómez (2009) Low-Temperature CO Oxidation and Long-Term Stability of $Au/In_2O_3{-}TiO_2$ Catalysts. *The Journal of Physical Chemistry C,* 113, 8911-8917.

Tisdale, W. A., K. J. Williams, B. A. Timp, D. J. Norris, E. S. Aydil & X.-Y. Zhu (2010) Hot-Electron Transfer from Semiconductor Nanocrystals. *Science,* 328, 1543-1547.

Venezia, A. M., G. Pantaleo, A. Longo, G. Di Carlo, M. P. Casaletto, F. L. Liotta & G. Deganello (2005) Relationship between Structure and CO Oxidation Activity of Ceria-Supported Gold Catalysts. *The Journal of Physical Chemistry B,* 109, 2821-2827.

Wang, J. & B. Hammer (2007) Oxidation state of oxide supported nanometric gold. *Topics in Catalysis,* 44, 49-56.

Xie, X., P. Shang, Z. Liu, Y. Lv, Y. Li & W. Shen (2010) Synthesis of Nanorod-Shaped Cobalt Hydroxycarbonate and Oxide with the Mediation of Ethylene Glycol. *The Journal of Physical Chemistry C,* 114, 2116-2123.

Xie, X. & W. Shen (2009) Morphology control of cobalt oxide nanocrystals for promoting their catalytic performance. *Nanoscale,* 1, 50-60.

Yang, D., L. Wang, Y. Sun & K. Zhou (2010) Synthesis of One-Dimensional $Ce_{1-x}Y_xO_{2-x/2}$ ($0 \leq x \leq 1$) Solid Solutions and Their Catalytic Properties: The Role of Oxygen Vacancies. *The Journal of Physical Chemistry C,* 114**,** 8926-8932.

Yuan, Q., H.-H. Duan, L.-L. Li, Z.-X. Li, W.-T. Duan, L.-S. Zhang, W.-G. Song & C.-H. Yan (2010a) Homogeneously Dispersed Ceria Nanocatalyst Stabilized with Ordered Mesoporous Alumina. *Advanced Materials,* 22**,** 1475-1478.

Zhang, X., H. Wang & B.-Q. Xu (2005) Remarkable Nanosize Effect of Zirconia in Au/ZrO_2 Catalyst for CO Oxidation. *The Journal of Physical Chemistry B,* 109**,** 9678-9683.

Zhou, H.-P., Y.-W. Zhang, H.-X. Mai, X. Sun, Q. Liu, W.-G. Song & C.-H. Yan (2008) Spontaneous Organization of Uniform CeO2 Nanoflowers by 3D Oriented Attachment in Hot Surfactant Solutions Monitored with an In Situ Electrical Conductance Technique. *Chemistry – A European Journal,* 14**,** 3380-3390.

Zhou, K., X. Wang, X. Sun, Q. Peng & Y. Li (2005) Enhanced catalytic activity of ceria nanorods from well-defined reactive crystal planes. *Journal of Catalysis,* 229**,** 206-212.

2.5.2. Photocatalysis

2.5.2.1. Introduction

Among all photocatalysts, titanium dioxide (TiO_2) has been intensively investigated as a semiconductor photocatalyst since Fujishima and Honda discovered the photocatalytic splitting of water on TiO_2 electrodes in 1972 (Fujishima and Honda 1972). Enhancement of the photocatalytic efficiency of anatase TiO_2 for decomposition of organic compounds and hydrolysis of water has been a challenging subject. When TiO_2 is exposed to UV light, electrons in the uppermost valence band will jump to the conduction band and create conduction band electrons and valence band holes. These electron-hole pairs, which are generated by band gap excitation of TiO_2, are transferred to surface-adsorbed reactants, as shown in Figure 2-17.

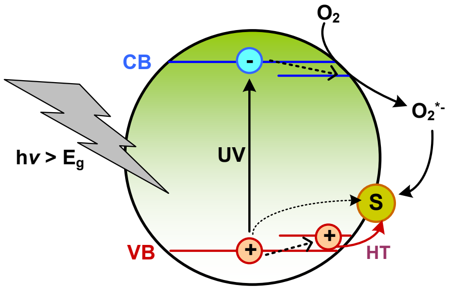

Figure 2.17. Photocatalytic mechanism of pure TiO_2 under UV illumination.

In TiO_2-based photocatalysts, the photogenerated electrons (e^-) and holes (h^+) migrate to the nanocrystal surface, where they act as redox sources, ultimately leading to the destruction of pollutants (Chen and Mao 2007). In most instances, the valence band holes and conduction band electrons simply recombine competitively liberating heat or light, a process known as mutual recombination. Because recombination is expected to occur on grain boundaries and crystalline defects, use of single-crystalline particles with a low density of defects is one of the possible strategies. Indeed, single-crystalline anatase particles exhibited a high level of photocatalytic activity when they had nanoscale particles and large specific surface area leading to more active catalytic sites. However, because of its large band gap (3.2 eV), TiO_2 mainly absorbs ultraviolet light, giving rise to a very low energy efficiency in utilizing solar light. Therefore, new photocatalysts that can be activated under visible light irradiation have been extensively exploited.

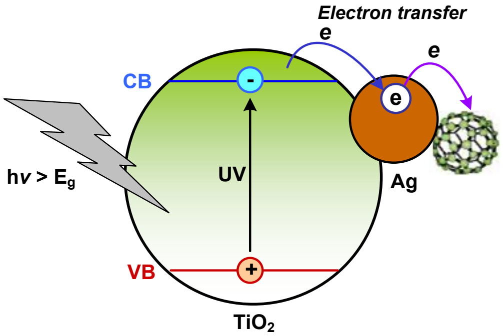

Figure 2.18. Photocatalytic mechanism of metal@TiO_2 under visible-light illumination.

To develop and design TiO_2-based photocatalysts that can operate under visible-light irradiation, modification of the electronic structure of the photocatalyst is indispensable. Two approaches are considered to control the electronic structure of TiO_2, namely (i) modification of the electronic structure of TiO_2 by depositing of metal particles (e.g., hybrid metal@semiconductor) and (ii) formation of a new valence band instead of O 2p by the addition of proper atoms into the lattice of TiO_2 by nonmetal doping (e.g. TiN) (Chen and Mao 2007). Following visible-light absorption, rapid charge separation takes place at the metal-semiconductor interface or in Ti-N lattice, and the separated charges can perform redox chemistry. If the redox potential is lower than the conduction band (CB) of

TiO_2, an electron may be injected from the excited state into the CB, and consequently the cationic radicals and CB electron are formed, as shown in Figure 2-18. Electrochemical and photochemical experiments have shown that the noble metal nanoparticles behave as a mediating role in storing and shuttling photogenerated electrons from the semiconductor to an acceptor in a photocatalytic process (Subramanian, Wolf and Kamat 2004). In recent years, several approaches for the fabrication of metal-semiconductor nanohybrids have been reported, including conventional impregnation and deposition-precipitation techniques, photodeposition (Costi, Saunders and Banin 2010).

2.5.2.2. Types of nanocatalysts

2.5.2.2.1. Single metal oxides

Recently, the application of TiO_2 photocatalysts has mainly been focused on decomposing toxic and hazardous organic pollutants in contaminated air and water, which is of great importance for the environmental protection (Chen and Mao 2007). TiO_2 exists in three main phases: rutile, anatase, brookite (Dambournet, Belharouak and Amine 2009). Structurally, both rutile and anatase crystallize in a tetragonal lattice, while the brookite has orthorhombic lattice. With regard to stability, rutile is thermodynamically the most stable phase of bulk TiO_2 because it has the lowest molecular volume among the three polymorphs. Anatase is less stable than rutile, but more efficient for photocatalytic application. The technological potential of titania is expected to be remarkably extended if a fine-tuning of particle morphology is somehow achieved. Generally, in spherical crystals, benefits arising from higher surface-to-volume ratio with decreasing the particle size are significantly offset by the increased e^-/h^+ recombination probability at surface trapping sites. As a consequence, lower photocatalytic quantum yields are observed for spherical nanocrystals smaller than a certain dimension (about 10 nm). In comparison, rod-shaped titania nanocrystals could lead to considerable advantages in both technological fields, when compared to nearly spherical particles (Cozzoli, Kornowski and Weller 2003). In nanorods, the surface-to-volume ratio is higher than that found in nanospheres, and this would guarantee a high density of active sites available for surface reactions as well as a high interfacial charge carrier transfer rate. Moreover, the increased delocalization of carriers in rods, where they are free to move throughout the length of the crystal, is expected to reduce the e^-/h^+ recombination probability. This could partially compensate for the occurrence of surface trap states and ensure a more efficient charge separation. Further, nanorods could potentially improve charge transport in photovoltaic devices if densely packed thin films were processed with a controlled orientation of the 1D inorganic electron transporters.

Representative TEM/SEM examples and photodegradation graphes of single metal oxide nanocrystals can be found in Figure 2-19. Furthermore the enhancement of photocatalytic efficiency of TiO_2 nanocrystals is dependent on the exposure degree of reactive facets. Yang et al.(Yang et al. 2008) synthesized single-crystalline anatase particles with a largely truncated octahedral shape with exposed {001} facets (Figure 2-19a). Because the {001} surface is more reactive for dissociative adsorption of reactant molecules compared with {101} facets, high photocatalytic efficiency was expected for the truncated octahedral-faceted {001} TiO_2 nanocrystals. The single-crystalline anatase TiO_2 truncated bipyramid-shaped nanocrystals with reactive {001} facets exposed were synthesized by Ohtani et al.(Amano et al. 2009) via the gas-phase reaction of $TiCl_4$. Figure 2-19b displays the extremely high photocatalytic activity for H_2 evolution from the oxidative organic decomposition of the {001}-faceted TiO_2 photocatalysts as compared to P25 that was explained by the low density of crystalline defects. Yang el al.(Yang et al. 2009) reported that synthesized anatase TiO_2 nanosheets having dominant {001} facets (64%) display superior photoreactivity (more than 5 times) compared to P25 as a benchmarking material. Unconventional polyhedron with high-index facets had a greater density of unsaturated atomic steps, edges, and kinks that could serve as active sites for breaking chemical bonds than conventional polyhedron with low-index facets such as octahedron, cube, tetrahedron, and so on. Wang et al.(Liu et al. 2010a) also indicated that the synthesized flower-like TiO_2 nanostructures with exposed {001} facets exhibited enhanced photocatalytic degradation of methylene blue dye under ultraviolet light irradiation (Figure 2-19c). The hollow TiO_2 microspheres composing anatase polyhedra (~20%{001} facets) exhibited the photocatalytic selectivity toward decomposition of azo dyes in water and their activity could be tuned by varying the percentage of {001} facets and by modifying the surface of anatase polyhedra (Liu, Yu and Jaroniec 2010b) (Figure 2-19d).

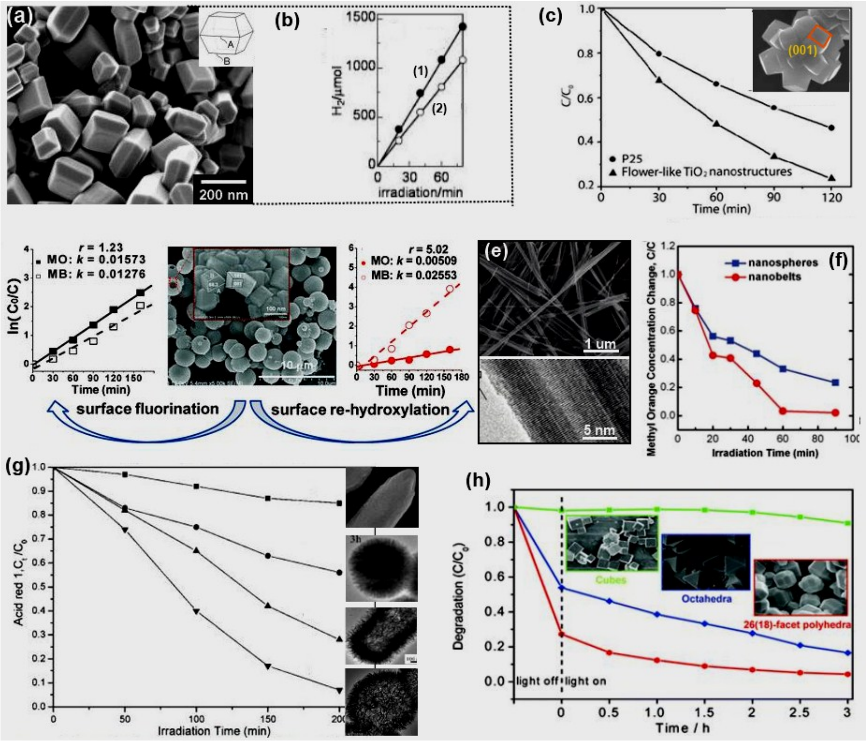

Figure 2.19. The shape-dependent catalytic properties for photodegradation over single metal oxide nanocatalysts: (a) decahedral TiO_2 nanoparticles and (b) photocatalytic H_2 evolution from an aqueous solution of 50 vol. % methanol under an Ar atmosphere in the presence of H_2PtCl_6 containing (1) decahedral TiO_2 nanoparticles and (1) P25-TiO_2 (Yang et al. 2008); (c) The variation of MB concentration by photoelectrocatalytic reaction with P25-TiO_2 powders and flower-like TiO_2 nanostructures, inset of flower-like TiO_2 nanostructures (Liu et al. 2010b); (d) A comparison of photocatalytic decomposition of methyl orange (MO) and methylene blue (MB) by hollow TiO_2 microspheres before and after surface modification (Liu et al. 2010b); (e) anatase TiO_2 nanobelts and (f) degradation of methyl orange in an aqueous solution by the TiO_2 nanobelts and the nanospheres (Liu et al. 2010a); (g) photodegradation of acid red 1 using different catalysts: NiO rod, NiO solid sphere, NiO hollow tube, NiO hollow spheres (Zhou et al. 2008); (h) Photodegradation of MO by Cu_2O polyhedra, octahedral, and cubes (Zhang et al. 2010b).

The morphology dependent-properties on the photocatalytic activity for acid red 1 pollutant decomposition of NiO micro/nanostructures prepared through the solvothermal process showed that hollow hierarchical structures had significantly higher activities than NiO nanorods (Figure 2-19g). Such dramatic activity enhancement could be due to the change of specific surface area (Zhou et al. 2008). Xu et al.(Zhang et al. 2010b) hydrothermally synthesized perfect mixed 26-facet and 18-facet polyhedra, octahedra, cubes of stearic acid-capped Cu_2O microcrystals. The 26-facet and 18-facet Cu_2O polyhedra had a higher adsorption and better photodegradation ability than octahedral and cubes. This finding further implies that the performance of catalysts could be enhanced by shape control as shape determines the number of atoms located at the edges, corners, or surfaces (Figure 2-19h). The hexagonal ZnO platelike particles with exposed reactive {001} facets were found to display ~5 times higher activity in the photocatalytic decomposition of methylene blue than the rod-shaped ZnO particles (McLaren et al. 2009). The hierarchical 10-20 μm WO_3 hollow shells including dendrites, spheres, dumbbells had been synthesized by calcining the acid-treated $PbWO_4$ and $SrWO_4$ precursors (Shevchenko et al. 2008). The morphology-dependent photocatalytic properties of WO_3 hollow shells for the rhodamine B degradation and 2-propanol photodecomposition were investigated. The hierarchical hollow nanostructures exhibited superior photocatalytic activity over the commercial WO_3, due to the large surface area, porous structure, and more surface active sites for hollow dendrites.

2.5.2.2.2. Mixed metal oxides

The enhancement of the photoactivity of the mixed metal oxide nanocrystals could originate from metal-oxide-metal interaction. Figure 2-20 shows photodegradation of organic contaminatants over mixed metal oxide nanocatalysts. The Ag_3VO_4 nanocrystals with a monoclinic structure exhibited photocatalytic activity for decomposing organic pollutants and splitting water under visible-light irradiation (Konta et al. 2003). The 2-3 wt.% RE^{3+} (Nd^{3+}, Eu^{3+}, and Sm^{3+})-loaded Ag_3VO_4 samples were found to exhibit higher photocatalytic activity for degradation of other organic pollutants than pure Ag_3VO_4 due to the synergetic effect of their larger adsorption ability. Nd^{3+}-loaded Ag_3VO_4 showed the highest activity among all of the rare-earth-loaded samples studied (Xu et al. 2009). Gao et al.(Gao et al. 2007) synthesized $BiFeO_3$ nanoparticles, which were used as efficient photocatalysts for the degradation of methyl orange. Li et al.(Li et al. 2010a) also demonstrated that, compared with $BiFeO_3$ microspheres and microcubes, the $BiFeO_3$ submicrocubes showed better photocatalytic activity for degradation of Congo Red under visible-light illumination. Shen et al.(Guo et al. 2010) illustrated the amount of Gd dopant in the $BiFeO_3$ nanoparticles strongly affected the photocatalytic activity for Rhodamine-B decomposition under visible-light illumination (Figure 2-20a,b).

The $NaTaO_3$ nanostructures showed the higher photocatalytic activity in the degradation of Safranine T dye and gaseous formaldehyde than those of solid-state-reacted counterparts and P25, due to their perfective crystallinity and larger surface areas (Li and Zang 2009). The influence of reaction temperature and time, as well as alkaline concentration, on the morphology of the photocatalysts was investigated. The photocatalytic activity of the samples increased with the reaction temperature used for preparing the nanocubes, owing to the better crystalline order of structure formed at higher temperatures. The $In_{1-x}Ni_xTaO_4$ (x = 0-0.2) photocatalysts induced direct splitting of water into oxygen and hydrogen under visible light irradiation that might provide a viable source for clean hydrogen fuel. The catalytic efficiency of the semiconductor system had been improved by increasing its surface area and suitable modifications of the surface sites (Zou et al. 2001). Kudo et al.(Kato and Kudo 2001) reported that $NiO/NaTaO_3$ photocatalysts showed the highest activity when the $NaTaO_3$ photocatalysts were prepared in the presence of excess sodium. Zhu et al.(Xu et al. 2006, Zhang et al. 2008) reported $CaNb_{2-x}Ta_xO_7$ photocatalysts with pyrochlore structure and monomolecular-layer $Ba_5Ta_4O_{15}$ nanosheet with hexagonal structure synthesized by hydrothermal method. Both nanosized particles and nanosheets showed high photocatalytic activity in the degradation of Rhodamine B and gaseous formaldehyde. Single-crystalline $Sr_{0.4}H_{1.2}Nb_2O_6.H_2O$ nanopolyhedrons and $SrNb_2O_6$ nanorods were selectively prepared through one-step hydrothermal reaction of $Nb_2O_5.nH_2O$ and $Sr(NO_3)_2$ under different pH values. The as-prepared nanocrystalline niobates showed the enhanced photocatalytic activity for degradation of methyl orange (MO) (Figure 2-20c,d,e). These results suggested that the mechanism of photocatalytic degradation of MO aqueous solution might be indirect oxidation by *OH or/and *O_2^- free radicals but not direct oxidation by hole (Li et al. 2010b).

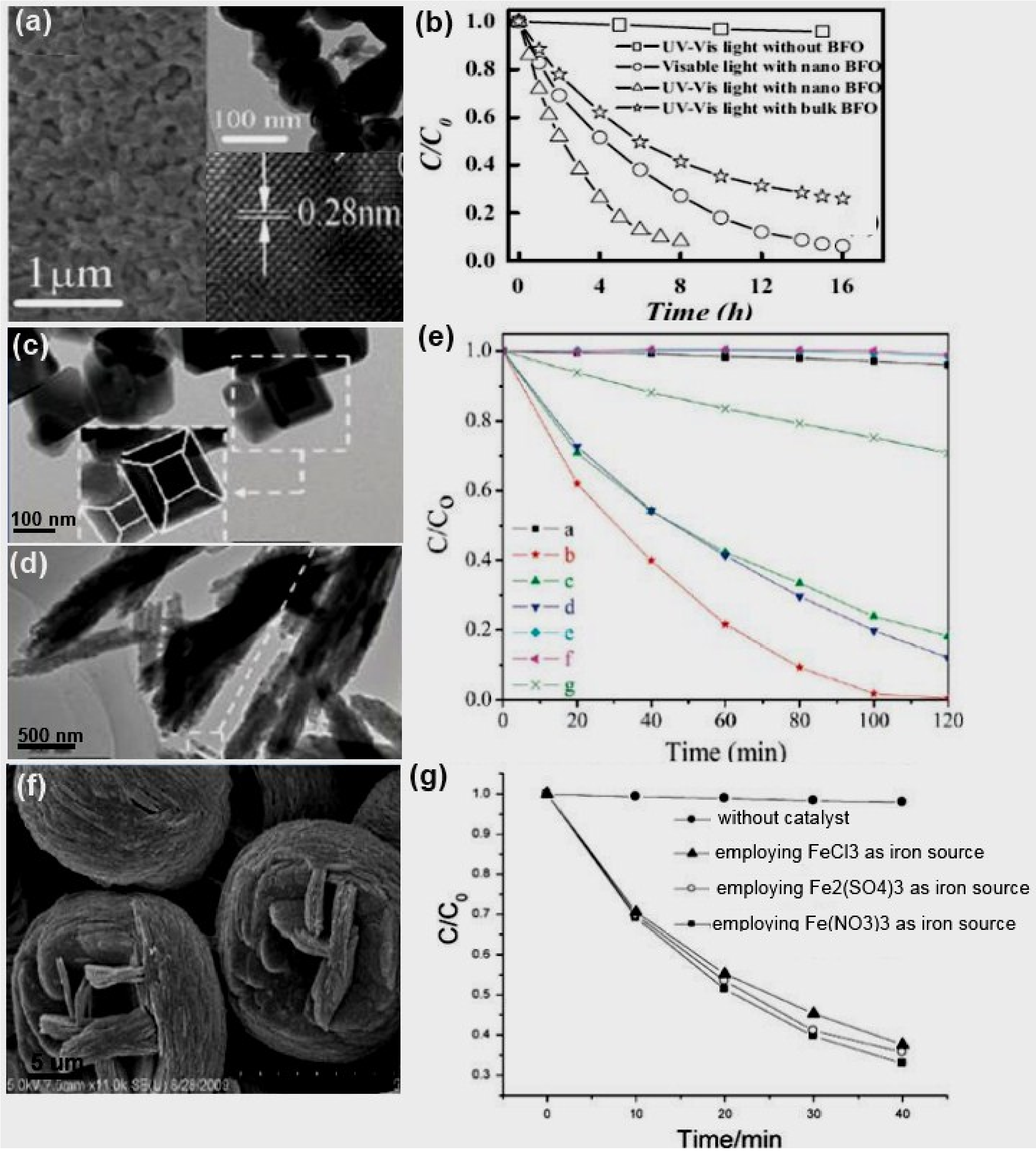

Figure 2.20. Photodegradation of organic contaminatants over mixed metal oxide nanocatalysts: (a) $BiFeO_3$ (BFO) nanoparticles and (b) photocatalysis of BFO nanoparticles and bulk on degradation of methyl orange under UV-vis light irradiation and visible light irradiation (Gao et al. 2007); (c) $Sr_{0.4}H_{1.2}Nb_2O_6.H_2O$ nanocrystals, (d) $SrNb_2O_6$ nanocrystals and (e) Photocatalytic degradation of MO over various photocatalysts under

O_2 flow and UV light irradiation (Li et al. 2010b); (f) self-assemblied $Fe_2(MoO_4)_3$ nanocrystals and (g) photodegradation efficiencies of bromo-pyrogallol red as a function of irradiation time with different catalysts (Zhang et al. 2010a).

The incorporation of transition metals into the anatase phase of TiO_2 has been frequently studied as a way to extend the spectral response to the visible range. In addition, certain $Ti_{1-x}M_xO_2$ phases showed an enhancement of the photoactivity due to structural and electronic modifications induced by the dopant. In this respect, the inclusion of Sn^{4+} in the rutile and the anatase structures led to a significant increment of the rate for the photocatalytic oxidation of acetone (Lin et al. 1999) or methylcyclohexane (Fresno et al. 2006) vapors. Similarly, $Ti_{1-x}M_xO_2$ materials with $x < 0.10$ presented higher photoactivity than anatase TiO_2 for the degradation of acetone in the gas phase (Yu, Lin and Kwok 1998). Besides, nanosized TiO_2-ZrO_2 binary oxides with multiphasic composition also exhibited an increment in the rate for the photocatalytic degradation of different pollutant in both air and aqueous solutions (Schattka et al. 2002). Xu et al.(Xu, Gao and Liu 2002) found that TiO_2 doped with seven different rare-earth ions (Gd-Sm) could enhance the photocatalytic activity as compared to bare TiO_2 for nitrite degradation. It has been demonstrated that the photocatalytic activity of Ce^{3+}-TiO_2 catalysts in 2-mercaptobenzothiazole degradation was significantly enhanced because of a higher adsorption capacity and better separation of electron-hole pairs.

It has been confirmed that tungstates such as Bi_2WO_6, $ZnWO_4$, $AgInW_2O_8$, etc show high photocatalytic activity on decontamination that has received considerable attention. The Bi_2WO_6 with complex flower-, tire-, helix-, plate-like shapes were found that the photocatalytic activities could be greatly improved by controlling the nanostructures, decreasing the particle sizes, etc (Anandan et al. 2007). The Bi_2WO_6 nanocages composing small nanoparticles with size of 50-80 nm exhibited excellent visible-light-driven photocatalytic efficiency, which was increased to nearly 10 times that of products prepared by traditional solid-state reactions and of commercial TiO_2. Close investigation revealed that the surface area and the porous hollow structure of the as-prepared Bi_2WO_6 nanocages could improve the photocatalytic activities (Shang, Wang and Xu 2008). Zhu et al.(Lin, Lin and Zhu 2007) synthesized $ZnWO_4$ nanoparticles and nanorods and studied their photocatalytic activity. The results showed the the photocatalytic activity for both FAD and RhB degradation of $ZnWO_4$ nanorods was much higher than that of nanoparticles. The [100]-preferred orientation growth of the nanorods and perfect crystallinity could enhance the photocatalytic activity of $ZnWO_4$ catalyst. Additionally the hydrogen-related defects could also have influences on the aqueous photodegradation system. Xue et al.(Zhang et al. 2010a) found the pancake-like $Fe_2(MoO_4)_3$ microstructures having the photocatalytic activity toward bromopyrogallol red photolysis directly (Figure 2-20f,g).

2.5.2.2.3. Hybrid metal@oxides

Several researchers reported that modification of the semiconductor surface with noble metal particles is promising as a tool to enhance the photocatalytic activity of semiconductor and to increase the quantum yield (Chen et al. 2010). Figure 2-21 shows photodegradation of organic contaminatants over hybrid metal-oxide nanocatalysts. A representative example of the band structure of Ag-ZnO heterojunction relative to the photocatalytic activity is discussed in literature (Lin et al. 2009). In Ag-ZnO system, electrons will migrate from Ag to the conduction band (CB) of ZnO through Ag-ZnO interaction to achieve the Fermi level equilibration because the chemical potential of ZnO (5.2 eV) is larger than that of Ag (4.26 eV). When the catalysts are illuminated by UV light with photon energy higher than the band gap of ZnO, electrons (e^-) in the valence band (VB) can be excited to the CB with simultaneous generation of the same amount of holes (h^+) left behind. The scheme for the photocatalytic process is shown in Figure 2-18. The deflexed energy band in the space charge region facilitates the rapid transfer of the as-excited electrons from ZnO to Ag nanoparticles, which increases the lifetime of the photogenerated pairs. Electrons accumulated at Ag particles or the conduction band of ZnO can be transferred to oxygen molecules adsorbed on the surface to form free oxygen radicals, such as $^\bullet O_2^-$, $^\bullet HO_2$, $^\bullet OH$, and so forth, while the photoinduced holes react with surface-bound H_2O or OH^- to produce the hydroxyl radical species ($^\bullet OH$) which is an extremely strong oxidant for the mineralization of organic chemicals.

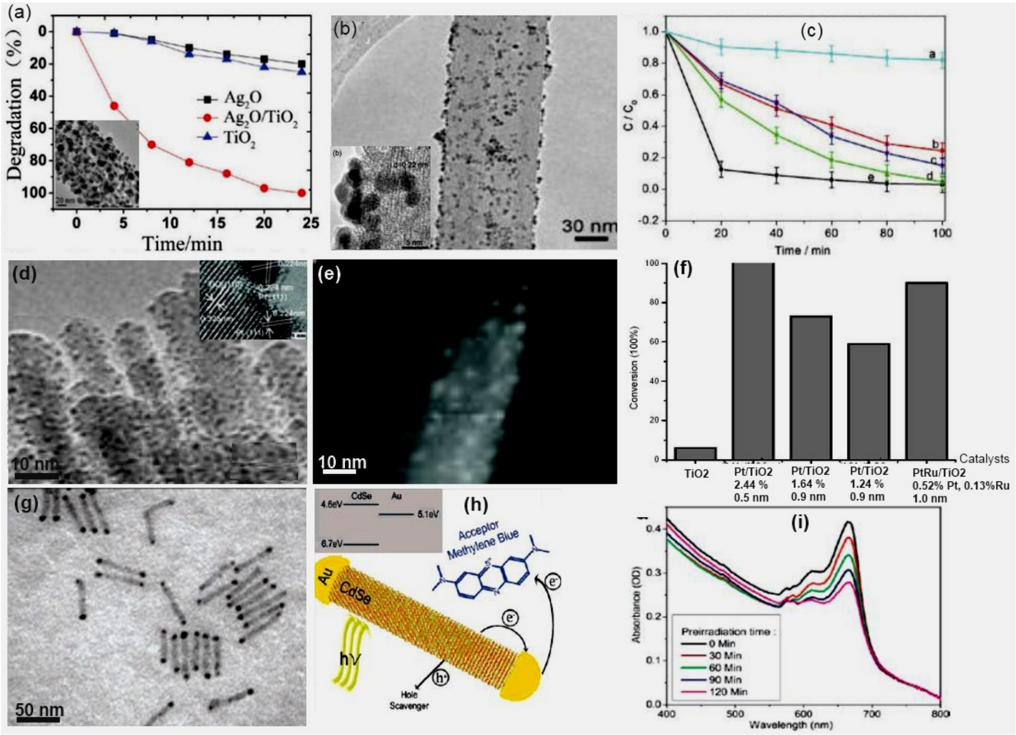

Figure 2.21. Photodegradation of organic contaminatants over hybrid metal-oxide nanocatalysts: (a) Photocatalytic degradation of MO in the presence of Ag_2O, TiO_2 nanobelts, Ag_2O/TiO_2 nanohybrids under UV light irradiation (Zhou et al. 2010); (b) 1 at % Pt/TiO_2 hybrid nanowires; (c) MB photodegradation of without photocatalysts, 2 at% Pt-TiO_2, 0.5 at% Pt-TiO_2, 1 at% Pt-TiO_2, and pure TiO_2 nanowires (Wang et al. 2010); (d,e) Pt/TiO_2 nanorods and (f) MB photodegradation of metallic Pt/TiO_2 and bimetallic $PtRu/TiO_2$ nanohybrids (Xie et al. 2009); (g) hybrid CdSe-Au nanodumbbells, (h) scheme of a light-induced charge separation mechanism in a nanodumbbell and (i) absorbance spectra of MB-nanodumbbells solution (Costi et al. 2008).

It is well-known that the photocatalytic activity closely relates to the diameter size, surface areas, the efficiency of electron-hole separation, etc., of the photocatalysts. Qi et al.(Wang et al. 2010) found that 1 atom% of 5 nm Pt particles on 100-200 nm TiO_2 nanowires had higher photocatalytic activity than 2 at% Pt-TiO_2, 0.5 at% Pt-TiO_2 relative to enhancing the electron-hole separation and charge transfer to dissolved oxygen (Figure 2-21b,c). The shift in the Fermi level of the hybrid system depended on the charge distribution between the smaller Au particles and TiO_2 supports. Hybrid 1.24-2.93 wt.%

Pt/TiO_2 photocatalysts with the Pt particle size ranging from ~0.5 to ~2.3 nm and very narrow size distribution were synthesized through the in situ redox reaction between the reductive titanium(III) oxide support and metal salt precursors in aqueous solution displayed dramatically improved photodegradation efficiency compared to the naked TiO_2 nanorods (Xie et al. 2009). The Pt/TiO_2 photocatalysts with loading of 2.44 wt % 0.5 nm-sized Pt showed the highest efficiency for this reaction, which could almost completely degrade phenol within 1 h (Figure 2-21d,e,f). The significantly enhanced activity should result from the strong synergy between the nanostructured TiO_2 support and tiny Pt particles. It has been widely accepted that Pt particles deposited on TiO_2 can suppress the recombination of electron-hole pairs in TiO_2, where the Pt particles act as electron traps aiding electron-hole separation.

The extensive investigations have been concentrated on the design and synthesis of nanocomposite metal oxides. The ZnO tetrapods coated with TiO_2 nanoparticles were also suggested for high efficiency photocatalysts. The ZnO/TiO_2 composite nanotubes were used for the evaluation of the effective photocatalytic degradation of humic acid. The Fe_3O_4/SiO_2/TiO_2 core-shell nanohybrids with enhanced photocatalytic activity had been synthesized by combining two steps of the sol-gel process with calcination (Ye et al. 2010). The photocatalytic efficiency of the TiO_2 nanocrystal shell increased in the presence of SiO_2 interlayer which helped the chemical and thermal stability of Fe_3O_4 core. Banin et al.(Costi et al. 2008) used visible light to activate a photoreduction reaction under the catalytic CdS-Au nanodumbells and this photocatalyst was possible to retain the charge-separated state for later use in reduction reactions (Figure 2-21g,h,i).

In this dissertation, our work on the catalytic activity of the nanohybrids for Methylene Blue photodegradation will be limited to Ag@TiO_2 nanocrystals as a respresentative sample.

References

Amano, F., O.-O. Prieto-Mahaney, Y. Terada, T. Yasumoto, T. Shibayama & B. Ohtani (2009) Decahedral Single-Crystalline Particles of Anatase Titanium(IV) Oxide with High Photocatalytic Activity. *Chemistry of Materials,* 21, 2601-2603.

Anandan, S., A. Vinu, K. L. P. Sheeja Lovely, N. Gokulakrishnan, P. Srinivasu, T. Mori, V. Murugesan, V. Sivamurugan & K. Ariga (2007) Photocatalytic activity of La-doped ZnO for the degradation of monocrotophos in aqueous suspension. *Journal of Molecular Catalysis A: Chemical,* 266, 149-157.

Chen, X. & S. S. Mao (2007) Titanium Dioxide Nanomaterials: Synthesis, Properties, Modifications, and Applications. *Chemical Reviews,* 107, 2891-2959.

Chen, X., S. Shen, L. Guo & S. S. Mao (2010) Semiconductor-based Photocatalytic Hydrogen Generation. *Chemical Reviews,* 110, 6503-6570.

Costi, R., A. E. Saunders & U. Banin (2010) Colloidal Hybrid Nanostructures: A New Type of Functional Materials. *Angewandte Chemie International Edition,* 49, 4878-4897.

Costi, R., A. E. Saunders, E. Elmalem, A. Salant & U. Banin (2008) Visible Light-Induced Charge Retention and Photocatalysis with Hybrid CdSe−Au Nanodumbbells. *Nano Letters,* 8, 637-641.

Cozzoli, P. D., A. Kornowski & H. Weller (2003) Low-Temperature Synthesis of Soluble and Processable Organic-Capped Anatase TiO_2 Nanorods. *Journal of the American Chemical Society,* 125, 14539-14548.

Dambournet, D., I. Belharouak & K. Amine (2009) Tailored Preparation Methods of TiO_2 Anatase, Rutile, Brookite: Mechanism of Formation and Electrochemical Properties†. *Chemistry of Materials,* 22, 1173-1179.

Fresno, F., D. Tudela, J. M. Coronado, M. Fernandez-Garcia, A. B. Hungria & J. Soria (2006) Influence of Sn^{4+} on the structural and electronic properties of Ti-SnO_2 nanoparticles used as photocatalysts. *Physical Chemistry Chemical Physics,* 8, 2421-2430.

Fujishima, A. & K. Honda (1972) Electrochemical Photolysis of Water at a Semiconductor Electrode. *Nature,* 238, 37-38.

Gao, F., X. Y. Chen, K. B. Yin, S. Dong, Z. F. Ren, F. Yuan, T. Yu, Z. G. Zou & J. M. Liu (2007) Visible-Light Photocatalytic Properties of Weak Magnetic $BiFeO_3$ Nanoparticles. *Advanced Materials,* 19, 2889-2892.

Guo, R., L. Fang, W. Dong, F. Zheng & M. Shen (2010) Enhanced Photocatalytic Activity and Ferromagnetism in Gd-Doped $BiFeO_3$ Nanoparticles. *The Journal of Physical Chemistry C,* 114, 21390-21396.

Kato, H. & A. Kudo (2001) Water Splitting into H_2 and O_2 on Alkali Tantalate Photocatalysts $ATaO_3$ (A = Li, Na, and K). *The Journal of Physical Chemistry B,* 105, 4285-4292.

Konta, R., H. Kato, H. Kobayashi & A. Kudo (2003) Photophysical properties and photocatalytic activities under visible light irradiation of silver vanadates. *Physical Chemistry Chemical Physics,* 5, 3061-3065.

Li, S., Y.-H. Lin, B.-P. Zhang, Y. Wang & C.-W. Nan (2010a) Controlled Fabrication of BiFeO3 Uniform Microcrystals and Their Magnetic and Photocatalytic Behaviors. *The Journal of Physical Chemistry C,* 114, 2903-2908.

Li, X., G. Chen, L. Yang, Z. Jin & J. Liu (2010b) Multifunctional Au-Coated TiO_2 Nanotube Arrays as Recyclable SERS Substrates for Multifold Organic Pollutants Detection. *Advanced Functional Materials,* 20, 2815-2824.

Li, X. & J. Zang (2009) Facile Hydrothermal Synthesis of Sodium Tantalate ($NaTaO_3$) Nanocubes and High Photocatalytic Properties. *The Journal of Physical Chemistry C,* 113, 19411-19418.

Lin, D., H. Wu, R. Zhang & W. Pan (2009) Enhanced Photocatalysis of Electrospun Ag−ZnO Heterostructured Nanofibers. *Chemistry of Materials,* 21, 3479-3484.

Lin, J., J. Lin & Y. Zhu (2007) Controlled Synthesis of the $ZnWO_4$ Nanostructure and Effects on the Photocatalytic Performance. *Inorganic Chemistry,* 46, 8372-8378.

Lin, J., J. C. Yu, D. Lo & S. K. Lam (1999) Photocatalytic Activity of Rutile $Ti_{1-x}SnxO_2$ Solid Solutions. *Journal of Catalysis,* 183, 368-372.

Liu, M., L. Piao, W. Lu, S. Ju, L. Zhao, C. Zhou, H. Li & W. Wang (2010a) Flower-like TiO_2 nanostructures with exposed {001} facets: Facile synthesis and enhanced photocatalysis. *Nanoscale,* 2, 1115-1117.

Liu, S., J. Yu & M. Jaroniec (2010b) Tunable Photocatalytic Selectivity of Hollow TiO_2 Microspheres Composed of Anatase Polyhedra with Exposed {001} Facets. *Journal of the American Chemical Society,* 132, 11914-11916.

McLaren, A., T. Valdes-Solis, G. Li & S. C. Tsang (2009) Shape and Size Effects of ZnO Nanocrystals on Photocatalytic Activity. *Journal of the American Chemical Society,* 131, 12540-12541.

Schattka, J. H., D. G. Shchukin, J. Jia, M. Antonietti & R. A. Caruso (2002) Photocatalytic Activities of Porous Titania and Titania/Zirconia Structures Formed by Using a Polymer Gel Templating Technique. *Chemistry of Materials,* 14, 5103-5108.

Shang, M., W. Wang & H. Xu (2008) New Bi2WO6 Nanocages with High Visible-Light-Driven Photocatalytic Activities Prepared in Refluxing EG. *Crystal Growth & Design,* 9, 991-996.

Shevchenko, E. V., M. I. Bodnarchuk, M. V. Kovalenko, D. V. Talapin, R. K. Smith, S. Aloni, W. Heiss & A. P. Alivisatos (2008) Gold/Iron Oxide Core/Hollow-Shell Nanoparticles. *Advanced Materials,* 20, 4323-4329.

Subramanian, V., E. E. Wolf & P. V. Kamat (2004) Catalysis with TiO_2/Gold Nanocomposites. Effect of Metal Particle Size on the Fermi Level Equilibration. *Journal of the American Chemical Society,* 126, 4943-4950.

Wang, C., L. Yin, L. Zhang, N. Liu, N. Lun & Y. Qi (2010) Platinum-Nanoparticle-Modified TiO_2 Nanowires with Enhanced Photocatalytic Property. *ACS Applied Materials & Interfaces,* 2, 3373-3377.

Xie, Y., K. Ding, Z. Liu, R. Tao, Z. Sun, H. Zhang & G. An (2009) In Situ Controllable Loading of Ultrafine Noble Metal Particles on Titania. *Journal of the American Chemical Society,* 131, 6648-6649.

Xu, A.-W., Y. Gao & H.-Q. Liu (2002) The Preparation, Characterization, and their Photocatalytic Activities of Rare-Earth-Doped TiO_2 Nanoparticles. *Journal of Catalysis,* 207, 151-157.

Xu, H., H. Li, L. Xu, C. Wu, G. Sun, Y. Xu & J. Chu (2009) Enhanced Photocatalytic Activity of Ag3VO4 Loaded with Rare-Earth Elements under Visible-Light Irradiation. *Industrial & Engineering Chemistry Research,* 48, 10771-10778.

Xu, T. G., C. Zhang, X. Shao, K. Wu & Y. F. Zhu (2006) Monomolecular-Layer Ba5Ta4O15 Nanosheets: Synthesis and Investigation of Photocatalytic Properties. *Advanced Functional Materials,* 16, 1599-1607.

Yang, H. G., G. Liu, S. Z. Qiao, C. H. Sun, Y. G. Jin, S. C. Smith, J. Zou, H. M. Cheng & G. Q. Lu (2009) Solvothermal Synthesis and Photoreactivity of Anatase TiO_2 Nanosheets with Dominant {001} Facets. *Journal of the American Chemical Society,* 131, 4078-4083.

Yang, H. G., C. H. Sun, S. Z. Qiao, J. Zou, G. Liu, S. C. Smith, H. M. Cheng & G. Q. Lu (2008) Anatase TiO_2 single crystals with a large percentage of reactive facets. *Nature,* 453, 638-641.

Ye, M., Q. Zhang, Y. Hu, J. Ge, Z. Lu, L. He, Z. Chen & Y. Yin (2010) Magnetically Recoverable Core–Shell Nanocomposites with Enhanced Photocatalytic Activity. *Chemistry – A European Journal,* 16, 6243-6250.

Yu, J. C., J. Lin & R. W. M. Kwok (1998) $Ti_{1-x}Zr_xO_2$ Solid Solutions for the Photocatalytic Degradation of Acetone in Air. *The Journal of Physical Chemistry B,* 102, 5094-5098.

Zhang, L., X.-F. Cao, Y.-L. Ma, X.-T. Chen & Z.-L. Xue (2010a) Pancake-like $Fe_2(MoO_4)_3$ microstructures: microwave-assisted hydrothermal synthesis, magnetic and photocatalytic properties. *New Journal of Chemistry,* 34, 2027-2033.

Zhang, L., H. Fu, C. Zhang & Y. Zhu (2008) Effects of Ta^{5+} Substitution on the Structure and Photocatalytic Behavior of the $Ca_2Nb_2O_7$ Photocatalyst. *The Journal of Physical Chemistry C,* 112, 3126-3133.

Zhang, Y., B. Deng, T. Zhang, D. Gao & A.-W. Xu (2010b) Shape Effects of Cu_2O Polyhedral Microcrystals on Photocatalytic Activity. *The Journal of Physical Chemistry C,* 114, 5073-5079.

Zhou, H.-P., Y.-W. Zhang, H.-X. Mai, X. Sun, Q. Liu, W.-G. Song & C.-H. Yan (2008) Spontaneous Organization of Uniform CeO_2 Nanoflowers by 3D Oriented Attachment in Hot Surfactant Solutions Monitored with an In Situ Electrical Conductance Technique. *Chemistry – A European Journal,* 14, 3380-3390.

Zhou, W., H. Liu, J. Wang, D. Liu, G. Du & J. Cui (2010) Ag_2O/TiO_2 Nanobelts Heterostructure with Enhanced Ultraviolet and Visible Photocatalytic Activity. *ACS Applied Materials & Interfaces,* 2, 2385-2392.

Zou, Z., J. Ye, K. Sayama & H. Arakawa (2001) Direct splitting of water under visible light irradiation with an oxide semiconductor photocatalyst. *Nature,* 414, 625-627.

Chapter 3 Principle of Synthetic Strategies of Colloidal Nanocrystals

3.1. Introduction

For the last 30 years, the synthesis of nanocrystals with sizes ranging from 1 to 50 nm has been intensively pursued, not only for their fundamental scientific interest, but also for their many technological applications (Schmid 2005, Lee et al. 2007, Bryan and Gamelin 2005, Rao, Müller and Cheetham 2005). This size effect has great potential for the design of nanocrystals, because the material properties can be tuned by varying the size and shape. Accordingly, the most important requirement in the synthesis of nanocrystals is the good controllability of their size and shape while maintaining their uniformity. In other words, to fully exploit the potential of nanocrystals with the desired properties, it is essential that they could be synthesized with uniform size and shape. Consequently, the synthesis of monodisperse nanocrystals is great challenging. Recently, several different colloidal solution-phase methods have been developed for the size- and shape-controlled synthesis of monodisperse nanocrystals of various materials including metal oxides (Cushing, Kolesnichenko and O'Connor 2004, Park et al. 2007), mixed metal oxides (Mao, Park and Wong 2005, Wang and Li 2007), and metal-oxide hybrids (Casavola et al. 2008, Mieszawska et al. 2007). The nuclei can be introduced externally or generated in the solution. If the crystallization proceeds with preexisting seeds, this process is called heterogeneous nucleation. Generally, the nucleation occurs randomly all the time during the crystallization process. The nucleation-growth process influences the particle size and shape of the crystal particles. Therefore, understanding of nucleation and growth kinetics of nanocrystal formation is critical for achieving control over size/shape and followed by nanocrystal properties.

3.2. Kinetics of Nucleation and Growth Process

In a typical synthesis of inorganic nanocrystals, the precursor compounds in bulk solution are hydrated or decomposed to generate oxide nuclei and followed by the precipitation starting from dissolved nuclei as building blocks to form the secondary nanocrystals. The thermodynamic driving force for the formation of a new phase is the supersaturation of the solution. A comprehensive good understanding of the process and parameters controlling the precipitation helps to improve the engineering of the growth of nanoparticles to the desired size and shape. The precipitation process then basically consists of a nucleation step followed by particle growth stages. Generally, there are three kinds of nucleation processes: homogeneous nucleation, heterogeneous nucleation, and secondary nucleation. Homogeneous nucleation happens due to the driving force of the thermodynamics because the supersaturated solution is not stable in energy. Seed formation proceeds according to the LaMer model, as shown in Figure 3.1.

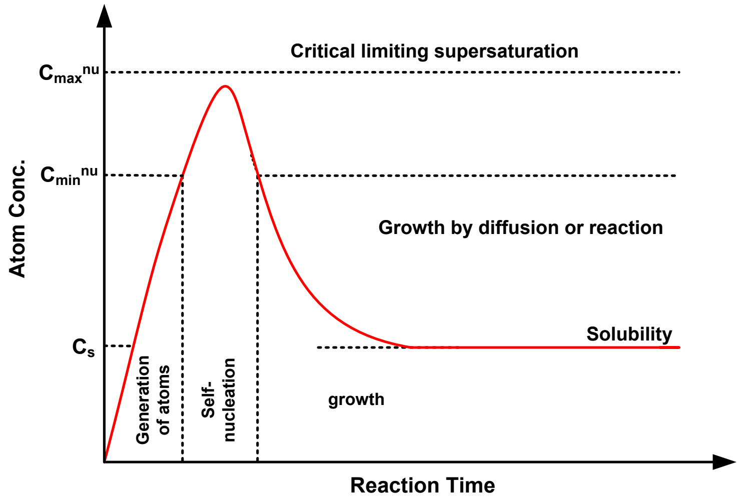

Figure 3.1. Plot of La Mer model for the generation of atoms, nucleation, and subsequent growth of colloidal synthesis.(LaMer and Dinegar 1950).

This mechanism reported in the early 50's on the basis of the crystallization study of the solution-phase synthesis of monodisperse sulfur colloids in ethanol (LaMer and Dinegar 1950). According to LaMer plot for the crystal nucleation process, in which the concentration of atoms steadily increases with time as the precursor is decomposed by heating, colloidal nanocrystal formation comprises the following three steps: (i) The atoms start to aggregate into nuclei via self-nucleation as increasing the monomer concentration in the solution to supersaturation levels; (ii) Then monomers continuously aggregate on the pre-existing nuclei or seed which leads to gradual decrease in the monomer concentration. As long as the concentration of reactants is kept below the critical level, further nucleation is discouraged; (iii) With a continuous supply of atoms via ongoing precursor decomposition, the nuclei will grow into nanocrystals of increasingly larger size until an equilibrium state is reached between the atoms on the surface of the nanocrystal and the atoms in the solution (Watzky and Finke 1997).

3.2.1. Nucleation

The zero-charge nanosized crystalline precursors were firstly produced from decomposing precursor molecules in bulk solution and then nucleated to form clusters such as dimers, trimers, tetramers, etc., in supersaturated solution and finally the initially formed seeds aggregate into larger secondary particles. The monomer is referred to as *M* in the equations. Nucleation increases when the concentration of growth units falls below the minimum supersaturation level. Nucleation involves the formation of a solid phase and the creation of a surface. The nucleation reaction can be regarded as the phase transition of the monomer from solution to crystal. Then, the reaction rate of nucleation can be written in the Arrhenius form (eq. 1):

$$\frac{dN}{dt} = A\exp[-\frac{\Delta G_N}{kT}] \qquad (1)$$

where N, A, k, and T are the number of nuclei, the pre-exponential factor, the Boltzmann constant, and temperature, respectively. ΔG_N is the overall free energy of nucleation and the derivation of ΔG_N is based on thermodynamic considerations. The driving force of crystallization is the change of the chemical potential and, thus, the free enthalpy (eq. 2) of the crystallization reaction.

$$\mu_2 - \mu_1 = \Delta\mu = -kT\ln S \qquad (2)$$

where μ_s and μ_L: the chemical potentials of the solid and the dissolved phase, respectively. $\Delta\mu$: change in the chemical potential during phase transformation of a phase with the chemical potential μ_L into the new phase with the chemical potential μ_s, k = Boltzmann constant, and T = thermodynamic temperature. When a nucleus of radius r forms from the homogeneous solution, the free energy (ΔG) change due to nucleation, in which the new surface with new volume is created that can be expressed by:

$$\Delta G = n(\mu_S - \mu_L) + A_\gamma = 4\pi r^2 \gamma + \frac{4}{3}\pi r^3 \Delta G_V \qquad (3)$$

where n: the number of moles in the nucleus, A: the surface area, and γ: the surface free energy per unit area at the solid-liquid interface, ΔG_V: the free energy per unit volume of crystal. ΔG_V is expressed as the difference between the free energy of the monomer in crystal and solution:

$$\Delta G_V = \frac{RT(\ln C_o - \ln C)}{V_m} = -\frac{RT \ln S}{V_m} \qquad (4)$$

where V_m is the molar volume of the monomer in crystal. C is the monomer concentration in the solution, and C_o is the equilibrium monomer concentration in bulk crystal. S is supersaturation, which is defined as the ratio C/C_o. S represents the driving force for both the nucleation and growth reactions.

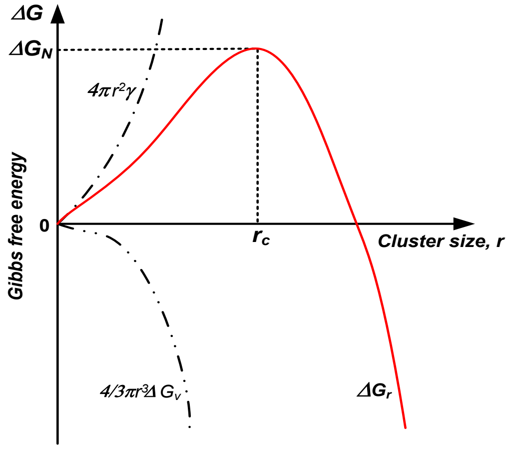

Figure 3.2. Gibbs crystallization free energy as a function of particle radius. The contributions from the surface (dash-dot) and the volume (dash) are plotted separately. r_c and ΔG_N are the critical radius and the corresponding free energy, respectively.

In the homogeneous solution, nucleation is accompanied by the formation of an interface between solution and crystal at the cost of an increase in the free energy. On the other hand, the monomer in crystal has a smaller free energy than that in solution if the solution is supersaturated ($S>1$). Therefore, there are two opposite tendencies in the nucleation reaction. The first is the increase in the free energy caused by the formation of the interface, which is reflected in the first term on the right-hand side of equation 3. This term is always positive. The other tendency is the decrease in the free energy caused by the formation of the crystal, which is shown in the second term, which is negative when $S>1$.

In Figure 3-2, the graph for equation 3 is shown. There is an optimum particle radius, known as the critical cluster size, $r*$, at which ΔG_N reaches a maximum and beyond this point, the formation of stable nuclei is favored. The number of nuclei formed is dependent on supersaturation levels as is the rate of their formation. Because the contributions from the surface and the volume of the nucleus are second- and third-order curves, respectively, their summation has a maximum point at $r = r_c$. The physical meaning of this graph is as follows: for a given value of S, all particles with $r > r^*$ will grow and all particles with $r < r*$ will dissolve. It can be seen from the above equation that a large saturation ratio S implies a small critical nuclei size $r*$. As a result, r_c is the minimum radius of a nucleus that can exist in the solution. The value of r_c can be found by using $d\Delta G/dr = 0$ at $r = r_c$.

$$r_c = -\frac{2\gamma}{\Delta G_V} \qquad (5)$$

Inserting this relation into equation 3 and using equation 4, we obtain the expression for ΔG_N.

$$\Delta G_N = \frac{16\pi\gamma^3}{3(\Delta G_V)^2} = \frac{16\pi\gamma^3 V_m^2}{3(RT\ln S)^2} \qquad (6)$$

Finally, by inserting equation 6 into equation 1, the nucleation rate equation is obtained (eq. 7).

$$\frac{dN}{dt} = A\exp[-\frac{16\pi\gamma^3 V_m^2}{3k^3 T^3 N_A^2 (\ln S)^2}] \qquad (7)$$

where N_A is Avogadro's number.

It can be concluded that the nucleation rate increases strongly with decreasing surface energy and increasing supersaturation. The supersaturation increases with decreasing solubility of the nuclei, and thus, the metal properties have a strong influence on the nucleation rate.

3.2.2. Growth

The growth of the crystal particle in the solution occurs via two processes. The first is the transport of monomers from the bulk solution onto the crystal surface and the second is the reaction of monomers on the surface. In this section, we derive separate equations describing these mechanisms, and then combine them to obtain the general growth rate equation. The description of the first process begins with Fick's law of diffusion:

$$J = -D\frac{dC}{dt} \qquad (8)$$

where J and D are the monomer flux and the diffusion constant, respectively. The concentration gradient near the surface of a nanocrystal particle is shown in Figure 3-2, along with a schematic of the diffusion layer structure. Let x be the radial distance from the center of the particle. The monomer concentration is C_s at the surface of the crystal ($x = r$). At a certain point far enough from the particle ($x = r + \delta$), the concentration reaches C_b, the bulk concentration of the solution. Now, consider a spherical surface of radius x whose center is identical to that of the nanocrystal. From equation 8, the diffusion rate of the monomers, dM/dt, through this surface is

$$\frac{dM}{dt} = J.A = -4\pi x^2 D\frac{dC}{dx} \qquad (9)$$

In the steady state, dM/dt is constant at any x. After dividing both sides with x^2, the equation can be integrated from r to $r + \delta$ and from C_s to C_b for left and right-hand sides, respectively. Then, getting $r << \delta$, we have

$$\frac{dM}{dt} = 4\pi Dr(C_s - C_b) \qquad (10)$$

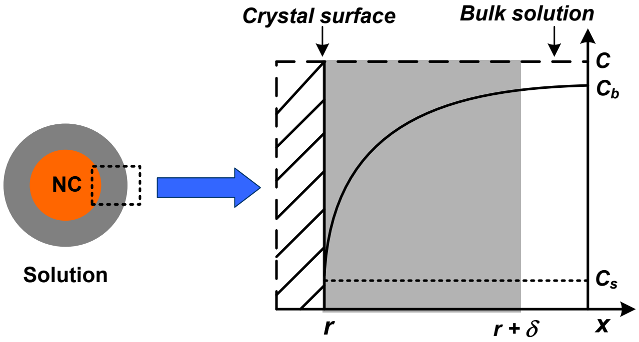

Figure 3.3. Schematic illustration of diffusion layer structure near the surface of a nanocrystal. The shaded area indicates the diffusion layer. Plot for the monomer concentration as a function of distance x.

The increasing rate of the particle volume is equal to the monomer supply rate. In equation form, this can be expressed as:

$$\frac{dM}{dt} = -\frac{4\pi r^2}{V_m}\frac{dr}{dt} \qquad (11)$$

Equating 10 and 11, we get

$$\frac{dr}{dt} = \frac{V_m D}{r}(C_b - C_s) \qquad (12)$$

This is a growth rate equation obtained by considering only the mass transport process. Although simplified, this equation is a good approximation when C_s varies little with r as is the case on the micrometer scale. The hyperbola shape of the graph in Figure 3-2 is derived from this equation. However, on the nanometer scale, C_s is very sensitive to r and equation 12 is far from accurate.

To modify equation 12, we need an expression of C_s as a function of r. This can be obtained by considering the second process of the crystal growth. On the crystal surface, the precipitation and dissolution reactions occur simultaneously. Let M^S and M^C be the monomer in the solution and in the crystal, respectively. Then, the equation for those two reactions is

$$\mathrm{nM^S} \underset{\mathrm{k_d}}{\overset{\mathrm{k_p}}{\rightleftharpoons}} \mathrm{mM_n^C} \tag{13}$$

where k_p and k_d are the reaction rate constants for the precipitation and dissolution, respectively. Their reaction rates are expressed as follows:

$$\frac{dM^C}{dt} = 4\pi r^2 k_p C_S \tag{14}$$

$$\frac{dM^S}{dt} = 4\pi r^2 k_d \tag{15}$$

Note that precipitation is assumed to be a first-order reaction of C_s, while dissolution is independent of it. To obtain the expression for C_s, we utilize the relation between *dM/dt, dM^C/dt, and dM^S/dt*.

$$\frac{dM}{dt} = \frac{dM^S}{dt} - \frac{dM^C}{dt} \tag{16}$$

By inserting equations 10, 13, and 15 into this equation and rearranging, we get an equation for C_s.

$$C_S = \frac{DC_b + k_d r}{D + k_p r} \tag{17}$$

However, because k_p and k_d in this equation are also functions of r, we have to know these functions to complete the derivation of the growth rate equation.

The relation between the chemical potential of a particle and its radius is known as the Gibbs-Thomson relation (Oxtoby 1998). Let μ^o_C and $\mu_C(r)$ be the chemical potentials of bulk crystal and a particle with radius r, respectively. Then, their difference $\Delta\mu$ is

$$\Delta\mu = \frac{2\gamma V_m}{r} \tag{18}$$

That is, the smaller particle has a higher chemical potential. The chemical potential of the particle often depends on the reaction kinetics of precipitation/dissolution of crystals. The smallest particle has the highest chemical potential and the precipitation reaction faces a higher energy barrier than the dissolution reaction. As the particle size increases, the chemical potential of the particle is lowered and the situation is reversed, that is, the barrier for dissolution is higher than the barrier for precipitation. Consequently, the increase of r results in a higher k_p and lower k_d.

The example above can be expressed by equations as follows: In general, the reaction constant is proportional to the term $exp(-\Delta E/RT)$, where ΔE is the molar activation energy. Then, the equations for k_p and k_d reflecting the change of the activation energy according to the chemical potential of the particle are

$$k_p = k_p^o \exp[-\alpha \frac{\Delta\mu}{RT}] \tag{19}$$

$$k_d = k_d^o \exp[(1-\alpha) \frac{\Delta\mu}{RT}] \tag{20}$$

In these equations, α is the transfer coefficient indicates that the parameter is for bulk crystal. Inserting Equation 18 into them yields

$$k_p = k_p^o \exp[-\alpha \frac{2\gamma V_m}{rRT}] \tag{21}$$

$$k_d = k_d^o \exp[(1-\alpha)\frac{2\gamma V_m}{rRT}] \qquad (22)$$

Lastly, putting together equations 12, 17, 21, and 22, we have the general growth rate equation:

$$\frac{dr^*}{d\tau} = \frac{S - \exp(1/r^*)}{r^* + K\exp(\alpha/r^*)} \qquad (23)$$

where the three normalized dimensionless variables are defined as follows:

$$r^* = \frac{RT}{2\gamma V_m} r \qquad (24)$$

$$\tau = \frac{R^2T^2Dk_d^o}{4\gamma^2 V_m k_p^o} t \qquad (25)$$

$$K = \frac{RT}{2\gamma V_m}\frac{D}{k_p^o} \qquad (26)$$

The features of the growth rate function are very important for understanding the size distribution control mechanism. The nucleation and growth occurs until the precursor concentration has equilibrated with the metal, which is determined by the solubility. In Figure 3-2, the graphs of equation 23 are shown. Generally, there is a maximum in the graph, and it converges to zero when $r^* \rightarrow \infty$ and diverges to negative infinity when $r^* \rightarrow 0$. The negative value of the growth rate means that the particle is dissolving. At this point, please recall that the mass transport process allows smaller particles to grow faster than larger ones. The growth rate graphs in Figure 3-2 describe how these two opposite effects compete with each other. Let $r^* = r^*_{max}$ be the position of the maximum in the growth rate. When $r^* < r^*_{max}$, the Gibbs-Thomson effect is overwhelming and the particles are too unstable to grow. In the region where $r^* > r^*_{max}$, the two tendencies take effect simultaneously and the balance between them is largely affected by two parameters, S and K, in which K is a ratio between the diffusion rate and the precipitation reaction rate.

After nucleation and growth, the particle size can change by aging processes, during which the total amount of solid material remains constant. The main aging processes for the evolution of particles are proposed by Ostwald ripening mechanism. According to the Gibbs-Thomson effect, smaller particles tend to dissolve rather than grow, because they are more thermodynamically unstable than larger particles. Coarsening is described by the Gibbs-Thomson equation:

$$c_r = c_{r \rightarrow \infty} \exp\left(\frac{2\gamma V_m}{RTr}\right) \qquad (27)$$

Equation 27 is called the critical nuclei in the given monomer solution because the solubility of particles of this size equals exactly the monomer concentration in the bulk solution. Any particles smaller than this critical size should have higher solubility, and thus should be unstable in the solution. Conversely, larger particles possesses low solubility and are stable under the given conditions. The equilibrium shape (Gibbs-Wulff theory) of a crystal is one that minimizes surface energy for a given enclosed volume (Rottman and Wortis 1981). If the surface energy is isotropic, the equilibrium shape will be spherical as the sphere has the minimum surface area. When the supersaturation level is low, the broadening of the size distribution occurs mainly via the Ostwald ripening process. In this process, a considerable number of the smaller particles dissolve, and the larger particles grow by receiving monomers from the dissolving particles. In some cases in which the particle size distribution is very broad initially, Ostwald ripening could contribute to improving the size uniformity by eliminating the smaller particles.

3.3. Kinetics of Oriented Attachment

The size and shape of nanocrystalline materials strongly impact their properties and reactivity. Thus, investigations into growth and coarsening mechanisms in the nanometer range are fundamental to a clear understanding of how anisotropic nanostructures are formed. Nanocrystal growth in solution typically involves the fast nucleation of primary particles followed by the subsequent growth by two primary mechanisms: coarsening and aggregation. Coarsening, also known as Ostwald ripening, is a mechanism driven by the fact that the chemical potential of a particle increases with a decrease in particle size, which is described by the Gibbs-Thompson equation, as illustrated above. Classical crystal coarsening has been described in terms of growth of large particles at the expense of smaller particles (Ostwald ripening). However, intense research on coarsening behaviour and morphology evolution of nanocrystalline oxide (e.g. titania) prepared under hydrothermal conditions has led to the formulation of a second mechanism of crystal growth. This so-called oriented attachment mechanism describes the spontaneous self-organization of adjacent particles, so that they share a common crystallographic orientation, followed by the joining of these particles at a planar interface. In this mechanism, the primary particles attach to one another at their high-energy faces, they crystallographically fuse and eliminate these faces to produce secondary anisotropic particle with new single crystals or pseudocrystals.

The concept of “oriented attachment” was first demonstrated by Banfield and co-workers in the hydrolytic synthesis of TiO_2 nanocrystals (Penn and Banfield 1999). Truncated diamond-shaped anatase TiO_2 nanocrystals have three different faces: {001}, {121}, and {101}. It is illustrated that the surface energy of the (001) is higher than those of the other surfaces. When there is a sufficient thermal energy in the system, the removal of high-energy surfaces is thermodynamically favorable. Therefore, the fusion of diamond-shaped nanocrystals along the [001] direction is facilitated by the oriented attachment process that results in a necklace-shaped nanocrystal (Figure 3-5a). This research direction has already been used by Huang et al.(Huang, Zhang and Banfield 2003) in the development of a kinetic model used to explain the growth of ZnS nanoparticles induced by hydrothermal treatments. Ribeiro et al.(Ribeiro et al. 2004) also proposed mechanism for oriented attachment growth in dispersed nanoparticles. The authors considered the growth behavior in SnO_2 colloidal suspensions. It was found that coalescence may also occur when particles with similar crystallographic orientations. Penn et al.(Penn and Banfield 1998) developed the kinetic model for oriented attachment. The author had considered primary nanoparticles as molecules. The two primary particles collide at the interface to irreversibly produce a two-dimensional structure with a compatible orientation, whereby kinetics of particle-particle coalescence in suspension may be interpreted as equation 28. P represents a primary particle, and the line represents the chemical bonds between two oriented primary particles. Figure 3-4 illustrates this reaction that shows a high-resolution transmission image of two nanoparticles coalesced in this way.

$$P + P \xrightarrow[-xH_2O]{k} P\text{-}P \qquad (28)$$

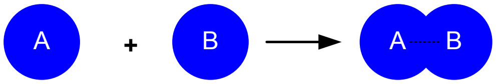

Figure 3.4. Mechanism of oriented collision leading to the colescence of two particles.

Intermediate steps may be related to the yield of effective collisions or to agglomeration and realignment processes. This interpretation has been used by some researchers aiming to gain a more thorough understanding of the growth behavior in colloidal suspensions of several systems. The first experimental observations of this unconventional coarsening behavior and morphology evolution were of nanocrystalline titania prepared under hydrothermal conditions. This work has stimulated many other observations and finally led to the formulation of the oriented-attachment mechanism. This mechanism that the rate of oriented attachment will be kinetic second-order in the number (concentration) of primary nanoarticles, describes the spontaneous self-organization of adjacent particles with a common crystallographic orientation (eq. 29).

$$d(P-P)/dt = k(P)^2 \qquad (29)$$

where $[P]$ is the concentration of primary (i.e., uncoalesced) particles (particles/volume) and k is the reaction constant. Assuming that the reaction occurs in a single step, $[P]$ is defined in terms of the initial concentration $[P]_o$ by equation (30):

$$[P] = \frac{[P]_o}{1 + 2k[P]_o t} \qquad (30)$$

Similar observation for oriented attachment process was made later by many research groups. Murray et al.(Cho et al. 2005) had performed the nonhydrolytic growth of

PbSe nanocrystal synthesis. Through aging processes, PbSe nanospheres were aligned and fused together along a specific axis (Figure 3-5b,c) and after surface reconstruction processes resulted in well-defined nanowires. Variations of either the shapes of the building blocks or the attachment directions yield a variety of nanocrystal shapes including wires, zigzags, helices, branches, and rings (Figure 3-5d,e). Some authors have reported that the formation of highly anisotropic structures (e.g. nanowires) occurs by oriented attachment and depends on the existence of a mechanism for organized agglomeration. Xu et al.(Zhang et al. 2007) demonstrated the influence of the alkylamine chain length of surfactant on the shape evolution of Y_2O_3:Tb nanostructures from spherical nanocrystals to self-assemblied anisotropic nanorods (Figure 3-5f).

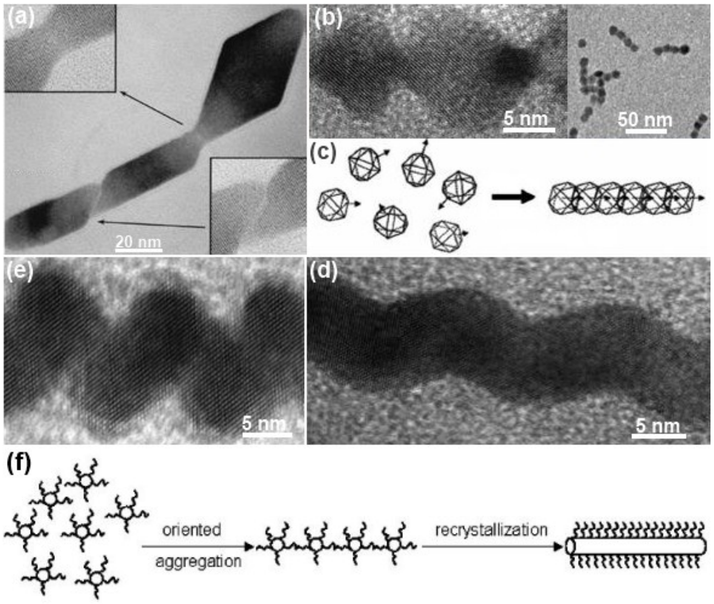

Figure 3.5. Schematic representations of oriented attachment process: (a) The initial 0D nanocrystals align and come together along their dipole direction. After surface reconstruction to minimize the surface energy, aligned diamond-shaped TiO_2 particles are obtained (Penn and Banfield 1999); (b) Aggregated oligomers of PbSe nanocrystals were intermediates during the oriented attachment processes; (c) oriented attachment mechanism, by controlling the reaction parameters, various shapes of nanocrystals including straight (e) PbSe zigzag chains and (d) helices are obtained (Cho et al. 2005); (f) the self-assembly mechanism of Eu^{3+}:Y_2O_3 nanorods (Zhang et al. 2007).

Li et al.(Meng et al. 2009) recently fabricated highly uniform coalescent moniliforme-shape α-Fe_2O_3 straight nanochains from the self-assembly of the primary polyhedron particles (Figure 3-6). The metastable oleic acid/oleylamine-capped α-Fe_2O_3 polyhedron particles emerge from the solution under a kinetic growth regime at the early stage. Through aging processes, the polyhedron particles attached to each other at the high energy facet {001} to generate α-Fe_2O_3 straight nanochains. When two nanoparticles approach each other closely, they are attracted by van der Waals forces. However, due to their thermal energy they can still rearrange to find the low-energy configuration represented by a coherent particle-particle interface. The particles appear fused almost end-to-end along the longitudinal axis and form linear chains. As has been widely accepted, the metastability of colloidal particles can be controlled not only according to the reaction conditions but also by the effects of surfactants selective adhesion, since the organic capping additive molecules as controlled aggregation agents can bind tightly to special crystal facets and restrain their growth while the others are restricted.

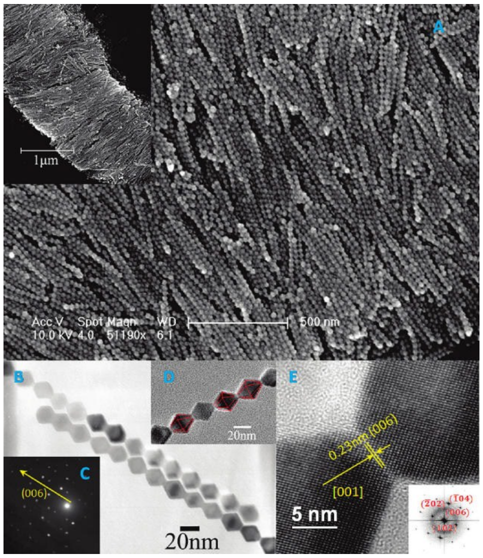

Figure 3.6. (A) SEM images of the moniliforme-shaped Fe_2O_3 nanostructures; (B) TEM image of two nanochains abutting each other side by side. The corresponding electron diffraction pattern is shown in part C; (D) TEM image of the truncated hexagonal bipyramid particle-units; (E) Lattice-resolved HRTEM image taken from the contact area of two contiguous particles and the associated FFT pattern (Meng et al. 2009).

References

Bryan, J. D. & D. R. Gamelin. 2005. *Doped Semiconductor Nanocrystals: Synthesis, Characterization, Physical Properties, and Applications*. John Wiley & Sons, Inc.

Casavola, M., R. Buonsanti, G. Caputo & P. D. Cozzoli (2008) Colloidal Strategies for Preparing Oxide-Based Hybrid Nanocrystals. *European Journal of Inorganic Chemistry,* 2008**,** 837-854.

Cho, K.-S., D. V. Talapin, W. Gaschler & C. B. Murray (2005) Designing PbSe Nanowires and Nanorings through Oriented Attachment of Nanoparticles. *Journal of the American Chemical Society,* 127**,** 7140-7147.

Cushing, B. L., V. L. Kolesnichenko & C. J. O'Connor (2004) Recent Advances in the Liquid-Phase Syntheses of Inorganic Nanoparticles. *Chemical Reviews,* 104**,** 3893-3946.

Huang, F., H. Zhang & J. F. Banfield (2003) The Role of Oriented Attachment Crystal Growth in Hydrothermal Coarsening of Nanocrystalline ZnS. *The Journal of Physical Chemistry B,* 107**,** 10470-10475.

LaMer, V. K. & R. H. Dinegar (1950) Theory, Production and Mechanism of Formation of Monodispersed Hydrosols. *Journal of the American Chemical Society,* 72**,** 4847-4854.

Lee, D. C., D. K. Smith, A. T. Heitsch & B. A. Korgel (2007) Colloidal magnetic nanocrystals: synthesis, properties and applications. *Annual Reports Section "C" (Physical Chemistry),* 103**,** 351-402.

Mao, Y., T.-J. Park & S. S. Wong (2005) Synthesis of classes of ternary metal oxide nanostructures. *Chemical Communications***,** 5721-5735.

Meng, L. r., W. Chen, C. Chen, H. Zhou, Q. Peng & Y. Li (2009) Uniform α-Fe_2O_3 Nanocrystal Moniliforme-Shape Straight-Chains. *Crystal Growth & Design,* 10**,** 479-482.

Mieszawska, A. J., R. Jalilian, G. U. Sumanasekera & F. P. Zamborini (2007) The Synthesis and Fabrication of One-Dimensional Nanoscale Heterojunctions. *Small,* 3**,** 722-756.

Oxtoby, D. W. (1998) Nucleation of First-Order Phase Transitions. *Accounts of Chemical Research,* 31**,** 91-97.

Park, J., J. Joo, S. G. Kwon, Y. Jang & T. Hyeon (2007) Synthesis of Monodisperse Spherical Nanocrystals. *Angewandte Chemie International Edition,* 46**,** 4630-4660.

Penn, R. L. & J. F. Banfield (1998) Imperfect Oriented Attachment: Dislocation Generation in Defect-Free Nanocrystals. *Science,* 281**,** 969-971.

Rao, C. N. R., A. Müller & A. K. Cheetham. 2005. *Nanomaterials – An Introduction*. Wiley-VCH Verlag GmbH & Co. KGaA.

Ribeiro, C., E. J. H. Lee, T. R. Giraldi, E. Longo, J. A. Varela & E. R. Leite (2004) Study of Synthesis Variables in the Nanocrystal Growth Behavior of Tin Oxide Processed by Controlled Hydrolysis. *The Journal of Physical Chemistry B,* 108**,** 15612-15617.

Rottman, C. & M. Wortis (1981) Exact equilibrium crystal shapes at nonzero temperature in two dimensions. *Physical Review B,* 24**,** 6274.

Schmid, G. 2005. *General Introduction*. Wiley-VCH Verlag GmbH & Co. KGaA.

Wang, X. & Y. Li (2007) Monodisperse nanocrystals: general synthesis, assembly, and their applications. *Chemical Communications***,** 2901-2910.

Watzky, M. A. & R. G. Finke (1997) Transition Metal Nanocluster Formation Kinetic and Mechanistic Studies. A New Mechanism When Hydrogen Is the Reductant: Slow, Continuous Nucleation and Fast Autocatalytic Surface Growth. *Journal of the American Chemical Society,* 119**,** 10382-10400.

Zhang, Y., J. Guo, T. White, T. T. Y. Tan & R. Xu (2007) Y_2O_3:Tb Nanocrystals Self-Assembly into Nanorods by Oriented Attachment Mechanism. *The Journal of Physical Chemistry C,* 111**,** 7893-7897.

Chapter 4 Size and Shape Control

4.1. Introduction

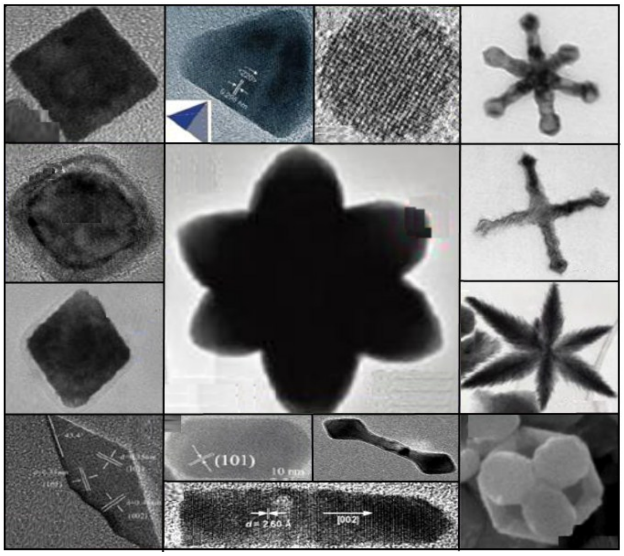

Figure 4.1. Galleries of representative colloidal inorganic nanocrystals with controlled shapes synthesized by surfactant-assistant pathways.

Nanocrystal formation can be simply understood as two-step processes: nucleation initiated by sudden increase of monomer concentration up to super-saturation levels and the subsequent growth from the seed with progressive consumption of monomers in solution. The final geometry of nanocrystals is determined by several parameters during these nucleation and growth processes. Figure 4-1 shows a gallery of multi-morphology of nanocrystals obtained by surfactant-assisted synthetic routes. Initially, the crystalline phase of the seed at the nucleating stage is the critical parameter for directing nanocrystal shapes due to its characteristic unit cell structure. The nanocrystal seeds are formed with a specific crystalline phase, several other factors for controlling the subsequent growth processes will affect the final geometry of nanocrystals. Such key factors include the intrinsic surface energy of different crystallographic surfaces, the role of surface selective capping agent, and the choice of the nanocrystal growth regime between thermodynamic and kinetic processes. We describe the effect of key factors on the nanocrystal shape determination, including crystalline phase effect of seeds, surface energy effect, and control of the growth regime. By variation of the type and relative concentration of the metal precursor and capping agent, as well as reaction conditions such as temperature and time, the size and shape of nanocrystals can be controlled. In this section, we review the key issues that need to be carefully considered the critical parameters for the size and shape control of colloidal nanocrystals.

4.2. Critical Parameters for Nanocrystal Size and Shape Determination

4.2.1. Effect of surfactant

The development of colloidal methods for the preparation of nanocrystals has opened interesting opportunities in nanoscience. Colloidal nanocrystals are particles grown in the solution phase. Nanocrystals with large surface area have a strong tendency to aggregate to relieve their high surface free energy. Using surfactant to reduce the surface tension of nanocrystals is essential in the colloidal chemical synthesis of nanocrystals. In these cases, the surfactant allows us to control the nanocrystal growth. The surfactant molecules are dynamically adsorbed to the surface of the growing crystal under the synthesis conditions. They must be mobile enough to provide access for the addition of monomer units, while stable enough to prevent the aggregation of nanocrystals. In addition, the surfactant molecules must be stable at the high temperatures (100-400 ^{o}C) required for the growth. The appreciative choice of surfactants is essential varying from case to case: an organic ligand molecule that binds too strongly to the surface of the crystal is not suitable, as it would not allow the crystal to grow. However, a weakly coordinating molecule would yield large particles, or aggregates. Most commonly used surface modification methods include fatty acids, alkyl amines, alkyl phosphines, phosphine oxides, aminoacids, nitrogen-containing aromatics, alkyl ammoniums, block copolymers, etc. In addition, the capping agent plays several different roles in the nanocrystal synthesis. The polar head groups of the surfactants cap on the surface of the nanocrystals and the long alkyl chains in the tail groups of the surfactants outward to reaction solvent to induce a good colloidal stability via so-called steric stabilization, as shown in Figure 4-2.

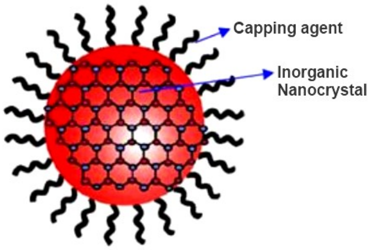

Figure 4.2. Structure of a colloidal organic ligand-capped inorganic nanocrystal.

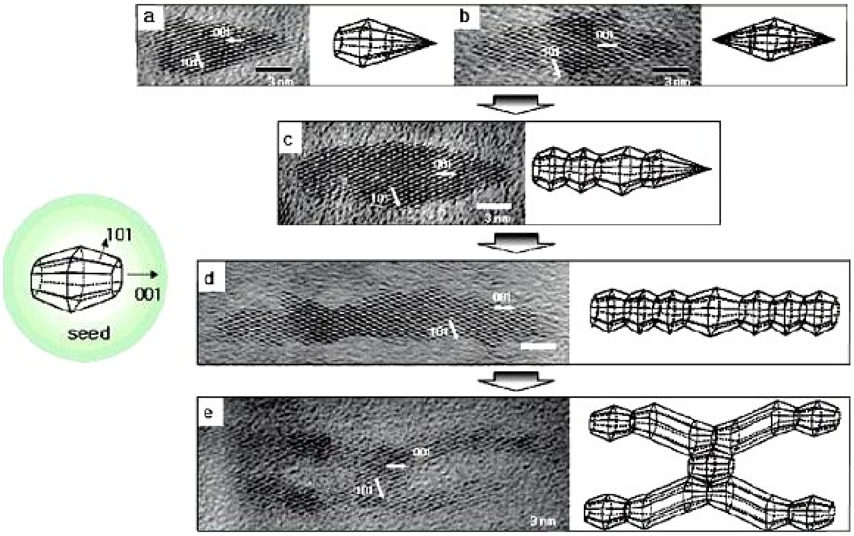

Figure 4.3. Shape evolution of TiO_2 nanocrystals depending on the concentration of lauric acid molecules: (a) bullets, (b) diamonds, (c) short rods, (d) long rods, (e) branched rods (Jun et al. 2003).

The advantage of colloidal surfactant-assisted methods is that they yield monodisperse inorganic nanocrystals and their size and shape can be easily manipulated. In order to control the growth, the surface energies must be changed by adjusting the types and amount of organic surfactants. By using mixed surfactants that bind differently to the different crystallographic faces, the shape of nanocrytals can be easily controlled by the selective absorption. Such surface energy (ΔG) difference results in significant growth rate differences between different crystallographic directions, since the growth rate is exponentially proportional to the surface energy. Through its chemical interaction with a metal surface, the presence of a capping agent can change the order of free energies for different crystallographic facets, and thus their relative growth rates. The growth processes should be quenched at appropriate times, since longer growth times can result in thermodynamically stable shapes of nanocrystals. Finally, the molecular precursor can decompose under mild condition, is critical for the kinetic growth process.

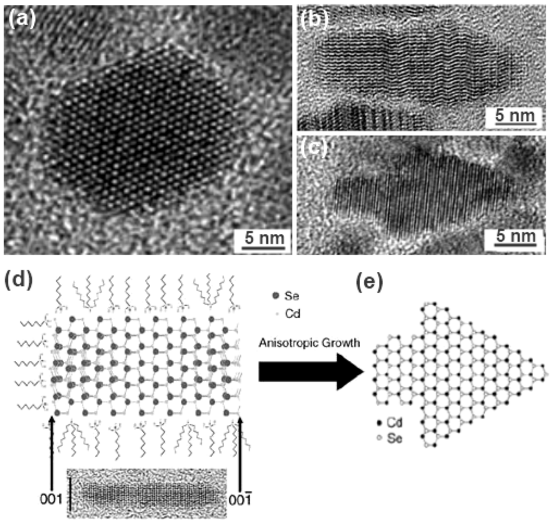

Figure 4.4. Shape control of CdSe nanocrystals: (a) A single CdSe nanocrystal looking down the [001] axis of the wurtzite structure, (b) an arrow-shaped and a tree-shaped (c) nanocrystal, (d) Proposed growth mechanism for CdSe nanorods and (e) arrow-shaped nanocrystals. The organic surfactants cannot coat one face of the nanocrystal, which raises the energy of this face allowing it to grow quickly and form a rod shape (Manna, Scher and Alivisatos 2000).

The one-dimensional shape evolution of anatase TiO_2 nanocrystals can also be a good example for examining the surface energy effect (Jun et al. 2003). TiO_2 anatase has a tetragonal structure and has been shown to nucleate as truncated octagonal-bipyramid seeds, exposing eight equivalent {101}-faces and two-equivalent {001}-faces (Figure 4-3). According to Donay-Harker rules, the surface energy of the {001}-faces is ~1.4 times larger than that for the {101}-faces. The significant difference of the intrinsic surface energy induces the formation of bullet- and diamond-shaped nanocrystals, arising from the shrinking of the {001}-faces and the complete elimination of the {001}-faces at one or two ends of the truncated octahedral bipyramid seed, respectively (Figure 4-3a,b). However, when organic acid molecules are involved as capping molecules in the reaction, the capping molecules selectively bind to the {001}-faces and reduce the growth rate along the {001}-directions. Under the reduced growth rate along the [001] direction, which is close to 2.7 times that of the [101] direction, monomers continuously grow further onto both the {001} and the {101}-faces of the truncated octahedral bipyramid seeds. This results in the progressive elongation along the [001] direction while the [001] surface area is preserved (Figure 4-3c,d). Further retardation of the growth rate along the [001] direction, at a higher concentration of organic acid, induces the formation of branched nanorods, which is a result of the growth from the equivalent {101}-faces of the truncated octahedral bipyramid seeds (Figure 4-3e).

The shape evolution of PbS nanocrystals with a symmetric rock-salt structure provides a good example of such processes (Lee et al. 2002). Rapid injection of a PbS molecular precursor into hot reaction solution induces the formation of tetradecahedron seeds that are terminated by {100} and {111) facets. Subsequent competitive growth on these two different types of crystalline faces determines the final shape. In rock-salt structures, the {111} surface typically has a higher surface energy than that of the {100} surface. When excess thermal energy is supplied by utilizing high growth temperature (~250 ^{o}C), the thermodynamic regime governs the growth process resulting in the faster growth on the {111} facets and favors the formation of cube-shaped PbS nanocrystals (~80 ^{o}C). However, in the presence of a dodecanethiol surfactant that binds strongly to the {111} surface while weakly binding to {100} facets, the surface energy of the {111} facets can be selectively lowered relative to that of the {100} faces. Therefore, under conditions of low temperature (120 ^{o}C) and in the presence of dodecanethiol as the capping molecule, the growth process shifts into the kinetic growth regime, growth on the {100} facets with high surface energy is preferred, and 1D rod-based single- and multi-pod structures result. Morever, at intermediate temperature (e.g., 180 ^{o}C), as a transient species, star-shaped nanocrystals possessing both the characteristics of 0D and 1D structure are formed.

Selective adhesion of surfactants is critical in the synthesis of CdSe nanorods (Manna et al. 2000, Peng et al. 2000). The choice of capping molecules can be a means of controlling the shape of nanocrystals. Since the capping molecules dynamically bind to the crystal surface during the nucleation and crystal growth, the conformation of crystal structure is highly affected by the identity of the capping molecules. When dimethylcadmium and TOPSe are injected into a hot surfactant mixture of TOPO and HPA, the amount of HPA that selectively binds to the {100}- and {110}-facets of the growing crystals modulates the growth pattern. At low HPA concentration or in the absence of HPA, only spherical nanocrystals are formed. However, with higher HPA concentrations, nanorods are obtained since the surface-bound HPA molecules serve to reduce the growth along {100} and {110} surfaces (Figure 4-4).

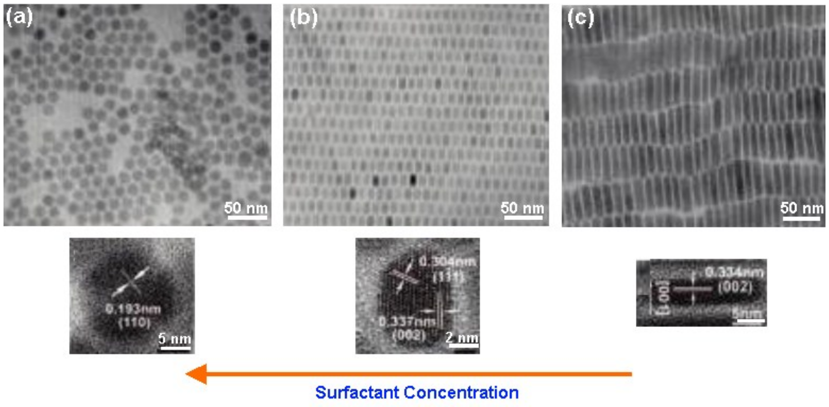

Figure 4.5. Effect of surfactant concentration on the evoluation shape. The shape of Cu_2S nanocrystals evolved from circular to elongate nanocrystal as increasing the content of Cu^{2+} and dodecanethiol: (a) 0.24 g Cu^{2+}: 3 ml dodecanethiol, (b) 0.12 g Cu^{2+}: 0.5 ml dodecanethiol (Zhuang et al. 2008).

The surface energy of the nanocrystals can be modulated by introducing surfactants that adsorb onto surfaces of growing crystallites. When surfactants stabilize a certain surface by "selective adhesion", the growth rate difference between different crystallographic directions can be accentuated. The formation of copper sulfide nanodiscs in the presence of surface selective alkanethiol surfactant is a good example (Zhuang et al. 2008). The alkanethiol molecules strongly adsorb on the {001} faces of Cu_2S and, by lowering the surface energy, 2D Cu_2S nanodiscs are formed (Figure 4-5). Shi et al.(Bu et al. 2009) ultilized a mixed surfactant of oleic acid/oleylamine as decisive structure-directing agent for the monodisperse $NaLa(MoO_4)_2$ and $NaLa(MoO_4)_2:Eu^{3+}$ bipyramid nanocrystals. Deprotonated oleic acid mainly led to the formation of well-defined tetragonal bipyramid morphology via the preferential adsorption of deprotonated oleic acid onto {101} and {001}, while facilitating the formation of bipyramid morphology with exposed {101} faces (Figure 4-6).

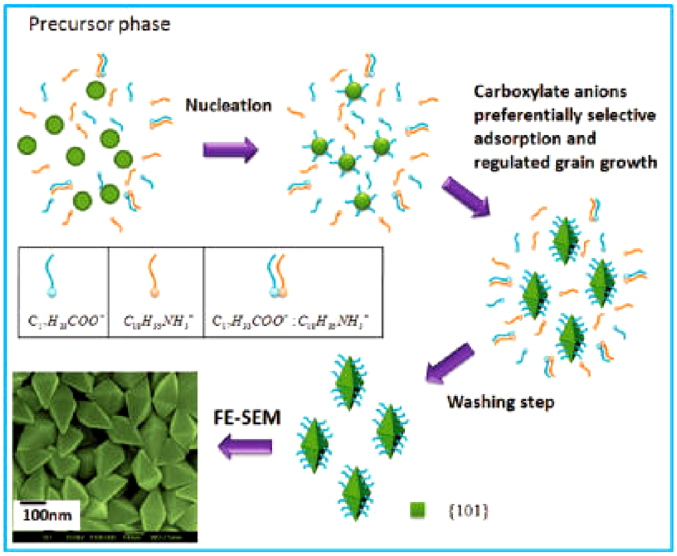

Figure 4.6. Schematic of the proposed oleic acid/oleylamine cooperative-controlled crystallization mechanism for the formation of monodisperse tetragonal bipyramid $NaLa(MoO_4)_2$ nanocrystals (Bu et al. 2009).

The selective binding or nonbinding of surfactant molecules to different faces of the growing nanocrystal can also control the product's morphology due to the possibility of breaking the limitations of crystal growth dynamically. Yan et al.(Si et al. 2005) demonstrated oleic acid binds more strongly than oleylamine to the surface atoms of the oxide nanocrystals, due to its higher oxophilicity. Due to the selective adsorption of the capping ligands on certain cubic faces during crystal growth, nanocrystals with different morphologies, such as nanopolyhedra, nanoplates, and nanodisks (Figure 4-7). The sterically diffusive kinetics concerning the length of alkyl chain of organic capping agent is crucial role in the elongated control of the colloidal nanocrystals. Herman et al.(Wang et al. 2007) varied the length of the alkylphosphonic acid ligands used in CdSe nanocrystal synthesis. Consequently, the shorter the ligand, the more elongated and branched were the resulting nanorods; when mixtures of alkylphosphonic acids were used, the higher the molar fraction of the shorter ligand, the more elongated and branched were the nanorods (Figure 4-8).

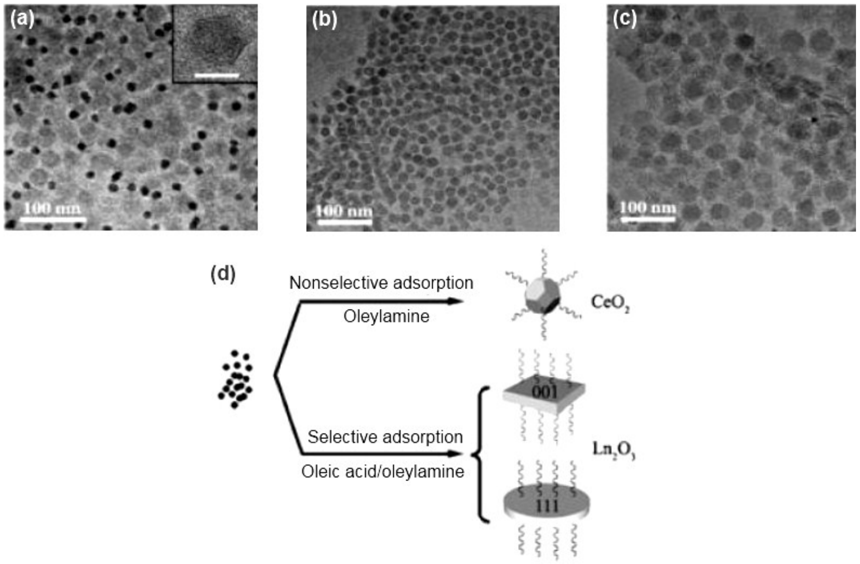

Figure 4.7. TEM images of the Eu_2O_3 nanocrystals: a) OA/OM=1:7, 310 °C, 1 h, b) OA/OM=3:5, 310 °C, 20 min, c) OA/OM=3:5, 330 °C, 1 h, d) formation of rare-earth oxide nanopolyhedra, nanoplates, and nanodisks (Si et al. 2005).

Similar growth patterns are observed in the $W_{18}O_{49}$, Mn_3O_4, and TiO_2 nanocrystals (Seo et al. 2005). The $W_{18}O_{49}$ has a monoclinic structure with a highly anisotropic *b*-axis (the *b*-axis being 0.2 times the *a*- and *c*-axes) with the highest atom packing density of {010}-faces. The Mn_3O_4 and the TiO_2 both have tetragonal structures with anisotropic *c*-axes (*c*-axis/*a*-axis ratio: ~1.7 (Mn_3O_4), ~2.7 (TiO_2) and the {001}-faces have the highest packing density. As expected by the surface energy trend, the $W_{18}O_{49}$ nanorods elongated along the [010] direction are formed by thermal reactions of tungsten chloride with capping molecule mixtures containing oleic acid and oleylamine, while Mn_3O_4 and TiO_2 rods, synthesized using $MnCl_2$ and $TiCl_2$ respectively, are formed by the unidirectional growth along the [001] direction.

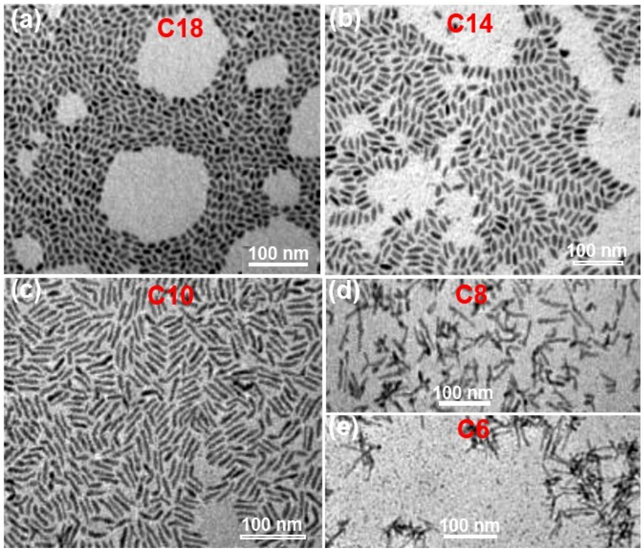

Figure 4.8. The elongation of shape of CdSe nanorods by decreasing the alkyl chain length of capping agents: (a) Octadecylphosphonic acid, (b) Tetradecylphosphonic acid, (c) Decylphosphonic acid, (d) octylphosphonic acid, (e) hexylphosphonic acid (Wang et al. 2007).

4.2.2. Effect of precursor monomer concentration

A balance between the kinetic and the thermodynamic growth regimes plays a key role in determining the final size/shape of the resulting nanocrystals. The critical nuclei can be much smaller than the ones for the synthesis of dots. In the extremely small size range, the relative chemical potential is highly size-dependent, and even very sensitive to the configuration of the nuclei. Thermodynamically, all of the nanocrystals will grow toward the shape having the lowest energy at equilibrium, which is governed by the classic theory. However, the formation dynamics can affect the shape of the formed nanocrystals. Indeed, the formation of nanocrystals is found to be a highly kinetics driven process. Isotropic growth of nanocrystals is preferred under the thermodynamic growth regime that is characterized by a sufficient supply of thermal energy and a low concentration of monomers. Spheres are the thermodynamically most stable shape with the lowest overall surface energy. In contrast, anisotropic growth along a specific direction with low activation energy barriers is facilitated under the nonequilibrium kinetic growth regime with a high concentration of monomers. It means that the formation of the intrinsic anisotropic nanocrystals is found to be a highly kinetics-driven process, which occurs far away from the thermodynamic equilibrium, and must be overdriven by high precursor monomer concentrations.

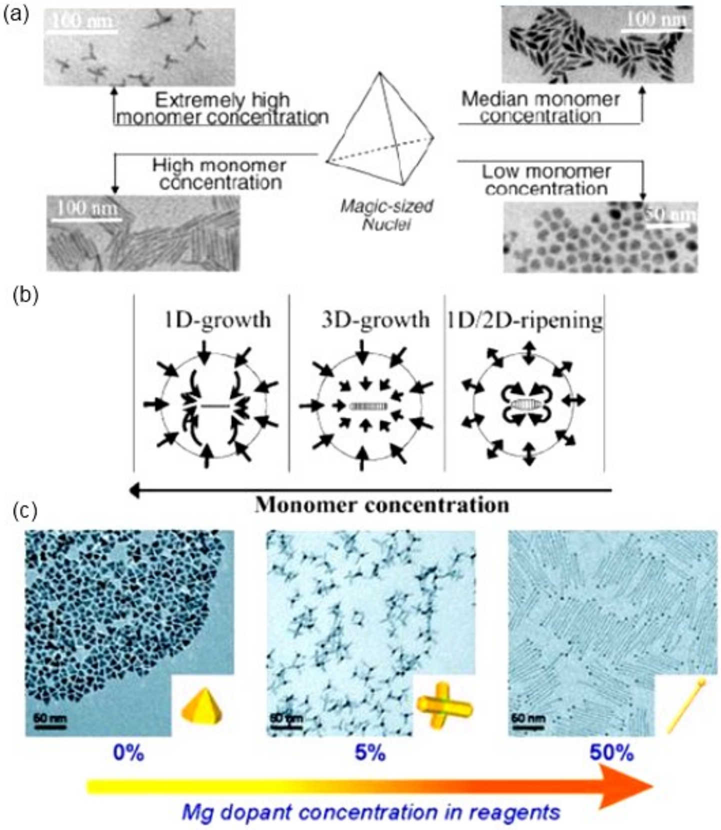

Figure 4.9. Effect of precursor monomer concentration on the evoluation shape: (a) Illustration of the growth conditions for different nanocrystal shapes: dot; spindle, rod, tetrapod (Peng 2003); (b) Illustration of the three growth stages of elongated CdSe nanocrystals at different monomer concentrations (Peng 2003); (c) Representative TEM images of the nanocrystals from the 0%, 5% and 50% $Mg(St)_2$ reactions, emphasizing the shape evolution of colloidal ZnO nanocrystals due to the increasing Mg dopant concentrations in the reagents (highlighted by the arrow) (Yang et al. 2010b).

Peng et al.(Peng 2003) first proposed a CdSe growth model that is controlled by the diffusion concentration of monomers. In their model, the CdSe nanocrystals were formed via the thermal decomposition of the pre-prepared Cd-alkylphosphonic acid complexes with maintaining a high monomer concentration. The author had achieved the control of the growth regime between kinetic *vs* thermodynamic by changing the precursor monomer concentration. In fact, the precursor monomer concentration remaining in the reaction solution is always depleted by the nucleation and growth of the nanocrystals. Consequently, the precursor monomer concentration effected on the shape evolution of CdSe nanocrystals. In summary, essentially at a low concentration of monomers at a fixed growth temperature, thermodynamically favorable, all isotropic wurtzite CdSe nanocrystals grew toward the lowest chemical potential environment, which results in the formation of only nanospheres. A median monomer concentration can support only an isotropic growth in a three dimensional growth stage and produces spindle shaped nanocrystals. However, at a higher monomer concentration, kinetically favorable, anisotropic growth along the [001] direction of the wurtzite CdSe is favored in resulting of the formation of rods or other elongated structures having metastability. If the remaining monomer concentration in the growth solution is extremely high, the solution could supply a sufficient amount of monomers for each seed to fully grow arms on the four (111) facets of the zinc blende structure of the tetrahedral seeds and yields tetrapod-shaped nanoparticles.

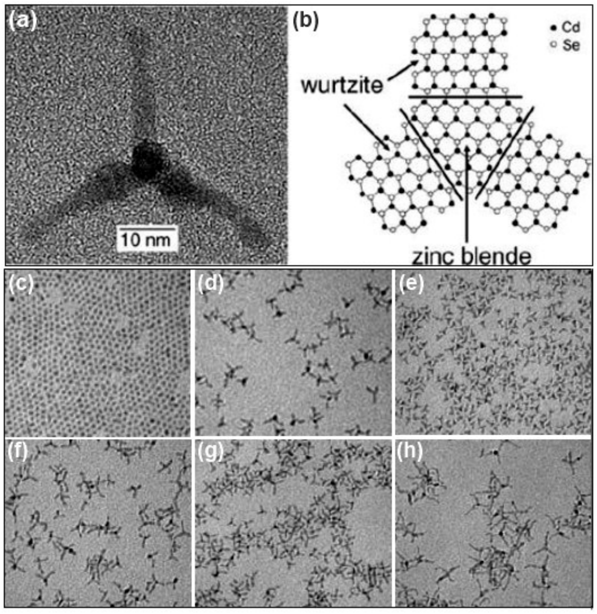

Figure 4.10. (a) HRTEM of a CdSe tetrapod looking down the [001] direction of one arm, (b) 2-dimensional representation showing the structure of a tetrapod. The nuclei is zinc blende, with wurtzite arms growing out of each of the four (111) equivalent faces. Three

arms are shown, with the fourth coming out of the page towards the reader (Wang and Lieber 2003, Manna, Scher and Alivisatos 2002); The evoluation shape of iron oxide nanocrystals from dot to tetrapod was achieved by varying amounts of $Fe(CO)_5$: (c) 0.8, (d) 1.4, (f) 2, (d) 2.6, (g) 3.2, (h) 4 mmol (Cozzoli et al. 2006).

During the synthesis, the monomer concentration should drop to a level lower than that required for a given shape. Figure 4-9a,b illustrates the three stages for the shape evolution of a rod-shaped nanocrystal as the monomer concentration decreases: i) 1D growth, ii) 3D growth, iii) 1D to 2D ripening (Peng 2003). During a 1D growth stage, a high diffusion concentration of monomers into the diffusion layer promotes the preferential 1D growth of monomers on the highest energy (001) surface. A median diffusion concentration induces an equi-directional growth of the nanocrystals. Due to the differences in chemical potential between different facets of the nanocrystals, the monomers on the nanocrystals move in an intraparticle manner to convert the rod-shaped nanocrystals to the dot-shaped ones (3D growth stage). When the monomer concentration is low, the system reaches equilibrium by dissolution and re-growth of the monomers from the (001) face onto the other faces (1D to 2D ripening stage). At very low monomer concentrations, the nanocrystals grow by an interparticular Ostwald ripening process. Ye et al.(Yang et al. 2010b) found that the relative concentration of dopant precursor in the reagents is one of the key factors that result in initial growth seeds with different crystallographic phases and shapes, which eventually lead to Mg-doped ZnO nanocrystals with different morphologies. Mg-doped ZnO nanocrystals with well-defined shapes, from tetrapods to ultrathin nanowires the shape evolution as increasing the concentration of dopant $Mg(St)_2$ precursor from 5% to 50%. Figure 4-9c illustrates the dopant-induced shape evolution of the Mg-doped ZnO nanocrystals. The formation of CdSe tetrapods from in situ assembling the (111) faces of the original zinc blende nucleus at high precursor monomer concentration was also reported by Alivisatos et al. (Manna et al. 2002) (Figure 4-10a,b). Cozzoli et al.(Cozzoli et al. 2006) revealed that evoluation shape of magnetic iron oxide nanocrystals from dot into three pods, depending on the amount of $Fe(CO)_5$ precursor injected (Figure 4-10c-h).

4.2.3. Effect of reaction temperature and time

In the classical crystallization theory, the flat surfaces of a crystal grow via layer-by-layer adsorption of solute atoms or molecules onto an existing crystal facet. When an atom/molecule approaches at the crystal surface from the solution, it is not immediately integrated into the crystal lattice but is can migrate on the crystal surface. These atoms form the so-called adsorption layer with a relative thickness of ~1 nm. The migrating atoms on the crystal surface become integrated into the crystal lattice at "active centers" where the attraction of the moving atoms to the lattice is greatest. The active centers are general corners, edges, twists of the growth surface. The heterogeneous nucleation of a new layer starts from surface nucleation of an island on the facet, which grows further by attachment of further atoms/ions to the corners, edges, or twists of the new layer until the crystal surface is completed. However, the growth of a surface is rarely perfect, and a number of defected crystals exist in the form of vacancies or screw dislocations on crystal surface. In addition, the absorbed atoms are not static and able to detach into solution even at equilibrium. Consequently, these different growth conditions can already lead to deviations from the equilibrium morphology for a crystal (Chattopadhyay, Ravishankar and Goswami 1997).

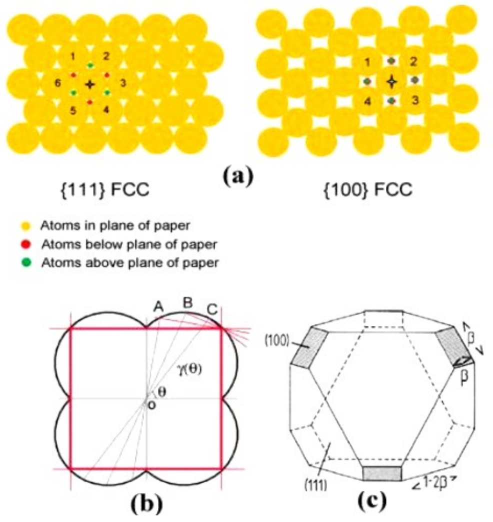

Figure 4.11. Steps involved in the construction of the equilibrium shape. (a) Obtaining the polar plot of surface energy as a function of orientation by bond counting. The surface

energy varies with orientation due to the fact that different surfaces have different densities of broken bonds; (b) Polar plot of surface energy $\gamma(\theta)$ for a hypothetical square lattice; (c) Polyhedral structure with an fcc crystal bounded by {111} and {100} facets based on the Wulff construction.

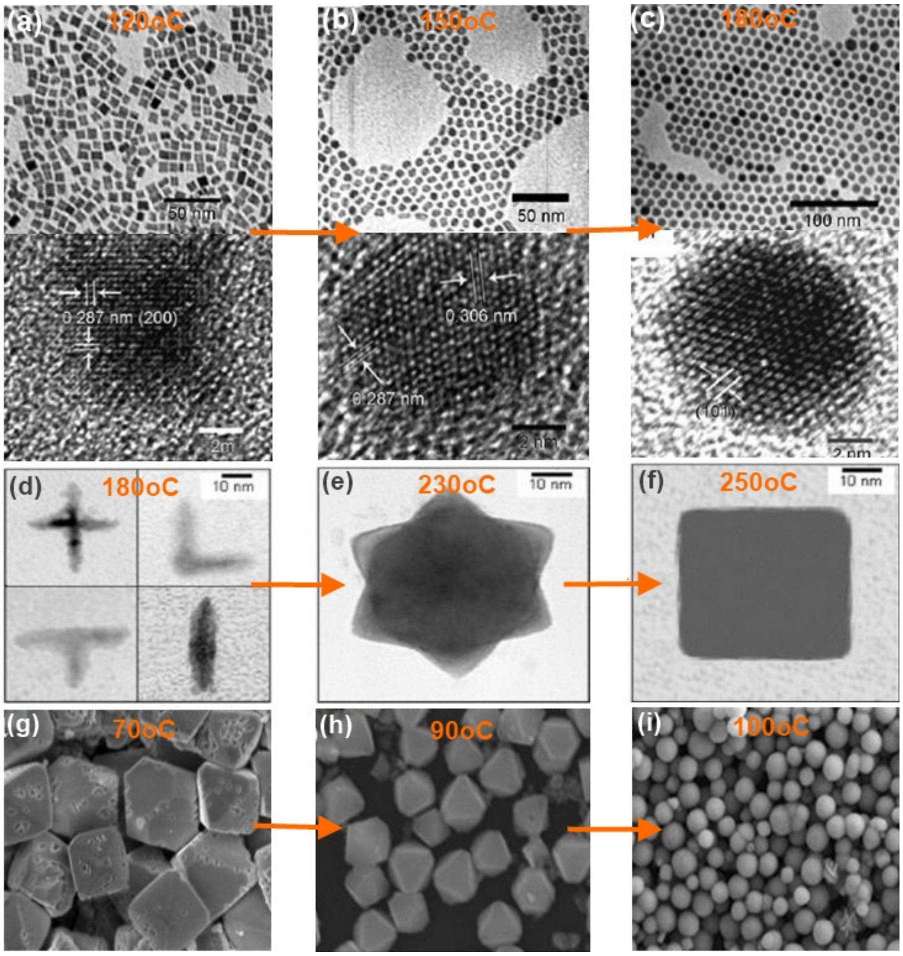

Figure 4.12. Effect of the reaction temperature on the shape transformation. Mn_3O_4 nanocrystals synthesized at different temperatures: (a) 120 ^{o}C, b) 150 ^{o}C, c) 180 ^{o}C (Zhao et al. 2008); (d) rod-based PbS multipods synthesized at 180 °C, (e) star-shaped nanocrystals at 230 °C, (f) truncated octahedrons at 250 °C, were observed (Lee et al. 2002); The samples synthesized for 2 h using 2.5 M poly(vinyl pyrrolidone) at different reaction temperatures: (g) 70; (h) 90; (i) 100 ^{o}C (Sui et al. 2009).

Under equilibrium conditions, the shape of single crystals is related to the intrinsic structure of the unit cell, and the crystal shape can reflect the unit-cell replication and amplification. However, the crystal morphology often varies significantly from the shape of the unit cell. From a thermodynamic viewpoint, the change of the diverse crystal shapes are dependent on the external growth environment, as proposed early last century by Wulff. In the Wulff construction, each facet of the crystal was described by its free surface and interfacial energies and the crystal shape results from minimizing these energies for a certain volume. However, the model was valid only at thermal equilibrium, and the resulting shape is therefore the equilibrium shape of the crystal. A proposed pseudo "Wulff construction" was based on the fact that the driving factor was not the equilibrium surface but rather the growth rate of each facet as determined by the kinetics. The normal distance from the crystal facets to the center of the crystal was then proportional to the corresponding growth velocity rather than the surface and interfacial energies. Generally speaking, the growth rate of a crystal facet is usually directly related to its surface energy if the same growth mechanism acts on each facet. With regard to facets that have high surface energies will grow quickly, have low surface areas, or disappear completely upon crystal growth to the final shape. While faces with low surface energies will grow slowly and dominate the final shape. This behavior predicted by Wulff's rule. The equilibrium shape of a single crystal is defined by its minimum surface free energy, which can be calculated as the sum of the products of surface energy and surface area of all exposed facets.

The most widely used classical model for shape control of crystals is given by the Gibbs-Curie-Wulff theorem.

$$\sum_i \gamma_i A_i = F_S \qquad (31)$$

with γ_i: surface energy of the surface i, A_i: area of surface i, and F_S: surface free energy. According to Wulff's rule, the shape of crystals will be affected by changing the surface energy of the surfaces. If this can be done in a facet-selective way, the equilibrium shape of a crystal can be tuned in a defined and predictable way. This strategy of crystal morphogenesis has been recognized for a long time and has even found industrial application mainly based on empirical observations.

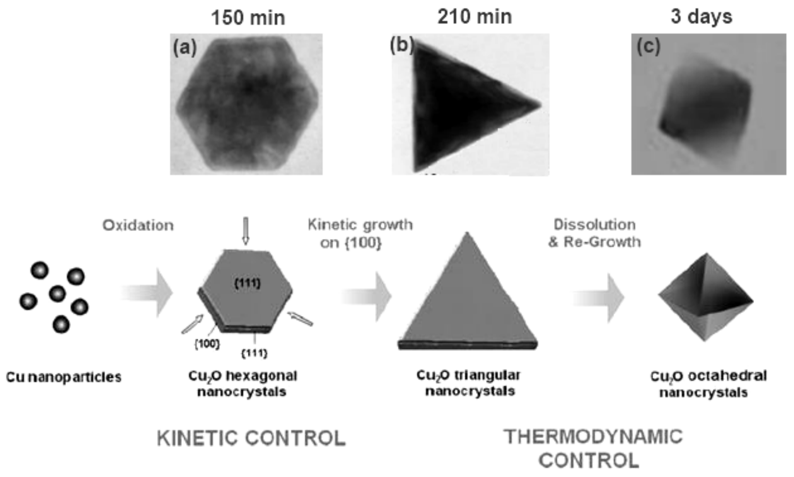

Figure 4.13. Effect of the reaction time on the shape transformation. Scheme for the growth of Cu_2O nanocrystals with different morphologies at 150, 210 min, and after an aging period of 3 days. Arrow indicates the diffusion directions of the monomers (Ng and Fan 2006).

Many authors have been used Wuff facets theory to explain the shape transformation of nanocrystals under adjusting the reaction time or temperature. For example, Ji et al. produced the Mn_3O_4 nanocrystals using manganese(II) stearate precursors in two-phase water-toluene system. When increasing the reaction temperature from 120 to 150 and 180 ^{o}C, the shape of Mn_3O_4 nanocrystals transferred from sphere to quasi-spheres, and cubic shapes (Figure 4-12a,b,c). Cheon et al.(Lee et al. 2002) found that the shape evolutions of a variety of novel PbS structures including 1-D rod-based structures, highly faceted star shapes, truncated octahedrons and cubes were also possible as a result of adjusting reaction temperature, as shown in Figure 4-12d,e,f. Zou et al.(Sui et al. 2009) also elucidaed that the reaction temperature was responsible for the shape-controlled synthesis of Cu_2O crystals, as shown in Figure 4-12g,h,i). Fan et al.(Ng and Fan 2006) revealed shape evolution of Cu_2O nanostructures via kinetic and thermodynamic controlled growth (Figure 4-13).

4.3. Self-Assembly/Aggregation of Nanocrystals

Nanocrystals are ideal building blocks for self-assembly of two- and three-dimensional supperlattice structures in which the particles behave like well-defined molecular to arrange orientational order for assembly formation. With different experimental conditions, a variety of organized structures have been achieved. Additionally by altering the substituents of the assembling building blocks, desirable changes in the assembly process are achieved. Organized or self-assembled nanostructures show remarkable collective properties, useful for superstructures or engineering nanoarchitectures. It has been demonstrated that the organized structures of nanocrystals in multi-dimensional superlattices can have collective physical properties that differ from the isolated nanoparticles due to coupling of the nanocrystals. The self-assembly of nanocrystals from solution is a fundamental problem by itself as it involves various interactions between the nanocrystals, substrate, and solvent. The desired properties and structural effects in the assembled materials can be accomplished using suitable templates. These properties can be tuned by controlling the size, shape, chemical composition of the nanocrystals as well as the interaction between the nanocrystals. The multi-dimensional assembly of nanoparticles with controlled morphology in highly ordered arrays is important for realizing their novel applications. Self-assembly is an important tool for generating integrated nanoscale devices.

Nanoparticle self-assembly is often achievable by using evaporation-based assembly producing spontaneously ordered superstructures, in which the surface properties and supramolecular chemistry directly effect on the final morphology of organized superlattice nanostructures. The relatively weak attraction forces between nanocrystals in the solution gain importance when the solvent is slowly evaporated, forcing nanoparticles to organize. Furthermore, other specific techniques are available such as Langmuir-Blodgett approach, layer-by-layer assembly, drying mediated assembly, and so forth. Non-covalent interactions such as hydrogen-bonding, electrostatic interactions, van der Waals interactions, surface free energy, chemical conjugations, templation are vital aspects of spontaneous or directed assembly. The interactions between nanoparticles are most likely dominated by van der Waals forces. However, it is further influenced by the size/shape of the particles and the thickness of the surface passivation layer.

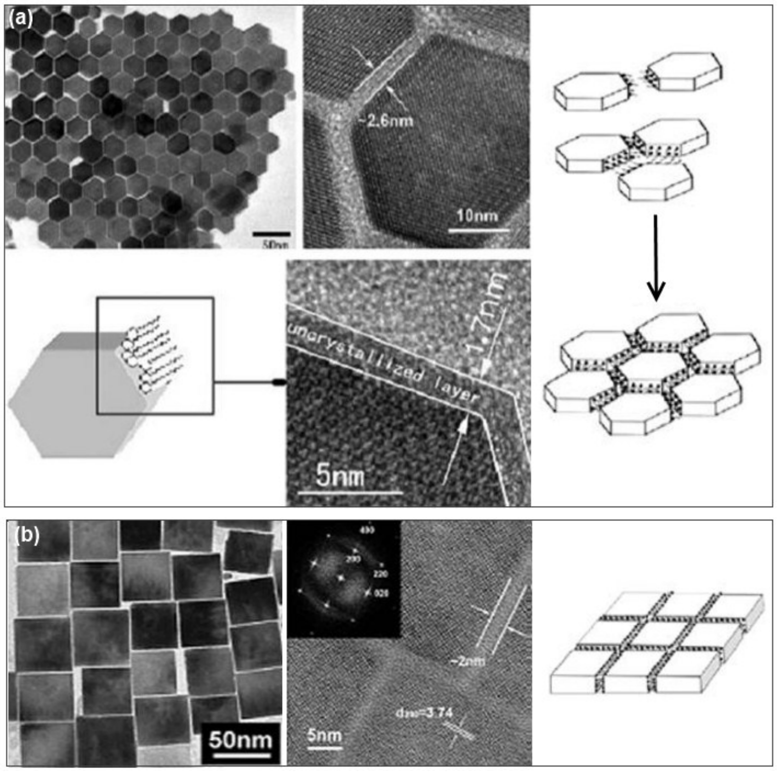

Figure 4.14. Assembly via the interaction of surfactants absorbed on the surfaces of nanocrystals (Wang and Li 2007): (a) TEM images of yttrium phosphate hydrate nanocrystals and HRTEM image on the edge of an yttrium phosphate hydrate (Huo et al. 2007); (b) TEM and HRTEM images of lanthanum vanadate nanocrystals (Liu et al. 2008a), Proposed schematic illustration of assembly of nanocrystals (right side).

In general, stabilized colloidal nanoparticles are most suited for controlled assembly processes. Figure 4-15 shows self-assembly via the interaction of surfactants absorbed on the surfaces of nanocrystals. The coupling interactions between different nanoparticles and the environment determine the physicochemical properties of the nanoparticles. In addition, the changes in the nanoparticle properties are attributed to the vicinity of nanoparticles and consequent dipole-dipole interactions leading to drastic changes in their electron-transport properties. For example, changing the length of the protecting ligands can affect quantum transitions and their electronic properties. Passivation of the nanoparticle surface with ligands, protecting them from agglomeration, gives the possibility of functional group tailoring through chemical reactions. Moreover, chemical patterning or surface electrostatic interactions are utilized to create specifically patterned nanoparticle assemblies. At the interfaces, reduction in the interfacial energies causes the spontaneous assembly. This path was also used to fabricate the superstructures from the assembly of the colloidal organic-capped nanoparticles, as shown in Figure 4-16 and Figure 4-17.

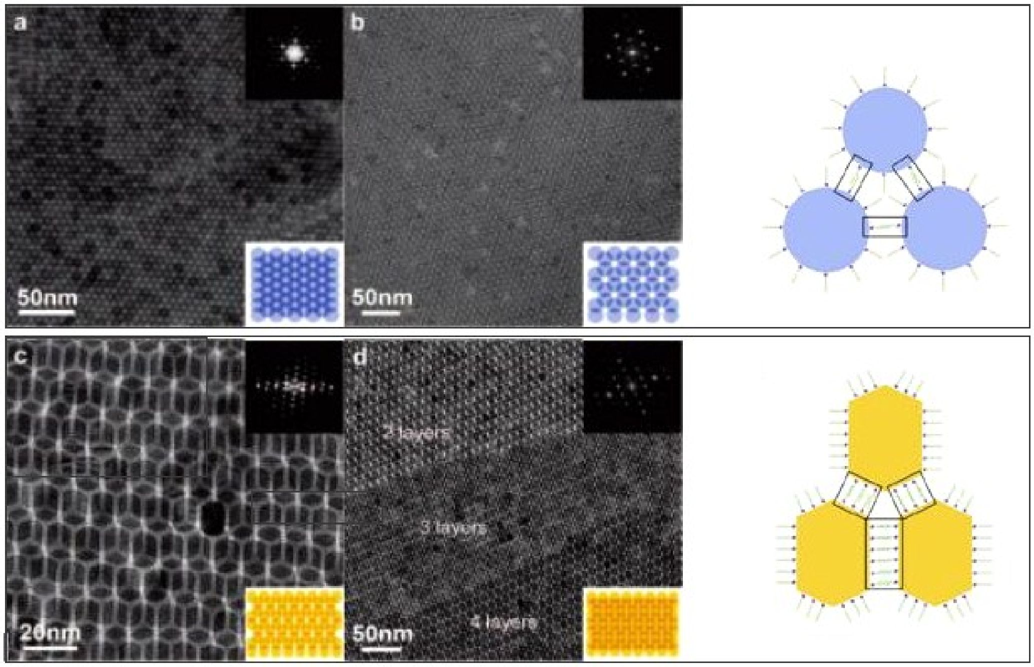

Figure 4.15. TEM images of Cu_2S nanocrystal assemblies: (a) fcc packed circular nanocrystals; (b) hcp packed circular nanocrystals; (c) two layers of close-packed elongated nanocrystals; (d) multilayers of elongated nanocrystals. The top insets are the corresponding FFT patterns, and the bottom insets are the schemes of the stacking of nanocrystals. Right side: detailed schemes and descriptions of the packing symmetry of nanocrystals (Zhuang et al. 2008).

In recent years, using bottom-up approaches of self-organization, a variety of organized nanostructures have been created. Evaporation-induced assembly of monodisperse nanoparticles of uniform size and shape generates hexagonal patterns of nanoparticle arrays. For example, PtFe nanoparticles form a hexagonal close-packed structure, if stabilized with oleic acid and oleyl amine, while with hexanoic acid and hexylamine they form cubic-packed monolayers (Sun et al. 2000). Banin et al.(Mokari et al. 2004) had achieved the asymmetric self-assembly of nanostructures to produce star-shaped nanocrystals and rod-shaped multipods or CdSe tetrapods with gold nanoparticles organized at their ends.

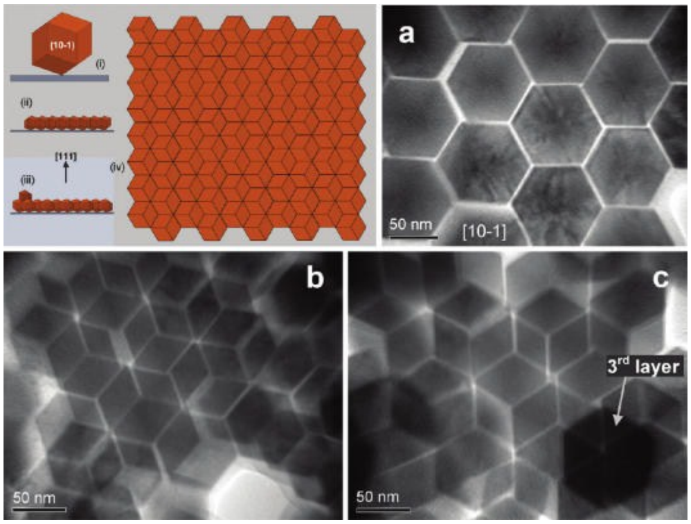

Figure 4.16. Self-assembly of Cu_2O rhombic dodecahedra (TEM images): (a) single layer array, (b) double layer arrangement, and (c) a dodecahedron standing on a double-layered structure (Yao et al. 2010).

O'Brien et al.(Redl et al. 2003) reported the self-assembly of PbSe semiconductor quantum dots and γ-Fe_2O_3 magnetic nanocrystals into precisely ordered three-dimensional AB_{13} or AB_2 superlattices. Such self-assembled superlattices or arrays of metal and semiconductor nanocrystals are a new form of materials of both fundamental interest and technological importance. This non-equilibrium aggregation process is also well explained using thermodynamics, where self-organization properties follow from the fact that the relevant interparticle attractions do not greatly exceed the thermal energies, thereby allowing formation of equilibrium structures as a function of temperature and concentration. Further, interfacial activity of reverse micelles and microemulsions is also exploited to self-assemble nanoparticles of $BaCrO_4$ in linear fashion. The assembly arose from the interdigitation of surfactant molecules, attached to specific nanoparticle crystal faces (Li et al. 1999b). Kotov et al.(Lee, Govorov and Kotov 2005b) achieved assembly of CdTe nanoparticles with gold nanocrystals using a thin layer of poly(ethyleneglycol) (PEG). The separation distances between the CdTe nanocrystal shells and the Au nanocrystal cores could be altered upon a change in the temperature (Lee, Govorov and Kotov 2005a). Similarly, negatively charged CdSe/CdS core-shell nnocrystals were also coated on positively charged gold nanorods (Wargnier et al. 2004).

References

Bu, W., Z. Chen, F. Chen & J. Shi (2009) Oleic Acid/Oleylamine Cooperative-Controlled Crystallization Mechanism for Monodisperse Tetragonal Bipyramid $NaLa(MoO_4)_2$ Nanocrystals. *The Journal of Physical Chemistry C,* 113**,** 12176-12185.

Cao, Y. C. (2004) Synthesis of Square Gadolinium-Oxide Nanoplates. *Journal of the American Chemical Society,* 126**,** 7456-7457.

Chattopadhyay, K., N. Ravishankar & R. Goswami (1997) Shapes of quasicrystals. *Progress in Crystal Growth and Characterization of Materials,* 34**,** 237-249.

Cozzoli, P. D., E. Snoeck, M. A. Garcia, C. Giannini, A. Guagliardi, A. Cervellino, F. Gozzo, A. Hernando, K. Achterhold, N. Ciobanu, F. G. Parak, R. Cingolani & L. Manna (2006) Colloidal Synthesis and Characterization of Tetrapod-Shaped Magnetic Nanocrystals. *Nano Letters,* 6**,** 1966-1972.

Guo, Q., X. Teng, S. Rahman & H. Yang (2002) Patterned Langmuir−Blodgett Films of Monodisperse Nanoparticles of Iron Oxide Using Soft Lithography. *Journal of the American Chemical Society,* 125**,** 630-631.

Huo, Z., C. Chen, D. Chu, H. Li & Y. Li (2007) Systematic Synthesis of Lanthanide Phosphate Nanocrystals. *Chemistry – A European Journal,* 13**,** 7708-7714.

Jun, Y.-w., M. F. Casula, J.-H. Sim, S. Y. Kim, J. Cheon & A. P. Alivisatos (2003) Surfactant-Assisted Elimination of a High Energy Facet as a Means of Controlling the Shapes of TiO_2 Nanocrystals. *Journal of the American Chemical Society,* 125**,** 15981-15985.

Kim, F., S. Kwan, J. Akana & P. Yang (2001) Langmuir−Blodgett Nanorod Assembly. *Journal of the American Chemical Society,* 123**,** 4360-4361.

Lee, J., A. O. Govorov & N. A. Kotov (2005a) Bioconjugated Superstructures of CdTe Nanowires and Nanoparticles: Multistep Cascade Förster Resonance Energy Transfer and Energy Channeling. *Nano Letters,* 5**,** 2063-2069.

Lee, S.-M., Y.-w. Jun, S.-N. Cho & J. Cheon (2002) Single-Crystalline Star-Shaped Nanocrystals and Their Evolution: Programming the Geometry of Nano-Building Blocks. *Journal of the American Chemical Society,* 124**,** 11244-11245.

Li, L.-s., J. Walda, L. Manna & A. P. Alivisatos (2002) Semiconductor Nanorod Liquid Crystals. *Nano Letters,* 2**,** 557-560.

Li, M., H. Schnablegger & S. Mann (1999) Coupled synthesis and self-assembly of nanoparticles to give structures with controlled organization. *Nature,* 402**,** 393-395.

Liu, J., W. Chen, X. Liu, K. Zhou & Y. Li (2008) Au/LaVO$_4$Nanocomposite: Preparation, characterization, and catalytic activity for CO oxidation. *Nano Research,* 1, 46-55.

Manna, L., E. C. Scher & A. P. Alivisatos (2000) Synthesis of Soluble and Processable Rod-, Arrow-, Teardrop-, and Tetrapod-Shaped CdSe Nanocrystals. *Journal of the American Chemical Society,* 122, 12700-12706.

Mokari, T., E. Rothenberg, I. Popov, R. Costi & U. Banin (2004) Selective Growth of Metal Tips onto Semiconductor Quantum Rods and Tetrapods. *Science,* 304, 1787-1790.

Ng, C. H. B. & W. Y. Fan (2006) Shape Evolution of Cu_2O Nanostructures via Kinetic and Thermodynamic Controlled Growth. *The Journal of Physical Chemistry B,* 110, 20801-20807.

Peng, X. (2003) Mechanisms for the Shape-Control and Shape-Evolution of Colloidal Semiconductor Nanocrystals. *Advanced Materials,* 15, 459-463.

Peng, X., L. Manna, W. Yang, J. Wickham, E. Scher, A. Kadavanich & A. P. Alivisatos (2000) Shape control of CdSe nanocrystals. *Nature,* 404, 59-61.

Redl, F. X., K. S. Cho, C. B. Murray & S. O'Brien (2003) Three-dimensional binary superlattices of magnetic nanocrystals and semiconductor quantum dots. *Nature,* 423, 968-971.

Santhanam, V., J. Liu, R. Agarwal & R. P. Andres (2003) Self-Assembly of Uniform Monolayer Arrays of Nanoparticles. *Langmuir,* 19, 7881-7887.

Seo, J.-w., Y.-w. Jun, S. J. Ko & J. Cheon (2005) In Situ One-Pot Synthesis of 1-Dimensional Transition Metal Oxide Nanocrystals. *The Journal of Physical Chemistry B,* 109, 5389-5391.

Si, R., Y.-W. Zhang, L.-P. You & C.-H. Yan (2005) Rare-Earth Oxide Nanopolyhedra, Nanoplates, and Nanodisks. *Angewandte Chemie International Edition,* 44, 3256-3260.

Sigman, M. B., A. Ghezelbash, T. Hanrath, A. E. Saunders, F. Lee & B. A. Korgel (2003) Solventless Synthesis of Monodisperse Cu_2S Nanorods, Nanodisks, and Nanoplatelets. *Journal of the American Chemical Society,* 125, 16050-16057.

Sui, Y., W. Fu, H. Yang, Y. Zeng, Y. Zhang, Q. Zhao, Y. Li, X. Zhou, Y. Leng, M. Li & G. Zou (2009) Low Temperature Synthesis of Cu2O Crystals: Shape Evolution and Growth Mechanism. *Crystal Growth & Design,* 10, 99-108.

Sun, S., C. B. Murray, D. Weller, L. Folks & A. Moser (2000) Monodisperse FePt Nanoparticles and Ferromagnetic FePt Nanocrystal Superlattices. *Science,* 287, 1989-1992.

Wang, D. & C. M. Lieber (2003) Inorganic materials: Nanocrystals branch out. *Nat Mater,* 2, 355-356.

Wang, W., S. Banerjee, S. Jia, M. L. Steigerwald & I. P. Herman (2007) Ligand Control of Growth, Morphology, and Capping Structure of Colloidal CdSe Nanorods. *Chemistry of Materials,* 19, 2573-2580.

Wang, X. & Y. Li (2007) Monodisperse nanocrystals: general synthesis, assembly, and their applications. *Chemical Communications*, 2901-2910.

Wargnier, R., A. V. Baranov, V. G. Maslov, V. Stsiapura, M. Artemyev, M. Pluot, A. Sukhanova & I. Nabiev (2004) Energy Transfer in Aqueous Solutions of Oppositely Charged CdSe/ZnS Core/Shell Quantum Dots and in Quantum Dot−Nanogold Assemblies. *Nano Letters,* 4, 451-457.

Yang, Y., Y. Jin, H. He, Q. Wang, Y. Tu, H. Lu & Z. Ye (2010) Dopant-Induced Shape Evolution of Colloidal Nanocrystals: The Case of Zinc Oxide. *Journal of the American Chemical Society,* 132**,** 13381-13394.

Yao, K. X., X. M. Yin, T. H. Wang & H. C. Zeng (2010) Synthesis, Self-Assembly, Disassembly, and Reassembly of Two Types of Cu_2O Nanocrystals Unifaceted with {001} or {110} Planes. *Journal of the American Chemical Society,* 132**,** 6131-6144.

Zhao, N., W. Nie, X. Liu, S. Tian, Y. Zhang & X. Ji (2008) Shape- and Size-Controlled Synthesis and Dependent Magnetic Properties of Nearly Monodisperse Mn_3O_4 Nanocrystals. *Small,* 4**,** 77-81.

Zhuang, Z., Q. Peng, B. Zhang & Y. Li (2008) Controllable Synthesis of Cu_2S Nanocrystals and Their Assembly into a Superlattice. *Journal of the American Chemical Society,* 130**,** 10482-10483.

Chapter 5 Experimental Synthetic Methodology

5.1. Introduction

Inorganic nanocrystals, as one kind of important nanomaterial, are still attractive to many researchers in chemistry, physics, materials science, biology, and other fields (Miller and Chandross 2010, Nozik et al. 2010, Ray 2010, Kobayashi et al. 2009, Leong and Vittal 2010). High-quality inorganic nanocrystals possess near monodispersity in terms of size, shape, defects in internal and external structures, and high crystallinity. Studies of high-quality nanometer-sized metal oxide, mixed metal oxide, and hybrid metal-oxide species provide powerful examples to build up hierarchically ordered structures with unique performance using controllable nanocrystals in size, shape, and surface chemistry. The nanocrystals serve as smaller units for the construction of nanomaterials. Therefore, the mapping of size- and shape-dependent properties for nanocrystals is a great challenge for fundamental nanotechnology and application areas.

There are several classical methods for synthesizing high-quality metal oxide, mixed metal oxide, and hybrid metal-oxide nanocrystals, such as the thermal decomposition (Park et al. 2007), the reverse micelle technique (Ingert and Pileni 2001, Whetten and Gelbart 1994), nonaqueous approaches (Garnweitner and Niederberger 2008), sol-gel process (Arachchige and Brock 2007, Schmidt et al. 2000), hydrothermal/solvothermal method (Rajamathi and Seshadri 2002), the liquid-solid-solution phase-transfer route (Wang et al. 2005b). However, most nanoparticles from sol-gel process and microemulsion still need post-treatment at a high temperature, the free-template solvo/hydrothermal method is not suitable for producing nanocrystals that have a wide size distribution and can not be completely dispersed in a nonpolar solvent. Also the thermal-decomposition approach requires a relatively high reaction temperature. Therefore, it is very beneficial for the researchers to develop a simple and highly reproducible approach to produce highly crystalline and uniformly sized and shaped nanocrystals. In this dissertation, we presented new approaches: (i) one-phase and (ii) two-phase hydro-solvothermal surfactant-assisted synthetic routes and (iii) seed-mediated growth, specific examples for the discussion of each synthetic pathway and corresponding formation mechanism. These synthetic approaches will be developed further in my Ph.D. work.

5.2. Hydro-Solvothermal One-Phase Synthesis

Hydrothermal and solvothermal processing where aqueous solutions, vapors, and/or fluids react with solid materials at high temperature, pressure, is a well-known process in mineralogy and geology fields for formation, alteration or deposit of minerals (Rajamathi and Seshadri 2002, Feng and Xu 2000). This method exploits the solubility of almost all inorganic substances in water at elevated temperatures, pressures and subsequent crystallization of the dissolved material from the fluid. The hydro-solvothermal surfactant-assisted syntheses involve heating the precursors in water or a solvent in the presence of surfactant at high temperatures and pressures. The solvents such as water, ethanol, or ethylene glycol at elevated temperatures plays an essential role in the precursor material transformation. The role of solvent is that of a pressure-transmitting medium and the solubility of the reactants is pressure and temperature dependent (Li et al. 1999). In a sealed vessel (bomb, autoclave, etc.), there is an increase of the autogenous pressures resulting from heating, therefore solvents can be brought to temperatures well above their boiling points. Performing a chemical reaction under such conditions is referred to as solvothermal processing or, in the case of water as solvent, hydrothermal processing. After sealing, the container is kept at high temperatures ranging from 100 to 500 ^{o}C inside an oven. The pressure of the container depends on the level of filling of the solvent (or water). During hydro-solvothermal treatment, metal cations initially precipitate in the form of polymeric hydroxides.

Over time, these hydroxides undergo dehydration to form the metal oxide crystal structures. A strong base could shift the equilibrium toward the formation of metal hydroxides. The concentration of alkali source was kept in excess relative to the metal salt concentration to ensure precipitation of all metal ions present in the solution. After synthesis, the products are capped by capping agents to precipitate at the bottom of autoclave. In addition, the ability of supercritical water to provide a good environment for oxidation in the presence of dissolved oxygen should be overcome. Because of its simplicity, low cost, and ambient pressure, crystal growth from solutions has been of considerable interest for a variety of materials and morphologies. Hydro-solvothermal surfactant-assisted method has an advantage of being safe, low temperature, and environmentally friendly (growth from aqueous solution instead of organic solvent) (Li et al. 1999).

In the past decades, there has been tremendous progress made in the area of hydro-solvothermal technology in the processing of advanced nanomaterials (Feng and Xu 2000). Hydro-solvothermal growth of different nanostructures depends on many apparatus such as growth temperature, precursors, addition of surfactants, solution pH value (Walton 2002). The effect of various experimental parameters on the reaction equilibria seems to be the key. Solution composition also affect the morphology of nanostructures, but it strongly depend on the crystal properties of the material because the crystal growth rates defer in different directions. Crystal planes which have higher surface energies typically have faster growth rate. However, this can be changed by addition of surfactants which selectively adsorb on certain crystal surfaces and it is the mechanism for surfactants. Furthermore, substrate modifications and solution concentrations all have impact on the morphology of final product of nanostructures. It was also found that different materials had different sensitivity to the changes of all these factors, so further work is still required to explore the hydro-solvothermal route for nanomaterials.

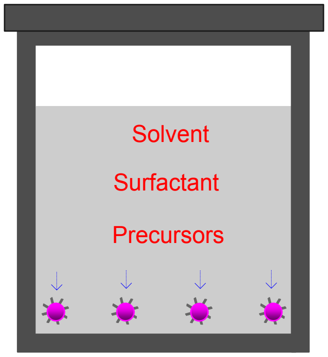

Figure 5.1. Hydro-solvothermal one-phase route for the synthesis of colloidal inorganic nanocrystals.

Among different types of materials which can be fabricated by this method, metal oxides and mixed oxides have been most commonly studied (Hayashi and Hakuta 2010, Demazeau 2008). Figure 5-1 shows a general scheme for the synthesis of colloidal surfactant-capped inorganic nanocrystals dispersible in a liquid. For oxide nanoparticle synthesis, either oxidation of metal sources or hydrolysis (or combination of the two) could be used for synthesis of nanoparticles. These features facilitate the fabrication of fine nanocrystals, generally well reacted and crystallized because the surrounding aqueous solutions accelerate these processes. One of the most important issues for practical applications is the achievement of precise control of the nanostructure size and shape.

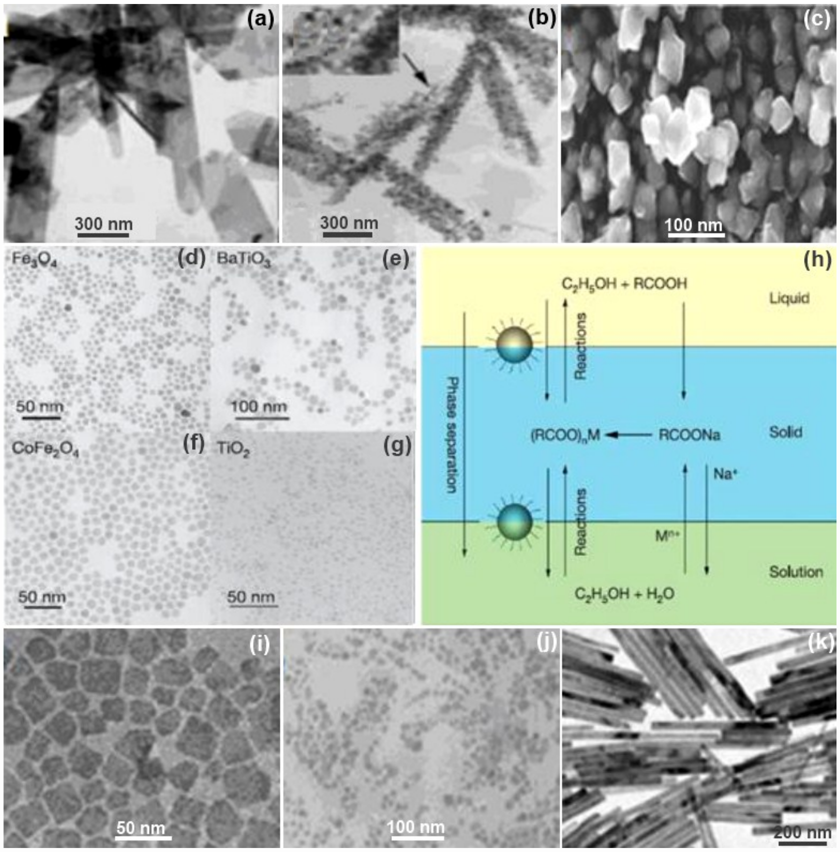

Figure 5.2. Gallery of representative TEM/SEM images illustrating examples of colloidal metal oxide and mixed oxide nanocrystals synthesized via hydrothermal one-phase route: (a) $Sm(OH)_3$ nanosheets, (b) $Y(OH)_3$ nanotubes coated with Au nanoparticles (Wang and Li 2003); (c) CeO_2 nano-octahedrons (Yan et al. 2008a); The general strategy for the nanocrystal synthesis in liquid-solid-solution hydrothermal process: (d) Fe_3O_4, (e) $BaTiO_3$,

(f) TiO_2, (g) $CoFe_2O_4$ nanocrystals, (h) Scheme of formation mechanism (Wang et al. 2005b); (i) YVO_4 nanosquares, (j) YPO_4 nanoparticles, (k) Eu^{3+}:$NaYF_4$ nanorods (Liu and Li 2007).

The hydrothermal precipitation route such as vapour-liquid-solid for synthesis of nanosized rare earth hydroxide nanocrystals (nanowires, nanotubles and fullerene-like nanoparticles) had been studied by Yadong Li (Wang and Li 2003) through controlling the temperature and pH in solution. The authors found that the particle size, morphology of the prepared rare-earth hydroxide strongly depended on pH value. Especially, the rare rearth hydroxyde nanosheets converted to uniform nanowires when the pH value of the solution is increased from 6-7 to 9 and followed by capping Au nanoparticles on the seeds (Figure 5-2a,b). By using H_2O_2 as the oxidizer and NH_4OH as the mineralizer the authors observed that the particle size was decreased with increasing concentration of oxidizer. Hydrothermal synthesis of CeO_2 nanocrystals had been also studied by Xing et al. (Figure 5-2c) (Yan et al. 2008a). However, this method is gerarally a thermodynamically driven tendency for aggregation of nanocrystals because nanocrystals are not a thermodynamically stable phase. Yadong Li et al.(Wang et al. 2005b) reported a generalized hydrothermal method for synthesizing a variety of different nanocrystals by a liquid-solid-solution reaction. The system consists of metal salt, sodium linoleate (solid), an ethanol-linoleic acid liquid phase, and a water-ethanol solution at different reaction temperatures under hydrothermal conditions. As illustrated in Figure 5-2d-h, this strategy is based on a general phase transfer and separation mechanism occurring at the interfaces of the liquid, solid and solution phases present during the synthetic process. The same synthetic strategy, they had been successfully employed multicomponent nanocrystals not only with mixed metal oxide nanocrystals ($LnVO_4$ and $LnPO_4$) (Figure 5-2i-j) but also with lanthanide doped $NaYF_4$ nanocrystals (Figure 5-2k) (Liu and Li 2007). Yu and coworkers (Yu, Fujino and Yoshimura 2003) noted that hydrothermal heating at 180 °C of an ammoniacal $FeCl_2$ solution containing metallic Zn leads to the formation of octahedrally-shaped $ZnFe_2O_4$ nanoparticles with an average size of 300 nm. While the purity of the ferrite material is controlled by the reaction time and temperature, its crystallinity was found to be significantly enhanced by increasing the concentration of ammonia in the reaction solution.

The reaction time and temperature as well as the dielectric constant of the reaction medium were also found to exert a significant effect on both the particle size and the crystallinity of the hydrothermally-prepared nanophase ferrites.

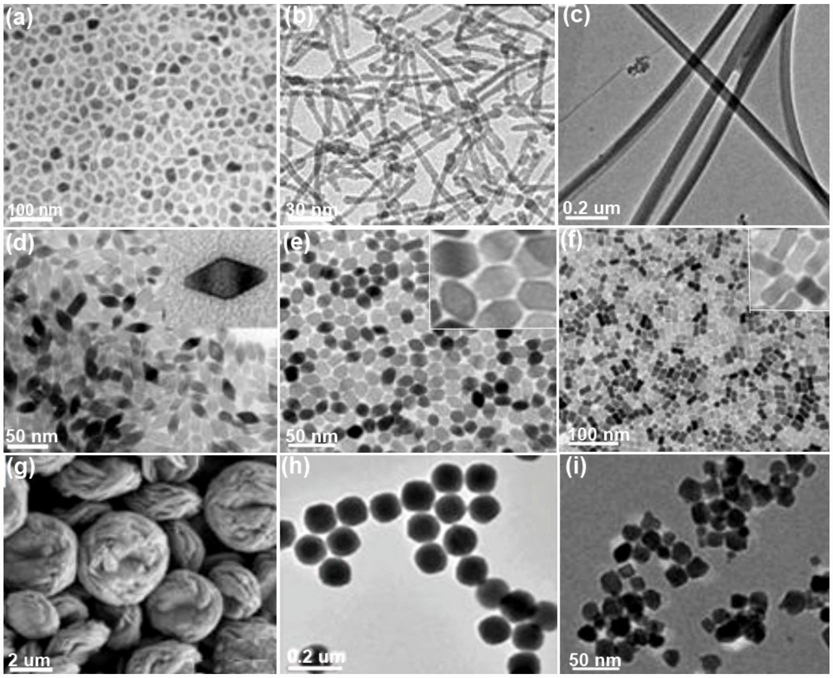

Figure 5.3. Gallery of representative TEM/SEM images illustrating examples of colloidal metal oxide and mixed oxide nanocrystals synthesized via solvothermal one-phase route: (a) TiO_2 nanoparticles, (b) TiO_2 nanorods (Li et al. 2006); (c) TiO_2 nanowires (Xie and Shang 2007); TiO_2 nanocrystals synthesized under the same method with the different shapes: (d) rhombic, (e) truncated rhombic, (f) dog-bone (Dinh et al. 2009); (g) hierarchical $FeWO_4$ cookielike-shaped microcrystals (Zhou et al. 2009); (h) nearly cubiclike CeO_2 nanocrystals (Liang et al. 2008); (i) In_2O_3 cubic-shaped nanocrystals (Yan et al. 2008b).

The solvothermal method has been also applied to synthesize TiO_2 nanocrystals with various shapes. For example, TiO_2 nanoparticles and nanorods could be obtained by solvothermal reaction of titanium butoxide, linoleic acid, triethylamine, and cyclohexane as reported by Li et al.(Li et al. 2006). The decomposition of NH_4HCO_3 which provide H_2O for the hydrolyzation reaction found to be an important factor to shape evolution of particles. In the presence of NH_4HCO_3, the fast hydrolyzation of precursors with the water leads to the formation of nanoparticles (Figure 5-3a). In the absence of NH_4HCO_3, in contrast, the slow nonhydrolytic condensation of precursors produces titania nanorods with uniform diameters of 3.3 nm, and a length of up to 25 nm (Figure 5-3b). TiO_2 nanowires could be also produced by solvothermal treatment of a mixture containing titanium tetroisopropoxide, ethylenediamine, and ethylene glycol (Figure 5-3c) (Xie and Shang 2007). TiO_2 nanocrystals with well-controlled shapes have been recently developed based on solvothermal technique using both acid oleic acid (OA) and oleyamine (OM) as two capping surfactants, and water vapor as hydrolysis agent (Dinh et al. 2009). It is demonstrated that, the presence of water vapor along with the desired OA:OM molar ratio plays crucial roles in controlling size and shape of TiO_2 nanocrystals. In particular, the shape of TiO_2 changed from rhombic to truncated rhombic and to sphere as the OA:OM ratio increased from 4:6 to 5:5 and to 6:4, respectively. Increasing the amount of titanium butoxide (TB) led to the formation of elongated particles. For example, when the TB:OA:OM molar ratio changed from 1:6:4 to 2:6:4, the shape of TiO_2 evolved from spheres to dog bone-like particles with uniform size (Figure 5-3d-f).

Many attempts have been made to the controllable synthesis of various nanocrystals. For example, Li et al.(Deng, Li and Li 2003) reported a facile solvothermal route to obtain II-VI group semiconductor nanocrystals including CdE (E = S, Se, Te) and ZnE (E = S, Se). Short-chain alkylamines such as ethylenediamine were used as structure-directing coordination molecular templates, which have been proven responsible for the morphologies of products. They also synthesized solvothermally size-controllable monodisperse PbSe and PbSe/PbS nanocrystals on scaled-up using lead acetate and Se powders (Xu, Ge and Li 2006). De et al.(Ghoshal et al. 2009) synthesized solvothermally cadmium-compound nanostructures using cadmium nitrate and ethanol as precursor and solvent. The single-crystalline CdO micro-octahedron, polycrystalline CdO nanowires, and $Cd(OH)_2$ nanorods obtained by only varying the amount of NaOH and reaction temperature. Electrical resistivity measurement revealed semiconducting behavior of the CdO nanocrystal sample due to the presence of oxygen vacancies or excess metal interstitial atoms. Fu et al.(Yan et al. 2008b) reported the phase-controlled synthesis of indium-compound nanocrystals by using the solvothermal reaction system containing indium nitrate and a binary solution of water and *N,N*-dimethylformamide (DMF). The composition of the products can be manipulated from cubic $In(OH)_3$ to orthorhombic InOOH and final to cubic In_2O_3 structure by adjusting the water amount (Figure 5-3i). Niederberger group developed a nonaqueous sol-gel approach for the synthesis a variety of oxide nanocrystals involving the solvothermal treatment of metallic alkoxide precursors in benzyl alcohol solvent (Garnweitner and Niederberger 2008).

The solvothermal method had also extended to synthesize the mixed metal oxide nanocrystals. For example, Yu et al.(Zhou et al. 2009) presented an effective ethylene glycol (EG)-assisted solvothermal method to synthesize hierarchical $FeWO_4$ microcrystals using $FeCl_3{\cdot}6H_2O$ and $Na_2WO_4{\cdot}2H_2O$ as precursors. It was found that the organic solvent EG played a critical role as both a reducing agent and a structure-directing agent in driving such architectures assembly by oriented attachment of primary nanoparticles. Moreover, a certain amount of CH_3COONa was necessary for the formation of such unique $FeWO_4$ microstructures. Figure 5-3g shows SEM images of platelike and cookielike hierarchical microcrystals of $FeWO_4$. Platelike $FeWO_4$ microcrystals show a small ferromagnetic at low temperature due to spin-canting of antiferromagnetic materials and their surface spins. Li group had successfully prepared a novel hollow CeO_2-ZrO_2 nanocages with controlled shapes, sizes, and compositions by adding zirconium(IV) into the glycol solution containing CeO_2 nanospheres under solvothermal treatment (Liang et al. 2008). Nearly monodisperse sphericallike CeO_2 nanoclusters the $Ce_{1-x}Zr_xO_2$ nanocages were demonstrated by TEM images shown in Figure 5-3h. The formation of cage-structured CeO_2-ZrO_2 nanomaterials was explained by on the basis of the Kirkendall effect. Namely, when Zr^{4+} ions were added into the system, they readily doped into ceria to form a solid solution of the type $Ce_{1-x}Zr_xO_2$; meanwhile, the diffusion rate of the special secondary nanostructure of the resulting clusters was obviously much faster than that of the single-element nanostructure, leading to the formation of hollow nanostructures of the $Ce_{1-x}Zr_xO_2$ type.

In this dissertation, we developed the modified solvo/hydrothermal “one-phase” surfactant-assistant approaches for the size-and shape-controlled synthesis of a variety of colloidal monodisperse metal oxide (Er_2O_3, V_2O_5, TiO_2, CeO_2, Y_2O_3, ZrO_2, In_2O_3) and mixed metal oxide (metal orthovanadate, tungstate, molybdate) nanocrystals.

5.3. Hydro-Solvothermal Two-phase Synthesis

The two-phase method is performed in two-phase water-organic system by mixing metal sources and capping agents. The two-phase reaction of the nucleation and growth of nanocrystals happened at the liquid-liquid interface of the organic and water phases under room-temperature reduction or hydro-solvothermal treatment in autoclave. The nuclei are formed, and then grow up at liquid-liquid interfaces, the surfactant-capped nanocrystal products could be highly dispersed in the nonpolar phase, and no product was observed in the water phase. The nanocrystal product in the organic phase was precipitated by adding excess of ethanol and recovered by centrifugation. Compared to the single-phase synthetic route, the two-phase strategy can also yield the products with good crystallinity under relatively mild conditions because the presence of the water phase in bulk solution generally increases the speed of the growth process. Particle size and shape can also be controlled because the nucleation process occurs with relatively slow rate at the interface.

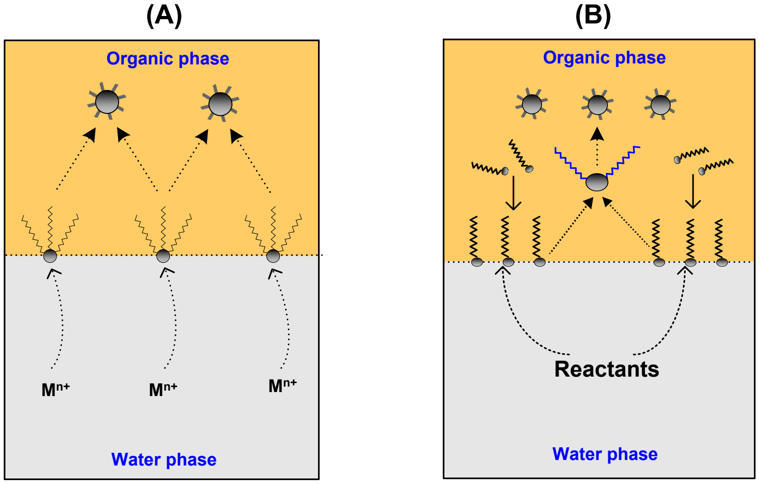

Figure 5.4. General two strategies for the hydro/solvothermal two-phase synthesis of colloidal inorganic nanocrystals in a two-phase toluene-water system using different types of precursor: (A) metal salt precursors disperse in aqueous phase and (B) metal-organic compound precursors disperse in organic phase.

Figure 5-4 shows two strategies to design two-phase aqueous-organic: (i) inorganic salt as precursor dissolve in water phase (Scheme 5-4A) and (ii) metal-ligand complex as precursor disperse in organic phase (Scheme 5-4B). In Scheme 5-4A, the metal hydroxides were formed under basic solution due to the hydrolysis of *tert*-butylamine as an activation agent in water to generate OH^- ions. Upon hydrothermal treatment, these metal hydroxides were dehydrated to oxide nuclei at the interfaces. In Scheme 5-4B, the metal-ligand complex is decomposed at the liquid-liquid interface to form oxide nuclei under catalyzing *tert*-butylamine. In both cases, after the synthesis reaction was terminated, the nanocrystal products will be pulled into the organic phase due to the capping agent. So, the metal oxide nanocrystals could disperse in organic phase. Two synthetic approaches will be presented in our synthetic result. It is well-known that for one-phase system, in order to gain monodisperse nanocrystals, the burst nucleation and then the separation of nucleation and growth must occur during synthesis. However, for the two-phase system, their nucleation and growth process is often much weakly compared with one-phase system, whereby the burst nucleation and the separated nucleation and growth processes are not essential and the resulting nanocrystals still have narrow size distributions. In a two-phase approach, in order to gain narrow the size distribution of well-shaped nanocrystals, the key point is how to slow the reaction rate including nucleation and growth rate. The low reactive precursors often lead to slow the reaction rate.

In 1994, the two-phase approach was first developed by Brust et al. (Brust et al. 1994) for the synthesis of gold nanocrystals, a phase transfer reagent, tetraoctylammonium bromide, was applied to increase the stirring step's efficiency in transferring gold cations to the organic phase (Figure 5-5A). The organic solution of the phase transfer reagent was added to the aqueous solution of $AuCl_4^-$ to form the two-phase system, which was later provided with dodecanethiol as the surfactant. The cationic part of the phase transfer reagent reacts with the anionic complex of Au^{3+}, as in equation 32, and an organic-soluble compound forms. Thus, in this method, the phase transfer reagent along with the surfactant plays the transferring role for metal cations. The first step is finished as soon as the aqueous phase becomes clear, meaning that $AuCl_4^-$ is quantitatively removed from this phase.

$$AuCl_4^-{}_{(aq)} + N(C_8H_{17})_4^+{}_{(toluene)} \rightarrow N(C_8H_{17})_4^+AuCl_4^-{}_{(toluene)} \quad (32)$$

The second step of this technique is the reduction of metal cations within reverse micelles by adding sodium borohydride, $NaBH_4$. The source of electron, BH_4^-, is also captured by free surfactant molecules that are floating at the interface. This second step is summarized in equation 33:

$$mAuCl_4^-{}_{(toluene)} + nC_{12}H_{25}SH_{(toluene)} + 3me^- \rightarrow 4mCl^-{}_{(aq)} + (Au)_m(C_{12}H_{25}SH)_{n(toluene)} \quad (33)$$

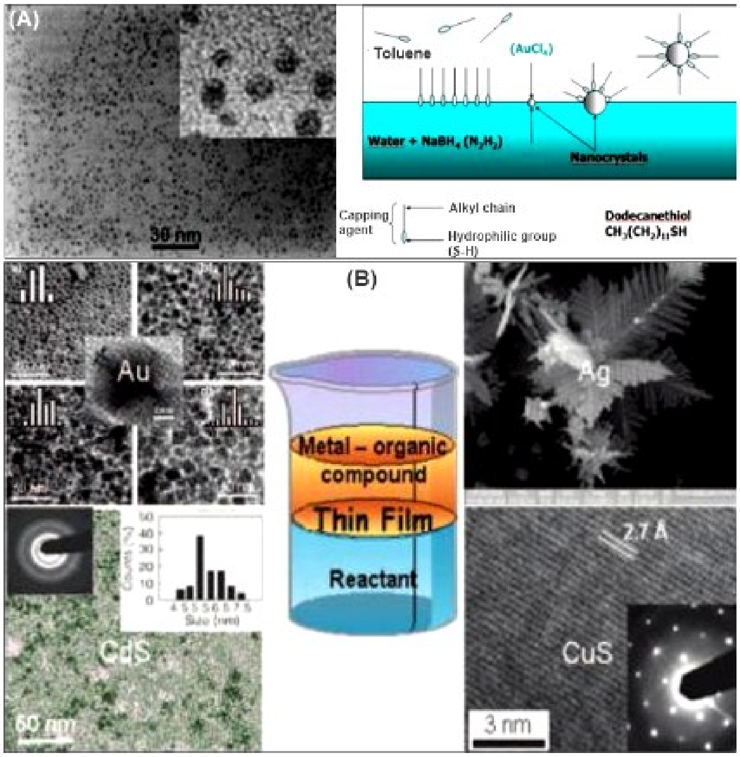

Figure 5.5. Gallery of representative TEM/HRTEM/SEM images illustrating examples of colloidal noble metal and semiconductor nanocrystals synthesized via two-phase route: (A) Au nanoparticles and corresponding formation mechanism of Au particles at toluene-water interface (1994); (B) A specific general two-phase route for the yield of a variety of metal (Au, Ag) and semiconductor (CdS, CuS) nanocrystals (Rao and Kalyanikutty 2008).

This preparative method has been refined repeatedly for different metals and stabilizing ligands. For instance, Ag, Pt, Pd and semiconductor nanoparticles (Figure 5-5B) have been successfully synthesized by the application of refined versions of the technique by Brust et al (Xia et al. 2009). Alkylamines have also substituted for alkanethiols to confirm the flexibility of this method for various kinds of surfactants. The surfactants, consisting of a coordinating head group and a long alkyl chain, adsorb reversibly to the surfaces of the growing nanocrystals, and thus provide a dynamic organic capping layer that stabilizes the nanocrystals in solution and also mediates their growth, providing excellent control of crystallite size and shape.

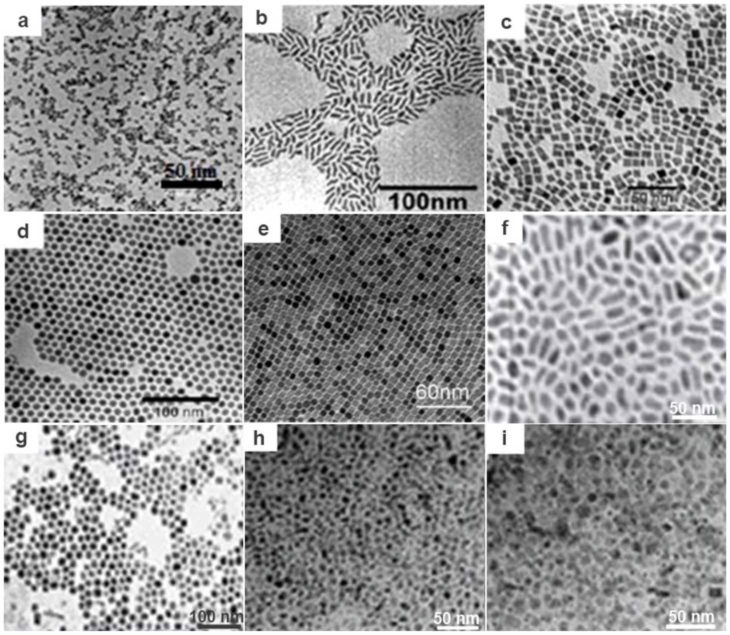

Figure 5.6. Gallery of representative TEM/HRTEM images illustrating examples of colloidal metal oxide and semiconductor nanocrystals synthesized via solvo/hydrothermal two-phase route: (a) TiO_2 nanoparticles (Pan et al. 2005b); (b) ZrO_2 nanorices (Zhao et al. 2006); (c) Mn_3O_4 nanocubes (Zhao et al. 2008); (d) Mn_3O_4 nanospheres (Zhao et al. 2008); (e) CeO_2 nanocubes (Zhang et al. 2007); (f) InOOH elongated nanocrystals (Zhao et al. 2010); (g) $Cr(OOH)_3$ nanospheres (Zhao et al. 2010); self-assembly of (c) Au-ZrO_2 and (d) Au-TiO_2 nanoparticles (Mrabet, Zahedi-Niaki and Do 2008).

Related progress using this two-phase approach was also extended to the synthesis of a variety of metal oxide and mixed oxide nanomaterials under solvo/hydrothermal treatment. The An group reported a modified two-phase approach for the synthesis of the

CdS nanocrystals which was produced at the water/toluene interface by mixing cadmium myristate toluene solution and thioure aqueous solution (Wang et al. 2005a). Additionally, the authors used a seeding-growth technique to change the CdS nanocrystal sizes. They also synthesized the CdSe and CdSe/CdS core/shell nanocrystals using selenourea as a selenium precursor by this two-phase approach. The CdSe/CdS core/shell nanocrystals exhibited quantum yields up to 60-80%, photoluminescence of nanocrystals can be clearly observed even without UV lamp irradiation (Pan et al. 2005a). By a growth technique, the authors also synthesized two multi-shell nanocrystals of CdS/CdSe/CdS/CdSe/CdS and CdSe/CdS/CdSe/CdS/CdSe/CdS nanocrystals (Pan et al. 2006). Xu et al.(Wang et al. 2009) had recently achieved two-phase solvothermal synthesis of rare-earth doped $NaYF_4$ upconversion fluorescent nanocrystals by using water/ethanol/rare-earth stearate/oleic acid system.

Moreover, metal oxide and mixed oxide nanocrystals can also be synthesized by a two-phase approach. The reaction mechanism is shown in Figure 5-4. Pan et al.(Pan et al. 2005b) reported on the synthesis of monodisperse TiO_2 nanocrystals from the hydrolysis of titanium(IV) *n*-propoxide in the water-toluene mixture. Alkoxide can be used as titanium precursor, *tert*-butylamine and oleic acid are used as an activation agent and capping agent, respectively. As an indirect band-gap semiconductor, the luminescence of resulting TiO_2 nanocrystals was also observed at room temperature. Ji et al.(Zhao et al. 2006) synthesized ZrO_2 nanocrystals with spherical-, teardrop-, rod-, and rice-shapes. The shapes of nanocrystals can be controlled by changing the zirconium(IV) *n*-propoxide concentration, the nature of capping agents, and the reaction temperature. Figure 5-6a,b shows typical TEM images of TiO_2 and ZrO_2 nanocrystals. Kaskel et al.(Du et al. 2007) also used this method to synthesize of $BaTiO_3$ nanocrystals using mixed titanium(IV)-*n*-butoxide and barium acetate precursors. Furthermore, Adschiri et al.(Zhang et al. 2007) modified this reaction system for the synthesis of CeO_2 nanocubes using cerium hydroxide precursors under supercritical water conditions (Figure 5-6e). The product shape could be controlled by tuning the interaction of organic molecules with various crystallographic planes of fluorite cubic ceria. In contrast to metal alkoxide precursors, metal stearates are cheaper and more stable; Ji et al.(Zhao et al. 2008) produced the Mn_3O_4 nanocrystals using manganese(II) stearate precursors. The spherical and cubic shapes and their particle size can be controlled by adjusting the reaction time and activation agent concentration, as shown in Figure 5-6c,d. Ji et al.(Zhao et al. 2010) recently developed a general two-phase approach to produce more kinds of monodisperse of inorganic nanocrystals with controlled size and shape (Figure 5-6f).

Recently, our group presented a modified two-phase method for the synthesis of alkyl chain-capped metal particles (e.g., Cu and Au) and metal oxide nanoparticles (TiO_2 and ZrO_2), followed by their cooperative assemblage into unusual hybrid metal/metal oxide nanocrystal mesostructured materials (Mrabet et al. 2008). Typical TEM images of the mixed oxide nanoparticles of Cu-ZrO_2, Cu-TiO_2, Au-ZrO_2, and Au-TiO_2 with an average diameters in the range of 3-8 nm are shown in Figure 5-6g-i. The catalytic activity of products for the CO oxidation was also employed. Indeed, these hybrid metal/metal oxide nanocatalysts exhibited high surface areas, narrow pore size distributions, and exceptional catalytic properties in the oxidation of CO, even surpassing the performance of commercial noble metal catalysts.

In this dissertation, we developed the modified solvo/hydrothermal "two-phase" surfactant-assistant approaches for the size-and shape-controlled synthesis of a variety of colloidal monodisperse metal oxide (CeO_2, Sm_2O_3, Y_2O_3, La_2O_3, Gd_2O_3, Mn_3O_4, Cr_2O_3, NiO, CeO_2, Y_2O_3, ZrO_2, In_2O_3) nanocrystals and colloidal nanostructured $Ce_xLa_{1-x}CO_3OH$ solid solution and their diverse oxides.

5.4. Seed-Mediated Growth

A seeded-growth approach provides a very effective method for generating heterogeneous inorganic nanocrystals with well-controlled nanostructures. By preventing secondary nucleation and by doing step-by-step growth on the pre-existing seed surfaces, the hybrid inorganic nanocrystals such as core/shell and dumbbell of good monodispersity can be obtained. When the secondary metal evenly deposits and sequential grow onto the surface of the preformed seed, core/shell nanostructures will be obtained, while dumbbell nanostructures can be synthesized if the deposition and growth of the second metal occur on specific site of the seed. Namely, each component can fused together to generate the dumbbell-shaped nanostrucuture when the individual components involved have similar crystal structures and lattice parameters. While the large lattice space difference of the individual components leads to the core-shell structure (Zeng and Sun 2008). Generally, in order to obtain hybrid nanostructures based on seeded-growth process, heterogeneous nucleation and simple growth via atomic addition must be achieved and homogeneous nucleation should be avoided.

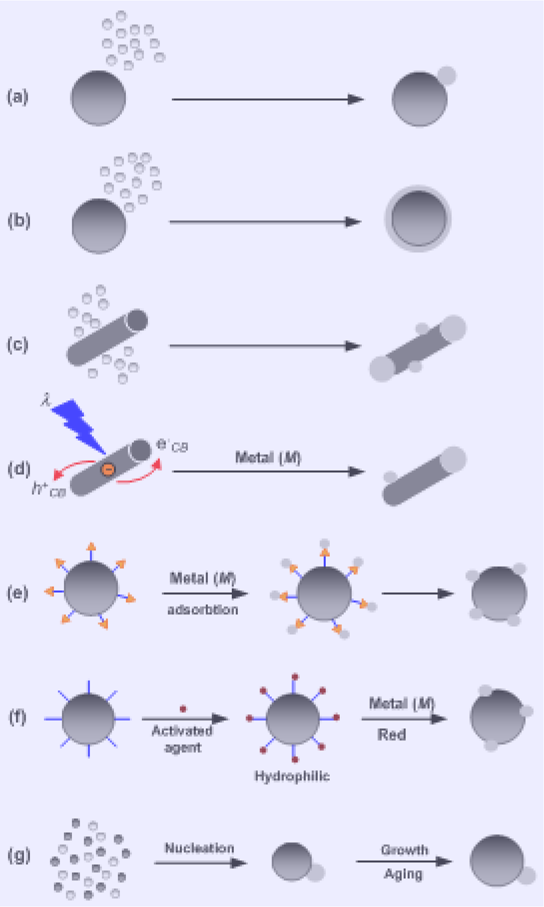

Figure 5.7. Sketch of reaction mechanisms for the formation of hybrid nanocrystals: (a-c) direct heterogeneous nucleation and growth of the metal precursors onto the preformed seed surfaces; (d) metal particles adsorb onto the opposite-charged-surfaced nanosupports by the photo-irradiation; (e) redox-precipitation of metal precursors on the hydrophilic-surfaced nanoislands; (f) metal precursor growth on the activated-surfaced nanosupports; (g) one-pot approaches by self-controlled nucleation-growth.

Colloidal nanohybrids are generated upon reaction of molecular precursors in a liquid solution in the presence of surfactant agents. Once the synthesis is activated at a suitable temperature, the monomers are generated, and then induce the nucleation of nanocrystals and sustain their subsequent enlargement. The organic surfactants play several key roles along the course of hybrid nanocrystal formation. Figure 5-7 shows the general seeded growth models for the fabrication of dumbbell- and core/shell-shaped hybrid nanocrystals, accordingly, it can be classified into five main synthetic approaches (Carbone and Cozzoli 2010): (i) direct heterogeneous nucleation and growth of the metal precursors onto the surfaces (facet sites or tips) of preformed seeds (Figure 5-7a-c); (ii) the small metal nanoparticles adsorb onto the opposite-charged surface of nanosupports by the photo-irradiation (Figure 5-7d); (iii) reduced-precipitated onto the colloidal nano-islands by the reduced reaction of the metal salt precursors previously adsorbed on their hydrophilic surface through ion exchange (Figure 5-7e); (iv) metal precursor growth after chemical activation of the surface of nanosupports (Figure 5-7f) ; (v) one-pot approaches by self-controlled nucleation growth (Figure 5-7g).

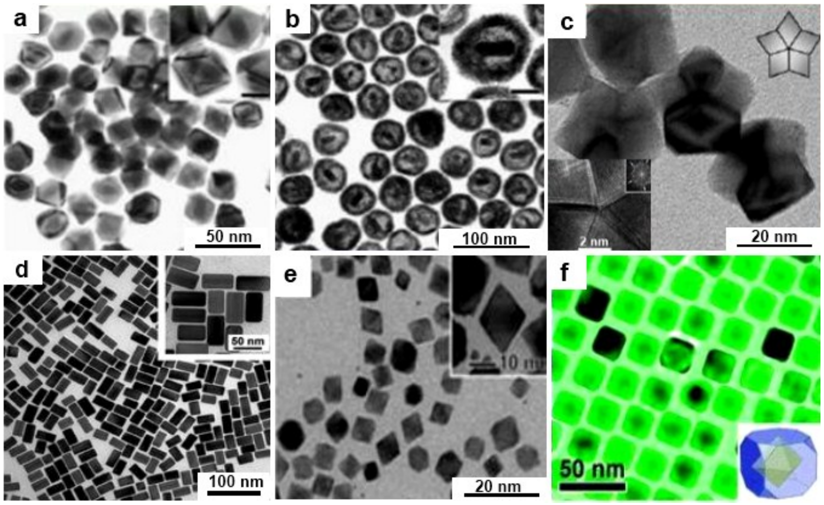

Figure 5.8. Gallery of representative TEM/HRTEM images illustrating examples of bimetallic nanohybrids: (a) Au@Ag core-shell nanostructures with a mean diagonal length of 64.8 nm (Cho, Camargo and Xia 2010); (b) Pt-based hollow nanostructures containing Au nanorods in the center (Cho et al. 2010); (c) alloy Pd-Pt star-shaped decahedrons (Lim

et al. 2009); (d) anisotropic Au-Ag core-shell nanorods (Okuno et al. 2010); (e) Pd-Pt core-shell octahedrons (Jiang et al. 2010); (f) Au@Pd core-shell nanocubes (Fan et al. 2008).

On the other hand, in order to further control the mode of overgrowth for a deposited metal, which can determine the morphology of final hybrid products, the kinetic parameters must also be carefully adjusted. As we know, the competing crystal growth on different side facets of preformed nuclei will result in the formation of nanohybrids with well-defined morphology exposing crystal planes that are most kinetically favored. Moreover, the growth rates on different facets can be artificially controlled to achieve the synthesis of nanohybrids with pre-designed morphology. A common method is to use proper stabilizing agent to change the kinetic stability of special facet utilizing the different interactions between stabilizing agent and surfaces. Therefore, the selection of kinetic parameters is crucial for the control of overgrowth mode in a seeded-growth process.

Figure 5-8 displays a gallery of representative TEM and HRTEM images of bimetallic nanohybrids. Xia et al.(Cho et al. 2010) reported on the synthesis of the uniform Au@Ag core shell materials with a uniform size distribution are composed of Ag nanocrystals containing Au nanorods in the center (Figure 5-8a,b). The dimensions of the core-shell nanostructures were easily tuned by using Au nanorods with different aspect ratios and/or by controlling the amount of $AgNO_3$ added into the reaction system. When no PVP was added, small Ag particles still deposited on Au nanorods to form octahedral nanocrystals via a homogeneous nucleation process. In the case without adding CTAB, Ag could not nucleate and grow on the Au nanorods. These were Au@Ag core-shell nanostructures that showed one broad peak at ~460 nm and a shoulder peak at ~350 nm. The formatyion of Ag shell on Au nanorod in hexadecyltrimethylammonium chloride (CTAC) and hexadecyltrimethylammonium bromide (CTAB) mixed micellar solutions were also achieved (Okuno et al. 2009). The extinction spectra, photographs of the dramatic changes in color from orange to green of the reaction solutions, and TEM images of the elongated shape of the anisotropic Au-Ag core-shell nanocrystals using $AgNO_3$ solutions at the different Ag/Au molar ratios are shown in Figure 5-8d (Okuno et al. 2010). Ag@Au core-shell nanocrystals were prepared by coating Au nanodumbbells with silver in an aqueous solution containing CTAB, $AgNO_3$, NaOH, ascorbic acid. The morphology observation showed that Ag grew on top of the Au dumbbell core, rather than growing on the side of Au. The Au@Ag core-shells served as excellent SERS substrates, as significantly higher enhancement factors were expected for silver as compared to gold (Fernanda Cardinal et al. 2010).

Ag@Au core-shell triangular bifrustum nanocrystals were synthesized in aqueous solution using a seed-mediated approach. The formation of the Ag layer on the Au nanoprism seeds led to structures with highly tunable dipole and quadrupole surface plasmon resonances (Yoo et al. 2009). Very recently, Xia group still used the seed-mediated growth process to synthesize the well-defined Au@Ag core-shell nanocubes (Saravanan et al. 2010). The synthetic procedure of the Au seeds was composed of two steps: (i) 2-3 nm Au nanoparticles were prepared by reducing $HAuCl_4$ with $NaBH_4$ in the presence of CTAB, and (ii) these Au particles grew into 11 nm Au nanocrystal seeds with cubo-octahedral shape in $HAuCl_4$/ascorbic acid/CTAC. The Au@Ag core-shell nanocubes were formed by depositing Ag on the as-prepared CTAC-capped Au seeds via adding $AgNO_3$, ascorbic acid, CTAC into an aqueous suspension containing the Au seeds at 60 °C. The Ag shell thickness could be finely tuned from 1.2 to 20 nm by varying the $AgNO_3$/Au molar ratio. When CTAC was displaced by CTAB as capping agent, the resultant core-shell nanocrystals with controlled cube shape became difficultly, possible due to the primary formation of AgBr precipitates. The Ag shells of the hybrid nanocubes could be transformed into porous Au shells with slightly enlarged dimensions while the Au cores were kept inside the shells via a galvanic replacement process because the reduction potential of Ag is the lower than that of Au.

For bimetallic Au and Pd system, it would be interesting to use Au nanocubes as the structure-directing cores for the overgrowth of Pd shells. Because of a significant lattice mismatch between gold and palladium, the resultant Au-Pd core-shell nanocrystals may exhibit unusual morphologies and high-index facets. Such nanocrystals with high catalytic activities may be obtained. The Pd-Au core-shell nanocubes and spherical nanostructures were formed by reducing $HAuCl_4$ with L-ascorbic acid in the presence of cubic Pd seeds in an aqueous solution (Figure 5-8f). The synthesized Pd-Au bimetallic nanocrystals which combine the properties of both Pd and Au, can generate the novel catalytic properties and potential applications including in situ monitoring of catalytic reactions via surface-enhanced Raman scattering (Lim et al. 2010). Two-step seed-mediated growth method for synthesizing single-crystalline 41.5 nm-sized Au@Pd nanocubes was performed in high yield via the overgrowth on the octahedral Au cores with 30 nm in diameter by reducing H_2PdCl_4 with ascorbic acid under the assistance of CTAB surfactant. The different deposition of metal shell on the core for the overgrowth core-shell process was revealed by Ostwald ripening mechanism. Synthetic parameters such as a reducing, capping agent, metal ion, and reaction temperature could also play an important role in the overgrowth process (Fan et al. 2008).

To date, disparate elaboration of metals, oxides, and semiconductors have been addressed by manipulating direct heterogeneous deposition pathways. In this dissertation, we developed the modified seed-mediated growth in the surfactant assistant for the size- and shape-controlled synthesis of many new types of metal@oxide (Cu@CeO_2, Ag@Y_2O_3, Ag@In_2O_3), metal@semiconductor (Ag@TiO_2), metal@mixed oxide (Au@$MnWO_4$, Au@$CoWO_4$, Ag@$MnWO_4$, Ag@$CoWO_4$) nanohybrids. These hybrid nanomaterials were used as excellent catalysts for CO oxidation conversion and Methylene Blue photodegradation in the catalytic application section of the thesis.

5.5. Characterization

5.5.1. X-Ray Diffraction (XRD)

X-ray diffraction (XRD) was used to determine the crystallographic structure and different phases in the nanocrystal products. Wide-angle ($2\theta > 10°$) X-ray diffraction studies are widely used for crystal structure identification and lattice constant determination. X-rays are produced by a beam of fast electrons bombarding a metal target in an evacuated tube. The energetic electrons excite the target atoms, which subsequently emit high frequency electromagnetic radiation as they decay back to their ground states. When an X-ray beam heats the atoms in the solid sample the electrons of these atoms start to oscillate and form constructive interference, which is characteristic of the arrangement of atoms in the crystal. The diffracted beam consists of in phase X-rays which mutually reinforce one another. The diffraction can be explained by incident and reflected rays and theta angle (θ) between them. Using Bragg's Law (eq. 34), the unit cell dimensions (d) can be determined as shown in Figure 5-9.

$$2d\sin\theta = n\lambda \qquad (34)$$

The average crystallite sizes of samples can be calculated from the XRD spectra using the Debye-Scherrer equation:

$$D = \frac{K_\alpha \lambda}{B\cos\theta_B} \qquad (35)$$

where D is the thickness of the crystal (Å); $K_\alpha = 0.9$ is a constant related to the crystal shape; λ is the X-ray wavelength (1.54051 Å for CuK_α); θ_B is the Bragg angle (between incident and diffracted beam); B is the line broadening, measured from the peak width at half the peak height; copper K_α was the radiation source. Spectrometric studies on this work were conducted using a Bruker SMART APEXII X-ray diffractometer (Department of Chemical Engineering, Laval University).

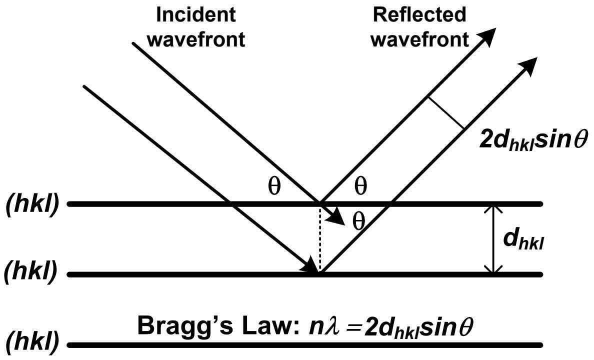

Figure 5.9. Schematic representation of the X-ray diffraction illustrating crystal planes and Bragg's law, the incoming X-rays diffract with θ angle in the lattice of the material and only the waves in face can be detected (*hkl*: the Miller indices).

Estimation of average crystal size: Scherrer equation is a very useful tool to estimate the average crystal size in submicrometric solids. Multiplying both sides of the Bragg's equation by an integer *"m"* such that $m \cdot d = t$, the thickness of the crystal, leads to:

$$m.\lambda = m.2.d_{hkl} \sin\theta \qquad (36)$$

$$m.\lambda = 2.t.\sin\theta \qquad (37)$$

Equation 37 can also be interpreted as the m^{th} order reflection from a set of planes with interplanar distance t. Differentiating both sides of equation 37, remembering that *"$m\lambda$"* is a constant, gives:

$$\theta = 2.\Delta t.\sin\theta + 2.t.\cos\theta.\Delta\theta \qquad (38)$$

$\Delta\theta$ can be positive or negative (only absolute values are of interest). Then:

$$t = \frac{\Delta t.\sin\theta}{2.\cos\theta.\Delta\theta} \qquad (39)$$

Sine the smallest increment in t is d, using $\Delta t = d$, and substituting $\lambda/2$ for $d.sin\theta$ (from Bragg's law) we get,

$$t = \frac{\frac{\lambda}{2}}{2.\cos\theta.\Delta\theta} \qquad (40)$$

Substituting B for $2\Delta\theta$, the angular width,

$$t = \frac{\lambda}{B.\cos\theta} \qquad (41)$$

Which is essentially Scherrer's equation. A more sophisticated analysis of the problem only adds a pre-factor of 0.95 to the right hand side of equation 41 and leads to the corrected Sherrer's equation:

$$t = \frac{0.95\lambda}{B.\cos\theta} \qquad (42)$$

In this equation, λ represents the wavelength of the X-ray radiation, B is the width of the diffraction peak at half its maximum intensity (in radians), and θ the maxium scattering angle.

5.5.2. Transmission Electron Microscopy (TEM)

One of the most common methods for determining the size and shape of nanomaterials is transmission electron microscopy (TEM) technique. A light source at the top of the microscope emits the electrons that travel through vacuum in the column of the microscope. Instead of glass lenses focusing the light in the light microscope, the TEM uses electromagnetic lenses to focus the electrons into a very thin beam. The electron beam then travels through the specimen you want to study. Depending on the density of the material present, some of the electrons are scattered and disappear from the beam. At the bottom of the microscope the unscattered electrons hit a fluorescent screen, which gives rise to a shadow image of the specimen with its different parts displayed in varied darkness according to their density. The image can be studied directly by the operator or photographed with a camera.

Characterization with TEM first involves creating dilute suspensions of a sample, placing a small drop (~20 microliters) on a copper grid, and allowing the sample to dry. The sample is bombarded with a uniform beam of electrons, with an acceleration voltage that can range from 100 kV to 3 MV, that pass through the sample to a detector. The interaction of the electrons with the atoms in the sample produces an image based on the electron cloud density of the sample. Samples with high density, such as metal and metal oxide, often generate images with a high degree of resolution and contrast. The advantages of TEM technique allow for the direct visualization of the sample and easily provide a direct measure of the morphology of nanocrystals, including the size, shape of the particles, size distribution, self-assembly, as well as their crystal lattice spacing. From the image, the sizes of the particles can be determined by comparison to the scale bar; and the size distribution is evaluated from the statistical measurement of hundreds of particles. Furthermore, this diffraction pattern, known as selected-area electron diffraction (SAED) pattern, is a good source of information to determine the crystalline structure of the sample. All the TEM specimens for this research were prepared by evaporating one drop of nanocrystal solution (using toluene or ethanol) on carbon-coated copper grids. The TEM micrographs were obtained using JEOL JEM 1230 transmission electron microscopes operating at 120 kV (Laval University).

5.5.3. Scanning Electron Microscopy

Scanning electron microscopy (SEM) is used to obtain information about the size and morphology of the powdered samples. In SEM the lenses do not form an image of the specimen. Instead, the lenses are used to generate a de-magnified, focused spot of electrons that is scanned over the surface of an electrically conductive specimen. As these electrons strike the specimen, they give rise to a variety of signals, including low energy secondary electrons from the uppermost layers of the specimen. Some of the secondary electrons are collected, processed, and eventually translated as a series of pixels on a cathode ray tube or monitor. For each point where the electron beam strikes the specimen and generates secondary electrons, a corresponding pixel is displayed on the viewing monitor. The brightness of the pixel is directly proportional to the number of secondary electrons generated from the specimen surface. Since the electron beam is scanned rapidly over the specimen, the numerous, minute points appear to blend into a continuous image composed of many density levels or shades of gray. The shading is similar to an ordinary black and white photograph in which light and dark tones give the impression of depth. However, a main disadvantage is that samples that are not conductive must undergo an additional preparative step of sputter coating with gold in order to obtain a reasonable image. SEM images of nanocrystal products on this work were obtained from a JEOL 6360 instrument working at 3 kV (Department of Chemical Engineering, Laval University).

5.5.4. Energy Dispersive X-ray Spectroscopy (EDS)

One of the chemical analysis systems of TEM or SEM is energy-dispersive X-ray spectroscopy (EDS) which can be applied to quantify the atomic ratios of the constituent elements accurately in the nanocrystal species synthesized. The technique relies on measuring the characteristic X-rays energies emitted when a transition of the outer shell electrons to inner shell occurs. A high energy incident electron beam creates an electron hole in the inner shell and causes the transition of an outer shell electron. Because all elements have a unique electronic structure the X-ray emitted through this process provides a characteristic signature used for elemental identification. The quantum transitions due to these excitations will cause many scattering signals, e.g., X-rays and Auger electrons. These signals are the fingerprints of the elements in the sample, and can be used as a source of quantitative chemical and electrical structural information. In EDS, we are concerned with the counting of the X-rays emitted from the beam-illuminated specimen region as a function of the photon energy. The probe size for the incident electron can be in the range of 2-3 nm, providing the possibility of taking EDS spectra from every single nanocrystal. EDS is mostly sensitive to heavy elements due to the fluorescence effect that is associated with Auger emission for light elements. We acquired EDS data for our samples during SEM analysis on a JEOL 6360 instrument to investigate the chemical compositions of synthesized nanocrystals.

5.5.5. X-ray photoelectron spectroscopy (XPS)

X-ray photoelectron spectroscopy was used to obtain surface compositions and chemical states of the metals in the electrocatalysts. The technique basically relies on photoelectric effect. When an element with a core level electron binding energy of E_B is illuminated with soft X-ray photon of energy hν, it causes the electrons to be emitted. The energy of the emitted photoelectrons is then analyzed by the spectrometer. Photoelectron spectroscopy is based upon a single photon in and/or electron out process and from many viewpoints this underlying process is a much simpler phenomenon than the Auger process. The energy of a photon of all types of electromagnetic radiation is given by the Einstein relation:

$$E = h\nu \qquad (47)$$

where h: Planck constant ($6.62.10^{-34}$ J.s); ν: frequency (Hz) of the radiation.

Photoelectron spectroscopy uses monochromatic sources of radiation (e.g., photons of fixed energy). The kinetic energy distribution of the emitted photoelectrons (e.g., the number of emitted photoelectrons as a function of their kinetic energy) can be measured using any appropriate electron energy analyser and a photoelectron spectrum can thus be recorded.

5.5.6. Braunauer-Emmer-Teller analysis (BET)

The textural properties of solid material can be characterized by porosity, surface area, pore volume, and pore size. Porous solids can have pores in the form of cavities, channels, or interstices. Some of these pores are closed, while open pores may have different shapes including cylindrical, blind with one open end, inkbottle or funnel shaped. Porosity is the ratio of the total pore volume to the apparent volume of the particles in the powder. For nanomaterials, pore size or pore diameter is the space of opposite particles. Pore size is important for the application of materials. They are divided into three pore size regions and characterized according to their sizes: microporous (diameter < 2 nm), mesoporous (2 nm < pore diameter < 50 nm), and macroporous (pore diameter > 50 nm). Porosity of these solids can be characterized by gas adsorption studies. The adsorption of gas over the surface of the material allows determination of the specific surface area, total pore volume, and pore size distribution of the sample. The free gas and absorbed gas are in dynamic equilibrium, and the surface coverage depends on the pressure of the gas. The fractional surface coverage measured at different pressures at a set temperature gives adsorption isotherms. The mathematical analysis of the adsorption isotherm gives necessary data for calculations of surface areas and porosity characteristics of the samples. Nitrogen is the gas traditionally used as the adsorbate and allows calculating the cross-sectional area of an adsorbate. The Branauer-Emmet-Teller equation (48) is widely used for determining of the surface area of solid materials.

$$\frac{1}{W(\frac{P_o}{P}-1)}=\frac{1}{W_mC}+\frac{C-1}{W_mC}(\frac{P}{P_o}) \qquad (48)$$

where W is the weight of the absorbed gas at relative pressure P/P_o, C is a constant related to the energy of adsorption in the first adsorbed layer, and W_m is the weight of a monolayer of adsorbate. The total surface area of the sample can be calculated by

$$S_t = \frac{W_m N A_{cs}}{M} \qquad (49)$$

where N is an Avogadro number (6.023 ×1023 molecules/mol) and M is a molecular weight of the adsorbate, and A_{cs} is a cross-sectional area (16.2 Å at 77 K). The specific surface area can be calculated from the total surface area and the weight of the material sample:

$$S = \frac{S_t}{w} \qquad (50)$$

The total pore volume can be calculated from the amount of vapor adsorbed at relative pressure close to unity. Besides, the pore size distribution can be calculated from the desorption branch of the isotherm. Pore size is calculated using the Kelvin equation:

$$r_K = \frac{-2\gamma V_m}{RT \ln \frac{P}{P_o}} \qquad (51)$$

where γ is a surface tension of nitrogen at its boiling point (8.85 ergs/cm^2 at 77 K), V_m is a molar volume of liquid nitrogen (34.6 cm^3/mol), R is a gas constant (8.314 × 107 ergs/degmol), T is a boiling point of nitrogen (77 K), P/P_o is a relative pressure of nitrogen, and r_K is a Kelvin radius of the pore. The analysis of gas adsorption on the surface of the material can provide information on the surface area and porosity. The adsorption isotherm is obtained by introducing known volumes of nitrogen and measuring the equilibrium pressure. The desorption isotherm is obtained by measuring the quantities of released gas from the samples as the relative pressure is lowered. All isotherms may be divided into five types according to the way the adsorption of nitrogen occurs.

Type I isotherm is associated with microporous materials where the adsorption of nitrogen is on the external surface area and is limited by the accessibility of the micropores.

Type II isotherms represents nonporous and macroporous materials where unrestricted multilayers of nitrogen can be adsorbed. Type III isotherm is characterized by the heat of adsorption which is less than the heat of adsorbate liquid faction and there is an additional adsorption through the interaction with the adsorbed layer. Type IV isotherm represents mesoporous materials where the mesopores are filled at higher elevated pressures. Finally, Type V isotherm is similar to the Type III isotherm but this type is common for mesoporous materials. The adsorption and desorption branches in Type I, Type II, and Type III isotherms are identical and hysteresis occurs very rarely. However, in Type IV and Type V isotherms there is a hysteresis effect between adsorption and desorption. The bottleneck shape of pores and differences in the meniscus of the condensing and evaporating nitrogen causes this effect.

In this dissertation, nitrogen adsorption/desorption isotherms were obtained by using a Quantachrome Autosorb-1 system. Prior to measurements, all samples were degassed at a temperature of 200 ^{o}C for ~2 h. The specific area was calculated from the linear part of the Brunauer-Emmett-Teller (BET) equation ($P/P_o \approx$ 0.05-0.20). The pore size distributions were obtained from the analysis of the desorption branch of the isotherms using the Barret-Joyner- Halenda (BJH) model.

5.5.7. FTIR Spectroscopy

Fourier transform infrared (FTIR) spectroscopy is a technique for collecting spectra and measuring the temporal coherence of its radiation source. It can be utilized to various spectroscopy methods including infrared spectroscopy. Molecular vibrations can be analyzed by infrared spectra, and since for each molecule these vibrations occur at specified frequencies, the spectra can be interpreted by checking the peaks with the IR database to determine the chemical structure of the sample. All of the FTIR spectra in this work were taken with a FTS 45 infrared spectrophotometer. A pellet of mixed the solid nanocrystal sample (0.1 wt.%) and pure KBr was created and its infrared spectra were recorded for the wavenumbers in the range of 400-4000 cm^{-1} with a resolution of 4 cm^{-1}. These spectra were compared with FTIR spectra of the pure surfactant to indicate whether the surfactant bonds to the surface of the nanocrystals.

5.5.8. Ultra Violet -Visible Spectroscopy (UV-Vis)

Measuring the optical properties of molecules provides insight into their band gap, size, and shape. In absorption measurements, incident light is selectively refracted, exposing the sample to one wavelength at a time. By comparing the molecule solution to the pure solvent, intrinsic wavelength versus absorption spectra can be obtained. Additionally, when electrons in semiconductor oxide are excited with energy greater than the band gap of semiconductor, the electrons relax by emitting photons at a wavelength of the band gap. This is due to the band theory of electrons where electrons can reside only in certain states. By measuring the wavelength of light emitted, the band gap can be readily determined. In UV-Vis, high energy electromagnetic radiation in the wavelength range of 200-800 nm is utilized to promote electrons to higher energy orbitals. Since orbitals have quantized energy, only certain transitions can occur in the UV-vis energy range. The differences in the incident and transmitted beam give us information about the frequencies which are absorbed by the sample molecules. Based on absorbance data, the sample chemical structure can be analyzed. In this work, absorption spectra of nanocrystal liquid (toluene, ethanol, or water) or solid (MgO) solution were obtained in the range of 250-800 nm via a Cary 300 Bio UV-visible spectrophotometer; and pure toluene, ethanol, water, MgO (depended on the nature of nanocrystal surface) were used as blank.

5.5.9. Thermal Analysis (TGA-DTA)

Thermogravimetric analysis (TGA) shows that heating a freshly prepared nanocrystal sample in air causes the desorption of physically adsorbed solvent and water from the surface at 100-200 ºC and decomposition of residual organic groups into carbon dioxide at 300-500 ºC. This method was used to determine the weight loss of organic residuals during the heat treatment. Attention must be directed to the removal of organics to avoid undesirable blackening of the sample from the reduction of organic residuals into pure carbon. Two major weight losses were observed. The first weight loss occurs during heating to 100-160°C and can be attributed to the remove of physisorbed water. The second weight loss occurs at 400 °C which is due to the removal of chemisorbed water and organic residuals of solvent. In parallel with TGA, differential thermal analysis (DTA) is characterized by the detection of any variation in energy taking place in the reaction of sample. The thermal analysis experiments and results reported here were conducted on Perkin-Elmer TGA thermogravimetric analyzer, a type of simultaneous TGA-DTA equipment. The heating rate was controlled at 10 °C/min under highly pure O_2 gas flow for all experiments.

5.5.10. Photoluminescence spectroscopy

Photoluminescence (abbreviated as PL) is a process in which a substance absorbs photons (electromagnetic radiation) and then re-radiates photons. Quantum mechanically, this can be described as an excitation to a higher energy state and then a return to a lower energy state accompanied by the emission of a photon. This is one of many forms of luminescence (light emission) and is distinguished by photoexcitation. The period between absorption and emission is typically extremely short, in the order of 10 nanoseconds. For a direct band gap transition photons with enough energy excite an electron from the ground state valence band into an excited state in the conduction band. In semiconductor physics terms, the incoming energy creates an electron-hole pair of positive and negative charges, and these pairs or excition retain that excited energy which is then released when the electron and hole recombia. Knowing the band gap when can estimate the average nanoparticle size using the effective mass approximation. Even the particle size distribution can be estimated using from the photoluminescence as a broad size distribution would be reflected by a broad emission signal. Further the distribution structure would also be mirrored in the emission signal, for example, a bimodal distribution would give a bimodal signal profile.

5.5.11. CO oxidation experiments

All catalytic tests were carried out with a high hourly space velocity (GHSV, e.g., short contact time) due to the fact that the subambient temperature experimental setup was not available in our laboratory. Figure 5-12 shows a schematic diagram of of the experimental catalytic CO oxidation system. A flow fix-bed microreactor was used to investigate the catalytic activity of nanocatalysts for the CO oxidation reaction. Typically, small amount (~300 mg) of sample catalyst was diluted with equal weight of glass beads (20-40 mesh) and introduced in a stainless-steel tubular reactor (i.d. = 4 mm). Then the catalyst first was activated by passing a flow of 30 mL/min of dry ultrapure helium at 250 °C and later using a mixture of H_2/helium (10% hydrogen). A stream of 60 mL/min reaction gas mixture containing 2.3% CO, 2.5% O_2, and the balance helium was passed on the catalyst bed at different temperatures for specified times. The reactor effluent was then analyzed by using an online IR gas analyzer (FTLA2000, ADD, Canada). The amounts of CO, CO_2, an oxygen were monitored in reaction products.

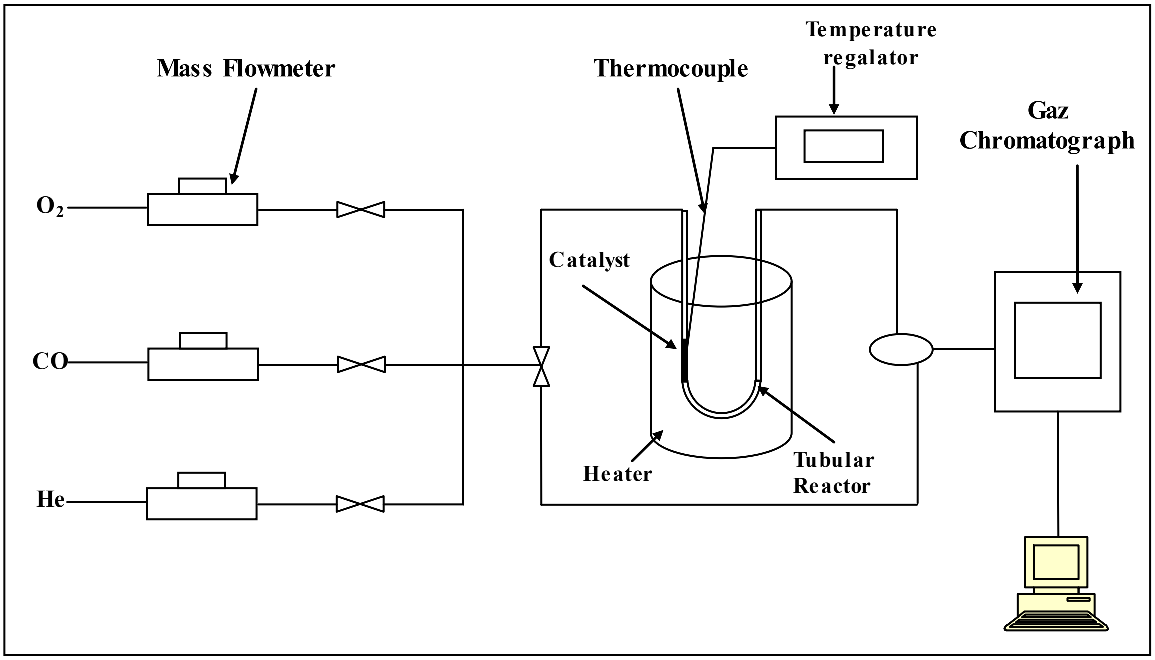

Figure 5.10. Schematic diagram of of the experimental catalytic CO oxidation system setup.

5.5.12. Photocatalytic experiments

Metylene Blue (MB) was selected as model chemicals to evaluate the activity and properties of the photocatalyst. In a typical experiment, an queous suspensions of MB and photocatalyst powders were placed in a 50 mL beaker. Prior to irradiation, the suspensions were magnetically stirred in the dark for ~30 min to establish adsorption/desorption equilibrium between the MB and the surface of the catalyst under room air equilibrated conditions. The solution was then exposed to UV-visible light irradiation under magnetic stirring. At given irradiation time intervals, the mixed solution were collected and centrifuged to remove the catalyst particulates for analysis. Figure 5-13 shows a schematic diagram of the experimental photocatalytic system. The residual MO concentration was detected using a Cary 300 Bio UV-visible spectrophotometer. The photocatalytic activity of photocatalytic samples was calculated from the absorbance peak area [ln(A)]. Nearly exact ($R^2 \approx 1$) logarithmic linearity was found between the MB absorbance and the UV exposure time.

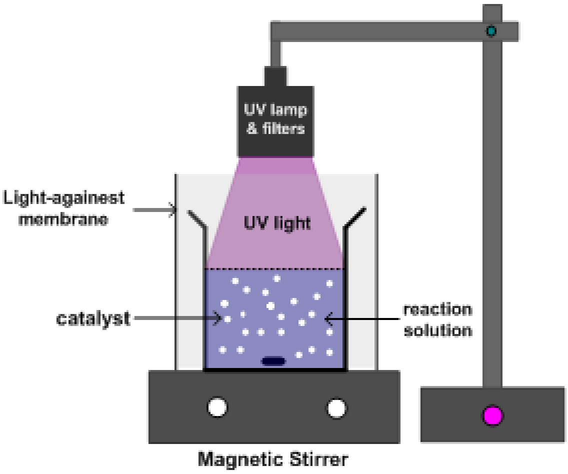

Figure 5.11. Schematic diagram of the experimental photocatalytic system setup.

References

Arachchige, I. U. & S. L. Brock (2007) Sol–Gel Methods for the Assembly of Metal Chalcogenide Quantum Dots. *Accounts of Chemical Research,* 40**,** 801-809.

Brust, M., M. Walker, D. Bethell, D. J. Schiffrin & R. Whyman (1994) SYNTHESIS OF THIOL-DERIVATIZED GOLD NANOPARTICLES IN A 2-PHASE LIQUID-LIQUID SYSTEM. *Chem. Commun.,* 7**,** 801-802.

Carbone, L. & P. D. Cozzoli (2010) Colloidal heterostructured nanocrystals: Synthesis and growth mechanisms. *Nano Today,* 5**,** 449-493.

Cho, E. C., P. H. C. Camargo & Y. Xia (2010) Synthesis and Characterization of Noble-Metal Nanostructures Containing Gold Nanorods in the Center. *Advanced Materials,* 22**,** 744-748.

Demazeau, G. (2008) Solvothermal reactions: an original route for the synthesis of novel materials. *Journal of Materials Science,* 43**,** 2104-2114.

Deng, Z.-X., L. Li & Y. Li (2003) Novel Inorganic−Organic-Layered Structures: Crystallographic Understanding of Both Phase and Morphology Formations of One-

Dimensional CdE (E = S, Se, Te) Nanorods in Ethylenediamine. *Inorganic Chemistry,* 42**,** 2331-2341.

Dinh, C.-T., T.-D. Nguyen, F. Kleitz & T.-O. Do (2009) Shape-Controlled Synthesis of Highly Crystalline Titania Nanocrystals. *ACS Nano,* 3**,** 3737-3743.

Du, H., S. Wohlrab, Wei & S. Kaskel (2007) Preparation of BaTiO3 nanocrystals using a two-phase solvothermal method. *Journal of Materials Chemistry,* 17**,** 4605-4610.

Fan, F.-R., D.-Y. Liu, Y.-F. Wu, S. Duan, Z.-X. Xie, Z.-Y. Jiang & Z.-Q. Tian (2008) Epitaxial Growth of Heterogeneous Metal Nanocrystals: From Gold Nano-octahedra to Palladium and Silver Nanocubes. *Journal of the American Chemical Society,* 130**,** 6949-6951.

Feng, S. & R. Xu (2000) New Materials in Hydrothermal Synthesis. *Accounts of Chemical Research,* 34**,** 239-247.

Fernanda Cardinal, M., B. Rodríguez-González, R. n. A. Alvarez-Puebla, J. Pérez-Juste & L. M. Liz-Marzán (2010) Modulation of Localized Surface Plasmons and SERS Response in Gold Dumbbells through Silver Coating. *The Journal of Physical Chemistry C,* 114**,** 10417-10423.

Garnweitner, G. & M. Niederberger (2008) Organic chemistry in inorganic nanomaterials synthesis. *Journal of Materials Chemistry,* 18**,** 1171-1182.

Ghoshal, T., S. Biswas, P. M. G. Nambissan, G. Majumdar & S. K. De (2009) Cadmium Oxide Octahedrons and Nanowires on the Micro-Octahedrons: A Simple Solvothermal Synthesis. *Crystal Growth & Design,* 9**,** 1287-1292.

Hayashi, H. & Y. Hakuta (2010) Hydrothermal Synthesis of Metal Oxide Nanoparticles in Supercritical Water. *Materials,* 3**,** 3794-3817.

Ingert, D. & M. P. Pileni (2001) Limitations in Producing Nanocrystals Using Reverse Micelles as Nanoreactors. *Advanced Functional Materials,* 11**,** 136-139.

Jiang, M., B. Lim, J. Tao, P. H. C. Camargo, C. Ma, Y. Zhu & Y. Xia (2010) Epitaxial overgrowth of platinum on palladium nanocrystals. *Nanoscale,* 2**,** 2406-2411.

Kobayashi, H., M. Ogawa, R. Alford, P. L. Choyke & Y. Urano (2009) New Strategies for Fluorescent Probe Design in Medical Diagnostic Imaging. *Chemical Reviews,* 110**,** 2620-2640.

Leong, W. L. & J. J. Vittal (2010) One-Dimensional Coordination Polymers: Complexity and Diversity in Structures, Properties, and Applications. *Chemical Reviews***,** null-null.

Li, J., Z. Chen, R.-J. Wang & D. M. Proserpio (1999) Low temperature route towards new materials: solvothermal synthesis of metal chalcogenides in ethylenediamine. *Coordination Chemistry Reviews,* 190-192**,** 707-735.

Li, X.-L., Q. Peng, J.-X. Yi, X. Wang & Y. Li (2006) Near Monodisperse TiO_2 Nanoparticles and Nanorods. *Chemistry – A European Journal,* 12**,** 2383-2391.

Liang, X., X. Wang, Y. Zhuang, B. Xu, S. Kuang & Y. Li (2008) Formation of CeO_2-ZrO_2 Solid Solution Nanocages with Controllable Structures via Kirkendall Effect. *Journal of the American Chemical Society,* 130**,** 2736-2737.

Lim, B., H. Kobayashi, T. Yu, J. Wang, M. J. Kim, Z.-Y. Li, M. Rycenga & Y. Xia (2010) Synthesis of Pd−Au Bimetallic Nanocrystals via Controlled Overgrowth. *Journal of the American Chemical Society,* 132**,** 2506-2507.

Lim, B., J. Wang, P. H. C. Camargo, C. M. Cobley, M. J. Kim & Y. Xia (2009) Twin-Induced Growth of Palladium–Platinum Alloy Nanocrystals. *Angewandte Chemie International Edition,* 48**,** 6304-6308.

Liu, J. & Y. Li (2007) General synthesis of colloidal rare earth orthovanadate nanocrystals. *Journal of Materials Chemistry,* 17**,** 1797-1803.

Miller, R. D. & E. A. Chandross (2010) Introduction: Materials for Electronics. *Chemical Reviews,* 110**,** 1-2.

Mrabet, D., M. H. Zahedi-Niaki & T.-O. Do (2008) Synthesis of Nanoporous Network Materials with High Surface Areas from the Cooperative Assemblage of Alkyl-Chain-Capped Metal/Metal Oxide Nanoparticles. *The Journal of Physical Chemistry C,* 112**,** 7124-7129.

Nozik, A. J., M. C. Beard, J. M. Luther, M. Law, R. J. Ellingson & J. C. Johnson (2010) Semiconductor Quantum Dots and Quantum Dot Arrays and Applications of Multiple Exciton Generation to Third-Generation Photovoltaic Solar Cells. *Chemical Reviews,* 110**,** 6873-6890.

Okuno, Y., K. Nishioka, A. Kiya, N. Nakashima, A. Ishibashi & Y. Niidome (2010) Uniform and controllable preparation of Au-Ag core-shell nanorods using anisotropic silver shell formation on gold nanorods. *Nanoscale,* 2**,** 1489-1493.

Okuno, Y., K. Nishioka, N. Nakashima & Y. Niidome (2009) Rapid Formation of Silver Shells on Gold Nanorods in a Micellar Solution of Hexadecyltrimethylammonium Chloride. *Chemistry Letters,* 38**,** 60-61.

Pan, D., Q. Wang, S. Jiang, X. Ji & L. An (2005a) Synthesis of Extremely Small CdSe and Highly Luminescent CdSe/CdS Core–Shell Nanocrystals via a Novel Two-Phase Thermal Approach. *Advanced Materials,* 17**,** 176-179.

Pan, D., Q. Wang, J. Pang, S. Jiang, X. Ji & L. An (2006) Semiconductor "Nano-Onions" with Multifold Alternating CdS/CdSe or CdSe/CdS Structure. *Chemistry of Materials,* 18**,** 4253-4258.

Pan, D., N. Zhao, Q. Wang, S. Jiang, X. Ji & L. An (2005b) Facile Synthesis and Characterization of Luminescent TiO_2 Nanocrystals. *Advanced Materials,* 17**,** 1991-1995.

Park, J., J. Joo, S. G. Kwon, Y. Jang & T. Hyeon (2007) Synthesis of Monodisperse Spherical Nanocrystals. *Angewandte Chemie International Edition,* 46**,** 4630-4660.

Rajamathi, M. & R. Seshadri (2002) Oxide and chalcogenide nanoparticles from hydrothermal/solvothermal reactions. *Current Opinion in Solid State and Materials Science,* 6**,** 337-345.

Rao, C. N. R. & K. P. Kalyanikutty (2008) The Liquid–Liquid Interface as a Medium To Generate Nanocrystalline Films of Inorganic Materials. *Accounts of Chemical Research,* 41**,** 489-499.

Ray, P. C. (2010) Size and Shape Dependent Second Order Nonlinear Optical Properties of Nanomaterials and Their Application in Biological and Chemical Sensing. *Chemical Reviews,* 110**,** 5332-5365.

Saravanan, G., H. Abe, Y. Xu, N. Sekido, H. Hirata, S.-i. Matsumoto, H. Yoshikawa & Y. Yamabe-Mitarai (2010) Pt_3Ti Nanoparticles: Fine Dispersion on SiO2 Supports, Enhanced Catalytic CO Oxidation, and Chemical Stability at Elevated Temperatures. *Langmuir,* 26**,** 11446-11451.

Schmidt, H., G. Jonschker, S. Goedicke & M. Mennig (2000) The Sol-Gel Process as a Basic Technology for Nanoparticle-Dispersed Inorganic-Organic Composites. *Journal of Sol-Gel Science and Technology,* 19, 39-51.

Walton, R. I. (2002) Subcritical solvothermal synthesis of condensed inorganic materials. *Chemical Society Reviews,* 31, 230-238.

Wang, M., J.-L. Liu, Y.-X. Zhang, W. Hou, X.-L. Wu & S.-K. Xu (2009) Two-phase solvothermal synthesis of rare-earth doped NaYF4 upconversion fluorescent nanocrystals. *Materials Letters,* 63, 325-327.

Wang, Q., D. Pan, S. Jiang, X. Ji, L. An & B. Jiang (2005a) A New Two-Phase Route to High-Quality CdS Nanocrystals. *Chemistry – A European Journal,* 11, 3843-3848.

Wang, X. & Y. Li (2003) Rare-Earth-Compound Nanowires, Nanotubes, and Fullerene-Like Nanoparticles: Synthesis, Characterization, and Properties. *Chemistry – A European Journal,* 9, 5627-5635.

Wang, X., J. Zhuang, Q. Peng & Y. Li (2005b) A general strategy for nanocrystal synthesis. *Nature,* 437, 121-124.

Whetten, R. L. & W. M. Gelbart (1994) Nanocrystal Microemulsions: Surfactant-Stabilized Size and Shape. *The Journal of Physical Chemistry,* 98, 3544-3549.

Xia, Y., Y. Xiong, B. Lim & S. E. Skrabalak (2009) Cover Picture: Shape-Controlled Synthesis of Metal Nanocrystals: Simple Chemistry Meets Complex Physics?. *Angewandte Chemie International Edition,* 48, 1-1.

Xie, R.-C. & J. Shang (2007) Morphological control in solvothermal synthesis of titanium oxide. *Journal of Materials Science,* 42, 6583-6589.

Xu, J., J.-P. Ge & Y.-D. Li (2006) Solvothermal Synthesis of Monodisperse PbSe Nanocrystals. *The Journal of Physical Chemistry B,* 110, 2497-2501.

Yan, L., R. Yu, J. Chen & X. Xing (2008a) Template-Free Hydrothermal Synthesis of CeO_2 Nano-octahedrons and Nanorods: Investigation of the Morphology Evolution. *Crystal Growth & Design,* 8, 1474-1477.

Yan, T., X. Wang, J. Long, H. Lin, R. Yuan, W. Dai, Z. Li & X. Fu (2008b) Controlled preparation of In_2O_3, InOOH and $In(OH)_3$ via a one-pot aqueous solvothermal route. *New Journal of Chemistry,* 32, 1843-1846.

Yoo, H., J. E. Millstone, S. Li, J.-W. Jang, W. Wei, J. Wu, G. C. Schatz & C. A. Mirkin (2009) Core−Shell Triangular Bifrustums. *Nano Letters,* 9, 3038-3041.

Yu, S.-H., T. Fujino & M. Yoshimura (2003) Hydrothermal synthesis of $ZnFe_2O_4$ ultrafine particles with high magnetization. *Journal of Magnetism and Magnetic Materials,* 256, 420-424.

Zeng, H. & S. Sun (2008) Syntheses, Properties, and Potential Applications of Multicomponent Magnetic Nanoparticles. *Advanced Functional Materials,* 18, 391-400.

Zhang, J., S. Ohara, M. Umetsu, T. Naka, Y. Hatakeyama & T. Adschiri (2007) Colloidal Ceria Nanocrystals: A Tailor-Made Crystal Morphology in Supercritical Water. *Advanced Materials,* 19, 203-206.

Zhao, N., W. Nie, X. Liu, S. Tian, Y. Zhang & X. Ji (2008) Shape- and Size-Controlled Synthesis and Dependent Magnetic Properties of Nearly Monodisperse Mn_3O_4 Nanocrystals. *Small,* 4, 77-81.

Zhao, N., W. Nie, J. Mao, M. Yang, D. Wang, Y. Lin, Y. Fan, Z. Zhao, H. Wei & X. Ji (2010) A General Synthesis of High-Quality Inorganic Nanocrystals via a Two-Phase Method. *Small,* 6**,** 2558-2565.

Zhao, N., D. Pan, W. Nie & X. Ji (2006) Two-Phase Synthesis of Shape-Controlled Colloidal Zirconia Nanocrystals and Their Characterization. *Journal of the American Chemical Society,* 128**,** 10118-10124.

Zhou, Y.-X., H.-B. Yao, Q. Zhang, J.-Y. Gong, S.-J. Liu & S.-H. Yu (2009) Hierarchical $FeWO_4$ Microcrystals: Solvothermal Synthesis and Their Photocatalytic and Magnetic Properties. *Inorganic Chemistry,* 48**,** 1082-1090.

Chapter 6 Size- and Shape-Controlled Synthesis and Characterization of Metal Oxide Nanocrystals

6.1. General Two-Phase Routes to Synthesize Colloidal Metal Oxide Nanocrystals: Large-Scale Synthesis and Their Ordered Self-Assembly Structures

Thanh-Dinh Nguyen and Trong-On Do

Department of Chemical Engineering, Laval University, Quebec G1K 7P4 Canada

Published in *J. Phys. Chem. C* **2008**, *112*, 15226-15235; **2009**, *113*, 11204-11214

Abstract

Different two-phase approaches have been developed for the synthesis of two classes of monodisperse colloidal metal oxide nanocrystals (NCs): rare earth oxide NCs and transition-metal oxide NCs. These routes were simple and inexpensive using metal salts instead of organometallic compounds, mild reaction conditions, easy size and shape control, and multi-gram-scale products. The obtained products were characterized by transmission electron microscopy (TEM), selected area electron diffraction (SAED), X-ray diffraction (XRD), X-ray photoelectron spectra (XPS), fourier transform infrared absorption spectroscopy (FTIR), and nitrogen adsorption-desorption isotherms (BET). The possible mechanisms for the formation and growth of nanocrystals were discussed. Accordingly, *tert*-butylamine (nucleophile agent) and ethanol (reduced agent) are as the key factors for the formation of rare earth oxide NCs and transition-metal oxide NCs, respectively. Different sizes and shapes of monodisperse nanoparticles such as spherical, cubic, peanut, rod, hexagonal NCs were obtained depending on the nature of metal precursors. Furthermore, the effect of monomeric precursor concentration, type of precursors, reaction time on the size and shape of products was also studied.

The SAED patterns of the obtained NC samples show a set of sharp spots which are characteristic of single crystalline structures indexed accordingly with the structures determined by the XRD spectra. The XPS results revealed that the presence of two oxidation states of cerium, samarium, manganese, and cobalt on the nanocrystal surface, whereas, it seems that only one oxidation state on the surface for Y, Cr, La, Gd, Er oxide nanocrystals is present. A large O 1s XPS peak attributed to two oxygen components for these Ce, Sm, Mn, Co oxide NC samples refer to the defected structure. Our approaches may be also applicable to synthesize other uniform metal oxide NCs as well as doped metal oxide NCs and multi-component NCs.

6.1.1. Introduction

Colloidal inorganic nanocrystals (NCs) with 1-100 nm in size are versatile building blocks for constructing diverse superstructures, functional mesocrystals, and new nanodevices, which can expect to find useful applications in catalysis, magnetic data storages, solar cells, lithium-ion batteries, and medicine, etc.[1-4] Assembling the single nanocrystals into ordered lattice structures that is "bottom up assembly", is an attractive way to design systems possessing the novel physico-chemical properties that differ drastically from their bulk counterparts.[5,6] Thus, the development and innovation of new synthetic strategies for high-quality oxide nanocrystals have been among the key issues in the scientific researches.[7]

Numerous methods have been well documented in several recent review articles for the synthesis of a broad range of nanocrystals including the hydrolytic and non-hydrolytic sol-gel process,[8] solvo-hydrothermal treatment,[9] and thermal decomposition.[10] Size and shape controls of nanocrystals can be obtained via either single-phase or two phase methods. Single-phase method is always used for the synthesis of colloidal oxide nanocrystals.[11,12] Furthermore, the two-phase synthetic method was first reported by Brust et al.[13] for the synthesis of gold nanoparticles and other noble metal nanoparticles such as Ag, Pt, Au.[14] Related progress using the two phase approach was also extended to the synthesis of metal oxide and semiconductor nanocrystals.[15] Compared to the single-phase approach, the two-phase strategy can obtain the products with well crystallinity under the relatively mild adopted conditions because the presence of water phase in bulk solution generally impulses the speed of the growth process, which was previously reported by our group.[16] The particle size and shape can be also controlled because of the quitely slow nucleation process, which was demonstrated by An et al.[17] Many attempts have been made to the design and synthesis of a variety of NCs using this two-phase approach to explore their properties and potential applications. For example, Pan et al.[18,19] reported a hydrothermal two-phase route to synthesize monodisperse TiO_2 and ZrO_2 NCs from the hydrolysis of titanium(IV) isopropoxide and zirconium(IV) isopropoxide, respectively, in the water-toluene mixture. Kaskel et al.[20] reported the synthesis of $BaTiO_3$ nanocrystals using mixed titanium(IV)-*n*-butoxide and barium acetate precursors. Furthermore, Adschiri et al.[21] modified this reaction system for the synthesis of CeO_2 nanocubes using cerium hydroxide precursors under supercritical water conditions. The product shape could be controlled by tuning the interaction of organic molecules with various crystallographic planes of fluorite cubic ceria. More recently, our group[22] developed a modified two-phase method for the synthesis of alkyl chain-capped metal particles (e.g., Cu and Au) and metal oxide nanoparticles (CeO_2, TiO_2, and ZrO_2) followed by their cooperative assemblage into unusual hybrid metal/metal oxide NCs mesostructured materials. Indeed, these metal/metal oxide hybrid materials exhibited high surface areas, narrow pore size distributions and exceptional catalytic properties in the oxidation of CO, even surpassing the performance of commercial noble metal catalysts. In addition, controlled size and shape of vanadia and samaria NCs were also developed using inexpensive metal precursors and multi-gram scales in single run.[16,23] Even though, the two-phase methods have been shown to synthesize various metal oxide nanocrystals, the development of general and simple two-phase methods for the synthesis of a variety of NCs with a desired shape and size control using inexpensive precursors still faces challenges.

In this paper, we report two different general two-phase approaches for the synthesis of two classes of colloidal metal oxide nanocrystals (NCs): rare earth oxide NCs and transition-metal oxide NCs, with controlled size and shape, through the hydrolysis of corresponding inorganic salts or metal-surfactant complexes in the water/toluene system. These synthetic approaches have several advantages including relatively mild conditions, easy manipulation, and large-scale production. The possible mechanisms for the formation of alkyl-capped oxide nanocrystals in each route are also proposed. Furthermore, the effect of various synthetic reaction parameters including precursor concentration, type of precursors, and reaction time on the shape evolution of nanocrystalline oxides are also studied.

6.1.2. Experimental Section

6.1.2.1. Starting Materials: All chemicals were used as received without further purification. Cerium(III) nitrate hexahydrate ($Ce(NO_3)_3.6H_2O$, 99.9%), cerium(III) acetate hydrate ($Ce(ac)_3.xH_2O$, 99.9%), samarium(III) nitrate hexahydrate ($Sm(NO_3)_3.6H_2O$, 99.9%), yttrium(III) nitrate hexahydrate ($Y(NO_3)_3.6H_2O$, 99.9%), lanthanium (III) nitrate hexahydrate ($La(NO_3)_3.6H_2O$, 99.9%), gadolinium(III) nitrate hexahydrate ($Gd(NO_3)_3.6H_2O$, 99.9%), erbium(III) nitrate hydrate ($Er(NO_3)_3.xH_2O$, 99.9%), manganese(III) nitrate tetrahydrate ($Mn(NO_3)_2.4H_2O$, 99%), chromium(III) chloride hexahydrate ($CrCl_3.6H_2O$, 99%), cobalt(II) nitrate hexahydrate ($Co(NO_3)_3.6H_2O$, 98%), nickel(II) nitrate hexahydrate ($Ni(NO_3)_2.6H_2O$, 99.999%), oleic acid ($C_{18}H_{35}COOH$ or OA, tech. grade, 90%), oleylamine ($C_{18}H_{35}NH_2$ or OM, tech. grade, 70%), potassium oleate ($C_{18}H_{35}COOK$, 40% water), and *tert*-butylamine ($(CH_3)_3CNH_2$, 98%), were purchased from Sigma-Aldrich. All solvents used such as toluene, absolute ethanol were of analytical grade and purchased from Reagent ACS.

6.1.2.2. Nanocrystal Synthesis: All NCs in this work were synthesized in two-phase system and stabilized with hydrophobic molecules containing long alkyl chains (C_{18}). Detailed information on the synthesis of metal oxide NCs is given below.

6.1.2.2.1. Synthesis of rare earth oxide nanocrystals

6.1.2.2.1.1. Synthesis of rare earth oxide nanocrystals (e.g., Sm_2O_3 and CeO_2 NCs) using rare earth salt precursors

Typically, 20 mL of an aqueous solution (0.015-0.120 mol/L) containing metal salt (0.3-2.4 mmol, $Sm(NO_3)_3.6H_2O$, or $Ce(NO_3)_3$. $6H_2O$, or $Ce(ac)_3$), *tert*-butylamine (0.15

mL) was mixed an organic solution of oleic acid (1.5 mL) and toluene (20 mL). The resulting mixture was transferred to a 60 mL Teflon-lined stainless-steel autoclave in the ambient environment without stirring. The sealed autoclave and heated up at 180 ^{o}C for 24 h. Afterthat, the system was cooled to room temperature by submerging the reactor in a water bath. The nanocrystal solution was precipitated with the excess volume of ethanol. The purified products were separated by centrifugation and easily re-dispersed in nonpolar solvent (e.g., toluene, hexane, chloroform). The precipitation-redispersion process was repeated several times to purify the producing nanocrystals.

6.1.2.2.1.2. Synthesis of rare earth oxide nanocrystals using rare earth surfactant complex precursors (e.g., RE = Er, Gd, La, Y)

The synthesis of rare earth oxide nanocrystals consists of two steps: (i) preparation of rare earth complex precursors from rare earth salts, and (ii) the formation of NCs.

(i) To prepare rare earth oleate complexes, an organic solution was produced from adding 20 mL of toluene into the ethanol solution (6.4 mL) containing potassium oleate (0.85 g or 1.1 mmol). Subsequently, the organic phase was mixed to 12.8 mL of aqueous solution of $RE(NO_3)_3.6H_2O$ (0.36 mmol, RE = Er, Gd, La, Y) and transfered to a flask. The stock two-phase mixture was heated to 70 ^{o}C for 60 min with stirring vigorously and the organic solution became light yellow after being reacted, indicating the occurrence of the coordinative reaction between rare earth cation and oleate anion for the complex formation. The RE^{3+}/oleate^{-} molar ratio is close to 1:3, $RE(OA)_3$. The upper homogeneous toluene supernatant phase (20 mL) containing RE-oleate complexes was isolated using a separatory funnel. The yields for these rare earth complexes were between 85 and 95%.

(ii) The formation of Er_2O_3, Gd_2O_3, La_2O_3, Y_2O_3 nanocrystals: Typically, 5 mL of oleylamine was added to the above prepared rare earth complex solution (20 mL, 0.018 mol/L) under stirring for 10 min. Then, the organic solution was transferred to a 60 mL Teflon-lined stainless-steel autoclave containing aqueous solution (20 mL) of *tert*-butylamine (0.15 mL). The autoclave was seated and heated to the crystallization temperature at 180 ^{o}C for 24 hours.

6.1.2.2.2. Synthesis of transition-metal oxide nanocrystals (TMO-NCs) (e.g., Mn_3O_4, Cr_2O_3, Co_3O_4, and NiO NCs using transition-metal salts as precursors

Typically, a homogeneous ethanol solution (10 mL) containing potassium oleate (3 g) was added the organic solution of toluene (20 mL) and oleic acid (2 mL), then mixed to 20 mL of an aqueous solution (0.08 M, 1.6 mmol) containing metal salt (including $Mn(NO_3)_3$, $CrCl_3$, $Co(NO_3)_2$, and $Ni(NO_3)_2$) for the formation of two-phase reactive mixture. In which the oleate anions disperse into the organic phase while the entering of the ethanol and potassium (K^+) cations into the aqueous phase. The two-phase mixture was transferred to Teflon-lined stainless-steel autoclave and heated to 180 ^oC for 24 h. The yield of the products was more than 85%.

6.1.3. Results and Discussion

All the syntheses in this study were carried out in a two-phase water/toluene system by mixing metal sources and capping agent. After hydrothermal synthesis, the capped nanocrystal products were highly dispersed in the toluene phase and no significant product was observed in the water phase. The NC product in the toluene phase was precipitated by adding excess of ethanol and recovered by centrifugation. Table 6.1.1 summarizes the synthesis conditions, the metal precursors and capping ligands for the synthesis of nanocrystals (NCs) as well as the size and shape of as-made samples determined by transmission electron microscopy (TEM). The morphologies of the corresponding as-synthesized samples after calcination proved unchanged significantly as shown in Supporting Information. In this study, we have developed two different simple and general two-phase routes for the synthesis of metal oxide NCs of two group elements: rare earths; Sm, Ce, Er, Gd, La, and Y (Schemes 6.1.1A and 6.1.1B) and transition metals; Mn, Cr, Co, and Ni (Scheme 6.1.2) using metal salts as starting precursors. These routes are particularly advantageous because of the use of inorganic salt precursors instead of expensive metal alkoxides and quite mild synthetic conditions. Furthermore, the shape and size of the NC products can be also controlled by various reaction parameters including the monomer concentration of metal precursors, the type of precursors, and the reaction time.

6.1.3.1. Synthesis of rare earth oxide nanocrystals

To date, a number of rare earth oxide nanocrystals are being studied intensively because of diverse application including electronic, magnetic, optical, and catalytic fields, due to their unique 4f electrons.[24] Many rare earth nanostructures have been synthesized through solution based routes.[25] Among them, the hydrothermal two-phase route is particularly versatile for the synthesis of diverse rare earth oxide nanocrytals. However, this approach is rather restricted, when metal alkoxides as precursors are either commercially not available or costly.

To overcome these drawbacks, in this work, we present two alternative two-phase routes to synthesize nanocrystalline rare earth oxides in water/toluene mixture in the presence of capping agents using (i) direct rare earth nitrate salts (Scheme 6.1.1A) and (ii) the rare earth-surfactant complexes prepared from the corresponding nitrate salts (Scheme 6.1.1B) as starting precursors.

6.1.3.1.1. Synthesis of earth oxide NCs using rare earth salt precursors

Nanocrystalline rare earth oxides were obtained by the hydrolyzed reaction of the corresponding nitrate salts in water/toluene mixture in the presence of capping molecules (fatty acid) and *tert*-butylamine (see Experimental Section). This synthetic route shows the distinct advantage of relatively low temperature compared with the supercritical water method reported by Adschiri et al.[21] The presence of the activation agent, *tert*-butylamine, in aqueous phase which strongly decreases the hydrolytic temperature of metal precursors from 400 ^{o}C to 180 ^{o}C for the nanocrystal formation. Sm_2O_3 and CeO_2 were selected to illustrate this approach, because they are widely recognized for their unique properties as supports and catalysts. The formation of rare earth oxide NCs was sketched in Scheme 6.1.1A.

For this way, the formation procedure of Sm_2O_3 and CeO_2 NCs can be expressed in Scheme 6.1.1A. It is known that the Ce^{4+} ions have the stable empty $4f^0$ sub-shells,[26] therefore, the Ce^{3+} ions were easily oxidized to the Ce^{4+} ions by the trace oxygen existing in the aqueous solution, which was suggested by Xing el al.[27] The metal hydroxides were formed under basic solution due to the dissociation of *tert*-butylamine in water to generate OH^- ions.[28] Upon hydrothermal treatment, these metal hydroxides were dehydrated to oxide nuclei at the interfaces.

Figure 6.1.1 shows the TEM images of Sm_2O_3 and CeO_2 NCs (samples 1 and 2 in Table 6.1.1) prepared at the high metal monomer concentration of the corresponding nitrate salts in the water solution (e.g., C = 0.12 M) following Scheme 6.1.1A. Under these synthesis conditions, single-crystalline Sm_2O_3 nanorods with ~7 nm in width and 100-160 nm in length (aspect ratio of ~19) were observed (Figure 6.1.1a), meanwhile, CeO_2 NCs composed of a mixture of nanocubes (6 nm) and elongated nanocubes (8 nm x 10 nm) were obtained. CeO_2 NCs had a tendency to assemble into 2D arrays (Figure 6.1.1c). The selected area electron diffraction (SAED) patterns taken by focusing the electronic beam on a single samaria and ceria particles are presented in Figures 6.1.1b and 6.1.1d, respectively, showing both the distinct diffraction rings of cubic structure, in good agreement with the XRD results (see below). This route would be especially benefical for industrial production at reduced cost. For example, at the cerium monomer concentration of 0.12 M, we were able to synthesize in large-scale as much as 3.4 g of OA-capped CeO_2 nanocubes with significantly unchanged morphology for a single preparation when the reaction size for the synthesis was increased by a factor of 12.5.

The size and shape evolution of CeO_2 NCs was found to be as a function of cerium monomer concentrations, e.g., $Ce(NO_3)_3$, in the water solution. Representative TEM images of the samples are shown in Figure 6.1.2. At a relatively low cerium monomer concentration in the water phase (C = 0.015 M), only ordered CeO_2 nanocubes were formed with an average diameter of 3 nm (Figure 6.1.2a). However, their cube size increased from 3 nm to 8 nm, when the cerium precursor concentration in the initial water phase was 0.068 M (Figure 6.1.2b). As careful high-magnification TEM examination (inset of Figure 6.1.2b), the monodisperse nanocubes had strong tendency to assemble into multilayer superlattices (2D). With increasing the monomer concentration to 0.120 M, it yields some elongated nanocubes (8 nm x 10 nm) with sharper edges and corners. The self-assembly of the mixture of cubes and elongated cubes NCs was observed (Figure 6.1.2c). The general trend is also sketched in Figure 6.1.2d. The elongation and size of ceria nanocubes increased as the concentration of cerium monomers in the initial water solution increased. It is clear that the concentration of cerium salts plays an important role for the size and shapes of the resulting nanocubes. Based on the Gibbs-Thompson theory,[29] the chemical potential of a crystal is proportional to its surface-atom ratio, however, the size and shape evolution of NCs is strongly dependent on metal monomer concentrations, as reported by Peng's group.[30,31] Generally, low monomer concentrations favour isotropic growth, whereas high monomer concentrations favour anisotropic growth.

Furthermore, the effect of the nature of cerium precursors on size and shape of NCs was also studied. When cerium nitrate replaced by cerium acetate (C = 0.068 M, acetate is weaker anion than nitrate[32,33]), some aggregated particles composed of two or three of the individual nanocubes with relatively larger size (8-10 nm) were observed (Figures 6.1.2e and 6.1.2f). This suggests that the nature of counter-anion ligands played a role in the growth of uniform nanocubes. Li et al.[32] also found that the variation of type of anion in the water phase could change the growth rate and consequently change the size and shape of Cu_2S nanocrystals.

Figure 6.1.3 shows the XRD patterns of the various calcined NC samples: Sm_2O_3 nanorods, CeO_2 nanocubes, and agglomerated CeO_2 nanocubes (samples 1, 2, 3 in Table 6.1.1). The results revealed the body-centered cubic (*bcc*) structure of these samples with cell parameters for Sm_2O_3: a = 10.93 Å (*Ia3*, JCPDS 86-2479); for CeO_2: a = 5.45 Å (*Fm*3*m*, JCPDS 34-0394). As seen in Figure 6.1.3, the XRD patterns show broad peaks due to the nanoscale size of the products and no peaks of others impurities was detected. The size of these samples corresponding to samples 2 and 3 in Table 6.1.1 was calculated from the half-widths of the (220) reflections[34] using the Debye-Scherrer equation ($d = 0.89\lambda/B\cos\theta$) are ~11.0 nm and ~10.5 nm, respectively, which are consistent with the TEM results.

The XPS spectra of metal oxides reveal that the metal core level binding energies and the full widths at half-maximum (FWHM) taken from nanoparticles are obviously higher than those from the counterpart bulk.[35] The upward shift of binding energies by ca.

0.5-1.5 eV might results from the dispersion of metal ion clusters on the particle surfaces, while the increasing FWHM of ca. 2.5-3.5 eV might causes a change in electronic properties with decreasing particle size.[36]

The obtained cerium oxide NC products before and after calcination have a light yellow color, but pure bulk CeO_2 powders have a white color, indicating that the chemical composition of cerium oxide NCs may be CeO_{2-x} ($0 < x < 2$). Replacement of the smaller Ce^{4+} ions (~0.92 Å in radii) by the a few larger Ce^{3+} ions (~1.034 Å in radii) into the crystal lattice may result in the color change from white color to light yellow color. To further confirm this observation, the Ce 3d core level XPS spectra (Figure 6.1.4) were recorded for the sample of ceria nanocubes (solid curve) and after (dotted curve) calcination (sample 2 in Table 6.1.1). It is interesting to note that no significant difference of the XPS spectrum before and after calcination of these samples was observed suggesting no significant change in the cerium oxidation state upon this thermal treatment. The Ce 3d states are splitted due to spin-orbit interaction into two lines Ce $3d_{5/2}$-Ce $3d_{3/2}$ with a spin-energy separation (Δ) of 18.3 eV and intensity $I(3d_{5/2})/I(3d_{3/2}) = 1.1$.[37] The complex spectrum of Ce 3d can be decomposed to six components with the assignment as defined in Figure 6.1.4. The bands at 887.50 eV (v''), 903.76 eV (u'') are the $3d^{10}4f^{1}$ initial electronic state of Ce^{3+} ion and the bands at 880.30 eV (v'), 887.50 eV (v''), 887.50 eV (v'''), 898.64 eV (u), 903.76 eV (u''), 916.35 eV (u''') are the $3d^{10}4f^{0}$ state of Ce^{4+} ion.[36] The atomic ratio of $Ce^{3+}/(Ce^{3+} + Ce^{4+})$ of the as-made and calcined ceria NC samples can be quasi-quantitatively determined by the ratio of $(I_{v''} + I_{u''})/(I_u + I_v + 2I_{v''} + 2I_{u''} + I_{v'''} + I_{u'''})$ is ~46%. Furthermore, the Ce/O ratio was found to be 1.00:1.67, corresponding the stoichiometric formula of CeO_{2-x} ($x = 0.33$). This suggests that distorted crystal structure of nanoceria due to the replacement of Ce^{4+} ions by Ce^{3+} ions, which causes oxygen vacancy creation in surface defects. The presence of two oxidation states (Sm^{2+}/Sm^{3+}) with 40% Sm^{2+} and the chemical composition of $Sm_2O_{(3-1.8)}$ on the samaria NC surface were observed in our recent study.[23]

A series of as-made OA-capped Sm_2O_3 nanocrystals were synthesized using the same chemical composition mixture, however, at different stages of reaction temperatures:

from 120°C to 140°C, 160°C, 180°C, and 200°C, respectively with a fixed reaction time - 24 h of each stage of temperature; oleic acid was used as a capping agent. Particle size analysis using TEM images shows that nanocrystal growth involves two mechanisms: coarsening well known as Ostwald ripening and oriented attachment (discussed below).

Figure 6.1.5 shows representative TEM images of this series of as-made samples. As shown in Figure 6.1.5, the morphology of Sm_2O_3 nanocrystals varies as a function of synthesis temperatures. When the synthesis temperature was at 120°C, monodisperse spherical nanoparticles as the sole products with a diameter of about 5 nm were obtained (Figure 6.1.5a). With a longer reaction time, from 24 to 48 h, no significant change in the morphology and size was observed suggesting that the equilibrium of growth kinetics was established after 24 h at this temperature. However, when the reaction temperature was increased to 140°C, after 24 h, a mixture of spherical particles and primary rod-like particles were observed. This can be explained by the well-known Ostwald ripening process, where the larger nanoparticles obviously grew at the expense of smaller particles (Figure 6.1.5b).[52-54] The formation of larger particles at the cost of the small ones could be due to the energy difference between large particles and the smaller particles of a higher solubility according to the Gibbs-Thomson law.[55] Closer TEM observation on numerous parts of the sample showed that a small amount (5%) of nanorods with ~6 nm in width and 50 nm in length have started to appear at this temperature; each “primary nanorod” is composed of several nanoparticles, although nanoparticles were still the exclusive products. It suggests that the larger nanoparticles grow involving the Ostwald ripening rather than the oriented attachment.

When the reaction temperature was increased to 160°C for 24 h, no nanoparticles were essentially observed, concomitantly, only the bundles composed of individual nanorods aligned along the common axis with ~6 nm width and 80-100 nm length were formed. It indicates a complete conversion from nanoparticles to “small” nanorods at this temperature after 24 h. Furthermore, the similar diameter of nanoparticles and nanorods substantiates the oriented attachment mechanism.[37-39] As seen in Figure 6.1.5c, nanoparticles appear fused almost end to end along the longitudinal axis and form linear chains. These nanorods tended to stack together to form extended rodlike nanobundles with ~15 nm width and ~100 nm length (Figure 6.1.5c) from inter-rod attachment of many "primary" nanorods. This phenomenon can be interpreted by the high-degree lateral agglomeration due to high surface energy of "primary" nanorods through van der Waals forces (electrostatic attraction).[52-54] The further studies the effect of the reaction temperatures and capping agent variations on the size of the nanobundles were not performed. However, when the reaction temperature was increased to 180°C, the nanobundles can be split up into individual nanorods. The nanobundles evolved into thicker and longer OA-capped nanorods (7 nm x 100-160 nm), the nanorod surfaces became smoother with relatively narrow size distributions (Figure 6.1.5d). At this stage of temperature, the oriented attachment is as a dominant mechanism by which the nanorods were formed.

Interestingly, while the synthesis temperature was increased from 180°C to 200°C, these nanorods had a strong self-assembling tendency to form parallel OA-capped nanorods with ~8 nm in width and ~160 nm in length, along their longitudinal axis (Figure 6.1.5e). A careful observation of the TEM images in several parts of the sample clearly reveals that the building blocks of the one-dimensional superstructures are, in fact, the aligned parallel of cross-sectional nanorods of Sm_2O_3 (Figure 6.1.5f). The parallel superstructures are composed of the OA-capped nanorods that are stacked side-to-side then they would look like raft-like nanostructures. However, at higher temperature (beyond 200°C) leads to the formation of bulky aggregated rods.

Based on these TEM results, it can be concluded that Sm monomer precursors were consumed for the formation of nanoparticles at relatively low temperatures ($\leq$140°C); only nanoparticles were formed at 120°C and few nanorods were observed at 140°C. At higher temperatures (>160°C), because no Sm monomer precursors were added during the synthesis, the Sm monomer concentration in the bulk solution is very low; nanocrystals can rearrange to find the low-energy configuration by a coherent particle-particle interface. Therefore, the formation of nanorods could be due to the oriented attachment process.[55,56] The length of the nanorods increases (from 50 nm at 140°C to 100-160 nm in length at

180°C) and the nanorods tend to be tilted along their axis direction with increasing the reaction temperature, however, no essential change in the diameter was observed. This means that the size control of nanorods (length and width) through oriented aggregation can be achieved by controlling primary particle size and reaction temperature.

The nanorods yield in toluene phase was ~94, 98 and 75% for the synthesis at 160, 180 and 200ºC, respectively. The nanorods yield was only 94% at 160ºC, even only nanorods were observed at this temperature. This could be due to the lost of some primary nanocrystals in leaching solvent during the precipitation-redispersion process to purify the product. The highest yield of rod (~98%) was indeed obtained at 180°C owing to the optimized balance between nucleation and growth.[2,5] Furthermore, the product yield decreased to ~75% when the reaction temperature increased to 200°C. It is observed that at 200°C, some aggregated rods were formed and they dropped into the water phase due to the loss of surface ligands, while the smaller ones stayed in the toluene phase. This could be the main reason why the product yield decreases at this temperature. Under the optimized reaction conditions (e.g., at 180°C for 24 h), we were able to synthesize in ultra-large-scale of as much as 50 g of the Sm_2O_3 nanorods in a single preparation as shown in Figure 6.1.6. Hence, this proves that the synthetic process is simple, high yield and readily scaled up for the production of Sm_2O_3 nanorods.

The formation of nanoparticles and the transformation of nanoparticles into nanorods at different stages of reaction temperatures are schematically illustrated in Scheme 6.1.3. It consists of two steps involving the two dominant growth mechanisms: "Ostwald ripening" and "oriented attachment". (i) The formation of nanocrystals and nanocrystal growth based on the "Ostwald ripening" mechanism[57-59] at relatively low temperature (120-140°C), (ii) followed by the aggregation of nanoparticles into nanorods based on the "oriented attachment" mechanism[37-39] at higher temperature (160-200°C).

To gain further insights into the influence of the alkyl chain length of surfactants on the morphologies of Sm_2O_3 nanocrystals, different capping agents were used, oleic acid (OA), myristic acid (MA) and decanoic acid (DA) corresponding to C_{18}, C_{14} and C_{10}, respectively for the synthesis of Sm_2O_3 nanocrystals, while keeping the other synthesis conditions unchanged. Figure 6.1.7 shows TEM images of the Sm_2O_3 samples synthesized at the low temperatures (e.g., 120°C) for 24 h. It is found that no significant difference in particles size was observed at 120°C. The average particle size is ~5, 5.5 and 5 nm for oleic acid, myristic acid and decanoic acid, respectively. When we had performed the experiments at higher temperatures (e.g., 180°C). Representative TEM images (Figure 6.1.8) of the obtained materials show that when the alkyl chain length of the capping agents decreases, the diameter of the nanorods tends to increase, while the length of the nanorods (100-160 nm) stayed essentially constant. The average diameter was found to be 7, 10 and 25 nm when using OA, MA and DA, respectively. This suggests that the alkyl chain length of the capping agents is taken advantage in controlling the diameter of nanorods, however the nanorods length essentially remains. The increase in the nanorod diameter with the decrease of the alkyl chain length of the capping agents could be explained by a lateral aggregation of primary nanorods;[24] when primary nanorods approach along their lateral faces, they are attracted by van der Waals forces and then fuse gradually, recrystallize into single crystalline nanorods. The length of capping alkyl ligands can control the growth kinetics. Longer capping alkyl ligands result in a slower rate of lateral aggregation because of the larger inter-distance of primary nanorods along the lateral faces, consequently, a smaller diameter of nanorods was finally formed (Figure 6.1.8d).

The calcined Sm_2O_3 nanorods sample is also studied by the X-ray photoelectron (XPS) technique. The samarium 3d states are split due to spin-orbit interaction into two lines Sm $3d_{5/2}$-Sm $3d_{3/2}$ with energy $\Delta = 30$ eV and intensity $I(3d_{5/2})/I(3d_{3/2}) = 3/2$. The deconvolution data of the spectra are summarized in Table 2. The XPS spectrum of Sm 3d consists of two components related to Sm^{3+} and Sm^{2+} (Figure 6.1.9). The first main peak pair related to the Sm^{3+} component is at 1083.5 (v_1) and 1110.8 eV (v_2), whereas the weak peak pair at 1095.9 (u_1) and 1121.3 eV (u_2) is assigned to Sm^{2+}.[61,62] These data indicate that the coexistence of two oxidation states on the Samaria surface owing to the in situ photoreduction of Sm^{3+} to Sm^{2+} under ultra high vacuum (UHV) conditions during XPS measurement.[63] The percentage of the Sm^{2+} surface concentration in the samaria nanorods determined from the ratio of $Sm^{2+}/(Sm^{3+} + Sm^{2+})$ can be quasi-quantitatively determined by the ratio of $(I_{u1} + I_{u2})/(I_{v1} + I_{v2} + I_{u1} + I_{u2})$ (see Table 6.1.2).[62] It was found to be 40%

indicating that the main valence of samarium in the sample is +3. Bao at el.[64] suggested that Sm^{2+} exists only on the surface, while Sm^{3+} inside of materials. Thus, the fraction of Sm^{2+} would mainly depend on the surface area and the size of nanoparticles.

6.1.3.1.2. Synthesis of rare earth oxide NCs using rare earth-surfactant complex precursors

Recently, we have reported the shape-selective synthesis of vanadium oxide nanocrystals (NCs) through decomposing of vanadium-ligand complexes in the water/toluene mixture in the presence of aliphatic amine.[16] It was found that the size and shape of NCs can be controlled by various synthesis parameters such as water content, steric ligands of vanadium complexes, and the alkyl chain length of capping agents. In addition, Ji group was also used to the two-phase route to produce the Mn_3O_4 nanocrystals by using manganese(II) stearate precursors.[38] The spherical and cubic shapes and their particle size can be controlled by adjusting the reaction time and activation agent concentration. However, the author had not further decribed a general route for rare earth oxide nanocrystal synthesis as well as studied on the reaction mechanism. From the points of view, we continue to develop further into a general method and study on the reaction mechanism for the synthesis of different types of rare earth oxide nanocrystals (REO-NCs) using rare earth oleate complexes. In this work, Er, Gd, La, and Y oxide NCs were selected and synthesized with controllable size and shape, due to their wide variety of technological applications and limited information available in the literature for the synthesis of these NCs through two-phase approach.[17]

The synthesis of REO- NCs involves two steps (Scheme 6.1.1B): (i) the preparation of rare earth oleate complexes from the reaction between rare earth nitrate and potassium oleate (KOA) in water/toluene system and (ii) the formation of colloidal REO-NCs in the autoclave containing the water/toluene mixture composed of capping oleylamine, *tert*-butylamine, and rare earth oleate complexes at 180 ºC. All the rare earth oleate complexes (Er, Gd, La, Y) were synthesized from the corresponding rare earth nitrate compounds using the same procedure.

The rare earth nanocrystals (RE-NCs) synthesized with different morphologies are summarized in Table 6.1.1. Figure 6.1.10 shows the XRD patterns of various types of the calcined NC products. The Er_2O_3, Gd_2O_3, and Y_2O_3 samples exhibit cubic structure, while La_2O_3 sample shows hexagonal structure. The calculated lattice constants are respectively 10.63 Å, 11.28 Å, 10.80 Å, 10.56 Å, and 3.39 Å for Y_2O_3 (JCPDS: 25-1200),[40] Gd_2O_3 (JCPDS: 86-2477),[41] Er_2O_3 (JCPDS: 08-0050),[42] and La_2O_3 (JCPDS: 05-0602).[43] The particle sizes of Gd_2O_3 and Er_2O_3 NCs calculated from the (222) reflections are about 20 nm and 30 nm, respectively, which are consistent with the sizes obtained by the TEM images. The XRD spectra of all the nanocrystal samples show much broader diffraction peaks compared to their bulk counterparts owing to their nanometer size.

It should be noted that *tert*-butylamine and rare earth oleate complexes play a key role for the formation of rare earths nanocrystals: for example, the synthesis of Y_2O_3 NCs, was carried out under the same synthesis conditions, except the absence of *tert*-butylamine in the synthesis mixture, no rare earth NC product was formed. When yttrium acetate compounds were used instead yttrium oleate complexes, keeping the other synthesis conditions constant (e.g., in the presence of capping oleylamine and *tert*-butylamine), only irregular Y_2O_3 nanospheres were obtained.

The formation of NCs using rare earth oleate complexes, capping oleylamine and *tert*-butylamine could be expressed in Equation 1. The formation of RE-NCs could consist of three steps during the hydrothermal synthesis: (i) *Tert*-butylamine as nucleophile attacks one carboxyl group of the oleate ligand through sharing lone-pair of electrons of the donor NH_2 group onto the electrophilic carboxyl center at the nucleation stage. Only *tert*-butylamine can react with the oleate group and not oleylamine because the basic property of *tert*-butylamine is stronger than that of oleylamine. Moreover, *tert*-butylamine well dispersed in aqueous phase and easily hydrolyzed to generate OH^- compared with oleylamine in organic phase. (ii) This nucleophilic reaction leads to the C-O bond cleavage, the release of a carbonyl group, and then the formation of REO nuclei at the water-toluene interfaces and (iii) the formation of NCs. A similar observation was also reported for the synthesis of ZnO nanocrystals in the mixture of zinc acetate and oleylamine.[44]

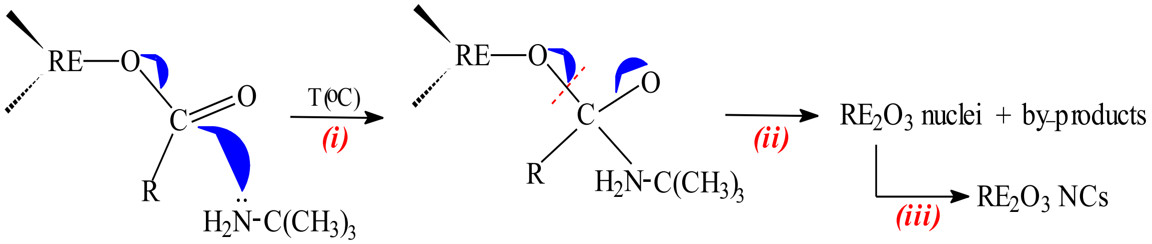

RE = Rare earth; R = $C_{18}H_{35}$

(1)

Figures 6.1.11-6.1.13 show representative TEM images and SAED patterns of different rare earth oxide NCs (see Table 6.1.1). Under the same synthesis conditions, different shapes of the final NC products were observed: spheres for Er_2O_3 (Figure 6.1.11), the mixture of spheres and peanuts for Gd_2O_3 (Figure 6.1.12), and rods for La_2O_3 and Y_2O_3 (Figure 6.1.13), and depending on metal oleate complexes. Er_2O_3 nanospheres with the size of about 10-20 nm were obtained meaning that no growth direction is dominant during the seeded growth, whereas nanorods were yielded for La_2O_3 and Y_2O_3. The La_2O_3 nanorods of 8 nm in width and 20 nm in length with an aspect ratio of ~2.5, while Y_2O_3 nanorods (10 nm x 80-120 nm) with the aspect ratio of ~10 were observed. However, for Gd_2O_3, the mixture of nearly round-shaped nanocrystals (10-20 nm) and partly nanopeanuts (10-20 nm x 20-40 nm) was identified. The corresponding SAED patterns of these Er_2O_3, Gd_2O_3, and Y_2O_3 NC samples exhibit a set of sharp spots which are characteristic of single crystalline cubic structure, the diffraction rings of the La_2O_3 NC sample corresponds to hexagonal structure, in good aggreement with the XRD results.[40-43] It seems that unit cell structure and crystallographic surface energy of seeds are critical for directing the intrinsic shapes of rare earth oxide NCs (see Figure 6.1.13d). This synthetic route also allows us to synthesize in relative large-scale production. For instant, an amount as much as 1.2 g of uniform OM-capped Er_2O_3 nanospheres obtained when increasing the reaction size for the synthesis to 12.5.

6.1.3.2. Synthesis of transition-metal oxide nanocrystals (TMO-NCs).

Transition-metal oxides have been widely used in many applications, especially for catalysis and fuel cell technology. In addition, size and shape of these materials provide a sensitive knob for tuning their properties.[47] A number of chemical routes has been developed to produce nanocrystals of transition-metal oxides with defined and controllable shapes.[48] In most cases, nanocrystals were formed at high temperatures. Therefore, the development of approaches for the synthesis of such nanocrystals under mild reaction conditions with size and shape control remains a challenge. We develop a new procedure for the synthesis of a large variety of monodisperse transition-metal oxide nanocrystals through a hydrothermal two-phase approach at relatively low temperature (150-180 ºC) using inexpensive compounds such as transition-metal salts and potassium oleate, instead of expensive organometallic compounds. The synthetic procedure is illustrated in Scheme 6.1.2. The biphasic mixture was composed of an aqueous phase of metal ion (e.g., metal nitrate or chloride), ethanol, water; and a toluene phase of potassium oleate and oleic acid. The metal-oleate complex was directly formed in water-toluene mixture from an ion exchange reaction of metal cation with oleate anion in early mass-transfer stage: $M^{n+} + n\text{RCOO}^- \rightarrow \text{M(COOR)}_n$.[49] Under the hydrothermal synthesis conditions, the resulting metal-oleate complexes were reduced by ethanol to generate tiny oxide nuclei at the interfaces and then form metal oxide nanocrystals, which were capped by fatty acid in organic phase; no NC product was observed in aqueous phase. To describe this approach, four different transition-metal oxides: Mn_3O_4, Cr_2O_3, Co_3O_4, and NiO, were selected and synthesized in this study (see Table 6.1.1). As seen in Figure 6.1.14, the XRD patterns of these samples are well-matched to tetragonal Mn_3O_4 (JCPDS: 16-0154) with a = 5.759 Å;[50] rhombohedra Cr_2O_3 (JCPDS: 05-0667) with a = 4.958 Å;[51] cubic Co_3O_4 (JCPDS: 48-1719) with a = 8.084 Å;[52] and cubic NiO (JCPDS: 04-0835) with a = 4.193 Å.[53] A broadening of XRD peaks indicates the nanocrystalline nature of these samples. Furthermore, no other phases were detected in the spectra suggesting the pure structure of products. The particle size calculated using the Scherrer equation from the (103), (110), (331), (200) reflections for Mn_3O_4, Cr_2O_3, Co_3O_4, and NiO NCs, respectively was about 12 nm, 7 nm, 5 nm, and 7 nm, which are further consistent with the TEM results.

Representative TEM images and SAED patterns of these samples are shown in Figure 6.1.15. The Mn_3O_4 and NiO NCs exhibit a hexagonal-like shape with an average diameter of nearly 10 nm and 8 nm, respectively. Closer TEM observation of the Mn_3O_4

NC sample shows that the single hexagon self-assembled two-dimensional (2D) networks. The Cr_2O_3 NC sample shows self-assemblied nanodots with an average diameter of about 3 nm. Furthermore, the 6 nm-sized nanospheres and a few truncated nanospheres of Co_3O_4 prefer to construct the ordered hexagonal self-assembly, as proposed simulation in inset of Figure 6.1.15e. The corresponding SAED patterns of these Mn_3O_4, NiO, Cr_2O_3, and Co_3O_4 NC samples exhibit the strong diffraction rings and can be well indexed to the tetragonal, cubic, rhombohedra, and cubic structures, respectively. Similarly, we could be obtained the large-scale amount of products, e.g., 2.0 g of OA-Co_3O_4 nanospheres, through this approach when increasing the reaction size for the synthesis to 12.5.

The self-assembly of Co_3O_4 nanocubes into nanospheres was also observed (Figure 6.1.16), as a function of reaction time, when all the synthesis condition kept constant (e.g., cobalt nitrate, solvent volume, potassium oleate and oleic acid, and reaction temperature corresponding to 0.08 M, 40 mL, 3 g, 2 mL, and 180 °C, respectively). After heating at 180 ºC for a relatively short time, 12 h, the TEM image of this sample shows two populations of particles size (Figure 6.1.16a): polydisperse small nanocubes (2-4 nm) and relatively monodisperse nanocubes self-assembly (~5 nm). However, after 18 h of synthesis, relatively uniform nanocrystals with the average size of 6 nm was observed (Figure 6.1.16b). Furthermore, when the synthesis time was extended to 24 h, the morphology of the product was remarkably changed; the corners and tips of cubes gradually became smooth and monodisperse spherial nanocrystals were formed (Figure 6.1.16c). These results indicate that a transformation of the nanocubes to monodisperse 6 nm-sized nanospherical self-assembly with extending the reaction time, as suggested in Figure 6.1.16d. The most model for shape control is the Gibbs-Curie-Wulff facet theorem[54,55] which suggests that the shape of a crystal is determined by the minimum surface energy of each facet of the crystal. It means that crystal growth should occur rapidly at high-free-energy facets. In the early stages, Co_3O_4 nanocubes can be formed in the anisotropic growth, which can relate to the selective absorption of oleic acid on these low-energy exposed crystal faces of {100}, {010}, and {001}.[56] It is known that the cubes correspond to cuboctahedral precursors with the specific growth of {111} facets compared to the {100} facets while spheres exist with symmetric faces.[57] When extending the reaction time, the monomer Co(II) oleate complex concentration was gradually depleted by the nucleation and growth of the nanocrystals. If the reaction time is sufficiently long (in this case, 24 h), the monomer concentration should drop to a level which is a lower than that required for a given cubic shape. The cubic shape should eventually evolve to the spherical shape which is most stable shape by moving monomers from {111} to {100} faces in an intraparticles due to the differences in chemical potential between different facets of the nanocrystals. In this case, a few truncated nanospheres were still observed may result the incomplete transformation of cubes to spheres owing to the insufficient ripening reaction time.

These NC samples: manganese oxide, cobalt oxide, and chromium oxide nanocrystals before and after calcination were characterized by the XPS technique. The XPS spectra before (solid curve) and after (dotted curve) calcination of these samples show almost the same suggesting no significant change in the oxidation state upon this thermal treatment (Figure 6.1.17). The deconvolution results of the Mn 2p, Co 2p, and Cr 2p peak XPS spectra are shown in Figures 6.1.17A,B,C. The Mn $2p_{3/2}$ peaks are centered at ~640.59-652.01 eV; Mn $2p_{1/2}$ peaks at ~642.20-653.60 eV, with $\Delta \approx 1.6$ eV, indicating those of pure Mn_3O_4 phase.[58] The O 1s peaks (not shown) were located at 529.76-531.76 eV are assigned to oxygen in Mn_3O_4 and the an another shoulder at 533.40 eV attributed to the presence of hydroxyl species or adsorbed water on the surface.

For the cobalt oxide NC sample, the two main Co 2p binding energies are ~779.63-794.85 eV (Co $2p_{3/2}$), ~781.70-796.35 eV (Co $2p_{1/2}$), and $\Delta \approx 2.1$ eV, and the shake-up satellites (I) with a low intensity at ~10.6 eV due to the main Co 2p band are characteristic of those of pure Co_3O_4.[59] The shake-up satellites (II) at ~5.6 eV from the weak Co 2p bands suggests the presence of NC surface hydroxyls. The Cr 2p spectrum of the chromium oxide NC sample shows the Cr $2p_{3/2}$ peak at 576.88-586.39 eV and Cr $2p_{1/2}$ peak 579.74-588.91 eV are attributed to Cr^{3+}.[60] The O 1s peak (not shown) is often believed to be composed of two peaks, related to two different chemical states of oxygen. The binding energies of each individual component are 531.80 (Cr^{3+}-O) and 533.35 eV (OH^-). Furthermore, the calculated atomic ratios of Mn:O, Co:O, and Cr:O are respectively found to be very close to

0.73:1.00, 0.85:1.00, and 0.98:1.49 corresponding to the stoichiometry of Mn_3O_{4-x} (x = 1.25), Co_3O_{4-x} (x = 1.47), and Cr_2O_3, respectively.

6.1.4. Conclusion

Different two-phase methods have been developed for the synthesis of two classes of monodisperse metal oxide nanocrystals: rare earth oxides and transition-metal oxides, using metal salts as starting precursors instead of expensive organometallic compounds. The results revealed that for the formation of rare earth oxide nanocrystals, *tert*-butylamine plays a key role as a nucleophile agent. However, in the case of transition-metal oxide nanocrystals, ethanol is an important agent for reducing the monomeric transition-metal precursors to induce the NC products. Various sizes and shapes of monodisperse nanoparticles such as cubic, spherical, hexagonal, peanut, and rod NCs were obtained depending on the nature of metal precursors. The size and shape evolution of CeO_2 NCs was found to be as a function of monomer concentration of cerium salts. The size and shape varied from 3 nm-sized cubes to 8 nm x 10 nm-sized elongated cubes when the cerium monomer concentration in the synthesis mixture increased from 0.015 M to 0.120 M, which is related to the increasing the chemical potential in bulk solution. The results revealed that the synthesis of samaria nanorods consists of two steps of growth: (i) the nanoparticles were formed at relatively low temperature (120-140ºC) by Ostwald ripening; (ii) followed by oriented attachment of these nanoparticles at higher temperature (160-200ºC) to produce the nanorods (average size of 7 nm x 160 nm). Furthermore, the width of nanorods can be controlled by the length of capping alkyl chain agents; based on the experimental results, it seems that a longer alkyl chain agent leads to thinner nanorods, however, the length of nanorods remains unchanged. In the case of Co_3O_4 nanocrystals, the morphology changed from nanocube to nanospheres when the reaction time increased from 12 h to 24 h at 180 ºC due to the differences in chemical potential between different facets of the nanocrystals.

The SAED patterns of the obtained NC samples show a set of sharp spots characteristic of single crystalline structure, and the strong diffraction rings indexed accordingly with the structures determined by the XRD spectra. The XPS results revealed that the presence of two oxidation states of cerium, samarium, manganese, and cobalt on the nanocrystal surface. However, it seems that only one oxidation state on the surface for Y, Cr, La oxide nanocrystals is present. Two different components of O 1s XPS large peak for these Ce, Sm, Mn, Co oxide NC samples refer to the defected structure.

These synthetic methods have several advantages including relatively mild conditions, easily to manipulate with controllable size and shape of NCs and to scale-up to the multi-gram-scale products using inexpensive metal salt precursors. These methods can be extended to the synthesis of other uniform NCs as well as doped and multi-component NCs. Further work is in progress in our laboratory.

6.1.5. References

(1) Jun, Y. W.; Seo, J. W.; Cheon, A. J. *Acc. Chem. Res.* **2008**, *41*, 179-189.

(2) El-Sayed, M. A. *Acc. Chem. Res.* **2004**, *37*, 326-333.

(3) Garcia, M. F.; Arias, A. M.; Hanson, J. C.; Rodriguez, J. A. *Chem. Rev.* **2004**, *104*, 4063-4104.

(4) Wang, X.; Peng, Q.; Li, Y. *Acc. Chem. Res.* **2007**, *40*, 635-643.

(5) Kinge, S.; Calama, M. C.; Reinhoudt, D. N. *ChemPhysChem* **2008**, *9*, 20-42.

(6) Rao, C. N. R.; Kulkarni, G. U.; Thomas, P. J.; Edwards, P. P. *Chem. Eur. J.* **2002**, *8*, 28-35.

(7) Daniel, M. C.; Astruc, D. *Chem. Rev.* **2004**, *104*, 293 346.

(8) Niederberger, M.; Garnweitner, G.; Buha, J; Polleux, J.; Ba, J; Pinna, N. *J. Sol-Gel Sci. Tech.* **2006**, *40*, 259-266.

(9) Wang, X.; Li, Y. *Chem. Commun.* **2007**, 2901-2910.

(10) Kwon, S. G.; Hyeon, T. *Acc. Chem. Res.* **2008**, 41, 1696-1709.

(11) Redl, F. X.; Cho, K. S.; Murray, C. B.; O'Brien, S. Nature **2003**, *423*, 968-971.

(12) Yin, Y.; Alivisatos, A. P. *Nature* **2004**, *437*, 664-670.

(13) Brust, M.; Walker, M.; Bethell, D.; Schiffrin, D. J.; Whyman, R. J. *Chem. Soc., Chem. Commun.* **1994**, 801-802.

(14) Xia, Y.; Xiong, Y.; Lim, B.; Skrabalak, S. E. *Angew. Chem. Int. Ed.* **2009**, *48*, 60-103.

(15) Pan, D.; Wang, Q.; Jiang, S.; Ji, X.; An, L. *Adv. Mater.* **2005**, *17*, 176-179.

(16) Nguyen, T. D; Do. T. O. *Langmuir* **2009**, *25*, 5322-5332

(17) Pan, D.; Wang, Q.; An, L. *J. Mater. Chem.* **2009**, *19*, 1063-1073.

(18) Pan, D.; Zhao, N.; Wang, Q.; Jiang, S.; Ji, X.; An, L. *Adv. Mater.* **2005**, *17*, 1991-1995.

(19) Zhao, N. N.; Pan, D. C.; Nie, W.; Ji, X. L. *J. Am. Chem. Soc.* **2006**, *128*, 10118-10124.

(20) Du, H.; Wohlrab, S.; Weiß. M.; Kaskel, S. *J. Mater. Chem.* **2007**, *17*, 4605-4610.

(21) Zhang, J.; Ohara, S.; Umetsu, M.; Naka, T.; Hatakeyama, Y.; Adschiri, T. *Adv. Mater.* **2007**, *19*, 203-206.

(22) Mrabet, D.; Zahedi-Niaki, M. H.; Do, T. O. *J. Phys. Chem. C* **2008**, *112*, 7124-7129.

(23) Nguyen, T. D; Mrabet, D.; Do. T. O. *J. Phys. Chem. C* **2008**, *112*, 15226-15235.

(24) Jun, Y. W.; Choi, J. S.; Cheon, J. *Angew. Chem., Int. Ed.* **2006**, *45*, 3414–3439.

(25) Yan, Z. G.; Yan, C. H. *J. Mater. Chem.* **2008**, *18*, 5046-5059.

(26) Cotton, F. A.; Wilkinson, G.; Murillo, C. A.; Bochmann, M. *Advanced Inorganic Chemistry*, Sixth Edition.

(27) Yan, L.; Yu, R.; Chen, J.; Xing, X. X. *Crystal Growth & Design* **2008**, *8*, 1474-1477.

(28) Knifton, J. F.; Grice, N. J., *Tert*-butylamine synthesis over montmorillonite clays, *US Patent 5304681*, **1994**.

(29) Mullin, J. W. In *Crystallization*, 3rd ed., Butterworth-Heinemann: Woburn, MA, **1997**.

(30) Peng, Z. A.; Peng, X. G. *J. Am. Chem. Soc.* **2002**, *124*, 3343-3353.

(31) Peng, X. G. *Adv. Mater.* **2003**, *15*, 459-463.

(32) Zhuang, Z.; Peng, Q.; Zhang, B.; Li, Y. *J. Am. Chem. Soc.* **2008**, *130*, 10482-10483.

(33) Wu, Q.; Zhang, F.; Xiao, P.; Tao, H.; Wang, X.; Hu, Z. *J. Phys. Chem. C* **2008**, *112*, 17076-17080.

(34) Taniguchi, T.; Watanabe, T.; Sakamoto, N.; Matsushita, N.; Yoshimura, M. *Cryst. Growth & Des.* **2008**, *8*, 3725-3730.

(35) Alivisatos, A. P. *J. Phys. Chem.* **1996**, *100*, 13226-13239.

(36) Kapteijn, F.; Langeveld, A. D. V.; Moulijn, J. A.; Andreini, A. Vuurman, M. A.; Turek, A. M.; Jehng, J. M.; Wachs, I. E. *J. Catal.* **1994**, *150*, 94-104.

(37) Zhang, F.; Wang, P.; Koberstein, J. Khalid, S.; Chan, S. C. *Surface Science* **2004**, *563*, 74-82.

(38) Zhao, N.; Nie, W.; Liu, X.; Tian, S.; Zhang, Y.; Ji, X. *small* **2008**, *4*, 77-81.

(39) Yongiu, L.; Xiaoyun, L.; Yizheng, W.; Junming, L.; Weili, S. *Journal of Rare Earths* **2006**, *24*, 34-38.

(40) Nelson, J. A.; Wagner, M. J. *Chem. Mater.* **2002**, *14*, 915-917.

(41) Soderlind, F.; Pedersen, H.; Petoral Jr, R. M.; Kall, P. O.; Uvdal, K. *Journal of Colloid and Interface Science* **2005**, *288*, 40-148.

(42) Han, K.; Zhang, Y.; Fang, Z.; Cheng, T.; Gao, M. *Chemistry Letters* **2007**, *36*, 1124-1125.

(43) Murugan, A. V.; Navale, S. C.; Ravi, V. *Mater. Lett.* **2006**, *60*, 848-849.

(44) Zhang, Z.; Lu, M.; Xu, H.; Chin, W. S. *Chem. Eur. J.* **2007**, *13*, 632-638.

(45) Van, T. T.; Chang, J. P. *Surface Science* **2005**, *596*, 1-11.

(46) Tuysuz, H.; Liu, Y.; Weidenthaler, C.; Schuth, F. *J. Am. Chem. Soc.* **2008**, *130*, 14108-14110.

(47) Thomas, J. M.; Simpson, E. T.; Kasama, T.; Borkowski, R. E. D. *Acc. Chem. Res.* **2008**, *41*, 665-674.

(48) Park, J.; Joo, J.; Kwon, S. G.; Jang, Y.; Hyeon, T. *Angew. Chem., Int. Ed.* **2007**, *46*, 4630-4660.

(49) Park, J.; An, K.; Hwang, Y.; Park, J. G.; Noh, H. J.; Kim, J. Y.; Park, J. H.; Hwang, N. M.; Hyeon, T. *Nat. Mater.* **2004**, *3*, 891-895.

(50) Lei, S.; Tang, K.; Fang, Z.; Zheng, H. *Cryst. Growth & Des.* **2006**, *6*, 1757-1760.

(51) Li, L.; Yan, Z. F.; Lu, G. L.; Zhu, Z. H. *J. Phys. Chem. B* **2006**, *110*, 178-183.

(52) Kumar, U.; Shete, A.; Harle, A. S.; Kasyutich, O.; Schwarzacher, W.; Pundle, A.; Poddar, P. *Chem. Mater.* **2008**, *20*, 1484-1491.

(53) Huang, C. N.; Chen, S. Y.; Shen, P. *J. Phys. Chem. C* **2007**, *111*, 3322-3327.

(54) Mullin, J. W. In *Crystallization*, 3rd ed., Butterworth-Heinemann: Woburn, MA, **1997**.

(55) Wulff, G.; Zeitschrift, F. *Beitr. Krystallogr. Mineral.* **1901**, 34, 449.

(56) Si, R.; Zhang, Y. W.; You, L. P.; Yan, C. H. *Angew. Chem.* **2005**, *117*, 3320-3324.

(57) Pileni, M. P. *J. Phys. Chem. C* **2007**, *111*, 9019-9038.

(58) Wang, W.; Ao, L. *Cryst. Growth & Des.* **2008**, *8*, 358-362.

(59) He, T., Chen, D., Jiao, X., Wang, Y., Duan, Y. *Chem. Mater.* **2005**, *17*, 4023-4030.

(60) Unveren, E.; Kemnitz, E.; Hutton, S.; Lippitz, A.; Unger, W. E. S. *Surf. Interface Anal.* **2004**, *36*, 92-95.

Table 6.1.1. Synthesis Conditions and Morphologies of the As-Made Capped Metal Oxide Nanocrystals via Hydrothermal Two-Phase Routes

Sample	Precursor	Precursor conc. [M]	Aqueous phase [mL]	Organic phase [mL]	Surfactant [mL]	Time [h]	Product	Morphology
Rare earth oxide nanocrystals (Schemes 6.1.1A,B)								
1	$Sm(NO_3)_3$	0.120	water, TBA [a]	Toluene	OA [a]	24	Sm_2O_3	rod
2	$Ce(NO_3)_3$	0.120	water, TBA	Toluene	OA	24	CeO_2	cubic/ elongated cubic self-assembly
3	$Ce(ac)_3$	0.120	water, TBA	Toluene	OA	24	CeO_2	agglomerated cubic self-assembly
4	Er-oleate	0.018	water, TBA	Toluene	OM [a]	24	Er_2O_3	spherical self-assembly
5	Gd-oleate	0.018	water, TBA	Toluene	OM	24	Gd_2O_3	peanut
6	La-oleate	0.018	water, TBA	Toluene	OM	24	La_2O_3	short rod
7	Y-oleate	0.018	water, TBA	Toluene	OM	24	Y_2O_3	long rod
Transition-metal oxide nanocrystals (Scheme 6.1.2)								
8	$Mn(NO_3)_2$	0.08	water, ethanol	Toluene, KOA [a]	OA	24	Mn_3O_4	hexagonal self-assembly
9	$CrCl_3$	0.08	water, ethanol	Toluene, KOA	OA	24	Cr_2O_3	dot
10	$Co(NO_3)_2$	0.08	water, ethanol	Toluene, KOA	OA	24	Co_3O_4	spherical self-assembly
11	$Co(NO_3)_2$	0.08	water, ethanol	Toluene, KOA	OA	18	Co_3O_4	cubic
12	$Co(NO_3)_2$	0.08	water, ethanol	Toluene, KOA	OA	12	Co_3O_4	cubic/assembled cubic
13	$Ni(NO_3)_2$	0.08	water, ethanol	Toluene, KOA	OA	24	NiO	hexagonal

* All samples were synthesized by solvothermal process at 180 °C.

(a) TBA: *tert*-butylamine; KOA: potassium oleate; OA: oleic acid; OM: oleylamine

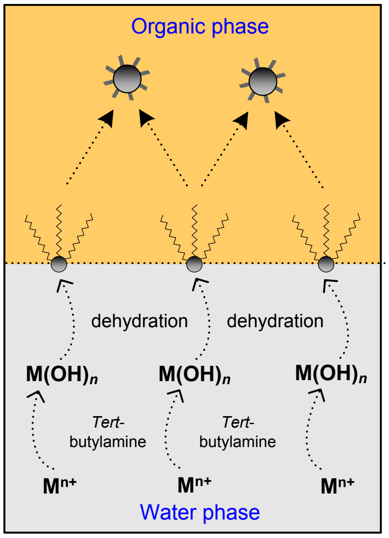

Scheme 6.1.1A. A two-phase route to synthesize the rare earth oxide nanocrystals using rare earth salt precursors.

$$RE(NO_3)_3 + 3KOA\ \text{(potassium oleate)} \longrightarrow \boxed{\begin{matrix} RE(OA)_3 \\ \text{complex} \end{matrix}} + 3KNO_3$$

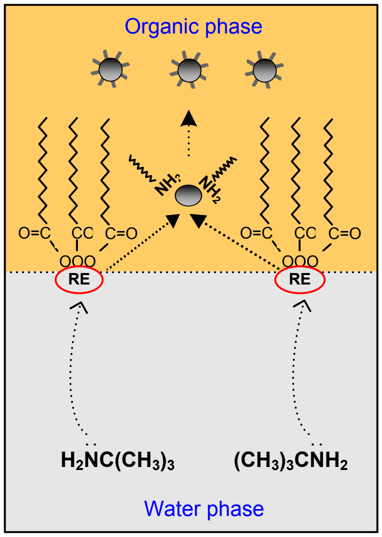

Scheme 6.1.1B. A two-phase route to synthesize the rare earth oxide nanocrystals using rare earth oleate complex precursors.

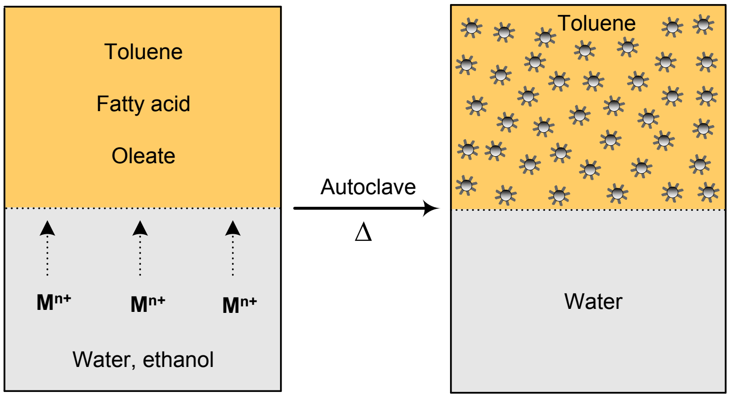

Scheme 6.1.2. A two-phase route to synthesize the transition-metal oxide nanocrystals using metal salt precursors.

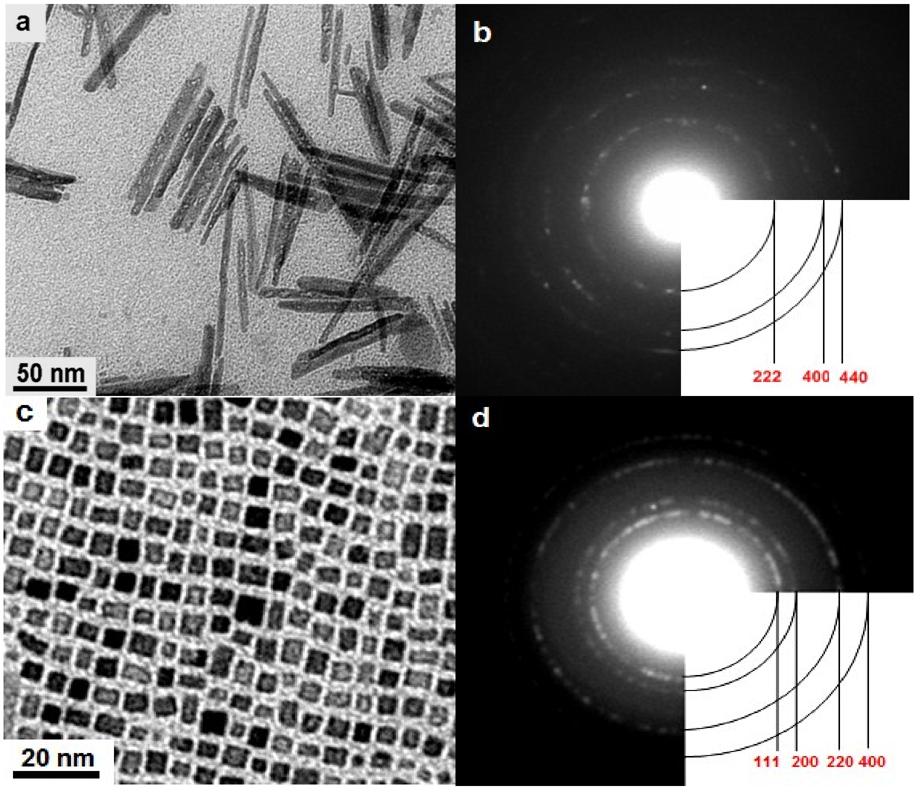

Figure 6.1.1. The rare earth oxide nanocrystals synthesized using the corresponding nitrate salts at a high monomer concentration (C = 0.120 M) following Scheme 6.1.1A: (a) TEM image and (b) SAED pattern of 7 nm x 100-160 nm-sized Sm_2O_3 nanorods (sample 1), (c) TEM image and (d) SAED pattern of the CeO_2 NC mixture of 8 nm-sized nanocubes and 8 nm x 10 nm-sized elongated nanocubes (sample 2).

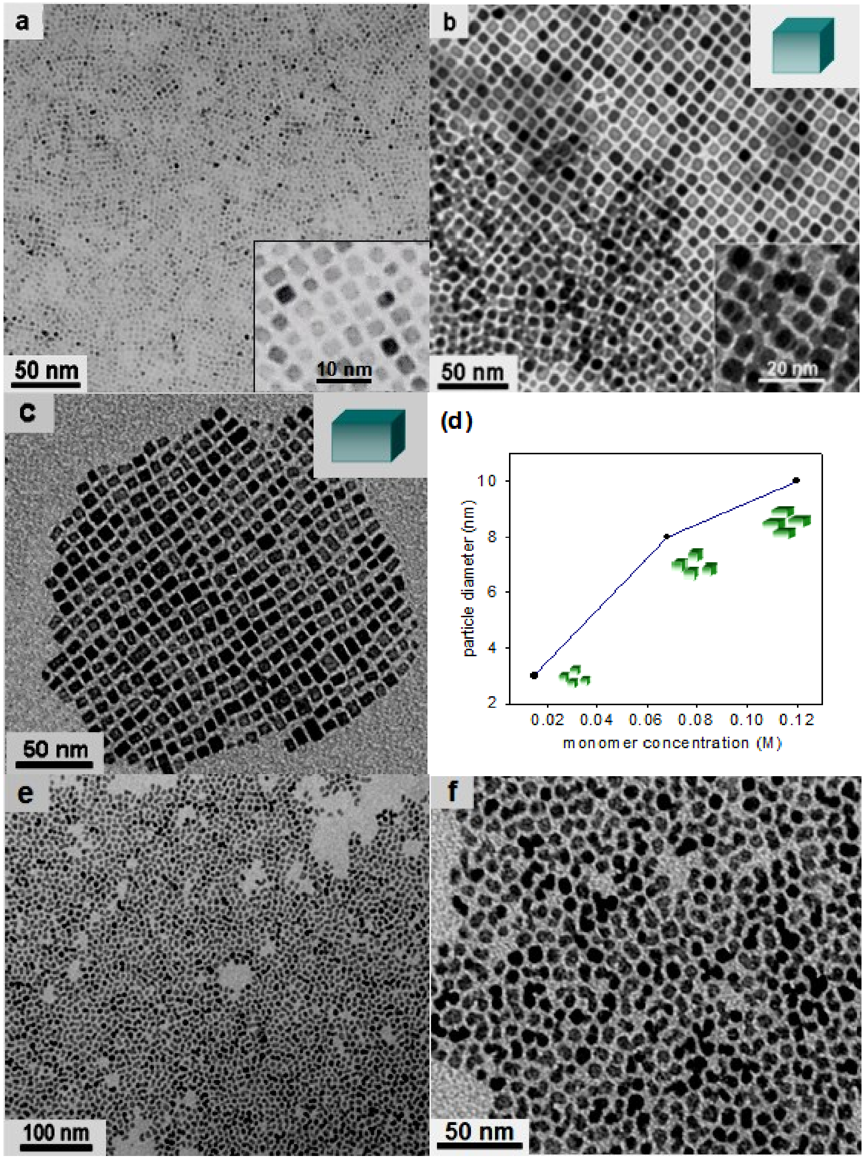

Figure 6.1.2. Shape and size evolution of CeO_2 nanocrystals as a function of the cerium monomer concentrations (*C*). TEM images of the CeO_2 NC samples prepared at: (a) C = 0.015 M, 3 nm-sized nanocubes, (b) C = 0.068 M, 8 nm-sized nanocubes, (c) C = 0.120 M, a mixture of 8 nm-sized nanocubes and 8 nm x 10 nm-sized elongated nanocubes, (d) Correlation plot showing the relationship of the cerium monomer concentration in water phase and average diameter of CeO_2 nanocubes, (e,f) 8-10 nm-sized agglomerated CeO_2 nanocubes obtained using $Ce(ac)_3$ precursors (C = 0.068 M, sample 3).

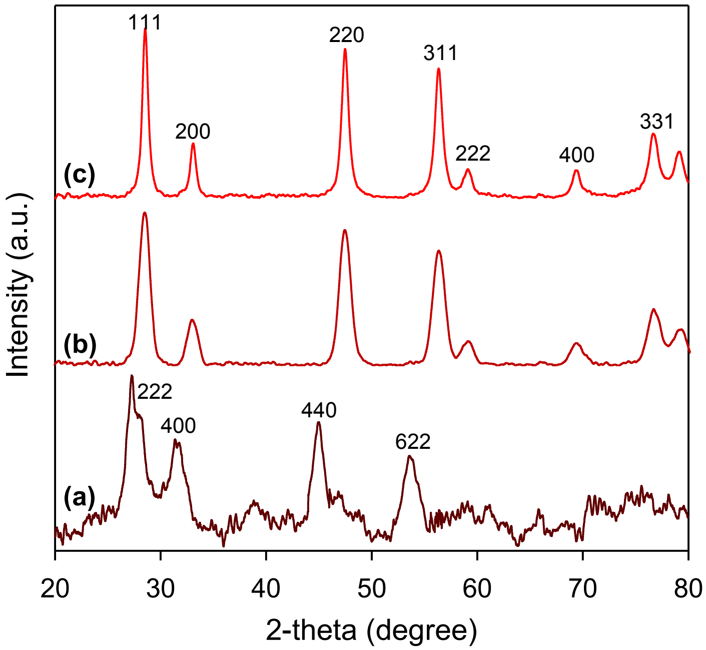

Figure 6.1.3. XRD patterns of the calcined rare earth oxide NC samples: (a) Sm_2O_3 nanorods (sample 1), (b) CeO_2 NC mixture of nanocubes and elongated nanocubes (sample 2), (c) agglomerated CeO_2 nanocubes (sample 3).

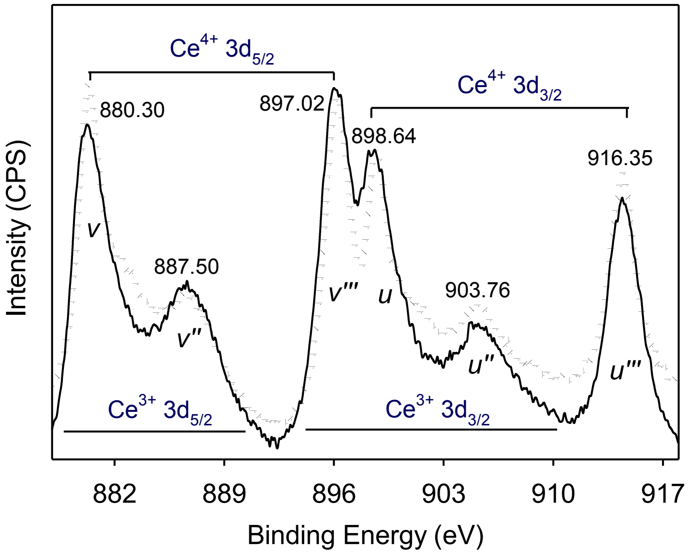

Figure 6.1.4. Ce 3d XPS spectra of the nanoceria (sample 2) before (solid curve) and after (dotted curve) calcination.

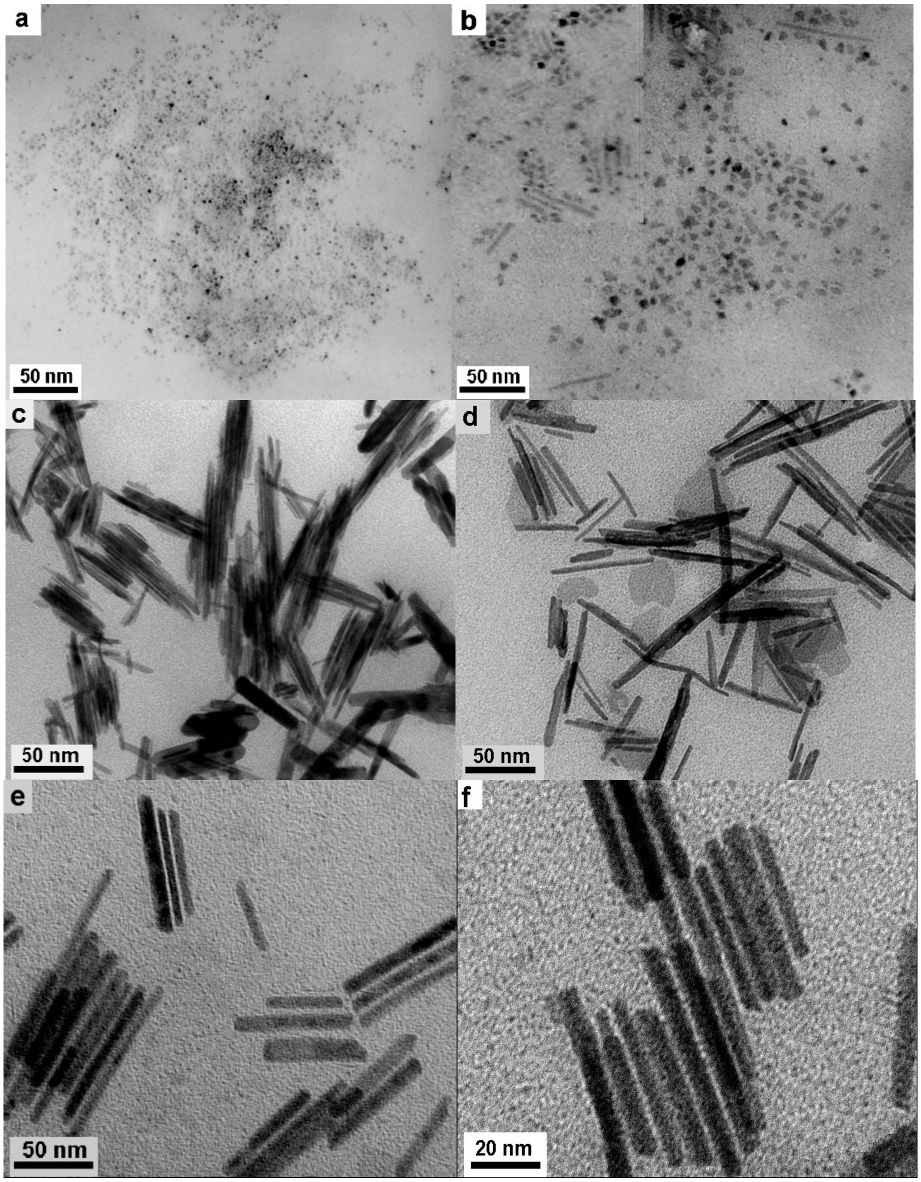

Figure 6.1.5. TEM images of Sm_2O_3 nanocrystals formed at different stages of synthesis temperature for 24 h of each stage, while keeping the other experimental conditions unchanged: (a) 5 nm-sized nanospheres synthesized at 120°C, (b) mixture of 6 nm-sized nanospheres and 6 nm x 50 nm-sized nanorods at 140°C, (c) 6 nm x 80-100 nm-sized rodlike nanobundles at 160°C, (d) 7 nm x 100-160 nm-sized nanorods at 180°C, (e, f) 8 nm x 160 nm-sized parallel nanorods at 200°C.

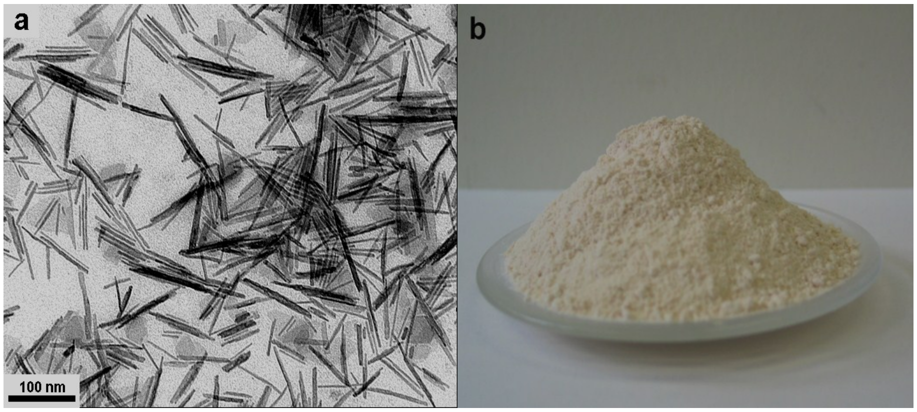

Figure 6.1.6. TEM image of the 7 nm x 100-160 nm sized Sm_2O_3 nanorods (a), and photograph of a Petri dish containing as-synthesized Sm_2O_3 nanorods in a large scale as much as 50 g (b).

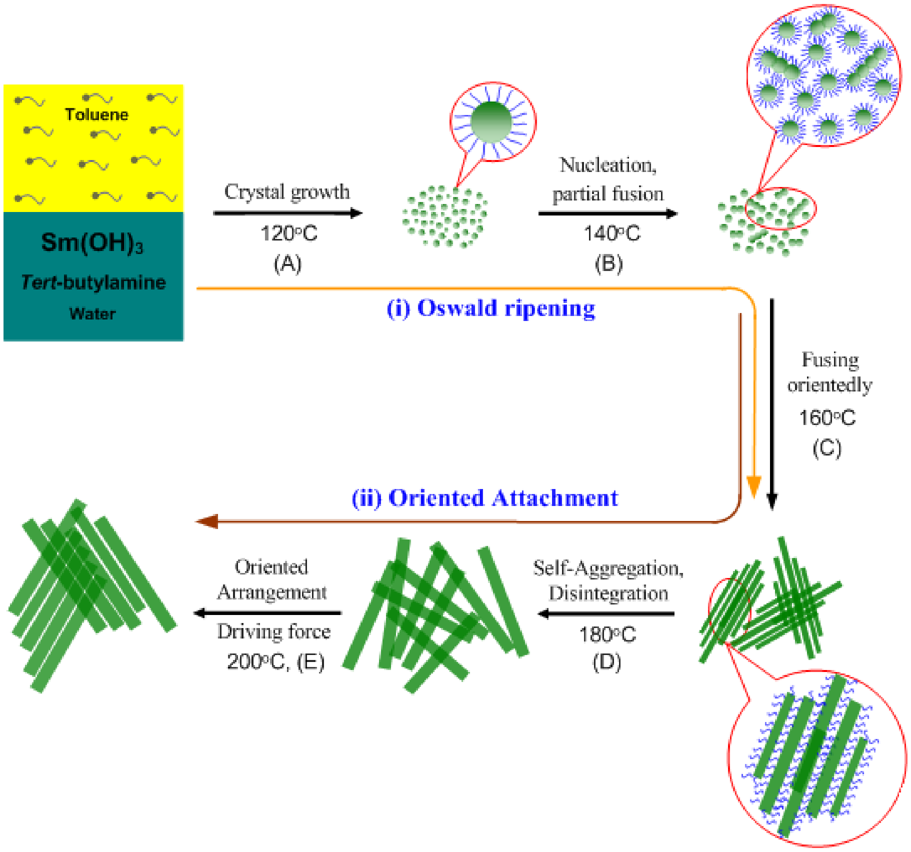

Scheme 6.1.3. Schematic illustration of the formation mechanism and shape evolution of Sm_2O_3 nanorods in the whole synthetic process.

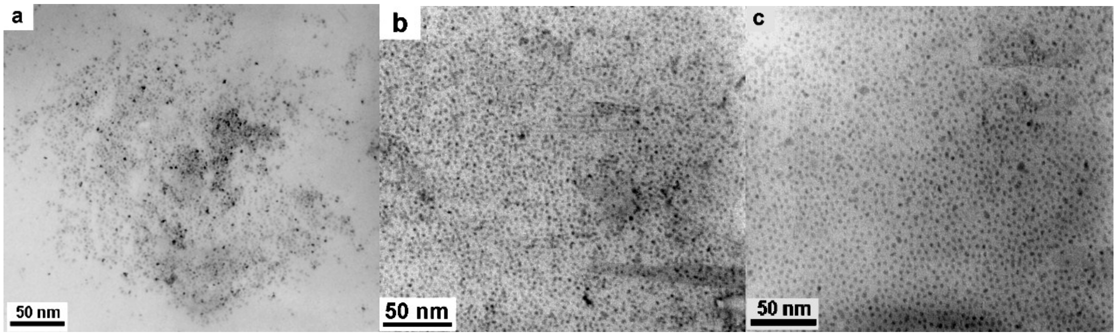

Figure 6.1.7. TEM images of the Sm_2O_3 nanospheres synthesized at 120°C for 24 h using various surfactants: a) Oleic acid, b) Myristic acid, c) Decanoic acid.

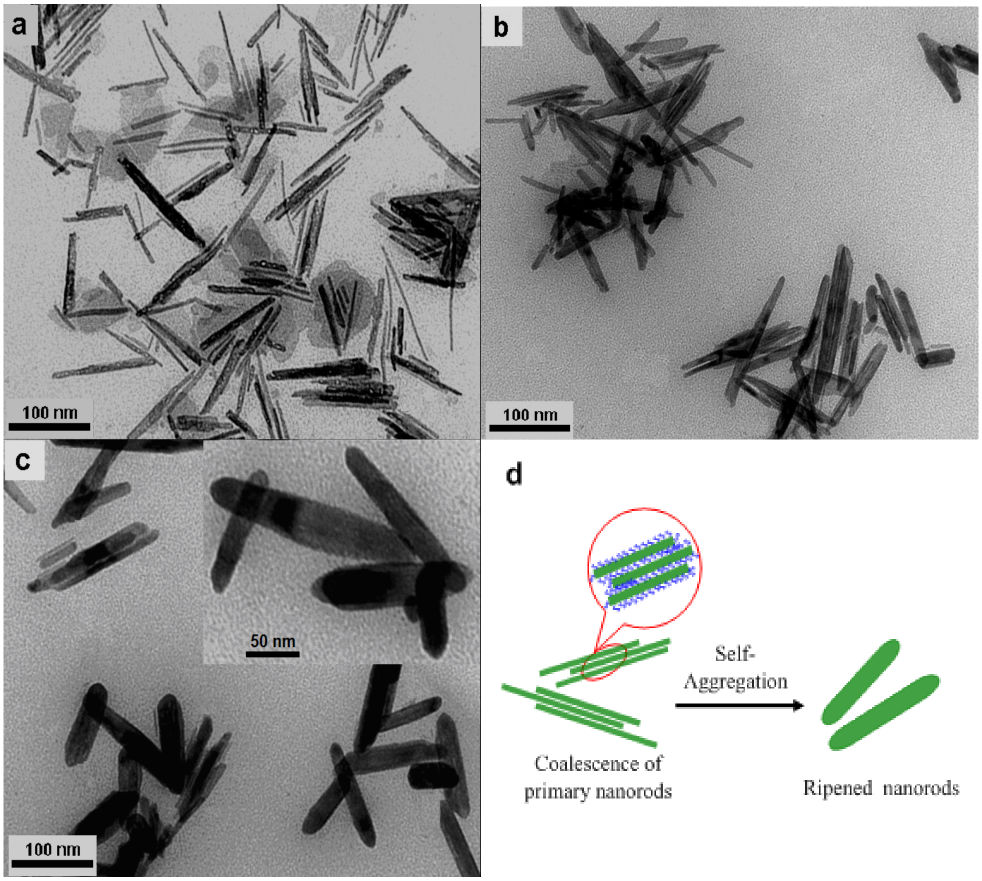

Figure 6.1.8. TEM images of the Sm_2O_3 nanorods synthesized at 180°C for 24 h using various surfactants: a) Oleic acid, b) Myristic acid, c) Decanoic acid; d) Schemetic illustration for the influence of the alkyl chain length of the capping agents on the lateral aggregation of primary nanorods into extended nanorods.

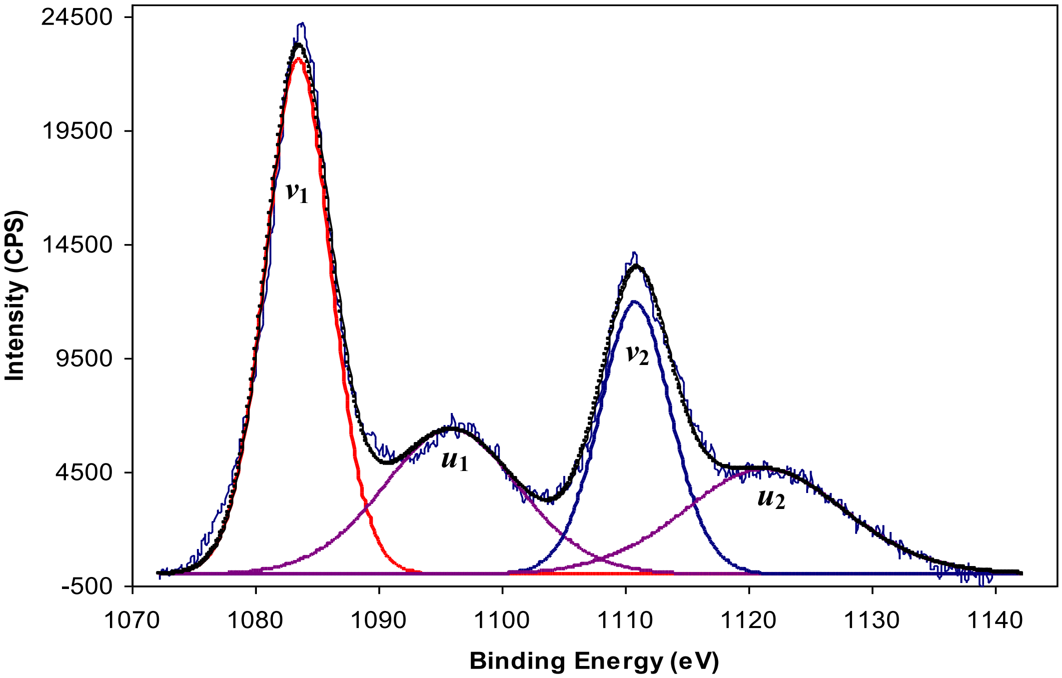

Figure 6.1.9. Sm 3d core level XPS spectrum of the calcined Sm_2O_3 nanorods.

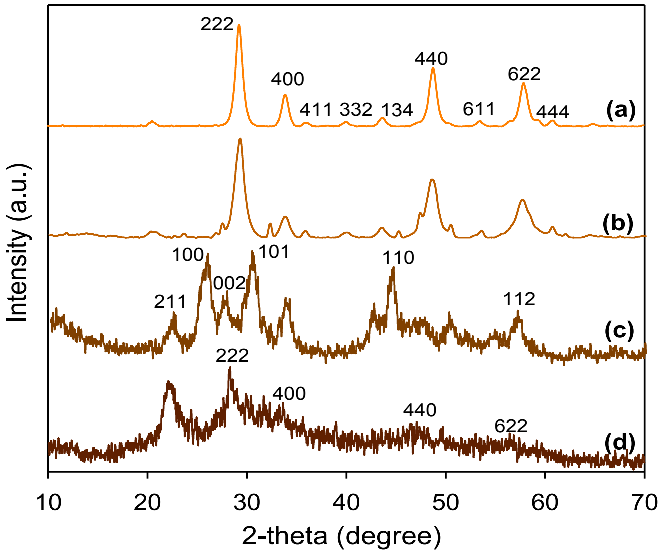

Figure 6.1.10. XRD patterns of the calcined rare earth oxide NC samples synthesized using the corresponding rare earth oleate complexes following Scheme 6.1.1B: (a) Er_2O_3 nanospheres (sample 4), (b) Y_2O_3 nanorods (sample 7), (c) La_2O_3 nanorods (sample 6), (d) Gd_2O_3 nanospheres/nanopeanuts (sample 5).

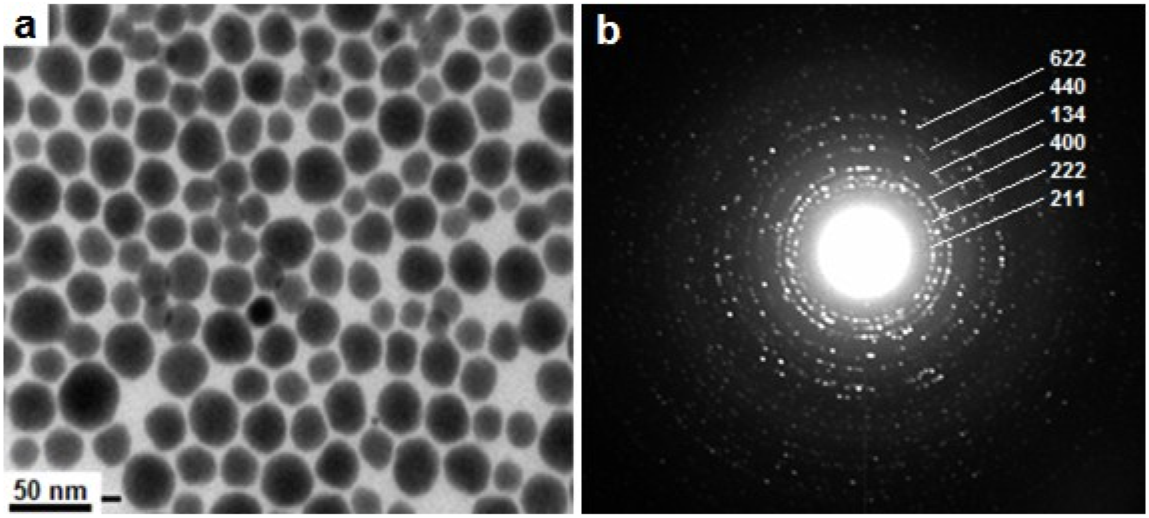

Figure 6.1.11. TEM images and corresponding SAED pattern of the Er_2O_3 nanospheres synthesized using the Er-oleate complexes.

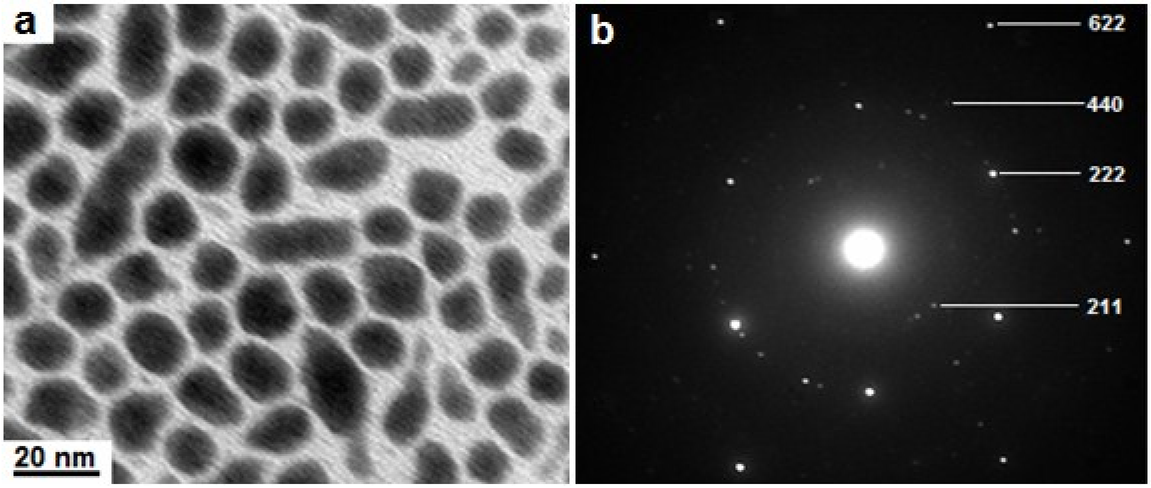

Figure 6.1.12. TEM images and corresponding SAED pattern of the Gd_2O_3 nanospheres/nanopeanuts synthesized using the Gd-oleate complexes.

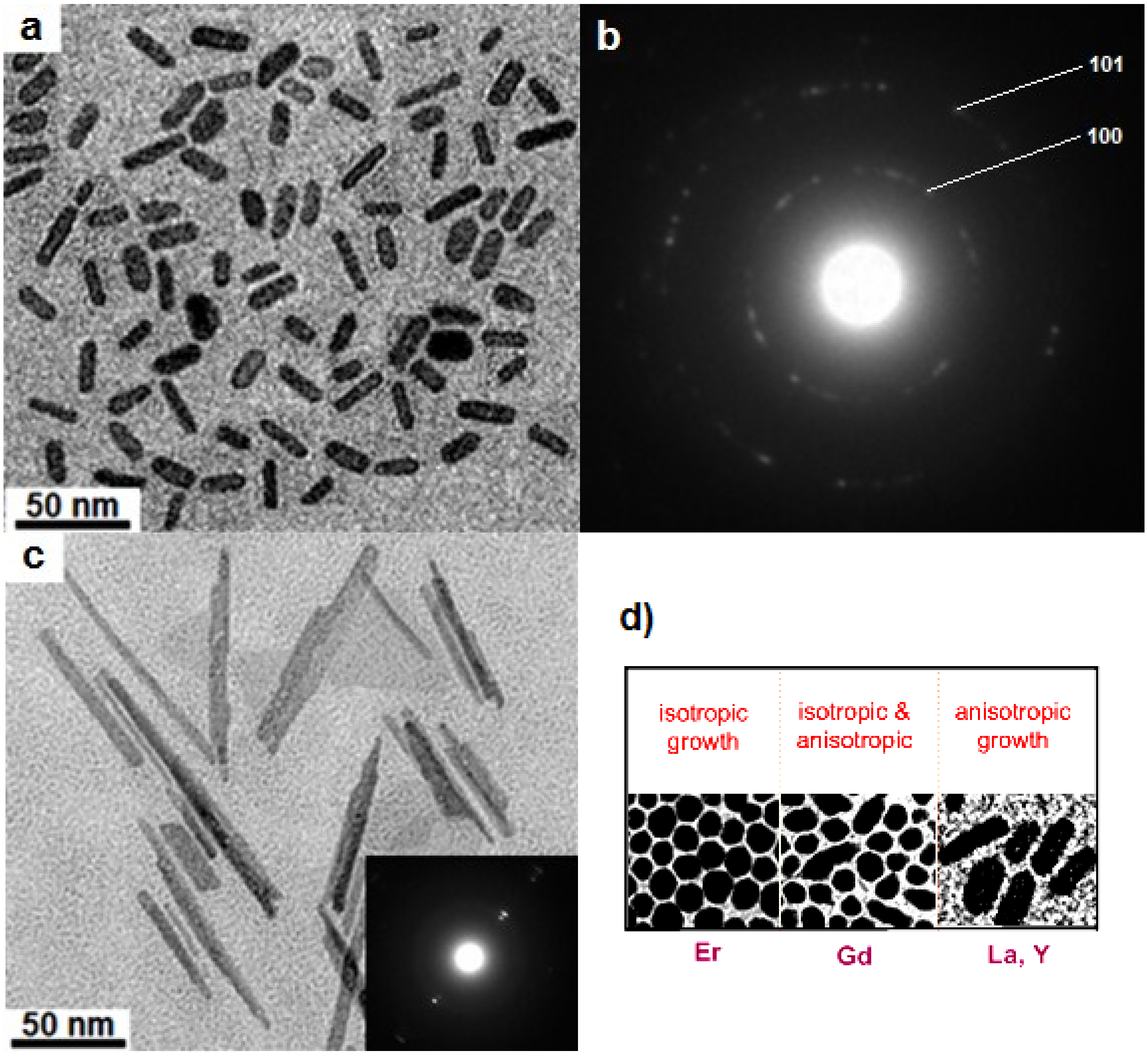

Figure 6.1.13. TEM images and corresponding SAED patterns of the rare earth oxide nanocrystals synthesized using the corresponding rare earth oleate complexes: (a,b) La_2O_3 nanorods, (c) Y_2O_3 nanorods, and d) Growth diagram of RE_2O_3 NCs (RE = Er ÷ Y).

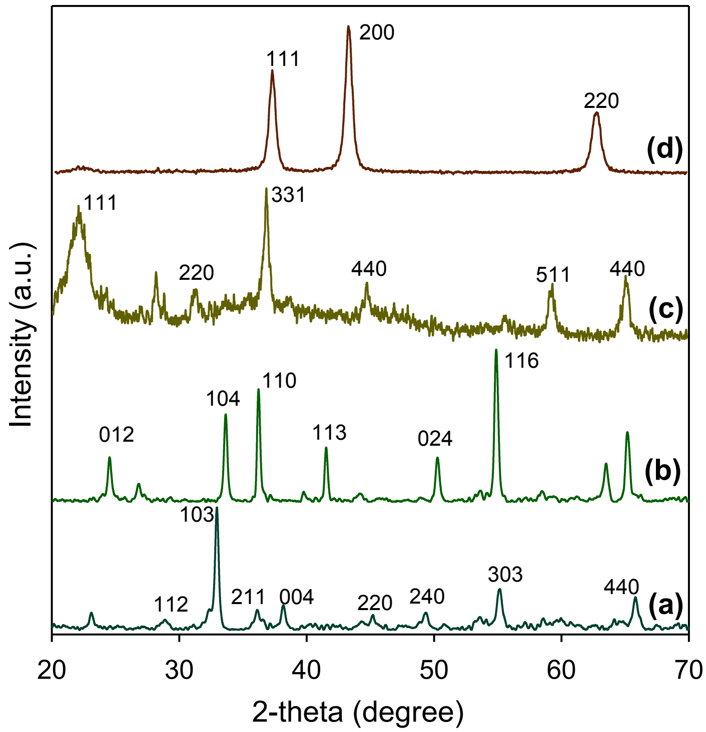

Figure 6.1.14. XRD patterns of the calcined transition-metal oxide NC samples: (a) hexagonal Mn_3O_4 nanocrystals (sample 8), (b) Cr_2O_3 nanodots (sample 9), (c) Co_3O_4 nanospheres (sample 10), and (d) hexagonal NiO nanocrystals (sample 13).

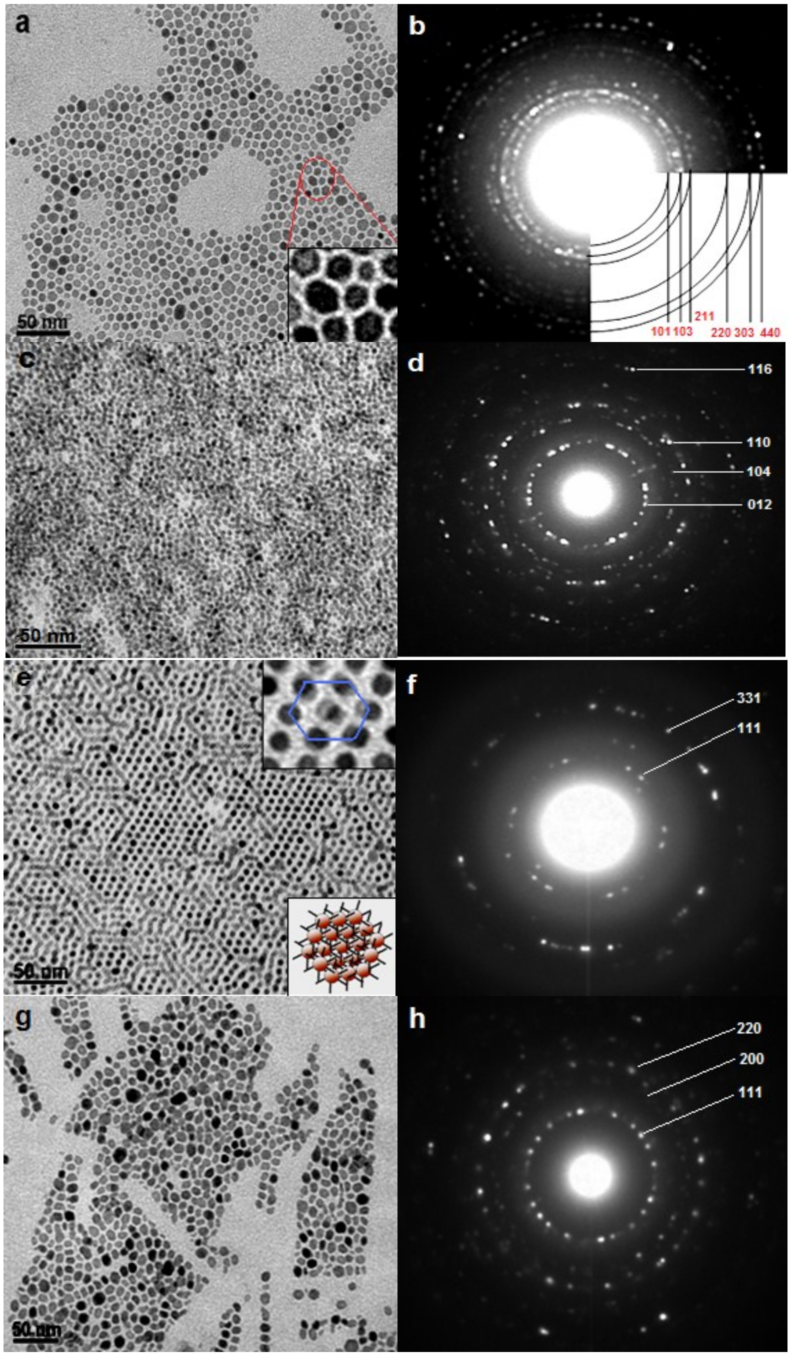

Figure 6.1.15. TEM images and corresponding SAED patterns of the transition-metal oxide nanocrystals synthesized using the corresponding metal salts following Scheme 6.1.2: (a,b) 10 nm-sized hexagonal Mn_3O_4 nanocrystals, (c,d) 3 nm-sized Cr_2O_3 nanodots, (e,f) 6 nm-sized nanospheres and a few truncated nanospheres of Co_3O_4, and (g,h) 8 nm-sized hexagonal NiO nanocrystals.

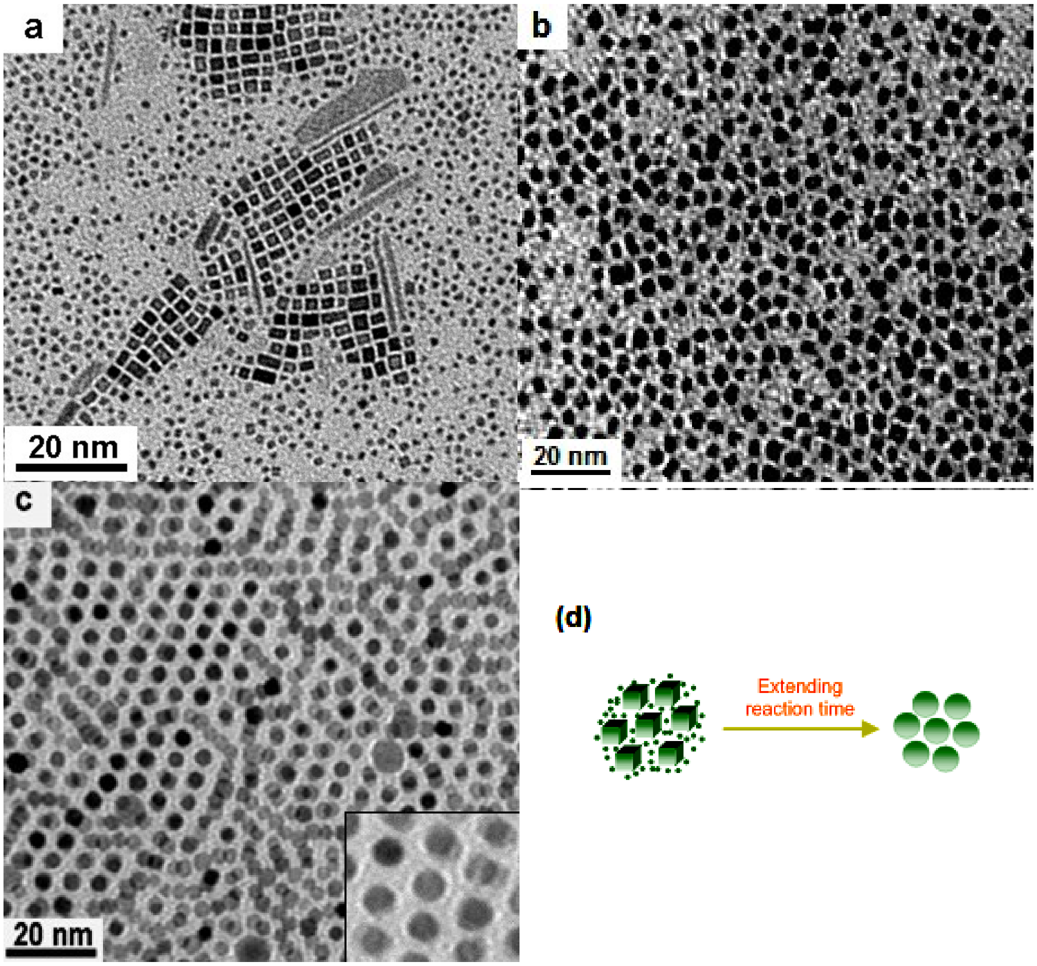

Figure 6.1.16. TEM images of Co_3O_4 NCs synthesized following Scheme 6.1.2 at various reaction times: (a) 12 h, a mixture of nanocubic and nanocubic self-assemblies (sample 12), (b) 18 h, nanocubes (sample 11), (c) 24 h, self-assemblied nanospheres and a few truncated nanospheres (sample 10). (d) A suggested scheme for the self-assembly of the cubic into spherical shape.

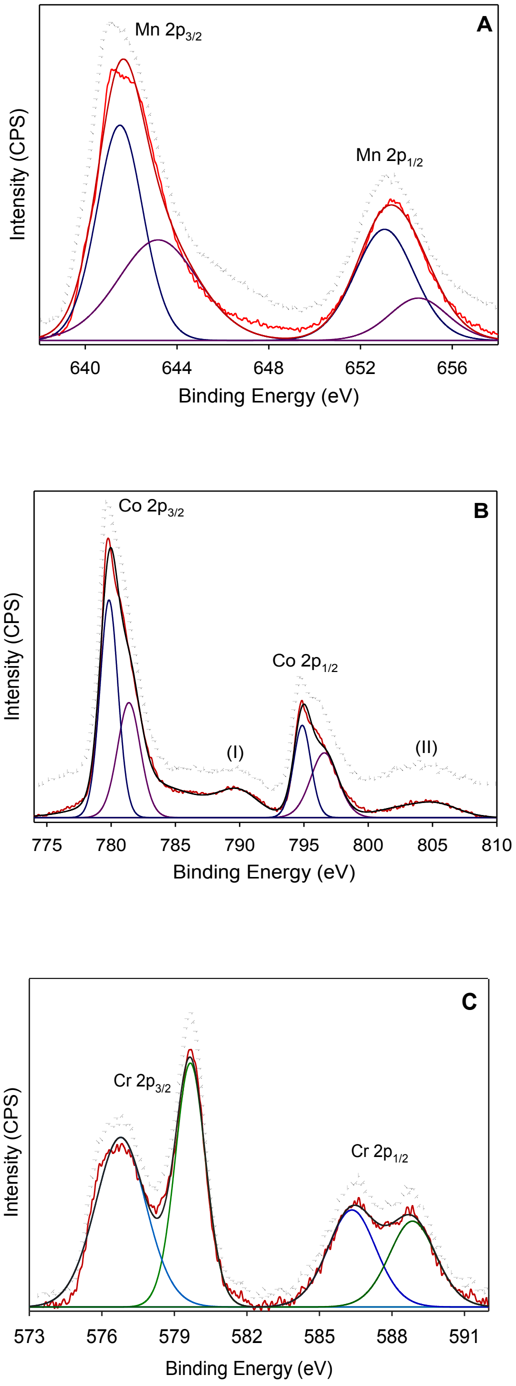

Figure 6.1.17. High-resolution XPS spectra of the transition-metal oxide NC samples before (solid curve) and after (dotted curve) calcination: (A) Mn 2p core level for hexagonal Mn_3O_4 nanocrystals (sample 8), (B) Co 2p core level for Co_3O_4 nanospheres (sample 10), and (C) Cr 2p core level for Cr_2O_3 nanodots (sample 9).

6.2. Solvo-Hydrothermal Approach for the Shape-Selective Synthesis of Vanadium Oxide Nanocrystals and Their Characterization

Thanh-Dinh Nguyen and Trong-On Do

Department of Chemical Engineering, Laval University, Quebec G1K 7P4 Canada

Published in *Langmuir* **2009**, *25*, 5322-5332

Abstract

A new solvo-hydrothermal method has been developed for the synthesis of uniform vanadium oxide nanocrystals (NCs) with various sizes and shapes in aliphatic amine/toluene/water using V(V) diperoxo alkylammonium complexes. The vanadium complex precursors were prepared from an ion exchange reaction of V(V) diperoxo gels and tetraalkylammonium bromide in the water-toluene mixture using H_2O_2 solution and commercial bulk V_2O_5 powders as starting vanadium gel source. The obtained VO_2 nanocrystal products were characterized by means of transmission electron microscopy (TEM), selected area electron diffraction (SAED), scanning electron microscopy (SEM), powder X-ray diffraction (XRD), X-ray photoelectron spectra (XPS), fourier transform infrared absorption spectroscopy (FTIR), thermogravimetric differential thermal analysis (TGA-DTA), and nitrogen adsorption/desorption (BET). The size and shape of nanocrystals can be controlled by different synthesis parameters such as water content, steric ligands of complexes, alkyl chain lengths of capping aliphatic amines as well as nature of solvent. Monodisperse vanadium oxide nanocrystals with various sizes and shapes: nanospheres, nanocubes, nanorices and nanorods can be easily achieved. The possible mechanisms for the formation of vanadium complex precursors and vanadium oxide nanocrystals as well as the shape evolution of NCs were also discussed. The as-made vanadium oxide products exhibited the monoclinic rutile VO_2 structure, which was however converted to the orthorhombic $V_2O_{4.6}$ structure after calcination in air. The XPS results also revealed that only one V^{4+} state for the as-made sample, however, the coexistence of V^{5+} and V^{4+} states and two components of oxygen associated with O=V and

O-V for the calcined samples on the vanadium oxide nanocrystal surface were observed. The surface chemical composition of both as-made and calcined sample was found to be VO_2 and V_2O_{5-x} (x = 0.4), respectively. Our approach may provide a novel route for the extended synthesis to other inorganic nanocrystals.

6.2.1. Introduction

Shape-selective synthesis of inorganic nanocrystals (NCs) is particularly attractive for exploring many their unique material properties with respect to their bulk counterparts, since they are potential building blocks for catalysis, advanced materials, and optoelectronic devices.[1-6] For the past few years, various template-based methods including sol-gel,[7] thermo-hydrolysis of organometallics,[8] reverse micelle technique,[9] solvo-hydrothermal treatment,[10-11] had been demonstrated a success in superior shape and size control. Among them, a solvothermal approach of decomposing metal complexes has been regarded as one of the most effective and economical routes,[12] as it has the merits of a single step low temperature synthesis.

Vanadium oxides (V_2O_{5-x}) are of interest due to their versatile redox activity and layered structures.[13] They are a key technological material widely used in fields such as chemical sensing,[14] actuators,[15] high-energy lithium batteries,[16] and electric field-effect transistors.[17] In particular, V_2O_{5-x} nanocrystals have high oxygen storage capacity (OSC) as a result of the multiple valence state, so they exhibit a good candidate for applications in catalysis such as the selective reduction of NO_x by NH_3[18] and oxidative dehydrogenation of propane.[19] Moreover, supported vanadium oxides are found to be selective catalysts in a number of catalytic reactions, for example, oxidation of methanol, methane, olefins; and oxidative convertion of o-xylene to phthalic anhydride.[20-22] Further research interests will continue in the direction of vanadium-based oxide nanocrystals because of their advantages of being cheap and especially display high positive redox potential for Li insertion.[22-24]

As a target for the shape-controlled nanocrystal synthesis, recent studies in vanadium oxide NCs have focused on the development of synthetic approaches toward nanotubes, nanobelts, nanofibers, nanowires, nanorods, etc., as well as their shape-dependent properties. Up to date, some research groups[25-27] reported the preparation of size-turnable mixed-valent VO_x nanotubes via the aging and hydrothermal process of various vanadium sources including bulk V_2O_5 powders, vanadium(V) peroxo gels, vanadium(V) triisopropoxides using aliphatic amines as structure-directing templates. Furthermore, the distance between the layers in the nanotubes can be also controlled by the alkyl chain length of the structure-directing templates. Zhang et al.[28] showed that the belt-, olive-, petal-shaped VO_2 nanocrystals could be synthesized with high concentrations of the reducing agent (specifically oxalic acid) through hydrothermal route. Baughman et al.[15] reported the synthesis of V_2O_5 nanofibres at room temperature from ammonium meta-vanadate and acidic ion exchange resin in water. The resulting V_2O_5 nanofibers could deliver dramatically higher specific discharge capacities than micrometer-sized V_2O_5 fibers. Recently, Whittingham's group has also developed a method to produce vanadium oxide nanofibers with dimensions less than 140 nm by coating oxides on polylactide fibers.[29] Park et al.[30] synthesized single-crystalline VO_2 nanowires with rectangular cross sections using a vapour transport method. Robert Schlogl et al.[31] presented a reverse micelle technique to prepare V_2O_5 nanorods and nanowires from a colloidal self-assembly made of sodium bis-(ethyl-2-hexyl) sulfosuccinate Na(AOT)/isooctane/H_2O. Chen's group synthesized vanadium oxide nanorods using such reverse micelle technique.[32] The aspect ratio (length/width) of the nanorods was found to be dependent on the water content in micelle system. Cao et al.[33] also synthesized V_2O_5 nanorods arrays using electrophoretic deposition combined with templating. Most of these synthetic methods are limited in the formation of 1-D nanostructures. Reports on the simple routes for the large-scale synthesis of 3-D nanostructures using commercial bulk V_2O_5 powders as starting vanadium source and studies on their shape transformation, however, remain uncommon. Furthermore, in order to obtain monodisperse nanocrystals with a narrow size distribution, suitable precursors that can generate stable monomers in bulk solution are necessary. In this study, V(V) diperoxo gel and tetraalkylammonium bromide are chosen as the vanadium source and ligand, respectively, for the preparation of complex precursors.

In this work, we demonstrate a new solvothermal route to synthesize uniform vanadium oxide nanocrystals using vanadium(V) diperoxo alkylammonium complexes in toluene or toluene/water media in presence of the capping agents (e.g., aliphatic amines). The complex precursors were produced using H_2O_2 solution and commercial bulk V_2O_5 powder as vanadium source. Different sizes and shapes of vanadium oxide nanocrystals including nanospheres, nanocubes, nanorices, and nanorods can be achieved by the control of various reaction parameters, such as water content, types of V(V) diperoxo alkylammonium complexes and alkyl chain length of capping agents in synthesis mixture.

6.2.2. Experimental Section

6.2.2.1. Starting materials: All chemicals were used as received without further purification. Vanadium penta-oxide (V_2O_5, 99.6%), tetraoctylammonium bromide ($[CH_3(CH_2)_7]_4NBr$ or TOA^+, ≥98%), cetyl trimethylammonium bromide ($[CH_3(CH_2)_{15}N(CH_3)_3]Br$ or CTA^+, 95%), tetrapropylammonium bromide ($[CH_3CH_2CH_2]_4NBr$ or TPA^+, 98%), oleylamine ($C_{18}H_{35}NH_2$ or OM, tech. grade, 90%), hexadecylamine ($C_{16}H_{33}NH_2$ or HA, tech. grade, 90%), dodecylamine ($C_{12}H_{25}NH_2$ or DD, 98%), octylamine ($C_8H_{17}NH_2$ or OC, 97%) were purchased from Sigma-Aldrich. Hydrogen peroxide (H_2O_2, 30%) and all solvents used such as toluene, absolute ethanol were of analytical grade and purchased from Reagent ACS.

6.2.2.2. Synthesis of vanadium oxide nanocrystals

6.2.2.2.1. Preparation of complex precursors: vanadium(V) diperoxo alkylammonium complexes.

Preparation of V(V) diperoxo tetraoctylammonium complexes, $VO(O_2)_2(TOA)$: 0.14 g (0.77 mmol) of commercial bulk V_2O_5 powders was dissolved in 20 ml of H_2O_2 solution (1.5%) and vigorously stirred at the room temperature for 30 min. V_2O_5 powders were completely reacted with dilute H_2O_2 solution to give a homogeneous deep orange V(V) diperoxo aqueous solution (~0.04 mol/L, final pH ≈ 1.5-2.0) as formula of $[VO(O_2)_2]^-$, according to the procedure reported by Zhang et al.[34] Then, 40 mL of toluene solution (0.05 mol/L) containing a cationic phase-transfer reagent ($[CH_3(CH_2)_7]_4NBr$ or TOA^+Br^-, 1.1 g) was added to the above solution and the $VO(O_2)_2^-/TOA^+$ molar ratio is close to 1.0:2.5. The two-phase mixture was vigorously stirred at room temperature. After 30 min, $[VO(O_2)_2]^-$

anions in aqueous phase were completely extracted into the toluene phase, and a deep orange toluene solution was observed. Subsequently, the upper deep orange supernatant toluene solution (40 mL) containing $VO(O_2)_2(TOA)$ complexes was isolated.

Preparation of V(V) diperoxo cetyl trimethylammonium, $VO(O_2)_2(CTA)$ and vanadium(V) diperoxo tetrapropylammonium, $VO(O_2)_2(TPA)$ complexes: The synthetic process of vanadate CTA compounds described by Livage et al.[35] was used with modification. In a typical preparation, 40 mL of CTA^+ aqueous solution (0.05 mol/L) (or TPA^+) was added to 20 mL of the above as-prepared V(V) diperoxo aqueous solution and the $VO(O_2)_2^-/CTA^+$ (or TPA^+) molar ratio is also close to 1.0:2.5. The resulting orange suspensive solution was stirred for 2 hours, and then the water was slowly evaporated at room temperature for 3 days giving rise to orange solids of $VO(O_2)_2(CTA)$ or $VO(O_2)_2(TPA)$ complexes.

6.2.2.2.2. Synthesis of vanadium oxide nanocrystals.

Synthesis of vanadium oxide nanospheres from $VO(O_2)_2(TOA)$ precursors: Typically, 0.015 mol (5 mL) of oleylamine (OM) was added to 40 mL of above as-prepared toluene solution containing $VO(O_2)_2(TOA)$ complexes under stirring. The reaction solution was transferred to a 60 mL Teflon-lined stainless-steel autoclave and heated at 180 °C for 5 h. The reaction system was cooled to the room temperature using tap water. The vanadium oxide products were easily precipitated by excess ethanol and redispersed preferably in non-polar solvents (e.g., toluene, hexane, etc). The precipitation-redispersion process was repeated several times to purify the producing black OM-capped vanadium oxide nanospheres.

Shape transformation of vanadium oxide nanospheres into nanorods by controlling the water content: To investigate the effect of water contents on the shape transformation of vanadium oxide nanospheres into nanorods during the solvo-hydrothermal synthesis, a fixed amount of distilled water (water/toluene ratio in volume, W/T = 0:40, 2:40, 8:40 and 20:40) was added to the solution containing $VO(O_2)_2(TOA)$ complexes. The autoclave was then sealed and heated at 180 °C for 5 h. The nanocrystal products recovered in toluene phase were also washed several times with ethanol to remove the residual oleylamine.

Size-controlled synthesis of vanadium oxide NCs (including nanospheres and nanoplatelets) from $VO(O_2)_2(CTA)$ and $VO_2(O_2)_2(TPA)$ precursors: The above orange complex solids of as-prepared $VO(O_2)_2(CTA)$ (0.80 g) complexes (or $VO(O_2)_2(TPA)$, 0.65 g) were completely dissolved in toluene medium (40 mL) under stirring giving clear orange solution. To this solution, 0.015 mol (5 mL) of oleylamine was then added. The reaction mixture was transferred to a 60 ml Teflon-lined stainless-steel autoclave and heated at 180 ^{o}C for 5 h.

Shape-controlled synthesis of vanadium oxide NCs by using various capping aliphatic amines and ethanol used as the synthesis medium instead of toluene: The obtained orange $VO(O_2)_2(TOA)$ complex solids (1.1 g) (the above toluene solution containing $VO(O_2)_2(TOA)$ complexes after toluene evaporation at room temperature) was added to 40 mL of ethanol solution containing other aliphatic amine compounds (0.015 mol) including OM, HA, DD, OC (depending on the desired particle shape) with stirring for 1 h at 70 ^{o}C. The resulting suspension solution was transferred to a 60 ml Teflon-lined stainless-steel autoclave and heated at 180 ^{o}C for 5 h. The reaction system was then cooled to the room temperature and the black products at the bottom of the vessel were collected. The colloidal alkyl amines-capped vanadium oxide nanocrystals were re-dispersed in toluene and then precipitated by excess ethanol. A similar procedure was employed in the synthesis of other samples as shown in Table 6.2.1.

6.2.3. Results and discussion

The vanadium oxide nanocrystals were obtained using V(V) diperoxo alkylammonium complexes in the presence of aliphatic amine compounds as capping agents through solvothermal or solvo-hydrothermal treatment at 180 ^{o}C for 5 h. Their size and shape were controlled by different reaction parameters: i) water content in the reaction mixture, ii) types of V(V) diperoxo alkylammonium complexes: $VO(O_2)_2(TOA)$, $VO(O_2)_2(CTA)$, $VO(O_2)_2(TPA)$, iii) nature of solvents: toluene, ethanol, and iv) nature of capping agents: oleylamine (OM), hexadecylamine (HA), dodecylamine (DD), octylamine (OC). The effect of these parameters on the size and shapes of the final products was systematically examined by TEM measurement. The vanadium oxide nanocrystal products obtained under different synthesis conditions were listed in Table 6.2.1.

The V(V) diperoxo gels were often obtained via the reaction between V_2O_5 powders and H_2O_2 solution.[36] Other metal peroxo gels were developed for the wet synthesis of transition metal oxides and lamellar structures.[34,37] However, in the case of using V(V) diperoxo gels (e.g., without organic ligands) as precursors, it is hard to control the size and shape of monodisperse nanocrystals due to the heterogeneity in nonpolar media. To overcome this problem, in this study we used V(V) diperoxo alkylammonium complexes instead of V(V) diperoxo gels.

The V(V) diperoxo tetraoctylammonium complexes, $VO(O_2)_2(TOA)$, were prepared from two-phase system of V(V) diperoxo aqueous solution and toluene containing tetraoctylammonium ligands (TOA^+) (Scheme 6.2.1). The formation of the complexes consists of two steps:

In the first step for the preparation of V(V) diperoxo compounds, the bulk V_2O_5 powders were completely dissolved in dilute H_2O_2 aqueous solution to give the deep orange solution, as seen in eq. 1.[34]

$$V_2O_{5\,(solid)} + 4H_2O_2 \rightarrow 2[VO(O_2)_2]^-_{(gel)} + 3H_2O + 2H^+ \quad (1)$$

The possible geometry of the $[VO(O_2)_2]^-$ anion is as the peroxide groups parallel each other, perpendicular to the oxo oxygen and with the vanadium atom raised 0.5 Å out of the plane.[39] Coordination of a TOA^+ ligand to the vanadium center resulted in the formation of the Pentagonal Pyramidal Oxodiperoxo Tetraoctylammnium structure.[38]

In second step, the $[VO(O_2)_2]^-$ anions incorporated with the TOA^+ ligands to yield the V(V) diperoxo tetraoctylammonium complexes $VO(O_2)_2(TOA)$ through the mass-transfer process of $[VO(O_2)_2]^-$ from aqueous phase into toluene phase. It is important to note that the change from a clear in-color to an orange color in the toluene phase, concomitantly, from a deep orange in water phase to in-color phase after this step, strongly suggests the presence of $[VO(O_2)_2]^-$ anions in toluene phase (see Scheme 6.2.1). The ion pairs of $VO(O_2)_2(TOA)$ complexes formed due to electrostatic interaction ($VO(O_2)_2^- \cdots TOA^+$) according to the equilibrium depicted by eq. 2.

$$[VO(O_2)_2]^-_{(water)} + TOA^+_{(toluene)} \rightarrow VO(O_2)_2(TOA)_{(toluene)} \quad (2)$$

The formation of the $VO(O_2)_2(TOA)$ complexes in the toluene phase is further supported by the FTIR and TGA data. The FTIR spectrum of the $VO(O_2)_2(TOA)$ complex solid (after toluene elimination) exhibits strong absorption FTIR bands characteristic of various vibrationally active groups (Figure 6.2.1). The well defined IR bands at 2959, 2918, 2878, 2852 cm^{-1} along with the bands at 733 cm^{-1} and 720 cm^{-1} are characteristic of the symmetric and asymmetric methyl and methylene stretches of the TOA^+ alkyl chains.[40-41] An IR band is observed at 1455 cm^{-1}, which is attributed to the stretching vibrations of the ammonium cation groups ($\equiv N^+$) of TOA^+.[42] The IR bands corresponding to stretches of the V(V) diperoxo appear in the 1000-500 cm^{-1} region: 960 cm^{-1} for $\nu(V{=}O)$, 926 cm^{-1} for $\nu(O_p\text{-}O_p)$ and 542 cm^{-1} for $\nu(V\text{-}O_p)$.[38,43] The TGA data for $VO(O_2)_2(TOA)$ complex solid species (Figure 6.2.2) reveal a mass loss of 34.8% in the temperature range 120-480 °C, which is attributed to the TOA^+ decomposition and the combustion of organic groups. Furthermore, the complex species were completely transformed to vanadium oxides as the heating temperature reached 480 °C. A slight increase in mass of approximately 2 wt.% between 550 °C and 650 °C due to the oxidation of reduced vanadium oxides into V_2O_5.[35,44] These results confirm the formation of $VO(O_2)_2(TOA)$ complexes through the transformation of $[VO(O_2)_2]^-$ from aqueous phase into toluene phase in which TOA^+ cations were coordinated with $[VO(O_2)_2]^-$ anions.

Effect of water content on the formation of nanocrystals: Under the solvothermal treatments (e.g., in absence of water in the synthesis solution), at high temperature (180 °C) in organic medium, $VO(O_2)_2(TOA)$ complex precursors are decomposed and generate vanadium monomers then vanadium nuclei. They are capped by oleylamine molecules. The resulting oleylamine capped nuclei are hydrophobic and easily dispersed within organic medium, which could grow into nanospheres through an Ostwald ripening process during the solvothermal synthesis. The probable reaction processes for the formation of capping vanadium oxide NCs can be as eq. 3.

It is important to note that a blue-black color was observed for all as-made vanadium oxide NCs, which corresponds to VO_2, according to the XRD and XPS results (see bellow). Figure 6.2.3a shows a TEM image of the sample which was synthesized at 180 °C for 5 h without water in the toluene medium (sample 1 in Table 6.2.1). It can be clearly seen that the vanadium product consists of uniform quasispherical nanocrystals with diameter of 4 nm. The selected area electron diffraction (SAED) pattern taken by focusing the electronic beam on a single vanadia particles (inset of Figures 6.2.3a and 6.2.3c) composed of bright spots of respective diffraction rings indicated the high crystallinity of vanadium oxide nanospheres.

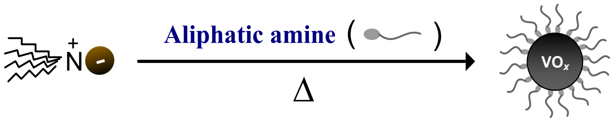

(3)

 : **Tetraoctylammonium cation (TOA^+)**; ● : **Vanadium(V) diperoxo anion ($[VO(O_2)_2]^-$)**

To verify the role of the TOA^+ ligands for the formation of nanocrystals, a similar experiment was carried out using V(V) diperoxo compound, $[VO(O_2)_2]^-$ as precursors (e.g., without TOA^+ ligands) instead of $VO(O_2)_2(TOA)$ complexes under the same synthesis conditions. The results showed that no nanospheres were obtained but irregular particles closely aggregated together were formed, suggesting the TOA ligands are a key factor for the formation of monodisperse vanadium oxide nanospheres in these synthesis conditions.

For the synthesis of vanadium oxide nanocrystals starting from $VO(O_2)_2(TOA)$ complex precursors, the significant effect of water content on the size and shape of vanadium oxide NCs was observed. In this study, the experiments were carried out with different amounts of water added in the synthesis solution (Table 6.2.1, samples 1-4), while the other synthesis conditions were kept constant. Keeping the toluene volume unchanged

(40 mL), the water/toluene ratio (W/T) in volume varied from 0:40 to 2:40, 8:40, and 20:40. It was found that the shape evolution of vanadium oxide nanocrystals is as a function of water contents. Figure 6.2.3 shows representative TEM images of these samples. In the absence of water in the synthesis medium, only uniform quasispherical nanocrystals with an average size of 4 nm were obtained (Figure 6.2.3a). While the W/T value was as low as 2:40, aggregated nanoparticles beside some un-uniformed small nanorods were formed. Most of the aggregated nanoparticles formed pearl-chain-like structures; however, few isolated nanospheres were still observed (Figure 6.2.3b).

When the W/T value increased to 8:40, most of short vanadium oxide nanorods (low aspect ratio) were generated. This indicates that with increasing the water content aggregated particles tend to align and form short rod,[47] however, the rod size distribution is broad with average diameter of about 6-7 nm and length of 20-30 nm (Figure 6.2.3c). It is noted that even the water content is increased (up to the W/T = 8:40), only one phase in the reaction solution was observed. This is ascribed to the water/toluene microemulsion system owing to nanosized water droplets dispersed in a continuous toluene medium and stabilized by surfactant molecules at the W/T interface. The highly dispersed water pools are ideal nano-reactors for producing monodispersed nanoparticles and controlling shapes.[48] However, when the W/T value increased to 20:40, the two water-toluene phases were clearly separated in the synthesis solution. Interestingly, only nanorod product was formed in the toluene phase (Figure 6.2.3d), while no vanadium oxide nanocrystals were essentially observed in the water phase. The vanadium product is composed of uniformly sized and shaped rods with ~20 nm in width and 150-300 nm in length. The high-magnification TEM image clearly demonstrates that the nanorods were quite smooth and straight along their entire length (inset Figure 6.2.3d). Furthermore, the rod diameters were quite uniform. The SAED pattern taken from a single vanadium oxide nanorods in the red square box (Figure 6.2.3d-inset) reveals the single crystal nature of the nanorods and further confirmed that the nanorods' elongation axis was along [101] direction. This elongated orientation may be believed to be come from a preferential oriented-aggregation mediated precursor growth of the [101] facets at W/T interface. The increase in nanorod diameter from 7 nm to 20 nm with the increase of water content to the W/T= 20:40 could be explained by a lateral aggregation of individual nanorods along the longitudinal axis and further their fusion to form aligned nanorods at the high water content in the mixture.[47] By far, this big rod morphology did not change (constant aspect ratio) when the W/T ratio was increased further to 20:40 (e.g., 30:40 or 40:40). This suggested that these nanorods can be only able to form when the amount of water added in the synthesis solution is just enough to maintain the two-phase system, in which the synthesis reaction occurs at the interface. We also believe that the dissolution and growth of vanadium monomers might also result in an overall growth of the nanorods. This suggests that particle size and shape can be controlled by the water content in the reaction mixture under these synthesis conditions.[45-47] A schematic illustration of the inference from the TEM observation demonstrating the transformation of nanospheres into nanorods is shown in Scheme 6.2.2.

In general, nanoporous materials have a large fraction of the atoms exposed at surfaces and access to reactant molecules that have attracted intensive for applications to catalysis.[49] For the surfactant capped nanoparticles, it is therefore necessary to remove surfactants to generate pority in the nanomaterial structure. Figures 6.2.3e and 6.2.3f represent the SEM images of vanadium oxide nanospheres (sample 1) and nanorods (sample 4) after calcination at 550 °C for 2 h. As seen in Figure 6.2.3e for the vanadium oxide nanospheres sample, the SEM image revealed that the spherical morphology with some interlinked 3-D microspheres aggregated into bigger ones was observed and inside each microsphere mainly composed of monodisperse 4 nm-sized nanospheres. While SEM image (Figure 6.2.3f) shows the calcined nanorods with smooth surface and individual distribution have with average diameter of about 20 nm and length of 150-300 nm, which are consistent with the high-magnification TEM result.

Figure 6.2.4 shows the wide-angle XRD patterns of the as-made vanadium oxide nanosphere (sample 1 in Table 6.2.1) and nanorod (sample 4) samples before and after calcination in air at 550°C for 2 h. The X-ray pattern (Figure 6.2.4a) of the as-made samples 1 and 4 corresponds to monoclinic rutile-type VO_2 (JCPDS Card No. 44-0253, P42/mnm, a = b = 0.4554 nm, c = 0.2856 nm).[50,51] However, after calcination, the XRD patterns of the samples 1 and 4 exhibit the orthorhombic V_2O_{5-x} phase (space group: *Pmmn*, a = 11.516 Å, b = 3.566 Å, c = 3.777 Å; JCPDS card no. 41-1426).[52] Furthermore, their color was changed from blue-black to yellow after calcination (see Figure 6.2.6d). This indicates the transformation from the monoclinic rutile phase to the orthorhombic phase of these samples (Figure 6.2.4b,c). No other phases were detected in the XRD patterns suggesting the pure orthorhombic structure of the V_2O_{5-x} nanocrystals. The particle size of the calcined vanadium oxide nanosphere sample calculated from the (001) reflections using the Debye-Scherrer equation is 5.2 nm,[53] which are in agreement with the sizes determined from the above TEM (Figures 6.2.3a, 6.2.5b). It is important to note that the relative intensity of (101) diffraction peak of the nanorods is much higher than that of the nanospheres, which indicates their anisotropic structure and is in agreement with TEM and SAED results (Figure 6.2.3d).

To study the influence of the alkyl chain length of vanadium complex ligands on the formation of vanadium oxide nanocrystals, three different types of V(V) diperoxo alkylammonium complexes with different alkyl chain ligands including $VO(O_2)_2(TOA)$, $VO(O_2)_2(CTA)$ and $VO(O_2)_2(TPA)$ (see details in the Experimental Section) were used as starting precursors. The alkyl chain length is in the order: TOA > CTA > TPA. The syntheses were conducted under the same conditions (samples 5 and 6, Table 6.2.1). According to their XRD patterns, all the calcined products obtained from these different complex precursors have the orthorhombic phase of V_2O_{5-x} (Figures 4 and 5). The particle size of the calcined sample 5 and sample 6 calculated from the (001) reflections[53] are ~12.0 nm and ~6.5 nm, respectively. Representative TEM images of these as-made NC products are also presented in Figure 6.2.6. The vanadium oxide sample prepared from $VO(O_2)_2(TPA)$ is composed of irregular nanoplatelets with diameters of 10-15 nm (Figure 6.2.6a). However, using $VO(O_2)_2(TOA)$ and $VO(O_2)_2(CTA)$, the quasispherical nanocrystals were obtained with average diameters of ~4 nm and ~5 nm, respectively (Figures 6.2.6b and 6.2.6c), in agreement with the particles sizes obtained by XRD spectra. The corresponding SAED patterns (inset) of these vanadium oxide samples also composed of bright diffraction spots indicated the high crystallinity of vanadium oxide nanocrystals. In general, the activity of monomer complexes and consequently, the size and shape of the resulting nanocrystals can be affected by steric ligands.[54] Metal complex precursors with longer alkyl chain ligands diffuse slower through growth solution, and they are also decomposed more slowly.[55] In the case of TPA as complex ligands, their alkyl chain is shortest, the complex activity was very high (rapid diffusion and decomposition), many nuclei were formed at the nucleation stage and aggregated immediately at the growth stage and as a result, larger particle size was obtained. However, longer alkyl chain ligands such as TOA, CTA, can balance the nucleation and growth rates producing smaller nanocrystals. Based on the TEM results, vanadium complexes with the longer alkyl chains (TOA and CTA), as compared to that of TPA, were decomposed more slowly to generate smaller nanoparticles. Therefore, it can be suggested that the particle sizes gradually increased from ~4 nm to ~5 and 10-15 nm, due to the decrease of alkyl chain length of complex ligands from TOA to CTA and then TPA.

It is important to note that, using this process, multi-gram-scale vanadium oxide nanocrystals can be achieved in a single batch. For example, using $VO(O_2)_2$(CTA) complexes as precursors, about 6.8 g of oleylamine-capped quasispherical vanadium oxide nanocrystals was obtained in a single run (Figure 6.2.6d). The blue-black color of the products suggests that V^{5+} ions had been reduced to V^{4+} by decomposing the precursors during synthesis,[44] which is further confirmed by the XPS results (see below).

To understand the role of solvent medium on the particle size and shape of the resulting vanadium oxide NCs during the synthesis,[56] the experiment was carried out using $VO(O_2)_2$(TOA) complexes, and ethanol instead of toluene as reaction medium, while the other parameters were kept constant. The uniform vanadium oxide nanocubes with sizes of ~5 nm in diameter were obtained (Figure 6.2.7a). This indicates the change in size and shape of vanadium oxide nanocrystals from ~4 nm-sized nanospheres (see Figure 6.2.3a) to ~5 nm-sized nanocubes, when toluene was substituted by ethanol as medium in the reaction system. However, the product yield remained unchanged. This phenomeon may be believed to be the influence by the dielectric constant of alcohol. Under relatively high polar medium (ethanol), the diffusion rate of the hydrophobic dissolved crystals and precursor monomers in an intraparticles can be reduced lead to barrier in the convert of cubes to spheres.[57,58]

Furthermore, to gain further insights into the steric effect of the capping ligands on the size and shape of vanadium oxide nanocrystals, different alkyl chain lengths of the capping aliphatic amines were used, such as oleylamine (OM, C_{18}), hexadecylamine (HD, C_{16}), dodecylamine (DD, C_{12}) and octylamine (OC, C_8). The syntheses were carried out in ethanol as reaction medium, and $VO(O_2)_2(TOA)$ complexes were used as vanadium precursors (Figure 6.2.7 and Table 6.2.1). The mass of $VO(O_2)_2(TOA)$ complex solid (1.1 g) and volume of ethanol (20 mL) were kept the same in all syntheses (see details in the Experimental Section). It is found that the vanadium oxide NCs exhibit various shapes including cubic, ricelike particle, rod, and spherical particles, when the alkyl chain length of aliphatic amines is altered (Figure 6.2.7). In general, inorganic oxide species capped by shorter alkyl chain ligands are more mobile and more reactive than those by longer ones, because they are less sterically impeded, which leads to faster diffusion and faster nucleation-growth kinetics.[59] This can affect the size and shape of NCs.[60] Moreover, the dispersity as well as self-assembly of the hydrophobic alkyl-capped nanocrystals on the grid surface strongly depend on the alkyl-chain length of capping agent. For example, longer capping alkyl ligands (C_{18}) result in the better dispersity of nanocrystals than that of the shorter capping alkyl ligands (C_{16}-C_9).[61] Our results revealed that when the long alkyl chain OM (C_{18}) was used, uniform vanadium oxide nanocubes with sizes of 5 nm in diameter were produced (Figure 6.2.7a). However, when HD (C_{16}) was used instead of OM, the elongated particles with ricelike shape and size of about 4 nm x 9 nm were formed (Figure 6.2.7b). Furthermore, when HD was substituted by DD (C_{12}), the formation of thin nanorods with an average size of 3 nm x 50 nm was observed (Figure 6.2.7c). This suggests that shorter alkyl-chain ligands favour an anisotropic growth resulting in the formation of nanorods. However, while very short alkyl chain ligands ($< C_{12}$), in this work, we used OC (C_8), only spherical particles with broad particle size distribution and large diameter of 20-25 nm were observed (Figure 6.2.7d). The corresponding SAED patterns (inset) of cubic, ricelike particle, and spherical vanadium oxide particles exhibit a set of sharp diffraction spots which are characteristic of single crystalline of monoclinic rutile-type VO_2 structure. While all the detectable diffraction spots of the thin nanorods are perfectly indexed to the same positions as those from 20 nm x 150-300 nm-sized vanadium oxide nanorods (sample 4, Figure 6.2.3d) suggesting their elongation along [101] direction. It is believed that short alkyl chain length of aliphatic amines (< C_{12}) as capping ligands could be hard to control the nucleation and growth, because of much fast diffusion and growth kinetics. This can be concluded that the shape evolution of nanocrystals can also depend on the alkyl chain length of the capping agents.

The X-ray photoelectron spectroscopy (XPS) is a surface-specific technique was also used to study the oxidation states and the surface composition of the as-made and calcined vanadium oxide nanosphere samples (sample 1 before and after calcination). The survey XPS spectra of these samples in a wide energy range are shown in Figure 6.2.8. Besides carbons, and nitrogens, no impurities were found. However, the intense C 1s and N 1s peaks of the as-made as compared to those of the calcined sample can be assigned to the oleylamine ligand capped on the nanocrystal surface. The positions of XPS peaks were corrected using the C 1s core level taken at 285 eV as a binding energy (BE) reference. The XPS spectra of V 2p together with the O 1s are presented in Figure 6.2.9. The deconvolution data of the spectra are summarized in Table 6.2.2.[62,63] Both the as-made and calcined vanadium oxide nanosphere samples show that the V 2p states composed of two components originating from the spin-orbit splitting of V $2p_{3/2}$ and V $2p_{1/2}$, which are restricted to a ratio of 1.8:1.0 and the separation energy Δ = 8.3 eV. The V $2p_{3/2}$ peak has a small full width, 2.5-3.0 eV, at half maximum (FWHM), the V $2p_{1/2}$ peak has a larger FWHM, 5.0-5.5 eV, due to multiplet effects.[64] For the as-made sample 1, V $2p_{3/2}$ and V $2p_{1/2}$ peaks at 516.2 eV and 524.1 eV which are attributed to V^{4+} were observed. Non XPS peaks corresponding to V^{5+} were detected (Figure 6.2.9a) suggesting that the surface chemical composition in the as-made nanocrystal sample is VO_2. However, the calcined sample 1 exhibits the presence of both V^{4+}/V^{5+} oxidation states (Figure 6.2.9b). Both V $2p_{3/2}$ and V $2p_{1/2}$ peaks at 517.2 eV and 525.5 eV, respectively which are characteristic of vanadium in the +5 oxidation state, are present. Simultaneously, the V $2p_{3/2}$ and V $2p_{1/2}$ peaks at 516.2 eV and 524.1 eV corresponding to the V^{4+} oxidation state were observed. From the relative areas of the V^{4+} and V^{5+} contributions, the surface vanadium was found to be ~65% of V^{5+} and ~35% of V^{4+} for the calcined nanosphere sample (see Table 6.2.2). It can be concluded that the change of color from blue-black to yellow upon calcination in air could be due to the transformation from V^{4+} into V^{5+} oxidation state (see Figure 6.2.6d).

Oxygen bonded to vanadium atoms in the as made vanadium oxide nanocrystal sample (sample 1) exhibits an O 1s peak (Figure 6.2.9a), related to O-V (530.7 eV).[65] However, the O 1s peak of this sample after calcination shows composed of two components. The deconvolution peak at 530.4 eV was assigned to the O=V groups, and another peak at higher binding energy of 531.0 eV was attributed to the O-V ones,[43] which are related to the oxygen in the crystal lattice of vanadium oxides.[66] Based on the corresponding areas of the vanadium and oxygen XPS peaks obtained by deconvolution, the molar ratio of V/O determined from the surface chemical composition of the as-made and calcined sample 1 was respectively (1.0):(2.0) and (1.0):(2.3). Thus the chemical surface formula is respectively VO_2 and $V_2O_{4.6}$.

Figure 6.2.10 shows TGA-DTA curves of the OM-capped VO_2 nanosphere and OM-capped VO_2 nanorod samples (samples 1 and 4 in Table 6.2.1). For the nanosphere sample (Figure 6.2.10a), the steep weight-loss (22%) appeared around 100-390 °C. However, the corresponding DTA curve shows two exothermic peaks at 215 ºC and 324 ºC, which are related to the decomposition and combustion of capping agents on the particle surfaces during heating. A gradual mass gain of VO_2 (~2%) above 411 ^{o}C, accompanied by a sharp endothermic peak at 593 ºC could be related to oxidation of the vanadium dioxide framework from V^{4+} to V^{5+}, as reported by Brandstatter and Riedmann.[40] The total mass loss of nanorods was 28%, quite similar to these of the nanospheres, 22% (samples 1 and 2). However, for the VO_2 nanorods sample (Figure 6.2.10b), the presence of an additional broad exothermic peak at higher temperature at 431 ºC could be due to strongly held surfactant molecules blocked between nanorods, in good agreement with our previously published.[47]

The FTIR spectrum of the as-made oleylamine (OM)-capped vanadium oxide nanosphere sample (e.g. sample 1 in Table 6.2.1) is shown in Figure 6.2.11. The FTIR bands at 2925-2852 cm^{-1} and 1625 cm^{-1} are assigned to the C-H and C=C stretching modes of alkyl chains in oleylamine, respectively. The band at 1458 cm^{-1} is attributed to the N-H bending and N-C stretching modes of $-NH_2$ groups in oleylamine capping on vanadium dioxides.[67] Furthermore, the IR bands at 620 and 927 cm^{-1} corresponding to the vibrations of V-O-V and O-$(V)_3$, respectively, along with an intense FTIR band at 1022 cm^{-1} attributing to the V=O vibration, they are characteristic of vanadium oxides.[68] The presence of these FTIR bands suggests that oleylamine molecules are bound to the surface of VO_2 nanocrystals. Similar results for the others aliphatic amines-capped vanadium oxide NC samples were also observed (not shown).

The BET specific surface areas and pore size distributions of the various samples after calcination were obtained by nitrogen adsorption/desorption isotherms and are summarized in Table 6.2.3. For the calcined nanospheres samples (samples 1 and 2 in Table 6.2.1), the BET surface area was 70.5 m^2/g and 68.5 m^2/g for sample 1 and sample 2, respectively. The BET surface area of sample 1 is higher than that of sample 2 due to its smaller particle sizes.[69] The average pore diameter with narrow mesopore size is around 16.5 nm and 19.5 nm for sample 1 and sample 2, respectively.

For the sample 3 and sample 4 (Table 6.2.1) after calcinations, the BET surface area values are 42.0 m^2/g and 32.0 m^2/g with an average pore size of 37.0 nm and 51.0 nm, respectively. The pore diameter of sample 4 is somewhat larger than that of sample 3 due to the length difference of rods. It is also noted that average pore diameters of the nanospheres samples (samples 1 and 2) are smaller than those of the nanorods samples (samples 3 and 4) due to the compact structure.[70] High specific surface areas of these nanoparticles samples after calcination can be explained by the particle surfaces protected by capping agent; and the nanoparticle surface preserved upon thermal procedures.[66] The properties of such nanocrystals could make them interesting system for future studies in catalysis.

6.2.4. Conclusion

We have developed a new solvo-hydrothermal route to synthesize monodisperse vanadium oxide nanocrystals from vanadium(V) diperoxo tetraalkylammonium complexes in aliphatic amine/toluene or aliphatic amine/toluene/water. Commercial bulk V_2O_5 powders were used as a starting vanadium source. This approach is simple, economical, and easily scaled up for products. The transformation of vanadium oxide nanospheres into short nanorods as well as aligned nanorods can be controlled by water content in the synthesis mixture. Furthermore, the shape evolution of vanadium oxide products from nanospheres to nanoplatelets, nanocubes and then to nanorods, was also controlled by the steric ligands of vanadium complexes as well as the alkyl chain length of capping aliphatic amine agents in ethanol medium.

The obtained vanadium oxide nanocrystal products before calcination are monoclilic rutile VO_2 structure with black color, which is however converted to the orthorhombic $V_2O_{4.6}$ structure with yellow color upon calcination procedure. The XPS results of these samples revealed that only V^{4+} was observed before calcination, while the coexistence of two vanadium oxidation states (V^{4+} and V^{5+}) and two components of oxygen corresponding to O=V and O-V groups on the vanadium penta-oxide nanocrystal surface was identified. The surface chemical composition of the vanadium oxide nanocrystal sample is VO_2 and V_2O_{5-x} (x = 0.4) before and after calcination, respectively. The high surface area of the vanadium oxide nanocrystal samples after calcination could be beneficial for potential applications in many fields of advanced nanotechnology, particularly in catalysis, chemical biological sensors. Furthermore, the synthetic method developed here can be extended to the synthesis of other nanocrystalline oxides and is potentially useful for large-scale production of the nanomaterials.

6.2.5. References

(1) Norris, D. J.; Efros, A. L.; Erwin, S. C. *Science* **2008**, *319*, 1776-1779.

(2) Pachon, L. D.; Rothenberg, G. *Appl. Organometal. Chem.* **2008**, *22*, 288-299.

(3) Lu, A. H., Salabas, E. L., Schuth, F. *Angew. Chem., Int. Ed.* **2007**, *46*, 1222-1244.

(4) Dumestre, F.; Chaudret, B.; Amiens, C.; Renaud, P.; Fejes, P. *Science* **2004**, *303*, 821-823.

(5) Clfen, H.; Mann, S. *Angew. Chem., Int. Ed.* **2003**, *42*, 2350-2365.

(6) Li, M.; Schnablegger, H.; Mann, S. *Nature* **1999**, *402*, 393-395.

(7) Pinna, N.; Niederberger, M. *Angew. Chem., Int. Ed.* **2008**, *47*, 2-15.

(8) Park, J.; An, K.; Hwang, Y.; Park, J. G.; Noh, H. J.; Kim, J. Y.; Park, J. H.; Hwang, N. M.; Hyeon, T. *Nat. Mater.* **2004**, *3*, 891-895.

(9) Zarur, A. J.; Ying, J. Y. *Nature* **2000**, *403*, 65-67.

(10) Wang, X.; Zhuang, J.; Peng, Q.; Li, Y. D. *Nature* **2005**, *437*, 121-124.

(11) Xu, J.; Ge, J. P.; Li, Y. D. *J. Phys. Chem. B* **2006**, *110*, 2497-2501.

(12) Peng, Z. A.; Peng, X. *J. Am. Chem. Soc.* **2001**, *123*, 1389-1395; **2002**, *124*, 3343-3353.

(13) Shah, P. R.; Khader, M. M.; Vohs, J. M.; Gorte, R. J. *J. Phys. Chem. C* **2008**, *112*, 2613-2617.

(14) Livage, J. *Chem. Mater.* **1991**, *3*, 578-593.

(15) Gu, G.; Schmid, M.; Chiu, P. W.; Minett, A.; Fraysse, J.; Kim, G. T.; Roth, S.; Kozlov, M.; Munoz, E.; Baughman, R. H. *Nat. Mater.* **2003**, *2*, 316-319.

(16) Poizot, P.; Grugeon, S.; Dupont, L.; Tarascon, J. M. *Nature* **2000**, *407*, 496-499.

(17) Muster, J.; Kim, G. T.; Krstic, V.; Park, J. G.; Park, Y. W.; Roth, S.; Burghark, M. *Adv. Mater.* **2000**, *12*, 420-424.

(18) Chae, H.; Nam, I.; Ham, S.; Hong, S. *Appl. Catal. B: Environmental* **2004**, *53*, 117-126.

(19) Barbero, B. P.; Cadus L. E.; Hilaire, L. *Appl. Catal. A: General* **2003**, *246*, 237-242.

(20) Blasco, T.; Lopez Nieto, J. M. *Appl. Catal. A: General* **1997**, *157*, 117-142.

(21) Centi, G. *Appl. Catal. A: General* **1996**, *147*, 267-298.

(22) Resini, C.; Milella, F.; Busca, G. *Phys. Chem. Chem. Phys.* **2000**, *2*, 2039-2045.

(23) Kim, G. T.; Muster, J.; Krstic, V.; Park, J. G.; Park, Y. W.; Roth, S.; Burghard, M. *Appl. Phys. Lett.* **2000**, *76*, 1875-1877.

(24) Karunakaran, C.; Senthilvelan, S. *J. Colloid Interface Sci.* **2005**, *289*, 466-471.

(25) Tenne, R. *Nature* **2004**, *431*, 640-641.

(26) Spahr, M. E.; Bitterli, P.; Nesper, R.; Muller, M.; Krumeich, F.; Nissen, H. U. *Angew. Chem., Int. Ed.* **1998**, *37*, 1263-1265.

(27) Corr, S. A.; Grossman, M.; Furman, J. D.; Melot, B. C.; Cheetham, A. K.; Heier, K. R.; Seshadr, R. *Chem. Mater.* **2008**, *20*, 6396-6404.

(28) Li, G.; Chao, K.; Peng, H.; Chen, K.; Zhang, Z. *Inorg. Chem.* **2007**, *46*, 5787-5790.

(29) Lutta, S. T.; Dong, H.; Zavalij, P. Y.; Whittingham, M. S. *Mater. Res. Bull.* **2005**, *40*, 383-393.

(30) Guiton, B. S.; Gu, Q.; Prieto, A. L.; Gudiksen, M. S.; Park, H. *J. Am. Chem. Soc.* **2005**, *127*, 498-499.

(31) Pinna, N.; Willinger, M.; Weiss, K.; Urban, J.; Schlogl, R. *Nano Lett.* **2003**, *3*, 1131-1134.

(32) Mai, L.; Guo, W.; Hu, B.; Jin, W.; Chen, W. *J. Phys. Chem. C* **2008**, *112*, 423-429.

(33) Takahashi, K.; Limmer, S. J.; Wang, Y.; Cao, G. *J. Phys. Chem. B* **2004**, *108*, 9795-9800.

(34) Yu, L.; Zhang, X. *Mater. Chem. Phys.* **2004**, *87*, 168-172.

(35) Bouhedja, L.; Steunou, N.; Maquet, J.; Livage, J. *J. Solid State Chem.* **2001**, *162*, 315-321.

(36) Dullberg, P. Z. *Z. Phys. Chem*. **1903**, *45*, 129.

(37) Do, T. O. *Langmuir* **1999**, *15*, 8561-8564.

(38) Butler, A.; Clague, M. J.; Meister, G. E. *Chem. Rev.* **1994**, *94*, 625-638.

(39) Bortolini, O.; Conte, V. *J. Inorg. Biochem.* **2005**, *99*, 1549-1557.

(40) Brandstatter, M. K.; Riedmann, M. *Mikrochim Acta [Wien]* **1989**, *II*, 173-184.

(41) Chalmers, J. M.; Bunn, A.; Willis, H. A.; Thorne, C.; Spragg, S. *Mikrochim. Acta [Wien]* **1988**, *I*, 287-290.

(42) Gole, A.; Orendorff, C. J.; Murphy, C. J. *Langmuir* **2004**, *20*, 7117-7122.

(43) Kaliva, M.; Giannadaki, T.; Salifoglou, A. *Inorg. Chem.* **2001**, *40*, 3711-3718.

(44) Carn, F.; Steunou, N.; Livage, J.; Colin, A.; Backov, R. *Chem. Mater.* **2005**, *17*, 644-649.

(45) Sigman, M. B.; Ghezelbash, J. A.; Hanrath, T.; Saunders, A. E.; Lee, F.; Korgel, B. A. *J. Am. Chem. Soc.* **2003**, *125*, 16050-16057.

(46) Banfield, J. F.; Welch, S. A.; Zhang. H.; Ebert, T. T.; Penn, R. L. *Science* **2000**, *289*, 751-754.

(47) Nguyen, T. D.; Mrabet, D.; Do, T. O. *J. Phys. Chem. C* **2008**, *112*, 15226-15235.

(48) Biais, J.; Clin, B.; Laolanne, P.; Microemulsions: Sturcture and Dynamics, Chapter 1. Edited by S. E. Friberg and P. Bothorel. *CRC Press, Boca Raton, FL,* **1987**.

(49) Concepcion, P.; Knozinger, H.; Lopez Nieto, J. M.; Martinez-Arias, A. *J. Phys. Chem. B.* **2002**, *106*, 2574-2582.

(50) Corr, S. A.; Grossman, M.; Furman, J. D.; Melot, B. C.; Cheetham, A. K.; Heier, K. R.; Seshadri, R. *Chem. Mater.* **2008**, *20*, 6396-6404.

(51) Gui, Z.; Fan, R. Mo, W.; Chen, X.; Yang, L.; Zhang, S.; Hu, Y.; Wang, Z.; Fan, W. *Chem. Mater.* **2002**, *14*, 5053-5056.

(52) Cao, A. M.; Hu, J. S.; Liang, H. P.; Wan, L. J. *Angew. Chem., Int. Ed.* **2005**, *44*, 4391-4395.

(53) O'Dwyer, C.; Lavayen, V; Fuenzalida, D.; Lozano, H.; SantaAna, M.; Benavente, E.; Gonzalez, G.; Torres, C. M. S. *small* **2008**, *4*, 990-1000.

(54) Hecht, S.; Frechet, M. J. *Angew. Chem., Int. Ed.* **2001**, *40*, 74-91.

(55) Kim, J. I.; Lee, J. K. *Adv. Funct. Mater.* **2006**, *16*, 2077-2082.

(56) Aghabozorg, H. R.; Mousavi, R.; Askari, S.; Aghabozorg, H. *J. Nano. Res.* **2007**, *9*, 497-500.

(57) Mullin, J. W. In *Crystallization*, 3rd ed., Butterworth-Heinemann: Woburn, MA, **1997**.

(58) Wulff, G.; Zeitschrift, F. *Beitr. Krystallogr. Mineral.* **1901**, *34*, 449.

(59) Lee, S. H.; Kim, Y. J.; Park, J. *Chem. Mater.* **2007**, *19*, 4670-4675.

(60) Scher, E. C.; Manna, L.; Alivisatos, A. P. *Philos. Trans. R. Soc. London, Ser. A* **2003**, *361*, 241-257.

(61) Zhao, N.; Pan, D.; Nie, W.; Ji, X. *J. Am. Chem. Soc.* **2006**, *128*, 10118-10124.

(62) Olivetti, E. A.; Kim, J. H.; Sadoway, D. R.; Asatekin, A.; Mayes, A. M. *Chem. Mater.* **2006**, *18*, 2828-2833.

(63) Barbero, B. P.; Cadus, L. E.; Hilaire, L. *Appl. Catal. A: General* **2003**, *246*, 237-242.

(64) Guimaraes, J. L.; Abbate, M.; Betim, S. B.; Alves, M. C. M. *J. Alloy. Comp.* **2003**, *352*, 16-20.

(65) Hecjingbottom, R; Linnett, J. W. *Nature* **1962**, *194*, 678.

(66) Chenakin, S. P.; Silvy, R. P.; Kruse, N. *J. Phys. Chem. B* **2005**, *109*, 14611-14618.

(67) Gibot, P.; Laffont, L. *J. Solid State Chem.* **2007**, *180*, 695-701.

(68) Chen, W.; Mai, L. Q.; Peng, J. F.; Xu, Q.; Zhu, Q. Y. *J. Mater. Sci.* **2004**, *39*, 2625-2627.

(69) Mrabet, D.; Zahedi-Niaki, M. H.; Do, T. O. *J. Phys. Chem. C* **2008**, *112*, 7124-7129.

(70) Jaroniec, M.; Choma, J.; Gorka, J.; Zawislak, A. *Chem. Mater.* **2008**, *20*, 1069-1075.

Table 6.2.1. Synthesis Conditions, Shapes and Sizes of the as-made Capped Vanadium Oxide Nanocrystals.

sample	figure	precursors[a] [mol]	surfactants [mol]	solvents[a] [mL]	T [°C]	t [h]	shape	size [nm]
1	3a,4b	$VO(O_2)_2$(TOA)	Oleylamine	W/T=0:40	180	5	spherical	4
2	3b	$VO(O_2)_2$(TOA)	Oleylamine	W/T=2:40	180	5	aggregated spherical	6-7
3	3c	$VO(O_2)_2$(TOA)	Oleylamine	W/T=8:40	180	5	short rod	~9x50
4	3d,e	$VO(O_2)_2$(TOA)	Oleylamine	W/T=20:40	180	5	aligned rod	20x300
5	4a	$VO(O_2)_2$(TPA)	Oleylamine	Toluene	180	5	platelet	10-15
6	4c	$VO(O_2)_2$(CTA)	Oleylamine	Toluene	180	5	spherical	5
7	5a	$VO(O_2)_2$(TOA)	Oleylamine	Ethanol	180	5	cubic	5
8	5b	$VO(O_2)_2$(TOA)	Hexadecylamine	Ethanol	180	5	rice	~4x9
9	5c	$VO(O_2)_2$(TOA)	Dodecylamine	Ethanol	180	5	thin rod	~3x50
10	5d	$VO(O_2)_2$(TOA)	Octylamine	Ethanol	180	5	spherical	20-25

(a) $[VO(O_2)_2]^-$ = Vanadium(V) diperoxo anion; TOA^+ = Tetraoctylammonium cation; CTA^+ = Cetyl trimethylammonium cation; TPA^+ = Tetrapropylammonium cation; W/T = Water/Toluene ratio in volume.

Table 6.2.2. XPS Binding Energies of O 2s, V 3p, V 3s, V 2p, O 1s Peaks in the As-made Vanadium Oxide Nanosphere Sample before and after Calcination at 550 °C for 2 h (sample 1 in Table 6.2.1).

Binding Energy (eV)^a									
				V 2p$_{3/2}$		V 2p$_{1/2}$		O 1s	
Sample 1	O 2s	V 3p	V 3s	V^{4+}	V^{5+}	V^{4+}	V^{5+}	O- V^{4+}	O- V^{5+}
As-made	22.5	42.6	71.0	516.2		524.1		530.7	
Calcined	22.5	42.6	71.0	516.2	517.2	524.1	525.5	531.0	530.4

^{a}BE = ± 0.1 eV

Table 6.2.3. BET Specific Surface Area and Average Pore Diameters of the As-made Vanadium Oxide NC Samples after Calcination at 550 °C for 2 h (samples 1-4 in Table 6.2.1).

sample	size & shape [nm]	S_{BET} [m^2/g]	V_{BJH} [cm^3/g]	average pore diameter [nm]
1	4 nm-spheres	70.5	0.100	16.5
2	6-7 nm-aggregated spheres	68.5	0.160	19.5
3	~9x50 nm-rods	42.0	0.210	37.0
4	20x500 nm-rods	32.0	0.215	51.0

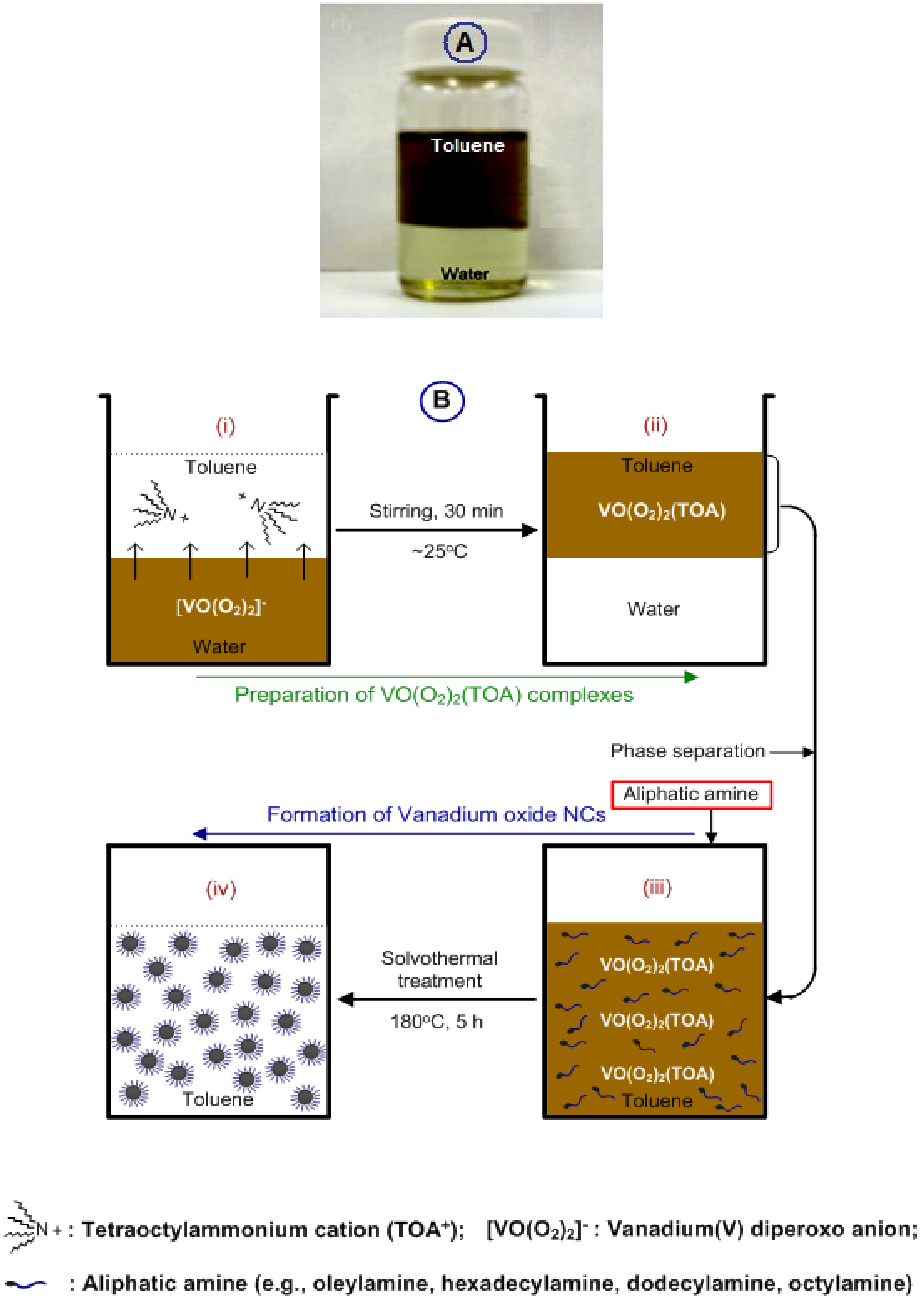

Scheme 6.2.1. (A) Photograph of a sample vial with the biphasic mixture after the transformation of vanadium(V) diperoxo anions from the water phase into the toluene phase. (B) Schematic illustration of the preparation of vanadium(V) diperoxo tetraoctylammonium ($VO(O)_2(TOA)$) complexes (the phase-transfer process accompanied by the corresponding deep orange color one), followed by the formation of alkyl amines-capped vanadium oxide nanocrystals.

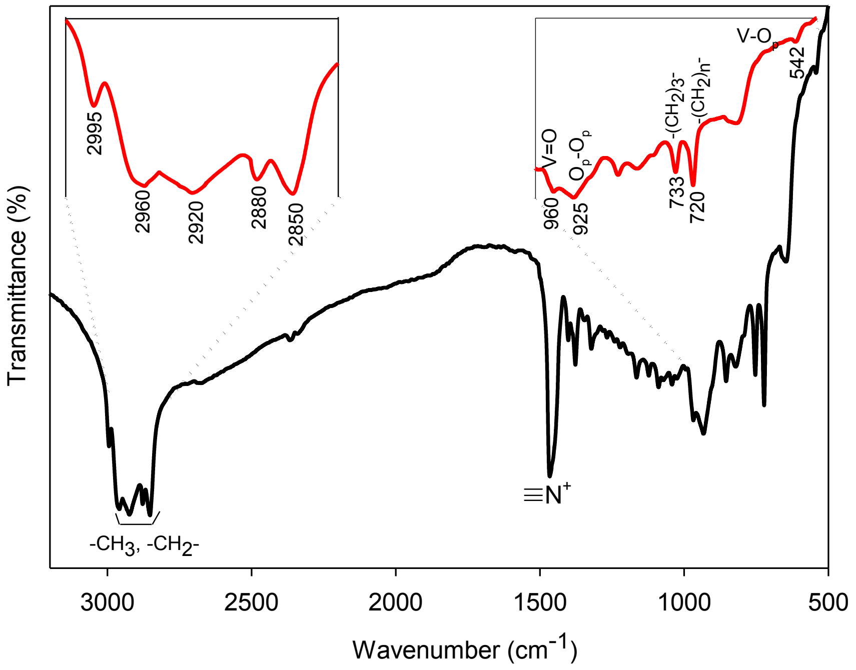

Figure 6.2.1. FTIR spectrum of the vanadium(V) diperoxo tetraoctylammonium complex solid.

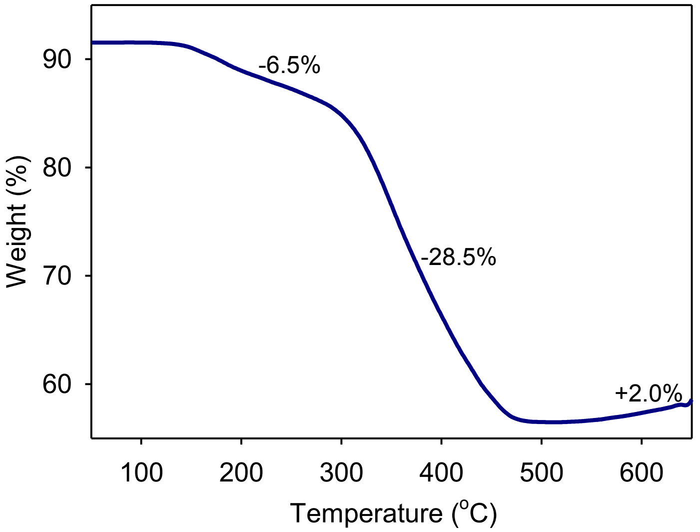

Figure 6.2.2. TGA curve of the vanadium (V) diperoxo tetraoctylammonium complex solid.

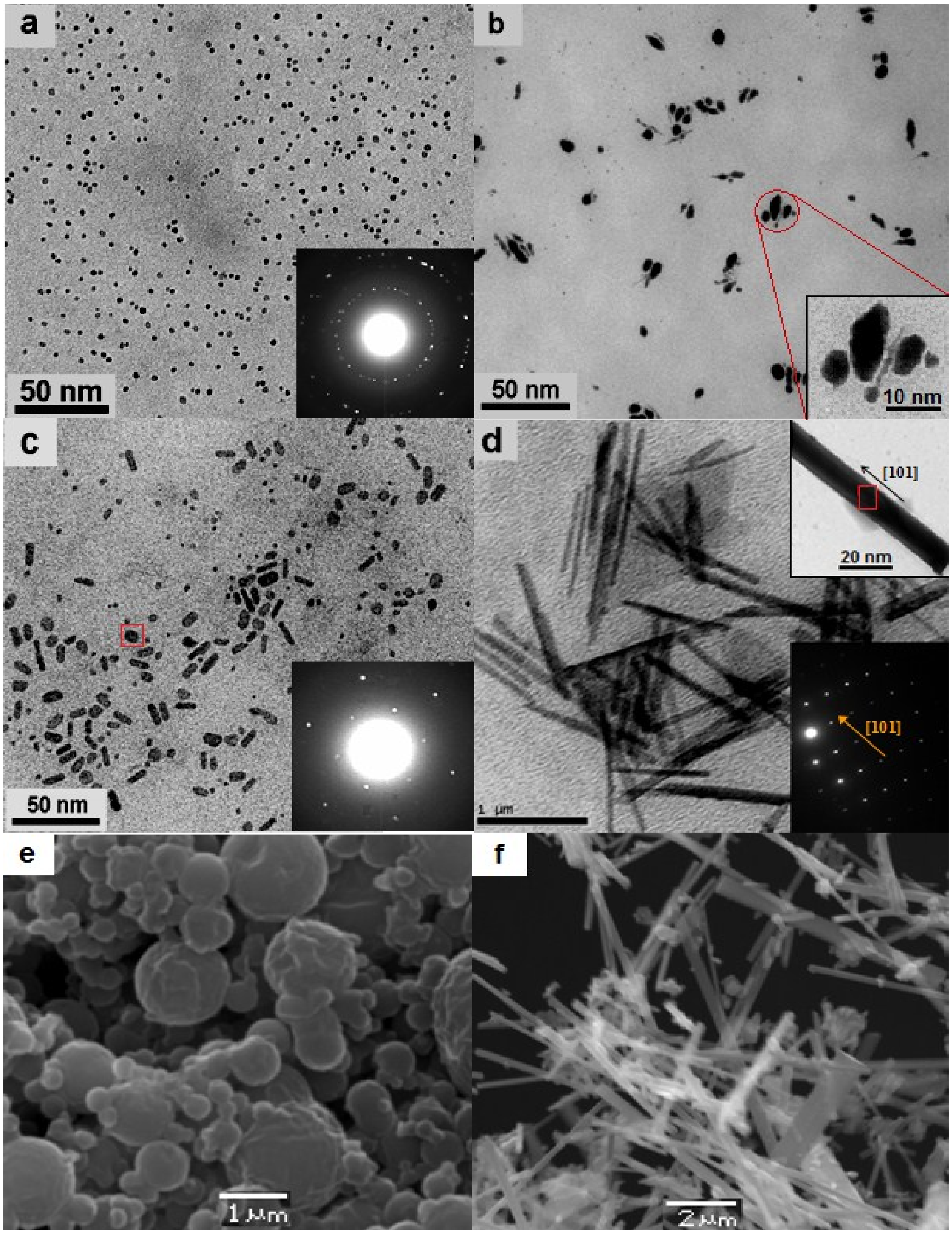

Figure 6.2.3. Effect of water content in the synthesis mixture on the shape transformation of nanospheres into nanorods. TEM images and corresponding SAED patterns of the as-made vanadium oxide nanocrystals synthesized from V(V) diperoxo tetraoctylammonium complexes (0.04 mol/L) in oleylamine (5 mL) at 180 ^{o}C for 5 h with various water/toluene solvent ratios in volume (W/T): a) W/T = 0:40, b) W/T = 2:40, c) W/T = 8:40, and d) W/T = 20:40. SEM images of (e) the calcined vanadium oxide nanospheres and (f) the calcined vanadium oxide nanorods (samples 1 and 4 in Table 6.2.1).

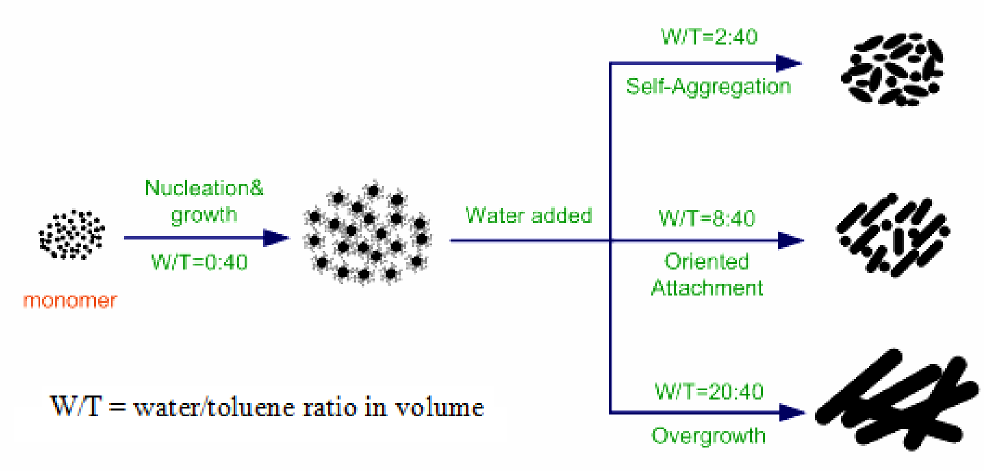

Scheme 6.2.2. Schematic illustration of the shape transformation of vanadium oxide nanocrystals from nanospheres into nanorods as a function of water content.

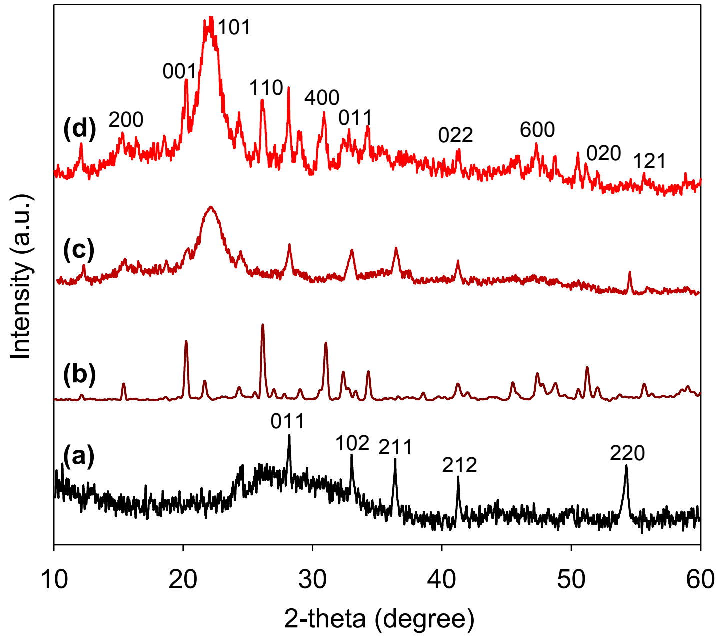

Figure 6.2.4. XRD patterns of the vanadium oxide NC samples before and after calcination: (a) as-made vanadium oxide nanospheres, (b) calcined vanadium oxide nanospheres, (c) as-made vanadium oxide nanorods, and (d) calcined vanadium oxide nanorods (samples 1 and 4 in Table 6.2.1).

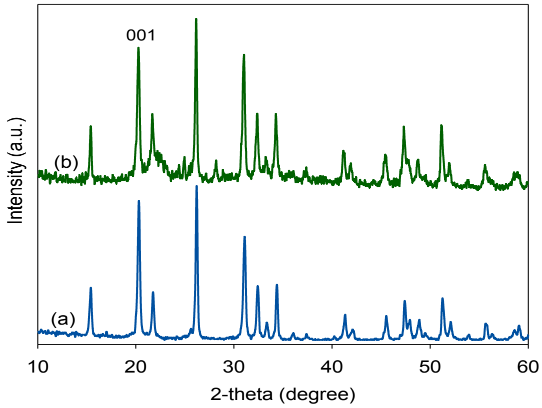

Figure 6.2.5. XRD patterns of the calcined vanadium oxide nanocrystals were synthesized from (a) $VO(O_2)_2$(TPA) and (b) $VO(O_2)_2$(CTA) (samples 5 and 6 in Table 6.2.1).

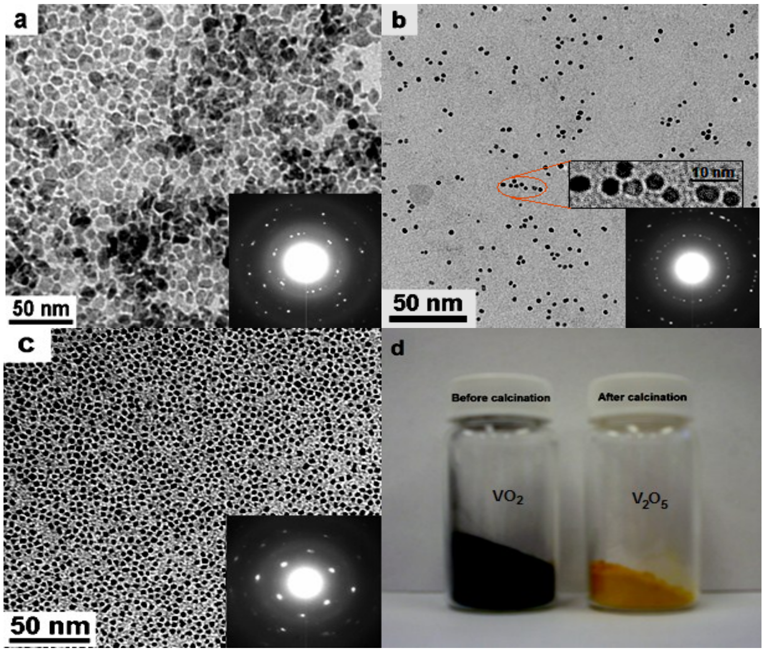

Figure 6.2.6. Effect of the steric ligands of vanadium complexes on the size of vanadium oxide nanocrystals. TEM images and corresponding SAED patterns of the VO_2 nanocrystals samples prepared from different vanadium complex precursors (e.g., various ligands): a) $VO(O_2)_2$(TPA), b) $VO(O_2)_2$(TOA), c) $VO(O_2)_2$(CTA). All of syntheses were carried out under the same condition as Sample 1 in Table 1. (d) Photograph of multi-grams of the as-made blue-black VO_2 nanosphere solids (6.8 g) and the calcined yellow V_2O_5 nanosphere solids (5.7 g) obtained in a single batch.

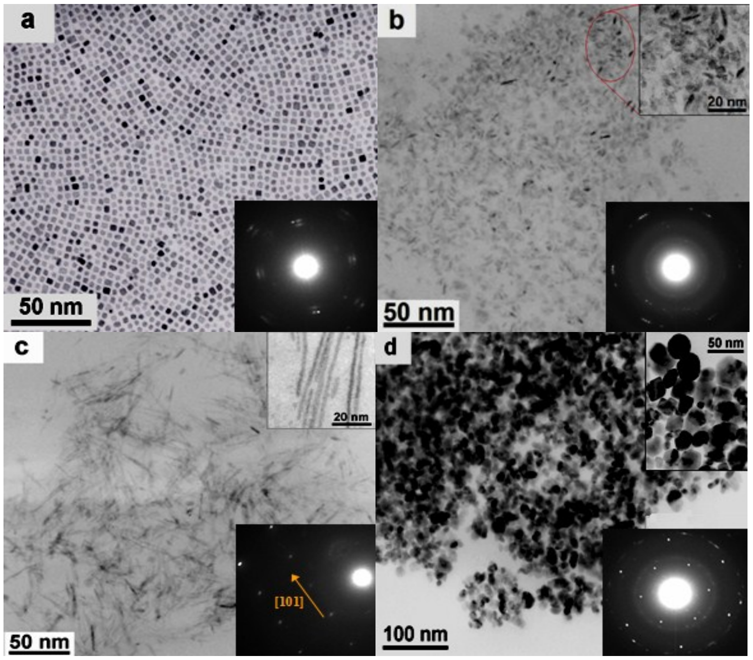

Figure 6.2.7. Shape evolution of vanadium oxide nanocrystals as a function of the alkyl chain length of the capping aliphatic amine agents. TEM images and corresponding SAED patterns of the as-made vanadium oxide NC samples prepared from: a) oleylamine (OM, C_{18}), b) hexadecylamine (HD, C_{16}), c) dodecylamine (DD, C_{12}) and d) octylamine (OC, C_8). All of syntheses were carried using $VO(O_2)_2$(TOA) complexes as vanadium precursors in ethanol medium.

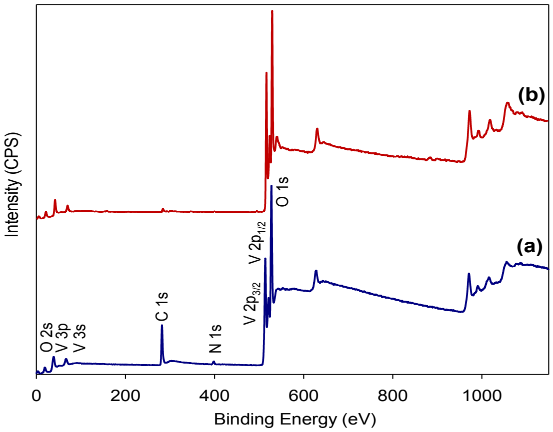

Figure 6.2.8. Survey XPS spectra of the as-made vanadium oxide nanospheres (a) before and (b) after calcination in air at 550 °C for 2 h (sample 1 in Table 6.2.1).

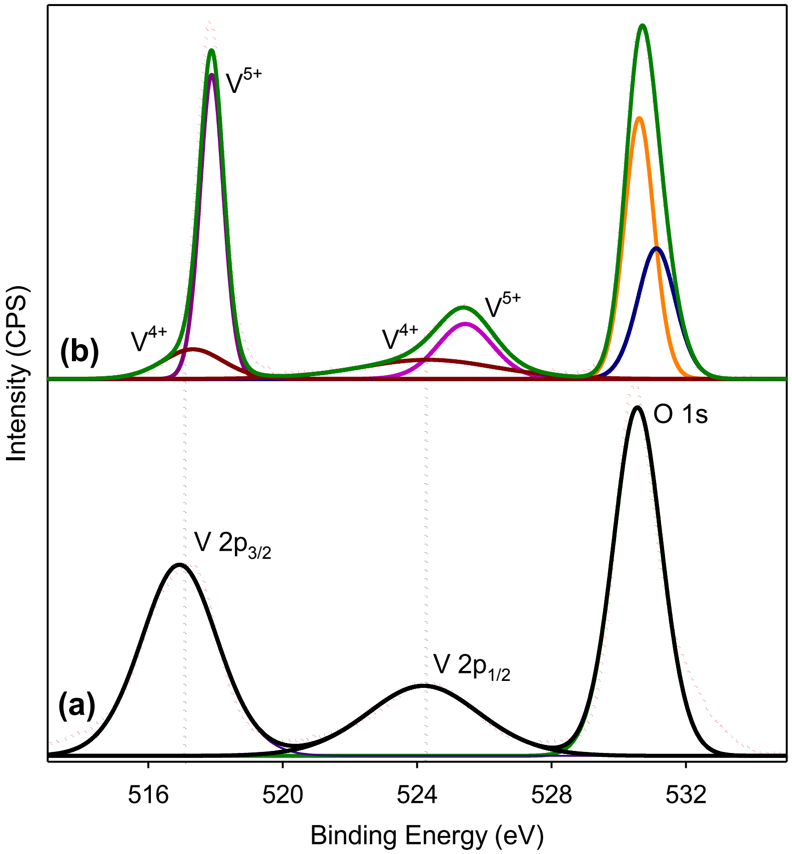

Figure 6.2.9. XPS spectra of V 2p and O 1s peaks and their deconvolution of the as-made vanadium oxide nanosphere sample (a) before and (b) after calcination at 550 ºC for 2 h.

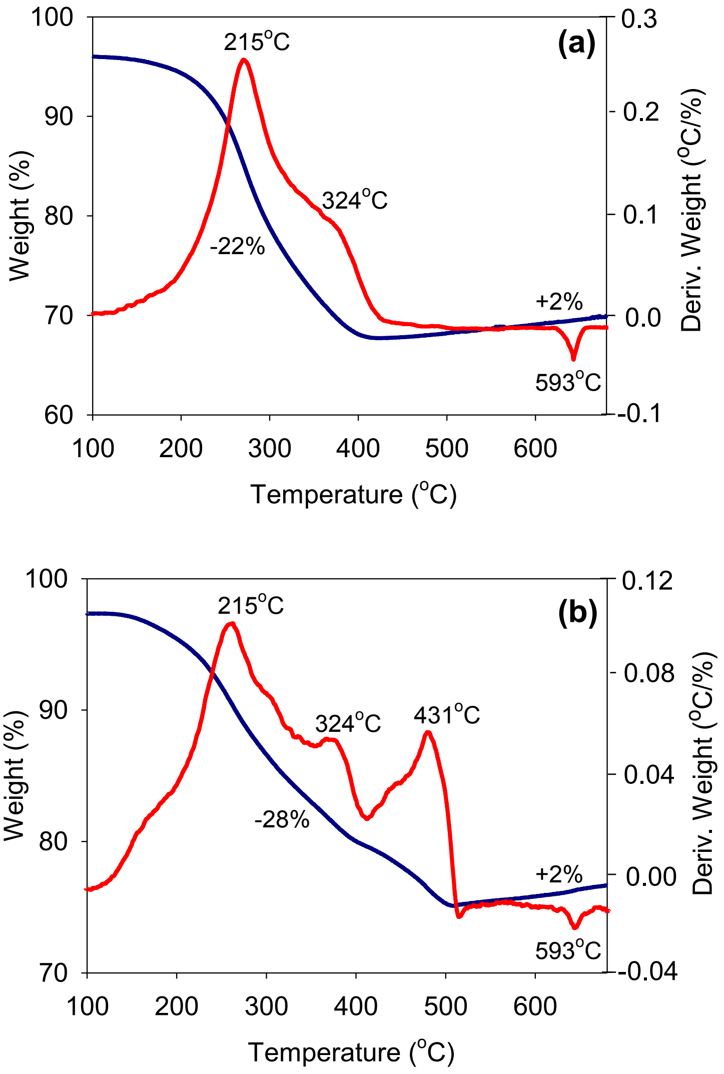

Figure 6.2.10. TGA/DTA curves of (a) the as-made OM-capped vanadium oxide nanospheres and (b) the as-made OM-capped VO_2 nanorods (samples 1 and 4 in Table 6.2.1).

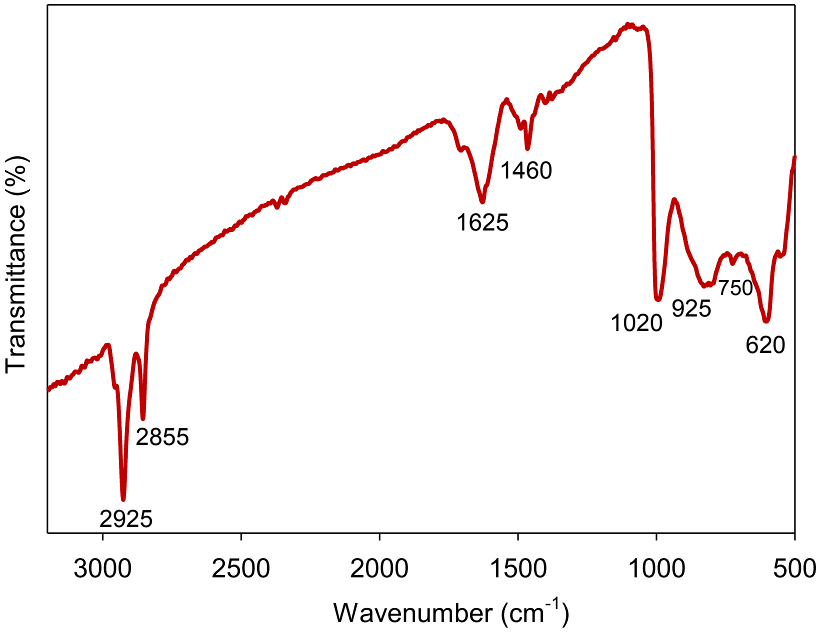

Figure 6.2.11. FTIR spectrum of the as-made OM-capped vanadium oxide nanospheres (sample 1 in Table 6.2.1).

6.3. Shape- and Size-Controlled Synthesis of Monoclinic ErOOH and Cubic Er_2O_3 from Micro- to Nanostructures and their Upconversion Luminescence

Thanh-Dinh Nguyen, Cao-Thang Dinh and Trong-On Do

Department of Chemical Engineering, Laval University, Quebec G1K 7P4 Canada

Published in *ASC Nano* **2010**, *4*, 2263-2273

Abstract

A general approach has been developed for the synthesis of monoclinic ErOOH and cubic Er_2O_3 structures with high yield via the solvo-hydrothermal reaction of erbium nitrate in water/ethanol/decanoic acid at temperature in the range of 120-180 ^oC for 24 h. The monoclinic ErOOH phase was formed at low temperatures (120-140 ^oC), however, this phase was converted to the cubic Er_2O_3 phase at higher temperatures (160-180 ^oC). By tuning different experimental parameters, the erbium-compounds with different sizes from 3 nm to 3 μm, and shapes including cores/dots to spheres, wrinkle-surfaced spheres, flowers, dog-bonds, wires, rods, bundles, straw-sheaves, and brooms can be controlled. The particle size of the product had a tendency decreasing from micro- to nanometer as increasing the decanoic acid concentration from 0.038 to 0.190 M. Their particle size significantly decreased from 18 nm sphere to 3 nm core by only using anhydrous ethanol instead of water-ethanol solvents. The anisotropic growth of the rod products was observed at high precursor monomer concentrations in the range of 76.25-152.50 mM. Based on this study, a correlation between the experimental parameters and the phase, shape, and size of the products was discussed. The upconversion luminescence properties depend not only on crystalline phase but also on particle size of the products. The luminescence intensity increases with the decrease of particle size from micro- to nanometers.

6.3.1. Introduction

The shape, size, and phase of materials with dependent properties are well established. The synthesis of metal oxide particles with controllable shape, size, and phase is thus a key goal in materials chemistry.[1,2] Specific morphologies such as nanorods, nanowires, nanocores, nanodots, nanobundles, nanospheres, nanoflowers show great promise in many applications, as they usually exhibit electronic, optical, magnetic, and catalytic properties which are distinct as compared to their corresponding bulk materials.[3-5] In addition, the specific properties of three-dimensional architecture assemblies can be observed due to the emergence of individual nanoscale componants as a result of the interparticle arrangement.[6,7] To achieve precise size/shape control, it is important to understand the relationship between product morphologies and experimental parameters. In the colloidal synthesis, the choice of appropriate surfactants and the synthesis conditions are crucial for controlling nucleation and growth in manipulating the size, shape, and phase of the resulting nanostructures.[8-12] The level of control also provides an advanced understanding on the particle formation and the interparticle forces for aggregation which based on Ostwald ripening,[13] oriented attachment,[14] and lateral-aggregation[15] mechanisms.

Erbium-compound (ErOOH and Er_2O_3) materials are recognized as one of the most important rare earth oxides for sensing applications in the lasers and optical amplifiers.[16-18] Indeed, the unique properties of these materials are produced by the intra Er^{3+} 4*f* shell transition from its first excited state ($^4I_{3/2}$) to the ground state ($^4I_{5/2}$). This is related to the emission band of around 1.54 μm that is one of the standard telecommunication wavelengths.[19,20] Previous investigations indicate that the intrinsic minimum optical absorption of erbium-compound materials strongly depends on shape and size, and crystalline phase.[21-24] A recent study is directed to erbium-compounds *due to* their special capability of near-infrared excitation (NIR)-to-visible upconversion (UC) emission.[25] Developing new and simple methods for shape-, size-, and phase-controlled synthesis of ErOOH and Er_2O_3 materials on the micro/nanoscales would thus open up new avenues for uncovering their remarkable properties and for achieving useful applications in optical telecomnication. Furthermore, *due to* their size-, shape-, phase-dependent properties, direct syntheses of tri-dimensional (3D) structures using surfactants have been extensively studied. However, little work has been reported concerning 3D erbium-compound materials with controllable size, from micro- to nanostructures, and shape such as spheres, wrinkle-surfaced spheres, and flowers. For example, Gao and coworkers[26] synthesized 200-300 nm-sized erbium oxide microspheres using urea as the precipitant of erbium ion precursors without any surfactants under hydrothermal condition. Li et al.[27] reported a simple hydrothermal route for the synthesis of erbium hydroxide nanobelts from the metal hydroxide precursors. The yielded products from these synthetic methods were hard to control the size and shape, *due to* the absence of capping agents. In a recent work, we have synthesized uniform Er_2O_3 nanospheres using the erbium-oleate complexes as precursor in two-phase (toluene-water) system containing *tert*-butylamine/oleylamine under autoclaving at 180 °C for 24 h.[28] It was illustrated that the nucleophilic reaction between $Er(oleate)_3$ complex and *tert*-butylamine as a catalytic agent occurred on the basis of S_N^1 mechanism to generate erbium monomers[29] and subsquently oleylamine-capped erbium oxide nuclei at the water-toluene interface. The resulting capped nuclei are hydrophobic and easily dispersed in toluene. These nuclei then grow into final Er_2O_3 nanospheres during the synthesis process. No product was observed in the water phase. *Due to* the thermal stability of the erbium-oleate complex as reported by Hyeon et al.,[30] the thermolysis of $Er(oleate)_3$ complex catalyzing by *tert*-butylamine to generate exclusive Er_2O_3 nuclei could not usually occur under 180 °C. Only the Er_2O_3 nanocrystal product can thus obtain at high temperatures (≥180 °C). This indicated that the solvo-hydrothermal two-phase progress is limited in controlling the composition and crystalline phase of the erbium-compounds because the metal oxyhydroxide is often yielded at low temperatures (≤140 °C).[31] To overcome to drawback for our further research work of these materials, a new water/ethanol-based approach have been developed for the systematical synthesis and characterization of luminescence properties of erbium-compound from micro- to nanostructures with different phases and shapes. In this water-ethanol solvent system, erbium nitrates are easily hydrolyzed to produce ErOOH at low temperatures. These intermediate compounds can be subsequently dehydrated to form Er_2O_3 at higher temperatures. These behaviors can not achieve as using the above mentioned two-phase method.

In this paper, we report a new and straightforward approach for the shape-, size-, and phase-controlled synthesis of ErOOH and Er_2O_3 micro- and nanostructures in high yield from the hydro-solvothermal reaction of erbium nitrate in water/ethanol solution in the presence of decanoic acid surfactant. By only tuning the temperature in the reaction system, monoclinic ErOOH and cubic Er_2O_3 phases can be controlled. Size and shape of erbium-compound crystals with the size ranging from thousands to tens of nanometers were selectively synthesized by controlling different synthesis conditions including the concentration of decanoic acid and erbium precursor and the amount of water. The crystalline phase- and particle size-dependent optical properties of these micro/nanomaterials were also discussed.

6.3.2. Experimental Section

Chemical: All chemicals were used as received without further purification. Erbium nitrate hexahydrate ($Er(NO_3)_3.6H_2O$, 99.9%) and decanoic acid ($C_{10}H_{22}COOH$ or DA, technical grade, 70%), were purchased from Sigma-Aldrich. Anhydrous ethanol and sodium hydroxide were purchased from Reagent ACS.

Synthesis of ErOOH and Er_2O_3 micro/nanostructures: $Er(NO_3)_2.6H_2O$ (0.30-6.10 mmol) was dissolved in 10 mL of distilled water to form clear light rose-colored solution. An homogenerous ethanol solution (30 mL) containing decanoic acid (1.52-9.15 mmol) was added into the above solution under magnetic stirring for 10 min. The obtained mixture was transferred into 70 mL autoclave with a Teflon liner at 120-180 °C for 24 h. The decanoic acid-capped products were collected in the bottom of the Teflon cup and can re-disperse in nonpolar organic solvents (*e.g.,* toluene or hexane). Erbium-compound micro/nanoparticles with different phases, sizes, and shapes, were obtained following the similar procedures by varying the reaction temperature, the surfactant/precursor molar ratio, the concentration and nature of precursor, water content in synthesis solution. In the case of using $Er(OH)_3$ as precursor instead of erbium nitrate salt, $Er(OH)_3$ gel was prepared by adjusting pH value of the aqueous erbium nitrate solution using 10% NaOH. Typically, $Er(NO_3)_2.6H_2O$ (0.135-2.70 g) was dissolved in 50 mL of distilled water to form clear light rose-colored solution. The pH was then adjusted with a 10% NaOH aqueous solution to 12.

After being stirred for about 30 min, the rose-colored $Er(OH)_3$ precipitate gel was filtered and washed several times with deionized water to remove any possible ionic remnants. The obtained $Er(OH)_3$ gel was dispersed in 10 mL of distilled water. The reaction solutions (40 mL) with different precursor concentrations (7.63; 76.25; 152.50 mM) were designed by mixing aqueous $Er(OH)_3$ gel solution (10 mL) and anhydrous ethanol solution (30 mL) containing decanoic acid (6.09 mmol).

6.3.3. Results and Discussion

The synthesis conditions, the crystalline phases, and the morphologies of a variety of particle size- and shape-controlled monoclinic ErOOH and cubic Er_2O_3 materials are summerized in Table 6.3.1. These erbium oxyhydroxide and oxide micro/nanomaterials were synthesized from the hydro-solvothermal reaction of erbium nitrates in a water/ethanol/decanoic acid mixture at 120-180 ^oC for 24 h. In this synthesis, erbium nitrate, decanoic acid (DA) and water/ethanol were used as precursor, capping agent, solvent, respectively. After the hydro-solvothermal synthesis, the products were capped by DA molecules and precipitated in the bottom of the vessel. The final products can be re-dispersible in nonpolar organic solvents. Note that the hydro-solvothermal reaction mechanism of the erbium-compound formation in one-phase (water-ethanol) system in the present work is obviously difference from the nucleophile one of the erbium oxide formation in two-phase (water-toluene) system as above mention.[28] Different well-defined morphologies of monoclinic erbium oxyhydroxide and cubic erbium oxide micro/nanostructures can be also obtained at the different reaction temperature stages in the synthesis process. The advantage of the current synthetic procedure utilized erbium nitrate as an inexpensive starting material and water-ethanol as environmentally benign solvents, as compared to the traditional organic-phase organometallic synthetic pathway. Generally, surfactant-capped particles are hydrophobic character, and ethanol is usually used to precipitate the particles out of the nonpolar solvents. It should be noted that, for the given synthetic conditions (Er^{3+} concentration, DA/Er, C_2H_5OH/H_2O, reaction temperature), the nucleation and growth occurred in the bulk solution. The particle product was spontaneously precipitated during the particle growth *owing to* the polar environment. The size and shape of the final particle products are essentially not disturbed by the continuous precipitation process. This led to the continued growth of the nanoparticles from *in situ* aggregation of the generated erbium precursor monomers in bulk solution on their surfaces was confined.[10]

The procedure for the synthesis of these materials is illustrated in Scheme 6.3.1. At early stages, erbium nitrate was hydrolyzed in water/ethanol solution in the presence of decanoic acid surfactant to generate erbium hydroxide nucleus. Resulting DA-capped $Er(OH)_3$ nucleus then dehydrated and grew into ErOOH particles in the synthesis solution at relatively low reaction temperatures (120-140 °C). These ErOOH particles were converted into Er_2O_3 ones in the hydro-solvothermal treatment at higher temperatures (160-180 °C).[27] The results in this study indicate that phase and morphology of ErOOH and Er_2O_3 micro/nanoparticles can be easily controlled by only changing the reaction temperature. A series of temperature-dependent experiments was performed to understand the formation of erbium-compound micro/nanostructures. The synthesis reactions were carried out at different temperatures: 120, 140, 160, 180 °C for 24 h of each stage of temperature using the same starting chemical composition mixture (*e.g.,* $[Er^{3+}]$ = 7.63 mM, DA/Er = 5:1, 30 mL C_2H_5OH and 10 mL H_2O).

The X-ray diffraction (XRD) patterns of the erbium-compound samples obtained at different reaction temperatures, while keeping other synthesis conditions unchanged, are shown in Figure 6.3.1. For the samples prepared at low temperatures (120 and 140 ^{o}C), the XRD patterns (Figure 6.3.1a,b) exhibit representative reflections for the monoclinic phase (ErOOH, $P2_1/m$, JCPDS 76-0700),[32,33] no other phase was observed indicating that only pure monoclinic-phase ErOOH products were formed. As the reaction temperature increases to 160 and 180 ^{o}C, the XRD patterns (Figure 6.3.1c,d) of these samples reveal the cubic-phase Er_2O_3 crystals with lattice constants a = 4.753 Å, b = 5.720 Å, c = 4.968 Å ($Fm3m$, JCPDS 08-0050).[28] This indicates that cubic Er_2O_3 phase instead of monoclinic ErOOH one was formed at higher temperatures. The broadening and intense diffraction peaks indicate small particle size and well-crystallized products. The average particle sizes of all the erbium-compound samples from (222) peak using Scherrer equation were ~25 nm implying that the ErOOH and Er_2O_3 microstructures were constructed from the aggregation of the small nanoparticles.

The TGA-DTA curves (Figure 6.3.2) were recorded for DA-capped ErOOH quasi-microspheres (sample 1). The TGA curve shows that the total weight loss of DA-capped ErOOH microsphere sample is ~36%, which attributed to that of both the combustion/elimination of decanoic acid and the dehydration of the conversion of ErOOH into Er_2O_3. An intensive exothermic peak at 313 °C along with a weak peak at 469 °C in the DTA profile attributed to the combustion and elimination of decanoic acids, respectively. The total weight loss of these processes determining from TGA curve is ~32.5%. The weight loss of the driving off of structural water molecules from ErOOH crystals calculating from TGA curve is ~3.5%, corresponding to a weak exothermic DTA peak at higher temperature (~612 ^{o}C). This experimental value (~3.5%) agrees well with the theoretical one of ~4% assuming a dehydration of $2ErOOH \rightarrow Er_2O_3 + H_2O$. Therefore, it could be concluded that monoclinic ErOOH is a metastable phase, whereas the cubic Er_2O_3 phase is formed and thermodynamically stable at high synthesis temperatures (≥160 ^{o}C).

The morphologies of the final products synthesized at different reaction temperatures in the range of 120-180 ^{o}C were also examined by SEM technique (Figure 6.3.3 and 6.3.4). When the synthesis reaction was performed at 120 ^{o}C, as shown in Figure 3a,b, the ErOOH product is composed of quasi-microspherical aggregates with an average diameter of approximately 3 μm and a coalescence of small particles on their surface. This indicates that the quasi-spherical aggregates consist of small particles, in agreement with XRD result. Increasing the reaction temperature to 140 °C, ErOOH microspherical aggregates were still observed, microspheres were however deformed; while the diameter of individual microspheres essentially intact and their surface is rather rough (Figure 6.3.3c,d). The surface morphology change should be *due to* the classical ion-mediated growth process in intraparticles because of the difference in chemical potential on the particle surface (Ostwald ripening) at 140 ^{o}C.[34]

At higher reaction temperature (>160 °C), the product was converted from monoclinic ErOOH into cubic Er_2O_3 phase as seen above in Figure 6.3.1. It is important to note that the Er_2O_3 microsphere morphology was significantly changed. Most wrinkle-surfaced microspheres with an average diameter of ~3 μm were observed (Figure 6.3.4a). These wrinkle-surfaced microspheres are attached together to form chainlike microsphere aggregates. From enlarged SEM image (Figure 6.3.4b), the structure of the spherical architecture was built from several dozen nanoplates with smooth surfaces. The nanoplates with a thickness of ~200 nm and a length of ~1.0 μm were connected to each other to form spherical hierarchical structures. The closer inspection of the SEM images reveals that the size of these microspheres seems to be unchanged. However, the formation of the wrinkle-surfaced microspheres may be *due to* the etching of Er_2O_3 microsphere surfaces in the presence of decanoic acid at this temperature.[35]

Eventually, when the synthesis reaction was performed at 180 °C, the microspheres were surrounded by the nanorods gathered together into larger Er_2O_3 microflowers (Figure 6.3.4c,d). Each microflower consists of a number of nanorods, which is adhibited with each other to construct the assemblied microflowers with an average diameter of each aggregate of approximately 3 μm. A careful observation of the enlarged SEM images in several parts of this sample clearly demonstrated that each petal of microflowers is of rodlike morphology. A number of nanorods was found to be highly oriented, vertically aligned with high density, and extended outward from the center of each microflower. Each individual nanorod has average diameter of ~0.1 μm and in length of ~0.7 μm. It may be established that a fractional oriented-assembly of the nanorods at high reaction temperatures arises in situations far from thermodynamic equilibrium where high driving force leads to the generation of the ordered microflower assembly.[36]

Furthermore, with a fixed DA/Er molar ratio of 20:1 instead of DA/Er = 5:1, a series of experiments was also carried out at different temperatures from 120 °C to 160 °C, a similar trend (from the pure monoclinic ErOOH phase to the pure cubic Er_2O_3) was also observed by the XRD spectra (not shown data). Moreover, the products exhibit magnificent morphologies as seen in Figure 6.3.5. At 120 °C, the main ErOOH products were bundles of nanowires with a diameter of about 100 nm and a length in the range of 0.4 μm (Figure 6.3.5a). At 140 °C, the abundance of nearly monodisperse ErOOH straw-nanosheaves with rough surface and the nanowire aggregates were formed (Figure 6.3.5b). The TEM image inset of Figure 5c clearly shows individual so-called ErOOH straw-nanosheaves which are strongly twisted in the middle part leading to the formation of the fanned dual fantails. These straw-nanosheaves with their extended dual fantails are closely bonded to each other in the middle part, and have a length in the range of 700 nm, a fantail diameter of about 150 nm and a middle diameter of about 70 nm. Increasing reaction temperature to 160 ^{o}C, the morphologies of ErOOH nanoarchitectures was almost broom-bundles with a broom diameter of about 150 nm and length in the range of 350-400 nm (Figure 6.3.5d). The SAED pattern (inset of Figure 6.3.5c) of the straw-nanosheaves clearly shows bright diffraction rings indicating that the nanowires as building units of the hierarchical nanobundle assemblies are polycrystalline rather than single crystalline. These small-thin nanowires have a higher chemical potential owing to a larger length-to-diameter ratio and thus are easier to coalesce leading to the nanobundles with lower surface energy.[37] In addition, the formation of the nanobundles for this DA/Er ratio (20:1) in the bulk solution could be illustrated by the lateral-aggregation mechanism *due to* relatively short alkyl chain of capping decanoic acid (C_{10}), in agreement with those reported by our group.[38,39]

The decanoic acid (DA) concentration in the bulk solution was also found to be as a crucial role in the size- and shape-controlled synthesis of erbium oxide nanocrystals. To investigate this parameter, a series of experiments was carried out at 180 ^{o}C with different DA concentrations, from 0.038 to 0.228 M in the bulk solution (*e.g.,* the DA/Er molar ratio increases from 5:1 to 30:1), while the other parameters kept the same ($[Er^{3+}]$ = 7.63 mM, 30 mL C_2H_5OH, 10 mL H_2O). Interestingly, the products exhibit size/shape-dependent DA concentration change. At the same reaction temperature (180 ^{o}C), increasing the DA concentration from 0.038 to 0.228 M, the particle size decreases from ~3 μm to ~3 nm (Figures 6.3.4c,d and 6.3.6). With relatively low DA concentrations, 0.038 M (*e.g.,* DA/Er = 5:1) and 0.076 M (*e.g.,* DA/Er = 10:1), Er_2O_3 microflowers with an average diameter of ~3 μm were found (see Figures 6.3.4c-d and 6.3.6a). However, with higher DA concentrations, only nanoparticles with different shapes were formed. Increasing the DA/Er ratio to 15:1, 18 nm-sized dog-bondlike nanocrystals companied with some nanocubes were found (Figure 6.3.6b). Only uniform 18 nm-sized nanospheres were formed, while the DA/Er ratio reached 20:1 (Figure 6.3.6c). Furthermore, almost the nanodots with an average diameter of 3 nm were produced as the DA/Er = 30:1 (Figure 6.3.6d).

The SAED pattern (inset of Figure 6.3.6c) of the Er_2O_3 nanospheres taken from a single sphere is indexed respectively to the strong concentric rings from the (222), (400), (440), (622) planes of a single cubic Er_2O_3 structure. The XRD patterns exhibit a pure cubic-phase Er_2O_3 structure for the both samples of Er_2O_3 nanospheres and nanodots (Figure 6.3.7, samples 10 and 11 in Table 6.3.1). Compared to the diffraction peaks for the erbium-compound microstructures, the XRD peaks for the Er_2O_3 nanospheres/nanodots are much broader, implying a smaller particle size. According to the Scherrer equation, the mean particle sizes of nanospheres and nanodots are estimated from (222) peak to be about 16.0 and 4.5 nm, respectively, which are consistent with the TEM results.

The reason for the size/shape-dependent DA concentration evolution should be *due to* the covering degree of capping agent on the particle surface. The above results suggest that the surfactant (decanoic acid) serves not only as a stabilizer to prevent the aggregation of the products but also as a strong shape-controller assisting to the formation of erbium-compound crystals during the crystal growth process. It is consistent with our previous results on the size-controlled synthesis of $SmVO_4$ nanospheres using oleylamine as capping agent.[40,41]

In order to study the effect of water content, nature of precursor, and precursor monomer concentration in bulk solution on size and shape of the final products, a series of experiments with different synthetic conditions was also carried out at 180 ^{o}C for 24 h with the Er/DA molar ratio of 20:1; *(i)* without water, *(ii)* with water, *(iii)* different erbium precursors: $Er(NO_3)_3$, $Er(OH)_3$, *(iv)* different $Er(OH)_3$ concentrations: $[Er(OH)_3]$ = 7.63 mM, 76.25 mM, 152.50 mM, respectively (see Table 6.3.1). $Er(OH)_3$ gel was prepared by adjusting pH value of the aqueous erbium nitrate solution using 10% NaOH (see Experimental Section). The TEM/SEM images of these products are shown in Figure 6.3.8. In the case of sample 12 which was synthesized under the same synthetic conditions (*e.g.,*

$Er(NO_3)_3$ = 7.63 mM) of sample 10 in Table 6.3.1 (Figure 6.3.6c), except that anhydrous ethanol (40 mL) was used as a reaction solvent instead of ethanol/water (30:10 mL) mixture. Uniform self-assembled Er_2O_3 nanocores with ~3 nm in diameter were obtained (sample 12 in Table 6.3.1 and Figure 6.3.8a). This indicates a decrease in particle size of erbium oxide nanospheres from 18 to 3 nm when only anhydrous ethanol was used as reaction medium. Futhermore, with the same ethanol/water ratio of 30:10 (mL), when $Er(OH)_3$ precursor was substituted by $Er(NO_3)_3$, 4 nm-sized Er_2O_3 nanodots (sample 13 in Table 6.3.1 and Figure 6.3.8b) were yielded instead of ~18 nm-sized nanospheres (Figure 6.3.6c). The effect of erbium precursors, $Er(NO_3)_3$ and $Er(OH)_3$, on particle size in this case could be *due mainly to* its influence on pH value in reaction solution, *e.g.,* pH~6 and 9.0 respectively.[27]

The $Er(OH)_3$ precursor concentration can also play a significant role in the morphological evolution of the products. As the $Er(OH)_3$ monomer concentration increased from 7.63 to 76.25 mM, the particle size and shape change from 4 nm-sized Er_2O_3 nanodots to 80 nm x 150 nm-sized Er_2O_3 nanowires was observed (samples 13,14 in Table 6.3.1 and Figure 6.3.8b,c). Increasing the precursor concentration to 152.50 mM, the products are mainly rods with ~ 0.25 μm in width and ~ 1 μm in length. These microrods were organized the aligned parallel together to form a large bundle (sample 14 and Figure 6.3.8d). This suggests that the growth of anisotropic structures occurred at a relatively high reactant concentration *due to* a relatively high chemical potential environment in the bulk solution.[42] Figure 6.3.9 shows the XRD patterns of the as-synthesized samples of nanocores and microrods (samples 12 and 15 in Table 6.3.1). The both samples starting from $Er(OH)_3$ precursors exhibit a pure cubic-phase Er_2O_3 structure, suggesting that the dehydration of erbium hydroxides to oxides occurs during hydro-solvothermal treatment at this temperature (180 °C). On the basis of the above experimental results, a schematic diagram of the growth process for the formation of monoclinic ErOOH and cubic Er_2O_3 micro/nanostructures in size and shape as a function of synthesis temperature and surfactant/precursor molar ratio are summarized in Scheme 6.3.2.

The X-ray photoelectron spectra (XPS) of the ErOOH quasi-microspheres (sample 1) and Er_2O_3 microflowers (sample 4) were measured to examine the chemical surface composition and oxidation state of erbium in erbium-compound structures. The survey XPS spectra reveal that these samples (not shown data) contain Er 4d, O 1s, C 1s, while no impurites are detected. The high-resolution Er 4d XPS spectra are presented in Figure 6.3.10A. The both samples exhibit the Er 4d states characterizing Er^{3+} in ErOOH and Er_2O_3 structures, respectively.[43] The main different point is found here, the Er 4d XPS spectrum of the ErOOH sample is composed of five component peaks at binding energies of 168.8, 171.0, 173.0, 184.0, 196.6 eV, while the Er 4d XPS spectrum of the Er_2O_3 sample consists of only four corresponding components, and the absence of peak at 171.0 eV. Furthermore, the difference of O 1s XPS spectra of the ErOOH and Er_2O_3 samples were also observed (Figure 6.3.10B). The ErOOH sample is composed of two oxygen components, whereas the Er_2O_3 sample exhibits only one oxygen component. For the ErOOH sample, the weak XPS peak at 529.4 eV is assigned to the HO-Er groups and the stronger second at 531.8 eV is attributed to the O-Er groups. The Er_2O_3 sample exhibits only one O 1s XPS peak at 531.8 eV related to O-Er bonds. This also indicates a high OH concentration on the particle surface of the ErOOH sample.

Figure 6.3.11A shows the C 1s XPS spectrum of the DA-capped ErOOH sample (sample 1). This spectrum consists of three peaks at 285.8, 286.0, and 288.8 eV which correspond to C-C, C=C and C-C=O of decanoic acid molecules, respectively. The C 1s XPS spectrum (not shown data) of the DA-capped Er_2O_3 sample also exhibits a similar result of sample 1. A color photograph of the transparent while- and rose-colored toluene solution dispersing the as-synthesized sample of ErOOH nanospheres and Er_2O_3 nanoflowers, respectively, are shown in inset of Figure 6.3.11A. These clearly suggest that the erbium-compound micro/nanomaterials were capped by the carboxyl groups of decanoic acid molecules and the exposed hydrophobic alkyl groups were well-immersed in toluene.[44] To further confirm this result, the FTIR spectra were also recorded for the two DA-capped ErOOH and Er_2O_3 samples (sample 1 and 4 in Table 6.3.1) and are shown in Figure 6.3.11B. The both samples exhibit an absorption band at 670 cm^{-1} which is characteristic of the Er-O stretching mode. The O-H stretching mode for the ErOOH sample was also observed at 3700 cm^{-1} which is a typical FTIR band of structural OH groups for erbium oxyhydroxide.[33] The FTIR bands at 2864 - 2944 cm^{-1} attributed to the C-H stretching mode of alkyl chains of decanoic acid molecules were observed for the two samples.[37] Two FTIR bands were observed at 1466 cm^{-1} and 1548 cm^{-1} which are attributed to the symmetric and asymmetric stretching vibrations of the carboxylate groups of decanoic acid, respectively.[37] A large band around 3500 cm^{-1} corresponds to the O-H stretching frequency of surface hydroxide groups which were observed in the ErOOH sample, in good agreement with the above XPS results. These data further confirm that the carboxylic groups of decanoic acid molecules capped on the particle surface.

The optical properties of micro/nanostructures of ErOOH and Er_2O_3 in toluene were characterized by UV/vis absorption and photoluminescence (PL) spectroscopy (Figure 6.3.12). The UV/vis spectra (Figure 6.3.12A) of 3 μm ErOOH quasi-microspheres (sample 1) and 18 nm Er_2O_3 nanospheres (sample 10 in Table 6.3.1) exhibit different peak shapes and the maximum excitonic peak shifted from 280 to 289 nm, illustrating the difference from the ErOOH and Er_2O_3 crystals.[33] It is also noteworthy that the color of the final products changed from white to light rose as the change from monoclinic ErOOH to cubic Er_2O_3 phase (*e.g.,* increasing the reaction temperature from 120 to 180 °C, inset of Figure 6.3.12A). The upconversion luminescence properties of various samples with different particle size: ErOOH wire-nanobundles (sample 5) and ErOOH quasi-microspheres (sample 1) compared with those of Er_2O_3 nanospheres (sample 10) and Er_2O_3 microflowers (sample 4) under 218 nm excitation are presented in Figure 6.3.12B,C. The colloidal solutions of the ErOOH and Er_2O_3 samples both show the different excitonic peak shapes but the same spectral peak positions corresponding to the following 4f-4f transitions: $^2H_{9/2} \rightarrow {}^4I_{15/2}$ (~424 nm), $^4F_{3/2} \rightarrow {}^4I_{15/2}$ (~448 nm), $^4F_{7/2} \rightarrow {}^4I_{15/2}$ (~485 nm), $^4S_{3/2} \rightarrow {}^4I_{15/2}$ (~560 nm).[33,45] In a comparison of the peak intensity, this indicates that erbium compound nanospheres/nanobundles clearly show much stronger luminescence than erbium compound microspheres. This is *due to* the decrease of particle size in the both cases: ErOOH and Er_2O_3 particles. This result can refer that the decrease of particle size leads to the increase of the number of active atoms located on the exposed particle surfaces.[25,46] As a result, variations in luminescence intensity are strongly related to quantum confinement effect and the change of the excited energy between valence band and conduction band of these materials.[47]

These results contribute to the understanding of the size and shape control of ebium-compound particles from micro- to nanoscturcture. This synthetic approach allows to the generation of a variety of shape, size, and phase controlled erbium-compound materials using erbium nitrate salts as a starting material and water/ethanol as an environmentally solvent. We believe that these materials with manifold morphologies will be useful for the further investigation in their optical telecommunications and sensing applications.

6.3.4. Conclusion

In conclusion, the micro- and nanostructures of monoclinic ErOOH and cubic Er_2O_3 have been synthesized by the hydro-solvothermal reaction of erbium nitrate in water/ethanol/decanoic acid at temperature in the range of 120-180 ^oC for 24 h. After the synthesis reaction, the products were capped by the carboxylic groups of decanoic acid molecules and precipitated in the bottom of an autoclave cup *due to* polar environment. The exposed hydrophobic alkyl groups were oriented outward leading to the final products can be re-dispersible in nonpolar organic solvents. This water/ethanol-based approach provides a simple, versatile, high-yield, and inexpensive pathway for the synthesis of erbium-compound micro/nanoarchitectures. Our results reveal that the monoclinic ErOOH phase obtained at low temperatures (120-140 ^oC) and it was converted into the cubic Er_2O_3 phase at higher temperatures (160-180 ^oC) through dehydration process.

The ErOOH and Er_2O_3 particles with different sizes from 3 nm to 3 μm, and shapes including cores/dots to spheres, wrinkle-surfaced spheres, flowers, dog-bonds, wires, rods, bundles, straw-sheaves, and brooms can be manipulated by controlling the reaction parameters. With increasing the decanoic acid surfactant concentration, the particle size of the product had a tendency decreasing from micro- to nanometer. Their particle size significantly decreased from 18 nm nanosphere to 3 nm nanocore, while anhydrous ethanol was used instead of water/ethanol (10:30 mL). The shape evolution of anisotropic products was overdriven by higher precursor monomer concentrations in bulk solution. The upconversion luminescence results indicated that the luminescence properties depend not only on the crystalline structure but also on the particle size of products. The luminescence intensity increases with a decrease of particle size. It is our hope that monoclinic ErOOH and cubic Er_2O_3 micro/nanostructures with manifold morphologies will lead to new opportunities for further practical applications in optical telecomnications and other fields.

6.3.5. References

(1) Min, Y.; Akbulut, M.; Kristiansen, K.; Golan, Y.; Israelachvili, J. The Role of Interparticle and External Forces in Nanoparticle Assembly, *Nat. Mater.* **2008**, *7*, 527-538.

(2) Wang, D.; Lieber, C. M. Inorganic Materials: Nanocrystals Branch Out, *Nat. Mater.* **2003**, *2*, 355-356.

(3) El-Sayed, M. A. Some Interesting Properties of Metals Confined in Time and Nanometer Space of Different Shapes, *Acc. Chem. Res.* **2001**, *34*, 257-264.

(4) Gao, J.; Gu, H.; Xu, B. Multifunctional Magnetic Nanoparticles: Design, Synthesis, and Biomedical Applications, *Acc. Chem. Res.* **2009**, *42*, 1097-1107.

(5) Xiong, Y.; Wiley, B. J.; Xia, Y. Nanocrystals with Unconventional Shapes-A Class of Promising Catalysts, *Angew. Chem. Int. Ed.* **2007**, *46*, 7157-7159.

(6) Zhuang, J.; Shaller, A. D.; Lynch, J.; Wu, H.; Chen, O.; Li, A. D. Q.; Cao, Y. C. Cylindrical Superparticles from Semiconductor Nanorods, *J. Am. Chem. Soc.* **2009**, *131*, 6084-6085.

(7) Shang, N.; Papakonstantinou, P.; Wang, P.; Zakharov, A.; Palnitkar, U.; Lin, I.; Chu, M.; Stamboulis, A. Self-Assembled Growth, Microstructure, and Field-Emission High-Performance of Ultrathin Diamond Nanorods, *ACS Nano* **2009**, *3*, 1032-1038.

(8) Choi, S. H.; Kim, E. G.; Hyeon, T. One-Pot Synthesis of Copper-Indium Sulfide Nanocrystal Heterostructures with Acorn, Bottle, and Larva Shapes, *J. Am. Chem. Soc.* **2006**, *128*, 2520-2521.

(9) Soumare, Y.; Garcia, C.; Maurer, T.; Chaboussant, G.; Ott, F.; Fievet, F.; Piquemal, J. Y.; Viau, G. Kinetically Controlled Synthesis of Cobalt Nanorods with High Magnetic Coercivity, *Adv. Funct. Mater.* **2009**, *19*, 1-7.

(10) Cao, T. D.; Nguyen, T. D.; Kleitz, F.; Do, T. O. Shape-Controlled Synthesis of Highly Crystalline Titania Nanocrystals, *ACS Nano* **2009**, *11*, 3737-3743.

(11) Wang, X.; Li, Y. Monodisperse Nanocrystals: General Synthesis, Assembly, and their Applications, *Chem. Comm.* **2007**, 2901-2910.

(12) Lou, X. W.; Archer, L. A.; Yang, Z. Hollow Micro-/Nanostructures: Synthesis and Applications, *Adv. Mater.* **2008**, *20*, 3987-4019.

(13) Ratke, L.; Voorhees, P. W. Growth and Coarsening: Ostwald Ripening in Material Processing, *Springer* **2002**, 117-118.

(14) Tang, J.; Alivisatos, A. P. Crystal Splitting in the Growth of Bi_2S_3, *Nano Lett.* **2006**, *6*, 2701-2706.

(15) Zhao, N. N.; Pan, D. C.; Nie, W.; Ji, X. L. *Two-Phase* Approach for the *Synthesis* of Shape-Controlled Colloidal *Zirconia Nanocrystals*, *J. Am. Chem. Soc.* **2006**, *128*, 10118-10124.

(16) Philippe, C.; et al. Erbium-doped fiber amplifiers (Optics and Photonics), *Academic Press* **1999**, USA.

(17) Solehmainen, K.; Kapulainen, M.; Heimala, O.; Polamo, M. Erbium-doped Waveguides Fabricated with Atomic Layer Deposition Method, *IEEE Photon Technol. Lett.* **2004**, *16*, 194-196.

(18) Michael, C. P.; Yuen, H. B.; Sabnis, V. A.; Johnson, T. J.; Sewell, R.; Smith, R.; Jamora, A.; Clark, A.; Semans, S.; Atanackovic, P. B.; Painter, O. Growth, Processing, and Optical Properties of Epitaxial Er_2O_3 on Silicon, *Optics Express* **2008**, *16*, 19649-19666.

(19) Sun, R. G.; Wang, Y. Z.; Zheng, Q. B.; Zhang, H. J.; Epstein, A. J. 1.54 μm Infrared Photoluminescence and Electroluminescence from an Erbium Organic Compound, *J. Appl Phys.* **2000**, *87*, 7589.

(20) Shuto, K.; Hattori, K.; Kitagawa, T.; Ohmori, Y.; Horiguchi, M. Erbium-doped Phosphosilicate Glass Waveguide Amplifier Fabricated by PECVD, *Electron. Lett.* **1993**, *29*, 139.

(21) Feng, W.; Sun, L.; Zhang, Y.; Yan, C. Solid-to-Hollow Single-Particle Manipulation of a Self-Assembled Luminescent $NaYF_4$:Yb,Er Nanocrystal Monolayer by Electron-Beam Lithography, *Small* **2009**, *5*, 2057-2060.

(22) Heer, S.; Kompe, K.; Gudel, H.; Haase, M. Highly Efficient Multicolour Upconversion Emission in Transparent Colloids of Lanthanide-Doped $NaYF_4$ Nanocrystals, *Adv. Mater.* **2004**, *16*, 2102-2105.

(23) Yang, J.; Li, C.; Quan, Z.; Zhang, C.; Yang, P.; Li, Y.; Yu, C.; Lin, J. Self-Assembled 3D Flowerlike Lu_2O_3 and $Lu_2O_3:Ln^{3+}$ (Ln = Eu, Tb, Dy, Pr, Sm, Er, Ho, Tm) Microarchitectures: Ethylene Glycol-Mediated Hydrothermal Synthesis and Luminescent Properties, *J. Phys. Chem. C* **2008**, *112*, 12777-12785.

(24) Yin, S.; Akita, S.; Shinozaki, M.; Li, R.; Sato, T. Synthesis and Morphological Control of Rare Earth Oxide Nanoparticles by Solvothermal Reaction, *J. Mater. Sci.* **2008**, *43*, 2234-2239.

(25) Wang, G.; Peng, Q.; Li, Y. Upconversion Luminescence of Monodisperse $CaF_2:Yb^{3+}/Er^{3+}$ Nanocrystals, *J. Am. Chem. Soc.* **2009**, *131*, 14200-14201.

(26) Han, K.; Zhang, Y.; Fang, Z.; Cheng, T.; Gao, M. A Simple Route to Preparation and Characterization of Er_2O_3 Microspheres, *Chemistry Letters* **2007**, *36*, 1124-1125.

(27) Wang, X.; Li, Y. Rare-Earth-Compound Nanowires, Nanotubes, and Fullerene-Like Nanoparticles: Synthesis, Characterization, and Properties, *Chem. Eur. J.* **2003**, *9*, 5627-5635.

(28) Nguyen, T. D.; Do, T. O. General Two-Phase Routes to Synthesize Colloidal Metal Oxide Nanocrystals: Simple Synthesis and Ordered Self-Assembly Structures, *J. Phys. Chem. C* **2009**, *113*, 11204-11214.

(29) Depner, S. W.; Kort, K. R.; Jaye, C.; Fischer, D. A.; Banerjee, S. Nonhydrolytic Synthesis and Electronic Structure of Ligand-Capped $CeO_{2-\delta}$ and CeOCl Nanocrystals, *J. Phys. Chem. C* **2009**, *113,* 14126-14134.

(30) Park, J.; An, K.; Hwang, Y.; Park, J. G.; Noh, H. J.; Kim, J. Y.; Park, J. H.; Hwang, N. M.; Hyeon, T. Ultra-Large-Scale Syntheses of Monodisperse Nanocrystals, *Nat. Mater.* **2004**, *3*, 891-895.

(31) Oaki, Y.; Imai, H. Chelation-Mediated Aqueous Synthesis of Metal Oxyhydroxide and Oxide Nanostructures: Combination of Ligand-Controlled Oxidation and Ligand-Cooperative Morphogenesis, *Chem. Eur. J.* **2007**, *13*, 8564-8571.

(32) Christensen, A. N. N.; Quezel, S. The Magnetic Structure of The Monoclinic Modification of ErOOH, *Solid State Communication* **1972**, *10*, 765-767.

(33) Assaaoudi, H.; Fang, Z.; Butler, I. S.; Kozinski, J. A. Synthesis of Erbium Hydroxide Microflowers and Nanostructures in Subcritical Water, *Nanotechnology* **2008**, *19*, 185606.

(34) Jun, Y. W.; Choi, J. S.; Cheon, J. Shape Control of Semiconductor and Metal Oxide Nanocrystals Through Nonhydrolytic Colloidal Routes, *Angew. Chem. Int. Ed.* **2006**, *45*, 3414-3439.

(35) An, K.; Kwon, S. G.; Park, M.; Na, H. B.; Baik, S. I.; Yu, J. H.; Kim, D.; Son, J. S.; Kim, Y. W.; Song, I. C.; Moon, W. K.; Park, H. M.; Hyeon, T. Synthesis of Uniform Hollow Oxide Nanoparticles through Nanoscale Acid Etching, *Nano Lett.* 2008, ***8***, 4252-4258.

(36) Ban, T.; Nakatani, T.; Uehara, Y.; Ohya, Y. Microstructure of Six-Pointed Starlike Anatase Aggregates, *Cryst. Growth Des.* **2008**, *8*, 935-940.

(37) Zhao, D.; Yang, Q.; Han, Z.; Sun, F.; Tang, K.; Yu, F. Rare Earth Hydroxycarbonate Materials with Hierarchical Structures: Preparation and Characterization, and Catalytic Activity of Derived Oxides, *Solid State Sciences* **2008**, *10*, 1028-1036.

(38) Nguyen, T. D.; Mrabet, D.; Do, T. O. Controlled Self-Assembly of Sm_2O_3 Nanoparticles into Nanorods: Simple and Large Scale Synthesis using Bulk Sm_2O_3 Powders, *J. Phys. Chem. C* **2008**, *112*, 15226-15235.

(39) Nguyen, T. D.; Do, T. O. Solvo-Hydrothermal Approach for the Shape-Selective Synthesis of Vanadium Oxide Nanocrystals and Their Characterization, *Langmuir* **2009**, *25*, 5322-5332.

(40) Nguyen, T. D.; Cao. D. T.; Dinh, T. N.; Do, T. O. A Novel Approach for Monodisperse Samarium Orthovanadate Nanocrystals: Controlled Synthesis and Characterization, *J. Phys. Chem. C* **2009**, *113*, 18584-18595.

(41) Nguyen, T. D.; Dinh, C. T.; Do, T. D. Monodisperse Samarium and Cerium Orthovanadate Nanocrystals and Metal Oxidation States on the Nanocrystal Surface, *Langmuir* **2009**, *25*, 11142-11148.

(42) Peng, Z. A.; Peng, X. Nearly Monodisperse and Shape-Controlled CdSe Nanocrystals via Alternative Routes: Nucleation and Growth, *J. Am. Chem. Soc.* **2002**, *124*, 3343-3353.

(43) Swami, G. T. K.; Stageberg, F. E.; Goldman, A. M. XPS Characterization of Erbium Sesquioxide and Erbium Hydroxide, *J. Van. Sci. Technol. A* **1984**, *2*, 767-770.

(44) Deng, Z.; Peng, B.; Chen, D.; Tang, F.; Muscat, A. J. A New Route to Self-Assembled Tin Dioxide Nanospheres: Fabrication and Characterization, *Langmuir* **2008**, *24*, 11089-11095.

(45) Que, W.; Zhou, Y.; Lam, Y. L.; Pita, K.; Chan, Y. C.; Kam, C. H. Luminescence Properties from Erbium Oxide Nanocrystals Dispersed in Titania/Organically Modified Silane Composite Sol-Gel Thin Films, *Appl. Phys. A* **2001**, *73*, 209-213.

(46) Devaraju, M. K.; Yin, S.; Sato, T. A Rapid Hydrothermal Synthesis of Rare Earth Oxide Activated $Y(OH)_3$ and Y_2O_3 Nanotubes, *Nanotechnology* **2009**, *20*, 305302.

(47) Yin, S.; Shinozaki, M.; Sato, T. Synthesis and Characterization of Wire-like and Near-Spherical Eu_2O_3-Doped Y_2O_3 Phosphors by Solvothermal Reaction, *Journal of Luminescence* **2007**, *126*, 427-433.

Table 6.3.1. Synthesis Conditions, Crystal Phases, and Morphologies of Monoclinic ErOOH and cubic Er_2O_3 Micro- and Nanostructures.[a]

Sample	Precursor (mM)	Ethanol mL	Water mL	Decanoic acid M	Temperature °C	Product	Structure	Shape	Size nm
1	7.63, Er^{3+}	30	10	0.038	120	ErOOH	monoclinic	quasi-sphere	3000
2	7.63, Er^{3+}	30	10	0.038	140	ErOOH	monoclinic	aggregated-sphere	3000
3	7.63, Er^{3+}	30	10	0.038	160	Er_2O_3	cubic	wrinkle-sphere	3000
4	7.63, Er^{3+}	30	10	0.038	180	Er_2O_3	cubic	flower	3000
5	7.63, Er^{3+}	30	10	0.152	120	ErOOH	monoclinic	wire-bundle	100x400
6	7.63, Er^{3+}	30	10	0.152	140	ErOOH	monoclinic	straw-sheaf	150x700
7	7.63, Er^{3+}	30	10	0.152	160	Er_2O_3	cubic	broom	150x350
8	7.63, Er^{3+}	30	10	0.076	180	Er_2O_3	cubic	flower	3000
9	7.63, Er^{3+}	30	10	0.114	180	Er_2O_3	cubic	dog-bond	18
10	7.63, Er^{3+}	30	10	0.152	180	Er_2O_3	cubic	sphere	18
11	7.63, Er^{3+}	30	10	0.190	180	Er_2O_3	cubic	dot	3
12	7.63, Er^{3+}	40	0	0.152	180	Er_2O_3	cubic	core	3
13	7.63, $Er(OH)_3$	30	10	0.152	180	Er_2O_3	cubic	dot	4
14	76.25, $Er(OH)_3$	30	10	0.152	180	Er_2O_3	cubic	wire	80x150
15	152.50, $Er(OH)_3$	30	10	0.152	180	Er_2O_3	cubic	rod	250x1000

(a) All samples were synthesized by hydro-solvothermal process for 24 h.

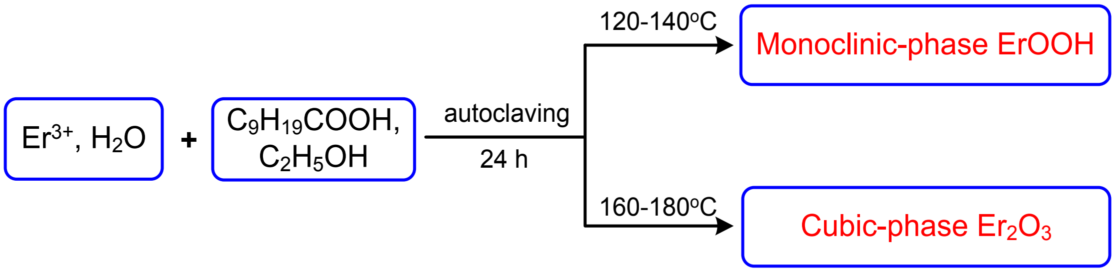

Scheme 6.3.1. A general synthetic procedure for controlled size, shape, and phase of erbium-compound micro- and nanostructures.

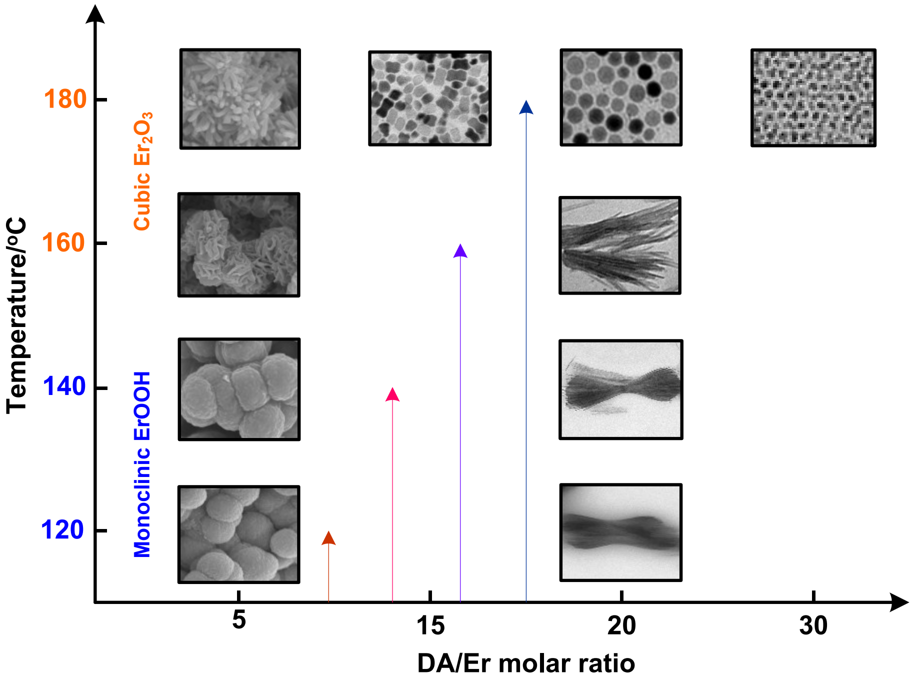

Scheme 6.3.2. ErOOH and Er_2O_3 micro- and nanostructures with different sizes, shapes, and phases obtained as a function of the reaction temperature and decanoic acid/erbium molar ratio.

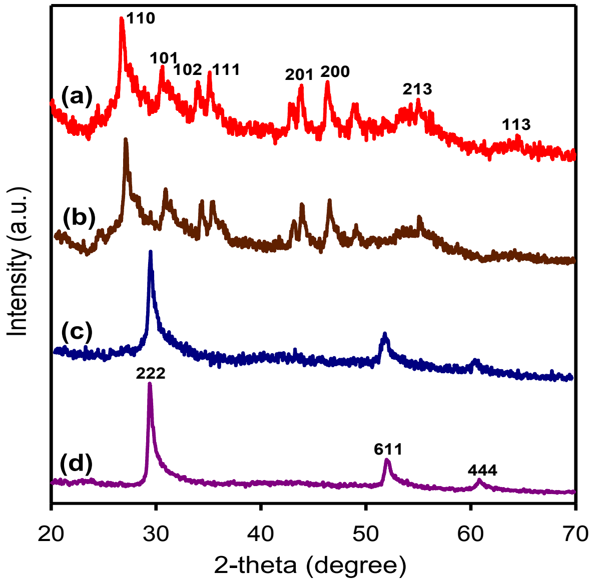

Figure 6.3.1. XRD patterns of the erbium-compound micro/nanostructures synthesized at different reaction temperatures: (a) monoclinic ErOOH, 120 °C; (b) monoclinic ErOOH, 140 °C; (c) cubic Er_2O_3, 160 °C; and (d) cubic Er_2O_3, 180 °C.

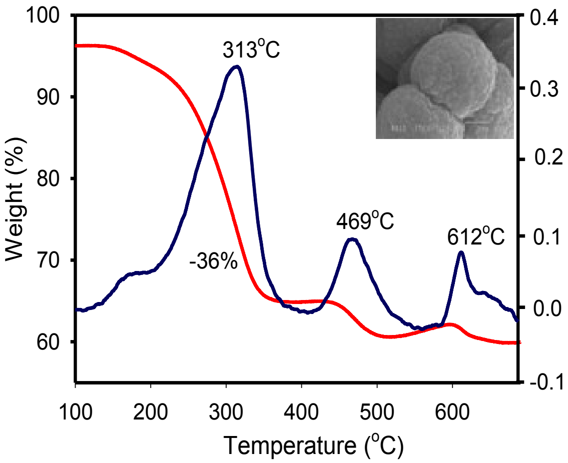

Figure 6.3.2. TGA-DTA curves of decanoic acid-capped ErOOH quasi-microspheres (sample 1).

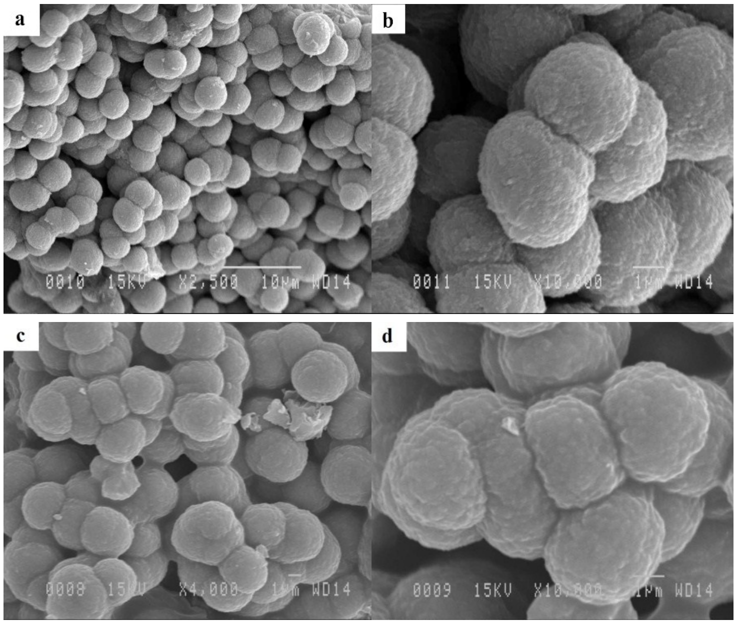

Figure 6.3.3. Different-magnification SEM images of the ErOOH structures synthesized at different reaction temperatures with the DA/Er ratio of 5/1: (a,b) quasi-microspheres, 120 °C; (c,d) attached microspheres, 140 °C.

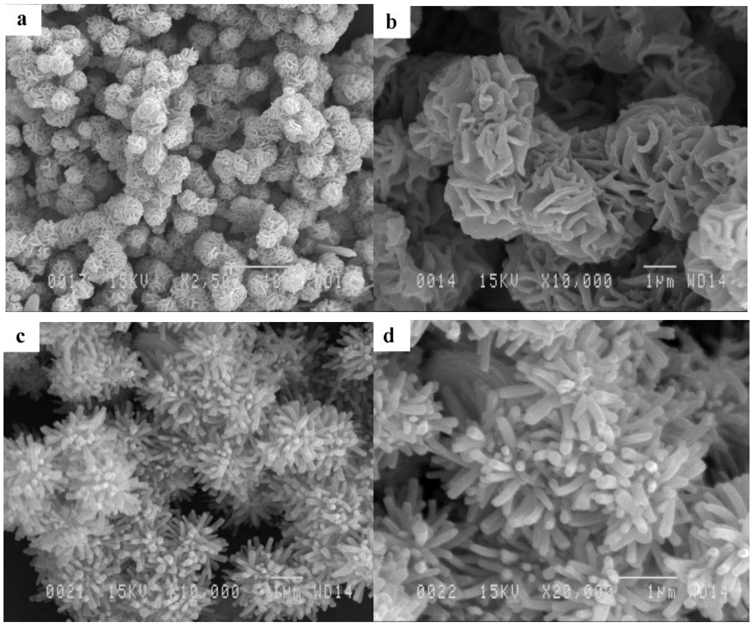

Figure 6.3.4. Different-magnification SEM images of the Er_2O_3 structures synthesized at different reaction temperatures with the DA/Er ratio of 5/1: (a,b) wrinkle-surfaced microspheres, 160 °C; (c,d) microflowers, 180 °C.

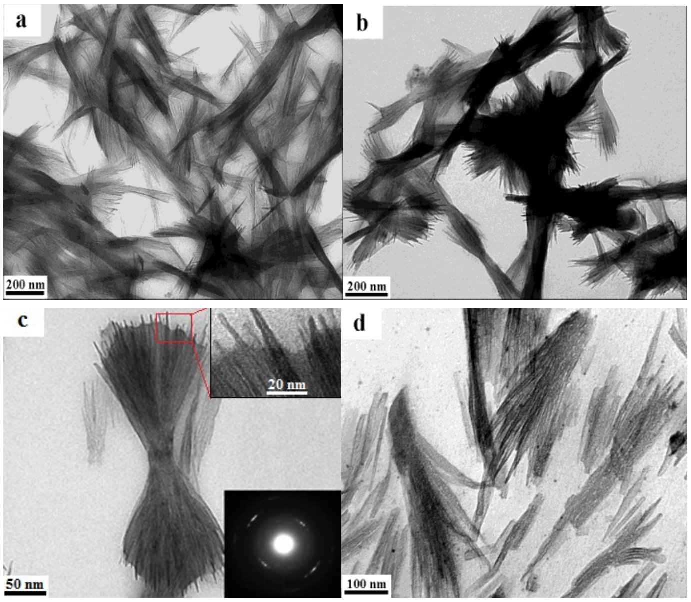

Figure 6.3.5. TEM images of the erbium-compound nanostructures synthesized with the DA/Er molar ratio of 20:1 at different reaction temperatures: (a) ErOOH wire-nanobundles, 120°C; (b,c) ErOOH straw-nanosheaves, 140°C, inset SAED; d) Er_2O_3 broom-nanobundles, 160°C.

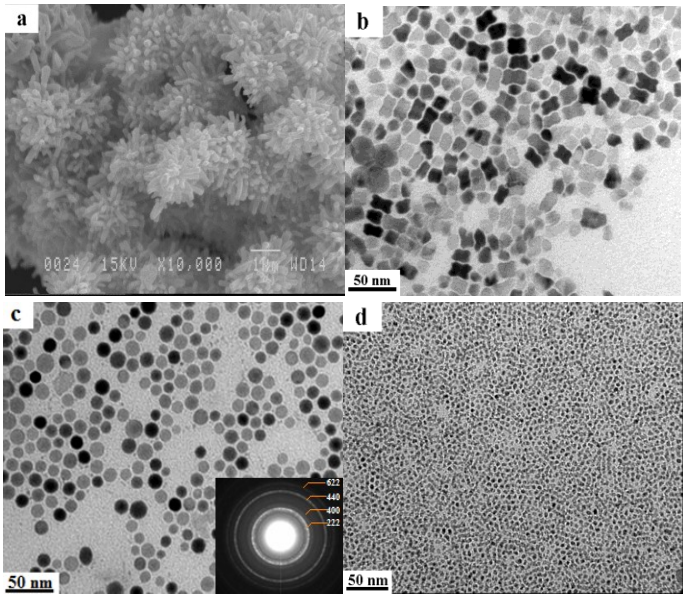

Figure 3.3.6. SEM/TEM images of the Er_2O_3 micro- and nanotructures synthesized at 180 °C, ethanol/water ratios of 30/10 (mL) with different DA/Er molar ratios: (a) 3 µm microflowers, DA/Er = 10:1; (b) 18 nm dog-bondlike nanocrystals, DA/Er = 15:1; (c) 18 nm nanospheres, DA/Er = 20:1, inset SAED; (d) 3 nm nanodots, DA/Er = 30:1.

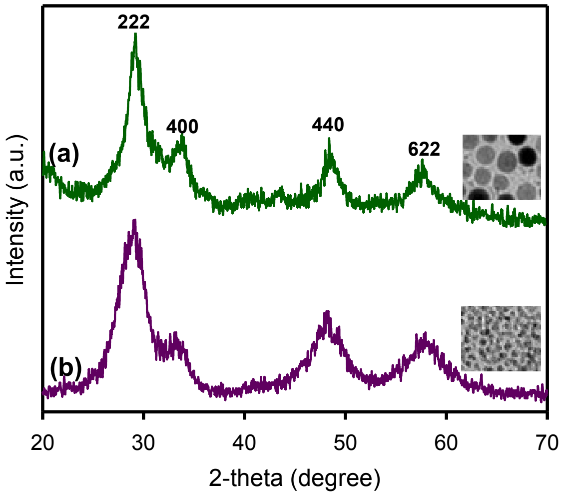

Figure 6.3.7. XRD patterns of (a) nanospheres and (b) nanodots of Er_2O_3

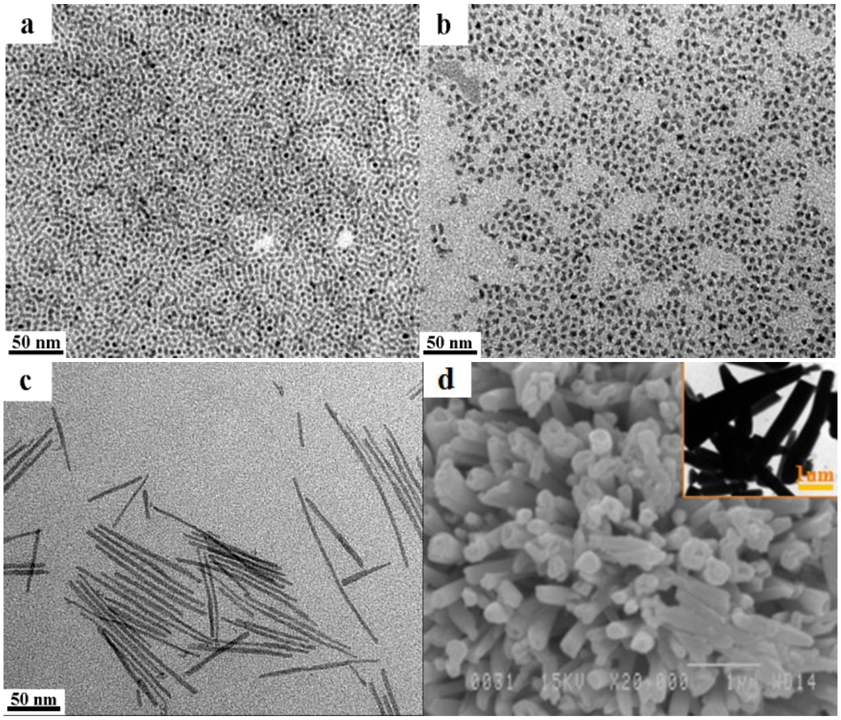

Figure 3.6.8. TEM/SEM images of the Er_2O_3 crystals synthesized with DA/Er = 20:1 at different reaction conditions: (a) 3 nm nanocores, $[Er(NO_3)_3]$ = 7.63 mM without water; (b) 4 nm nanodots, $[Er(OH)_3]$ = 7.63 mM; (c) 80 nm x 150 nm nanowires, $[Er(OH)_3]$ = 76.25 mM; (d) 250 nm x 1000 nm microrods, $[Er(OH)_3]$ = 152.50 mM.

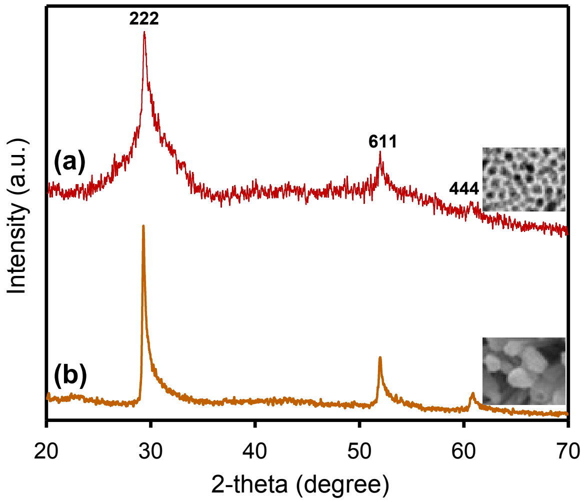

Figure 6.3.9. XRD patterns of (a) nanocores and (b) microrods of Er_2O_3

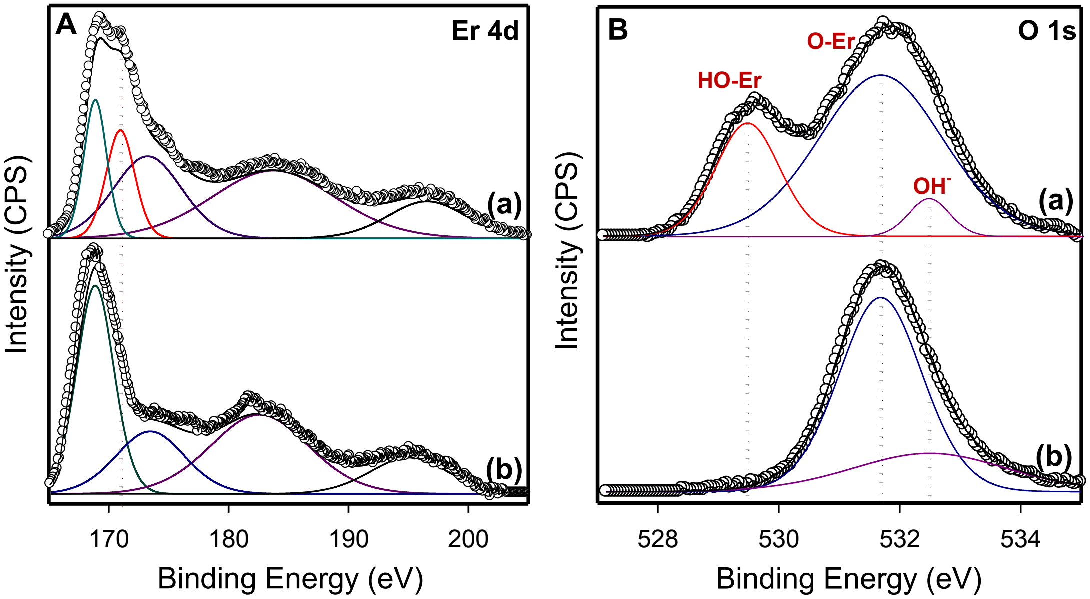

Figure 6.3.10. High-resolution (A) Er 4d and (B) O 1s XPS spectra of (a) 3 μm ErOOH quasi-microspheres (sample 1) and (b) 3 μm Er_2O_3 microflowers (sample 4).

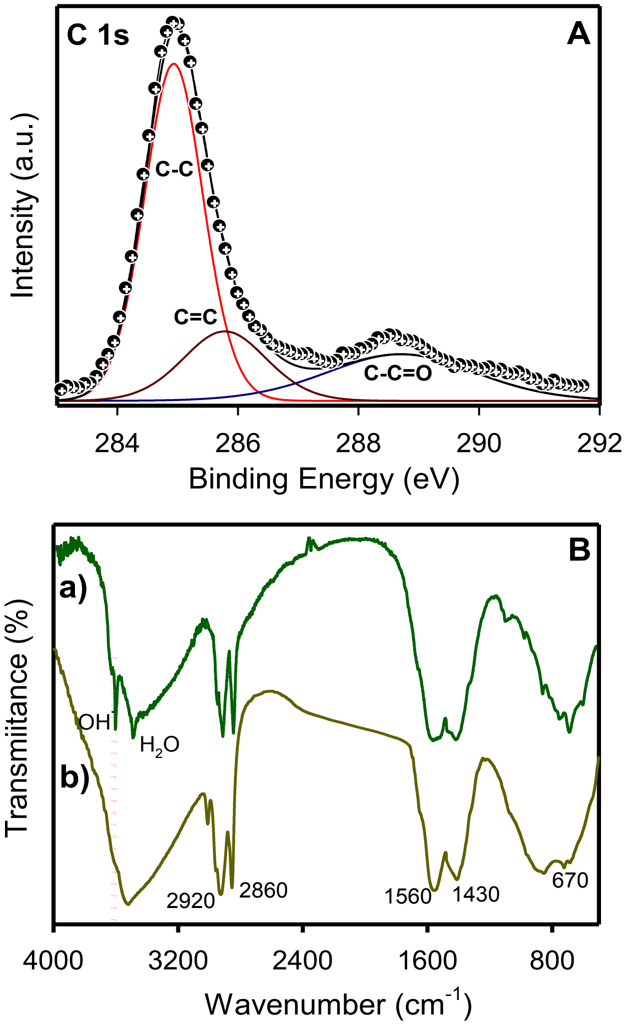

Figure 6.3.11. (A) C 1s XPS spectrum of DA-capped ErOOH quasi-microspheres; (B) FTIR spectra of (a) DA-capped ErOOH quasi-microspheres (sample 1) and (b) DA-capped Er_2O_3 microflowers (sample 4).

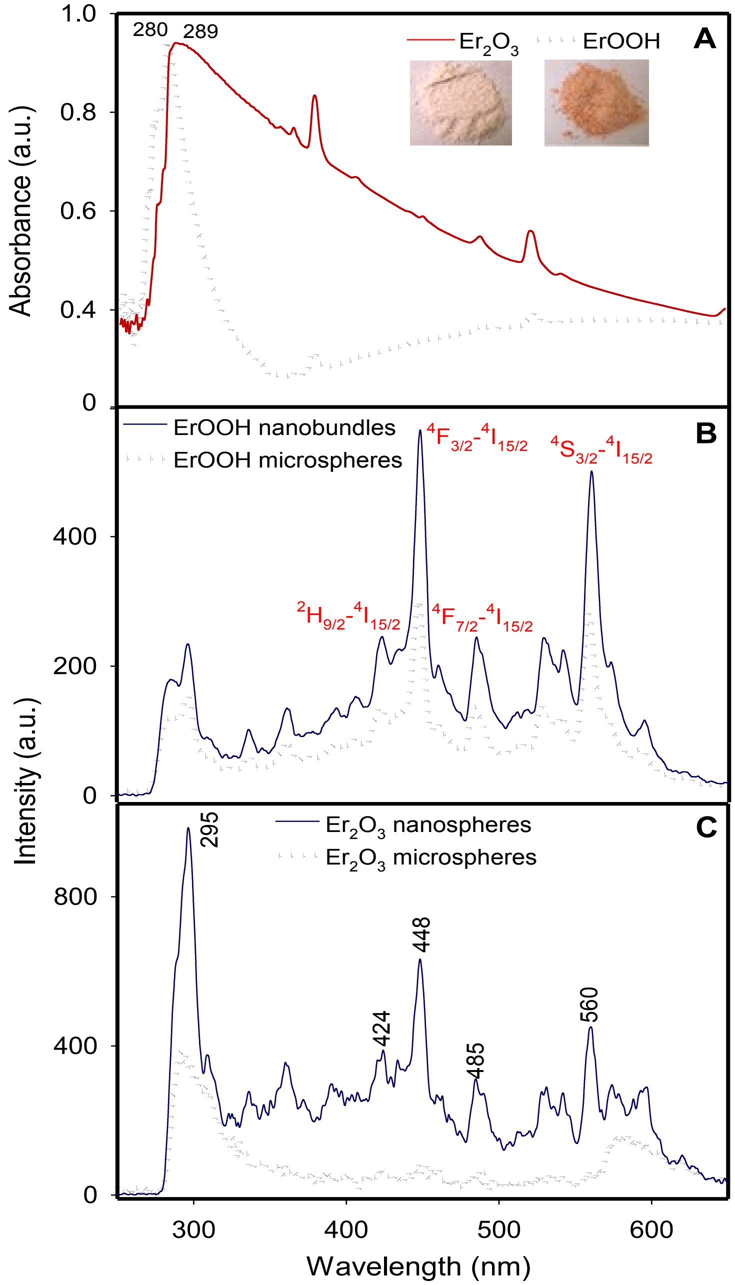

Figure 6.3.12. (A) UV/vis absorption spectra of 3 μm ErOOH quasi-microspheres (sample 1) and 3 nm Er_2O_3 nanospheres (sample 10), inset pictures show color change of the final products at different synthesis temperatures. Photoluminescence (PL) spectra of: (B) 100 nm x 400 nm ErOOH wire-nanobundles (sample 5) and 3 μm ErOOH quasi-microspheres (sample 1); (C) 18 nm Er_2O_3 nanospheres (sample 10) and 3 μm Er_2O_3 microflowers (sample 4).

Chapter 7 Size- and Shape-Controlled Synthesis and Self-Assembly of Mixed Oxide Nanocrystals

7.1. A Novel Approach for Monodisperse Samarium Orthovanadate Nanocrystals: Controlled Synthesis and Characterization

Thanh-Dinh Nguyen,[a] Cao-Thang Dinh,[a] Dinh-Tuyen Nguyen,[b] and Trong-On Do*[a]

Department of Chemical Engineering, Laval University, Quebec G1K 7P4 Canada,[a] and Institute of Chemistry, Vietnamese Academy of Science and Technology (VAST) [b]

Published in *J. Phys. Chem. C* **2009**, *113,* 18584-18595; *Langmuir* **2009**, *25*, 11142-11148

Abstract

A new solvothermal approach has been developed for the synthesis of monodisperse and well-crystallized $SmVO_4$ nanocrystals with different morphologies from the reaction of $Sm(OA)_3$ and $VO_4(TOA)_3$ complexes in toluene in the presence of surfactant (oleylamine or oleic acid) through a solvothermal pathway. The present solvothermal approach is simple, reproduction, and relatively mild reaction temperature. The obtained $SmVO_4$ nanocrystals were characterized by means of TEM, SAED, XRD, EDS, XPS, UV-visible, TGA-DTA, FTIR, BET techniques. The SAED and XRD patterns confirmed that the synthesis of the $SmVO_4$ nanocrystals is single-crystalline tetragonal structure. The size, shape, and aspect ratio of products can be readily controlled by adjusting the reaction parameters such as the nature and amount of surfactant, reaction temperature, and the concentration of metal complex precursors. The $SmVO_4$ nanocrystals with spherical and hexagonal shapes were obtained by using oleylamine or oleic acid as nonselective and selective surfactant, respectively, under the same synthesis conditions. Furthermore, the average particle size is tunable from 30 to 3 nm by increasing the oleylamine concentration from 0.025 to 0.43 M in the synthesis solution. By increasing the reaction temperature from 150 to 180 ^{o}C, $SmVO_4$ NCs can converted from cubic-shaped

$SmVO_4$ to uniform nanospheres. The shape evolution from nanocores to nanowires can be also obtained by increasing the metal complex precursor concentration; it is associated with the increase of chemical potential in the reaction solution. The XPS results revealed only one oxidation state for Sm^{3+} and V^{5+} on the $SmVO_4$ nanocrystal surface, even after calcinations compared to two oxidation states (e.g., Sm^{2+}/Sm^{3+} and V^{4+}/V^{5+}) of the single samarium oxide and vanadium oxide NPs, respectively. Our synthetic approach can be further extended to the synthesis of other uniform rare earth orthovanadate, molybdate, and tungstate nanocrystals.

7.1.1. Introduction

The synthesis of mixed metal oxide nanocrystals (NCs) composed of two or more different components has attracted particular interest due to the possibility of mergence of material properties together, which are not usually attainable in single-component nanocrystals.[1-3] Monodisperse mixed oxide nanocrystals with small dimensions are often referred to as 'artificial atoms' with novel properties because of their atomic-like behaviours which are not achieved by their bulk counterparts.[4,5] The synthesis of monodisperse mixed oxide nanocrystals with controllable morphologies is thus a key goal in modern materials chemistry and has attracted rapidly growing interest in recent years.[6-10] Furthermore, because of size- and shape-dependant properties of nanocrystals, a precise control over size and shape can lead to the formation of materials with the unique physical and chemical properties.[11-13] For example, zero- and one-dimensional (0D/1D) nanostructures such as nanospheres and nanowires show great promise in many applications.[14-16] In the bottom-up syntheses, the sterically diffusive kinetics and selective binding or nonbinding of surfactant molecules to different faces of the growing nanocrystal can also control the product's morphology due to afford the possibility of breaking the limitation of crystal growth dynamically.[17-21] In some cases, the formation of the intrinsic anisotropic nanocrystals is found to be a highly kinetics-driven process, which occurs far away from the thermodynamic equilibrium, and must be overdriven by high precursor monomer concentrations.[22]

The $SmVO_4$ nanocrystals have been extensively studied as a promising material for recent years, because they exhibit unique properties and applications in many fields such as catalysis,[23] gas sensors,[24] optical polarizers,[25] lithium intercalated electrode,[26] thin film phosphors,[27] laser host materials,[28] solar cells,[29] and unusual magnetic materials.[30] For example, these $SmVO_4$ nanocrystals exhibit high activity and selectivity as catalysts for many organic reactions such as oxidative dehydrogenation of alkanes, olefins, ethylbenzene, and oxidation of hydrogen sulfide to elemental sulphur.[31-35] Their high catalytic activity has been correlated to the redox cycle between V^{5+} and V^{4+} in the $SmVO_4$ crystal lattice and cation vacancies sites, which occurs during the oxidation dehydrogenation.[35,36] The unstable surface active sites are oxygen vacancies associated with V^{4+} ions. The activation of oxygen species generating the adsorbed O_2 or O^- takes place on the V^{4+} sites. The oxidation selectivity of the rare earth orthovanadates ($REVO_4$) is higher than that of vanadia might be explained by more difficult removing a lattice oxygen from the RE-O-V bond in $REVO_4$ than from the V-O-V bond in V_2O_5.[37] The dehydrogenation yield of $SmVO_4$ is much better than that of the corresponding single oxide catalysts (vanadia and samaria), which might be due to the reducibility difference between vanadium and samarium cations.[38] Consequently, oxygens in $SmVO_4$ lattice are less labile than those of both vanadia and samaria.[38] Furthermore, numerous studies not only demonstrated that mild reactions are structure sensitive, but also highlight that particle size and shape may play a key role in defining activity and selectivity in those catalytic processes.[39-41]

To date, most of the strategies for the synthesis of $SmVO_4$ nanocrystals are focused on the solid-state reaction and hydrothermal methods. The conventional solid-state reaction was used for the synthesis of these materials by heating the constituent bulk single metal oxide powders in stoichiometric ratio at relatively high temperature. For example, Saito et al.[42] synthesized the $SmVO_4$ crystals by heating at 1000-1100 °C after mechanical milling the mixture of single oxides of Sm_2O_3 and V_2O_5 powders. Nevertheless, this route was hard to control over the kinetics of nucleation-growth process, often giving particle agglomeration, low chemical homogeneity and poor crystallinity. The solution-based route, in contrast, was considered as one of the most convenient methods for the controlled synthesis of $SmVO_4$ nanocrystals. For example, Sun et al.[43] reported that $SmVO_4$ nanorods can be formed in the absence of surfactant or template agents using inorganic salts as raw materials. Ramanan et al.[44] had also directly precipitated these salts for the formation of the flaky-shaped $SmVO_4$ microcrystals. The synthesis of regular-square shaped $SmVO_4$ nanocrystals from the reaction of samarium nitrates and ammonium vanadates in water/ethanol/oleic acid system was recently published by Li group.[45] Despite these exciting developments, the precise size and shape manipulation of uniform $SmVO_4$ nanocrystals, particularly spherical- and wire-like morphologies, as well as the investigation of their oxidation states have not been reported so far.

It can thus be expected that developing a low cost and convenient method for the synthesis of monodisperse $SmVO_4$ nanocrystals with controlled well-defined sizes, shapes and structure opens enormous possibilities for engineering catalysts with enhanced the activity and selectivity.[46,47] For this purpose, the solvothermal method is widely accepted as a valuable process used for the preparation of such materials with well-controlled morphology, crystal growth orientation, and structural properties due to the kinetic equilibrium between dissolution and decomposition of the precursors in organic media at relatively mild reaction temperature.[48-50] Recently, our group have developed a solvothermal approach for the shape-selective synthesis of vanadium oxide nanocrystals through the decomposition of vanadium diperoxo-tetraalkylammonium complexes in the toluene/aliphatic amine system. It was found that the desired size and shape can be controlled by different synthesis parameters such as steric ligands of complexes, alkyl chain lengths of capping agents as well as the nature of solvent.[51]

In this present study, we report a new approach for the controllable synthesis of monodisperse and well-crystallized $SmVO_4$ mixed oxide nanocrystals with different shapes such as spherical, hexagonal, core, and wire from the reaction of $Sm(OA)_3$ and $VO_4(TOA)_3$ complexes in toluene in the presence of surfactant (oleylamine or oleic acid) through a solvothermal pathway. $Sm(OA)_3$ and $VO_4(TOA)_3$ complex precursors were pre-synthesized from the reaction of the inorganic sources and organic ligands. The obtained nanocrystals are highly dispersible in nonpolar organic solvents. The effect of the nature and amount of surfactant as well as metal complex precursor concentration on size and shape of the resulting $SmVO_4$ nanocrystals is studied. The possible mechanism for the formation of the nanocrystals with various sizes and shapes is also proposed.

7.1.2. Experimental Section

Starting materials: All chemicals were used as received without further purification. Samarium nitrate hexahydrate ($Sm(NO_3)_3.6H_2O$, 99.9%), vanadium pentaoxide (V_2O_5, 99.6%), tetraoctylammonium bromide ($[CH_3(CH_2)_7]_4NBr$ or TOABr, ≥98%), potassium oleate ($C_{17}H_{34}COOK$ or KOA 40 wt.% paste in water), oleylamine ($C_{18}H_{35}NH_2$ or OM, tech. grade, 70%), oleic acid ($C_{18}H_{35}COOH$ or OA, tech. grade, 90%), were purchased from Sigma-Aldrich. Sodium hydroxide (NaOH, 97.0%) and all solvents used such as toluene, ethanol were of analytical grade and purchased from Reagent ACS.

Synthesis of $SmVO_4$ nanocrystals

Preparation of $Sm(OA)_3$ complexes: To prepare rare earth oleate complexes, an organic solution was produced from adding 40 mL of toluene into the ethanol solution (10 mL) containing potassium oleate (KOA, 6.4-24.8 g or 0.008-0.031 mol). The organic solution was mixed to 30 mL of a $Sm(NO_3)_3.6H_2O$ aqueous solution (0.086-0.346 M) with Sm^{3+}:OA^- molar ratio of 1:3, and then transfered to a flask. The two-phase mixture was heated to 70 °C for 60 min with stirring vigorously and the organic solution became light yellow after being reacted, indicating the occurrence of the coordinated reaction of Sm^{3+} and OA^- for the complex formation. Subsequently, the upper deep orange supernatant toluene solution (40 mL) containing $Sm(OA)_3$ complexes (0.065 - 0.260 M) was isolated.

Preparation of $VO_4(TOA)_3$ complexes: 0.24-0.96 g (0.0013-0.0052 mol) of commercial bulk V_2O_5 powders was dissolved in 20 mL of an aqueous NaOH solution and vigorously stirred at the room temperature for 30 min. V_2O_5 powders were completely dissolved in the dilute NaOH solution to give a homogeneous light orange Na_3VO_4 aqueous solution (0.133 - 0.520 M). Then, 40 mL of toluene solution (0.040-0.159 M) containing a cationic phase-transfer reagent ($[CH_3(CH_2)_7]_4NBr$ or TOABr, 0.87-3.48 g) was added to the above solution and the VO_4^{3-}:TOA^+ molar ratio is close to 1:3. The two-phase mixture was vigorously stirred at room temperature. After 30 min, VO_4^{3-} anions in aqueous phase were completely extracted into the toluene phase, and a light orange toluene solution was observed. Subsequently, the upper light orange supernatant toluene solution (40 mL) containing $VO_4(TOA)_3$ complexes (0.065-0.260 M) was isolated.

Synthesis of $SmVO_4$ nanocrystals: Typically, two above toluene solution containing $Sm(OA)_3$ and $VO_4(TOA)_3$ complexes (0.065 - 0.260 M) were mixed together with the Sm:V molar ratio of 1:1, and 1-20 mL of oleylamine (OM) or oleic acid (OA) (0.025-0.43 M) was added under stirring. The reaction solution was transferred into a 140-mL Teflon-lined stainless steel autoclave and was heated at 180 °C for 16 h in an oven. After the reaction, the autoclave was cooled in tap water, and the obtained products were easily precipitated by excess ethanol and re-dispersed preferably in nonpolar solvents (e.g., toluene, hexane, etc.). The precipitation-redispersion process was repeated several times to purify the producing $SmVO_4$ nanocrystals. The different reaction conditions such as the nature and amount of surfactant and the metal complex precursor concentration were tested to control the sizes and the shapes of the $SmVO_4$ nanocrystals. The obtained samples for all of the measurements shown in this article are directly from synthesis without any size-selection process.

7.1.3. Results and Discussion

In this study, $SmVO_4$ nanocrystals were synthesized using pre-synthesized $Sm(OA)_3$ and $VO_4(TOA)_3$ complexes as precursors, oleylamine or oleic acid as capping surfactants, and toluene as solvent. Monodisperse $SmVO_4$ nanocrystals were obtained effectively through the synthetic reaction of the two pre-synthesized complex precursors, $Sm(OA)_3$ and $VO_4(TOA)_3$, with the Sm/V molar ratio of 1 in toluene containing surfactant at 180 ^{o}C for 16 h. Their size and shape were also controlled by the nature and amount of capping surfactant as well as the metal complex precursor concentration. The formation of monodisperse $SmVO_4$ nanocrystals with different shapes are shown in Scheme 1 (see also Experimental Section). The detailed synthesis conditions, and various sizes and shapes of the obtained nanocrystals are summarised in Table 7.1.1. The synthetic approach for the formation of $SmVO_4$ nanocrystals consists of two steps: i) the pre-synthesis of $Sm(OA)_3$

and $VO_4(TOA)_3$ complex precursors from the corresponding inorganic sources ($Sm(NO_3)_3$ and bulk V_2O_5 powders) and organic ligands (tetraoctylammonium bromide and potassium oleate), which are depicted by equations 1 and 2; (ii) the formation of $SmVO_4$ nanocrystals from the pre-synthesized $Sm(OA)_3$ and $VO_4(TOA)_3$ complexes in toluene containing capping molecules under solvothermal treatment as described in equation 3 (see Experimental Section).

$$Sm^{3+}{}_{(aqueous)} + 3OA^{-}{}_{(toluene)} \rightarrow Sm(OA)_3{}_{(toluene)} \qquad (1)$$

$$VO_4{}^{3-}{}_{(aqueous)} + 3TOA^{+}{}_{(toluene)} \rightarrow VO_4(TOA)_3{}_{(toluene)} \qquad (2)$$

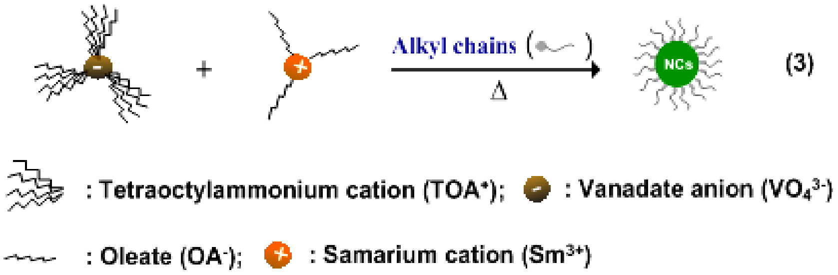

The formation of the complex precursor solids, $Sm(OA)_3$ and $VO_4(TOA)_3$ (after toluene elimination) was supported by the FTIR and TGA results, (Figure 7.1.1). The FTIR spectra of the $Sm(OA)_3$ and $VO_4(TOA)_3$ complexes show the absorption bands at 745 cm^{-1} and 500-700 cm^{-1} which are assigned to the stretching vibrations of the Sm-O and V-O bonds, respectively.[51,52] The well-defined IR bands at 2925-2860 cm^{-1} are characteristic of the symmetric, asymmetric methyl and methylene stretches of the alkyl chains. The absorption bands at 1465-1550 cm^{-1} are attributed to the stretching vibrations of the carboxylate groups of oleate ligands (Figure 7.1.1A-a).[52] As shown in Figure 7.1.1A-b, an IR band at 1455 cm^{-1} is attributed to the stretching vibrations of the ammonium cation groups ($\equiv N^+$) of TOA^+.[51] Furthermore, the TGA data for these $Sm(OA)_3$ and $VO_4(TOA)_3$ complex solids exhibit a mass loss of 21.5% and 23.0%, respectively, in the temperature range 150-470 ^oC, which are attributed to the decomposition and combustion of organic

OA^- and TOA^+ ligands, respectively. This indicates the formation of the $Sm(OA)_3$ and $VO_4(TOA)_3$ complexes.

To study the effect of the nature of surfactant on the size and shape of nanocrystals, two surfactants with different functional groups such as amines or acids having different binding strengths were used. In general, oleylamine possesses a stronger binding strength (e.g., as nonselective surfactant) to the particle surface compared to that of oleic acid (e.g., as selective surfactant). In this work, we used either oleylamine (OM) or oleic acid (OA), while the other reaction conditions remained unchanged. $SmVO_4$ nanocrystals were typically synthesized by mixing the equimolar quantity of the two pre-synthesized complexes ($[Sm(OA)_3] = [VO_4(TOA)_3] = 0.065$ M) in toluene containing capping surfactant (0.129 M) at 180 °C for 16 h. The reaction mixture consisted of the corresponding 4:1 molar ratio of surfactant and (Sm+V) complex precursors.

Figure 7.1.2 displays TEM images of the $SmVO_4$ nanocrystals with two different magnifications obtained using two different surfactants (e.g., oleylamine and oleic acid), and the corresponding SAED patterns. When oleylamine was used, (see Figures 7.1.2a_1,a_2), nanospheres with ~17 nm in diameter were obtained. However, using oleic acid as capping surfactant instead of oleylamine under the same synthesis conditions, hexagonal-like $SmVO_4$ nanocrystals with no significant change in particle size (~17 nm in diameter) were formed (Figures 7.1.2b_1,b_2). Both nanospheres and nanohexagons exhibited a high uniformity and were assembled to form the ordered nanostructures. The SAED patterns taken from individual spherical and hexagonal nanocrystals are shown in Figure 7.1.2a_3,b_3. The SAED results revealed that both the samples are indexed to a tetragonal $SmVO_4$ single crystal with strong spots originating from the (101), (200), (112), and (312) planes which are consistent with the XRD results (see below). It is clear that capping surfactants have distinct effects on the shape of the final product during the crystal-growth process depending on their nature, as also depicted in Figure 7.1.2c. Furthermore, when extending reaction time (180 °C for 24 h instead of 16 h), the morphology of both the spherical and hexagonal nanocrystal products did not change significantly, however, a broadening of the size distribution was observed. The particle size distributions further broadened suggesting the desired balance between nucleation and growth in these reaction conditions.[53]

Figure 7.1.3 show the X-ray diffraction (XRD) patterns of the as-synthesized $SmVO_4$ nanospheres and nanohexagons. Both samples display the XRD peaks which are well indexed to tetragonal zircon-type structure with lattice contents of $SmVO_4$: $a = b =$ 7.265 Å, $c = 6.389$ Å (*Fm*3h*m*, JCPDS No. 17-0876).[54] No XRD peaks correspond to single metal oxides of V_2O_5[51] and Sm_2O_3[52] was detected indicating that the pure tetragonal zircon-type structure of $SmVO_4$ nanocrystals can be achieved by this method. The well-resolved diffraction and intense broadening of the peaks indicate a high crystallinity and a small particle size of the nanocrystals products. The average particle size of these $SmVO_4$ nanocrystals calculated from the (200) peak[55] using Scherrer formular are ~13.5 nm which is consistent with the TEM results. It can be also concluded that the formation of the pure tetragonal $SmVO_4$ phase results in the complete reaction of the 1:1 ratio of Sm^{3+} cation and VO_4^{3-} anion monomers in the bulk solution during the synthesis.

The shape of $SmVO_4$ could be controlled by the synthesis temperature. TEM images, SEAD patterns, and particle size distribution (PSD) diagrams of the samples synthesized solvothermally at 150 ºC and 180 ºC for 16 h are shown in Figures 7.1.4. Nearly cubic-shaped $SmVO_4$ nanocrystals with an average diameter of 15 nm were found at 150 °C. When the synthesis temperature increased to 180 °C for 16 h, both uniform $SmVO_4$ nanospheres were observed, however, the diameter is unchanged. The color of synthesis solution changed from light-yellow to brown when increasing the reaction temperature from 150 to 180 °C illustrating the shape transformation of these samples. The inset SAED patterns taken from single particle are also indexed to a tetragonal $SmVO_4$ and $CeVO_4$ single crystal with strong ring patterns from the (200), (112), (301), (312), and (420) planes which are consistent with the XRD results. PSD diagrams of these samples were obtained from the statistical treatment of particle diameters from representative TEM images, as shown in Figures 7.1.4. It is observed that $SmVO_4$ particles become uniformer and PSD becomes narrower with increasing reaction temperature. This feature can be rationalized considering that the isotropic growth of the particles occurs by the recrystallization process.

The transformation of both cubic-shaped $SmVO_4$ NCs into uniform nanospheres, while preserving the particle size by increasing synthesis temperature from 150 ºC to 180 ºC can be explained by Wuff facets theory. Because no monomer precursors were added during the synthesis, at the relatively low reaction temperature (e.g., 150 ^oC), the cubic-shaped $SmVO_4$ nanocrystals were formed in the anisotropic growth of high-energy crystal faces owing to high monomer metal concentration in bulk solution.[26] The differences in cubic and round shapes of the $SmVO_4$ nanocrystals, respectively, should result from the different nature of their corresponding rare earth metals. At higher synthesis temperature (e.g., 180 ^oC), the transformation of both the cubic- and round-shaped nanocrystals into uniform nanospheres results in the depletion of remaining metal monomer concentration in bulk solution to a level lower than that required for a given anisotropic shapes. Consequently, the monomers of the dissolved crystals, which may occur preferably at high energy faces, could move to the low energy faces of the cubic and round-shaped nanocrystals because of the differences in chemical potential between different crystal faces. As a result, the corners and the tips of the cubic-shaped $SmVO_4$ nanocrystals were “smoothed” which leads to the formation of stable nanospheres.

To investigate the role of oleylamine (OM) in the formation of $SmVO_4$ nanoparticles, one synthesis without OM in the bulk solution were carried out. Without OM, only irregular nanocrystals with aggregated pearl-chain-like structures were formed. Furthermore, these nanocrystals were not dispersed in nonpolar solvents indicating also their polyparticle sizes. However, an appropriate amount of surfactant (0.025-0.43 M) was added to the synthesis solution, monodisperse nanocrystals with controlled size can be obtained depending on the OM concentration. To gain further insight into the mechanistic aspect of this process, a series of experiments was performed with different oleylamine (OM) concentrations in the synthesis solution: 0.025, 0.060, 0.129, 0.230, 0.034, and 0.43 M, corresponding to the OM/(Sm+V) molar ratios (denoted as OM/P) of 0.8, 2, 4, 8, 12, and 17, while the other components and reaction conditions remained unchanged (e.g., $[Sm(OA)_3] = [VO_4(TOA)_3] = 0.065$ M, 80 mL toluene, and at 180 ^oC for 16 h). It is found that the $SmVO_4$ nanocrystal size varies as a function of OM concentration. Figure 7.1.5 shows representative TEM images of these samples varying from ~30 to ~3 nm. At low

OM concentrations in the synthesis solution, for example, OM/P = 0.8, irregular particles with an average diameter of 30 nm were observed (Figure 7.1.5a). When the OM/P ratio was increased to 2, uniform 20 nm-sized nanospheres in company with some irregularly large spheres were found (Figure 7.1.5b). When the OM/P ratio reached 4, the exclusive formation of uniform nanospheres with an average diameter of 17 nm is produced (Figure 7.1.5c). Furthermore, as the OM/P ratio increased from 4 to 8, 12, and then 17, the spherical particle size gradually decreased from 17 nm to 10 nm, 5 nm, and then 3 nm, respectively (Figures 7.1.5d-f).

These results clearly indicate that irregular and large particle sizes of nanocrystals were formed at low OM surfactant concentrations (≤ 0.25 M or OM/P = 0.8). At higher OM surfactant concentrations in the synthesis reaction, from 0.025 to 0.43 M (e.g., OM/P ratio from 0.8 to 17), the spherical crystal size is decreased from 30 nm to 3 nm.

The reason for this behaviour may be due to the high degree of surfactant protection and stabilization of nanocrystals with increasing the OM concentrations in the bulk reaction solution. The larger and irregular sizes of the nanocrystals at low OM concentrations as compared to those obtained at high OM concentrations may result in insufficient coverage to the nanocrystal surface and induce their aggregation. Furthermore, in all the cases, the spherical nanocrystals were produced. The formation of spherical NPs could be due to the nonselective surfactant character of oleylamine (OM).[18,56]

The corresponding SAED patterns (inset of Figure 7.1.5) of individual $SmVO_4$ particles exhibit the well-defined single-crystalline structure. The XRD patterns of the $SmVO_4$ nanocrystals synthesized using different oleylamine concentrations are also shown in Figure 7.1.6. Their average particle sizes were further calculated from (200) XRD peak using the Debye-Sherrer equation. The particle size is decreased from 28.5 nm, 18 nm, 15.0 nm to 8.5 nm when increasing the OM/P molar ratio from 0.8, 2, 4 to 8. The nanocrystal sizes estimated using TEM and XRD techniques is presented in Figure 7.1.7. The similar trend and no significant difference in particle size using these two techniques were observed indicating that each individual particle is single crystal.[57]

The influence of metal complex precursor concentrations on size and shape of final nanocrystal products was also systematically studied. A series of $SmVO_4$ nanocrystals was synthesized at the same reaction conditions: Sm/V of 1, oleyamine/(Sm+V) complex precursors of 4 (denoted as OM/P), and at 180 °C for 16 h, however, using different initial precursor concentrations of $Sm(OA)_3$ and $VO_4(TOA)_3$ from low to high (Sm+V) concentrations, e.g., from 0.065 to 0.130, 0.195, and 0.260 M. Representative TEM images and corresponding SAED patterns of the resulting nanocrystals are shown in Figure 7.1.8. It is clear that the shape evolution of nanocrystal products is as a function of initial complex precursor concentration, from nanocores to nanowires. This observation also indicates that low monomer concentrations favour isotropic growth, whereas high monomer concentrations favour anisotropic growth.[58,59] At low precursor monomer concentration, (e.g., 0.065 M), almost the core-shaped nanocrystals with an average diameter of 3 nm was produced (Figure 7.1.8a). It is also noted that at the lower monomer concentration (< 0.065 M), no formation of nanocrystals was observed. This could be due to the monomer concentration lower than that required for the formation of nuclei. Furthermore, under the same synthesis conditions, increasing the precursor monomer concentration to 0.130 M, about 40% of primary thin nanorods with 3 nm in width and ~10-50 nm in length were observed, although nanocores were still the exclusive products (Figure 7.1.8b).

When the precursor monomer concentration was increased from 0.130 to 0.195 M, no nanocores were essentially observed; concomitantly, only the individual nanowires grew along their longitudinal axis with ~3 nm in width and 200 nm in length were yielded, the aspect ratio (length/width) of ~ 66 (Figure 7.1.8c). This indicates a complete conversion from nanocores into nanowires at this monomer concentration. Finally, when the precursor monomer concentration was increased further to 0.260 M, a large amount of nanowires was produced, but no obvious change in their morphology (constant aspect ratio) suggesting that the equilibrium of growth kinetics may be established at this range of monomer concentrations (Figure 7.1.8d). These results reveal that the shape evolution from 3 nm-sized nanocores to 3 nm x 200 nm-sized nanowires can be controlled by increasing the precursor monomer concentration from 0.065 to 0.260 M, which is strongly associated with the increase of chemical potential in the bulk solution as well as the dominant oriented attachment for the formation of nanowires, as also reported recently by our group.[52,60]

The corresponding SAED patterns (inset of Figure 7.1.8) of these nanocrystal samples also exhibit their single-crystalline structure. The XRD patterns of the as-synthesized nanocores and nanowires also show a pure tetragonal phase $SmVO_4$ structure (Figure 7.1.9). No diffraction peaks from any corresponding single metal oxide species are detected. The intense broadening of the peaks is caused by the small particle sizes. The particle size of nanocores calculated from the (200) peak[55] using Scherrer formular is about 3.7 nm, which nearly equals to that observed by the TEM result (Figures 7.1.8a). It is important to note that the relative intensity of (200) diffraction peak of the nanowires is much higher than that of the nanocores suggesting their elongation along [200] direction.

Schematic illustration for the formation mechanism of $SmVO_4$ nanocrystals and their size and shape evolution under different reaction stages in the whole synthetic process can be overall summarised in detail in Scheme 7.1.2.

Elemental dispersive spectrum (EDS) analysis of these as-made $SmVO_4$ nanospheres (Figure 7.1.10A) qualitatively indicates that the sample is elementally composed solely of Sm, V, and O. Further evidence for the chemical composition and oxidation states on the surface of the as-made and calcined samarium orthovanadate nanospheres was analysed by the XPS technique. The survey XPS spectra of these samples in a wide energy range are shown in Figure 7.1.10B. Core levels of Sm 3d, V 2p, O 1s, N 1s, and C 1s can be identified. However, the intense N 1s and C 1s peaks of the as-made as compared to those of the calcined sample can be assigned to the oleylamine ligand capped on the nanocrystal surface. The molar ratio of Sm:V determined from the surface chemical composition of both the as-made and calcined samples was very close to 1:1, agreeing with the formula of $SmVO_4$. It is interesting to note that no difference of the Sm 3d and V 2p XPS spectra before and after calcination at 550 ^{o}C of these samples was observed suggesting no significant change in the samarium and vanadium oxidation state upon this thermal treatment. As shown in Figures 7.1.11A,B, the Sm 3d and V 2p XPS spectra of both the as-made and calcined nanospherical $SmVO_4$ samples exhibit only one oxidation state of Sm^{3+} and V^{5+} at the nanoscale and even in a ultrahigh vacuum for XPS measurements. The Sm^{3+} $3d_{5/2,3/2}$ peaks at 10834.0-1111.0 eV and the V^{5+} $2p_{3/2,1/2}$ peaks at 517.5-535.5 eV were observed.[51,52] Both spectra show that non XPS peaks corresponding to Sm^{2+} and V^{4+} were detected indicating the formation of stable tetragonal $SmVO_4$ structure. However, for the single spherical nanovanadia[51] and nanosamaria[52] samples which were synthesized following the methods reported previously by our group, [51,52] the Sm 3d and V 2p XPS spectra exhibit two additional weak peaks: at 1095.9-1121.3 eV for Sm^{2+} $3d_{5/2,3/2}$; at 516.2-524.1 eV for V^{4+} $2p_{5/2,3/2}$; as compared to those of the mixed oxide $SmVO_4$ nanospherical sample. This difference is due to the fact that, for each single metal oxides, the single Sm-O-Sm bonds in Sm_2O_3, and the V-O-V bonds in V_2O_5 allow the multiple oxidation states, whereas, for the mixed metal oxides, the presence of mixed Sm-O-V bonds in $SmVO_4$ requires only the formation of Sm^{3+}-V^{5+} species.[36,38,61,62] Figure 7.1.12 shows the O 1s XPS spectrum of the as-made $SmVO_4$ nanospheres. A peak at 530.5 eV is attributed to both O-Sm and O-V bonds in the tetragonal $SmVO_4$ lattice[63] which consists of VO_4 tetrahedra which sharing corners and edges with SmO_8 dodecahedra,[64,65] and the smaller peak at 532.2-533.1 eV is ascribed to the presence of hydroxyl species or adsorbed water on the nanocrystal surface. In addition, the appearance of one broader peak at ~526.8 eV could be assigned to a Sm Auger peak.[66]

The UV-visible absorption spectrum of the as-synthesized $SmVO_4$ nanosphere sample was recorded to characterize its optical properties (Figure 7.1.13). It can be seen that a strong absorption peak at 265 nm is present, which is attributed to the charge transfer from the oxygen ligands to the central vanadium atom inside the VO_4^{3-} groups in the samarium orthovanadate.[67] The TGA-DTA curves (Figure 7.1.14A) of the oleylamine (OM)-capped $SmVO_4$ nanospheres (sample 1 in Table 7.1.1) exhibit the weight loss of 22% appeared around 150-550 °C companied by an exothermic peak at 305 ºC, which are related to the decomposition and combustion of oleylamine molecules bounded on the particle surfaces during heating. The FTIR spectrum (Figure 7.1.14B) of this as-made sample shows at 2920 - 2870 cm^{-1} and 1630 cm^{-1} which are assigned to the C-H and C=C stretching modes of alkyl chains in oleylamine, respectively.[51] The band at 1440 cm^{-1} is attributed to the N-H bending and N-C stretching modes of $-NH_2$ groups in oleylamine capped on the $SmVO_4$ nanocrystal surface.[51] The IR bands at 820 cm^{-1} attributed to the Sm-O-V vibrations of $SmVO_4$.[61] Residual water and a hydroxide group are detected with a large band around 3500 cm^{-1}, corresponding to the O-H stretching frequency due to the bending vibration of associated water. These data suggest oleylamine molecules bound to the nanocrystal surface and further confirm that the $SmVO_4$ is formed under this synthetic condition.

Figure 7.1.15 shows the N_2 adsorption/desorption isotherms and pore diameter distributions of the calcined $SmVO_4$ nanosphere and nanowire samples. It can be seen from Figures 15A,B that both the samples exhibit a type IV isotherm. Futhermore, the H_3 hysteresis loop at the 0.4-1.0 P/P_o and H_1 hysteresis loop at the 0.4-0.8 P/P_o pressure range for the nanosphere and nanowire samples, respectively indicate the presence of the mesopore structure in these samples.[68,69] The pore diameters (inset of Figures 7.1.15A,B) calculated using the BJH method are about 19.5 and 57.0 nm, respectively, which were originated from the interparticle space formed by the aggregation of the $SmVO_4$ nanocrystals upon calcination. The BET specific surface area of the nanospheres is 110 m^2g^{-1}, which is higher than that of the nanowires (70 m^2g^{-1}). This could be logically due to the difference in the sphere and wire shapes of these samples.

It is well known that shape and size of the well-defined nanocrystals are key factors which determine their chemical and physical properties. For example, single CeO_2 nanospheres with even higher surface area and smaller particle size have a lower catalytic activity for the CO oxidation reaction compared to that of single CeO_2 nanorods; these unusual results inspire us to hope that specific planes are indeed a determining factor that will prove useful.[70]

This new approach for the shape-controlled synthesis of this type of mixed metal oxide $SmVO_4$ nanocrystals in the present work is an important role for designing novel catalysts with desired performance. Further work to gain insight into the study of the catalytic properties of these $SmVO_4$ nanomaterials with various shapes as well as novel metal doped $SmVO_4$ nanocrystals are in progress in our laboratory.

7.1.4. Conclusion

We have developed a new approach for the controllable synthesis of monodisperse and well-crystallized $SmVO_4$ nanocrystals with various shapes from the reaction of $Sm(OA)_3$ and $VO_4(TOA)_3$ complexes in toluene in the presence of capping surfactant (either oleylamine or oleic acid) through a solvothermal pathway. The $Sm(OA)_3$ and $VO_4(TOA)_3$ complex precursors were pre-synthesized from the inexpensive inorganic sources and organic ligands. This solvothermal approach is simple, reproducible, and occurring at relatively mild reaction temperature. By varying the reaction parameters such as the nature and amount of surfactant, and metal complex precursor concentration, the different morphologies of the $SmVO_4$ nanocrystals can be easily controlled. By increasing the reaction temperature from 150 ºC to 180 ºC, $SmVO_4$ NCs converted from cubic-shaped $SmVO_4$ to uniform nanospheres. The formation of the $SmVO_4$ nanocrystals with spherical and hexagonal shapes using oleylamine and oleic acid as capping surfactants, respectively. It could be due to the different binding strengths of these surfactants (as nonselective and selective surfactant). Tuning the surfactant concentration in the synthesis solution is a crucial step for the discrete, monodisperse, and size-controlled $SmVO_4$ nanospheres. Increasing the oleylamine concentration from 0.025 to 0.43 M induces the decrease of particle size from ~30 to ~3 nm. Furthermore, the shape evolution of nanocrystals was also controlled by tuning the initial metal complex precursor concentration. This is associated with the increase of chemical potential in bulk solution. At the low metal complex precursor concentration range from 0.065 to 0.130 M, only nanocores or a mixture of nanocores and primary thin nanorods of the $SmVO_4$ crystals were produced. At the higher precursor concentration range from 0.195 to 0.260 M, uniform $SmVO_4$ nanowires with ~3 nm in diameter and ~200 nm in length were obtained.

The SAED patterns of the $SmVO_4$ nanocrystal samples show a set of sharp spots characteristic of single crystalline structure, and the strong diffraction rings indexed accordingly with the pure tetragonal structure determined by the XRD patterns. The XPS results reveal only one oxidation state for Sm^{3+} and V^{5+} on the $SmVO_4$ nanocrystal surface, whereas two oxidation states of Sm^{3+}/Sm^{2+} and V^{5+}/V^{4+} were found for the single samarium oxide and vanadium oxide nanospheres, respectively. We believe that this approach can also be extended for the synthesis of other uniform rare earth orthovanadate, molybdate, and tungstate nanocrystals in tailoring different sizes and shapes.

7.1.5. References

(1) Redl, F. X.; Cho, K. S.; Murray, C. B.; O'Brien, S. Nature ***2003, 423***, 968-971.

(2) Zarur, A. J.; Ying, J. Y. *Nature* **2000**, *403*, 65-67.

(3) Schrinner, M.; Ballauff, M.; Talmon, Y.; Kauffmann, Y.; Thun, J.; Möller, M.; Breu, J. *Science* **2009**, *323*, 617-620.

(4) Ferrando, R.; Jellinek, J.; Johnston, R. L. *Chem. Rev.* **2008**, *108*, 845-910.

(5) Maye, M. M.; Nykypanchuk, D.; Cuisinier, M.; Lelie, D.; Gang, O. *Nat. Mater.* **2009**, *8*, 388-391.

(6) Cushing, B. L.; Kolesnichenko, V. L.; O'Connor, C. J. *Chem. Rev.* **2004**, *104*, 3893-3946.

(7) Dahl, J. A.; Maddux, B. L. S.; Hutchison, J. E. *Chem. Rev.* **2007**, *107*, 2228-2269.

(8) Kwon, S. G.; Hyeon, T. *Acc. Chem. Res.* **2008**, 41, 1696-1709.

(9) Wang, X.; Peng, Q.; Li, Y. *Acc. Chem. Res.* **2007**, *40*, 635-643.

(10) Mutin, P. H.; Vioux, A. *Chem. Mater.* **2009**, *21*, 582-596.

(11) Sun, Y.; Xia, Y. *Science* **2002**, *298*, 2176-2179.

(12) Tian, N.; Zhou, Z. Y.; Sun, S. G.; Ding, Y.; Wang, Z. L. *Science* **2007**, *316*, 732-735.

(13) Jun, Y. W.; Seo, J. W.; Cheon, J. *Acc. Chem. Res.* **2008**, *41*, 1630-1640.

(14) Polshettiwar, V.; Baruwati, B.; Varma, R. S. *ACS Nano* **2009**, *3*, 728-736.

(15) El-Sayed, M. A. *Acc. Chem. Res.* **2004**, *37*, 326-333.

(16) Yang, S. M.; Kim, S. H.; Lima, J. M.; Yi, G. R. *J. Mater. Chem.* **2008**, *18*, 2177-2190.

(17) Liang, X.; Gao, L.; Yang, S.; Sun, J. *Adv. Mater.* **2009**, *21*, 1-4.

(18) Watt, J.; Young, N.; Haigh, S.; Kirkland, A.; Tilley, R. D. *Adv. Mater.* **2009**, *21*, 1-6.

(19) Si, R.; Zhang, Y. W.; You, L. P.; Yan, C. H. *Angew. Chem.* **2005**, *117*, 3320-3324.

(20) Park, J.; Koo, B.; Yoon, K. Y.; Hwang, Y.; Kang, M.; Park, J. G.; Hyeon, T. *J. Am. Chem. Soc.* **2005**, *127*, 8433-8440.

(21) Niu, W.; Zheng, S.; Wang, D.; Liu, X.; Li, H.; Han, S.; Chen, J.; Tang, Z.; Xu, G. *J. Am. Chem. Soc.* **2009**, *131*, 697-703.

(22) Peng, Z. A.; Peng, X. *J. Am. Chem. Soc.* **2001**, *123*, 1389-1395.

(23) Au, C. T.; Zhang, W. D. *J. Chem. Soc. Faraday Trans.* **1997**, *93*, 1195-1204.

(24) Tsipis, E. V.; Patrakeev, M. V.; Kharton, V. V.; Vyshatko, N. P.; Frade, J. R. *J. Mater. Chem.* **2002**, *12*, 3738-3745.

(25) Chen, F.; Wang, X.; Li, S.; Fu, G.; Wang, K.; Lu, Q.; Shen, D.; Nie, R.; Ma, H. *J. Appl. Phys.* **2003**, *94*, 4708-4710.

(26) Picardi, G.; Varsano, F.; Decker, F.; Krasovec, U. O.; Surca, A.; Orel, B. *Electrochim. Acta.* **1999**, *44*, 3157-3164.

(27) Yu, M.; Lin, J.; Wang, S. B. *Appl. Phys. A: Mater. Sci. Proc.* **2005**, *80*, 353.

(28) Fields, R. A.; Birnbaum, M.; Fincher, C. L. *Appl. Phys. Lett.* **1987**, *51*, 1885-1856.

(29) Liu, J. F.; Yao, Q. H.; Li, Y. D. *Appl. Phys. Lett.* **2006**, *88*, 173119.

(30) Gaur, K.; Lal, H. B. *J. Mater. Sci. Lett.* **1983**, *2*, 744.

(31) Stouwdam, J. W.; Raudsepp, M.; Veggel, F. V. *Langmuir* **2005**, *21*, 7003-7008.

(32) Matta, J.; Courcot, D.; Abi-Aad, E.; Aboukais, A. *Chem. Mater.* **2002**, *14*, 4118-4125.

(33) Au, C. T.; Zhang, W. D., Wan., H. L. *Catalysis Letters* **1996**, *37*, 241-246.

(34) Sugunan, S.; Renuka, N. K. *Bull. Chem. Soc. Jpn.* **2002**, *75*, 463-471.

(35) Mamedov, E.A.; Corberfin, V. C. *Applied Catalysis A: General* **1995**, *127*, 1-40.

(36) Barbero, B. P.; Cadus, L. E. *Applied Catalysis A: General* **2003**, *244*, 235-249.

(37) Li, K. T.; Chi, Z. H. *Applied Catalysis A: General* **2001**, *206*, 197-203.

(38) Barbero, B. P.; Cadus, L. E. *Applied Catalysis A: General* **2002**, *234*, 245-258.

(39) Lee, I.; Morales, R.; Albiter, M. A.; Zaera, F. *PNAS* **2008**, *105*, 15241-15246.

(40) Tao, F.; Grass, M. E.; Zhang, Y.; Butcher, D. R.; Renzas, J. R.; Liu, Z.; Chung, J. Y.; Mun, B. S.; Salmeron, M.; Somorjai, G. A. *Science* **2008**, *322*, 932-934.

(41) Friedrich, H.; Jongh, P. E.; Verkleij, A. J.; Jong, K. P. *Chem. Rev.* **2009**, *109*, 1613-1629.

(42) Tojo, T.; Zhang, Q.; Saito, F. *Journal of Alloys and Compounds* **2007**, *427*, 219-222.

(43) Fana, W.; Zhao, W.; You, L.; Songa, X.; Zhanga, W.; Yua, H.; Sun, S. *J. Sol. Sta. Chem.* **2004**, *177*, 4399-4403.

(44) Mahapatra, S.; Ramanan, A. *Journal of Alloys and Compounds* **2005**, *395*, 149-153.

(45) Liu, J.; Li. Y. *Mater. Chem.* **2007**, *17*, 1797-1803.

(46) Liu, J.; Chen, W.; Liu, X.; Zhou, K.; Li, Y. *Nano Res* **2008**, *1*, 46-55.

(47) Wang, D.; Xie, T.; Li, Y. *Nano Res* **2009**, *2*, 30-46.

(48) Sheldrick, W. S.; Wachhold, M. *Angew. Chem., Int. Ed.* **1997**, *36*, 206-224.

(49) Demazeau, G. *J. Mater. Chem.* **1999**, *9*, 15-18.

(50) Walton, R. I. *Chem. Soc. Rev.* **2002***, 31*, 230-238.

(51) Nguyen, T. D.; Do, T. O. *Langmuir* **2009**, *25*, 5322-5332.

(52) Nguyen, T. D.; Mrabet, D.; Do, T. O. *J. Phys. Chem. C* **2008**, *112*, 15226-15235.

(53) Kwon, S. G.; Piao, Y.; Park, J.; Angappane, S.; Jo, Y.; Hwang, N. M.; Park, J. G.; Hyeon, T. *J. Am. Chem. Soc.* **2007**, *129*, 12571-12584.

(54) Fana, W.; Zhao, W.; You, L.; Songa, X.; Zhanga, W.; Yua, H.; Sun, S. *J. Sol. Sta. Chem.* **2004**, *177*, 4399-4403.

(55) Mialon, G.; Gohin, M.; Gacoin, T.; Boilot, J. P. *ACS Nano* **2008**, *2*, 2505-2512.

(56) Xie, T.; Li, S.; Peng, Q.; Li, Y. *Angew. Chem.* **2009**, *121*, 202-206.

(57) Shevchenko, E. V.; Talapin, D. V.; Schnablegger, H.; Kornowski, A.; Festin, Ö.; Svedlindh, P.; Haase, M.; Weller, H. *J. Am. Chem. Soc.* **2003**, *125*, 9090-9101.

(58) Peng, Z. A.; Peng, X. *J. Am. Chem. Soc.* **2002**, *124*, 3343-3353.

(59) Yin, Y.; Alivisatos, A. P. Nature ***2004, 437***, 664-670.

(60) Nguyen, T. D.; Do, T. O. *J. Phys. Chem. C* **2009**, *113*, 11204-11214.

(61) Hughes, M. D.; Xu, Y. J.; Jenkins, P.; McMorn, P.; Landon, P.; Enache, D. I.; Carley, A. F.; Attard, G. A.; Hutchings, G. J.; King, F.; Stitt, E. H.; Johnston, P.; Griffin, K.; Kiely, C. J. Nature ***2005, 437***, 1132-1135.

(62) Patel, D.; Andersen, P. J.; Kung, H. H. *J. Catal.* **1990**, *125*, 132-145.

(63) Jia, C. J.; Sun, L. D.; Luo, F.; Jiang, X. C.; Wei, L. H.; Yan, C. H. *Appl. Phys. Lett.* **2004**, *45*, 5305-5307.

(64) Mahapatra, S.; Ramanan, A. *Journal of Alloys and Compounds* **2005**, *395*, 149.

(65) Deng, H.; Yang, S.; Xiao, S.; Gong, H. M.; Wang, Q. Q.*J. Am. Chem. Soc.* **2008**, *130*, 2032.

(66) Moulder, J. F.; Stickle, W. F.; Sobol, P. E.; Bomben, K. D. *Handbook of X-ray photoelectron spectroscopy*; Perkin-Elmer corporation, Physical Electronics Division: **1992**.

(67) Selvan, R. K.; Gedanken, A.; Anilkumar, P.; Manikandan, G.; Karunakaran, C. *J Clust Sci* **2008**, DOI 10.1007/s10876-008-0229-y.

(68) Mrabet, D.; Zahedi-Niaki, M. H.; Do, T. O. *J. Phys. Chem. C* **2008**, *112*, 7124-7129.

(69) Song, J.; Ren, L.; Yin, C.; Ji, Y.; Wu, Z.; Li, J.; Xiao, F. S. *J. Phys. Chem. C* **2008**, *112*, 8609-8613.

(70) Wang, X.; Li, Y. *Chem. Comm.* **2007**, 2901-2910.

Table 7.1.1. Synthesis Conditions and Corresponding Morphologies of the As-made $SmVO_4$ Nanocrystals.[a]

Sample	$Sm(OA)_3$[b] [M]	$VO_4(TOA)_3$[b] [M]	OM[b] [mol]	OA[b] [mol]	Shape	Size[c] [nm]	Size[d] [nm]
1	0.065	0.065	0.011		Sphere	17	15.0
2	0.065	0.065		0.011	Hexagon	17	15.0
3	0.065	0.065	0.002		Irregular round	30	28.5
4	0.065	0.065	0.005		Sphere	20	18.0
5	0.065	0.065	0.021		Sphere	10	8.5
6	0.065	0.065	0.032		Sphere	5	5.7
7	0.065	0.065	0.043		Core	3	3.7
8	0.130	0.130	0.043		Core and thin Rod	3&3x10-50	
9	0.195	0.195	0.043		Wire	3x200	
10	0.260	0.260	0.043		Wire	3x200	

(a) All samples were synthesized by solvothermal process at 180 °C for 16 h.

(b) OA^-: Oleate anion; TOA^+: Tetraoctylammonium cation; OM: Oleylamine; OA: Oleic acid

(c) Average particle size estimated by TEM

(d) Average particle size estimated by XRD

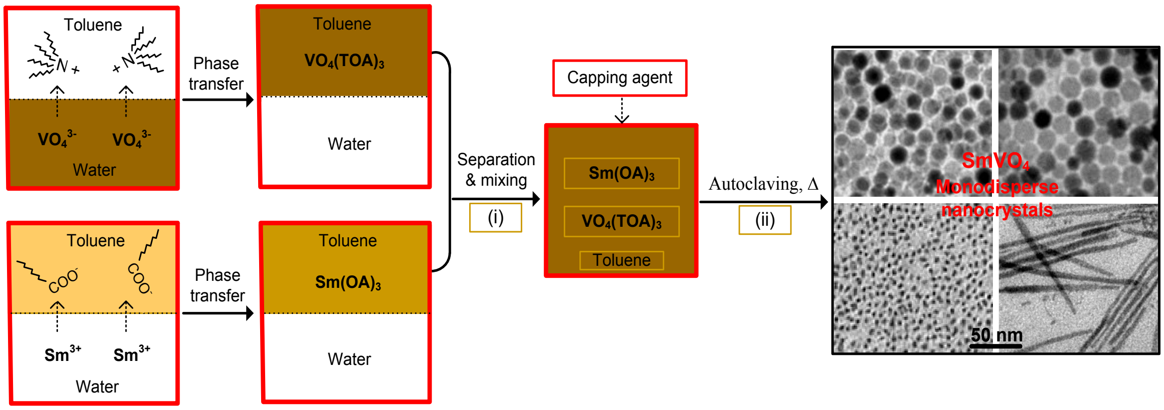

Scheme 7.1.1. Scheme illustrating the formation of the Sm(OA)$_3$ and VO$_4$(TOA)$_3$ complexes (i) and the capping SmVO$_4$ nanocrystals (ii).

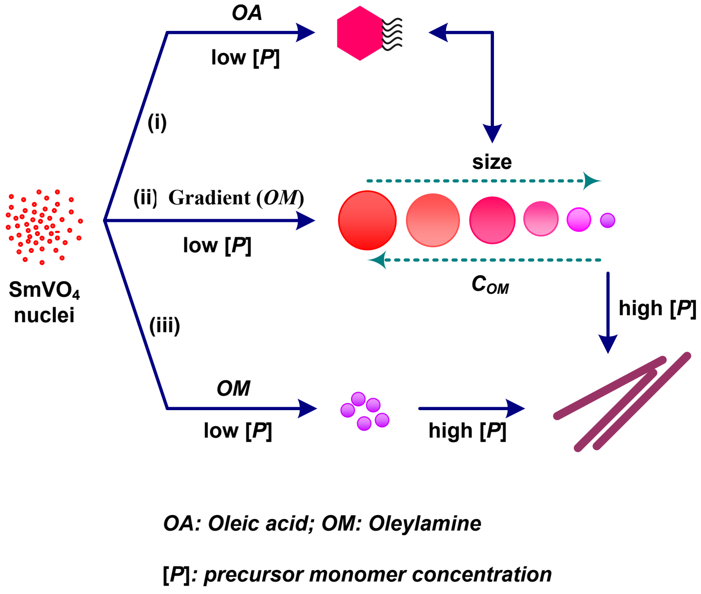

Scheme 7.1.2. The overall schematic illustration of the size and shape control of alkyl-capped SmVO$_4$ nanocrystals.

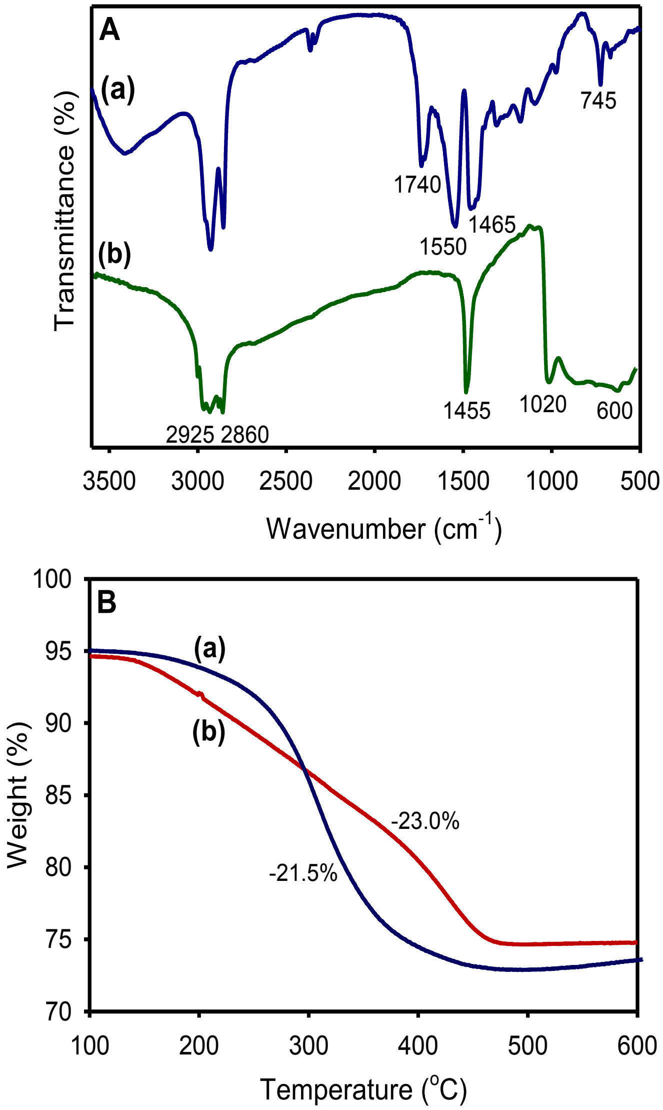

Figure 7.1.1. FTIR spectra and TGA curves of (a) Sm(OA)$_3$ and (b) VO$_4$(TOA)$_3$ complex solids.

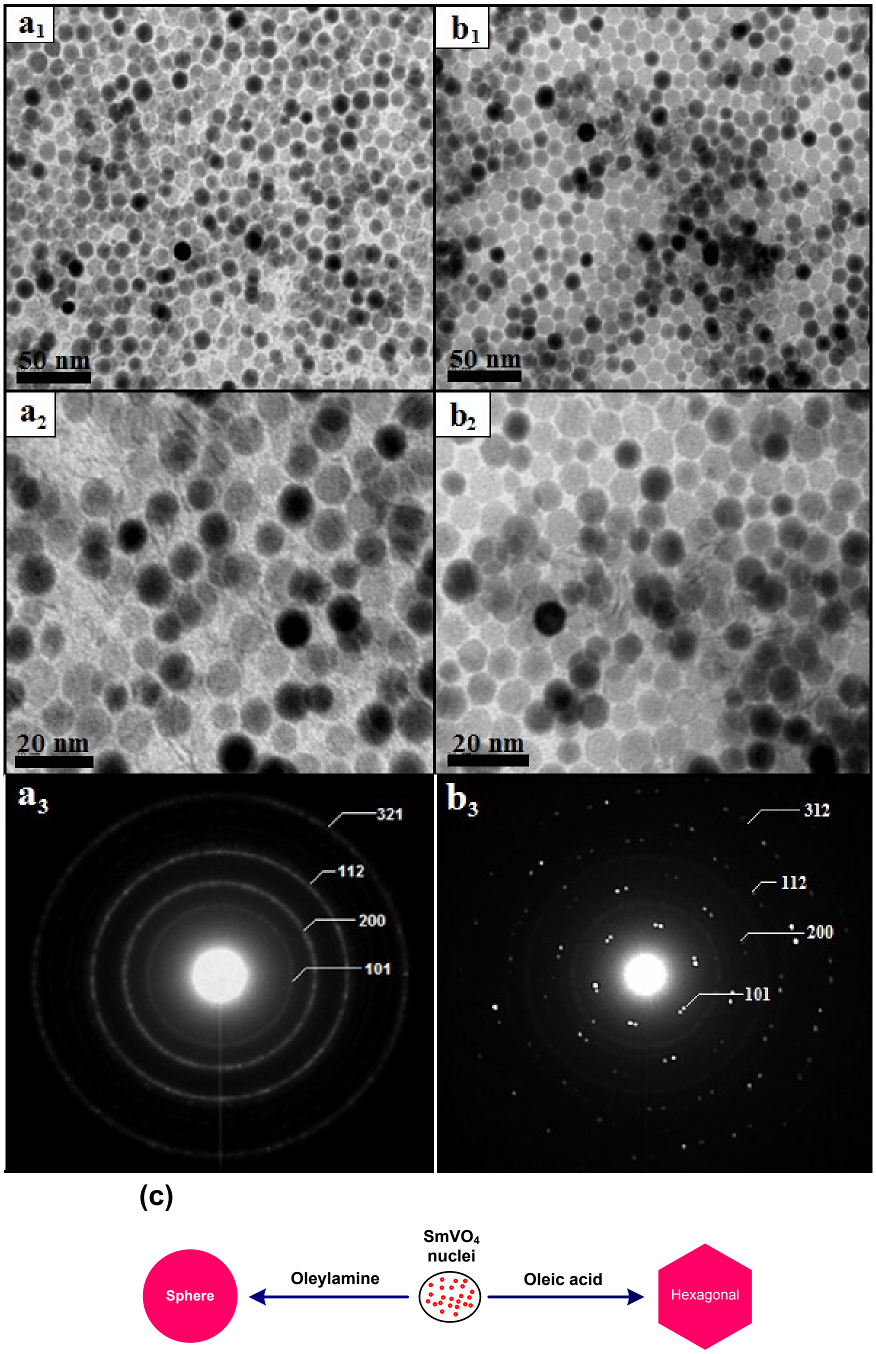

Figure 7.1.2. Effect of the surfactants with different functional groups on the shape control. TEM images and SAED patterns of the $SmVO_4$ nanocrystals synthesized from a 1:1 mixture of $Sm(OA)_3$ and $VO_4(TOA)_3$ in toluene using various surfactants: (a_1,a_2,a_3) oleylamine, 17 nm nanospheres (sample 1), (b_1,b_2,b_3) oleic acid, 17 nm nanohexagons (sample 2), and (c) Schematic illustration for the shape control of the $SmVO_4$ nanocrystals.

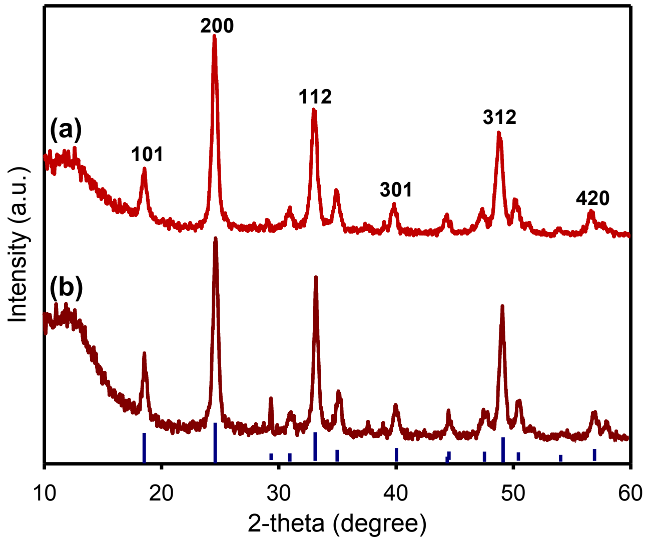

Figure 7.1.3. XRD patterns of the as-synthesized $SmVO_4$ samples: (a) nanospheres and (b) nanohexagons. Vertical bars denote the peak positions and relative intensities of the tetragonal zircon-type structure (JCPDS No 17-0876).

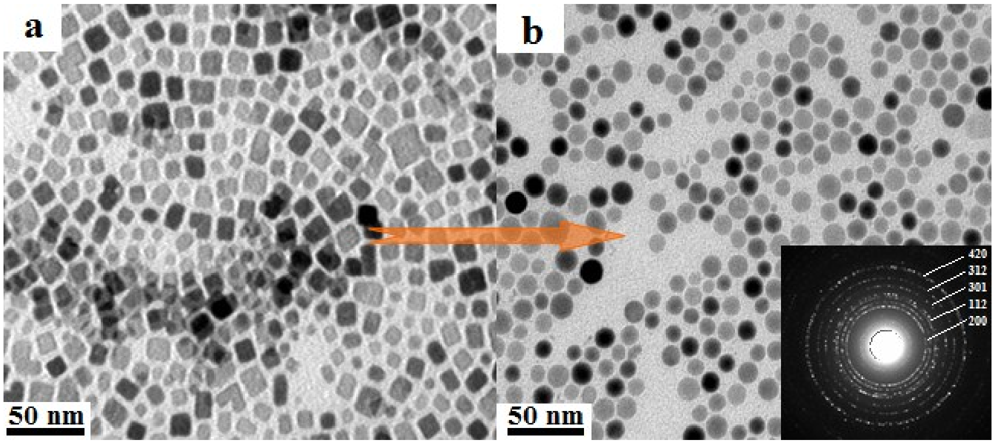

Figure 7.1.4. TEM images of 15 nm-sized $SmVO_4$ nanocrystals synthesized at different temperatures for 16 h: (a) nanocubes at 150 °C; (b) nanospheres at 180 °C (inset, SAED).

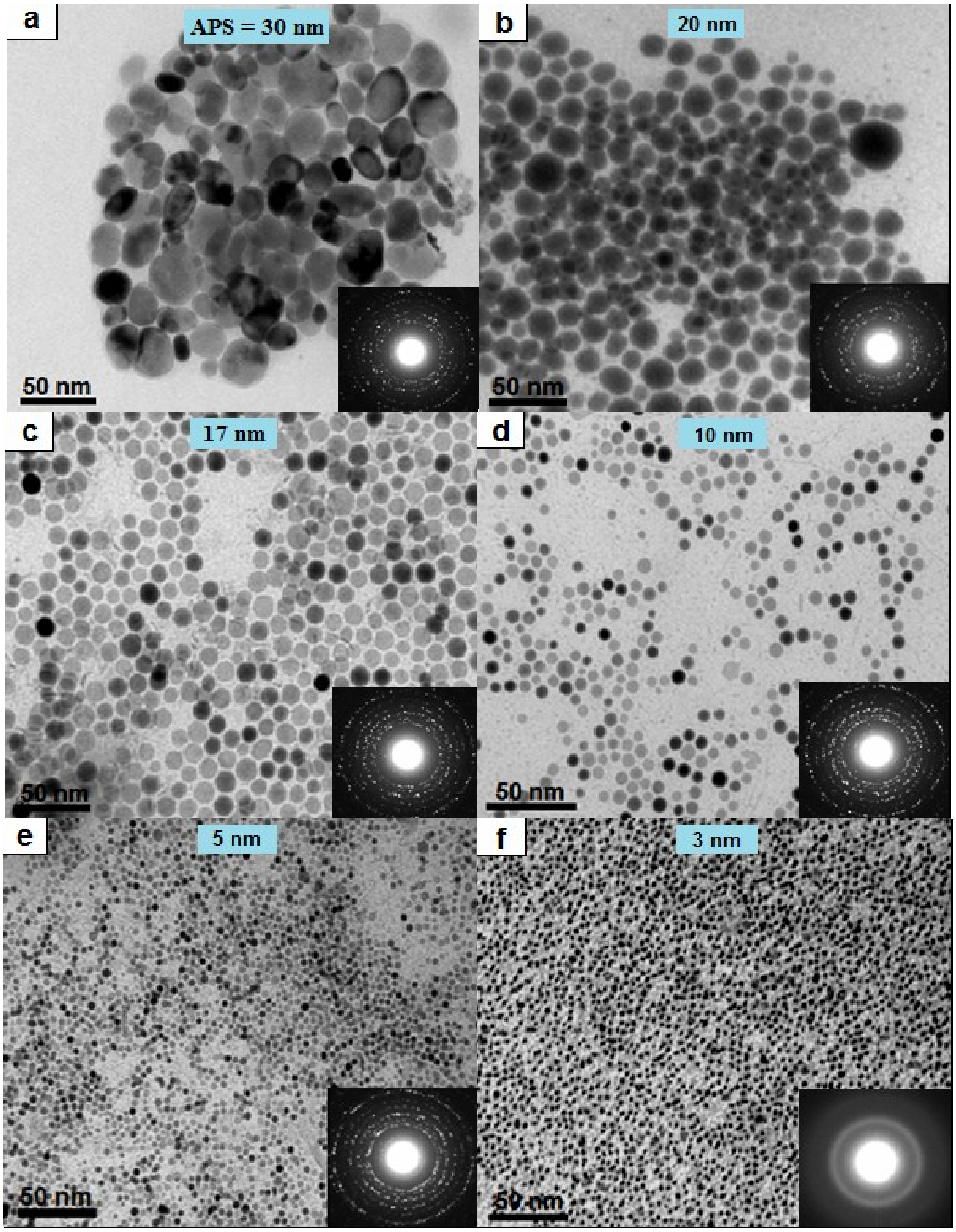

Figure 7.1.5. Effect of the oleylamine concentration in the bulk solution on the particle size. TEM images and corresponding inset SAED patterns of the $SmVO_4$ nanocrystals synthesized using the different molar ratios of oleylamine:precursor (*OM:P*): (a) *OM:P* = 0.8, 30 nm roundlike nanocrystals (sample 3), (b) *OM:P* = 2, 20 nm nanospheres (sample 4), (c) *OM:P* = 4, 17 nm nanospheres (sample 1), (d) *OM:P* = 8, 10 nm nanospheres (sample 5), (e) *OM:P* = 12, 5 nm nanospheres (sample 6), and (f) *OM:P* = 17, 3 nm nanocores (sample 7). Average particle size = APS.

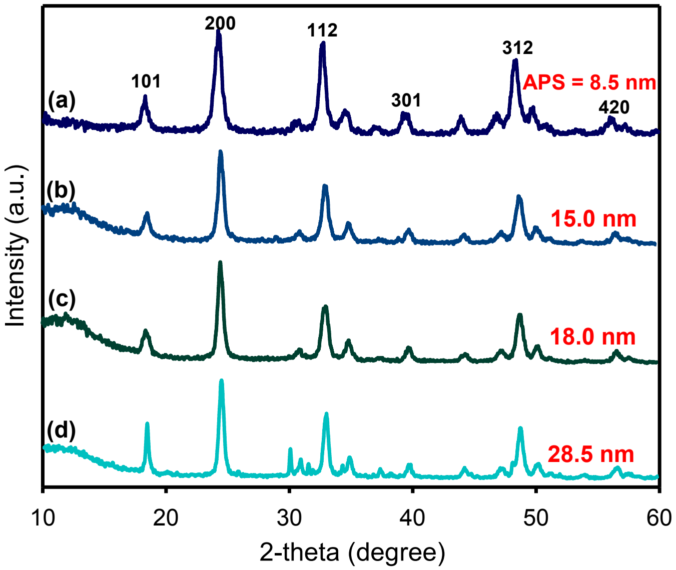

Figure 7.1.6. XRD patterns of the $SmVO_4$ nanocrystals synthesized using different molar ratios of oleylamine and precursor (*OM:P*): (a) *OM:P* = 0.8, (b) *OM:P* = 2, (c) *OM:P* = 4, and (d) *OM:P* = 8. The average particle sizes (APS) were calculated from (200) peak using the Debye-Sherrer equation.

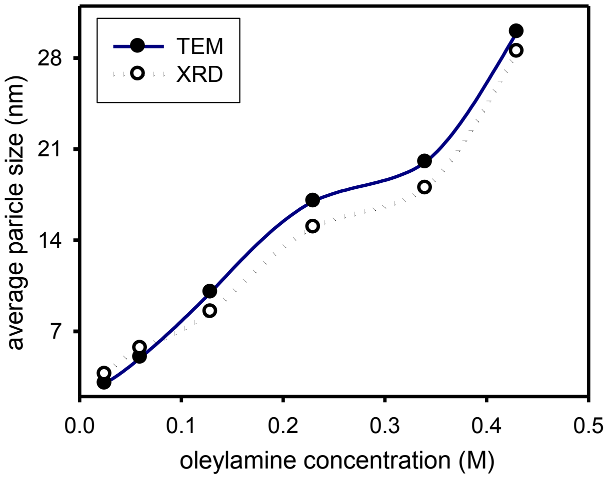

Figure 7.1.7. Effect of oleylamine concentration on the average particle size of $SmVO_4$ nanocrystals estimated by TEM (solid curve) and XRD (dotted curve).

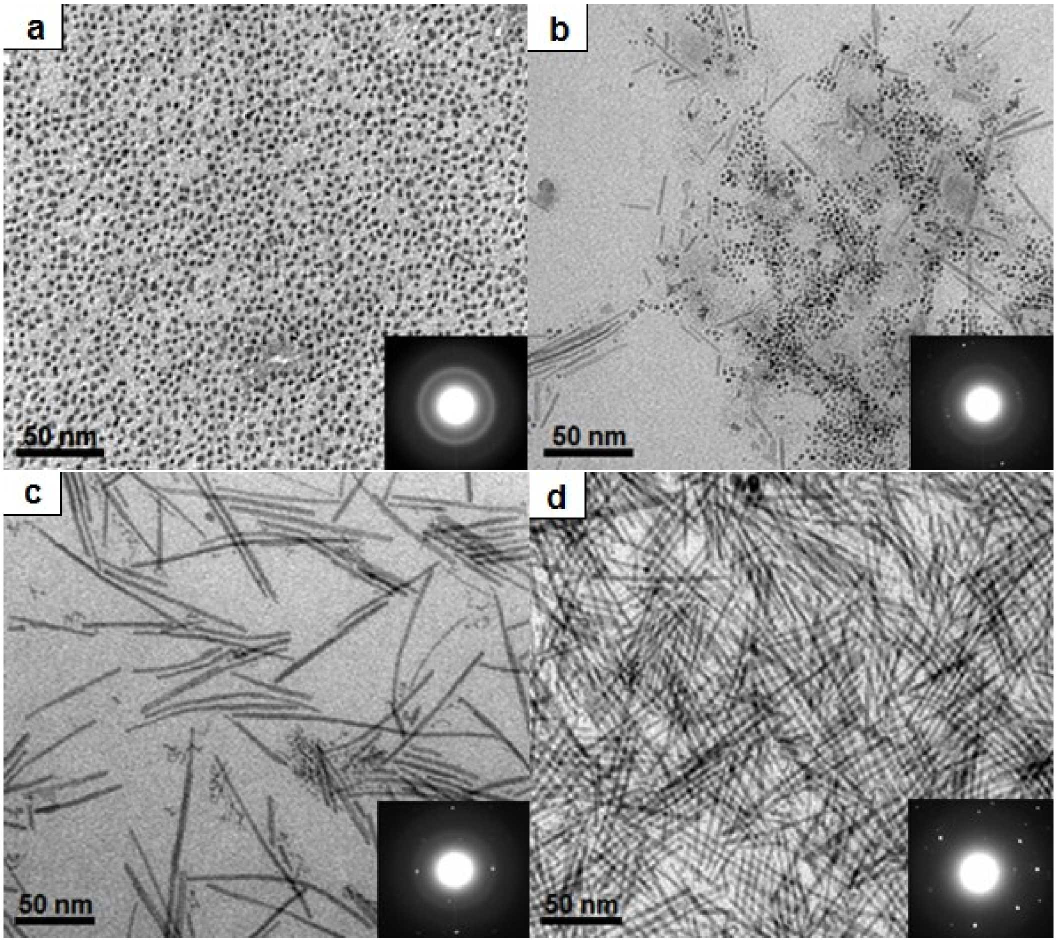

Figure 7.1.8. Effect of the precursor monomer concentration in the bulk solution on the shape evolution from nanocores to nanowires. TEM images and corresponding inset SAED patterns of the $SmVO_4$ nanocrystals synthesized using the different precursor concentrations, while keeping the Sm/V molar ratio = 1 (C = [$Sm(OA)_3$] = [$VO_4(TOA)_3$]): (a) C = 0.065 M, 3 nm nanocores (sample 7), (b) C = 0.130 M, mixture of 3 nm nanocores and 3 nm x 10-50 nm thin nanorods (sample 8), (c) C = 0.195 M, 3 nm x 200 nm nanowires (sample 9), and (d) C = 0.260 M, 3 nm x 200 nm nanowires (sample 10).

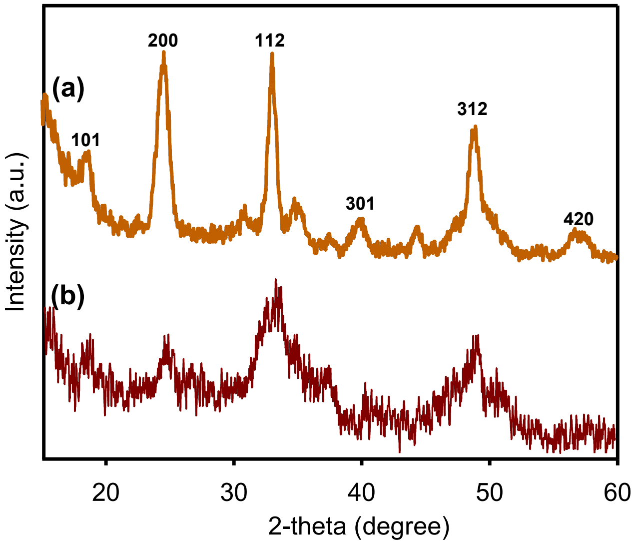

Figure 7.1.9. XRD patterns of the as-synthesized $SmVO_4$ samples: (a) nanowires (sample 10) and (b) nanocores (sample 7).

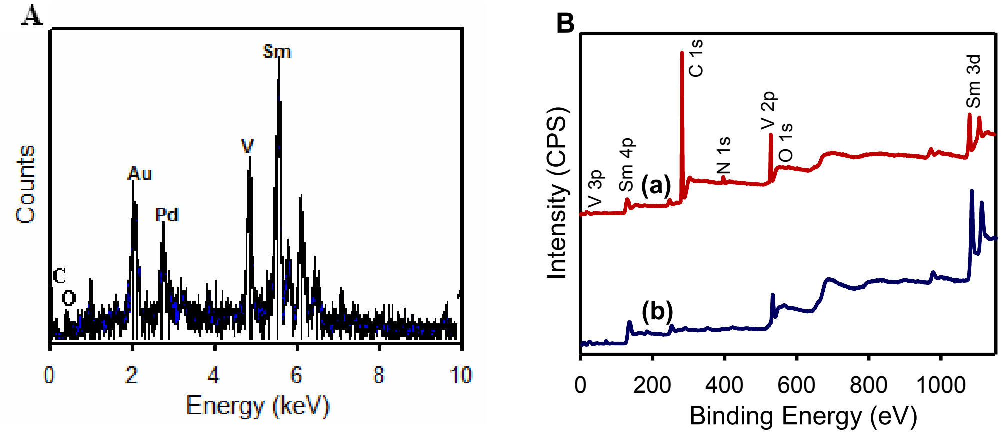

Figure 7.1.10. (A) Energy disperse X-ray (EDS) spectrum of the as-synthesized $SmVO_4$ nanospheres and (B) Survey XPS spectra of the $SmVO_4$ nanospheres before (a) and after (b) calcination at 550 °C for 2 h.

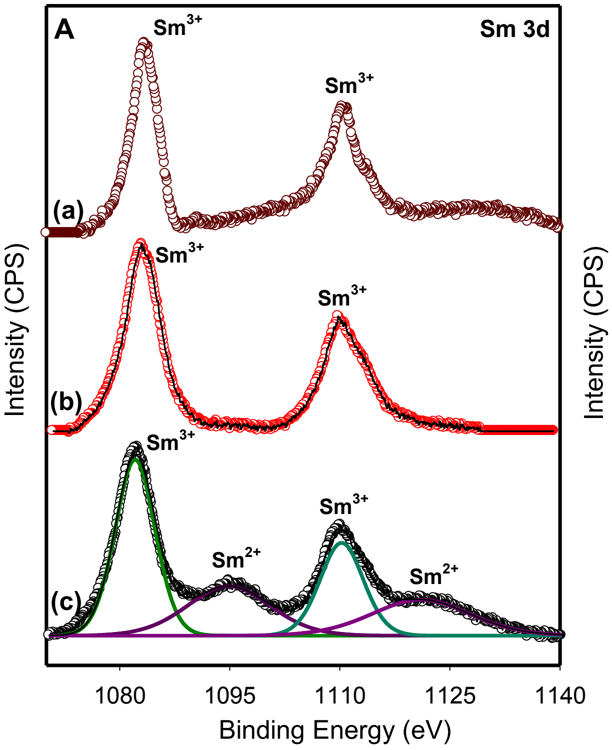

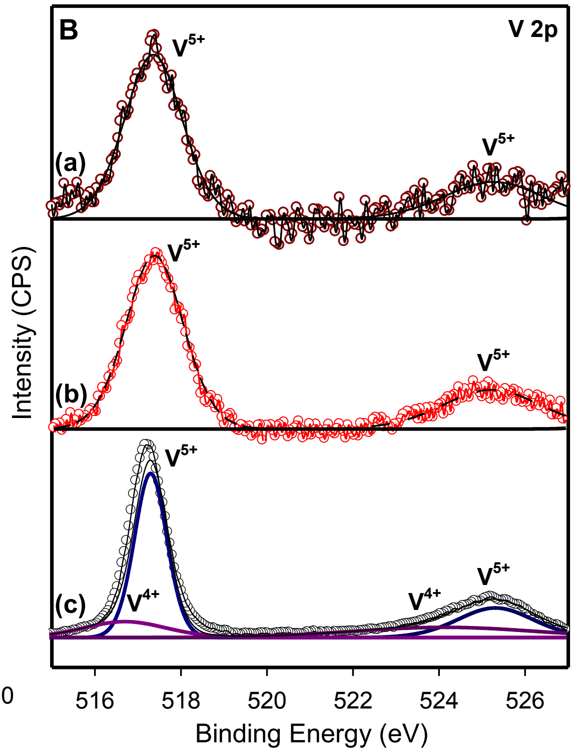

Figure 7.1.11. (A) Sm 3d XPS spectra of: (a) the as-made $SmVO_4$ nanospheres, (b) the calcined $SmVO_4$ nanospheres, and (c) the calcined Sm_2O_3 nanospheres. (B) V 2p XPS spectra of: (a) the as-made $SmVO_4$ nanospheres, (b) the calcined $SmVO_4$ nanospheres, and (c) the calcined V_2O_5 nanospheres.

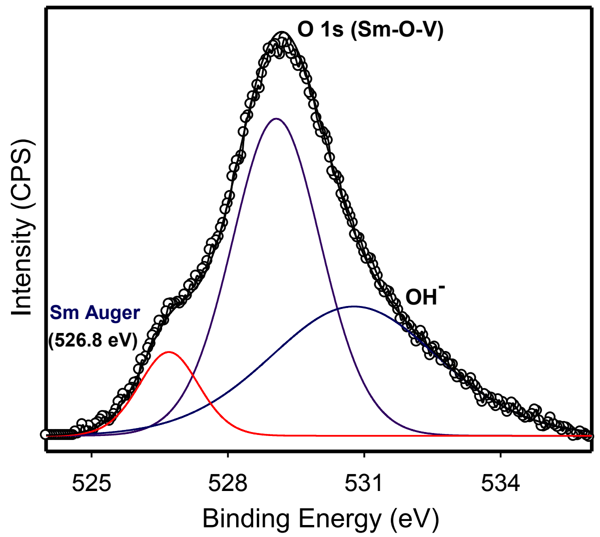

Figure 7.1.12. O 1s XPS spectrum of the as-made SmVO$_4$ nanospheres.

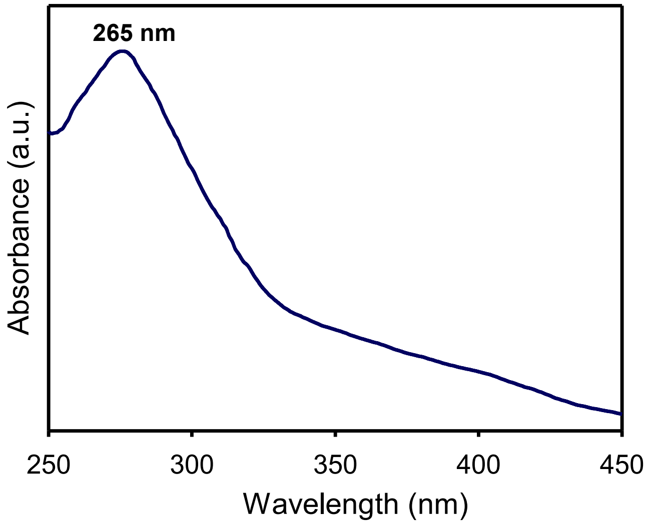

Figure 7.1.13. UV-visible absorption spectrum of the as-synthesized SmVO$_4$ nanospheres.

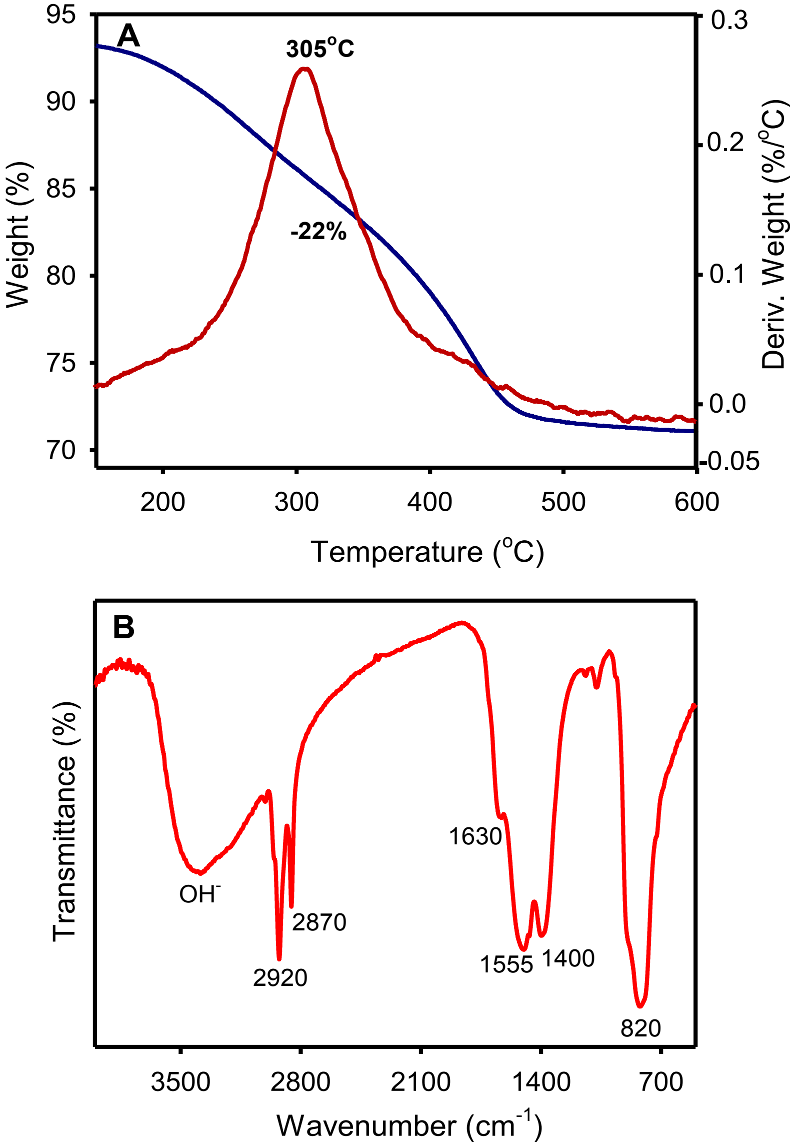

Figure 7.1.14. (A) TGA-DTA curves and (B) FTIR spectrum of oleylamine (OM)-capped $SmVO_4$ nanospheres (sample 1).

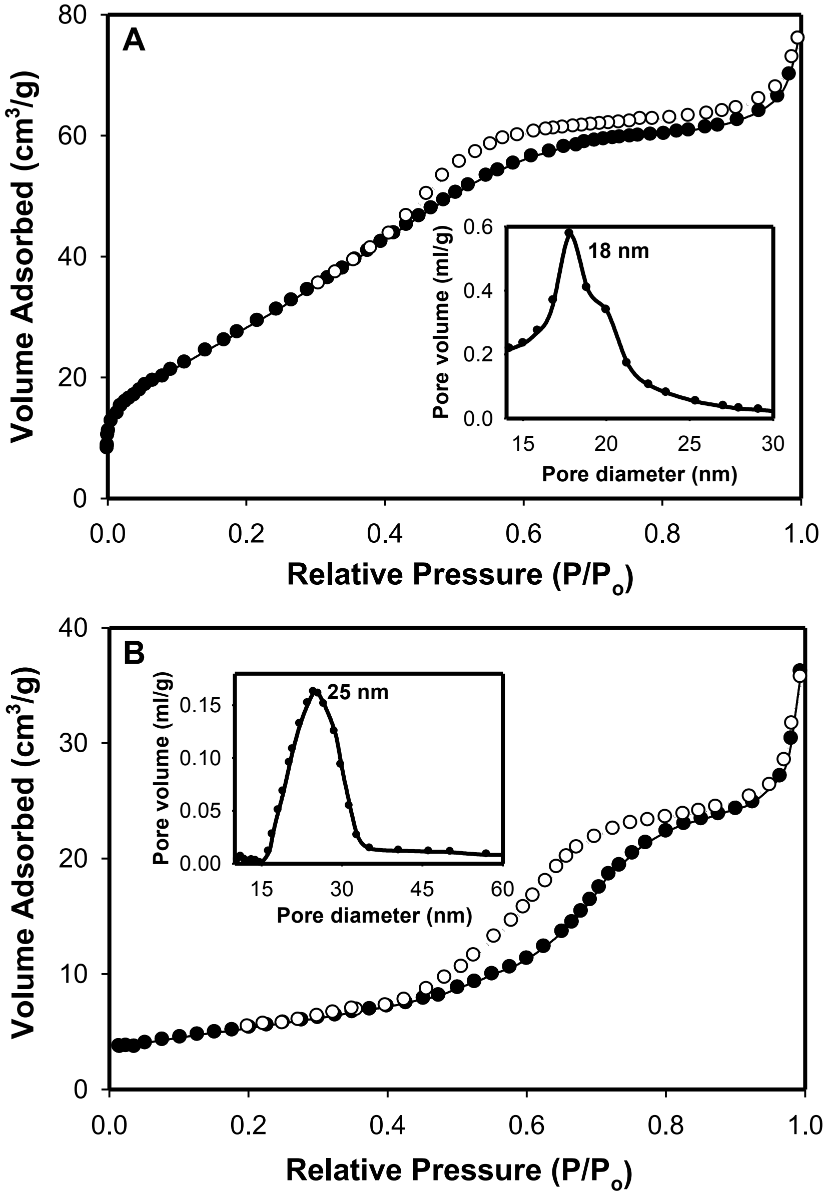

Figure 7.1.15. Nitrogen adsorption (filled symbols) and desorption (open symbols) isotherms and inset BJH pore diameter distribution of: (A) the calcined $SmVO_4$ nanospheres (sample 1) and (B) the calcined $SmVO_4$ nanowires (sample 10).

7.2. Biomolecule-Assisted Route for Shape-Controlled Synthesis of Single Crystalline $MnWO_4$ Nanoparticles and Spontaneous Assembly of Polypeptide-Stabilized Mesocrystal Microspheres

Thanh-Dinh Nguyen, Driss Mrabet, Vu Thi Thuy-Duong, Cao-Thang Dinh and Trong-On Do

Department of Chemical Engineering, Laval University, Quebec G1K 7P4 Canada

Published in *CrystEngComm* **2011**, *13*, 1450-1460

Abstract

Single-crystalline mixed metal oxide nanoparticles and 3D hierarchical mesocrystal microspheres of $MnWO_4$ have been synthesized on a large scale by a facile single-step hydrothermal method using $Mn(NO_3)_2$ and Na_2WO_4 precursors, and capping bifunctional amino acid biomolecules with different alkyl chain lengths, and water or water/ethylene glycol medium. The resulting single-crystalline $MnWO_4$ nanoparticles with different uniform shapes including bar, rod, square, quasisphere, sphere, hexagonal crystals were obtained by tuning the synthetic conditions such as the concentration and the alkyl chain length of amino acids, pH, and reaction temperature. By decreasing the Mn^{2+} and WO_4^{2-} precursor monomer concentration from 0.0150 to 0.0076 M in aqueous media, polypeptide-stabilized $MnWO_4$ mesocrystal hierarchical microspheres were achieved, due to the spontaneous-assembly of primary nanoparticles through the backbone-backbone intermolecular hydrogen-bonding interactions of polypeptide chains. Nanoplatelet-based like-microapples with two holes on their poles were also obtained under the same synthetic conditions for the microspheres, except that the use of water/ethylene glycol (10:30 mL) instead of water medium. The photoluminescence (PL) results revealed that the PL emission intensity of the $MnWO_4$ nanobars is higher than that of the self-assembled $MnWO_4$ microspheres. This green chemistry method is simple and highly reproducible, using

inexpensive reagents, and water as reaction solvent. The uniform $MnWO_4$ nanorods with the control of aspect ratio (length/width) can be produced in a large quantity as much as 16 grams in a single preparation. The current approach is quite general and able to be extended to a variety of other well-defined metal oxide and mixed oxide nanomaterials with controlled shapes.

7.2. 1. Introduction

Over the past decade, shape-controlled syntheses of mixed metal oxide nanoparticles have become one of the essential topics in nanomaterials science, since their unique properties are generally not available in single metal oxide nanoparticles.[1] Mixed metal oxides nanoparticles with different shapes are thus gained much attraction in the fields of catalysis, electronics, optics, sensors, biology, magnetic and luminescence properties, and drug delivery.[2,3] The shape of nanomaterials is an important factor that dictates their physicochemical properties because the number of active atoms located at the edges/corners and exposed facets of crystals.[4,5] In addition, the self-assembly of tailored nanobuilding units into three-dimensional (3D) mixed metal oxide microarchitectures has recently received considerable interest.[6,7] Many novel and fascinating properties of these materials are predicted depending not only on the complex morphology but also on the order degree of single-crystalline nanoparticles in microarchitectures.[8] For example, the photoluminescence (PL) from single-disk spherical superparticles of CdSe/CdS nanorod building blocks did not have a significant linear polarization, but individual bilayer spherical superparticles exhibited strongly linearly polarized emissions.[9] Therefore, exquisite shape and control of both uniform single-crystalline mixed oxide nanoparticles and self-assembled hierarchical microarchitectures are highly desirable for tailoring their specific properties and are also required for high performance in many applications.

Managanese tungstate ($MnWO_4$) is one of the promising mixed metal oxide nanomaterials, which exhibits high sensitivity to humidity change and unique magnetic property.[10-13] Hence, it has attracted considerable research interest in the potential applications such as photocatalysts, humidity sensors, optical fibers, photoluminescence and scintillator materials.[14-18] These exciting applications originate from its electrical-conductivity property, which depends on the shape of the products.[19-21] Therefore, several efforts have been devoted to the synthesis of $MnWO_4$ nanoparticles and especially focused on the shape and dimensional control. For instance, a general hydrothermal route for the synthesis of single-crystalline tungstate AWO_4 (A = Mn, Fe, Zn) nanorods/nanowires with wolframite structures was reported by Qian et al.[22] Thongtem et al.[23] prepared $MnWO_4$ nanostructures through a cyclin microwave-assisted spay method. Yu et al.[24] hydrothermally fabricated three-dimensional (3D) urchin-like $MnWO_4$ microspheres assembled by nanorods with the aid of cationic surfactant cetyltrimethyl ammonium bromide (CTAB). Our group has recently developed some new routes for the synthesis of shape-controlled oxide and mixed oxide nanocrystals using surfactant-stabilized precursors.[25-29] So far, recent efforts have been focused on the assembled restructuring of the individual nanocomponents into microspheres through the interaction of functionalized nanoparticles. Generally, two "bottom-up" approaches for the hierarchical microarchitectures have been widely used: (i) "two-step" synthesis has mostly employed the replacement of hydrophobic ligands by hydrophilic ones or *in situ* grow a hydrophilic shell on a pre-synthesized nanoparticles in emulsions or ionic liquids.[30,31] However, the addition of a template to the reaction system involves a complicated process and may result in impurities due to the incomplete removal of the template. (ii) "One-step" one has carefully examined by various reaction factors to organize artificial nanobuilding blocks into 3D architectures with the aid of the surface functional groups.[32,33] The latter method thus seems to be more attractive and promising, owing to its higher yield and simplicity. To our best knowledge, no aqueous-based amino acid-assisted method for "one-step" synthesis of single-crystalline $MnWO_4$ nanoparticles with diversely controllable shapes and architectures in terms of low cost and potential for large-scale production has been reported.

In the present study, we report a new approach for the aqueous-phase synthesis of uniform single-crystalline $MnWO_4$ nanoparticles with controlled shape and the self-assembled mesocrystal microspheres/microapples with high yield using $Mn(NO_3)_2$ and Na_2WO_4 as presursors and bifunctional amino acid biomolecules as capping agent. This work consists of two parts. In the first part, we focus on the large-scale synthesis of single-crystalline $MnWO_4$ nanoparticles with various shapes by tuning the concentration and the alkyl chain length of amino acid surfactants, pH, and reaction temperature. Secondly, we describe a "single-step" synthesis of 3D hierarchical $MnWO_4$ mesocrystal microspheres and micro like-apples from the spontaneous assembly of individual nanoparticles by adjusting the precursor monomer concentration in water or in water/ethylene glycol medium. The possible mechanisms for the formation of single-crystalline $MnWO_4$ nanoparticles and their self-assembled microspheres are proposed. The optical properties of these $MnWO_4$ samples with various morphologies are also reported.

7.2.2. Experimental Section

Chemicals: All chemicals were used as received without further purification. Manganese(II) nitrate tetrahydrate ($Mn(NO_3)_2.4H_2O$, 99%), sodium tungstate dihydrate ($Na_2WO_4.2H_2O$, 99.9%), 5-aminovaleric acid ($HOOCC_4H_8NH_2$, or AVA, 97%), 6-aminohexanoic acid ($HOOCC_5H_{10}NH_2$, or AHA, 70%), 2-aminononanoic acid ($HOOCC_9H_{19}NH_2$ or ANA, 90%), hexamethylenediamine ($NH_2(CH_2)_6NH_2$, 98%), were purchased from Sigma-Aldrich. Nitric acid (HNO_3, 63%) and ethylene glycol ($HOCH_2CH_2OH$, 99.8%) are of analytical grade and purchased from Reagent ACS.

(i) Synthesis of $MnWO_4$ Nanoparticles with Bar, Rod, Square, quasi-Sphere, Sphere, Hexagonal Shapes: $Mn(NO_3)_2{\cdot}6H_2O$ (0.61 mmol, 0.153 g) and 6-aminohexanoic acid (1.22 mmol, 0.16 g) were dissolved in 20 mL of distilled water. Twenty militers of an aqueous $Na_2WO_4.2H_2O$ 30.5 mM solution was added to the above aqueous solution under magnetic stirring for about 10 min at room temperature. A white colored amorphous $MnWO_4$ precipitate appreared immediately because of the combination of Mn^{2+} cations and WO_4^{2-} anions. The resulting reaction mixture (40 mL) was transferred to a Teflon-lined stainless steel autoclave of 70 mL capacity and treated at desired temperature in the range of 180 ^{o}C for 20 h, and then cooled naturally to room temperature. The obtained product was filtered out, washed several times by ethanol, and dried at 60 °C for 2 h. The $MnWO_4$ nanoparticles with various shapes (including bar, rod, square, quasi-sphere, sphere, hexagonal) have been controlled by varying reaction parameters such as concentration of 6-aminohexanoic acid (0.031 - 0.915 M), alkyl chain length of amino acid surfactants (e.g., 5-aminovaleric acid, 6-aminohexanoic acid, 2-aminononanoic acid), pH of synthesis solution (ranging from 9 to 6, the pH value was adjusted to a desired pH value using 1 mol.L^{-1} HNO_3 solution), and reaction temperature (180-220 ^oC).

(ii) Synthesis of Self-Assembled $MnWO_4$ Microspheres and Micro-like Apples: $MnWO_4$ hierarchical microspheres were produced in water medium when the precursor monomer concentration of $Mn(NO_3)_2$ and Na_2WO_4 salts in bulk solution decreased from 0.0150 to 0.0076 M, while keeping the other synthesis conditions unchanged ($[Mn^{2+}]$ = $[WO_4^{2-}]$ = 1:1, 0.031 M of 6-aminohexanoic acid, pH = 9, 180 ^oC, 20 h). The nanoplatelet-based microapples obtained under the same reaction conditions for the synthesis of microspheres, except that water/ethylene glycol (10:30 mL) medium was used instead of distilled water (100%).

7.2.3. Results and Discussion

Uniform single-crystalline nanoparticles and 3D hierarchical mesocrystal microspheres of $MnWO_4$ were synthesized by a simple “one-step” hydrothermal method using $Mn(NO_4)_2$ and Na_2WO_4 as starting materials, 6-aminohexanoic acid as capping agent, and distilled water or water/ethylene glycol as synthesis medium at 180-220 °C for 20 h. Bifunctional amino acid molecules which were used in this study are composed of an alkyl chain (e.g., C_5, C_6 or C_{10}) and two head ends of -NH_2/-COOH groups. Table 7.2.1 summerized the synthesis conditions and various morphologies of the as-prepared $MnWO_4$ samples via bifunctional amino acid-assisted hydrothermal process. In the early stage of the synthesis, $MnWO_4$ nuclei were formed by the combination of Mn^{2+} cations and WO_4^{2-} anions. This stage is followed by the crystal growth process. The nanoparticle products were capped by the amino head groups of amino acid biomolecules and their surface become hydrophilic owing to other end of the uncoordinated carboxylic groups (see Scheme 7.2.1 and 7.2.2). Due to the hydrophilic surface character, the final products can be suspended in water medium. Various shapes of particle products can be controlled depending on synthetic conditions (see Table 7.2.1). The influence of synthetic conditions on shape was systematically studied by altering the concentration of reaction reagents, alkyl chain length of amino acid surfactant, pH of solution, and reaction temperature. Different precursor monomer concentrations ranging from 0.0120 to 0.0076 M in water or water/ethylene glycol medium were studied to determine the optimal conditions for the formation of polypeptide-stabilized $MnWO_4$ mesocrystal microspheres and microlike-apples (see Scheme 7.2.2).

Using 6-aminohexanoic acid (AHA) as a capping agent, the experimental results revealed that the AHA concentration in the aqueous solution plays an important role in tuning the lengths and aspect ratios (length/width) of $MnWO_4$ nanoparticles. Figure 7.2.1 shows TEM/HRTEM images of four representative samples synthesized under the same synthesis conditions (e.g., 0.015 M of $Mn(NO_3)_2$, 0.015 M of Na_2WO_4, Mn:W molar ratio = 1:1, pH = 9, 180 ^oC for 20 h), however, only the 6-aminohexanoic acid concentration in the reaction solution was changed from low to high; for example, from 0.031 to 0.305, 0.610, 0.915 M, corresponding to the AHA/(Mn+W) molar ratio ranging from 2:1 to 10:1, 20:1, 30:1. When the AHA/(Mn+W) molar ratio was 2:1, uniform single-crystalline nanobars (short rod) with an average diameter of 25 nm, a length of 50 nm, and an aspect ratio of 2.0 were obtained (Figure 7.2.1a). They were slightly truncated at the corners and their surface presented without any dislocation and stacking fault; however, some defects as pinholes were found. Figure 7.2.1b shows high-resolution TEM images with different scales of a $MnWO_4$ nanobar with the aspect ratio of 2.0, suggesting that the nanobar is single crystal with an interplanar spacing of 0.30 nm, which corresponds to the separation between the (200) lattice planes of monoclinic $MnWO_4$.[34] The side surfaces of the nanobar were bounded by (100) plane. The ends of the nanobar were enclosed by the (021) plane. This single-crystalline nanobar shows resolvable planes corresponding to the [100] and [021] directions, as illustrated in the inset of Figure 7.2.1b. The (100) planes are oriented parallel to the nanobars' growth axis, suggesting that the growth direction of the single-crystalline nanobar occurs preferentially along the [100] direction (*c*-axis). As a result, a strong (100) diffraction peak in the XRD pattern was observed (see below). A selected area electron diffraction (SAED) pattern (Figure 7.2.1c) taken from a single nanobar (inset of Figure

7.2.1b) also confirms the preferential [100]-oriented growth of a monoclinic $MnWO_4$ single-crystal structure. Further, an increase of the molar ratio to 10:1, the shape evolution of nanobar into nanorod with the average length elongated from 50 to 100 nm was yielded, while the diameter of ~25 nm remained almost unchanged (Figure 7.2.1d). When the molar ratio was increased from 10:1 to 20:1, the average length of nanorod increased significantly from 100 to 150 nm and their diameter was still unchanged (Figure 7.2.1e). Eventually, as this molar ratio was increased further to 30:1, the length of 25 nm x 150 nm-sized nanorods was still maintained (Figure 7.2.1f). Further, bar-shaped $MnWO_4$ nanocrystals were still produced but no well-shape when the synthetic reaction was performed at lower temperature (140-160 ^{o}C), indicating that a thermodynamic equilibrium of nanobars was being established at a wide range of the temperature.

The elongation of nanoparticles from 25 nm x 50 nm-sized nanobar to 25 nm x 150 nm-sized nanorods with increasing 6-aminohexanoic acid (AHA) concentration from 0.031 to 0.610 M was clearly observed. The general trend is sketched in Figure 7.2.1g. This observation indicates that the high surfactant concentration (0.610 M) favors the overgrowth of an anisotropic $MnWO_4$ structure and a long nanorod (high aspect ratio) was obtained. However, with higher surfactant concentrations (≥0.915 M), no significant change in the aspect ratio was observed suggesting that the equilibrium of growth kinetics could be established at this surfactant concentration. These experimental results suggest that the (021) faces of nanocrystals were selectively adsorbed and stabilized by AHA molecules, while the (100) faces were uncovered. The crystal grew anisotropically along the [100] direction due to their higher surface energies resulting in the nanorod product. Because AHA adsorbed onto only specific (021) faces, the nanorods with high aspect ratios produced at high AHA concentration could be due to the oriented attachment of nanocrystals predominantly during the synthesis.[35] To study the effect of the pH of synthesis solution as well as the reaction temperature on shape of the $MnWO_4$ products, a series of experiments was carried out under the same reaction conditions, except that either the pH of solution or the reaction temperature changed. As seen in Figure 7.2.1a, for sample 1 in Table 7.2.1, at 180 ^{o}C, with pH of 9, 25 nm x 50 nm nanobars were obtained. Under the same synthesis conditions, however, the pH of initial solution was 6 instead of 9.

The pH of 6 in the initial solution was adjusted by using 1M HNO_3 solution. $MnWO_4$ square-like nanosheets with the particle size of ~25 nm were produced (Figure 7.2.2a). This indicates the change of shape from the nanobars to the square-like nanosheets by only decreasing the pH of solution from 9 to 6. The pH change in the reaction solution could influence the binding and selective adsorption of the surfactant molecules on the particle surface leading to the shape change of the products. In this case, the shape change could be due to the protonation/deprotonation and consequently a decrease of selective adsorption of 6-aminohexanoic acid molecules (AHA) to crystal faces with the pH change from 9 to 6. Figure 7.2.2 also shows TEM images of the $MnWO_4$ nanoparticles synthesized with the pH of 6 instead of 9 for 20 h at different reaction temperatures: 180, 200, 220 ^oC, and keeping the other conditions unchanged ($[Mn^{2+}] = [WO_4^{2-}] = 0.015$ M, AHA/(Mn+W) = 2:1).

Under these synthetic conditions (with pH = 6) as increasing the temperature from 180 to 200 ^oC, 18 nm-sized quasi-nanospheres were produced (Figure 7.2.2b). At the reaction temperature of 220 ^oC, nanospheres were found instead of quasi-nanospheres (Figure 7.2.2c). SAED pattern of a single sphere, as seen in Figure 7.2.2d, exhibits strong ring patterns assigned to (100), (011), (111), (002), (102) planes, corresponding to a pure monoclinic phase of $MnWO_4$, and proves a single-crystal structure of the nanospheres, which is consistent with the XRD data (see below). These results indicate that for the pH of 6, increasing reaction temperature from 180 to 220 ^oC, the shape of $MnWO_4$ nanoparticles was changed from square into sphere, while preserving their particle size and monoclinic structure. This shape change could be explained by the Wuff facets theory.[36,37] According to this theory, the growth rate of a crystal facet depends exponentially on the surface energy. High-energy facets thus grow more quickly than others and they were minimized surface energies during growth.[38]

Because no monomer precursors were added during the synthesis, at the relatively low reaction temperature (e.g., 180 ^oC), the $MnWO_4$ nanosquares were formed in the anisotropic growth of high-energy crystal faces owing to high precursor monomer concentration in bulk solution. At higher synthesis temperature (e.g., 200-220 ^oC), the shape change of the nanoparticles from square to quasi-sphere and final to uniform sphere may result in the insufficient coverage of AHA molecules toward crystal faces owing to weak interactions between AHA and nanoparticles. The depletion of remaining precursor monomer concentration in bulk solution to a level lower than that required for a given anisotropic shape. Consequently, the monomers of the dissolved crystals at higher energy faces could move thermodynamically to the lower energy faces to minimize the surface energies. As a result, the corners and tips of the square-shaped $MnWO_4$ nanoparticles were "rounded", which leads to the formation of stable nanospheres with a minimum face energy.

Figure 7.2.3 shows XRD patterns of the $MnWO_4$ samples of 25 nm x 50 nm nanobars and 18 nm nanospheres. All the diffraction peaks of both samples are well indexed to monoclinic $MnWO_4$ phase with lattice parameters of a = 4.819 Å, b = 5.771 Å, c = 5.005 Å, which are comparable with reported database values of a = 4.829 Å, b = 5.759 Å, c = 4.998 Å for bulk $MnWO_4$ (JCPDS File No. 13-0434).[39] The broadening and intense diffraction peaks indicate the small particle size and high crystallinity of the as-synthesized products. An average particle size of nanospheres estimated from the broadening (111) peaks using the Debye-Scherrer equation is about 16.5 nm, which is in agreement with the particle size observed from TEM images. No other phases of either single manganese oxides or tungsten oxides were detected in the $MnWO_4$ nanoparticles indicating that a pure monoclinic $MnWO_4$ phase obtained by this synthetic approach. It is observed that the intensity of the diffraction peak from (100) plane of the nanobars is stronger than that of the nanospheres. This also indicates a growth orientation of the (100) plane in a single-crystalline $MnWO_4$ nanobar, which is consistent with the HRTEM analysis.

Furthermore, to gain further insights into the steric effect of the capping ligands on the shape of $MnWO_4$ nanoparticles, two additional amino acid surfactants with different alkyl chain lengths: 5-aminovaleric acid (AVA, C_5) and 2 aminononanoic acid (ANA, C_{10}) were employed, compared to 6-aminohexanoic acid (AHA, C_6). TEM images of these samples shown in Figure 7.2.4 indicate that when using 5-aminovaleric acid (C_5) instead of 6-aminohexanoic acid (C_6), no significant change in the shape of nanobars (25 nm x 50 nm) was observed (Figure 7.2.4a and Figure 7.2.1a). However, using amino acid with a longer alkyl chain length, e.g., 2-aminononanoic acid (C_{10}), 18 nm-sized $MnWO_4$ nanohexagons were produced (Figure 7.2.4b). A representative TEM image of this sample also exhibits a self-assembled 2D array of nanohexagons with a nearest-neighbor spacing of ~2 nm. It can be concluded that the increase of alkyl chain length of amino acid surfactant led to the change of shape: from anisotropic (nanobar) into isotropic nanocrystal (nanosphere/nanohexagon). This is also consistent with our previous report for the synthesis of vanadium oxide nanocrystals that longer alkyl chain lengths generated smaller particles owing to the slower nucleation and growth rate.[40]

The chemical composition and oxidation state on the surface of 6-aminohexanoic acid-capped manganese tungstate nanobars (sample 1 in Table 7.2.1) were analysed by the XPS technique. The survey XPS spectrum of 25 nm x 50 nm $MnWO_4$ nanobars shows the presence of Mn 2p, W 4f, O 1s, N 1s, C 1s (data not shown). Elemental dispersive spectrum (EDS) analysis of this sample (data not shown) also exhibits the presence of Mn, W, O. The Mn:W molar ratio determined from both techniques was close to 1:1. Figure 7.2.5 shows high-resolution Mn 2p and W 4f XPS spectra of this sample. For the Mn 2p XPS spectrum (Figure 7.2.5a), two Mn $2p_{3/2}$ and Mn $2p_{1/2}$ peaks at 640.5 - 650.0 eV and 642.8 - 653.7 eV, respectively, are similar to those of bulk MnO,[41] corresponding to the oxidation state of Mn^{2+}. For the W 4f XPS spectrum (Figure 7.2.5b), W $4f_{7/2}$ and W $4f_{5/2}$ peaks at 35.4 and 37.5 eV, respectively, were assigned to the oxidation state of W^{6+}.[42] The O 1s XPS spectrum (data not shown) is composed of two peaks at 530.0 and 531.8 eV, which can be assigned to Mn-O-W bond in $MnWO_4$ and O-C bond in 6-aminohexanoic acid, respectively.[43,44] This suggests that the stoichiometric ratio is close to $MnWO_4$ on the nanobar surface. The N 1s and C 1s XPS spectra of this sample (data not shown) indicate that 6-aminohexanoic acid molecules bound on the $MnWO_4$ nanobar surface. The N 1s region contains a main peak at 399.8 eV, which was assigned to nitrogen in $-NH_2$ group.[45] The C 1s region consists of three XPS peaks at 285.8, 286.0, 288.0 eV assigning to C-C, C-N, C-C=O groups of 6-aminohexanoic acid molecules, respectively.[45]

To understand the nature of the interaction between 6-aminohexanoic acid molecule and $MnWO_4$ nanoparticle surface, an experiment was carried out under the same reaction conditions for the synthesis of $MnWO_4$ nanoparticles, except for using hexamethylenediamine (two amino head-groups at the two ends of the molecule) instead of 6-aminohexanoic acid. $MnWO_4$ nanobars were obtained almost the same shape of the product prepared using 6-aminohexanoic acid. FTIR spectrum (data not shown) of hexamethylenediamine-capped $MnWO_4$ nanobars shows the bands at 2920-2845 cm^{-1} are assigned to the C-H stretching modes of alkyl chain in hexamethylenediamine. The bands at 1458 and 3330 cm^{-1} are attributed to the C-N and N-H stretching modes of amino groups in hexamethylenediamine capping on $MnWO_4$ surface, respectively.[46] The bands at 600 - 830 cm^{-1} corresponding to the WO_4^{2-} vibrations are characteristic of $MnWO_4$.[47] It suggests that in order to keep the same shape of nanobar in both cases ($MnWO_4$ nanobars prepared using capping 6-aminohexanoic acid and hexamethylenediamine), the amino ($-NH_2$) functional groups capped on the nanobar surface possibly due to the predominant donor of their free electron pair. This is further illustrated by the FTIR spectra of free 6-aminohexanoic acid and 6-aminohexanoic acid-stabilized $MnWO_4$ sample (see below).

In this synthesis approach, water is adopted as the continuous solution phase and inorganic salts were used as starting materials. Due to the high solubility of the salts in aqueous solution, we could be applicable to synthesize the nanoparticles in scale up by using the high precursor monomer concentrations. This aqueous-based method is thus a promising way in the academic laboratory as well as can be expanded to the industrial scale in a simple way. The effect of precursor monomer concentration on the critical shape of the $MnWO_4$ nanobars for the large-scale synthesis was studied. The synthesis experiments were performed with different precursor (Mn+W) monomer concentrations from medium to high; from 0.122 to 0.305 M, and keeping other synthesis conditions unchanged (AHA/(Mn+W) molar ratio = 2:1, pH = 9, 180 ^{o}C, 20 h). Interestingly, as increasing the precursor monomer concentration from 0.122 to 0.305 M, the shape of the final product was not affected (nanobars with the aspect ratio of ~2.5), as shown in Figure 7.2.6a. This may refer that the thermodynamically stability of the nanobars is established in a wide range of precursor monomer concentration (0.015 - 0.305 M). In fact, we obtained as much as 16 grams of ~25 nm x 50 nm $MnWO_4$ nanobars per single run in a 700 mL-sized autoclave when the high precursor concentration of 0.122 M was used (Figure 7.2.6). A schematic illustration for the formation and shape control of the products under different synthetic conditions can be overall summarized in details in Scheme 7.2.1.

Sacrificial organic surfactants can act as structure-directing agents or soft templates and are widely used to design nano/microstructures with peculiar morphologies.[48] For example, with the use of amino acid molecules, a variety of three-dimensional complex microarchitectures has been constructed.[49] In this work, we also found that the formation of 3D hierarchical $MnWO_4$ microspheres from the spontaneous assembly of primary $MnWO_4$ nanoparticles is very sensitive with low monomer precursor concentrations in the synthesis solution (e.g., 0.0120-0.0076 M) of Mn^{2+} cation and WO_4^{2-} anion precursors, in the presence of 6-aminohexanoic acid surfactant. A series of experiments was carried out at the gradual decreased precursor concentration from 0.015 to 0.012, 0.0076 M, corresponding to the (Mn+W)/AHA molar ratio of 0.48:1, 0.39:1, 0.25:1, while keeping other reaction conditions unchanged ($[Mn^{2+}] = [WO_4^{2-}] = 1:1$, 0.031 M of AHA, pH = 9, 180 ^{o}C, 20 h). The morphologies and microstructures of the final products examined by SEM, TEM, SAED, XRD are shown in Figure 7.2.7 and 7.2.10.

It is important to note that with the precursor monomer concentration of 0.015 M, only monodisperse single-crystalline nanobars with an average dimension of 25 nm x 50 nm were formed, and no nanobar aggregation was observed (see Figure 7.2.1a). When the (Mn+W)/AHA molar ratio decreased from 0.48:1 to 0.39:1 (reducing 1.27 times of the precursor concentration in the initial solution), 25 nm x 50 nm-sized nanobars were intact. Polydisperse $MnWO_4$ microspheres with an average diameter of ~7 µm were however self-assembled from primary nanobars. Some nanobar stacks and individual nanobars were still observed at this precursor concentration. It is worth pointing that when the (Mn+W)/AHA molar ratio decreased to 0.25:1 (reducing 2 times), the shape of the $MnWO_4$ nanobars (~25 nm x 50 nm) was still unchanged. These individual nanobars however had a greater tendency to form quite monodisperse hierarchical microspheres were formed, which are constituted from randomly individual nanorods. Figure 7.2.7 shows SEM images of this product. The overall morphology of the $MnWO_4$ microsphere sample shows in Figure 7.2.7a indicating that numerous microspheres with quite monodispersity with two size populations, 3-5 μm and 8-16 μm were achieved with this precursor concentration. Figure 7.2.7b shows a single $MnWO_4$ microsphere with a diameter of 16 μm. As seen in Figure 7.2.7c, the peripheral surface of the microsphere is rough and each microsphere is composed of numerous disordered nanobars suggesting that the formation of microspheres is likely driven by the interaction of inter-nanobars.

This observation was further confirmed by TEM measurements. Figure 7.2.7d displays a single $MnWO_4$ microsphere with an average diameter of 16 μm. Higher-magnification TEM image (Figure 7.2.7e) taken at a border of this microsphere also exhibits the self-assembly of individual ~25 nm x 50 nm $MnWO_4$ nanobars, in good agreement with SEM observation. These nanobars were arranged disorderly instead of regularly on the surface. SAED pattern taken from a selected microsphere shows diffuse rings (inset Figure 7.2.7e), indicating that the microsphere is polycrystalline, because it is composed of numerous primary nanobars. To obtain information about the inner structure of the hierarchical microspheres, $MnWO_4$ microspheres were cracked by ultrasonic treatment in a water batch for 30 min. As seen in Figure 7.2.7f, their inner structure consists of nanobar blocks. It can be concluded that the formation of self-assemblied $MnWO_4$ hierarchical microspheres from nanobars is favorable at relatively low precursor concentration (0.0076 M) of Mn^{2+} cation and WO_4^{2-} anion precursors in the initial synthesis solution.

Furthermore, when water/ethylene glycol (10:30 mL) medium was used instead of 100% distilled water under the same synthetic conditions ($[Mn^{2+}] = [WO_4^{2-}] = 0.0076$ M, 0.031 M of AHA, pH = 9, 180 °C, 20 h) for the synthesis of $MnWO_4$ hierarchical microspheres (sample 8 in Table 7.2.1). The morphology and crystalline structure of the products are shown in Figure 7.2.8.

Novel 3 μm-sized nanoplatelet-based microapples with two holes on their poles were observed (Figure 7.2.8a-c). Figure 7.2.8d presents TEM image of the $MnWO_4$ microapples with the same size. The whole microapple surface is composed of densely packed nanoplatelets aligned forming the apple-like structure. The nanoplatelets with an average thick of 15 nm are arranged regularly but not connected to each other. The formation of small nanoplatelets seems to be caused by the slow growth of $MnWO_4$ nuclei in the high viscous environment of ethylene glycol solvent.

The porosity of the $MnWO_4$ hierarchical microspheres (sample 9 in Table 7.2.1) was generated by a removal of 6-aminohexanoic acid molecules upon calcination at 550 ^oC for 2 h. SEM/TEM images of this calcined sample are shown in Figure 7.2.9 indicating that the microspherical morphology was well remained even after calcination. XRD patterns of the as-made microspheres, as-made microapples, calcined microspheres of $MnWO_4$ (Figure 7.2.10a-c) also show a pure monoclinic structure similar to the crystalline phase of the $MnWO_4$ nanobars. The broadening diffraction peaks also indicate that the $MnWO_4$ microspheres are composed of nanobars. Figure 7.2.11a shows thermogravimetric analysis (TGA) curve of 6-aminohaxanoic acid-capped $MnWO_4$ microspheres (sample 9), from which only one weight-loss step (~24%) was observed. This step is in the range of 135 to 450 °C, corresponding to combustion and elimination of 6-aminohexanoic acid molecules. N_2 adsorption/desorption isotherms (Figure 7.2.11b) of this calcined $MnWO_4$ microspheres exhibit a typical type-IV isotherm with a hysteretic loop in the range of 0.6-1.0P/P_o, indicating the presence of mesoporosity in this material.[50] BET surface area, pore volume, BJH pore radius of this sample are ~30 m^2g^{-1}, ~0.38 cm^3g^{-1}, ~26 nm, respectively. The generated mesoporosity in this calcined material is owing to the inter-nanobar spaces, and a large mesopore size distribution could be due to a disordered aggregation of single-crystalline $MnWO_4$ nanoparticles. This clearly illustrates the formation of the mesocrystal microspheres.[51,52] Both the mesocrystal microspheres and micro-like apples are expected to have potential applications as many functional materials and reduced resistance to diffusion for adsorption and reaction, particularly, for large molecular guest species.

The formation of the $MnWO_4$ microspheres at the low monomer Mn/W precursor concentration could be associated with the peptide process of the carboxylic and amino groups of neighboring 6-aminohexanoic acid molecules in aqueous solution to form dipeptide and/or polypeptide chains.[53] They can serve as polymer template like polyvinyl pyrrolidone (PVP),[54] to assemble nanoparticles yielding a second structure of $MnWO_4$ microspheres through the hydrogen-bonding interaction of polypeptides.[55]

To clarify the assembly mechanism of microspheres, FTIR spectra of free 6-aminohexanoic acid (AHA) and AHA-capped $MnWO_4$ microspheres (sample 9 in Table 7.2.1) were measured to assess the interaction between 6-aminohexanoic acid and nanobars, as well as the formation of peptide bonds. Figure 7.2.12 indicates that FTIR bands at 2855 - 2950 cm^{-1} are attributed to the C-H stretching vibrations of methylene groups of the AHA molecule for both samples.[56] A band at 1386 cm^{-1} corresponding to C-N stretching mode of AHA molecules was identified in the both samples, which illustrated the binding of amino groups to the $MnWO_4$ nanobar surface.[57] The spectrum for free AHA shows two peaks at 1536 and 1560 cm^{-1} corresponding to the symmetric and asymmetric stretching vibrations of uncoordinated $-COO^-$ terminus of free AHA. For the AHA-capped $MnWO_4$ microsphere sample, the IR bands at 1536 and 1560 cm^{-1} were absent, however, an IR band at 1631 cm^{-1} corresponding to the stretching frequency of the C=O groups from peptide bonds (O=C···N-H) was observed.[58] Furthermore, a specific peak at 1160 cm^{-1} appeared corresponding to the stretching vibration of the peptide backbone.[59] These results prove that only the amino ($-NH_2$) group of AHA molecules capped on the surface of $MnWO_4$ nanoparticles and the free carboxylic (-COOH) terminus was oriented outward. The polypeptide chains were formed through the interaction between this uncoordinated carboxylic group on the nanobar surface and the amino group of residual 6-aminohexanoic acid in aqueous solution. These demonstrations indicate that the concentration of formed peptide chains in bulk solution is a critical factor during the self-assembly of the peptide structure and consequently affects the morphology and the formation of assembled $MnWO_4$ microspheres. The microsphere morphology can thus be controlled by adjusting the concentration of the peptide, that is, the concentration of 6-aminohexanoic acid.

This phenomenon can be considered that with a low concentration of Mn^{2+} and WO_4^{2-} precursors (0.0076 M, (Mn+W)/AHA molar ratio of 0.25:1), consequently, a low nucleation of $MnWO_4$ atoms, and a small amount of $MnWO_4$ nanoparticles was produced.[60,61] Due to the relatively high surfactant concentration (0.031 M), an excess amount of free 6-aminohexanoic acid exists in the aqueous synthesis solution, the dipeptide/polypeptide process of both $-NH_2$ and -COOH groups of free 6-aminohexanoic acid occurred on the basis of nucleophile mechanism,[62] resulting in the formation of polypeptide chains (polymer template). Because only small amount of $MnWO_4$ nanobars was yielded in bulk solution and the high AHA concentration, the peptide reaction continued and the reaction between the amino groups of the formed amino acid sequence of protein (see Figure 7.2.13) and the uncoordinated carboxylic groups on the nanoparticle surface to generate the polypeptide-stabilized $MnWO_4$ nanobars. Subsequently, highly oriented backbone-backbone intermolecular hydrogen-bonding interactions of numerous amphiphilic polypeptide chains via either antiparallel or parallel arrangements were proceeded to spontaneous-assemble into polypeptide-stabilized $MnWO_4$ microspheres. These interactions are thermodynamically favorable due to the reduction of the particle surface energy when the interface is eliminated. On the contrary, a large amount of monodisperse nanobars was yielded using a higher precursor monomer concentration (0.015 M, (Mn+W)/AHA molar ratio of 0.48:1) with a faster nucleation of $MnWO_4$ atoms. The excess amount of free 6-aminohexanoic acid in synthesis solution decreased strongly because they were consumed more for the capping on nanobar surface. We believe that, herein, the construction of self-assembled microspheres can be confined because the dipeptide or/and polypeptide process of residual 6-aminohexanoic acid on the particle surface occurred in very low degree. A possible proposed mechanism of the "one-step" formation of self-assemblied $MnWO_4$ hierarchical microspheres is illustrated in Scheme 7.2.2.

Figure 7.2.14 shows UV/vis absorption and photoluminescence (PL) spectra of the sample 1: 25 nm x 50 nm $MnWO_4$ nanobar and sample 9: 7 μm $MnWO_4$ microspheres in Table 7.2.1. It is commonly accepted that the optical properties of the metal tungstate materials are strongly dependent on their morphology and crystallinity. Changes in shape would modify the electronic structures of tungstate leading to change in optical properties.[63] The UV/vis absorption spectra (Figure 7.2.14A) of both nanobars and microspheres exhibit a single absorption peak at 284 nm, attributing to a charge-transfer transition between the O 2p orbitals and the empty d orbitals of the central W ion.[64] The broadening absorption of the nanobars could result of the smaller particle size of products owing to quantum confinement effect.[65]

The PL emission spectra (Figure 7.2.14B) of these samples show the same blue emission bands at 449, 483, 527, 559 nm under the 253 nm excitation. These emission bands are attributed to the transition from the $^1A_1$ ground-state to the high vibration level of $^1T_2$ and from the low vibration level of $^1T_2$ to the $^1A_1$ ground-state within the tetragonal WO_4^{2-} groups.[21] This is due to the excitation of WO_4^{2-} group from charge-transfer p-d transition. As a result, the emission band positions are not strongly dependent on the morphology of the $MnWO_4$ lattices. However, using the same particle concentration under the identical measurement conditions, the nanobars show a higher upconversion efficiency than that the microspheres. The relative intensity of the nanobars is almost 2.5 times higher than that of the microspheres. Because the size of nanobars (~25 nm x 50 nm) is almost the same for the both samples, a lower PL emission intensity of the $MnWO_4$ microspheres compared to that of the $MnWO_4$ nanobars could be due to a part of nanobars inside of microspheres. It also indicates that an exposed surface of the microspheres under the excitation is lower than that of nanobars.

7.2.4. Conclusion

In conclusion, we have developed a facile single-step approach for the large-scale synthesis of the single-crystalline $MnWO_4$ nanoparticles and 3D hierarchical mesocrystal microspheres from the hydrothermal reaction in water or water/ethylene glycol medium using $Mn(NO_3)_2$ and Na_2WO_4, as starting precursors and capping bifunctional amino acid biomolecules with different alkyl chain lengths such as 5-aminovaleric acid, 6-aminohexanoic acid, 2-aminononanoic acid. Monodisperse $MnWO_4$ nanoparticles were capped by the amino head group of amino acid biomolecules and the uncoordinated carboxylic terminus were oriented outward to provide the water-dispersible nature of the hydrophilic nanoparticles. The uniform single-crystalline $MnWO_4$ nanoparticles with bar, rod, square, quasi-sphere, sphere, hexagonal shapes were achieved by tuning the synthesis parameters such as the concentration and the alkyl chain length of amino acids, pH of solution, and reaction temperature. Furthermore, by decreasing the Mn^{2+} and WO_4^{2-} precursor monomer concentration from 0.0150 to 0.0076 M in water medium, rigid $MnWO_4$ mesocrystal hierarchical microspheres were formed from the spontaneous-assembly of primary nanoparticles through the backbone-backbone intermolecular hydrogen-bonding interactions of polypeptide chains. Using water/ethylene glycol (10:30 mL) instead of distilled water medium, novel nanoplatelet-based microapples with two holes on their poles were yielded. The mesocrystal microspheres with relatively high porosity were generated after removal of surfactant upon calcination.

The photoluminescence results indicate that the PL emission intensity of the $MnWO_4$ nanobars is higher than that of the $MnWO_4$ microspheres indicating the decrease in the luminescence efficiency of the microspheres due to nanobars inside of microspheres. This current approach is easy to scale up (for example, uniform $MnWO_4$ nanobars can be produced in a large quantity of ~16 grams in a single preparation run), using inexpensive precursors, amino acid biomolecules as bifunctional surfactant, water as environmentally solvent. We believe that these shape-controlled $MnWO_4$ nanoparticles and 3D hierarchical $MnWO_4$ mesocrystal microspheres have highly potential applications in photocatalysis, humidity sensor, etc. The synthetic procedure can be extended to the "green" synthesis of other nanomaterials.

7.2.5. References

(1) U. Banin, *Nat. Mater.* **2007**, *6*, 625.

(2) Z. Nie, A. Petukhoval, E. Kumacheval, *Nat. Nanotech.* **2010**, *5*, 15.

(3) A. V. Blaaderen, *Nature* **2009**, *461*, 892.

(4) C. B. Burda, X. B. Chen, R. Narayanan, M. A. E. Sayed, *Chem. Rev.* **2005**, *105*, 1025.

(5) H. G. Yang, C. H. Sun, S. Z. Qiao, J. Zou, G. Liu, S. C. Smith, H. M. Cheng, G. Q. Lu, *Nature* **2008**, *453*, 638.

(6) X. W. Lou, L. A. Archer, Z. Yang, *Adv. Mater.* **2008**, *20*, 3987.

(7) S. C. Glotzer, M. J. Solomon, *Nat. Mater.* **2007**, *6*, 557.

(8) W. Fan, M. A. Synder, S. Kumar, P. S. Lee, W. C. Yoo. A. V. Mccormick, R. L. Penn, A. Stein, M. Tsapatsis, *Nat. Mater.* **2008**, *7*, 984.

(9) J. Zhuang, A. D. Shaller, J. Lynch, H. Wu, O. Chen, A. D. Q. Li, Y. C. Cao, *J. Am. Chem. Soc.* **2009**, *131*, 6084.

(10) W. M. Qu, W. Wlodarski, J. U. Meyer, *Sens. Actuators B* **2000**, *64*, 76.

(11) A. H. Arkenbout, T. T. M. Palstra, T. Siegrist, T. Kimura, *Phys. Rev. B.* **2006**, *74*, 184431.

(12) O. Heyer, N. Hollmann, I. Klassen, S. Jodlauk, L. Bohaty, P. Becker, J. A. Mydosh, T. Lorenz, D. Khomskii, *J. Phys.: Condens. Matter* **2006**, *18*, L471.

(13) K. Taniguchi, N. Abe, T. Takenobu, Y. Iwasa, Arima, T. *Phys. Rev. Lett.* **2006**, *97*, 203.

(14) Y. Xing, S. Song, J. Feng, Y. Lei, M. Li, H. Zhang, *Solid State Sci.* **2008**, *10*, 1299.

(15) L. Zhang, C. Lu, Y. Wang, Y. Cheng, *Materials Chemistry and Physics* **2007**, *103*, 433.

(16) W. Qu, W. Wlodarski, J. U. Meyer, *Sensors and Actuators B* **2000**, *64*, 76.

(17) R. Bharat, R. A. Singh, *Phys. Chem. Solids* **1982**, *43*, 641.

(18) M.A.K.L. Dissanayake, P.A.R.D. Jayathilaka, Bokalawela, R.S.P. *Electrochim. Acta* **2005**.

(19) Y. X. Zhou, Q. Zhang, J. Y. Gong, S. H. Yu, *J. Phys. Chem. C* **2008**, *112*, 13383.

(20) L. Zhang, C. Lu, Y. Wang, Y. Cheng, *Materials Chemistry and Physics* **2007**, *103*, 433.

(21) F. Zhang, Y. Yiu, M. C. Aronson, S. S. Wong, *J. Phys. Chem. C* **2008**, *112*, 14816.

(22) S. H. Yu , B. Liu , M. S. Mo , J. H. Huang , X. M. Liu , Y. T. Qian, *Adv. Func. Mater.* **2003**, *13*, **639.**

(23) S. Thongtem, S. Wannapop, A. Phuruangrat, T. Thongtem, *Materials Letters* **2009**, *63*, 833.

(24) Y. X. Zhou, Q. Zhang, J. Y. Gong, S. H. Yu, *J. Phys. Chem. C* **2008**, *112*, 13383.

(25) D. Mrabet, M. H. Zahedi-Niaki, T. O. Do, *J. Phys. Chem. C* **2008**, *112*, 7124.

(26) T. D. Nguyen, D. T. Cao, T. N. Dinh, T. O. Do, *J. Phys. Chem. C* **2009**, *113*, 18584.

(27) T. D. Nguyen, C. T. Dinh, T. D. Do, *Langmuir* **2009**, *25*, 11142.

(28) C. T. Dinh, T. D. Nguyen, F. Kleitz, T. O. Do, *ACS Nano* **2009**, *3*, 3737.

(29) T. D. Nguyen, C. T. Dinh, T. O. Do, *ACS Nano* **2010**, *4*, 2263-2273.

(30) D. Wang, T. Xie, Q. Peng, Y. Li, *J. Am. Chem. Soc.* **2008**, *130*, 4016.

(31) E. E. Lees, T. L. Nguyen, A. H. A. Clayton, P. Mulvaney, *ACS Nano* **2009**, *3*, 1121.

(32) B. Liu, H. C. Zeng, *J. Am. Chem. Soc.* **2004**, *126*, 8124.

(33) W. S. Wang, L. Zhen, C. Y. Xu, B. Y. Zhang, W. Z. Shao, *J. Phys. Chem. B* **2006**, *110*, 23154.

(34) S. Lei, K. Tang, Z. Fang, Y. Huang, H. Zheng, *Nanotechnology* **2005**, *16*, 2407.

(35) R. L. Penn, *J. Phys. Chem. B* **2004**, *108*, 12707.

(36) J. W. Mullin, Crystallization, 3rd ed.; Butterworth-Heinemann: Woburn, MA, **1997**.

(37) G. Wulff, F. Zeitschrift, *Beitr. Krystallogr. Mineral.* **1901**, *34*, 449.

(38) Y. Yin, A. P. Alivisatos, *Nature* **2005**, *437*, 664.

(39) Joint Committee on Powder Diffraction Standards diffraction data file no. 13-434, International Center for Diffraction Data, Newtown Square, PA, USA, **1963**.

(40) T. D. Nguyen, T. O. Do, *Langmuir* **2009**, *25*, 5322.

(41) J. F. Moulder, W. F. Stickle, P. E. Sobol, K. D. Bomben, Handbook of X-ray photoelectron spectroscopy; Perkin-Elmer corporation, Physical Electronics Division: **1992**.

(42) F. Zhang, M. Y. Sfeir, J. A. Misewich, S. S. Wong, *Chem. Mater.* **2008**, *20*, 5500.

(43) Q. Zhang, X. Chen, Y. Zhou, G. Zhang, S. H. Yu, *J. Phys. Chem. C* **2007**, *111*, 3927.

(44) V. V. Atuchin, V. G. Kesler, N. Y. Maklakova, L. D. Pokrovsky, D. V. Sheglov, *Eur. Phys. J. B* **2006**, *51*, 293.

(45) Z. Deng, B. Peng, D. Chen, F. Tang, A. Muscat, J. *Langmuir* **2008**, *24*, 11089.

(46) J. Yang, J. Y. Ying, *Nat. Mater.* **2009**, *8*, 683.

(47) Y. X. Zhou, Q. Zhang, J. Y. Gong, S. H. Yu, *J. Phys. Chem. C* **2008**, *112*, 13383.

(48) B. L. Cushing, V. L. Kolesnichenko, C. J. O'Connor, *Chem. Rev.* **2004**, *104*, 3893.

(49) F. C. Meldrum, H. Colfen, *Chem. Rev.* **2008**, *108*, 4332.

(50) Y. Li, M. Cao, L. Feng, *Langmuir* **2009**, *25*, 1705.

(51) A. N. Kulak, P. Iddon, Y. Li, S. P. Armes, H. Colfen, O. Paris, R. M. Wilson, F. C. Meldrum, *J. Am. Chem. Soc.* **2007**, 129, 3729.

(52) R. Q. Song, H. Colfen. *Adv. Mater.* **2010**, *22*, 1301.

(53) J. D. Hartgerink, E. Beniash, S. I. SStupp, *Science* **2001**, *294*, 1684.

(54) M. H. Kim, B. Lim, E. P. Lee, Y. Xia, *J. Mater. Chem.* **2008**, *18*, 4069.

(55) S. Kiyonaka, K. Sada, I. Yoshimura, S. Shinkai, N. Kato, I. Hamachi, *Nat. Mater.* **2004**, *3*, 58.

(56) T. D. Nguyen, D. Mrabet, T. D. Do, *J. Phys. Chem. C* **2008**, *112*,15226.

(57) L. Polavarapu, Q. H. Xu, *Nanotechnology* **2008**, *19*, 075601.

(58) N. T. Whilton, P. J. Vickers, S. Mann, *J. Mater. Chem.* **1997**, *7*, 1623.

(59) Z. Zhang, D. Gao, H. Zhao, C. Xie, G. Guan, D. Wang, S. H. Yu, *J. Phys. Chem. B* **2006**, *110*, 8613.

(60) R. Xie, Z. Li, X. Peng, *J. Am. Chem. Soc.* **2009**, *131*, 15457.

(61) S. G. Kwon, Y. Piao, J. Park, S. Angappane, Y. Jo, N. M. Hwang, J. G. Park, T. Hyeon, *J. Am. Chem. Soc.* **2007**, *129*, 12571-12584.

(62) H. Matsui, B. Gologan, H. Schaffer, F. Adar, D. Seconi, O. Phanstiel, *Langmuir* **2000**, *16*, 3148.

(63) L. Xu, J. Shen, C. Lu, Y. Chen, W. Hou, *Crystal Growth & Design* **2009**, *9*, 3129.

(64) Q. Zhang, X. Chen, Y. Zhou, G. Zhang, S. H. Yu, *J. Phys. Chem. C* **2007**, *111*, 3927.

(65) M. A. El-Sayed, *Acc. Chem. Res.* **2004**, 37, 326.

Table 7.2.1. Synthesis Conditions and Morphologies of the Monoclinic $MnWO_4$ Nano- and Microstructures via Amino Acid-Assisted Hydrothermal Process.[a]

Sample	Cation Precursor M	Anion Precursor M	Solvent mL	Amino acid M	pH	T°C	Size & Shape nm
1	0.015, $Mn(NO_3)_2$	0.015, Na_2WO_4	H_2O	0.031 AHA	9	180	25x50 nm-bar
2	0.015, $Mn(NO_3)_2$	0.015, Na_2WO_4	H_2O	0.305 AHA	9	180	25x100 nm-rod
3	0.015, $Mn(NO_3)_2$	0.015, Na_2WO_4	H_2O	0.610 AHA	9	180	25x150 nm-rod
4	0.015, $Mn(NO_3)_2$	0.015, Na_2WO_4	H_2O	0.031 AHA	6	180	25 nm-square
5	0.015, $Mn(NO_3)_2$	0.015, Na_2WO_4	H_2O	0.031 AHA	6	200	18 nm-quasi-sphere
6	0.015, $Mn(NO_3)_2$	0.015, Na_2WO_4	H_2O	0.031 AHA	6	220	18 nm-sphere
7	0.015, $Mn(NO_3)_2$	0.015, Na_2WO_4	H_2O	0.031 AVA	9	180	25x50 nm-bar
8	0.015, $Mn(NO_3)_2$	0.015, Na_2WO_4	H_2O	0.031 ANA	9	180	18 nm-hexagonal
9	0.0076, $Mn(NO_3)_2$	0.0076, Na_2WO_4	H_2O	0.031 AHA	9	180	7 µm-microsphere
10	0.0076, $Mn(NO_3)_2$	0.0076, Na_2WO_4	water/EG	0.031 AHA	9	180	3 µm-microapple

(a) All samples were synthesized by hydrothermal process for 20 h; 5-aminovaleric acid (AVA), 6-aminohexanoic acid (AHA), 2-aminononanoic acid (ANA), water/ethylene glycol (10:30 mL).

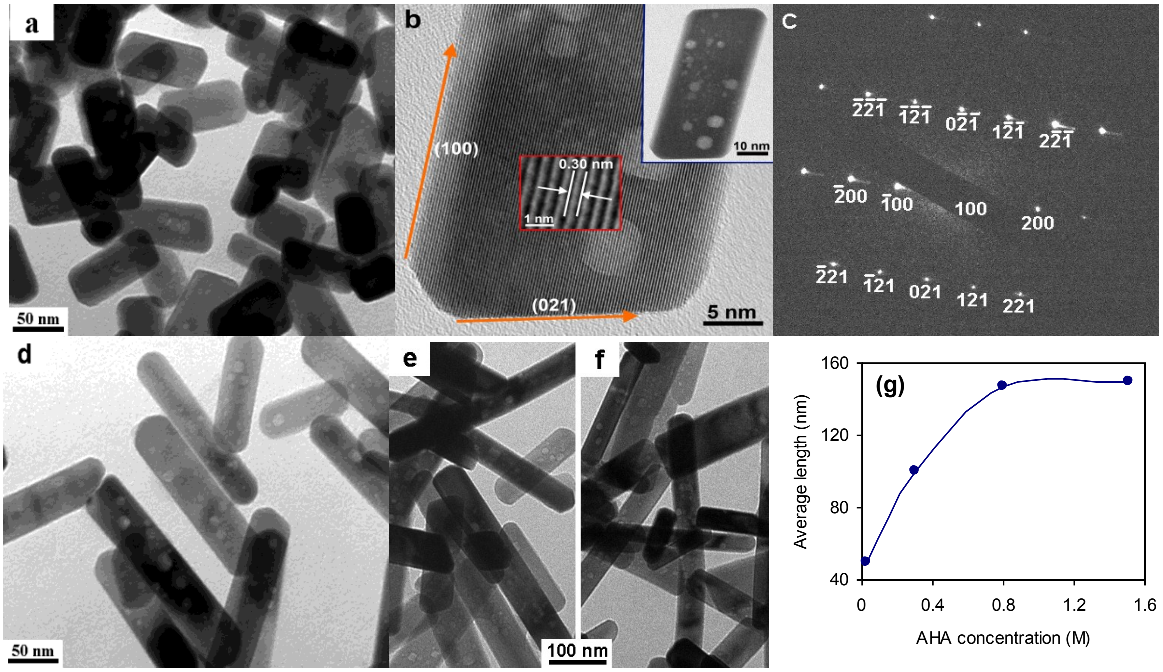

Figure 7.2.1. TEM images of the $MnWO_4$ nanoparticles synthesized from an aqueous solution of 0.015 M $Mn(NO_3)_2$ and 0.015 M Na_2WO_4, pH = 9, 180 °C for 20 h, using the different 6-aminohexanoic acid/(Mn+W) molar ratios (*AHA/P*): (a) 25 nm x 50 nm nanobars, *AHA/P* = 2:1; (b) HRTEM image of an individual nanobar; (c) SAED pattern of a single bar taking along [100] zone axis; (d) 25 nm x 100 nm nanorods, *AHA/P* = 10:1; (e) 25 nm x 150 nm nanorods, *AHA/P* = 20:1; (f) 25 nm x 150 nm nanorods, *AHA/P* = 30:1; (g) Correlation plot showing the relationship of 6-aminohexanoic acid concentration and average length of $MnWO_4$ nanorods.

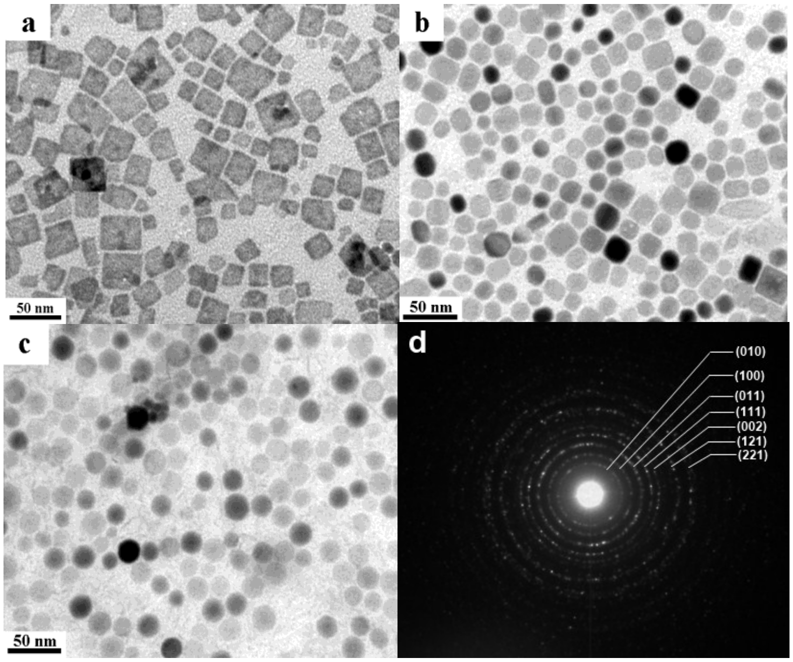

Figure 7.2.2. TEM images of the $MnWO_4$ nanoparticles synthesized from an aqueous solution of 0.015 M of $Mn(NO_3)_2$ and 0.015 M of Na_2WO_4, AHA/(Mn+W) molar ratio of 2:1, pH = 6, at the different reaction temperatures: (a) 18 nm square-like nanosheets, 180 ^{o}C; (b) 18 nm quasi-nanospheres, 200 ^{o}C; (c) 18 nm nanospheres, 220 ^{o}C; (d) SAED pattern of a single sphere in panel c, showing the single-crystal nature.

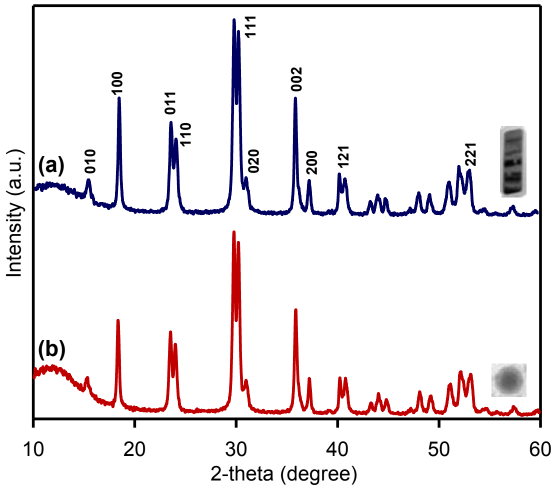

Figure 7.2.3. XRD patterns of the as-synthesized $MnWO_4$ samples: (a) nanobars (sample 1) and (b) nanospheres (sample 6 in Table 7.2.1).

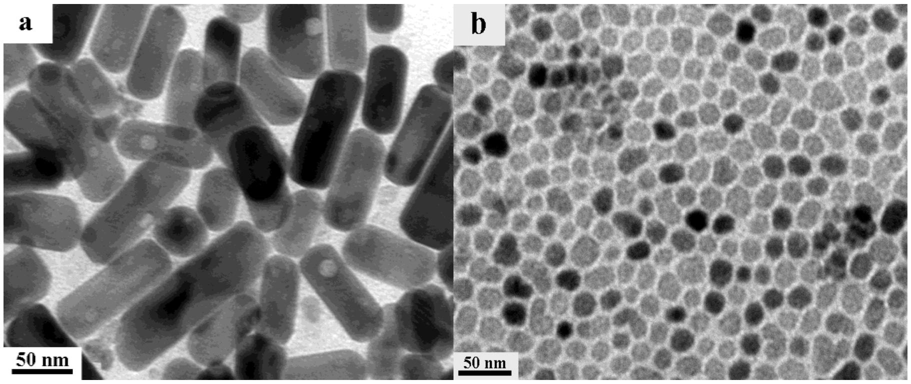

Figure 7.2.4. TEM images of the $MnWO_4$ nanoparticles synthesized using the different alkyl chain lengths of amino acids: (a) 25 nm x 50 nm nanobars, 5-aminovaleric acid (C_5); (b) 18 nm nanohexagons, 2-aminononanoic acid (C_{10}).

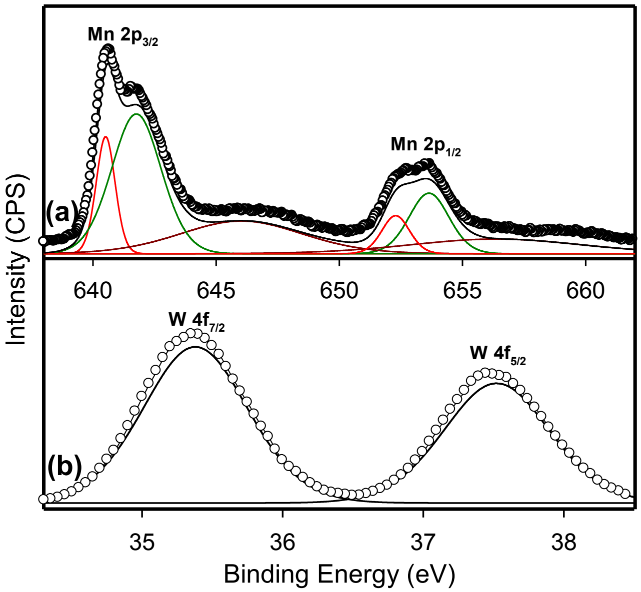

Figure 7.2.5. High-resolution (a) Mn 2p and (b) W 4f XPS spectra of 6-aminohexanoic acid-capped $MnWO_4$ nanobars (sample 1 in Table 7.2.1).

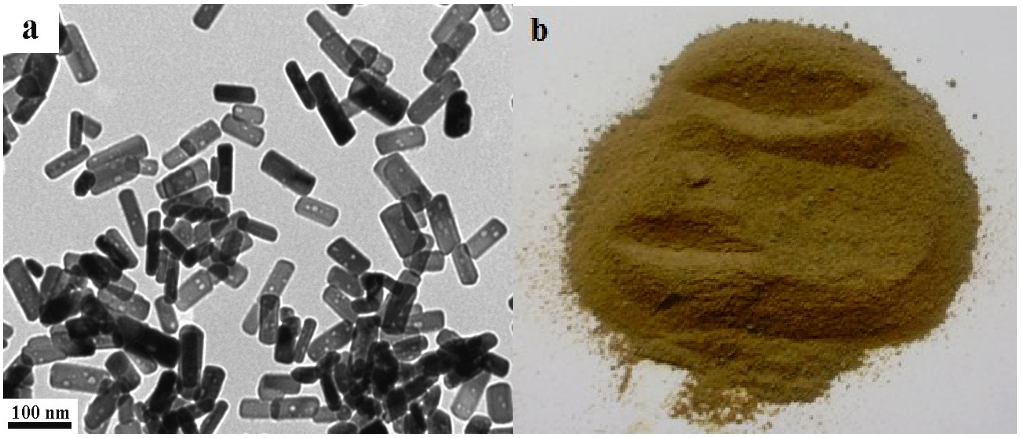

Figure 7.2.6. (a) Typical TEM image of 25 nm x 50 nm $MnWO_4$ nanobars and (b) one photograph of ~16 grams of 6-aminohexanoic acid-capped $MnWO_4$ nanobar powders synthesized using $[Mn^{2+}] = [WO_4^{2-}]$ of 0.122 M, 0.243 M of AHA, pH = 9, 180 °C for 20 h, in a 700 mL-sized autoclave.

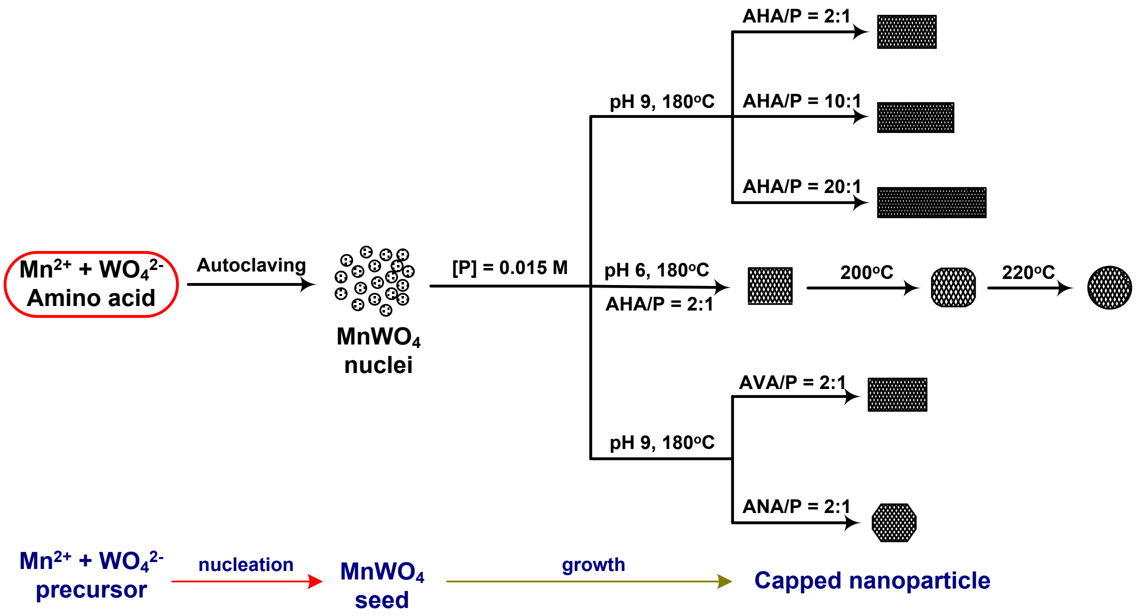

Scheme 7.2.1. Schematic illustration of the overall formation and various shape control of the monodisperse $MnWO_4$ nanoparticles using high precursor monomer concentration (0.015 M).

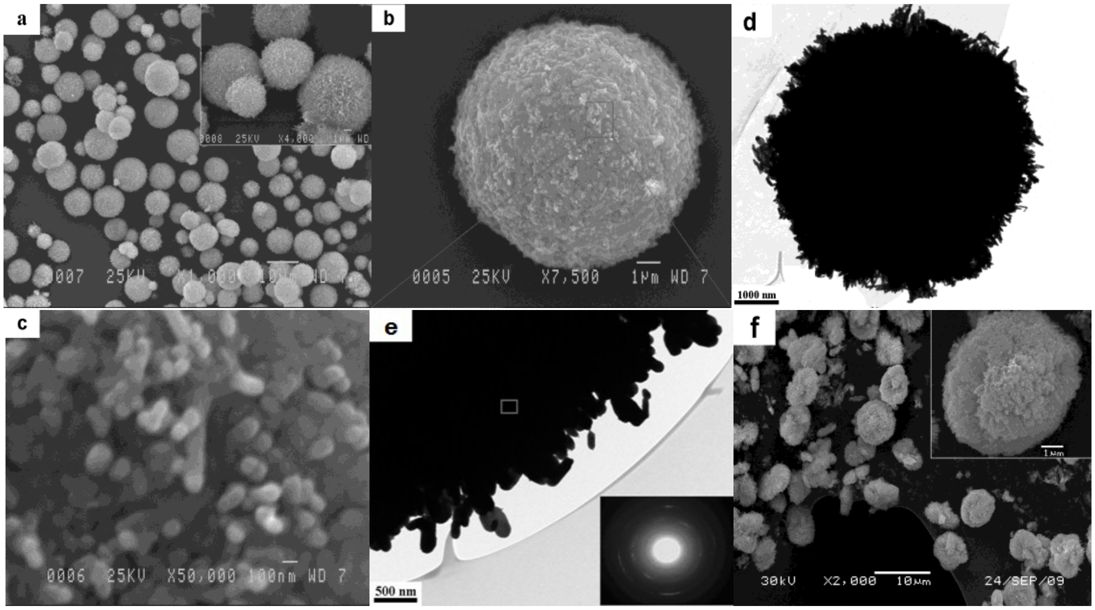

Figure 7.2.7. Different-magnification SEM (a-c) and TEM (d,e) images, inset SAED pattern of the self-assembled $MnWO_4$ hierarchical microspheres synthesized using $[Mn^{2+}] = [WO_4^{2-}]$ of 0.0076 M, 0.0305 M of AHA, pH = 9, 180 °C for 20 h. (f) SEM image of the broken $MnWO_4$ microspheres achieving ultrasonic treatment.

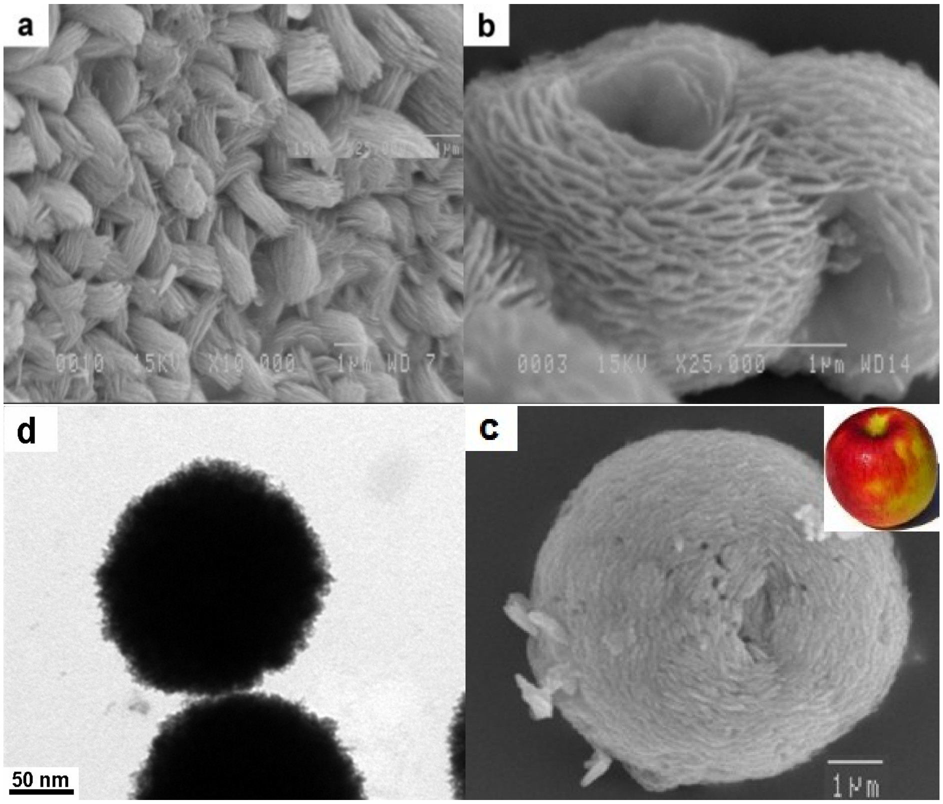

Figure 7.2.8. Different-magnification SEM (a-c) and TEM (d) images of the nanoplatelet-based $MnWO_4$ micro-like apples synthesized in water/ethylene glycol medium (10:30 mL), $[Mn^{2+}] = [WO_4^{2-}]$ of 0.0076 M, 0.0305 M of AHA, at 180 °C for 20 h.

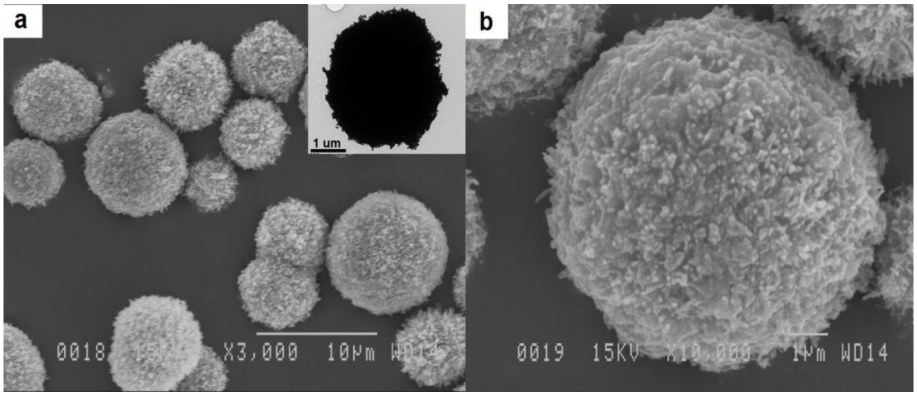

Figure 7.2.9. Different-magnification SEM and inset TEM images of the as-synthesized $MnWO_4$ microspheres (sample 9 in Table 7.2.1) after calcination at 550°C for 2 h.

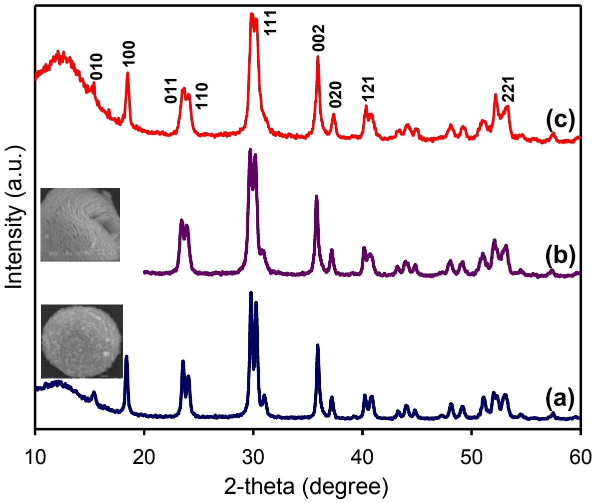

Figure 7.2.10. XRD patterns of the $MnWO_4$ microstructure samples: (a) as-made microspheres (sample 9); (b) as-made micro-like apples (sample 10 in Table 7.2.1); (c) calcined microspheres.

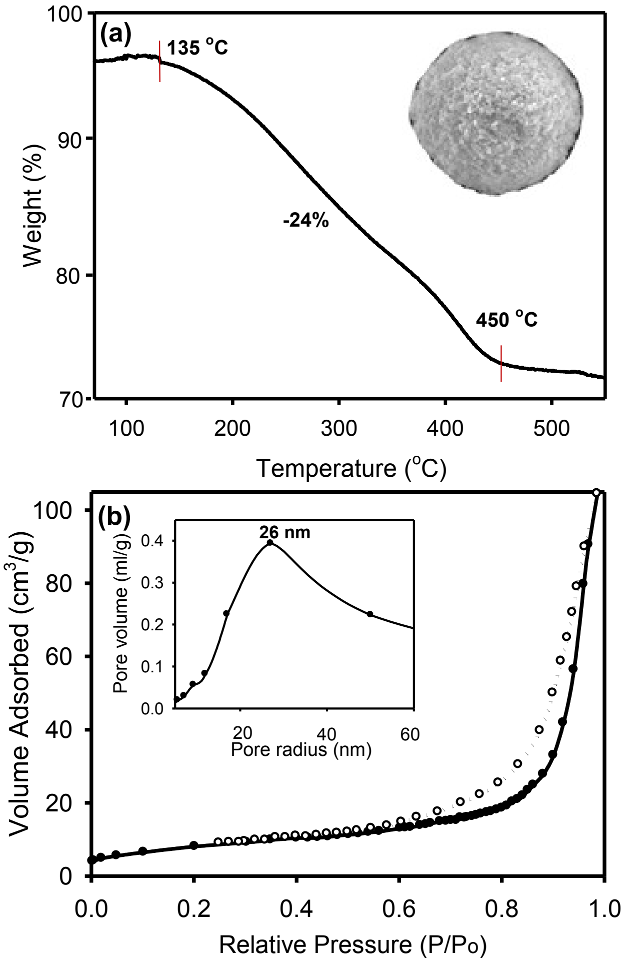

Figure 7.2.11. (a) TGA curve of AHA-capped $MnWO_4$ microspheres (sample 9 in Table 7.2.1), inset SEM image of calcined microspheres and (b) nitrogen adsorption (filled symbols) and desorption (open symbols) isotherms and inset BJH pore radius distribution of the calcined $MnWO_4$ microspheres.

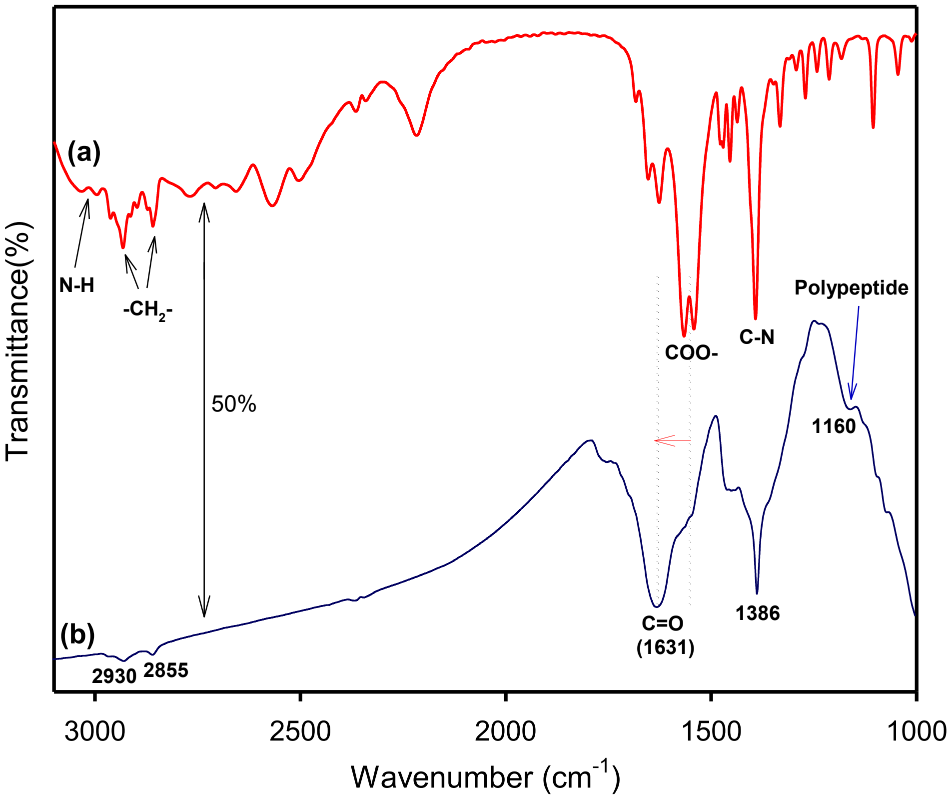

Figure 7.2.12. FTIR spectra of (a) free 6-aminohexanoic acid (AHA) and (b) AHA-capped $MnWO_4$ microspheres (sample 9 in Table 7.2.1).

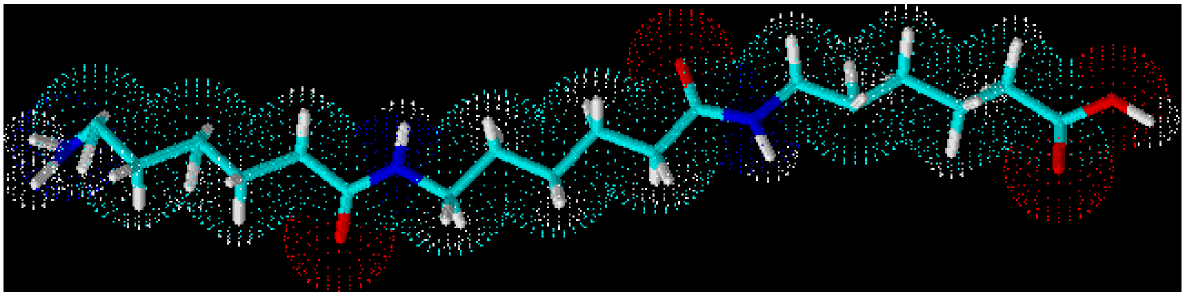

Figure 7.2.13. Structural simulation of a polypeptide chain as protein molecule producing by the peptide process of 6-aminohexanoic acids.

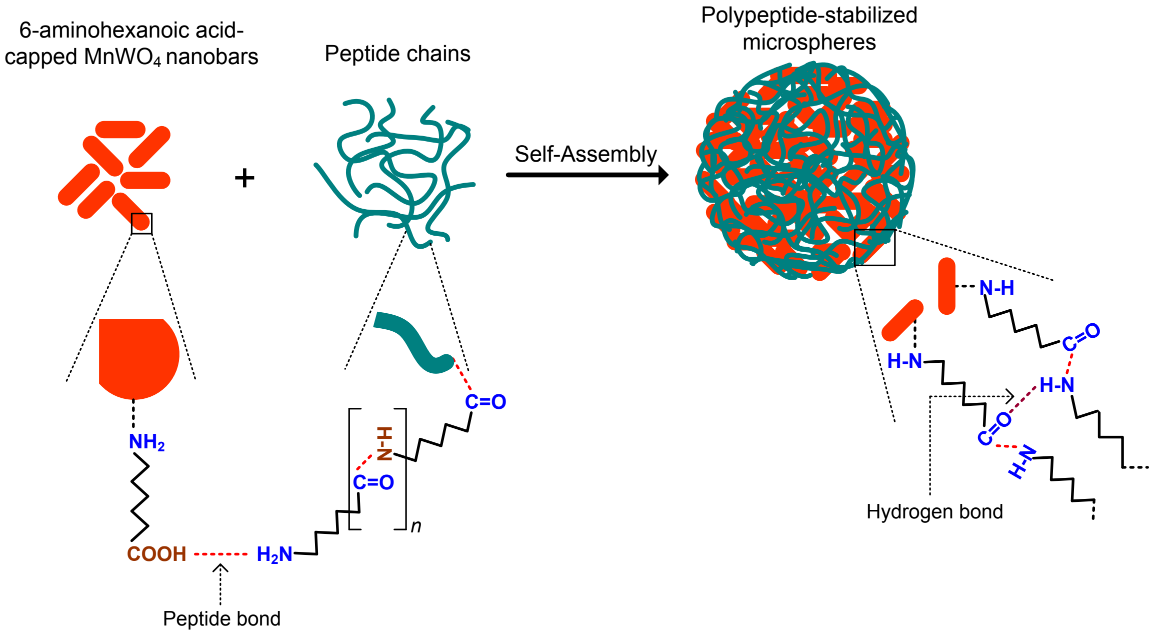

Scheme 7.2.2. A possible proposed mechanism for the construction of 3D hierarchical $MnWO_4$ microspheres from spontaneous-assembly of nanobars using low precursor monomer concentration (0.0076 M).

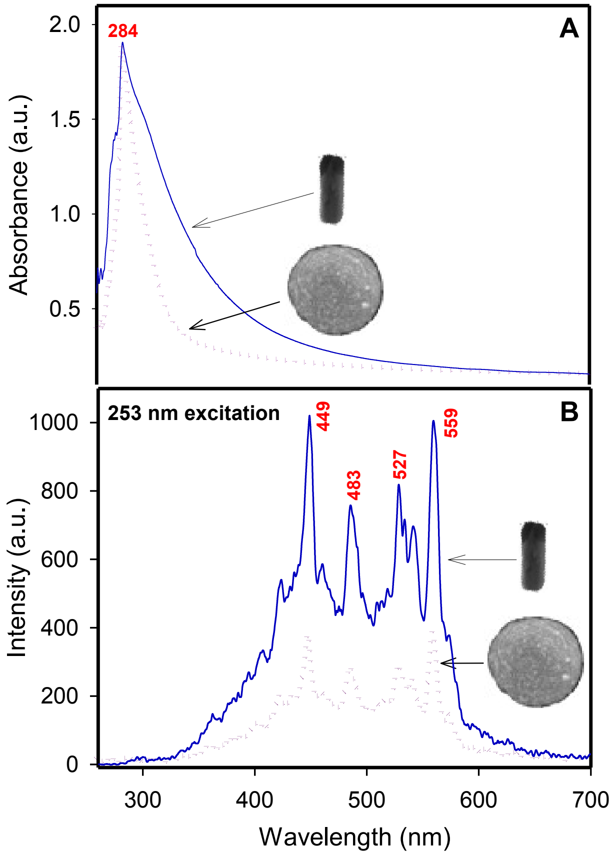

Figure 7.2.14. (A) UV/vis absorption and (B) photoluminescence emission spectra of 25 nm x 50 nm $MnWO_4$ nanobars (sample 1) and 7 μm $MnWO_4$ micropheres (sample 9 in Table 7.2.1).

7.3. Two-Phase Synthesis of Colloidal Annular-Shaped $Ce_xLa_{1-x}CO_3OH$ Nanoarchitectures Assemblied from Small Particles and Their Thermal Conversion to Derived Mixed Oxides

Thanh-Dinh Nguyen, Cao-Thang Dinh and Trong-On Do

Department of Chemical Engineering, Laval University, Quebec G1K 7P4 Canada

Published in *Inorganic Chemistry*, **2011**, *50*, 1309-1320.

Abstract

Undoped and cerium doped $LaCO_3OH$ annular-shaped nanoarchitectures with high specific surface area have been fabricated via the thermolysis of $Ce_xLa_{1-x}(oleate)_3$ (x = 0 - 20 mol%) complexes in toluene-water system containing *tert*-butylamine/oleylamine. The products exhibit 400 nm-sized monodisperse annular-shaped nanoarchitectures, which are constituted of 3-5 nm-sized primary particles. A possible mechanism of the reaction of $Ce_xLa_{1-x}(oleate)_3$ and *tert*-butylamine for the formation of annular-shaped $Ce_xLa_{1-x}CO_3OH$ nanoarchitectures is proposed. The thermal conversion of $Ce_xLa_{1-x}CO_3OH$ to $Ce_xLa_{1-x}(CO_3)O_2$ at 600 °C, to $Ce_xLa_{1-x}(OH)_3$ at 800 °C, final to $(Ce_xLa_{1-x})_2O_{3-\delta}$ at 900 °C were employed, while the original morphology was essentially unchanged. The dopant concentration was varied from five to twenty of cerium ions per $LaCO_3OH$ nanoparticle. The XRD results reveal that the cerium dopant could enter easily into the $LaCO_3OH$ structural lattice, whereas copper could be unlikely into their lattice due to their large ionic radius difference. The cerium oxidation state was controlled by changing doping concentration. The XPS results reveal that only one Ce^{3+} oxidation state is in the as-synthesized $Ce_xLa_{1-x}CO_3OH$ samples with cerium concentration ranging from 5 to 20 mol%, whereas both 3+ and 4+ ones coexisted in 20 mol%Ce:$LaCO_3OH$ structure. Remarkable luminescence emission intensity enhancement of 1.5-9.0 times were observed for $Ce_xLa_{1-x}CO_3OH$ samples with cerium concentration ranging from 5 to 20 mol%, after doping with an undoped $LaCO_3OH$.

7.3.1. Introduction

Self-assembled doped oxide nanostructures with specific morphology have attracted considerable attention in both fundamental research and potential application in recent years.[1-4] Incorporating metal ions of appropriate elements into host lattices yields a homogeneous mixed oxide solid-solution with desirable properties because the electronic state of dopant is confined to a small volume as a quantum confinement.[5] The interfacial interactions of the heterojunction nanocomposites that originate from electron transfer across the nanometer contact at the interface of dopant atoms and particles.[6] This electron exchange interaction introduces crystalline defects from the presence of oxygen vacancies in the structural lattices, which is expected to be significantly enhanced the application performance.[7,8] Controlled doping of metal atoms/molecules into oxide structures can manipulate their electronic and optical properties because the number of active electrons is modified.[9] The controlled syntheses of mesoporous metal doped oxide nanocomposites with large surface area have drawn rapidly growing interest not only due to the additional dopant-dependent functional properties but also *in situ* assembly of small particles as a building block into larger complex architectures.[10,11] The novel properties of assemblied three-dimensional (3D) nanoarchitectures depend on the emergence of nanoscale properties as a result of the interparticle arrangement.[12] The realization of metal ion doped oxide nanoarchitectures with advanced functions thus requires the development of efficient synthetic approaches for the combination of the building blocks into complicated structures.

Due to the empty 4f shell of La^{3+} and the lack of electronic f-f transitions, cerium doped lanthanum(III) carbonate hydroxide ($Ce_xLa_{1-x}CO_3OH$) has drawn a great deal of interest as a promising luminescent material.[13,14] This advance is mainly due to their unique electronic and optical properties arising from the 4f electrons of cerium.[15] Cerium dopant incorporation is as a substitutional ion with compensating oxygen vacancies, which can be improved the reactive performance of $LaCO_3OH$ materials because of the generation of the crystalline defects.[16,17] These make cerium doped $LaCO_3OH$ materials to find various potential applications in catalysts,[18] high-quality phosphors,[19] up-conversion materials,[20] oxygen-ion conducting electrolytes.[21] Lanthanide carbonate hydroxide can be formed readily from the combination of lanthanide oxide with carbonate or carbonyl species in the presence of water or hydroxide.[22] Upon annealing at high temperature in ranging of 600 - 900 °C, lanthanide carbonate hydroxides could be converted to their respective oxides by decarbonation and dehydration processes.[22] Considerable efforts have recently been devoted to preparing $LaCO_3OH$ micro/nanomaterials. For example, Fang et al.[23] synthesized the hexagonal-phase $LaCO_3OH$ microspheres from the hydrothermal reaction of $La(NO_3)_3.6H_2O$ in the presence of $CO(NH_2)_2$. Popa et al.[24] reported the solvent-free synthesis of $LaCO_3OH$ superstructures from the thermal dissociation of the lanthanum acetate hydrate precursor under autogenic pressure at elevated temperature process. Han et al.[25] synthesized the $LaCO_3OH$ nanowires via a solvothermal process controlling the volume ratio of tetramethylguanidinium lactate to water solvent. Nevertheless, it is often difficult to bring cerium into the bulk interior of $LaCO_3OH$ nanoparticles by these methods. The obtained doped materials where cerium is located on the surface or in the surface region or where at least the doping level is low. Thus, major limitations still emerge the urgency of advanced synthetic approaches for $Ce_xLa_{1-x}CO_3OH$ homogenerous structure and their mixed oxide derivative with large surface area, possibly due to the difficulty in choosing appropriate precursors and synthetic method. In order to obtain monodisperse and homogenerous $Ce_xLa_{1-x}CO_3OH$ nanocomposites, using binary cerium-lanthanum complex as precursor with similar decomposition temperature to generate stable mixed precursor monomers in bulk solution is really required.[26] This can reduce the diffusion path of the spontaneous crystallization of cerium and lanthanum nuclei for the formation of the compositional and structural uniformity of $Ce_xLa_{1-x}CO_3OH$. One of the more successful protocols is a powerful two-phase method for synthesizing novel metal,[27] metal oxide,[28] semiconductor[29] nanoparticles. Very recently, we reported the general synthesis of rare earth oxide nanocrystals via thermolysis of the rare earth-oleate complex precursors in two-phase system containing *tert*-butylamine/oleylamine under autoclaving at 180 °C for 24 h.[30] This protocol allowed a variety of oxide nanocrystals to be synthesized in toluene-water mixture using metal complexes as staring materials, which is inexpensive, low reaction temperature, and easily obtained.

In the continuation of the development of a simple two-phase approach of synthesizing uniform-sized nanocrystals, herein, we report the fabrication of undoped and cerium doped $LaCO_3OH$ annular-shaped nanoarchitectures with large specific surface area via the thermolysis of binary source precursor, Ce_xLa_{1-x}(oleate)$_3$ complex (x = 0-20 mol%), in water-toluene system containing *tert*-butylamine/oleylamine. A possible growth mechanism for the self-assemblied $Ce_xLa_{1-x}CO_3OH$ annular-shaped nanoarchitectures was proposed. After annealing at 900 °C, the $Ce_xLa_{1-x}CO_3OH$ structure was easily converted to the derived mixed oxide particles, which kept their original morphology. The partial replacement of lanthanum by cerium ion and the surface composition and oxidation state of cerium dopant in $LaCO_3OH$ structural lattice were confirmed by XRD and XPS techniques. The luminescence emission intensity of the cerium-doped $LaCO_3OH$ samples was found to enhance as compared to that of undoped $LaCO_3OH$ sample.

7.3.2. Experimental Section

Starting Materials. All chemicals were used as received without further purification. Lanthanium(III) nitrate hexahydrate [$La(NO_3)_3 \cdot 6H_2O$, 99.9%], cerium(III) nitrate hexahydrate ($Ce(NO_3)_3 \cdot 6H_2O$, 99.9%), copper(II) nitrate hexahydrate [$Cu(NO_3)_3 \cdot 6H_2O$, 98%], oleylamine ($C_{18}H_{35}NH_2$ or OM, technical grade, 70%), potassium oleate ($C_{18}H_{35}COOK$, 40% water), and *tert*-butylamine [$(CH_3)_3CNH_2$, 98%] were purchased from Sigma-Aldrich. All solvents used such as toluene and ethanol were of analytical grade and purchased from Reagent ACS.

Annular-shaped $Ce_xLa_{1-x}CO_3OH$ (x = 0-20 mol%) nanoarchitectures consist of two steps: The preparation of Ce_xLa_{1-x}(oleate)$_3$ complex (i) and the formation of nanoannular products (ii).

(i) Preparation of Ce_xLa_{1-x}(oleate)$_3$ complex: An organic solution was prepared by adding 160 mL of toluene into ethanol solution (80 mL) containing potassium oleate (21.31 g or 26.64 mmol). Subsequently, the organic phase was mixed with 80 mL of an aqueous solution of $Ce(NO_3)_3 \cdot 6H_2O$ (0 - 1.78 mmol) and $La(NO_3)_3 \cdot 6H_2O$ (8.88 - 7.10 mmol) with designed lanthanide molar ratios, and transferred to a flask. The stock two-phase mixture was heated to 70 °C for 6 h with stirring vigorously, and the organic solution turned light yellow after the reaction, indicating the occurrence of the coordinative reaction between binary metal (Ce^{3+},La^{3+}) cations and oleate anions for the complex formation. The Ce^{3+},La^{3+}/oleate molar ratio is close to 1:3, $Ce_xLa_{1-x}(oleate)_3$ with x of 0, 5, 10, 15, 20 mol%. The upper homogeneous toluene supernatant phase (160 mL) containing $Ce_xLa_{1-x}(oleate)_3$ complexes was washed several times with distilled water in a separatory funnel. After washing and drying in oven at 80 °C for 24 h, the toluene and traced water was evaporated off, yielding the $Ce_xLa_{1-x}(oleate)_3$ complex in solid form. 5.0 mol%Cu,La(oleate)$_3$ complex obtained from a toluene/water-ethanol mixture containing 0.44 mmol $Cu(NO_3)_2.6H_2O$, 8.43 mmol $La(NO_3)_3.6H_2O$, 21.31 g potassium oleate, in which the preparative procedure carried out under the same as that used to prepare $Ce_xLa_{1-x}(oleate)_3$ complex.

(ii) Synthesis of annular-shaped $Ce_xLa_{1-x}CO_3OH$ nanoarchitectures: 0.72 grams of $Ce_xLa_{1-x}(oleate)_3$ complex solid (after toluene elimination) was dissolved in 20 mL of toluene solution under stirring at room temperature for 24 h. Five militers of oleylamine was added to the above homogenerous complex solution under stirring for 10 min. This organic solution was then transferred to a 70 mL Teflon-lined stainless steel autoclave containing an aqueous solution (20 mL) in the presence of *tert*-butylamine (0.15 mL). The autoclave was seated and heated to the crystallization temperature at 180 °C for 24 h. The colloidal nanoparticle products in the toluene phase were precipitated by adding excess of ethanol and recovered by centrifugation. This approach was extended to synthesize the copper-doped $LaCO_3OH$ heterogenerous nanoarchitectures. Typically, this sample was synthesized using 5.0 mol% Cu,La(oleate)$_3$ complexes under the same synthetic conditions of annular-shaped $Ce_xLa_{1-x}CO_3OH$ nanoarchitectures.

7.3.3. Results and Discussion

Two-phase synthesis of undoped and cerium doped $LaCO_3OH$ ($Ce_xLa_{1-x}CO_3OH$, x = 0-20 mol%) homogenerous annular-shaped nanoarchitectures involves two steps, as shown in Scheme 7.3.1: (i) the preparation of $Ce_xLa_{1-x}(oleate)_3$ complex from the reaction between respective lanthanide nitrate and potassium oleate in a water-toluene mixture; (ii) the formation of mesoporous $Ce_xLa_{1-x}CO_3OH$ annular-shaped nanoarchitectures in an autoclave containing a water-toluene mixture composed of $Ce_xLa_{1-x}(oleate)_3$/*tert*-

butylamine/oleylamine at 180 °C for 24 h. According to the classical LaMer diagram,[31] the formation process of the colloidal $Ce_xLa_{1-x}CO_3OH$ nanoarchitectures can be well understood by the reported two-stage growth model, in which nanosized crystalline precursors are nucleated first in supersaturated solution at the water-toluene interface and then the initially formed seeds aggregate into larger secondary nanoarchitecture. The $Ce_xLa_{1-x}CO_3OH$ nanoarchitectures were capped by the amine groups of oleylamine molecules, the exposed hydrophobic alkyl groups were well-immersed in toluene, and guaranteed the good dispersibility of the product in toluene phase. No product was observed in the water phase. The solid-solution cerium-lanthanum oxide particles were produced from the decarbonation and dehydration of $Ce_xLa_{1-x}CO_3OH$ upon annealing.

Undoped lanthanum-compound sample synthesized using La(oleate)$_3$ complex. XRD pattern (Figure 7.3.1a) of the formed product without cerium dopant reveals that all diffraction peaks were perfectly indexed to a pure hexagonal-phase $LaCO_3OH$ structure with cell constants of a = 5.22 Å, b = 5.22 Å, c = 11.42 Å, which consists with a reference pattern (JCPDS No. 05-0602).[32] No $La(OH)_3$ or La_2O_3 was found. The strong and sharp diffraction peaks demonstrate high crystallinity of the products. The broadening of the peaks confirms the nanoscale nature of $LaCO_3OH$ structure. The average particle size assesses from (302) peak at $2\theta = 30.2^o$ using Scherrer equation, revealing that the resulting product consists of the small particles of ~3-5 nm in size. This indicates that the $LaCO_3OH$ nanostructures are composed of numerous small particle assemblies. SEM image in Figure 7.3.1b shows that uniform population of $LaCO_3OH$ nanostructures with an interesting annular each containing an interior concavity in sphere were observed. The monodisperse annular-shaped nanoarchitectures presented a rough surface, narrow size distribution, and an average particle diameter of ~ 400 nm. TEM images in Figure 7.3.1c indicate that the distribution of small particles at the center of each big $LaCO_3OH$ annular-shaped nanoarchitecture is less than that of their edges, confirming the annular structure. Dark-field TEM image (Figure 7.3.1d) of this sample shows a clear contrast between ring and interior concavity, confirming the doughnut structure. Figure 7.3.1d shows a single $LaCO_3OH$ annular-shaped nanoarchitecture with a diameter of ~400 nm. From the HRTEM image shown in Figure 7.3.1e,f, the lattice space of a single particle was clearly observed, and it further displays that the annular is constituted of numerous small interconnected primary nanoparticles with a size of 3-5 nm, in good agreement with the XRD result. SAED pattern (inset of Figure 7.3.1d) confirms the polycrystalline nature of the self-assembled annulars. Fast Fourier Transform (FFT) analysis (inset of Figure 7.3.1e) shows the crystallographic nature of the small particle assembly.

Oleylamine-capped $LaCO_3OH$ annular-shaped nanoarchitectures were characterized by XPS technique for the evaluation of the surface composition, oxidation state, capping oleylamine on the particle surface (Figure 7.3.2). Survey XPS spectrum and elemental dispersive spectrum (EDS) analysis detected the presence of La, C, O elements. La 3d XPS spectrum (Figure 7.3.2a) shows that the La $3d_{5/2}$ peaks center at ~ 640.59 - 652.01 eV, and La $3d_{3/2}$ peaks center at ~642.20-653.60 eV, with $\Delta \approx 1.6$ eV, corresponding to La^{3+}, which is consistent with those of bulk La_2O_3 phase.[33] The splitting (Δ) is due to spin orbit interaction and charge transfer from O 2p to La 4f. The N 1s region (Figure 7.3.2b) contained a single peak at 399.8 eV, assigning to nitrogen in $-NH_2$ group of the oleylamine molecule. The C 1s spectrum (Figure 7.3.2c) exhibits that the peaks at 284.6, 288.3, 288.3 eV were attributed to alkyl chain, C-N, carbonate, respectively, indicating that the $LaCO_3OH$ nanoarchitectures were covered with the oleylamine molecules.[34] FTIR spectrum of oleylamine-capped $LaCO_3OH$ nanoarchitectures is shown in Figure 7.3.2d. The shape absorption peaks at 3625 and 3468 cm^{-1} are assigned to the stretching vibration of structural OH and adsorbed H_2O, respectively.[35] The peaks at 2850-2925 cm^{-1} attributed to the C-H stretching mode of alkyl chains of oleylamine molecules.[30] The strong peak at 1412 cm^{-1} assigned to the stretching vibration of the $-NH_2$ group of oleylamine.[30] Four modes of CO_3^{2-} ion of $LaCO_3OH$ appeared at 1070-1100 cm^{-1} (ν_1), 850-880 cm^{-1} (ν_2), 1400 cm^{-1} (ν_3), and 690-730 cm^{-1} (ν_4).[35] Moreover, one photograph of the transparent toluene solution containing colloidal $LaCO_3OH$ nanoarchitectures is shown in inset Figure 7.3.2d. These data further confirm that the $-NH_2$ groups of oleylamine molecules capped on the particle surface. The exposed hydrophobic alkyl groups oriented outward and thus the capped products were highly dispersed in toluene.

The oleylamine is fully decomposed when the $LaCO_3OH$ nanoarchitectures thermally treated at 550 °C for 2 h. The thermal-stabilized nanoarchitectures therefore become mesoporous, as shown in SEM image (inset of Figure 7.3.3). Figure 7.3.3 shows the calcined $LaCO_3OH$ sample reveals a typical type-IV isotherm with H1-type hysteresis, characteristic of mesoporous materials,[36] with Brunauer-Emmett-Teller (BET) surface area of ~100 m^2g^{-1}. The large surface area of nanodoughnuts is due to the small size of particles. Pore size distribution obtained using Barrett-Joyner-Halenda (BJH) method (inset of Figure 7.3.3) shows that the binary pore distributions at 20 and 16 nm were evident, which is consistent with the results of SEM/TEM observations. The void structure is expected to arise from the self-assembly of 3-5 nm particles. Large external pores were generated by the formation of a large concavity in the centre of annular-shaped structures, while tiny internal pores were formed the interstitial voids inside the annular-shaped $LaCO_3OH$ nanoarchitectures. Obviously, such novel mesoporous $LaCO_3OH$ nanoarchitectures with high surface area and rough surface can be favorable for the catalytic performance.

Due to the $La(oleate)_3$ complex solid (after toluene elimination) having high thermal stability, the thermolysis rate of these complexes at the water-toluene interface is relatively slow. The oleylamine-capped seeds with small in size were produced. These formed small seeds are active because of their high surface energy and tend to aggregate growth, leading to the formation of larger aggregates to minimize interface energy. A possible formation mechanism of $LaCO_3OH$ structure using $La(oleate)_3$ complex, *tert*-butylamine, and capping oleylamine, could be depicted in equation 1. The formation of $LaCO_3OH$ structure could consist of three steps during the solvo-hydrothermal synthesis: (i) *Tert*-butylamine as nucleophile attacks one carboxyl group of the oleate ligand through a S_N^1 mechanism. In which a lone pair of electrons of the donor NH_2 group shares with the electrophilic carboxyl center at the nucleation stage. *Tert*-butylamine can react with the oleate group but not with oleylamine because its basic property is stronger than that of oleylamine. Moreover, *tert*-butylamine is dispersed an aqueous phase and easily hydrolyzed to generate OH^- compared with oleylamine in organic phase. (ii) This nucleophilic reaction leads to C-O bond cleavage and the release of lanthanum-oxyl and carbonyl species. (iii) The

$LaCO_3OH$ structure was formed from the combinative reaction of lanthanum-oxyl, carbonyl, and hydroxyl species at the water-toluene interface.

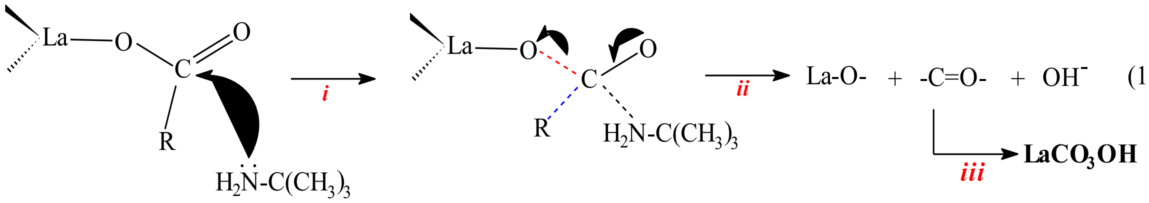

(1)

The seed-mediated growth has recently been employed for the synthesis of larger metallic nanoparticles on smaller seeds, meaning that the growth process is separated from additional nucleation.[37] For example, Hyeon and co-workers[38] synthesized the monodisperse iron oxide nanoparticles with continuous size spectrum of 6-13 nm from the combination of various-sized iron oxide nanoparticles and the iron-oleate complex solution via thermal decomposition. In this work, a similar principle is expected to apply for the synthesis of colloidal $LaCO_3OH$ nanospheres by the additional incremental growth. The annular-shaped $LaCO_3OH$ nanoarchitecture as seed and $La(oleate)_3$ complex as additional growth source were used. Twenty miligrams of pre-synthesized 400 nm $LaCO_3OH$ annular-shaped nanoarchitectures was dispersible to 10 mL of toluene under stirring, and then added to a water-toluene (20:10 mL) mixture containing 0.24 grams $La(oleate)_3$ and 0.05 mL *tert*-butylamine. Under autoclaving at 180 ^{o}C for 10 h, $La(oleate)_3$ complexes were decomposed to produce $LaCO_3OH$ nuclei under catalyzing *tert*-butylamine. These nuclei directly grow on the surface of $LaCO_3OH$ doughnut seeds by a digestive ripening mechanism leading to the formation of final annular-shaped $LaCO_3OH$ nanoarchitectures. SEM image (Figure 7.3.4a) depicts the morphology of the product is in the sphere shape with the diameter unchanged (~400 nm) but any voids at the center of each sphere were not observed. TEM image (Figure 7.3.4b) indicates that the self-assembled nanospheres without void consist of small particles. XRD pattern (Figure 7.3.4c) of the as-synthesized $LaCO_3OH$ nanospheres also exhibit a pure hexagonal structure and the intense and broadening diffraction peaks are significantly unchanged. A schematic drawing of the shape change from annular-shaped architecture into sphere by the seed-mediated growth is illustrated in Figure 7.3.4d.

$LaCO_3OH$ compound can be doped with various lanthanide elements to form a nanostructured mixed oxides. Exploiting this sensitivity can allow their physical and chemical properties to be controlled with atomic-scale precision, and can result in materials tailored to possess specific properties. In this second work, the cerium doped $LaCO_3OH$ samples with cerium dopant concentration of 5, 10, 15, 20 mol% using binary complex precursor, Ce_x,La_{1-x}(oleate)$_3$ with x of 5, 10, 15, 20 mol%, respectively. SEM images in Figure 7.3.5 show that the particle size and shape of all the $Ce_xLa_{1-x}CO_3OH$ samples with various doping levels (5-20 mol%) are similar to those of undoped $LaCO_3OH$ annular-shaped nanoarchitectures. The 400 nm-sized $Ce_xLa_{1-x}CO_3OH$ annular-shaped nanoarchitectures with various doping levels were made up of many particles and were polycrystalline nature as indicated by inset TEM and SAED results (inset of Figure 7.3.5a-f). Corresponding elemental dispersive spectrum (EDS) analysis (Figure 7.3.5e) of a representative 15 mol% cerium doped $LaCO_3OH$ sample reveals the molar ratio of Ce and La content is similar with the original ratio of reagents. The morphology of the doped products did not substantially vary when an increase in the amount of doping further, suggesting that cerium ions tend to solubilize into the $LaCO_3OH$ lattice leading to a homogenerous $Ce_xLa_{1-x}CO_3OH$ structure. The segregation of cerium ions on the surface of the annular-shaped nanoarchitecture seems to be limited.

Figure 7.3.6(a-d) displays XRD patterns of the as-synthesized cerium doped $LaCO_3OH$ annular-shaped nanoarchitecture samples with doping levels of 5, 10, 15, 20 mol%. The introduction of cerium seems not to modify the crystalline structure of pure $LaCO_3OH$. Indeed, cerium doped $LaCO_3OH$ still presents the hexagonal phase for all doping concentrations tested. All the doped samples show no additional diffraction peaks corresponding to either cerium oxide or cerium hydroxide were detected at the current doping levels. This indicates that the cerium ions are completely dissolved in the $LaCO_3OH$ host lattice by substitution for lanthanum ions to yield a homogenerous $Ce_xLa_{1-x}CO_3OH$ structure. The calculation of the average particle sizes of four doped samples using (302) peak at $2\theta = 30.2^o$ also suggest that the $Ce_xLa_{1-x}CO_3OH$ nanoarchitectures are composed of the small particles of 3-5 nm in size. It is known that La ion can exist in only one oxidation state of 3+ having an ionic radii of 1.172 Å, whereas Ce can exist in 3+ (1.143 Å) and 4+

(0.97 Å). The cerium oxidation state in the as-synthesized 5-15 mol% Ce:$LaCO_3OH$ samples existed in Ce^{3+} only, while both Ce^{3+} (38%) and Ce^{4+} (62%) oxidation states in 20 mol% Ce:$LaCO_3OH$ (see the XPS result below). It was found that for 5-15 mol% Ce^{3+}:$LaCO_3OH$ samples without Ce^{4+}, no significant shift of the peak position (2θ) of the $Ce_xLa_{1-x}CO_3OH$ samples as compared to the undoped $LaCO_3OH$ sample was observed in the XRD patterns (Figure 7.3.6a-c). The significantly unchanged lattice parameters of the doped samples can be attributed to the very small ionic radii difference between Ce^{3+} (1.150 Å) and La^{3+} (1.172 Å), which allows the replacement of La^{3+} by trivalent Ce^{3+} ions in $LaCO_3OH$. For 20 mol% cerium doped $LaCO_3OH$ sample with the presence of Ce^{4+}, (302) peak was shifted lightly toward lower angle side owning to the partial substitution of Ce^{4+} with La^{3+} in $LaCO_3OH$ lattice (Figure 7.3.6d). We reasoned that the ionic radius of La^{3+} (1.172 Å) is larger than Ce^{4+} (0.97 Å), leading to the expansion in unit-cell volume is expected.

TGA-DTA curves (Figure 7.3.7) were recorded for oleylamine (OM)-capped $Ce_xLa_{1-x}CO_3OH$ annular-shaped nanoarchitectures. The TGA curve shows that the total weight loss of the OM-capped $Ce_xLa_{1-x}CO_3OH$ sample is ~46%, which is attributed to the combustion/elimination of oleylamine and the decarbonation of the conversion of $Ce_xLa_{1-x}CO_3OH$ to $Ce_xLa_{1-x}(OH)_3$ and final to $(Ce_xLa_{1-x})_2O_{3-\delta}$. An intense exothermic peak at 351 °C in the DTA profile is attributed to the combustion and elimination of oleylamine. The weight loss due to the decarbonation of $Ce_xLa_{1-x}CO_3OH$ into $(Ce_xLa_{1-x})_2O_{3-\delta}$ is ~7%, corresponding to weak exothermic DTA peaks at higher temperature (~680-830 °C). A representative as-synthesized 10 mol% cerium doped $LaCO_3OH$ annular sample was heat-treated at 300, 600, 800, 900 °C for 12 h in air to investigate the thermal stability and induce the formation of derived mixed oxide solid-solution. The thermal decomposition of $Ce_xLa_{1-x}CO_3OH$ structure at different calcined temperatures could be expressed in Equation 2,3,4.

$$2Ce_xLa_{1-x}CO_3OH \xrightarrow{600^\circ C} (Ce_xLa_{1-x})_2(CO_3)O_2 + CO_2 + H_2O \quad (2)$$

$$(Ce_xLa_{1-x})_2(CO_3)O_2 + 3H_2O \xrightarrow{800^\circ C} 2Ce_xLa_{1-x}(OH)_3 + CO_2 \quad (3)$$

$$2Ce_xLa_{1-x}(OH)_3 \xrightarrow{900^\circ C} (Ce_xLa_{1-x})_2O_{3-\delta} + 3H_2O \quad (4)$$

From evidence of SEM images (Figure 7.3.8A), the samples annealed at 300, 600, 800 ^{o}C, show the quite similar morphology to the untreated sample, indicating that the annular shape has high thermal stability. When treated at 900 ^{o}C, the annular-shaped nanoarchitectures become smooth and the agglomeration between both annular appears due to the effect of sintering. Figure 7.3.8B shows XRD patterns of the $Ce_xLa_{1-x}CO_3OH$ nanoarchitectures calcined at 300, 600, 800, 900 ^{o}C, which evidences the conversion of composition. The doped sample calcined at 300 ^{o}C still remains the hexagonal $Ce_xLa_{1-x}CO_3OH$ phase. This structure was converted into hexagonal $(Ce_xLa_{1-x})_2(CO_3)O_2$ intermediate at 600 ^{o}C and into hexagonal $Ce_xLa_{1-x}(OH)_3$ at 800 ^{o}C by decarbonation. At 900 ^{o}C, $Ce_xLa_{1-x}(OH)_3$ was converted into hexagonal $(Ce_xLa_{1-x})_2O_{3-\delta}$ by dehydration process. The width of diffraction peaks in the XRD patterns of the samples treating at 300, 600, 800 ^{o}C has no previous difference, suggesting that the small particle (~3-5 nm) in these samples was still remained. However, as the treatment temperature was raised to 900 °C, the mean nanoparticle size is increased to 8.5 nm, confirming further the agglomeration of particles by heating.

The surface composition, the oxidation state, and the binding energy change of cerium element in the doped $LaCO_3OH$ samples were identified by XPS. The N 1s and C 1s XPS and FTIR data of these doped samples also reveal their particle surface was capped by $-NH_2$ groups of oleylamine molecules. La 3d XPS spectrum of the doped sample is similar to that of the undoped $LaCO_3OH$ nanoarchitectures. As can be noted, with increase of dopant concentration, there is no change in the position and intensity of the La 3d core level peaks. Survey XPS results of these doped samples determined no other contaminants are detected, except for the above-mentioned elements. The Ce-to-La molar ratio of 5%Ce:$LaCO_3OH$, 10%Ce:$LaCO_3OH$, 15%Ce:$LaCO_3OH$, 20%Ce:$LaCO_3OH$ samples was spectrally estimated to be 4.5:96.5, 8.7:91.3, 13.1:86.9, 19.2:80.8, respectively, corresponding to $Ce_{0.045}La_{0.965}CO_3OH$, $Ce_{0.087}La_{0.913}CO_3OH$, $Ce_{0.131}La_{0.869}CO_3OH$, $Ce_{0.192}La_{0.808}CO_3OH$ formulae. The detected cerium concentrations were slightly lower than the initial starting concentrations of Ce_xLa_{1-x}(oleate)$_3$ complexes, indicating the atomic mixing nature of the cerium and lanthanum ion sites.

Ce 3d XPS spectra (Figure 7.3.9Aa-c) of the as-synthesized samples of 5 mol%Ce:LaCO$_3$OH, 10 mol%Ce:LaCO$_3$OH, 15 mol%Ce:LaCO$_3$OH exhibit Ce 3d$_{5/2,3/2}$ peaks at 885.7-904.0 eV is attributed to Ce^{3+}.[33] No peak was observed in the binding energy region of Ce^{4+}. However, Ce 3d$_{5/2,3/2}$ XPS spectrum (Figure 7.3.9Ad) of the as-synthesized 20 mol%Ce:LaCO$_3$OH sample displays that cerium is in mixed valence states of 3+ (880.40, 885.5, 898.81, 903.7 eV) and 4+ (882.7, 888.96, 898.2, 901.3, 907, 916.7 eV).[33] Based on the peak areas, the surface concentration of Ce^{3+} and Ce^{4+} was found to be ~38 and 62%, respectively. These results evidence the presence of Ce in predominantly 3+ oxidation state in the Ce$_x$La$_{1-x}$CO$_3$OH samples with dopant concentration ranging from 5 to 15 mol%. Both 3+ and 4+ oxidation states coexist in 20 mol%Ce:LaCO$_3$OH, in which a part of Ce^{3+} ions would be converted into Ce^{4+} during synthesis process. It is particularly noted that the Ce 3d peaks showed the shift by ~0.8-1.0 eV toward lower binding energy with increasing dopant concentration. The decrease in binding energy can be attributed to increase in valence electron density and the formation of Ce-La bonding structure.[39]

It was predicted that the oxidation state change of cerium dopant in lanthanide compound is often related to crystalline defects and generated oxygen vacancy concentration, which would greatly influence the chemical properties.[40] Figure 7.3.9B shows the modifications of cerium oxidation states of a representative 10 mol%Ce:LaCO$_3$OH sample, calcined at 300, 600, 800, 900 °C for 12 h. From the analysis of the XPS spectra, cerium ion in the samples calcined at 300 and 600 °C still exist in one oxidation state of 3+ (Figure 7.3.9Ba,b), whereas two cerium oxidation states (Ce^{3+} and Ce^{4+}) coexist in the samples calcined at 800 and 900 °C (Figure 8Bc,d). The Ce^{4+} concentration in the doped sample calcined 800 °C was found to be ~41.2%, which increased to ~75.5% upon annealing at 900 °C. The partial conversion of Ce^{3+} ion to Ce^{4+} took place on their surface upon annealing due to the oxidation of Ce^{3+} in air atmosphere. The difference of O 1s XPS spectra of the Ce$_x$La$_{1-x}$CO$_3$OH and (Ce$_x$La$_{1-x}$)$_2$O$_{3-\delta}$ samples were also observed (Figure 7.3.10). The Ce$_x$La$_{1-x}$CO$_3$OH sample is composed of two oxygen components, whereas the (Ce$_x$La$_{1-x}$)$_2$O$_{3-\delta}$ sample exhibits only one oxygen component. For the Ce$_x$La$_{1-x}$CO$_3$OH sample, the weak XPS peak at 529.4 eV is assigned to the hydroxide group and the intense second one at 531.8 eV is attributed to the carbonate group. The $(Ce_xLa_{1-x})_2O_{3-\delta}$ sample exhibits only one O 1s XPS peak at 531.8 eV related to O-La,Ce bonds. This also indicates a high OH concentration on the particle surface of the $Ce_xLa_{1-x}CO_3OH$ sample.

To understand the effect of the cerium dopant concentration on the upconversion emission, photoluminescence (PL) emission spectra (Figure 7.3.11) of the colloidal $Ce_xLa_{1-x}CO_3OH$ nanoarchitectures with various doping levels (x = 0-20 mol%) in toluene were recorded on exciting at 360 nm. Using the same particle concentrations, the colloidal solutions of these $Ce_xLa_{1-x}CO_3OH$ samples show the same spectral peak positions at 424, 448, 486, 529, 560 nm, which can be attributed to the charge-transfer transition in $Ce_xLa_{1-x}CO_3OH$ structure. The broad backgrounds of the luminescence spectra of these doped samples can be due to the self-assembly of small particles (3-5 nm) for the formation of the aggregated $Ce_xLa_{1-x}CO_3OH$ structure with annular shape.[41] However, the observed effect of variation in emission can be correlated to the dopant concentration. Namely, the intensity was found to increase with increase in dopant concentration. We obtained the PL intensity enhancement of 1.5, 2.2, 5.0, 9.0 times for $Ce_xLa_{1-x}CO_3OH$ with doping level of 5, 10, 15, 20 mol%, respectively, after doping with an undoped $LaCO_3OH$. The emission intensity of $Ce_xLa_{1-x}CO_3OH$ sample increases with increase in cerium concentration to 20 mol% and then exhibits a gradual decrease upon further increase in cerium dopant content. The relationship between the cerium dopant concentration in $LaCO_3OH$ sample and the PL intensity ratio was shown in inset of Figure 7.3.11. The initial increase in emission intensity can be associated with the increase in relative concentration of the defects in crystal structure. The subsequent decrease in emission intensity can be primarily attributed to the increase in particle size of the formed Ce doped $LaCO_3OH$ heterogenerous structure.

To validate our hypothesis, 5.0 mol% copper ion was introduced to $LaCO_3OH$ annular-shaped nanoarchitectures under the same lanthanide doping approach, except that 5.0 mol%Cu,La(oleate)$_3$ complex was used. XRD pattern (Figure 7.3.12a) of the as-synthesized Cu doped $LaCO_3OH$ sample shows that there are separate phase: hexagonal $LaCO_3OH$, monoclinic CuO,[42] and cubic Cu_2O[43] phases. No shift of the diffraction peak of the hexagonal $LaCO_3OH$ phase was observed. This demonstrates that the copper ions cannot enter the lattice of $LaCO_3OH$ by occupying the La^{3+} ion sites. They crystallized to form two new separate phases of CuO and Cu_2O dispersing on the $LaCO_3OH$ annular surface. Actually, Cu ion clusters can chemically bonded with oxygen ions to form oxide traces on the surface or in the shallow layer of $LaCO_3OH$ annular-shaped nanoarchitectures. The main reason for this was attributed to the radius of La^{3+} ion was much larger than that of Cu^+ ion ($r(La^{3+}) = 1.172$ Å, $r(Cu^{2+}) = 0.87$ Å, $r(Cu^+) = 0.91$ Å). This is also supported by SEM image of 5.0 mol% Cu/$LaCO_3OH$ sample as shown in Figure 7.3.12b. It is clearly that the basic morphology of Cu/$LaCO_3OH$ sample is similar to annular shape of undoped $LaCO_3OH$. As evidence in TEM image (Figure 7.3.12c), 3 nm-sized CuO/Cu_2O particles segregating on the surface of 400 nm-sized $LaCO_3OH$ annular-shaped nanoarchitectures were observed. The segregation of copper(I,II) oxide on the surface of $LaCO_3OH$ nanoarchitectures is probably due to the different decomposition temperature of the Cu- and La-oleate. The different crystallization rates of copper and lanthanum nuclei lead to the formation of heterogenerous structure. Survey XPS spectrum of this sample also reveals the presence of Cu on the surface layer of annular-shaped nanoarchitectures. The main peak at 932.2 eV belongs to Cu $2p_{3/2}$, and can be divided into two peaks at 932.2 and 934.6 eV, attributed to Cu^+ and Cu^{2+}, respectively, corresponding to CuO_x,[44] in agreement with the XRD data. The surface composition of the 5.0 mol% Cu/$LaCO_3OH$ sample was found to contain 7.3 mol% Cu at the surface. The tendency for excess surface enrichment of copper ions is mainly due to the segregation of copper on the $LaCO_3OH$ surface instead of incorporation into the structural lattice.

Because the aggregation is energetically favored, the primary particles tended to aggregate into larger annular-shaped nanoarchitectures to lower the system energies at longer reaction time. Time-dependent experiments of 10 mol%Ce:$LaCO_3OH$ nanoarchitectures were carried out at 180 °C for 4, 12, 24 h. The growth process of the monodisperse homogeneous annular-shaped nanoarchitectures was carefully examined by using TEM. As depicted in Figure 7.3.13, some seed aggregates appeared after aging for 4 h (Figure 7.3.13a). When the aging time was prolonged to 12 h, these aggregated particles tend to assemble further to form irregular annulars (Figure 7.3.13b). They evolved into the perfect 400 nm sized-nanoannulars as the aging time was prolonged to 24 h (Figure

7.3.13c). A feasible formation mechanism of the annular-shaped $Ce_xLa_{1-x}CO_3OH$ nanoarchitectures is proposed to involve different growth processes as illustrated in Figure 7.3.13d. With increased reaction time, more inner $Ce_xLa_{1-x}CO_3OH$ crystals with higher energy gradually dissolved possibly due to the presence of capping oleylamine in homogenerous toluene phase,[45] which finally led to a void space in the center, in result of mesostructured $Ce_xLa_{1-x}CO_3OH$.

7.3.4. Conclusion

In conclusion, mesoporous undoped and cerium doped $LaCO_3OH$ homogenerous annular-shaped nanoarchitectures with large specific surface area have been synthesized through the thermolysis of $Ce_xLa_{1-x}(oleate)_3$ (x = 0 - 20 mol%) complexes in toluene-water mixture containing *tert*-butylamine/oleylamine at 180 °C for 24 h. The mechanism of the decomposed reaction of $Ce_xLa_{1-x}(oleate)_3$ under catalyzing *tert*-butylamine for the formation of $Ce_xLa_{1-x}CO_3OH$ structure and the growth of self-assemblied nanoarchitectures were proposed. The conversion of $Ce_xLa_{1-x}CO_3OH$ structure to $Ce_xLa_{1-x}(CO_3)O_2$ at 600 °C, to $Ce_xLa_{1-x}(OH)_3$ at 800 °C, and eventually to $(Ce_xLa_{1-x})_2O_{3-\delta}$ at 900 °C were employed. The XRD results reveal that because cerium and lanthanum have the similar ionic radii, the cerium dopant could enter easily into the $LaCO_3OH$ structural lattice. Whereas copper could be unlikely into their lattice due to the large ionic radius difference. The XPS results reveal that only one Ce^{3+} oxidation state is in the as-synthesized $Ce_xLa_{1-x}CO_3OH$ samples with doping level in ranging from 5 to 15 mol%, whereas both 3+ and 4+ ones coexisted in 20 mol%Ce:$LaCO_3OH$. Upon annealing at high temperatures (800 - 900 °C) under air atmosphere, the partial conversion of Ce^{3+} into Ce^{4+} occurring on the surface of mixed cerium-lanthanum hydroxide or oxide was observed. The significant luminescence emission intensity of the as-synthesized $Ce_xLa_{1-x}CO_3OH$ samples was found to increase from 1.5 to 9.0 times with increase in cerium dopant concentration from 5 to 20 mol%. This approach was extended to synthesize Cu_2O/CuO doped $LaCO_3OH$ heterogenerous nanoarchitectures. We expect that these mesoporous nanomaterials could offer opportunities for investigating their collective properties and open the door for other technologically important applications.

7.3.5. References

(1) Talapin, D. V.; Shevchenko, E. V.; Bodnarchuk, M. I.; Ye, X.; Jun Chen, Murray, C. B. *Nature* **2009**, *461*, 964-967.

(2) Yang, Y.; Wang, C. *Chem. Soc. Rev.* **2009**, *38*, 2576-2589.

(3) Zhao, Y.; Jiang, L. *Adv. Mater.* **2009**, *21*, 1-18.

(4) Pileni, M. P. *Macromol. Symp.* **2008**, *270*, 14-26.

(5) Galli, G. *Nature* **2005**, *436*, 32-33.

(6) Erwin, S. C.; Zu, L.; Haftel, M. I.; Efros, A. L.; Kennedy, T. A.; Norris, D. J. *Nature* **2005**, *436*, 91-94.

(7) Yu, J. H.; Liu, X.; Kweon, K. E.; Joo, J.; Park, J.; Ko, K. T.; Lee, D. W.; Shen, S.; Tivakornsasithorn, K.; Son, J. S.; Park, J. H.; Kim, Y. W.; Hwang, G. S.; Dobrowolska, M.; Furdyna, J. K.; Hyeon, T. *Nat. Mater.* **2010**, *9*, 47-53.

(8) **Ristein, J.** *Science* **2006**, *313*, 1057-1058.

(9) Wang, F.; Han, Y.; Lim, C. S.; Lu, Y.; Wang, J.; Xu, J.; Chen, H.; Zhang, C.; Hong, M.; Liu, X. *Nature* **2010**, *463*, 1061-1065.

(10) Simon, J.; Protasenko, V.; Lian, C.; Xing, H.; Jena, D. *Science* **2010**, *327*, 60-64.

(11) Claridge, S. A.; Castleman, A. W.; Khanna, S. N.; Murray, C. B.; Sen, A.; Weiss, P. S. *ACS Nano* **2009**, *3*, 244-255.

(12) Lou, X. W.; Archer, L. A.; Yang, Z. *Adv. Mater.* **2008**, *20*, 3987-4019.

(13) Koen Binnemans, *Chem. Rev.* **2009**, *109,* 4283-4374.

(14) Bunzli, J. C. G. *Chemical Reviews* **2010**, DOI: 10.1021/cr900362e.

(15) Su, L. T.; Tok, A. I. Y.; Zhao, Y.; Ng, N.; Boey, F. Y. C. *J. Phys. Chem. C* **2009**, *113*, 5974-5979.

(16) Meiser, F.; Cortez, C.; Caruso, F. *Angew. Chem. Int. Ed.* **2004**, *43*, 5954-5957.

(17) Ding, S. J.; Zhang, D. W.; Wang, P. F.; Wang, J. T. *Materials Chemistry and Physics* **2001**, *68*, 98-104.

(18) Sun, C. W.; Sun, J.; Xiao, G. L.; Zhang, H. R.; Qiu, X. P.; Li, H.; Chen, L. Q. *J. Phys. Chem. B* **2006**, *110*, 13445-13452.

(19) Mai, H. X.; Zhang, Y. W.; Si, R.; Yan, Z. G.; Sun, L. D.; You, L. P; Yan, C. H. *J. Am. Chem. Soc.* **2006**, *128*, 6426-6436.

(20) Auzel, F. *Chem. Rev.* **2004**, *104*, 139-173.

(21) Etsell, T. H.; Flengas, S. N. *Chem. Rev.* **1970**, *70*, 339-376.

(22) Foger, K.; Hoang, M.; Turney, T. W. *Journal of Materials Science* **1992**, *27*, 77-82.

(23) Zhang, Y.; Han, K.; Cheng, T.; Fang, Z. *Inorg. Chem.* **2007**, *46*, 4713-4717.

(24) Pol, V. G.; Thiyagarajan, P.; Moreno, J. M. C.; Popa, M. *Inorg. Chem.* **2009**, *48*, 6417-6424.

(25) Li, Z.; Zhang, J.; Du, J.; Gao, H.; Gao, Y.; Mu, T.; Han, B. *Materials Letters* **2005**, *59*, 963-965.

(26) Bao, N.; Shen, L.; Wang, Y.; Padhan, P.; Gupta, A. *J. Am. Chem. Soc.* **2007**, *129*, 12374-12375.

(27) Castro, E. G.; Salvatierra, R. V.; Schreiner, W. H.; Oliveira, M. M.; Zarbin, A. J. G. *Chem. Mater.* **2010**, *22*, 360-370.

(28) Nguyen, T. D.; Mrabet, D.; Do, T. O. *J. Phys. Chem. C* **2008**, *112*, 15226-15235.

(29) Pan, D.; Jiang, S.; An, L.; Jiang, B. Adv. Mater. ***2004,*** 16*, 982-985.*

(30) Nguyen, T. D.; Do, T. O. *Phys. Chem. C* **2009**, *113*, 11204-11214.

(31) Meldrum, F. C.; Colfen, H. *Chem. Rev.* **2008**, *108*, 4332-4432.

(32) Joint Committee on Powder Diffraction Standards diffraction data file no. 13-434, International Center for Diffraction Data, Newtown Square, PA, USA, **1963**.

(33) Moulder, J. F.; Stickle, W. F.; Sobol, P. E.; Bomben, K. D. Handbook of X-ray photoelectron spectroscopy; Perkin-Elmer corporation, Physical Electronics Division: **1992**.

(34) Deng, Z.; Peng, B.; Chen, D.; Tang, F.; Muscat, A. J. *Langmuir* **2008**, *24*, 11089-11095.

(35) Sun, J.; Kyotani, T.; Tomita, A. *Journal of Solid State Chemistry* **1986**, *65*, 94-99.

(36) Li, Y.; Cao, M.; Feng, L. *Langmuir* **2009**, *25*, 1705-1712.

(37) Chen, A.; Hindle, P. H. *Chem. Rev.* **2010**, DOI: 10.1021/cr9003902.

(38) Park, J.; Lee, E.; Hwang, N. M.; Kang, M.; Kim, S. C.; Hwang, Y.; Park, J. G.; Noh, H. J.; Kim, J. Y.; Park, J. H.; Hyeon, T. *Angew. Chem.* **2005**, *117*, 2932-2937.

(39) Ahmad, A.; Shah, J. A.; Buzby, S.; Shah, S. I. *Eur. J. Inorg. Chem.* **2008**, 948-953.

(40) Luque, M. P. R.; Hernandez, J. C.; Yeste, M. P.; Bernal, S.; Cauqui, M. A.; Pintado, J. M.; Omil, J. A. P.; Stephan, O.; Calvino, J. J.; Trasobares, S. *J. Phys. Chem. C* **2008**, *112*, 5900-5910.

(41) Itoh, T.; Kikkawa, Y.; Biju, V.; Ishikawa, M.; Ikehata, A.; and Ozaki, Y. *J. Phys. Chem. B* **2006**, *110*, 21536-21544.

(42) Zhou, H.; Wong, S. S. *ACS Nano* **2008**, *2*, 944-958.

(43) Hung, L. I.; Tsung, C. K.; Huang, W.; Yang, P. *Adv. Mater.* **2010**, *22*, 1-5.

(44) Sun, X.; Zhang, Y. W.; Si, R.; Yan, C. H. *small* **2005**, *1*, 1081-1086.

(45) An, K. Kwon, S. G.; Park, M.; Na, H. B.; Baik, S. I.; Yu, J. H.; Kim, D.; Son, J. S.; Kim, Y. W.; Song, I. C.; Moon, W. K.; Park. H. M.; Hyeon, T. *Nano Lett.* **2008**, *8*, 4252-4258.

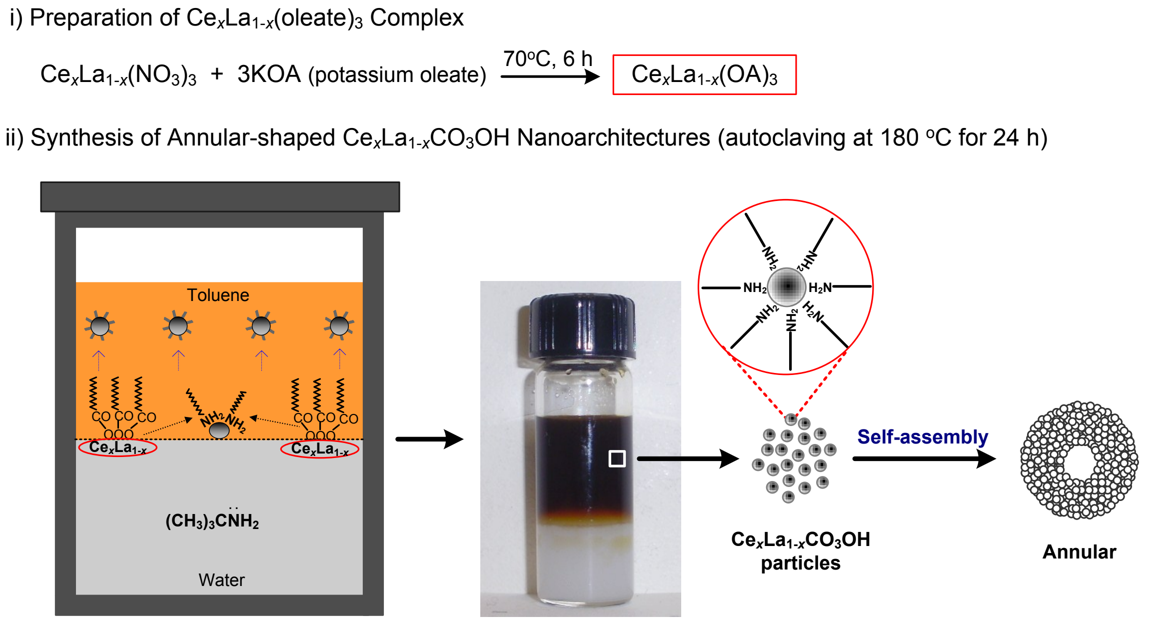

Scheme 7.3.1. Two-phase protocol for the synthesis of the undoped and cerium doped $LaCO_3OH$ annular-shaped nanoarchitectures.

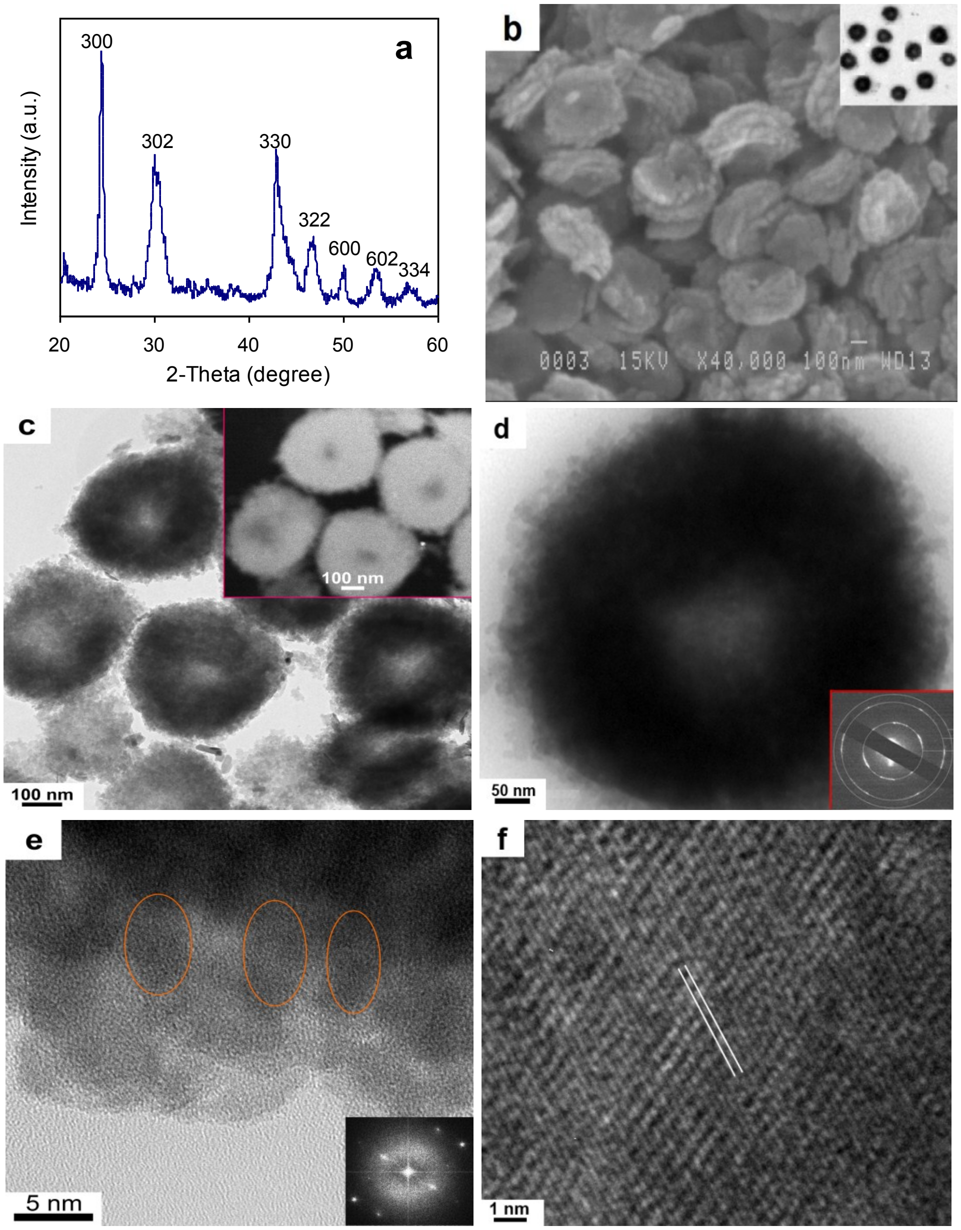

Figure 7.3.1. (a) XRD; (b) SEM; (c) and (d) TEM, inset dark-field TEM, inset SAED; (e) and (f) HRTEM, inset FFT pattern of the as-synthesized $LaCO_3OH$ annular-shaped nanoarchitectures.

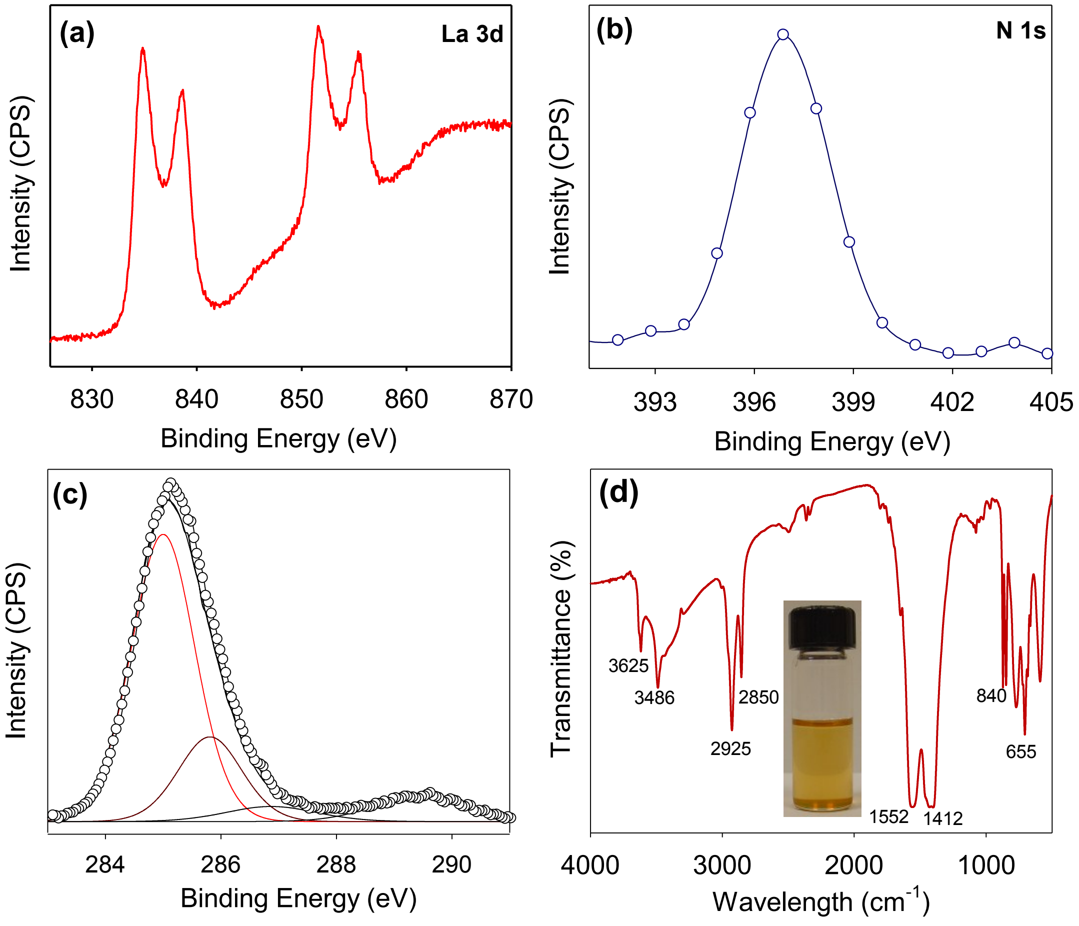

Figure 7.3.2. (a) La 3d; (b) N 1s; (c) C 1s XPS; (d) FTIR spectra of the as-synthesized $LaCO_3OH$ nanoannulars; Inset of (d): one photo of transparent toluene solution containing the colloidal $LaCO_3OH$ nanoannulars.

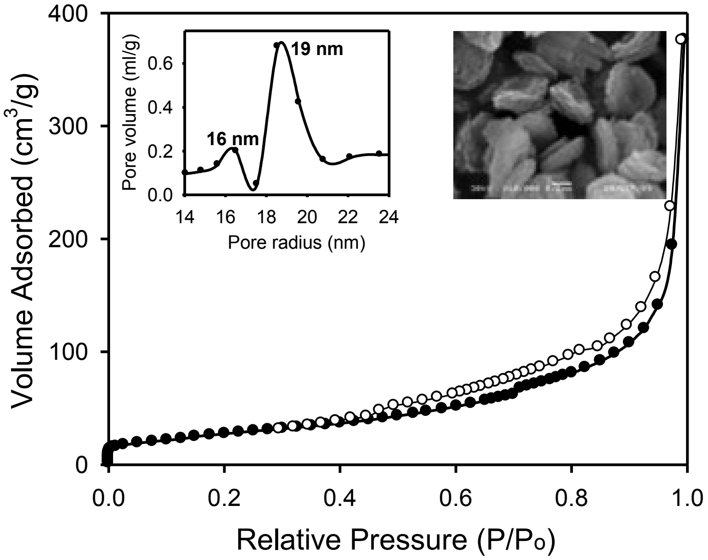

Figure 7.3.3. Nitrogen adsorption-desorption and pore size distribution of the as-made $LaCO_3OH$ nanoannulars after annealing at 550 °C for 2 h. Inset SEM image of the calcined $LaCO_3OH$ annular sample.

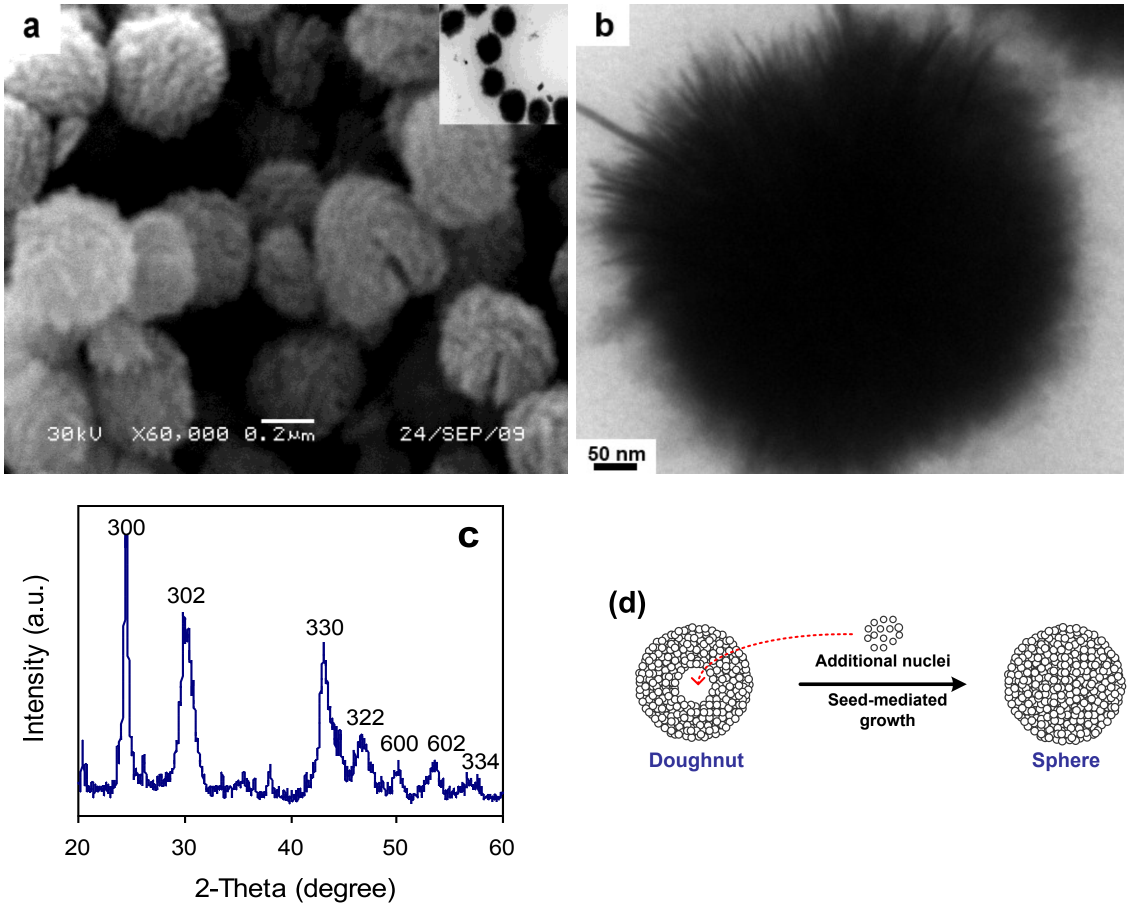

Figure 7.3.4. (a) SEM; (b) TEM; (c) XRD pattern of the as-synthesized $LaCO_3OH$ nanospheres; (d) A schematic model of the shape change from annular into sphere by the seed-mediated growth.

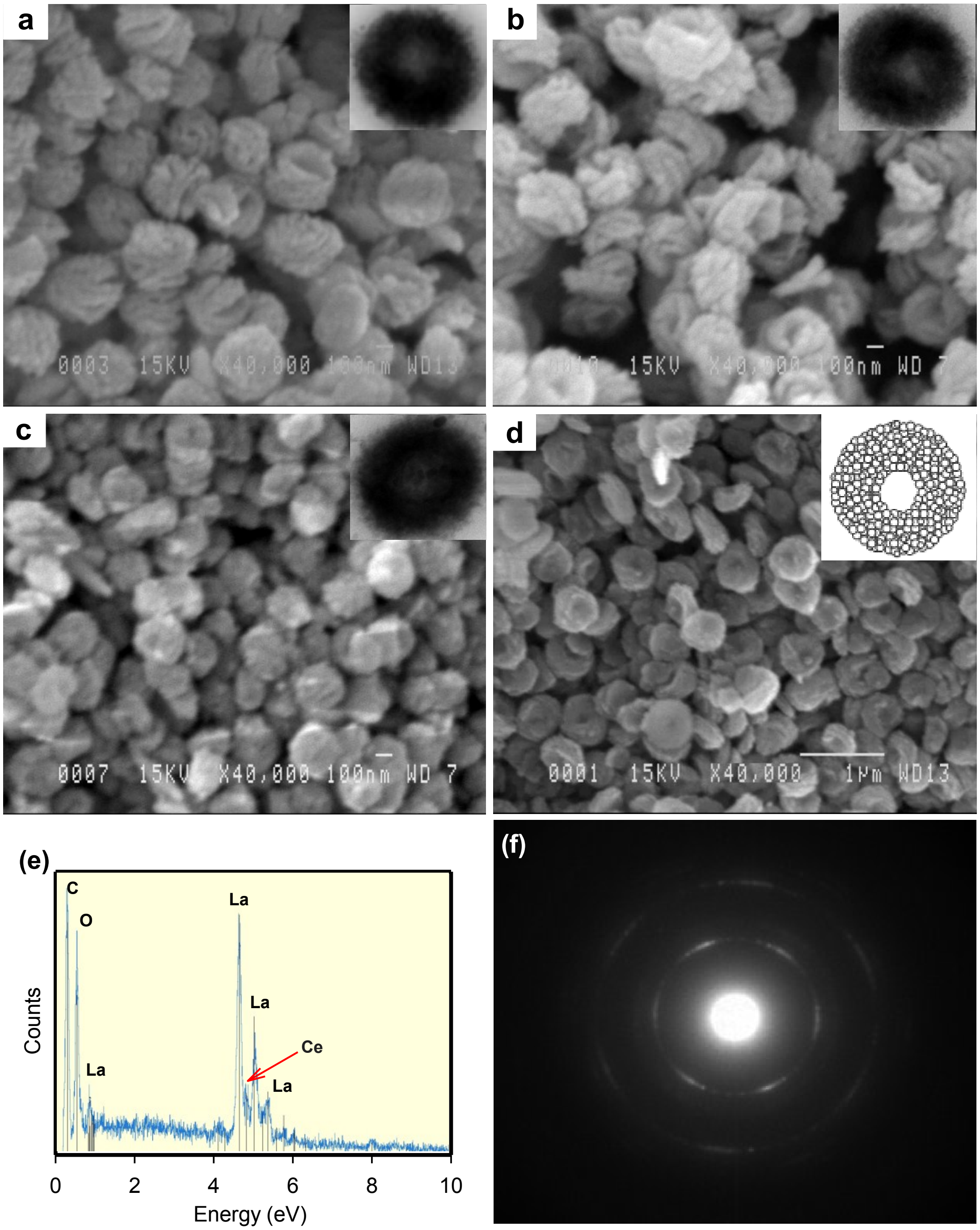

Figure 7.3.5. SEM images of the $Ce_xLa_{1-x}CO_3OH$ nanoannulars with various doping level (mol%): (a) $x = 5$; (b) $x = 10$; (c) $x = 15$; (d) $x = 20$; (e) EDS and (f) SAED pattern of 15 mol% cerium doped sample. The upper insets in (a-c) showing the TEM images of a corresponding annular. The upper inset in (d) showing a drawn scheme of an annular structure.

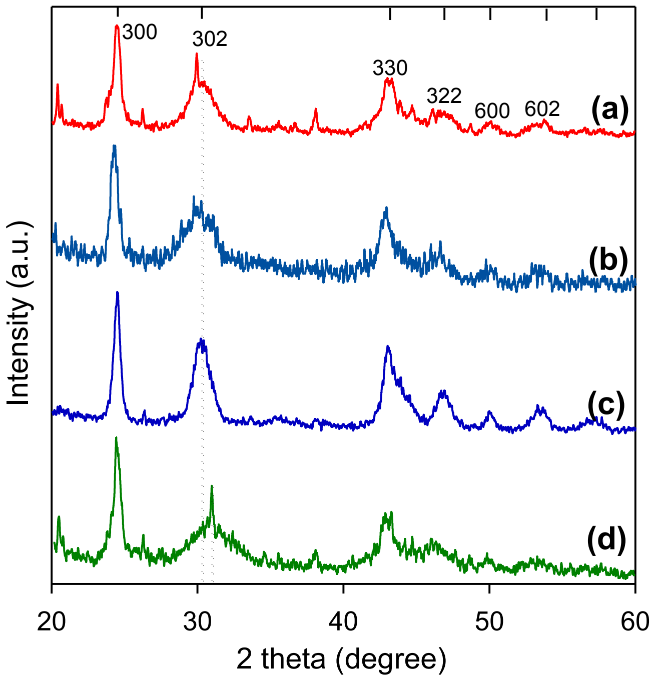

Figure 7.3.6. XRD patterns of the as-synthesized $Ce_xLa_{1-x}CO_3OH$ nanoannular samples with various doping levels (mol%): (a) $x = 5$; (b) $x = 10$; (c) $x = 15$; (d) $x = 20$.

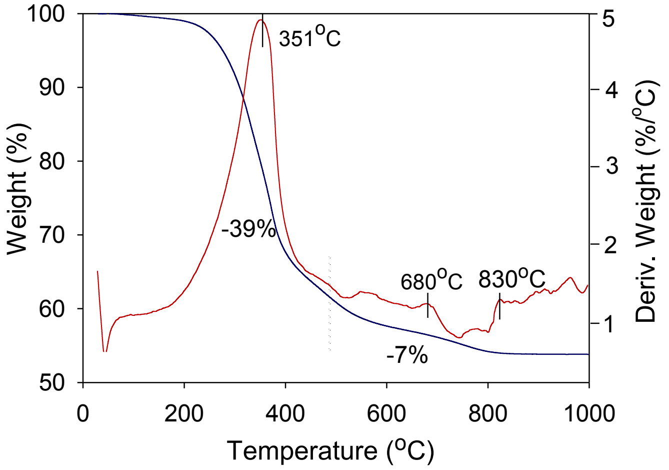

Figure 7.3.7. TGA-DTA curves of the as-synthesized oleylamine-capped Cerium-doped LaCO$_3$OH nanoannulars.

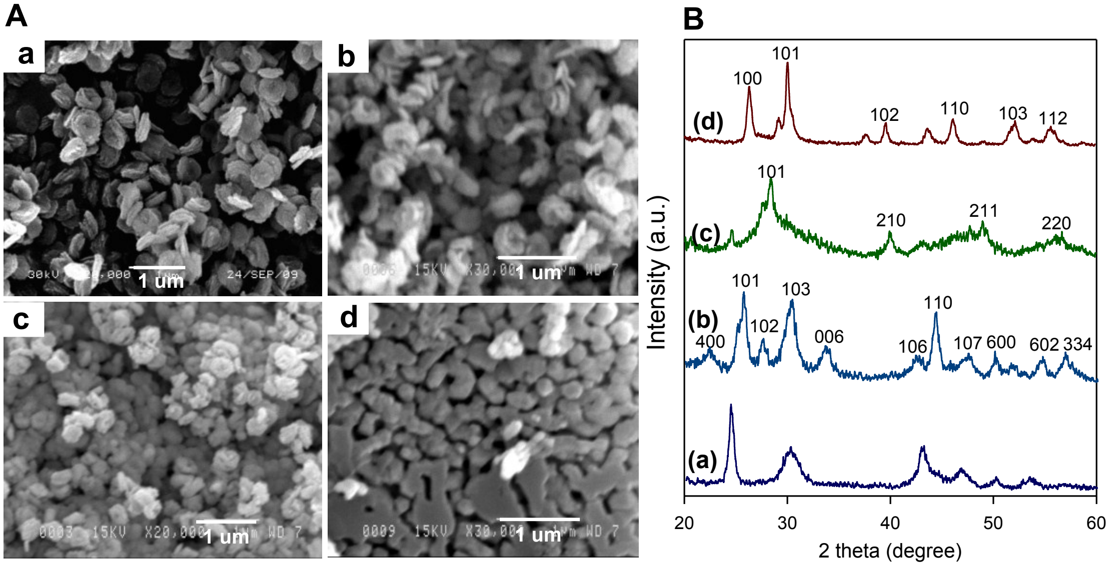

Figure 7.3.8. (A) SEM images and (B) XRD patterns of the as-synthesized 10 mol% cerium doped LaCO$_3$OH samples calcined at the different temperatures for 12 h: (a) Ce$_x$La$_{1-x}$CO$_3$OH, 300 °C; (b) Ce$_x$La$_{1-x}$(CO$_3$)O$_2$, 600 °C; (c) Ce$_x$La$_{1-x}$(OH)$_3$, 800 °C; (d) (Ce$_x$La$_{1-x}$)$_2$O$_{3-\delta}$, 900 °C.

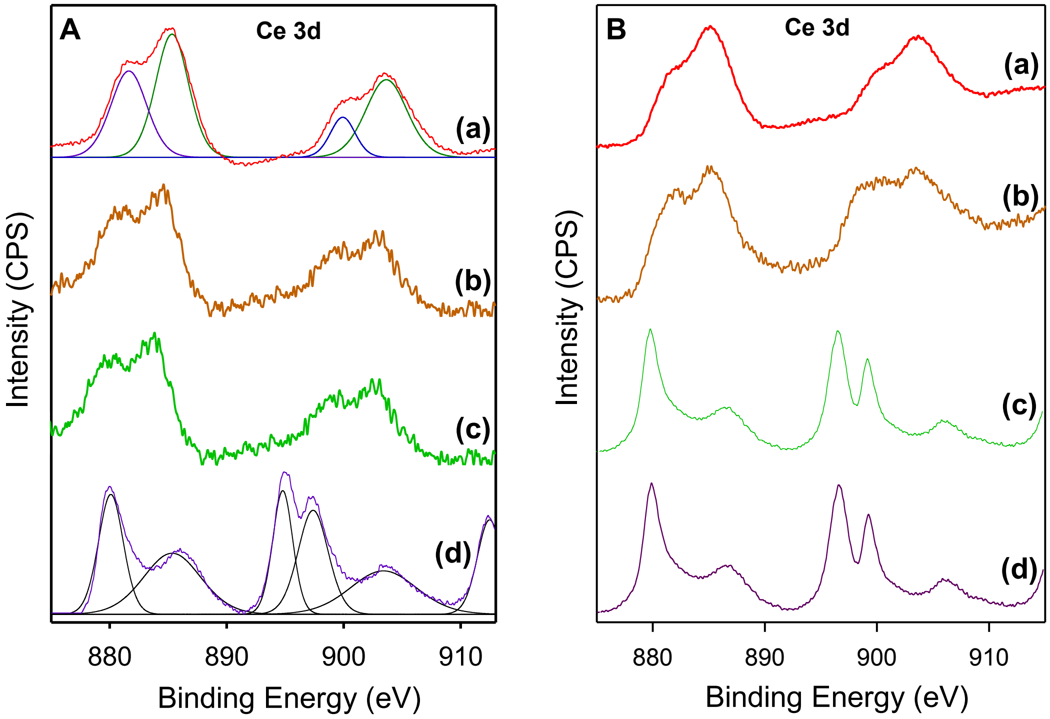

Figure 7.3.9. (A) Ce 3d XPS spectra of the as-synthesized $Ce_xLa_{1-x}CO_3OH$ samples with various doping levels (mol%): (a) x = 5; (b) x = 10; (c) x = 15; (d) x = 20. (B) Ce 3d XPS spectra of 10 mol% cerium doped $LaCO_3OH$ samples calcined at different temperatures for 12 h: (a) 300 °C; (b) 600 °C; (c) 800 °C; (d) 900 °C.

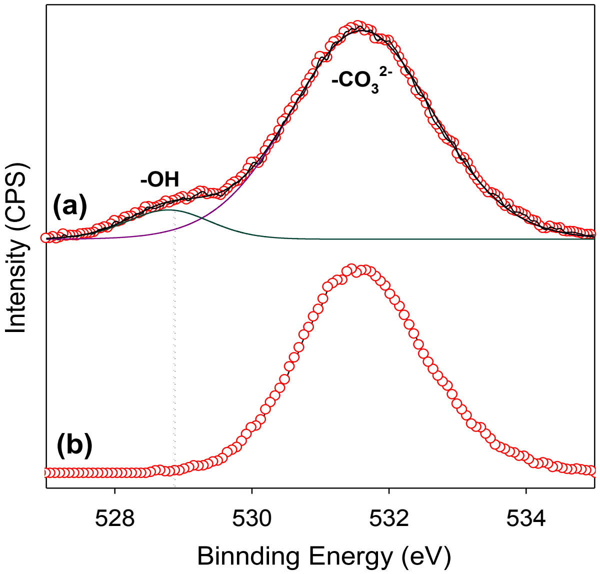

Figure 7.3.10. O 1s XPS spectra of (a) $Ce_xLa_{1-x}CO_3OH$ and (b) $(Ce_xLa_{1-x})_2O_{3-\delta}$ samples.

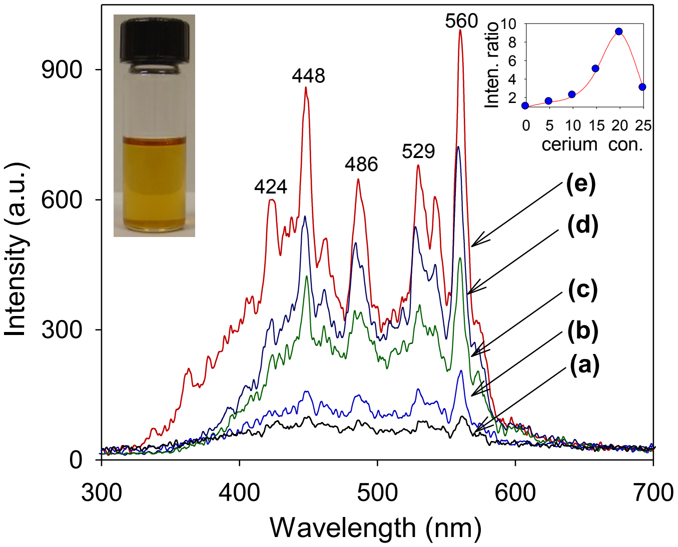

Figure 7.3.11. Photoluminescence emission spectra (under excitation at 360 nm) of the as-synthesized $Ce_xLa_{1-x}CO_3OH$ nanoannular samples with various doping levels (mol%): (a) $x = 0$; (b) $x = 5$; (c) $x = 10$; (d) $x = 15$; (e) $x = 20$. Inset: one photo of transparent toluene solution containing colloidal 10 mol% cerium doped $LaCO_3OH$ nanoannulars and the relationship between the cerium concentration and the PL intensity ratio.

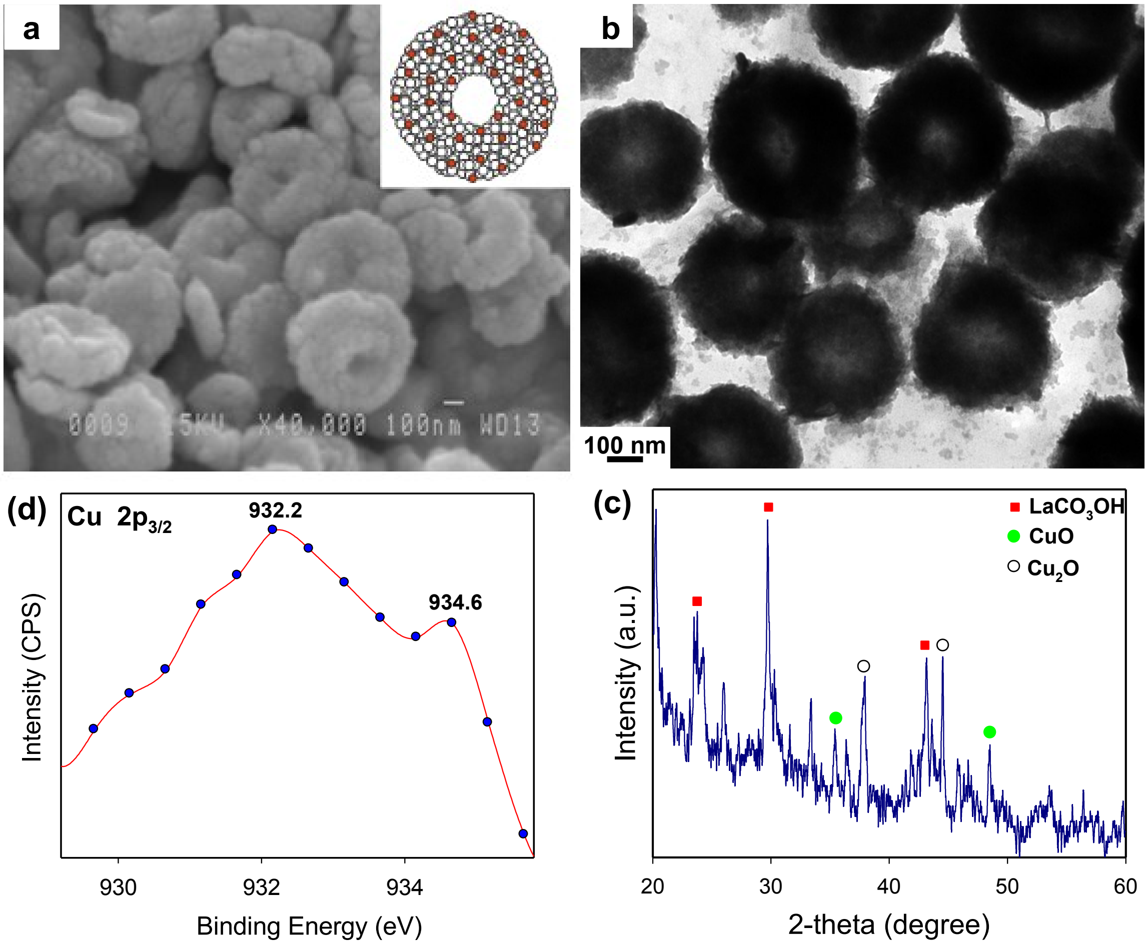

Figure 7.3.12. (a) SEM; (b) TEM, inset SAED; (c) XRD; (d) Cu 2p$_{3/2}$ XPS patterns of the as-synthesized Cu/LaCO$_3$OH nanoannulars. Upper inset in (a) shows the simulated structure of a Cu/LaCO$_3$OH annular.

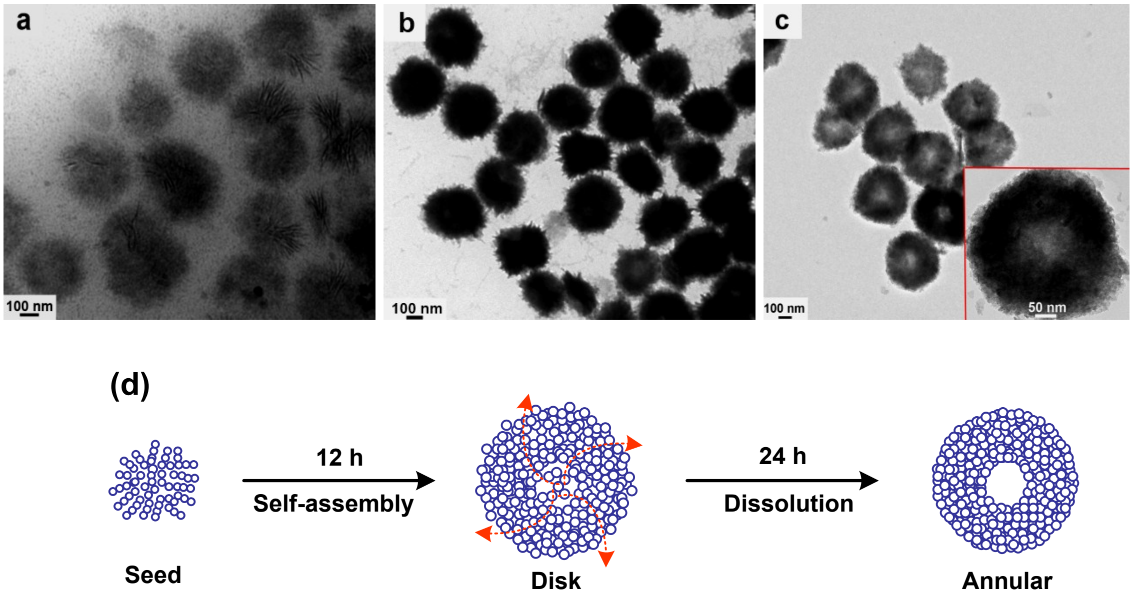

Figure 7.3.13. TEM images of 10 mol% cerium doped $LaCO_3OH$ samples synthesized at 180 °C with a reaction time of (a) 4 h, (b) 12 h, (c) 24 h. (d) A schematic diagram for the formation of annular-shaped nanoarchitectures.

Chapter 8 Synthesis of Hybrid Metal@Oxide Nanocrystals and Their Catalytic Applications

8.1. Cu particles on Single-Crystalline CeO_2 Nanocubes as a Synergistic Catalyst for Preferential CO Oxidation

Thanh-Dinh Nguyen, Driss Mrabet, Dinh-Thang Cao and Trong-On Do

Department of Chemical Engineering, Laval University, Quebec G1K 7P4 Canada

Submitted to *Advanced Materials* - **2011**

Abstract

Well-shaped and single-crystalline {100}-faceted CeO_2 nanocubes with ~120 nm edge length were synthesized via hydrothermal reaction of cerium nitrates in basic medium in the presence of hexamethylenediamine (HEA) as the capping agent. The electrostatic attraction between Cu^{2+} deposits and negatively charged surface of HEA-capped CeO_2 nanocubes is a crucial for the formation of $Cu@CeO_2$ nanohybrids. The $Cu@CeO_2$ nanomaterials are used as a synergistic catalyst for preferential CO conversion originating from entirely exposed active {100} facet and interfacial copper-ceria interaction.

8.1.1. Introduction

Inorganic nanohybrids containing two or more nanoscale components have drawn considerable interest in many other areas of materials science.[1] A particle-particle interaction between the components of such systems may significantly improve the existing local electronic structure and induce new synergistic chemical properties. Here we report a new approach for the synthesis of efficient nanohybrids consisting of decoration of Cu particles on the reactive {100} facets of single-crystalline ceria (CeO_2) nanocubes. An interfacial interaction between copper and ceria species could facilitate the formation and migration of oxygen vacancies in a controlled-manner hybrid structure, resulting in as a synergistic catalyst for preferential CO conversion.[2]

Cu@CeO_2 nanohybrids as a much more cost-effective catalyst with morphological and positional control of the components have been viewed as a promising candidate for preferential oxidation (PROX).[3] Ceria has been widely established as a principal oxygen carrier that originates from its high oxygen storage capability (OSC) due to nonstoichiometric oxides, CeO_{2-x} ($0 < x \leq 0.5$).[4, 5] A synergistic interaction of metal-support in Cu@CeO_2 nanosystem results in an increase of more oxygen vacancies, leading to increase OSC and enhance catalytic performance.[6] In a ceria crystal, the surface reactivity on {100} facet with a distinct surface atomic arrangement is considerably higher than on either {110} or {111}.[7, 8] Consequently, ceria nanocubes with a high exposed percentage of {100} facet are supposed to be a most active support.[8-10] Thereby to gain a high catalytic activity, tiny copper particles often have to well-disperse on the {100} facets of ceria support.[11] In addition, the high-crystalline and relative large-sized ceria nanosupports often have thermal stability–resulting in enhancing the durability of the hybrid catalysts.[12]

The most recent progress of surfactant-assisted techniques has been performed to fabrication of more elaborate hybrid nanocrystals via deposition/coating of either colloidal oxides or semiconductors with metallic clusters. We recently synthesized the different hybrid systems and extensively studied their size-dependent photocatalytic activities, in which metal particles were coupled with the oxide nanocrystals using either seed-mediated growth in assistance of bifunctional organic linker[13] or photodeposition technique.[14] El-Shall et al.[15] reported the synthesis of selected nanoalloys supported on ceria nanocatalysts for low-temperature CO oxidation. The particle size-dependent catalytic properties were reported in the literature.[16] Prince et al.[17] loaded Cu particles on commercial CeO_2 micropowders via conventional impregnation and proved a low-temperature CO conversion due to CO adsorption on copper in the vicinity of reactive ceria facets. However, no much information has been reported for the synthesis of efficient nanohybrids, consisting of size-controlled Cu particles on the reactive {100} facets of single-crystalline ceria nanocubes, as a synergistic catalyst for CO conversion.

8.1.2. Experimental Section

Chemicals: All chemicals were used as received without further purification. Cerium nitrate hexahydrate ($Ce(NO_3)_3.6H_2O$, 99%), commercial cerium (IV) oxide powder (CeO_2 with particle size < 5 μm, 99.9%), copper nitrate ($Cu(NO_3)_2$, 99.99%), silver nitrate ($AgNO_3$, 99.99%), hexamethylenediamine ($H_2NC_5H_{10}NH_2$, or HEA, tech. grade, 70%), sodium borohydride ($NaBH_4$, >98%), were purchased from Sigma-Aldrich. Sodium hydroxide was purchased from Reagent ACS.

Synthesis of Single-Crystalline CeO_2 Nanocubes: In typical synthesis, 0.03 mol $Ce(NO_3)_3.6H_2O$ was poured to aqueous hexamethylenediamine solution (10 mL, 1.5 M) under stirring and then a NaOH solution (15 M, 20 mL) was poured. The pH value of the initial solution was ~12. The resulting reaction mixture (30 mL) was transferred to a 50 mL Teflon-lined stainless steel autoclave and treated to 180 ^oC for 3 days, and then allowed to cool naturally to room temperature. The obtained products were filtered out and washed by distilled water for several times to remove the excess amount of impurities and dried at 60 °C for 2 h.

Preparation of $Cu@CeO_2$ Nanohybrids: An aqueous $Cu(NO_3)_2$ solution (5 mL, 8.58-25.78 mM) was injected into 5 mL of an aqueous CeO_2 nanocube suspension (0.2 g for synthesized CeO_2 NC powder) under stirring. Cu^{2+} precursors were adsorbed on the hydrophilic surface of ceria nanocrystals and then reduced to zerovalent metallic copper particles by injecting 10 mL of aqueous $NaBH_4$ solution 0.019-0.057 M. The pH value of the reaction solution was ~7.0. The whole loading content of metallic copper was controlled from 5 to 15 wt.%. The reaction mixture (20 mL) was then stirred vigorously and placed in a 30 ^oC water bath. Within 4 h, the color of the reaction solution changed to light brown for Cu, indicating the formation of the deposited metallic Cu particles. A precipitated powder was collected and washed with distilled water for several times to remove impurities. The sample for characterization was further dried at 60 °C for 2 h. $Ag@CeO_2$ sample synthesized extensibility using the same above synthetic procedure.

8.1.3. Results and Discussion

In this study, we used a seeded-growth method to prepare nanohybrids consisting of Cu particles attached to CeO_2 nanocubes. Briefly, hexamethylenediamine (HEA)-capped CeO_2 nanocubes were prepared by a hydrothermal reaction of cerium nitrates in basic medium in the presence of hexamethylenediamine (HEA) as a capping agent. Upon heating, the cerium precursors chemically transformed into $Ce(OH)_4$ monomers and then dehydrated to CeO_2 nuclei, whose subsequent growth into single-crystalline nanocubes is affected by capping HEA molecules. The hydrophilic-surfaced ceria nanocrystals were used to direct the growth of Cu particles from copper ions (see Supporting Information). The use of bifunctional HEA linker as a metallic trap is essential for linking two components through oppositely charge interaction. A proposed scheme for the formation of Cu@CeO_2 nanohybrids is expressed in Scheme 8.1.1. The overall procedure is simple and readily scalable because it does not require high-temperature reaction or any other complicated steps.

For the synthesis of nanocrystalline CeO_2 support, the vital role of HEA capping agent in determining the shape of CeO_2 nanocrystals was found. Under the same synthetic conditions, however, without HEA, only irregular particles with a wide population were formed. Figure 8.1.1 show PXRD, TEM, SAED patterns of the synthesized CeO_2 nanocrystals with HEA:Ce molar ratio of 1:2. The PXRD spectrum (Figure 8.1.1a) exhibits intense reflected peaks assigning to (111), (200), (220), (311) planes characteristic of a cubic phase with very high crystallinity (*Fm*3*m*, JCPDS 34-0394).[15] There is not any other impurities of $Ce(OH)_3$ structure detected. As seen in Figure 8.1.1b, TEM images show most single-crystalline and well-shaped CeO_2 nanocubes with a mean edge length of 120 nm. The projection views of most particles are perfect square shape, clear-cut edge, and very smooth surface without obvious defects. These ultrafine and highly symmetrical cube-shaped ceria nanocrystals have not almost been reported before.

The single-crystalline feature of the nanocubes was also confirmed by dark-field TEM image, as seen in Figure 8.1.1c. SAED pattern (Figure 8.1.1d) taken from a ceria nanocube exhibits very high crystallinity with the percentage of exposed {100} facets up to 100%. Panel e in Figure 8.1.1 shows four free-standing single 3D nanocubes displayed four differently projected shapes under TEM, depending on their orientations relative to the electron beam. Each cube has six well-defined {100} facets exposed, whose the surface energy is considered as the highest among {110} and {111} facets. When the HEA:Ce molar ratio increased from 1:2 to 10:1 and to 20:1, the particle size reduced from 120 to 40 nm, and its shape gradually transformed from nanocube (Figure 8.1.2a) into quasi-nanosphere (Figure 8.1.2b), respectively. The density of surface atoms in ceria crystal follows the order {100} > {110} > {111}.[7, 8] At low HEA concentration, the formed nanocubes could result in blocking the {100} facets by -NH_2 groups of HEA molecules, and the growth along these facets is considerably restricted. The decrease of the particle size along with a tendency to isotropic-shaped particle transformation at the higher capping agent concentrations could be relevant to a high degree of equal surfactant protection at all of the facets, providing regime the growth of ceria crystals.

The results reveal that the growth of ceria crystals proceeded by particle coalescence. Figure 8.1.4 shows representative TEM images of the ceria samples prepared at 180 ^{o}C for each duration of 1, 2, 3 days, using the same starting chemical composition. At a short stage (1 day), numerous small particles (less than 20 nm) were emerged, in which some of them coalesced into large particles with sizes of 50-70 nm (Figure 8.14a). Small particles had a tendency to disappear gradually with prolonged reaction time (2 days) and large particles kept growing by means of surface attachment and subsequent recrystallization (Figure 8.1.4b). The well-shaped nanocubes with relatively large size of ~120 nm dominantly produced after 3 days reaction (Figures 8.1.1b-e, 8.1.4c). The coalescence event could be explained by Ostwald ripening process for which the primary particles act as seeds for direct growth of ceria monomers.[18]

Ce 3d XPS spectrum (Figure 8.1.5) exhibits two oxidation states of Ce^{3+} (18%) and Ce^{4+} (82%) existing on the ceria surface.[19] The calculation of spectral areas indicates a defected structure CeO_{2-x} ($x = 0.3$) of the synthesized sample, contributing an essential role in catalysis. TGA-DTA curves (Figure 8.1.6) of the HEA-capped CeO_2 sample indicate a steep weight loss of ~1 wt.% only, appearing around 200-450 °C, accompanied by an exothermic peak at 523 °C, assigning to decomposition of HEA molecules. The content of surfactant capping on nanocrystal surface is very low (~1wt.%) because of low HEA:Ce ratio of 1:2 used. A gradual mass gain of ceria (~0.4 wt.%) above 450 °C could be related to partial oxidation of cerium oxide framework from Ce^{3+} to Ce^{4+}, demonstrating a defected CeO_{2-x} structure as XPS result. FTIR spectrum (Figure 8.1.7) of the capped nanocubes shows the bands at 1465-1665 cm^{-1} associated with N-H stretching modes of amino groups of HEA. C 1s and N 1s XPS spectra (Figure 8.1.4b,c) of this sample were also detected. A weak O 1s XPS peak (Figure 8.1.4d) at 532.2 eV was observed associated with a small amount of hydroxide groups located on the ceria surface. These negatively charged groups (amine and hydroxide) groups, that made the hydrophilic-surfaced ceria nanocrystals dispersible in water, exhibit a strong affinity for metal cations compatible with the formation of metal@ceria hybrids.

Nanohybrids consisting of ceria cubes coupled with copper clusters were achieved at different initial Cu contents ranging from 5 to 10 and 15 wt.%, corresponding to 4.9, 9.1, 13.8 wt.% in the calcined $Cu@CeO_2$ solids that were determined by XPS and EDS spectra. These works exploit the strong ability of metallic copper to bind covalently to the predominant donor of their free electron pair of the terminal $-NH_2$ groups of HEA molecules. The copper contents before and after calcination did not see any difference proving that copper species mostly migrated on the ceria surfaceinstead of incorporating into their lattice. TEM images in Figure 8.1.8a-f displays the $Cu@CeO_2$ nanohybrids with corresponding copper contents described as deposited 3D cubes viewing from the different directions. In most cases, overall Cu particles are epitaxial protrusions on {100} facets and edges/corners of the CeO_2 nanocubes. No evidence of large aggregates of Cu particles occurred and existed separately aside from the hybrid products. At low copper concentration (5 wt.%), small 2-3 nm Cu particles were formed on the ceria nanocubes (Figure 8.1.8a,b). When Cu loading was increased to 10 wt.%, a well-dispersion of 4-5 nm Cu particles on the CeO_2 nanocubes was observed (Figure 8.1.8c,d). A narrow distribution, small particle size, and high dispersion were found intwo cases. With higher Cu loading (15 wt.%), Cu particles with larger particle size (7-9 nm), broad size distribution and some coalescence of Cu particles were found (Figure 8.1.8e,f). The results imply that the growth of metallic Cu particles on hydrophilic-surfaced ceria through attachment role of $-NH_2$ groups is dependent on copper concentration.

Calcination of the capped Cu@CeO_2 hybrids to remove HEA linkers generated the nanocatalysts. The size and shape of Cu particles and CeO_2 supports in the calcined nanohybrids remain essentially unchanged without aggregation (Figure 8.1.9). BET surface area of the calcined Cu@CeO_2 sample is ~10 $m^2.g^{-1}$ similar to the theoretical surface area calculated from the TEM average particle size (e.g., ~14.3 $m^2.g^{-1}$). The status of copper particles coupled with ceria nanocubes was detected by XRD, EDS, XPS techniques. Metallic copper or copper oxide species were unable to detect by PXRD up to 15 wt.% copper content, possibly due to their low crystallinity, high dispersion, and tiny particle size. XPS and EDS spectra of the calcined Cu@CeO_2 samples however provide a clear evidence of the existence of Cu elements in the hybrid materials. Cu 2p XPS spectrum (Figure S10a) exhibits a Cu $2p_{3/2}$ peak at 932.3-943.1 eV which is associated with a mixture of Cu^o and partial Cu^+ species, no Cu^{2+} formed due to the absence of shake-up peak at 939-944 eV.[20, 21]

Catalytic activity of the Cu@CeO_2 nanocatalysts for CO oxidation was tested in comparison with pure CeO_2 samples. The evolution of the CO conversion over the different catalysts as a function of temperature is presented in Figure 8.1.10. For the pure CeO_2 samples, the maximum-half CO conversion was at 400 ^oC for commercial CeO_2 powders and at 340 ^oC for 40 nm CeO_2 nanospheres, while 120 nm CeO_2 nanocubes exhibits at lower temperature (300 ^oC). The nanocubes sample exhibits better catalytic efficiency than the nanospheres even though their lower surface area. This result clearly depicts that the exposed {100} facets in nanocubes contain more reactive atoms in determining catalytic activity for pure CeO_2. Regarding Cu@CeO_2 catalysts, the 100% CO conversion was reached at 200 ^oC for 9.1 wt.% Cu@CeO_2, at 225 ^oC for 4.9 wt.% Cu@CeO_2, and at 300 ^oC for 13.8 wt.% Cu@CeO_2. The catalytic activity of 9.1 wt. % Cu@CeO_2 is higher than that of 4.9 wt.% Cu@CeO_2 and 13.8 wt.% Cu@CeO_2 samples. This behavior could be mainly due to Cu particle size on CeO_2 surface concerning their interfacial interaction. It can be concluded that the catalytic efficiency of Cu@CeO_2 catalysts is much higher than pure ceria. This can be associated with metallic copper and copper (I) oxide particles considered as active sites on the CeO_2 surface and a synergistic interaction between copper and ceria facilitating the formation of oxygen vacancies. The adsorbed CO molecules on the active sites would react with oxygen extracting from the support surface leaving oxygen vacancy to convert intermediate carbonate species and finally its decomposition to CO_2.[6]

The electrostatic attraction between Ag^+ deposits and HEA-capped CeO_2 supports is instructive for the formation of Ag@CeO_2 hybrids using a similar procedure, as illustrated representative TEM and XPS data in Figure 8.1.11a,b. Free exposed H_2N-C_5H_{10}-NH_2-capped CeO_2 nanocubes provide a number of intermediate sites for attachment of metallic species on the {100} facets, thus enabling the formation of metal particles with a narrow distribution. The catalytic activity of the 4.7 wt.% Ag@CeO_2 hybrids is similar to 9.1 wt.% Cu@CeO_2 (Figure 8.1.11c). We suppose that the well-shaped single-crystalline CeO_2 nanocubes with hydrophilic surface character can be considered a useful oxygen carrier in the fabrication of diverse hybrid materials for enhanced catalytic activity.

8.1.4. Conclusion

In conclusion, we have demonstrated a versatile approach for the synthesis of CeO_2 nanocubes and the decoration of Cu particles on CeO_2 nanocubes as a synergistic catalyst for preferential CO oxidation. The enhanced catalytic efficiency of the hybrid Cu@CeO_2 catalysts results in the high exposure of reactive {100} facet in ceria nanocube and interfacial copper-ceria interaction. The shape-dependent catalytic activity of pure CeO_2 particles is demonstrated. CeO_2 nanocubes shows a better catalytic activity for CO oxidation compared to nanospheres and commercial powders. The size of the deposited particle in hybrid Cu@CeO_2 system depending on the catalytic activity can be controlled by tuning the copper content. The significance of the current method lies mainly in its simplicity and controllable ability towards variable factors in determining the activity of hybrid nanocatalysts.

8.1.5. References

1. Costi, R., A.E. Saunders, and U. Banin, *Colloidal Hybrid Nanostructures: A New Type of Functional Materials.* Angewandte Chemie International Edition, 2010. **49**(29): p. 4878-4897.
2. Razeghi, A., et al., *Activity enhancement of Cu-doped ceria by reductive regeneration of CuO–CeO_2 catalyst for preferential oxidation of CO in H_2-rich streams.* Chemical Engineering Journal, 2010. **164**(1): p. 214-220.

3. Snytnikov, P., et al., *Copper-cerium oxide catalysts for the selective oxidation of carbon monoxide in hydrogen-containing mixtures: II. Physicochemical characterization of the catalysts.* Kinetics and Catalysis, 2007. **48**(3): p. 448-456.
4. Wang, D., et al., *Synthesis and Oxygen Storage Capacity of Two-Dimensional Ceria Nanocrystals.* Angewandte Chemie International Edition, 2011. **50**(19): p. 4378-4381.
5. Campbell, C.T. and C.H.F. Peden, *Oxygen Vacancies and Catalysis on Ceria Surfaces.* Science, 2005. **309**(5735): p. 713-714.
6. Tschöpe, A., J.Y. Ying, and Y.-M. Chiang, *Processing and structural evolution of nanocrystalline* Cu/CeO_{2-x} *catalysts.* Materials Science and Engineering: A, 1995. **204**(1-2): p. 267-271.
7. Sayle, D.C., S.A. Maicaneanu, and G.W. Watson, *Atomistic Models for* $CeO_2(111)$*, (110), and (100) Nanoparticles, Supported on Yttrium-Stabilized Zirconia.* Journal of the American Chemical Society, 2002. **124**(38): p. 11429-11439.
8. Sayle, D.C., et al., *"Simulating Synthesis": Ceria Nanosphere Self-Assembly into Nanorods and Framework Architectures.* Journal of the American Chemical Society, 2007. **129**(25): p. 7924-7935.
9. Fu, Q., H. Saltsburg, and M. Flytzani-Stephanopoulos, *Active Nonmetallic Au and Pt Species on Ceria-Based Water-Gas Shift Catalysts.* Science, 2003. **301**(5635): p. 935-938.
10. Yang, S. and L. Gao, *Controlled Synthesis and Self-Assembly of* CeO_2 *Nanocubes.* Journal of the American Chemical Society, 2006. **128**(29): p. 9330-9331.
11. Cao, A. and G. Veser, *Exceptional high-temperature stability through distillation-like self-stabilization in bimetallic nanoparticles.* Nat Mater, 2010. **9**(1): p. 75-81.
12. Yu, T., B. Lim, and Y. Xia, *Aqueous-Phase Synthesis of Single-Crystal Ceria Nanosheets.* Angewandte Chemie, 2010. **122**(26): p. 4586-4589.
13. Nguyen, T.-D., C.-T. Dinh, and T.-O. Do, *A general procedure to synthesize highly crystalline metal oxide and mixed oxide nanocrystals in aqueous medium and photocatalytic activity of metal/oxide nanohybrids.* Nanoscale, 2011. **3**(4): p. 1861-1873.
14. Dinh, C.-T., et al., *A New Route to Size and Population Control of Silver Clusters on Colloidal* TiO_2 *Nanocrystals.* ACS Applied Materials & Interfaces, 2011. **3**(7): p. 2228-2234.
15. Abdelsayed, V., et al., *Microwave Synthesis of Bimetallic Nanoalloys and CO Oxidation on Ceria-Supported Nanoalloys.* Chemistry of Materials, 2009. **21**(13): p. 2825-2834.
16. Chen, M. and D.W. Goodman, *Catalytically Active Gold: From Nanoparticles to Ultrathin Films.* Accounts of Chemical Research, 2006. **39**(10): p. 739-746.
17. Matolin, V., et al., *Photoemission Spectroscopy Study of* Cu/CeO_2 *Systems: Cu/CeO2 Nanosized Catalyst and* $CeO_2(111)/Cu(111)$ *Inverse Model Catalyst.* The Journal of Physical Chemistry C, 2008. **112**(10): p. 3751-3758.
18. Yin, J., et al., *Low-Symmetry Iron Oxide Nanocrystals Bound by High-Index Facets.* Angewandte Chemie, 2010. **122**(36): p. 6472-6476.
19. Nguyen, T.-D. and T.-O. Do, *General Two-Phase Routes to Synthesize Colloidal Metal Oxide Nanocrystals: Simple Synthesis and Ordered Self-Assembly Structures.* The Journal of Physical Chemistry C, 2009. **113**(26): p. 11204-11214.

20. Gustafson, B.L. and P.S. Wehner, *XPS and XRD studies of supported Pd-Cu bimetallics.* Applied Surface Science, 1991. **52**(4): p. 261-270.
21. Avgouropoulos, G. and T. Ioannides, *Effect of synthesis parameters on catalytic properties of CuO-CeO$_2$.* Applied Catalysis B: Environmental, 2006. **67**(1-2): p. 1-11.

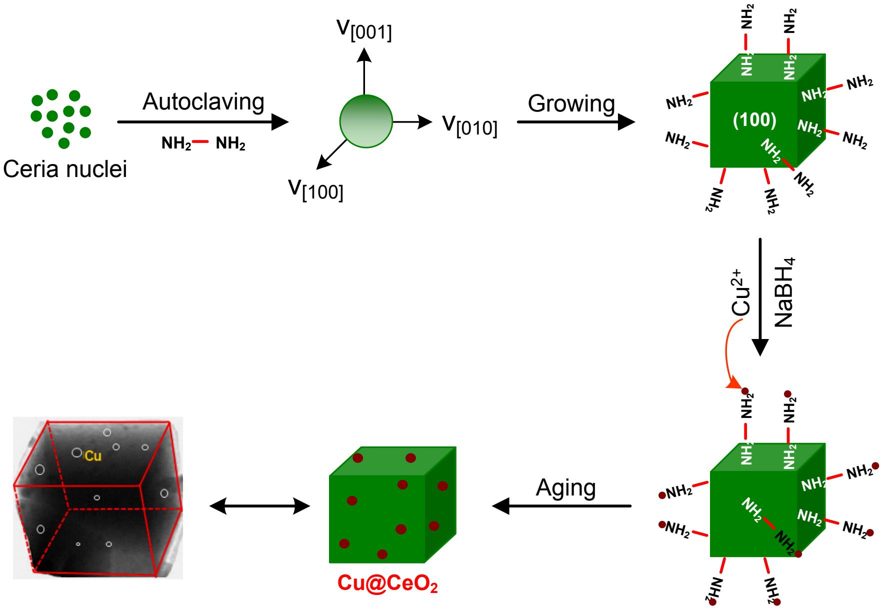

Scheme 8.1.1. A proposed mechanism for the evolution of single-crystalline CeO$_2$ nanocubes and the formation of Cu@CeO$_2$ nanohybrids.

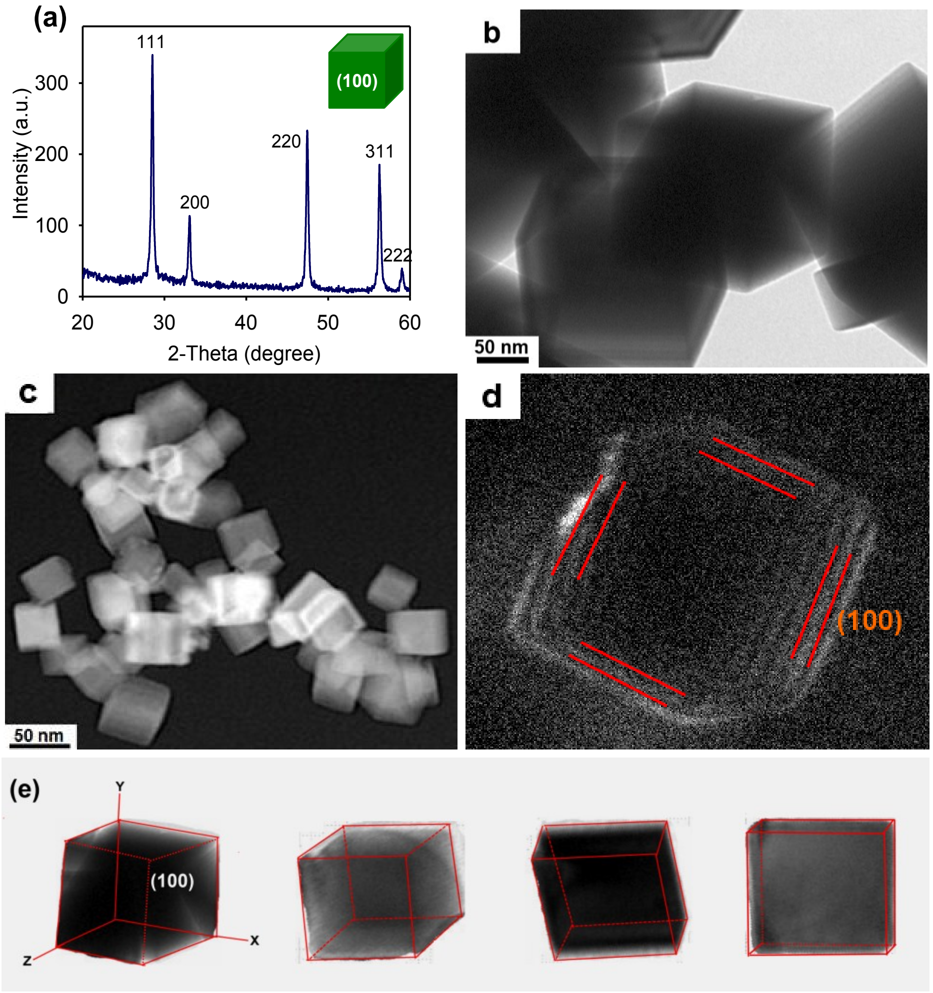

Figure 8.1.1. CeO_2 nanocubes synthesized using HEA:Ce molar ratio of 1:2. (a) PXRD; (b) TEM; (c) Dark-field TEM; (d) SAED pattern; (e) TEM images of a single nanocube taken at different orientations.

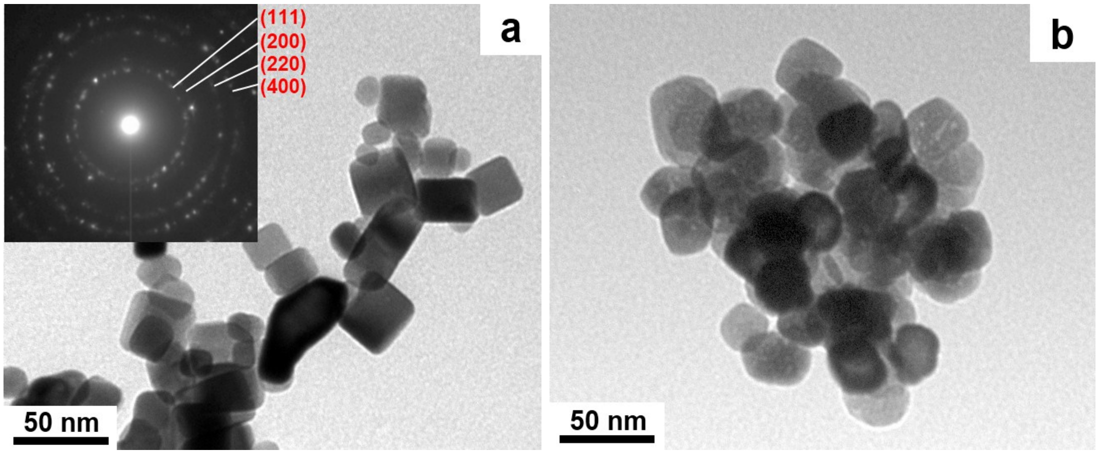

Figure 8.1.2. Size- and shape-controlled CeO_2 nanocrystals. TEM images (inset of SAED) of the samples synthesized using HEA:Ce molar ratio of 10:1 (a) and 20:1 (b).

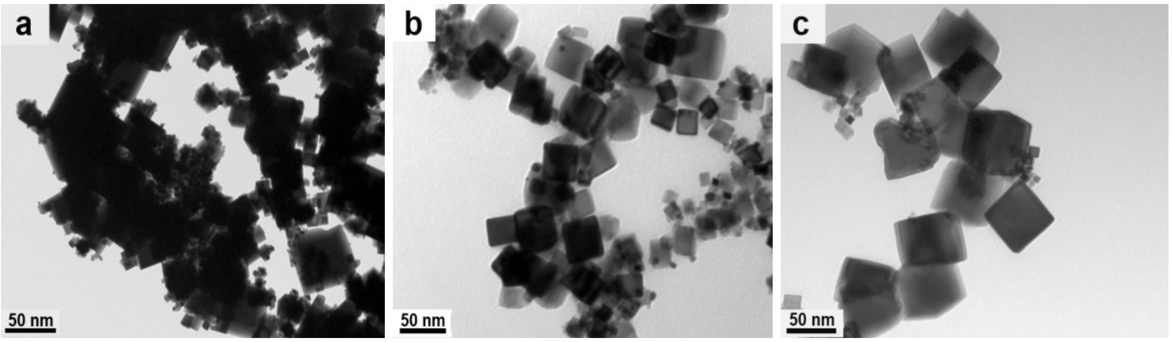

Figure 8.1.4. TEM images of CeO_2 nanocube samples synthesized at 180 °C for different reaction times (t): (a) $t = 1$ day, (b) $t = 2$ days, (c) $t = 3$ days.

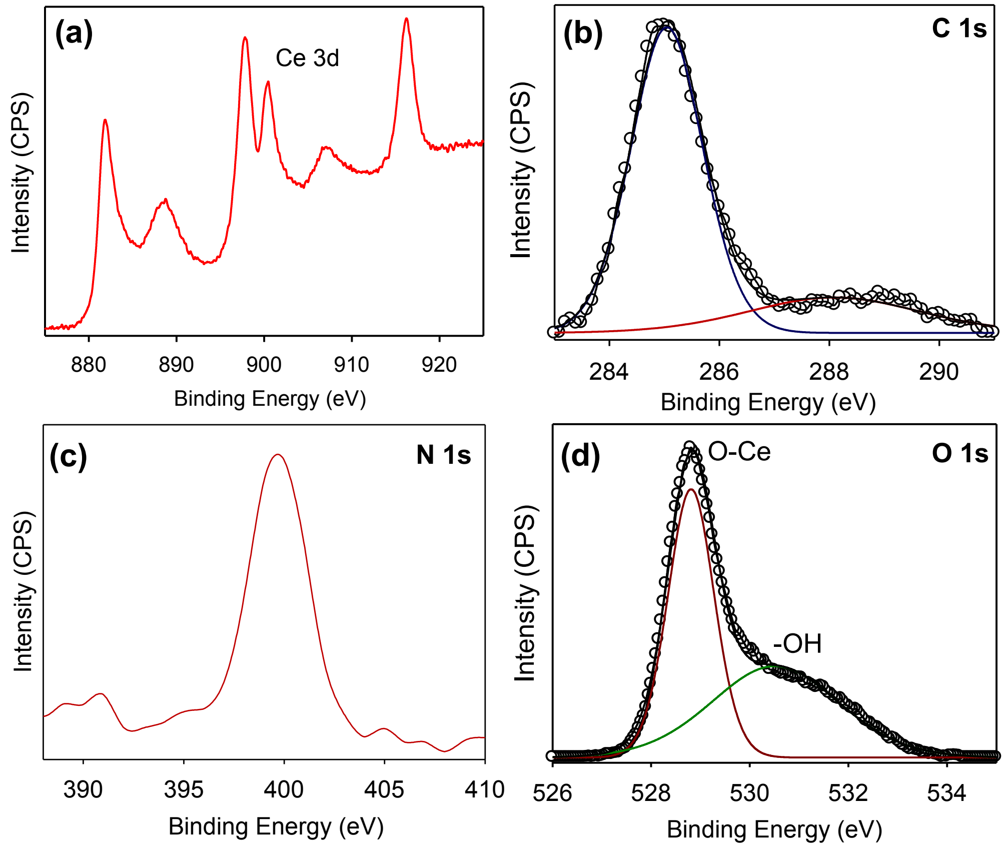

Figure 8.1.5. (a) Ce 3d, (b) C 1s, (c) N 1s, (d) O 1s XPS spectra of hexamethylenediamine-capped CeO_2 nanocubes.

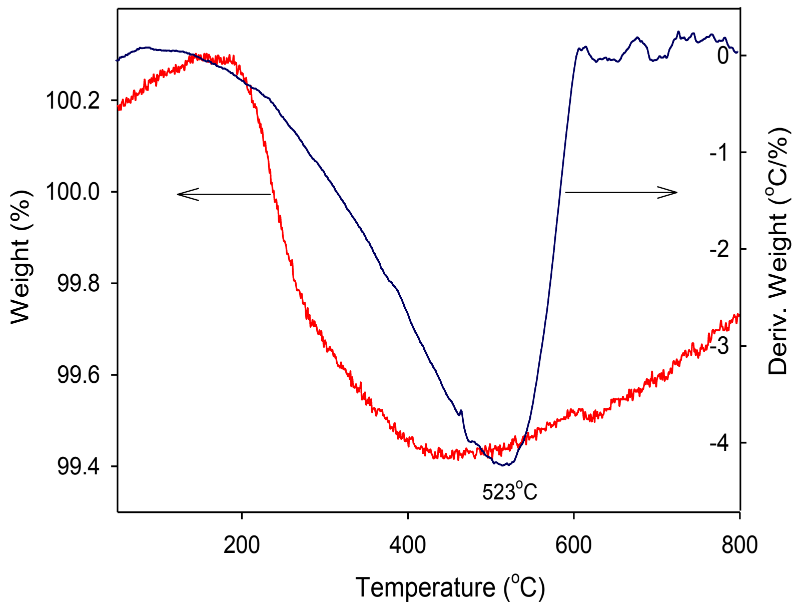

Figure 8.1.6. TGA-DTA curves of hexamethylenediamine-capped CeO_2 nanocubes.

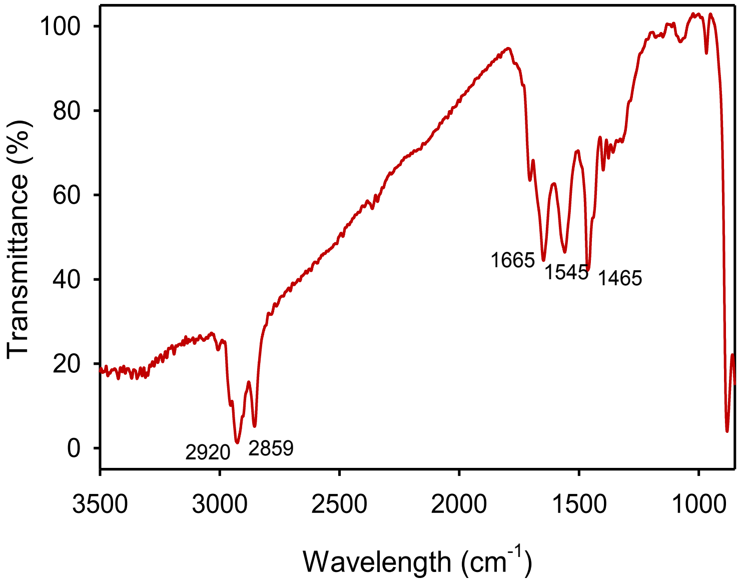

Figure 8.1.7. FTIR spectrum of hexamethylenediamine-capped CeO_2 nanocubes.

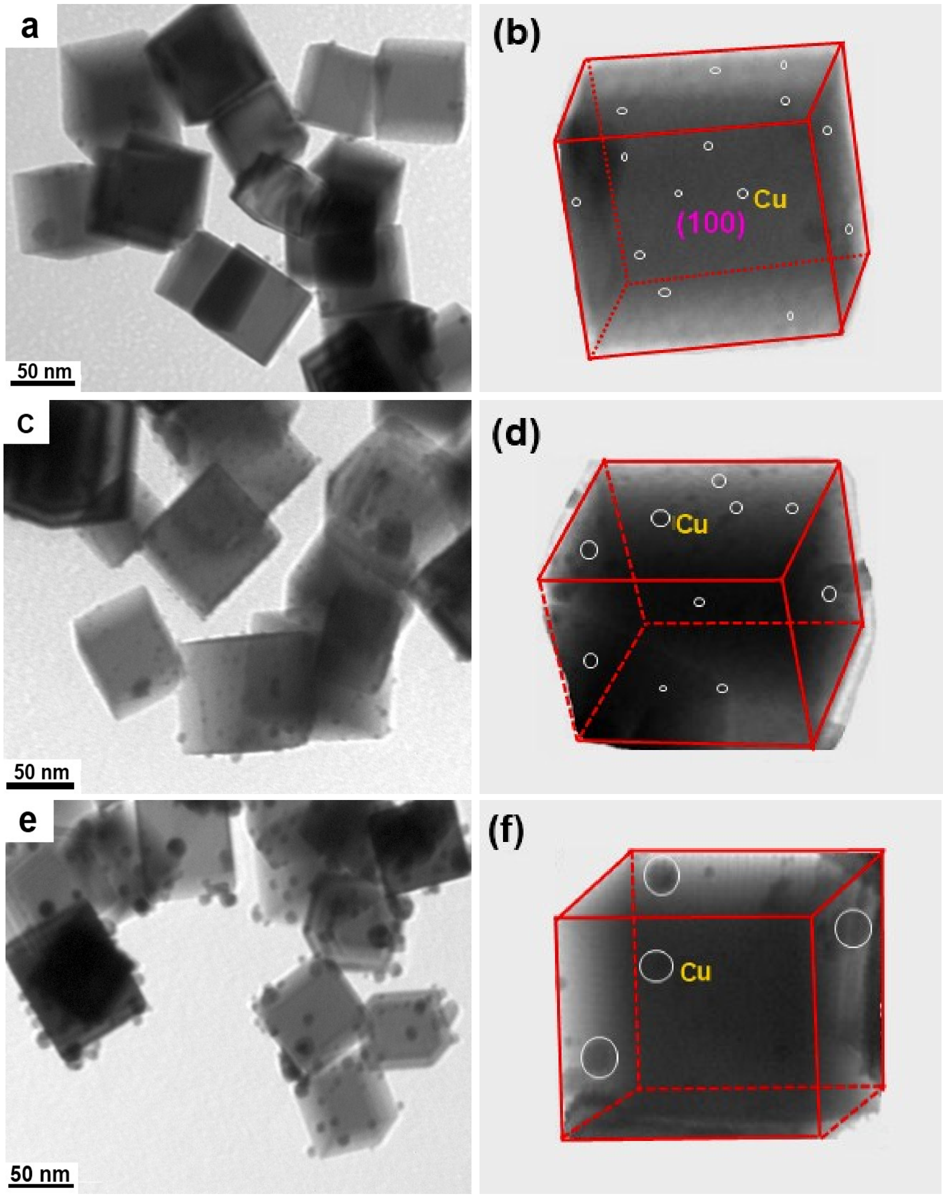

Figure 8.1.8. TEM images described the effect of copper content (C = wt.%) on size (d, nm) of Cu particles on {100}-faceted CeO_2 nanocubes. (a,b) C = 4.9 wt.%, d = 2-3 nm; (c,d) C = 9.1 wt.%, d = 4-5 nm; (e,f) C = 13.8 wt.%, d = 7-9 nm.

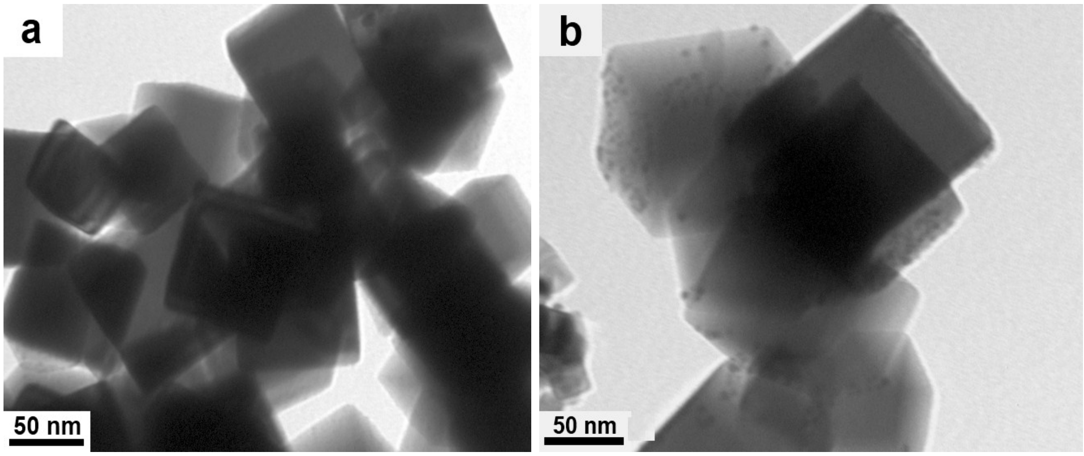

Figure 8.1.9. TEM images of single-crystalline CeO_2 nanocubes and 9.1 wt.% Cu@CeO_2 nanohybrids calcined at 550 °C for 3 h.

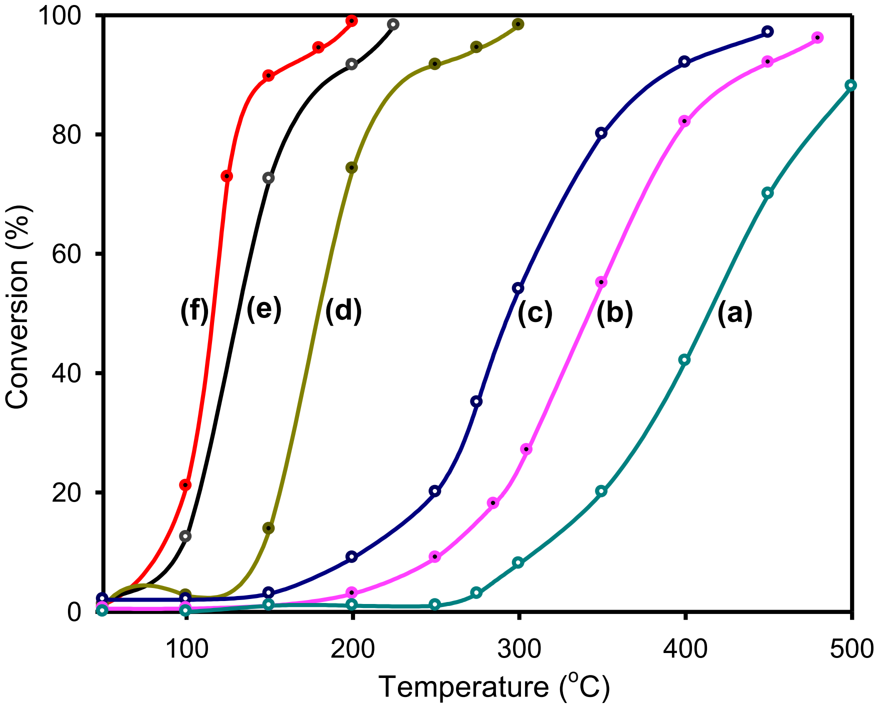

Figure 8.1.10. CO oxidation catalytic activity of hybrid Cu@CeO_2 *vs* pure CeO_2 catalysts with different particle sizes and components: (a) commercial CeO_2 powders; (b) 40 nm CeO_2 quasi-nanospheres; (c) 120 nm CeO_2 nanocubes; (d) 13.8 wt.% Cu@CeO_2; (e) 4.9 wt.% Cu@CeO_2; (f) 9.1 wt.% Cu@CeO_2.

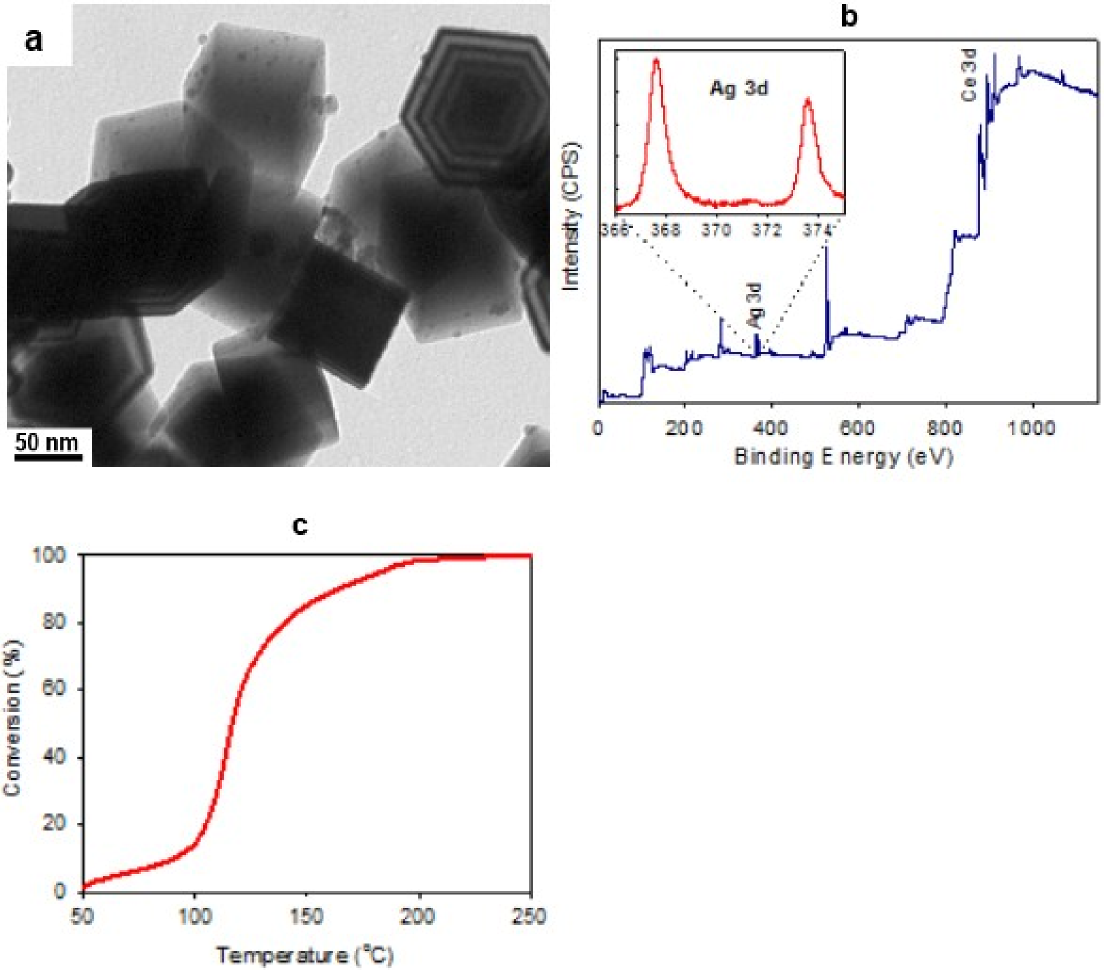

Figure 8.1.11. (a) TEM image and (b) XPS spectrum of 4.7 wt.% Ag@CeO_2 sample, (c) catalytic activity of the calcined Ag@CeO_2 catalyst (100% CO conversion at 200 °C).

8.2. A General Procedure to Synthesize Highly Crystalline Metal Oxide and Mixed Oxide Nanocrystals in Aqueous Medium and Photocatalytic Activity of Metal/Oxide Nanohybrids

Thanh-Dinh Nguyen, Cao-Thang Dinh and Trong-On Do

Department of Chemical Engineering, Laval University, Quebec G1K 7P4 Canada

Published in *Nanoscale*, **2011**, *3*, 1861-1873

Abstract

A conventional and general route has been exploited to the high yield synthesis of many kinds of highly crystalline metal oxide (and mixed oxide nanocrystals with different morphologies including belt, rod, truncated-octahedron, cubic, sphere, sheet via the hydrothermal reaction of inorganic precursors aqueous solution in the presence of bifunctional 6-aminohexanoic acid (AHA) molecules as a capping agent. This method is a simple, reproducible, and general route and is becoming as powerful an approach as other aqueous-based synthetic approaches to high-crystalline inorganic nanocrystals in scale-up. The shape of some nanocrystals (e.g., $CoWO_4$, $La_2(MoO_4)_3$) can be controlled by simple adjusting the synthesis conditions including pH solution and reaction temperature. Further by tuning precursor monomer concentration, the mesocrystal hierarchical aggregated microspheres (e.g., $MnWO_4$, $La_2(MoO_4)_3$) can be achieved due to the spontaneous assembly of individual AHA-capped nanoparticles. Additionally, we demonstrate that these obtained AHA-capped nanocrystals are the excellent support for the synthesis of a variety of hybrid metal/oxide nanocrystals in which noble metal particles are uniformly deposited on the surface of each individual nanosupport. The photocatalytic activity of Ag/TiO_2 nanobelts as a typical hybrid sample for Methylene Blue degradation was studied.

8.2.1. Introduction

Metal oxide, mixed oxide, and hybrid noble-metal/oxide nanocrystals (NCs) have great potential for electronic, magnetic, optical, and photocatalytic applications.[1-3] Mixed oxide system composed of two or more different components has attracted particular interest because their unique properties are not usually attainable in single components.[4] Metal highly dispersed on nanosupport surfaces show active catalysts for a variety of reactions. The origins of their high catalytic activity have been proposed to originate from one or more of three contributions: (i) presence of low coordinative metal sites; (ii) charge transfer between the support and metal; (iii) quantum size effect.[5] For example, the metal-semiconductor (TiO_2) interface can promote effective charge carrier transfers to favor charge separation under band gap excitation and subsequently high photo-catalytic performance.[6] Noble metals deposited on the NC surface act as sinks for transferring the photoexcited electron from semiconductor surface to reagents to perform the oxidation.[7] Therefore, the charge distribution between semiconductor and metal plays an important role in the photocatalytic process. Even though a large number of studies have been reported in the literature, the key factors for improved performance in metal/oxide nanocomposites are yet to be fully understood. Thus, the development of a general approach for the fabrication of many new types of metal/oxide nanohybrids is a great challenge.

Numerous methods have been documented in the recent reviews for the synthesis of a broad range of metal oxide and mixed oxide NCs.[8-10] For example, Li et al.[11] reported a new route for the synthesis of a variety of nanocrystals including magnetic/dielectric, semiconducting, rare earth fluorescent nanoparticles, which is based on a phase transfer and separation mechanism at the liquid-liquid interface, through the liquid-solid-solution process. Ying et al.[12] reported a protocol to transfer metal ions from an aqueous solution to an organic medium and their application in the synthesis of nanocrystals in organic solvent. Recently, our group reported the general two-phase routes for the synthesis of two classes of monodisperse metal oxide nanocrystals: rare earth oxides and transition metal oxides, using metal salts as starting precursors instead of expensive organometallic compounds.[13] The same synthetic protocol, we have successfully synthesized multicomponent nanocrystals with controlled size and shape, such as doughnut- and sphere-shaped $LaCO_3OH$ nanocrystals and cerium doped $LaCO_3OH$.[14] The shape-controlled vanadium oxide and rare earth orthovanadate nanocrystals using pre-prepared metal-ligand complexes were also obtained via a surfactant-mediated solvothermal process.[15-17]

It is well-known that the morphology of target nanocrystals could be controlled by capping agents through kinetic and thermodynamic regulations of nuclei growth.[18] Using conventional surfactants, such as fatty acids, aliphatic amines, alkyl thiols, alkyl phosphine oxides, the resulting surfactant-capped NC products are usually hydrophobic and separated in water solution, which may not be compatible for practical applications, in which water is used as reaction solvent. Recently, using amphiphilic amino acid biomolecules have received great attention to synthesize the water-dispersible nanocrystals in aqueous medium and the formed products can be compatible for biotechnology.[19] For example, Xu et al.[20] synthesized the amino acid-capped Au nanochains by reducing aqueous $AuCl_4^-$ with $NaBH_4$ in the presence of the amino acid (glutamic acid and histidine) as a capping agent. The interaction between hydrophilic-surfaced groups (-COOH and $-NH_2$) could be the result of the oriented-attachment process for the formation of the Au nanochains from 10-15 nm nanospheres. Peptide-capped gold nanospheres with ~10 nm in diameter were recently synthesized by Aizawa et al.[21] Several approaches for the controllable synthesis of titania nanocrystals and erbia micro/nanostructures in water/ethanol media have been developed in our research group.[22, 23] Very recently, we used bifunctional 6-aminohexanoic acid as a capping agent to the controlled shape of $MnWO_4$ nanoparticles and their self-assemblied microspheres in water medium.[24] For this purpose, we extent this protocol for the synthesis of a variety of highly crystalline metal oxide and mixed oxide nanocrystals with various morphologies and high yield.

On the other hand, heterogeneous photocatalysis is an economically alternative and environmentally safe technology of advanced oxidation processes for removal of organic contaminants and bacterial detoxification from water.[25] Photocatalytic nanoscale systems used to date were based mostly on noble metal-deposited oxide semiconductor hybrid nanocrystals and were usually operational under UV illumination.[26] Due to large band-gap oxide semiconductors such as titania and transition metal tungstate, metal islands deposited on the support structures serve to promote charge separation and also exhibit charge retention. Moreover, the precise control of small metal particle size, well-dispersion, and composition of metal deposited on support is deemed as an essential and powerful knob to turn their band gaps, which determines the photocatalytic characteristic of this system.[27, 28]

Especially, as the sizes of Au particles fall about 3 nm, the composites display exceptional catalytic behavior.[28] Two main routes have typically been used for the growth of such oxide hybrids. The first route employed light-induced growth of the metal onto the pre-synthesized oxide nanocrystals, as recently illustrated by our group.[22, 29] This synthetic method allows us not only to control the population of uniform metal clusters on each individual TiO_2 surface but also to control their particle size. The resulting hybrid materials exhibit much higher catalytic performance compared to that of commercial catalysts. The second route is via the reduced solution reaction of metal salt on the oxide nanocrystals. Available examples by these two processes include Au@CdS nanorods[30] and Ag@Pt nanorods.[31]

In this article, we report a convenient and general route for the aqueous-phase synthesis of highly crystalline metal oxide and mixed oxide nanoparticles via bifunctional surfactant-assisted hydrothermal process. The synthesis based on the crystallization of inorganic precursors in water medium in the presence of 6-aminohexanoic acid. The role of 6-aminohexanoic acid biomolecule is as a chelating agent to control the morphology and to stabilize the formed nanocrystals in water medium because of their hydrophilic surface. The deposition of small noble-metal on the oxide nanocrystals was performed in water medium using metal salt and $NaBH_4$ as metal source and reducing agent, respectively. The optical property and photocatalytic activity of the representative metal nanodots/ semiconductor oxide (Ag/TiO_2) hybrid nanocrystals were studied.

8.2.2. Experimental Section

Chemicals: All chemicals were used as received without further purification. Indium nitrate hydrate ($In(NO_3)_3.xH_2O$, 99.99%), anhydrous zirconium(IV) chloride ($ZrCl_4$, 99.99%), commercial titanium oxide powder (TiO_2, 99.8%), cobalt nitrate hexahydrate ($Co(NO_3)_2.6H_2O$, 98%), manganese nitrate tetrahydrate ($Mn(NO_3)_2.4H_2O$, 99%), zincate nitrate hexahydrate ($Zn(NO_3)_2.6H_2O$, 99.9%), cadimium nitrate hexahydrate ($Cd(NO_3)_2.6H_2O$, 99.9%), lanthanium nitrate hexahydrate ($La(NO_3)_3.6H_2O$, 99.9%), neodymium nitrate hexahydrate ($Nd(NO_3)_3.6H_2O$, 99.9%), yttrium nitrate hexahydrate ($Y(NO_3)_3.6H_2O$, 99.9%), cerium nitrate hexahydrate ($Ce(NO_3)_3.6H_2O$, 99.9%), samarium nitrate hexahydrate ($Sm(NO_3)_3.6H_2O$, 99.9%), gadolinium nitrate hexahydrate ($Gd(NO_3)_3.6H_2O$, 99.9%), erbium nitrate hydrate ($Er(NO_3)_3.xH_2O$, 99.9%), sodium tungstate dihydrate ($Na_2WO_4.2H_2O$, 99.9%), vanadium pentaoxide (V_2O_5, 99.6%), silver nitrate ($AgNO_3$), chlorauric acid ($HAuCl_4$. $3H_2O$), 6-aminohexanoic acid ($HOOCC_5H_{10}NH_2$, or AHA, tech. grade, 70%), sodium borohydride ($NaBH_4$), were purchased from Sigma-Aldrich. Sodium hydroxide and anhydrous ethanol were purchased from Reagent ACS.

Synthesis of Metal Oxide NCs (In_2O_3, Y_2O_3, ZrO_2, TiO_2, CeO_2): Metal oxide NCs were prepared by a standard alkali hydrothermal treatment process. In a typical synthesis, 0.03 mol of each inorganic precursor ($In(NO_3)_3$, $Y(NO_3)_3$, $ZrCl_4$, commercial TiO_2 powder, $Ce(NO_3)_3$) was poured to 6-aminohexanoic acid aqueous solution (10 mL, 1.5 M) under stirring and then a NaOH solution (15 M, 20 mL) was poured. The pH value of the initial solution was ~12. The resulting reaction mixture (30 mL) was transferred to a 50 mL Teflon-lined stainless steel autoclave and treated to 180 ^{o}C for 20 h, and subsequently to cool naturally to room temperature. The obtained products were filtered out and washed by distilled water for several times to remove impurities, and dried at 60 °C for 2 h.

Synthesis of Mixed Metal Oxide NCs (Tungstate, Vanadate, Molybdate): (i) Vanadate and molybdate precursors were prepared from bulk V_2O_5 and bulk MoO_3 powders, respectively. Typically, bulk V_2O_5 powder (0.30 mmol, 0.055 g) and NaOH solution (20 mL, 0.09 M) were mixed for the formation of 0.03 M Na_3VO_4 solution; bulk MoO_3 powders (0.92 mmol, 0.13 g) and NaOH solution (20 mL, 0.09 M) were mixed for the formation of 0.045 M Na_2MoO_4 solution at room temperature under magnetic stirring for about 30 min. **(ii)** For the synthesis of mixed metal oxide NCs, metal nitrates (0.61 mmol), 6-aminohexanoic acid (1.22 mmol, 0.16 g), were dissolved in 20 mL distilled water. An aqueous 0.03 M sodium tungstate, 0.03 M vanadate, or 0.045 M molybdate solution (20 mL) was dissolved in the above solution under stirring for 10 min at room temperature. An amorphous precipitates were generated immediately from the combination of metal cation and tungstate/vanadate/molybdate anion. The pH value of the initial solution was ~8. The resulting reaction mixture (40 mL) was transferred to a 70 mL Teflon-lined stainless steel autoclave and treated to 180 ^oC for 20 h. The obtained products were filtered out and washed by distilled water, and dried at 60 °C for 2 h.

Synthesis of Metal (Ag, Au)/Oxide Hybrid NCs: A $AgNO_3$ or $HAuCl_4$ aqueous solution (5 mL, 3.82-11.45 mM) was injected into 5 mL of an aqueous oxide suspension (0.2 g for each the pre-synthesized CeO_2, TiO_2, In_2O_3, Y_2O_3, $CoWO_4$, $MnWO_4$, $La_2(MoO_4)_3$ NC powders) under stirring. Ag or Au ion precursors were adsorbed on the hydrophilic surface of oxide semiconductor nanocrystals and were then reduced to zerovalent metal particles by injecting 10 mL of 0.019 M $NaBH_4$ aqueous solution. The pH value of the reaction solution was ~7. The whole loading amount of metal in synthesis solution was changed from 5.0 to 15.0 weight percent. The reaction mixture (20 mL) was then stirred vigorously and placed in a 30 ^oC water bath. Within 4 h, the color of the reaction solution changed to gray for Ag and to light pink for Au, indicating the formation of the deposited metallic Ag and Au particles, respectively. A precipitated powder was collected and washed by distilled water for several times to remove impurities. The sample was further dried at 60 °C for 2 h.

8.2.3. Results and Discussion

The synthetic conditions, crystalline phases, and morphologies of a variety of metal oxide and mixed metal oxide nanocrystals are summarized in Table 8.2.1. The metal oxide and metal mixed oxide nanocrystals (NCs) were formed from the hydrothermal crystallization in an aqueous solution containing inorganic precursor and 6-aminohexanoic acid (AHA) at 180 °C for 20 h. These obtained nanocrystals were capped by $-NH_2$ heads of bifunctional AHA molecules and free -COOH groups of other end of AHA molecules were available for further derivativation in polar solvent.[24] Furthermore, noble metal highly dispersed on the oxide NC surface was also prepared via the controllable deposition of noble-metal precursors on the hydrophilic surface of these oxide NCs. The role of capping 6-aminohexanoic acid is to capture metal ion by its interaction with -COOH group, which favors for the formation of highly dispersed metal on the oxide surface during the synthesis. This synthetic procedure is simple, high yield, and large-scale production, so that it may be a green process and convenient to transfer to industrial application. Scheme 8.2.1 represents a general route for the high-yield synthesis and highly crystalline metal oxide and mixed oxide NCs as well as noble-metal dispersed oxide hybrid nanocrystals with different morphologies.

Metal oxides including In_2O_3, Y_2O_3, ZrO_2, TiO_2, CeO_2, were selected to illustrate our approach (Scheme 8.2.1A) because they are widely recognized for their unique properties as supports and catalysts. Metal oxide NCs were obtained by hydrolysis of the corresponding metal nitrate or bulk oxide powder in basic environment (pH~12) in the presence of 6-aminohexanoic acid ligand. Under the hydrothermal treatment, metal ions were hydrolyzed to form metal hydroxide and then dehydrated to metal oxide, which further condenses into primary oxide clusters. These clusters aggregated to produce the nuclei, subsequently the oxide nanocrystals were formed via further growth of these nuclei. As seen in Figure 8.2.1, XRD patterns of the resulting samples are well-matched to cubic In_2O_3 (JCPDS 006-0416), monoclinic Y_2O_3 (JCPDS 44-0399), monoclinic ZrO_2 (JCPDS 37-1484), pure brookite TiO_2 (JCPDS 291-361) without mixture of rutile or anatase phase, and cubic CeO_2 (JCPDS 34-0394). The broadening and well-resolved diffraction peaks can be attributed to the nanoscale nature and high crystallinity of the samples; no peaks of any other phases or impurities were detected. Figure 8.2.2 shows representative SEM/TEM images of the nanocrystalline samples of In_2O_3, Y_2O_3, ZrO_2, TiO_2, CeO_2. The In_2O_3 and Y_2O_3 NCs both exhibit a long rod shape with an average diameter of 80 nm and length of 6 μm (Figure 8.2.2a-d), while the ZrO_2 sample shows short nanorod with an average diameter of 0.5 μm and length of 1 μm (Figure 8.2.2e,f). TiO_2 nanocrystals with high aspect ratio (60 nm x 8 μm) were mostly belt-like shape (Figure 8.2.2g,h). Unlike the rod morphology of above oxides, the product CeO_2 is mainly composed of ultrafine nanocubes with a mean edge length of 50 nm (Figure 8.2.2l). These hydrophilic-surfaced oxide nanocrystals with high crystallinity could be used as an interesting support for the fabrication of novel metal-dispersed oxide hybrid nanocrystals with improved catalytic performance.

The procedure (Scheme 8.2.1A) was further used to synthesize mixed metal oxide nanocrystals such as mixed metal tungstates, orthovanadates, and molybdates. Three types of these mixed oxide materials have been the subjects of extensive research in recent years due to their potential applications in various fields.[32-34] For example, metal tungstates are a good photocatalyst for the degradation of organic compounds under UV irradiation in order to purify wastewater from households and industries;[35] rare earth molybdates are a promising candidate in laser hosts and up-conversion lasing application.[36] Rare earth vanadates are highly active and selective catalysts for many organic reactions including oxidative dehydrogenation of alkanes/olefins.[37] However, the synthesis of these materials with hydrophilic surface still remain challenge. For this purpose, we developed a simple method for the synthesis of these hydrophilic-surfaced nanocrystals via the hydrothermal reaction of an aqueous mixture containing corresponding metal cation (transition metal, rare earth) and anion (WO_4^{2-}, VO_4^{3-}, MoO_4^{2-}) in the presence of 6-aminohexanoic acid ligand (Scheme 8.2.1B). XRD patterns of the as-synthesized transition-metal tungstate NC samples are shown in Figure 8.2.3. The diffraction peaks of all samples are well-indexed to pure monoclinic structure: $CoWO_4$ (a = 4.947 Å, b = 5.682 Å, c = 4.669 Å, JCPDS 30-0443), $MnWO_4$ (a = 4.80 Å, b = 5.71 Å, c = 4.97 Å, JCPDS 80-0134), $ZnWO_4$ (a = 4.689 Å, b = 5.724 Å, c = 4.923 Å, JCPDS 15-0774), and $CdWO_4$ (a = 5.026 Å, b = 5.078 Å, c = 5.867 Å, JCPDS 14-676). The XRD patterns show broadening and intensive diffraction peaks due to their nanometer size and high crystallinity. No other XRD peaks for impurities were observed.

Representative TEM images of $CoWO_4$, $MnWO_4$, $ZnWO_4$, $CdWO_4$ nanocrystals are shown in Figure 8.2.4. Under the same synthesis conditions (pH~9, 180 ^oC, 20 h), the $CoWO_4$ nanocrystals mainly display truncated octahedron-like shape with uniform size distribution (Figure 8.2.4a). A single truncated octahedron is ~40 nm in size as measured along the longest edge. The surface of the truncated octahedral nanocrystals is smooth with no obvious defects. It also found that the pH of synthesis solution effected on the shape of $CoWO_4$ nanocrystals. The pH value in the initial solution was adjusted by using 1 M NaOH solution. When the pH was increased from 9 to 10, to 11, the shape of $CoWO_4$ species evolved from truncated nanooctahedral nanocrystals to elongated nanocrystals (~40 x 50 nm) and to nanorods (~40 x 200 nm), respectively (Figure 8.2.4b,c). The pH increase in the reaction solution may influence the selective adsorption of the surfactant molecules on the growth surface of particles leading to the shape elongation of the products. For the $MnWO_4$, $ZnWO_4$, and $CdWO_4$ NC samples, the anisotropic morphologies of all products were found. The differences in the average aspect ratio (length/width namely as AAR) of the final NC products were observed: 25 nm x 50 nm-sized $MnWO_4$ nanobars, AAR of 2.0 (Figure 8.2.4f); 15 nm x 70 nm-sized $ZnWO_4$ nanorods, AAR of 4.7 (Figure 8.2.4h); 50 nm x 160 nm-sized $CdWO_4$ nanorods, AAR of 3.2 (Figure 8.2.4l), depending on the nature of transition metals. Interestingly, when the monomer precursor concentration decreases from 0.0150 to 0.0076 M in water medium, polypeptide-stabilized tungstate mesocrystal hierarchical microspheres (e.g., 3 μm-sized $MnWO_4$) were achieved. This could be due to the spontaneous-assembly of primary nanoparticles through the backbone-backbone intermolecular hydrogen-bonding interactions of polypeptide chains (Figure 8.2.4g), as illustrated in our recent work.[24]

For the rare earth orthovanadate NC samples ($REVO_4$, RE = La, Ce, Nd, Sm, Gd, Er), XRD patterns of these samples are shown in Figure 8.2.5. It is known that rare earth orthovanadates crystallize in two polymorphs including tetragonal phase (*t*-) and monoclinic phase (*m*-).[38] With an increase of ionic radius of rare earth (RE^{3+}), RE^{3+} ions show a strong tendency toward *m*-phase orthovanadate due to its higher oxygen coordination number; 9 compared to 8 of the *t*-phase orthovanadate. Because La^{3+} ion has the largest ionic radius in all rare earth ions, the thermodynamically stable state of *m*-$LaVO_4$ is much easier than the metastable state of *t*-$LaVO_4$. In some cases, the tetragonal (*t*-) zircon type to monoclinic (*m*-) monazite type transformation often occurs at 850 - 900 ^{o}C or turns the pH value of synthesis solution.[39] In our present case, the monazite-type monoclinic $LaVO_4$ structure with cell parameters a = 7.043 Å, b = 7.279 Å, c = 6.721 Å (JCPDS 50-0367) were formed (Figure 8.2.5a). On the contrary, the XRD patterns of all other samples (Figures 8.2.5b-f) show that all diffraction peaks of different products were well-indexed as pure tetragonal-zircon structure of $REVO_4$ (RE = Ce, Nd, Sm, Gd, Er). All the XRD patterns also show broad peaks due to their nanoscale size and no peaks of any other phases or impurities were detected.

As seen in Figure 8.2.6, representative TEM images of these rare earth orthovanadate NCs (from panel a to l) exhibit two distinct shapes: rod for La, Ce, Nd, and ellipsoid/cube/sphere for Sm, Gd, Er. In Figure 8.2.6a-c, TEM images of $REVO_4$ NCs (RE = La, Ce, Nd) clearly reveal a rod shape with an average size of 8 nm x 40 nm for $LaVO_4$; 10 nm x 30 nm for $CeVO_4$; and 10 nm x 35 nm for $NdVO_4$. However, TEM images in Figure 8.2.6g-l exhibit ellipsoid for $SmVO_4$, cube for $GdVO_4$, and sphere for $ErVO_4$ with an average diameter of 30 nm. Further the selected area electron diffraction (SAED) pattern (Figure 8.2.6d) of the corresponding typical $NdVO_4$ sample are indexed to a monoclinic-phase single crystal, which are consistent with the above XRD data. Elemental dispersive spectrum (EDS) analysis (Figure 8.2.6e) of the $NdVO_4$ sample determined the Nd:V molar ratios of 1:1. From a series of our present experiments, we found that under the same synthetic conditions, light rare earth orthovanadates (RE = La, Ce, Nd) readily form nanorods, whereas heavy rare earth orthovanadates (RE = Sm, Gd, Er) yield nanocubes/spheres. It seems that the shape of $REVO_4$ nanocrystals depend on ionic radius of rare earth. For the larger lanthanide ions (La, Ce, Nd), the corresponding orthovanadates exhibit rod shapes, whereas for the smaller ones (Sm, Gd, Er), the corresponding orthovanadates were found to be cube/sphere shapes. Similar results for this type of rare earth vanadate materials were also reported by Li et al.[40]

The recent researches demonstrated that the rare earth doped orthovanadate nanocrystals have attracted great interest in view of luminescent applications.[41-43] In this work, Eu^{3+} doped $NdVO_4$ NCs as a typical example were synthesized with a similar method and their optical properties were studied. The doping Eu^{3+} ion in low concentration (5.0 % mol) would not influence the morphology of the $NdVO_4$ nanorods (Figure 8.2.6f). Figure 8.2.7 shows UV-visible adsorption and photoluminescent (PL) excitation and emission spectra of the as-prepared 5.0 mol% Eu^{3+}-doped $NdVO_4$ nanorods suspension in water. The UV region (Figure 8.2.7a) of this sample exhibits a strong absorption edge at ~283 nm attributing to the charge transfer from the oxygen ligands to the central vanadium atoms inside the VO_4^{3-} ions.[44] As shown in Figure 8.2.7b, under 218 nm excitation and emission, the excitation spectrum of this sample exhibits the excitation peaks (434 nm, ^7F_o-$^5L_6$; 529 nm, ^7F_o-$^5D_2$) of Eu^{3+} within its $4f^6$ configuration.[44-46] The presence of the VO_4^{3-}

absorption band in the excitation spectrum of Eu^{3+} reveals an energy transfer takes place from VO_4^{3-} to Eu^{3+} in the Eu^{3+}:$NdVO_4$.[47] The emission spectrum of this sample consists of the characteristic emission peaks (449 nm, ^5D_o-$^7F_1$; 486 nm, ^5D_o-$^7F_2$; 560 nm, ^5D_o-$^7F_4$) of the f-f transition of Eu^{3+}, as reported previously for Eu^{3+}:YVO_4 nanocrystals.[41]

Furthermore, for the synthesis of rare earth molybdate NCs ($RE_2(MoO_4)_3$, RE = La, Ce, Gd, Y, Er), typical XRD patterns of these samples are shown in Figure 8.2.8. The diffraction peaks of $La_2(MoO_4)_3$ sample were well-indexed to the tetragonal-phase structure with lattice parameters of a = b = 5.343 Å, c = 11.780 Å (JCPDS 45- 0407). All the other $RE_2(MoO_4)_3$ (RE = Ce, Gd, Y, Er) were also well-indexed to the tetragonal-phase structure.[48] The XRD patterns also exhibit broad and intensive diffraction peaks due to their nanometer size and high crystallinity. The (112) peak is more intense than other reflection peaks, which implies the highly preferential oriented growth of the $RE_2(MoO_4)_3$ nanosheets, as seen in following SAED results. The morphologies of a series of $RE_2(MoO_4)_3$ nanocrystals were also examined by TEM/SEM images (Figure 8.2.9a-f). TEM images of all samples, including $La_2(MoO_4)_3$, $Ce_2(MoO_4)_3$, $Gd_2(MoO_4)_3$, $Y_2(MoO_4)_3$, $Er_2(MoO_4)_3$ NCs, shared thin sheet shape, and their corner and edge were mostly broken or damaged. All the resulting nanosheets have an average side dimension of 200-300 nm and a thickness of ~2 nm. The SEM observation (inset also indicates that almost 100% of the as-prepared products are superthin nanosheets and no other types of nanoparticles was found. Corresponding SAED patterns (inset of Figure 8.2.9a-f) of all samples revealed the single-crystalline nature and indexed to tetragonal-phase $RE_2(MoO_4)_3$. From the above results presume that all the $RE_2(MoO_4)_3$ nanocrystals maintained the superthin sheet morphology, indicating that no significant influence of rare earth ionic radius on morphology of the products was observed. Further the shape of $RE_2(MoO_4)_3$ nanocrystals was changed at low reaction temperatures (<180 °C). Taking $La_2(MoO_4)_3$ sample as a typical example, performing the synthesis reaction at 100, 130, 160 °C, the products of $La_2(MoO_4)_3$ nanocrystals obtained with corresponding shapes: ~300 nm microsphere; ~110 nm x 340 nm nanorod; ~2 nm x 200-300 nm sheet-shaped nanosquare (Figure 8.2.9g-l). These shape changes may close to minimize the surface energy of particle during growth.

Similarly, as in the case of metal tungstate materials (Figure 8.2.4g), these molybdate nanocrystals, for example, $La_2(MoO_4)_3$ could offer nanobuilding blocks for the further construction of the hierarchical aggregated microsphere materials, as seen in Figure 8.2.9b. We expect that the 2D nanosheets or 3D assemblied microspheres of rare earth molybdate materials have promising applications in electronic and optical fields, which mainly arise from their structural anisotropy, nearly perfect crystallinity, and quantum confinement effects in the thickness.[49] Furthermore, such materials could act as a stable support for the preparation of doped nanomaterials, in particular, of nitrogen doped nanosheets to reduce the band-gap energy, which enhances their activity.[50]

To understand the formation mechanism of the $RE_2(MoO_4)_3$ nanosheets, we systematically tracked the time course of the sheet growth process of representative $La_2(MoO_4)_3$ sample. Figure 8.2.10a-c shows three TEM images of the $La_2(MoO_4)_3$ samples synthesized at the different reaction times of 2, 6, and 20 h, while keeping the other experimental conditions unchanged (La/Mo of 2:3, AHA/(La+Mo) of 2:1, 180 ^oC). All small particles tend to agglomerate together for the formation of the dense aggregates with size of ~200 nm was observed when the aging time reached 2 h (Figure 8.2.10a). A careful examination of high-magnification TEM image (inset of Figure 8.2.10a) clearly suggests that all the aggregates are made up of small particles of ~2 nm. By further prolonging the reaction time to 6 h, these aggregates crystallized into the chains of irregular sheets, which were self-assembled into 2-D arrays onto the amorphous carbon-coated copper grid (Figure 8.2.10b). These irregular species grew into the quite uniform nanosheets when the reaction lasted as long as 20 h (Figure 8.2.10c).

On the basis of these TEM results, we considered that the interesting transformation of dense aggregates of primary particles into $RE_2(MoO_4)_3$ nanosheets of can be the effect of among Ostwald ripening,[51] lateral-aggregation,[52] and dissolution/recrystallization[53] processes, which may be probably attributed to the presence of 6-aminohexnoic acid molecules in water medium. The whole process is illustrated in Figure 8.2.10d. When two precursor solutions of La^{3+} cations and MoO_4^{2-} anions are mixed together in the presence of 6-aminohexanoic acid, an high supersaturation degree will be reached, and amorphous

$La_2(MoO_4)_3$ particles will form immediately. The tiny crystalline nuclei was firstly generated in a supersaturated solution at elevated temperature and then grew into nanoparticles by controlled crystallization and growth of the crystals through the process known as Ostwald ripening. Subsequently, the primary nanoparticles quickly build anisotropically and spontaneously self-aggregated along the 2D direction; the nanosheets were grown until all the particles were consumed through lateral-aggregation mechanism. Finally, the shape transformation of the crystallized nanosheets in synthesis solution often operate through a classical dissolution-recrystallization mechanism to minimize the surface energy of the system, resulting in the formation of the quite uniform nanosheets.

Furthermore, a small amount (corresponds to ~2.0 atomic conc.% of nitrogen of -NH_2) of capping 6-aminohexanoic acid molecules on the surface of $La_2(MoO_4)_3$ nanosheets was determined by XPS spectrum (data not shown). The O1s, C 1s, N 1s, C 1s XPS spectra of this sample suggest that 6-aminohexanoic acid molecules bound on the $La_2(MoO_4)_3$ NC surface. This result is suitable to the initial chemical components, in which AHA ligand was used at low concentration (AHA/precursor = 2:1). Besides only a small amount of surfactant capped on nanocrystal surface can result in the partial removal of the several washes by distilled water. This result was also confirmed further by FTIR spectrum. Figure 8.2.11 shows that an IR band at 2900 cm^{-1} attributed to the C-H stretching vibrations of methylene groups of the AHA molecules were observed. Two bands at 1400 and 3460 cm^{-1} correspond to C-N bending and -NH_2 stretching modes of AHA molecules, respectively. These indicated that the adsorption of -NH_2 groups on the oxide nanocrystal surface and free -COOH groups were oriented outward, consequently the colloidal AHA-capped oxide nanocrystals became hydrophilic and dispersed in water medium, as previously illustrated by our group.[24]

As compared to the nonaqueous synthetic routes using hydrophobic organic surfactants such as fatty acids, aliphatic amines, alkyl phosphine oxides, ect, our aqueous-based approach has many advantages including: water is adopted as the continuous solution phase and inorganic salts were used as starting materials; amphiphilic 6-aminohexanoic acid biomolecule is an interesting stabilizer to yield the biocompatible nanocrystal products. Because of the high solubility of the salts in aqueous solution, we could be applicable to synthesize the nanoparticles in scale up by using the high precursor monomer concentrations. It is interesting to find that the morphology of products was significantly unchanged as strongly increasing the synthesis volume. For examples of representative TiO_2 and $CoWO_4$ samples, we were able to synthesize in ultralarge quantities of 31 g of 60 nm x 8 μm TiO_2 nanobelts (inset of Figure 8.2.2g) and 18.9 g of 20 nm-sized $CoWO_4$ nanooctahedrons (inset of Figure 8.2.4e) per single run in a 700 mL-sized autoclave when increasing the synthesis volume to 10 times. The average yield of synthesis reaction was about 93% for metal oxides and 96% for mixed oxides (see Table 8.2.1). The products have quite purity because only a very small amount of biomolecule organic AHA surfactant (~2.0 atomic conc.% N) absorbed on the nanocrystal surface, as above-mentioned XPS result. Hence, the current aqueous-based route is readily applicable to the large-scale synthesis for the academic laboratory as well as the industrial application in a simple way because of their simplicity, high yield, and the use of nontoxic cheap reagents.

Recently, noble-metal deposited semiconductor nanocrystals have been received much attention due to their unique photocatalytic performance.[54, 55] Our synthetic approach for such noble-metal dispersed semiconductor NCs relies on two sequential seeded-growth steps, as sketched in Scheme 8.2.1C. Using the pre-synthesized AHA capped oxide nanocrystals as nanosupport and metal nitrate as metal source, the amine group of AHA ligand was bonded to the surface of oxide nanocrystals and other end uncoordinated carboxylic acid of AHA was outwarded to water.[25] In water medium (pH ~ 7.5), noble-metal precursor cations strongly adsorbed on the negatively charged surface of 6-aminohexanoic acid-stabilized oxide nanocrystals through electrostatic attraction, due to the deprotonation of -COOH groups (see Experimental Section). This technique guarantees preferential heterogeneous nucleation and growth metal precursors on the surface of the substrate seeds via the interaction between noble-metal precursor and uncoordinated carboxylic group of AHA-capped oxide nanocrystals followed by reduction using $NaBH_4$. This leads to the high dispersion of tiny metal particles on the nanosupport. Here we selected four metal oxide NCs: CeO_2, TiO_2, In_2O_3, Y_2O_3 and three mixed oxide NCs: $CoWO_4$, $MnWO_4$, $La_2(MoO_4)_3$, and two noble metals: Ag, Au, as typical examples for the syntheses of metal-semiconductor nanohybrids. Nanohybrids of Ag/CeO_2, Ag/Y_2O_3, Ag/In_2O_3, Ag/$MnWO_4$, Au/$MnWO_4$, Ag/$CoWO_4$, Au/$CoWO_4$, Au/$La_2(MoO_4)_3$ were successfully prepared. The whole loading amount of metal was kept to 10.0 weight percent. The structural-compositional details of the heterostructures have been studied by multi-technique combination including TEM, XRD, XPS, UV-vis analyses.

TEM images of a variety of metal/oxide nanohybrids with a noble-metal content of 10.0 wt.% show that such nanohybrids consisted of metallic clusters/dots and oxide NC supports, as presented in Figure 8.2.12. Also, one can see that numerous deposited metallic nanoparticles were attached to a oxide nanocrystal support. The 5-7 nm-sized Ag nanodots were observed, while the tiny Au nanodots with smaller diameter of 2-3 nm were dispersed effectively on the hydrophilic surface of support. Metal aggregates were also not found by the TEM observation. In all cases, after decorating with a metallic ion precursor, tiny Ag or Au nanodots formed and grew on the surface and the surfaces become coarse. It was noteworthy that no separated noble-metal particles were observed, indicating that the AHA-stabilized oxide nanocrystals provide a large number of adsorption sites for the noble metal nucleated and grown on the oxide NC surface under our experimental conditions. The resulting metal nanoclusters/dots thus are evenly distributed over the entire NC surface without significant overlap. For the metal (Ag, Au)/oxide hybrid samples, XRD spectra (Figure 8.2.14 and 8.2.15) exhibited two sets of strong diffraction peaks, indicating that the hybrid products are composite materials with high crystallinity. Those marked with "*" can be indexed to face-centered cubic (*fcc*) Ag structure (JCPDS. 74-1728),[56] and face-centered cubic (*fcc*) Au structure (JCPDS. 01-1174),[57] while the others can be indexed to corresponding oxide structure.

The particle size dependence of the electronic properties has been reported in the literature.[30, 58, 59] In this work, the Ag/TiO_2 nanobelt sample was selected as a typical example. In this case, the size of Ag particles and their distribution on the TiO_2 nanobelt surface were conducted by tuning the silver precursor concentrations in the synthesis solution. Figure 8.2.13 shows TEM images of hybrid Ag/TiO_2 nanobelts prepared with different Ag contents ranging from 5.0 to 10.0 and 15.0 wt.% in the synthesis solution. The

Ag concentration in solid solution was determined by XPS technique. The Ag amount in 5.0 wt.% Ag/TiO_2, 10.0 wt.% Ag/TiO_2, 15.0 wt.% Ag/TiO_2 samples was estimated to be 4.8, 9.5, 14.6 wt.%, respectively, corresponding to 4.8 wt.% Ag/TiO_2, 9.5 wt.% Ag/TiO_2, 14.6 wt.% Ag/TiO_2. When 4.8 wt.% Ag was deposited on TiO_2 nanobelts, very small Ag nanoclusters with an average diameter of ~2-3 nm were observed (Figure 8.2.13a). When the Ag loading was increased to 9.5 wt.% Ag nanodots with a particle size of 5-7 nm was observed (Figure 8.2.13b). In both the case, they were highly dispersed on the nanobelt surface. No evidence of Ag aggregates was detected. With higher Ag loading (14.6 wt.%), the Ag particles with a larger size (15-20 nm) and a broad distribution were found (Figure 8.2.13c). Further increasing this ratio (e.g., >14.6 wt.%), large Ag particles and only few smaller particles were observed, indicating that a coalescence of Ag particles occurred during the synthesis. The crystalline feature of the as-prepared nanohybrids was also confirmed by dark-field TEM analysis (Figure 8.2.13d). Using this approach, a high dispersion of Ag nanoparticles can be obtained, and their size can be tuned by Ag concentration in the synthesis solution.

The as-prepared 9.5 wt.% Ag/TiO_2 nanobelt sample was characterized by XPS technique for the evaluation of the metal oxidation state. High-resolution XPS spectra for Ti 2p and Ag 3d species (data not shown). The Ti 2p spectrum exhibits two peaks. The Ti $2p_{3/2}$ and Ti $2p_{1/2}$ peaks are centered at 450.3 and 456.1 eV, respectively, with $\Delta \approx 5.8$ eV, indicating those of pure TiO_2 phase.[60] The Ag $3d_{5/2}$ peak is centered at 367.7 eV, which are attributed to metallic Ag.[61] Remarkably, this Ag $3d_{5/2}$ binding energy value of the Ag/TiO_2 sample is lower as compared to that of the pure metallic Ag (368.0 eV). O 1s XPS spectrum exhibits two peaks; one peak at 528.8 eV corresponds to oxygen in the lattice of TiO_2 NCs and other one at 530.7 eV can be attributed to the adsorbed oxygen on the TiO_2 NC surface. The results indicate that the shift of the binding energy of Ag $3d_{5/2}$ to the lower site can be mainly ascribed to the electrostatic interaction between the deposited Ag clusters and TiO_2 nanobelts.

UV-visible spectra of the synthesized Ag/TiO_2 samples with Ag loadings of 4.8, 9.5, 14.6 wt.% are shown in Figure 8.2.16. For pure TiO_2 nanobelts, the optical absorption threshold peak is located approximately at 280-290 nm which corresponds to the band gap energy value of 3.18 eV.[62] This value is very close to that of the commercial TiO_2 (Degussa P-25, E_g = 3.2 eV).[63] For the Ag/TiO_2 nanobelts with different Ag loadings, an additional peak at 352 nm was observed. This peak is attributable to the metallic Ag nanodots on the Ag/TiO_2 heterostructures.[56] The intensity of this peak increases as a function of Ag loading in the Ag/TiO_2 sample. Its intensity increases gradually with an increase of the Ag content from 4.8 to 14.6 wt.%, possible due to the size-dependent surface Plasmon resonance effect of metallic Ag clusters and arising the interaction between Ag clusters and TiO_2 NCs.

The metal-semiconductor nanohybrids are expected to exhibit high photocatalytic efficiency. To evaluate the photocatalytic performance, we selected the 9.5 wt.% Ag/TiO_2 sample for the photocatalytic decomposition of methylene blue (MB) in water under UV illumination. The 9.5 wt.% Ag/TiO_2 hybrid nanobelt sample after calcination at 500 ^oC at 2 h possesses a surface area of 32 $m^2.g^{-1}$ and large pore volumes of 0.42 cm^3g^{-1} (data not shown). The samples of pure TiO_2 nanobelts, commercial TiO_2-P25, 9.5 wt.% Ag/TiO_2 nanohybrids and 9.5 wt.% Ag/TiO_2-P25 were compared under the same testing conditions. As seen in Figure 8.2.17A, UV-visible spectra of the MB aqueous solution (16 mL, 0.05 mM) containing 0.015 g catalysts were recorded at different time intervals. The absorption double peaks at 609 and 667 nm are characteristic of methylene blue. The intensity of these peaks decreases as a function of irradiation time, indicating the decomposition of MB. For the 9.5 wt.% Ag/TiO_2 hybrid catalyst, after 80 min of reaction time, these peaks completely disappeared, indicating the complete degradation of methylene blue in the aqueous solution. The pure TiO_2 nanobelts show a slightly higher catalytic activity than that of commercial TiO_2-P25. This could be due to the shape effect on the photocatalytic efficiency (Figure 8.2.17B). Both hybrid Ag/TiO_2 materials show better photocatalytic activity than that of pure TiO_2 materials. However, the hybrid Ag/TiO_2 nanobelts clearly exhibit a much higher performance for the photocatalytic degradation of MB as compared to Ag/P25. The high photocatalytic activity of Ag/TiO_2 NCs could be due to a very high dispersion of Ag clusters on the individual TiO_2 NCs and the TiO_2 shape effect.

A possible photocatalytic mechanism of Ag/TiO_2 system is proposed in Scheme 8.2.2. In Ag-TiO_2 system, electrons will migrate from Ag to the conduction band (CB) of TiO_2 to achieve the Fermi level equilibration through Ag-TiO_2 interaction. When the catalysts are illuminated by UV light with photon energy higher than the band gap of TiO_2, electrons (e^-) in the valence band (VB) can be excited to the CB with simultaneous generation of the same amount of holes (h^+) left behind. The deflexed energy band in the space charge region facilitates the rapid transfer of the as-excited electrons from TiO_2 to Ag nanoparticles, which increases the lifetime of the photogenerated pairs. Electrons accumulated at Ag particles or the conduction band of TiO_2 can be transferred to oxygen molecules adsorbed on the surface to form free oxygen radicals, such as $^{\bullet}O_2^-$, $^{\bullet}HO_2$, $^{\bullet}OH$, while the photoinduced holes are apt to react with surface-bound H_2O or OH^- to produce the hydroxyl radical species ($^{\bullet}OH$) which is an extremely strong oxidant for the mineralization of organic chemicals (e.g., MB).

8.2.4. Conclusion

In summary, we have demonstrated a general method for the hydrothermal high-yield synthesis of many kinds of the highly crystalline metal oxide (e.g., In_2O_3, Y_2O_3, ZrO_2, CeO_2) and mixed oxide nanocrystals (MWO_4, $REVO_4$, $RE_2(MoO_4)_3$, M = Co, Mn, Cd, Zn; RE = La, Ce Gd, Nd, Y, Er) with various morphologies including belt, rod, truncated-octahedron, cubic, sphere and sheet. The synthetic procedure was based on the hydrothermal crystallization of inorganic precursors in water medium in the presence of bifunctional 6-aminohexanoic acid (AHA) as a capping agent. The resultant AHA-capped nanocrystals are suspended in water medium due to their hydrophilic surface character. The shape of some nanocrystals (e.g., $CoWO_4$, $La_2(MoO_4)_3$) can be controlled by simple adjusting the synthesis conditions such as pH solution and reaction temperature. Further at low precursor monomer concentration (e.g., 0.0075 M) in synthetic water solution, the mesocrystal hierarchical aggregated microspheres of $MnWO_4$ and $La_2(MoO_4)_3$ obtained from the spontaneous assembly of individual AHA-capped nanoparticles. This synthesis method is simple, inexpensive (metal salts instead of metal alkoxides as starting metal sources in water medium), and easy to scale-up to multigram-scale products (e.g., ~31 g of

AHA-capped TiO_2 nanobelts and ~18 g AHA-capped $CoWO_4$ nanooctahedrons per a single preparation).

These AHA-capped oxide nanocrystals are excellent support for the preparation of a variety of metal/oxide hybrid nanocrystals, in which noble metal (Ag, Au) particles with the average size of 2-7 nm were deposited on the hydrophilic surface of individual supports. We have demonstrated that hybrid Ag/TiO_2 nanobelts show a much higher performance for the photocatalytic degradation of MB as compared to Ag/commercial P25. Such hybrid metal/oxide nanomaterials have potential applications in many fields, such as environmental clean-up, optical coating, photovoltaic cells, gas sensors, optoelectronic, and so on. The present study on such metal/oxide nanohybrids motivates us to further explore other promising applications such as optical coating, photovoltaic cells, gas sensors, optoelectronic devices, and so on.

8.2.5. References

1. Fernández-García, M., et al., *Nanostructured Oxides in Chemistry: Characterization and Properties.* Chemical Reviews, 2004. **104**(9): p. 4063-4104.
2. Ferrando, R., J. Jellinek, and R.L. Johnston, *Nanoalloys: From Theory to Applications of Alloy Clusters and Nanoparticles.* Chemical Reviews, 2008. **108**(3): p. 845-910.
3. Talapin, D.V., et al., *Prospects of Colloidal Nanocrystals for Electronic and Optoelectronic Applications.* Chemical Reviews, 2009. **110**(1): p. 389-458.
4. Taylor, A.F., et al., *Dynamical Quorum Sensing and Synchronization in Large Populations of Chemical Oscillators.* Science, 2009. **323**(5914): p. 614-617.
5. Xie, Y., et al., *In Situ Controllable Loading of Ultrafine Noble Metal Particles on Titania.* Journal of the American Chemical Society, 2009. **131**(19): p. 6648-6649.
6. Jakob, M., H. Levanon, and P.V. Kamat, *Charge Distribution between UV-Irradiated TiO_2 and Gold Nanoparticles: Determination of Shift in the Fermi Level.* Nano Letters, 2003. **3**(3): p. 353-358.
7. Subramanian, V., E.E. Wolf, and P.V. Kamat, *Green Emission to Probe Photoinduced Charging Events in ZnO−Au Nanoparticles. Charge Distribution and Fermi-Level Equilibration†.* The Journal of Physical Chemistry B, 2003. **107**(30): p. 7479-7485.
8. Chakrabortty, S., et al., *Asymmetric Dumbbells from Selective Deposition of Metals on Seeded Semiconductor Nanorods.* Angewandte Chemie International Edition, 2010. **49**(16): p. 2888-2892.
9. Kwon, S.G. and T. Hyeon, *Colloidal Chemical Synthesis and Formation Kinetics of Uniformly Sized Nanocrystals of Metals, Oxides, and Chalcogenides.* Accounts of Chemical Research, 2008. **41**(12): p. 1696-1709.

10. Niederberger, M., *Nonaqueous Sol–Gel Routes to Metal Oxide Nanoparticles.* Accounts of Chemical Research, 2007. **40**(9): p. 793-800.
11. Wang, X., et al., *A general strategy for nanocrystal synthesis.* Nature, 2005. **437**(7055): p. 121-124.
12. *A general phase-transfer protocol for metal ions and its application in nanocrystal synthesis.* Nat. Mater., 2010. **9**(2): p. 179-179.
13. Nguyen, T.-D. and T.-O. Do, *General Two-Phase Routes to Synthesize Colloidal Metal Oxide Nanocrystals: Simple Synthesis and Ordered Self-Assembly Structures.* The Journal of Physical Chemistry C, 2009. **113**(26): p. 11204-11214.
14. Long, S., et al., *Phase Transition from Two Z' = 1 Forms to a Z' = 2 Form of a Concomitant Conformational Polymorphic System.* Crystal Growth & Design, 2011. 11(2): p. 414-421.
15. Nguyen, T.-D. and T.-O. Do, *Solvo-Hydrothermal Approach for the Shape-Selective Synthesis of Vanadium Oxide Nanocrystals and Their Characterization.* Langmuir, 2009. **25**(9): p. 5322-5332.
16. Nguyen, T.-D., et al., *A Novel Approach for Monodisperse Samarium Orthovanadate Nanocrystals: Controlled Synthesis and Characterization.* The Journal of Physical Chemistry C, 2009. **113**(43): p. 18584-18595.
17. Nguyen, T.-D., C.-T. Dinh, and T.-O. Do, *Monodisperse Samarium and Cerium Orthovanadate Nanocrystals and Metal Oxidation States on the Nanocrystal Surface.* Langmuir, 2009. **25**(18): p. 11142-11148.
18. Jun, Y.-w., J.-s. Choi, and J. Cheon, *Shape Control of Semiconductor and Metal Oxide Nanocrystals through Nonhydrolytic Colloidal Routes.* Angewandte Chemie International Edition, 2006. **45**(21): p. 3414-3439.
19. Meldrum, F.C. and H. Cölfen, *Controlling Mineral Morphologies and Structures in Biological and Synthetic Systems.* Chemical Reviews, 2008. **108**(11): p. 4332-4432.
20. Lakshminarayana, P. and X. Qing-Hua, *A single-step synthesis of gold nanochains using an amino acid as a capping agent and characterization of their optical properties.* Nanotechnology, 2008. **19**(7): p. 075601.
21. Serizawa, T., Y. Hirai, and M. Aizawa, *Novel Synthetic Route to Peptide-Capped Gold Nanoparticles.* Langmuir, 2009. **25**(20): p. 12229-12234.
22. Dinh, C.-T., et al., *Shape-Controlled Synthesis of Highly Crystalline Titania Nanocrystals.* ACS Nano, 2009. **3**(11): p. 3737-3743.
23. Nguyen, T.-D., C.-T. Dinh, and T.-O. Do, *Shape- and Size-Controlled Synthesis of Monoclinic ErOOH and Cubic* Er_2O_3 *from Micro- to Nanostructures and Their Upconversion Luminescence.* ACS Nano, 2010. **4**(4): p. 2263-2273.
24. Nguyen, T.-D., et al., *Biomolecule-assisted route for shape-controlled synthesis of single-crystalline* $MnWO_4$ *nanoparticles and spontaneous assembly of polypeptide-stabilized mesocrystal microspheres.* CrystEngComm, 2011.
25. Hoffmann, M.R., et al., *Environmental Applications of Semiconductor Photocatalysis.* Chemical Reviews, 1995. **95**(1): p. 69-96.
26. Smith, A.M. and S. Nie, *Semiconductor Nanocrystals: Structure, Properties, and Band Gap Engineering.* Accounts of Chemical Research, 2009. **43**(2): p. 190-200.
27. Corma, A., P. Serna, and H. García, *Gold Catalysts Open a New General Chemoselective Route to Synthesize Oximes by Hydrogenation of α,β-Unsaturated*

Nitrocompounds with H2. Journal of the American Chemical Society, 2007. **129**(20): p. 6358-6359.

28. Chen, M. and D.W. Goodman, *Catalytically Active Gold: From Nanoparticles to Ultrathin Films.* Accounts of Chemical Research, 2006. **39**(10): p. 739-746.
29. Sun, Y., et al., *Carbon-in-Al4C3 Nanowire Superstructures for Field Emitters.* ACS Nano, 2011: p. null-null.
30. Menagen, G., et al., *Au Growth on Semiconductor Nanorods: Photoinduced versus Thermal Growth Mechanisms.* Journal of the American Chemical Society, 2009. **131**(47): p. 17406-17411.
31. Feng, L., et al., *Well-Controlled Synthesis of Au@Pt Nanostructures by Gold-Nanorod-Seeded Growth.* Chemistry – A European Journal, 2008. **14**(31): p. 9764-9771.
32. Yu, S.-H., et al., *Synthesis of Very Thin 1D and 2D* $CdWO_4$ *Nanoparticles with Improved Fluorescence Behavior by Polymer-Controlled Crystallization.* Angewandte Chemie, 2002. **114**(13): p. 2462-2466.
33. Santato, C., et al., *Crystallographically Oriented Mesoporous* WO_3 *Films: Synthesis, Characterization, and Applications.* Journal of the American Chemical Society, 2001. **123**(43): p. 10639-10649.
34. Rossinyol, E., et al., *Synthesis and Characterization of Chromium-Doped Mesoporous Tungsten Oxide for Gas Sensing Applications.* Advanced Functional Materials, 2007. **17**(11): p. 1801-1806.
35. Zhang, L., et al., Bi_2WO_6 *Nano- and Microstructures: Shape Control and Associated Visible-Light-Driven Photocatalytic Activities.* Small, 2007. **3**(9): p. 1618-1625.
36. Stevens, S.B., et al., $NaLa(MoO_4)_2$ *as a laser host material.* Physical Review B, 1991. **43**(10): p. 7386.
37. Downing, E., et al., *A Three-Color, Solid-State, Three-Dimensional Display.* Science, 1996. **273**(5279): p. 1185-1189.
38. Fan, W., et al., *Selected-Control Hydrothermal Synthesis and Formation Mechanism of Monazite- and Zircon-Type* $LaVO_4$ *Nanocrystals.* The Journal of Physical Chemistry B, 2006. **110**(46): p. 23247-23254.
39. Jia, C.-J., et al., *Selective Synthesis of Monazite- and Zircon-type* $LaVO_4$ *Nanocrystals.* The Journal of Physical Chemistry B, 2005. **109**(8): p. 3284-3290.
40. Wang, X., et al., *Hydrothermal Synthesis of Rare-Earth Fluoride Nanocrystals.* Inorganic Chemistry, 2006. **45**(17): p. 6661-6665.
41. Wang, G., et al., *Enhanced Photoluminescence of Water Soluble* $YVO_4:Ln^{3+}$ *(Ln = Eu, Dy, Sm, and Ce) Nanocrystals by* Ba^{2+} *Doping.* The Journal of Physical Chemistry C, 2008. **112**(44): p. 17042-17045.
42. Mialon, G., et al., *New Insights into Size Effects in Luminescent Oxide Nanocrystals.* The Journal of Physical Chemistry C, 2009. **113**(43): p. 18699-18706.
43. Antic-Fidancev, E. and et al., *Simulation of the energy level scheme of* Nd^{3+} *and* Eu^{3+} *ions in rare-earth orthovanadates and phosphates.* Journal of Physics: Condensed Matter, 1991. **3**(35): p. 6829.
44. Liu, J. and Y. Li, *General synthesis of colloidal rare earth orthovanadate nanocrystals.* Journal of Materials Chemistry, 2007. **17**(18): p. 1797-1803.

45. Wu, X., et al., *Preparation of Single-Crystalline $NdVO_4$ Nanorods, and Their Emissions in the Ultraviolet and Blue under Ultraviolet Excitation.* The Journal of Physical Chemistry B, 2005. **109**(23): p. 11544-11547.
46. Jandl, S., et al., *Raman active phonon and crystal-field studies of Yb^{3+} doped $NdVO_4$.* Optical Materials, 2010. **32**(11): p. 1549-1552.
47. Yu, C., et al., *Spindle-like Lanthanide Orthovanadate Nanoparticles: Facile Synthesis by Ultrasonic Irradiation, Characterization, and Luminescent Properties.* Crystal Growth & Design, 2008. **9**(2): p. 783-791.
48. Bu, W., et al., *Controlled Construction of Uniform Pompon-Shaped Microarchitectures Self-Assembled from Single-Crystalline Lanthanum Molybdate Nanoflakes.* Langmuir, 2007. **23**(17): p. 9002-9007.
49. Ma, R. and T. Sasaki, *Nanosheets of Oxides and Hydroxides: Ultimate 2D Charge-Bearing Functional Crystallites.* Advanced Materials, 2010. **22**(45): p. 5082-5104.
50. Matsumoto, Y., et al., *N Doping of Oxide Nanosheets.* Journal of the American Chemical Society, 2009. **131**(19): p. 6644-6645.
51. Tang, J. and A.P. Alivisatos, *Crystal Splitting in the Growth of Bi_2S_3.* Nano Letters, 2006. **6**(12): p. 2701-2706.
52. Nguyen, T.-D., D. Mrabet, and T.-O. Do, *Controlled Self-Assembly of Sm_2O_3 Nanoparticles into Nanorods: Simple and Large Scale Synthesis using Bulk Sm_2O_3 Powders.* The Journal of Physical Chemistry C, 2008. **112**(39): p. 15226-15235.
53. Luo, Z., et al., *Synthesis of BaMoO4 Nestlike Nanostructures Under a New Growth Mechanism.* Crystal Growth & Design, 2008. **8**(7): p. 2275-2281.
54. Costi, R., A.E. Saunders, and U. Banin, *Colloidal Hybrid Nanostructures: A New Type of Functional Materials.* Angewandte Chemie International Edition, 2010. **49**(29): p. 4878-4897.
55. Cozzoli, P.D. and L. Manna, *Asymmetric nanoparticles: Tips on growing nanocrystals.* Nat Mater, 2005. **4**(11): p. 801-802.
56. Chen, M., et al., *Silver Nanoparticles Capped by Oleylamine: Formation, Growth, and Self-Organization.* Langmuir, 2007. **23**(10): p. 5296-5304.
57. Wu, X.-F., et al., *Synthesis of Core−Shell Au@TiO_2 Nanoparticles with Truncated Wedge-Shaped Morphology and Their Photocatalytic Properties.* Langmuir, 2009. **25**(11): p. 6438-6447.
58. Macdonald, J.E., et al., *Hybrid nanoscale inorganic cages.* Nat. Mater., 2010. **9**(10): p. 810-815.
59. Costi, R., et al., *Electrostatic Force Microscopy Study of Single Au−CdSe Hybrid Nanodumbbells: Evidence for Light-Induced Charge Separation.* Nano Letters, 2009. **9**(5): p. 2031-2039.
60. Chen, X. and C. Burda, *The Electronic Origin of the Visible-Light Absorption Properties of C-, N- and S-Doped TiO_2 Nanomaterials.* Journal of the American Chemical Society, 2008. **130**(15): p. 5018-5019.
61. Sieb, N.R., et al., *Hollow Metal Nanorods with Tunable Dimensions, Porosity, and Photonic Properties.* ACS Nano, 2009. **3**(6): p. 1365-1372.
62. Tahir, M.N., et al., *Facile Synthesis and Characterization of Functionalized, Monocrystalline Rutile TiO_2 Nanorods.* Langmuir, 2006. **22**(12): p. 5209-5212.

63. Nagaveni, K., et al., *Solar photocatalytic degradation of dyes: high activity of combustion synthesized nano TiO_2*. Applied Catalysis B: Environmental, 2004. **48**(2): p. 83-93.

Table 8.2.1. Synthesis Conditions, Structures, and Morphologies of a Variety of High-Crystalline Metal Oxide and Metal Mixed Oxide Nanocrystals via 6-Aminohexanoic Acid-Assisted Hydrothermal Process[a]

Sample	Inorganic Precursor	Yield %	Solvent	Product	Structure	Shape	Size nm
Metal Oxide NCs							
1	In^{3+}	93	basic medium	In_2O_3	cubic	rod	80 x 6000
2	Y^{3+}	93	basic medium	Y_2O_3	monoclinic	rod	80 x 6000
3	Zr^{4+}	93	basic medium	ZrO_2	monoclinic	rod	0.5 x 1000
4	Ti^{4+}	93	basic medium	TiO_2	brookite	belt	60 x 8000
5	Ce^{3+}	93	basic medium	CeO_2	cubic	cubic	50
Transition Metal Tungstate NCs							
6	Co^{2+}, WO_4^{2-}	96	water	$CoWO_4$	monoclinic	truncated octahedral	40
7	Mn^{2+}, WO_4^{2-}	96	water	$MnWO_4$	monoclinic	rod	25 x 50
8	Zn^{2+}, WO_4^{2-}	96	water	$ZnWO_4$	monoclinic	rod	15 x 70
9	Cd^{2+}, WO_4^{2-}	96	water	$CdWO_4$	monoclinic	rod	50 x 160
Rare Earth Orthovanadate NCs							
10	La^{3+}, VO_4^{3-}	96	water	$LaVO_4$	monazite	rod	8 x 40
11	Ce^{3+}, VO_4^{3-}	96	water	$CeVO_4$	tetragonal	rod	10 x 30
12	Nd^{3+}, VO_4^{3-}	96	water	$NdVO_4$	tetragonal	rod	10 x 35
13	Sm^{3+}, VO_4^{3-}	96	water	$SmVO_4$	tetragonal	cubic	30
14	Gd^{3+}, VO_4^{3-}	96	water	$GdVO_4$	tetragonal	quasi-sphere	30
15	Er^{3+}, VO_4^{3-}	96	water	$ErVO_4$	tetragonal	sphere	30
Rare Earth Molybdate NCs							
16	La^{3+}, MoO_4^{2-}	96	water	$La_2(MoO_4)_3$	tetragonal	sheet	2 x 200-300
17	Ce^{3+}, MoO_4^{2-}	96	water	$Ce_2(MoO_4)_3$	tetragonal	sheet	2 x 200-300
18	Gd^{3+}, MoO_4^{2-}	96	water	$Gd_2(MoO_4)_3$	tetragonal	sheet	2 x 200-300
19	Y^{3+}, MoO_4^{2-}	96	water	$Y_2(MoO_4)_3$	tetragonal	sheet	2 x 200-300
20	Er^{3+}, MoO_4^{2-}	96	water	$Er_2(MoO_4)_3$	tetragonal	sheet	2 x 200-300

(a) All samples were hydrothermally synthesized using 6-aminohexanoic acid as a capping agent at 180 °C for 20 h.

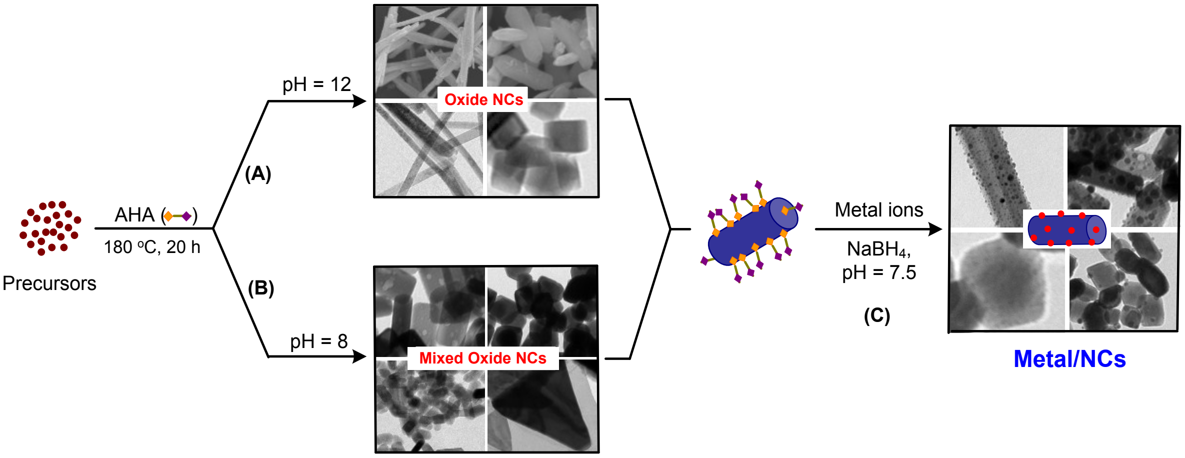

Scheme 8.2.1. A general procedure to synthesize highly crystalline metal oxide, mixed oxide, and hybrid metal/oxide nanocrystals in aqueous medium.

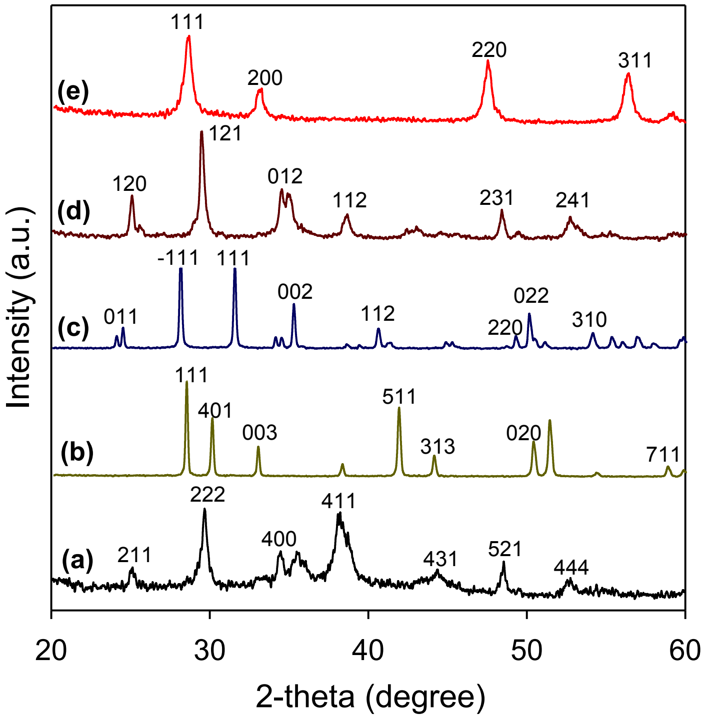

Figure 8.2.1. XRD patterns of the as-synthesized metal oxide NC samples: (a) In_2O_3, (b) Y_2O_3, (c) ZrO_2, (d) TiO_2, and (e) CeO_2.

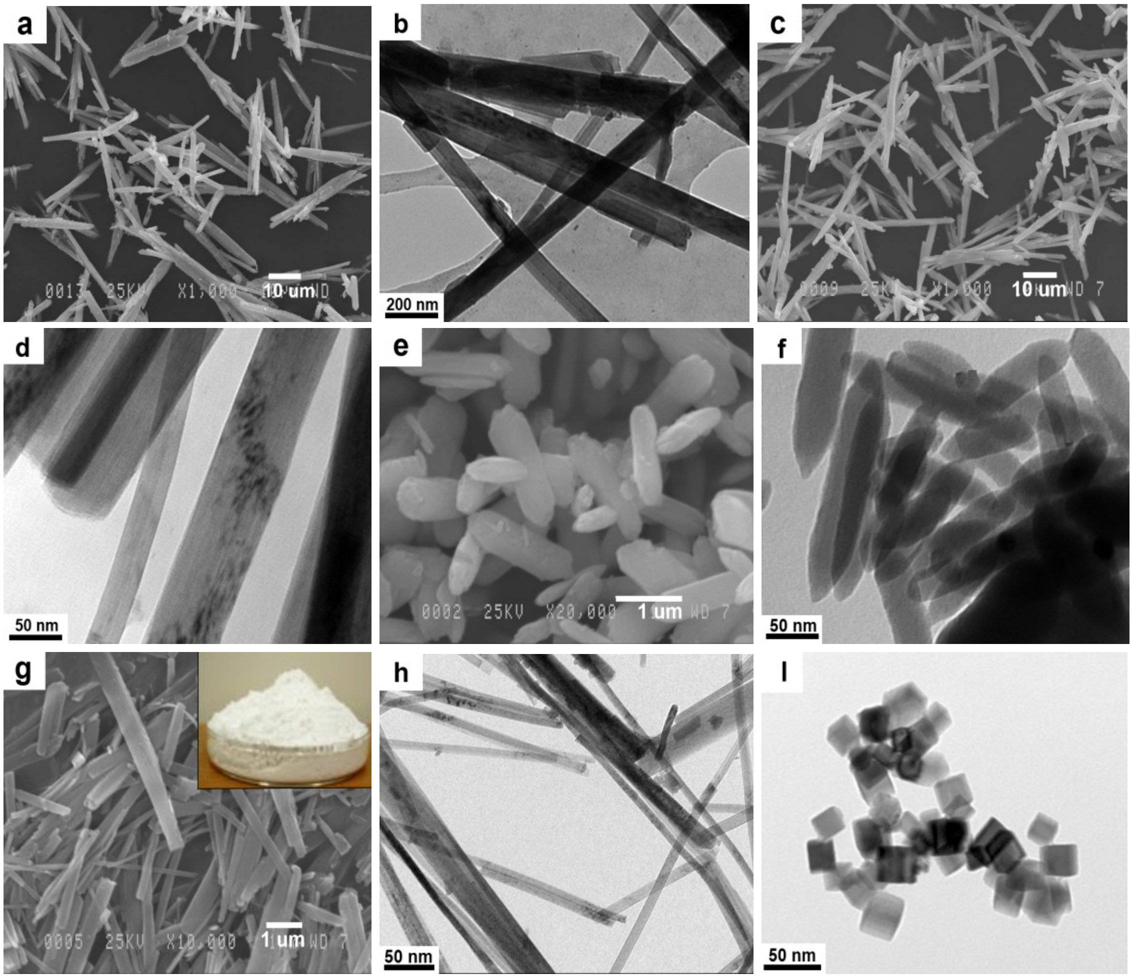

Figure 8.2.2. SEM/TEM images of the metal oxide NCs samples: (a,b) 80 nm x 6 μm In_2O_3 nanorods, (b,c) 80 nm x 6 μm Y_2O_3 nanorods, (d,e) 0.5 μm x 1 μm ZrO_2 nanorods, (f,g) 60 nm x 8 μm TiO_2 nanobels, inset of Figure 2f, 31 g of the AHA-capped TiO_2 nanobelts obtained in a single preparation from 300 mL of the reaction solution using a 700 mL autoclave, and (h) 50 nm CeO_2 nanocubes.

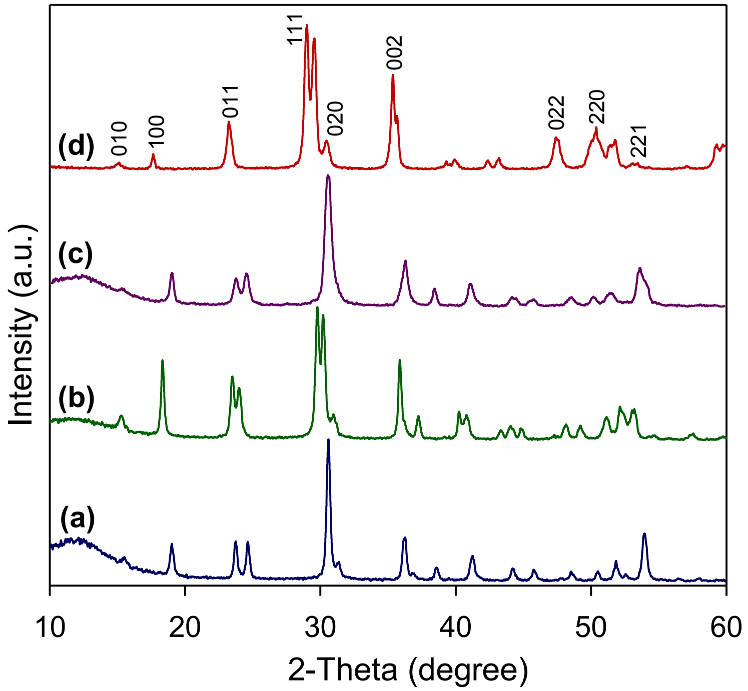

Figure 8.2.3. XRD patterns of the as-synthesized transition metal tungstate NC samples: (a) $CoWO_4$, (b) $MnWO_4$, (c) $ZnWO_4$, and (d) $CdWO_4$.

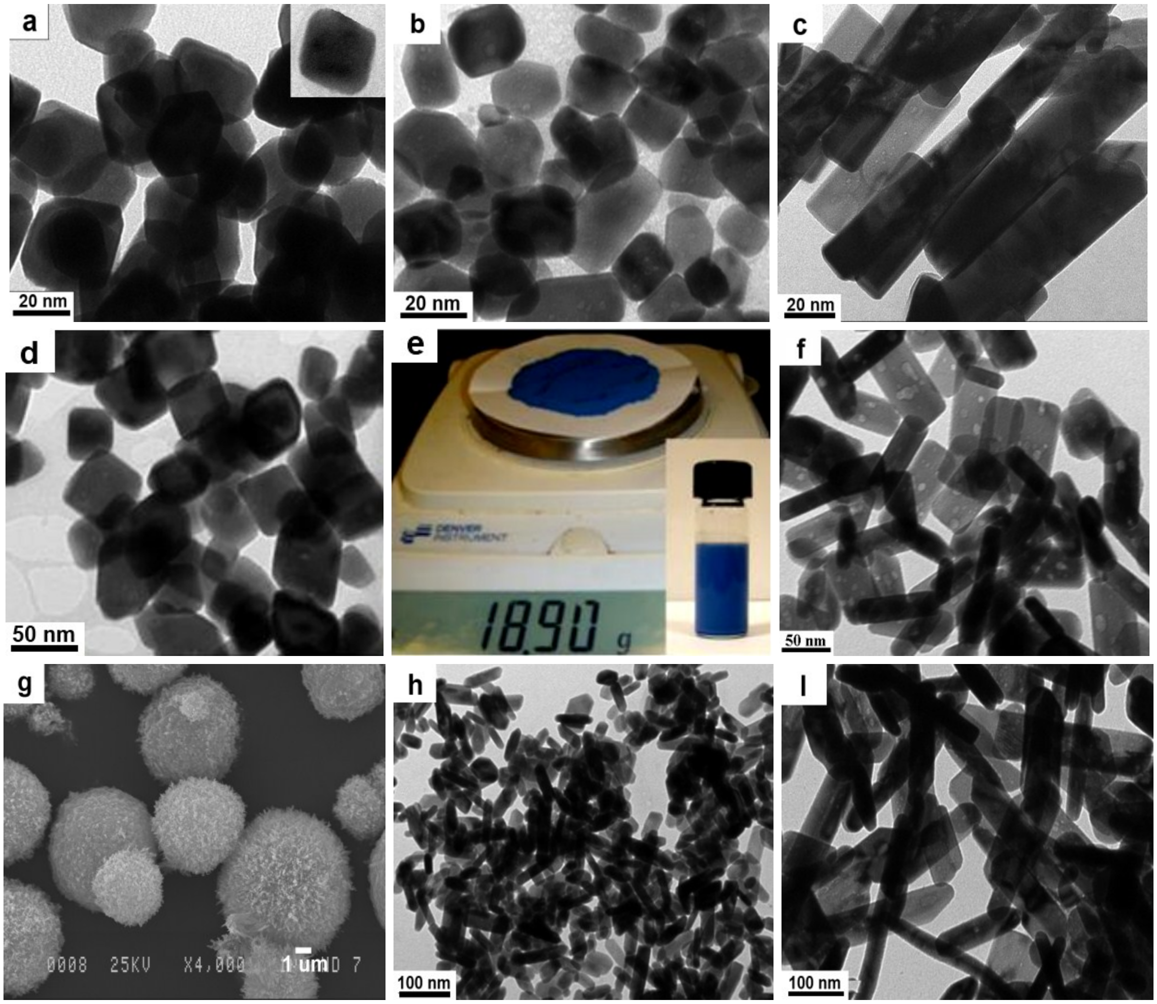

Figure 8.2.4. TEM/SEM images of the transition-metal tungstate NC samples: $CoWO_4$ nanocrystals with various shapes of (a) truncated nanoctahedron, (b) nanobar, (c) nanorods synthesized at different pH of 9, 10, 11, respectively; (d) $CoWO_4$ truncated nanoctahedron synthesized in scale-up and (e) photograph of ~18 g of AHA-capped $CoWO_4$ truncated nanoctahedron obtained per single run from from 500 mL of the reaction solution using a 700 mL autoclave, inset of a vial of aqueous $CoWO_4$ NC suspension, (f) 25 nm x 50 nm $MnWO_4$ nanobars, (g) 3 μm $MnWO_4$ microspheres, (h) 15 nm x 70 nm $ZnWO_4$ nanorods, and (l) 50 nm x 160 nm $CdWO_4$ nanorods.

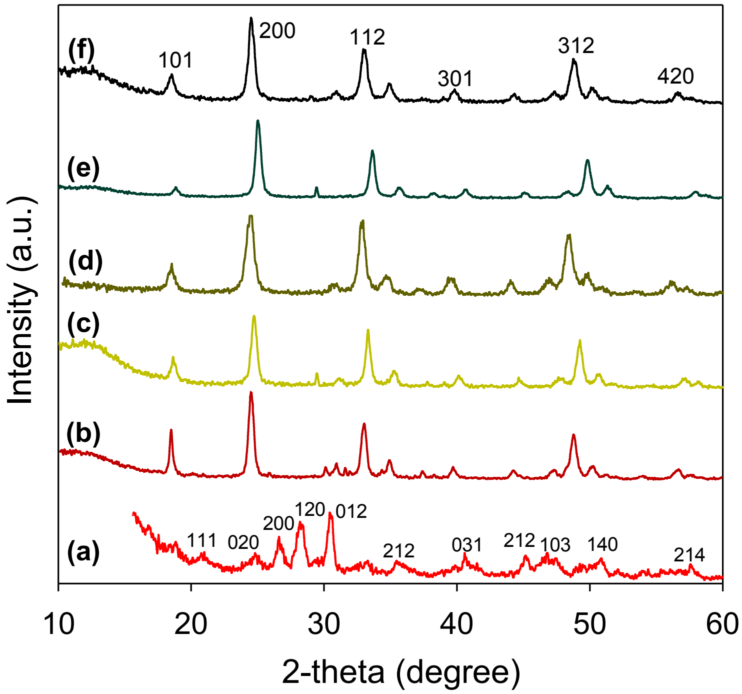

Figure 8.2.5. XRD patterns of the as-synthesized rare earth orthovanadate NC samples: (a) $LaVO_4$, (b) $CeVO_4$, (c) $NdVO_4$, (d) $SmVO_4$, (e) $GdVO_4$, and (f) $ErVO_4$.

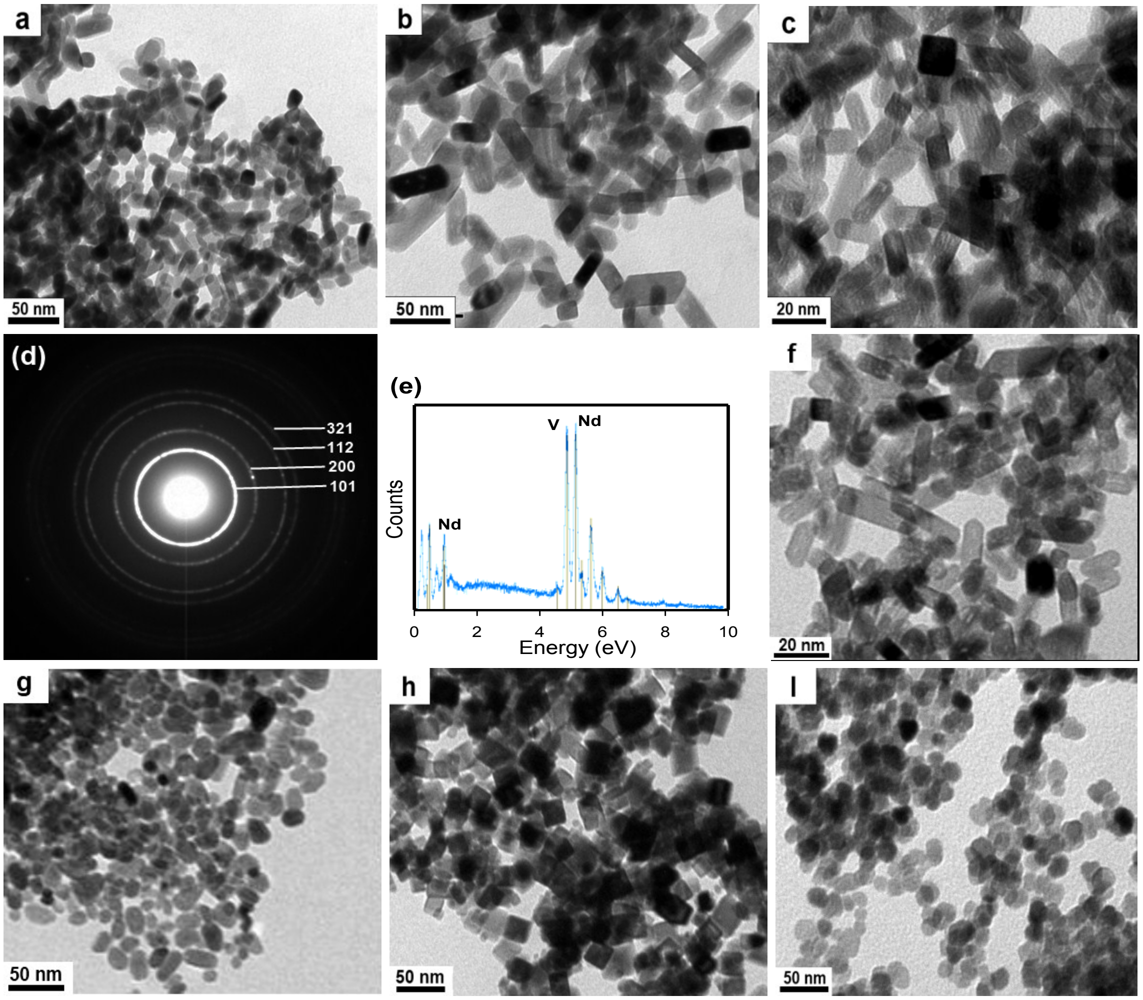

Figure 8.2.6. TEM images of the rare earth orthovanadate NCs samples: (a) 8 nm x 40 nm $LaVO_4$ nanorods, (b) 10 nm x 30 nm $CeVO_4$ nanorods, (c) 10 x 35 nm $NdVO_4$ nanorods, (d) SAED and (e) EDS patterns of corresponding $NdVO_4$, (f) 5.0 mol% Eu^{3+}:$NdVO_4$ nanorods, (g) 30 nm $SmVO_4$ nanoellipses, (h) 30 nm $GdVO_4$ nanocubes, and (l) 30 nm $ErVO_4$ nanospheres.

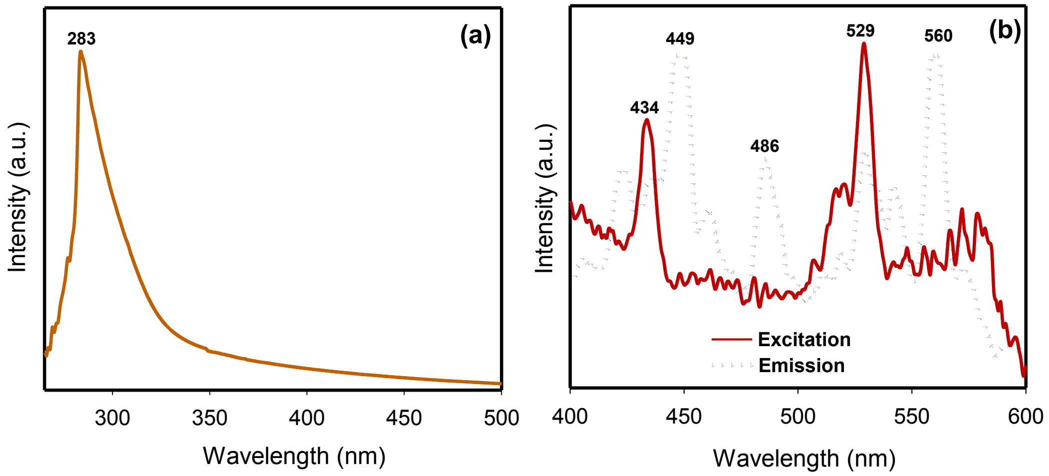

Figure 8.2.7. (a) UV-visible adsorption and (b) photoluminescence (PL) spectra of 5.0 mol% Eu^{3+}:$NdVO_4$ nanorods dispersion in water.

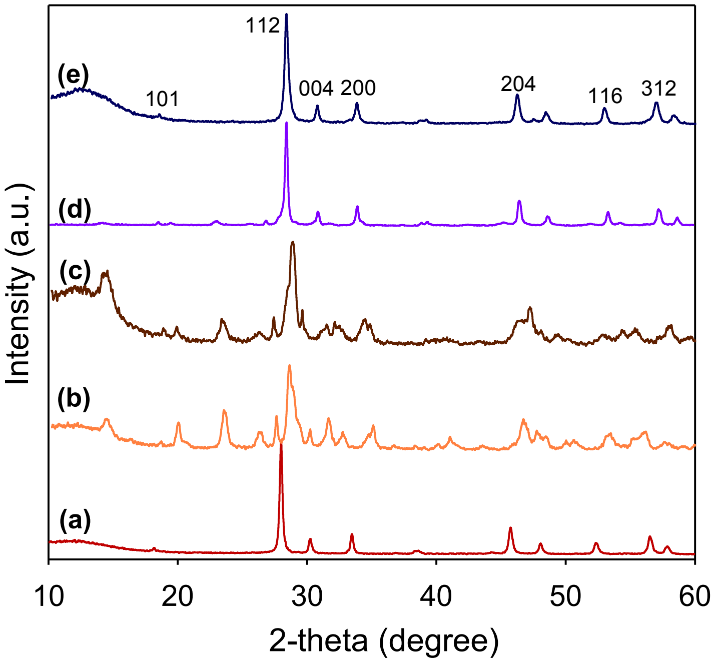

Figure 8.2.8. XRD patterns of the as-synthesized rare earth molybdate NCs samples: (a) $La_2(MoO_4)_3$, (b) $Ce_2(MoO_4)_3$, (c) $Gd_2(MoO_4)_3$, (d) $Y_2(MoO_4)_3$, and (e) $Er_2(MoO_4)_3$.

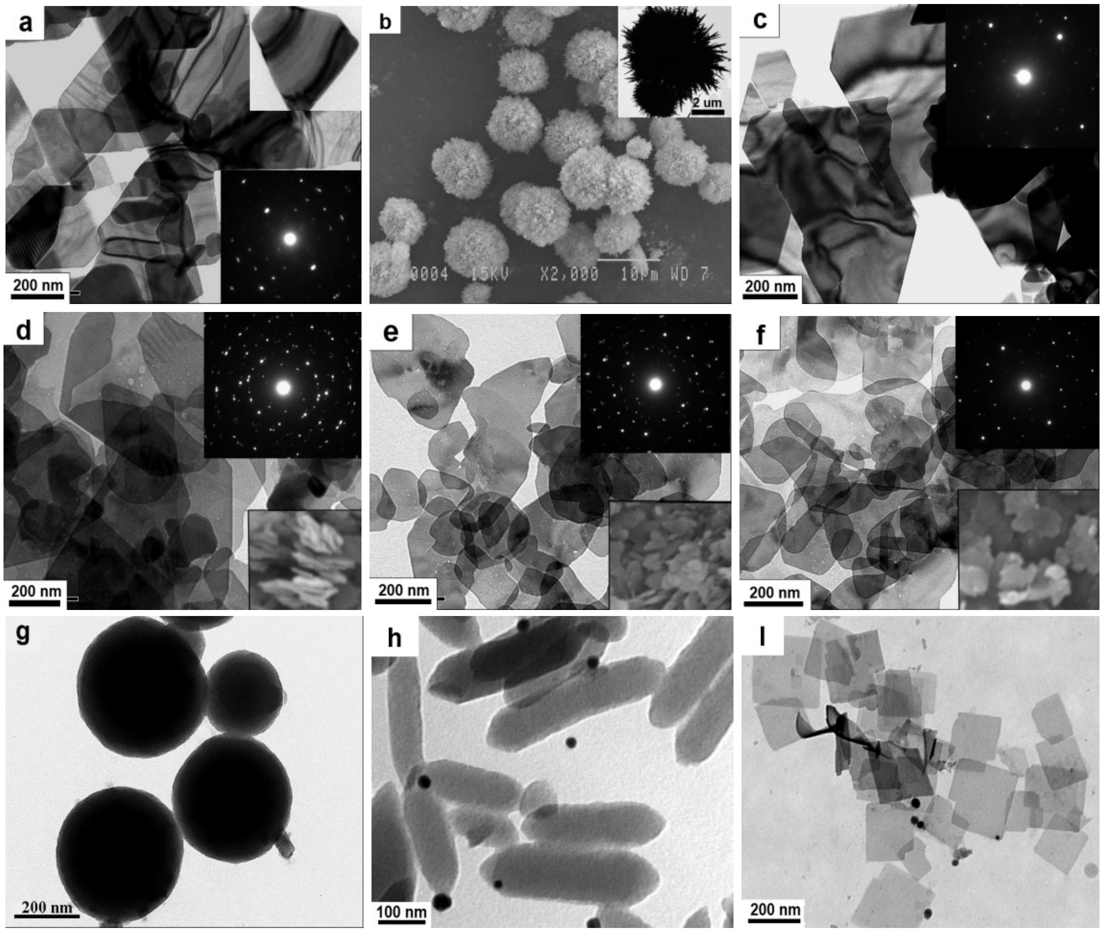

Figure 8.2.9. TEM/SEM and inset SAED patterns of 2 nm x 200-300 nm-sized rare earth molybdate nanosheets: (a) $La_2(MoO_4)_3$, (b) $La_2(MoO_4)_3$ microspheres, (c) $Ce_2(MoO_4)_3$, (d) $Gd_2(MoO_4)_3$, (e) $Y_2(MoO_4)_3$, and (f) $Er_2(MoO_4)_3$. Effect of reaction temperature on the shape of $La_2(MoO_4)_3$ crystals: (g) 100 ^{o}C, microspheres, (h) 130 ^{o}C, nanorods, (l) 160 ^{o}C, sheet-shaped nanosquares.

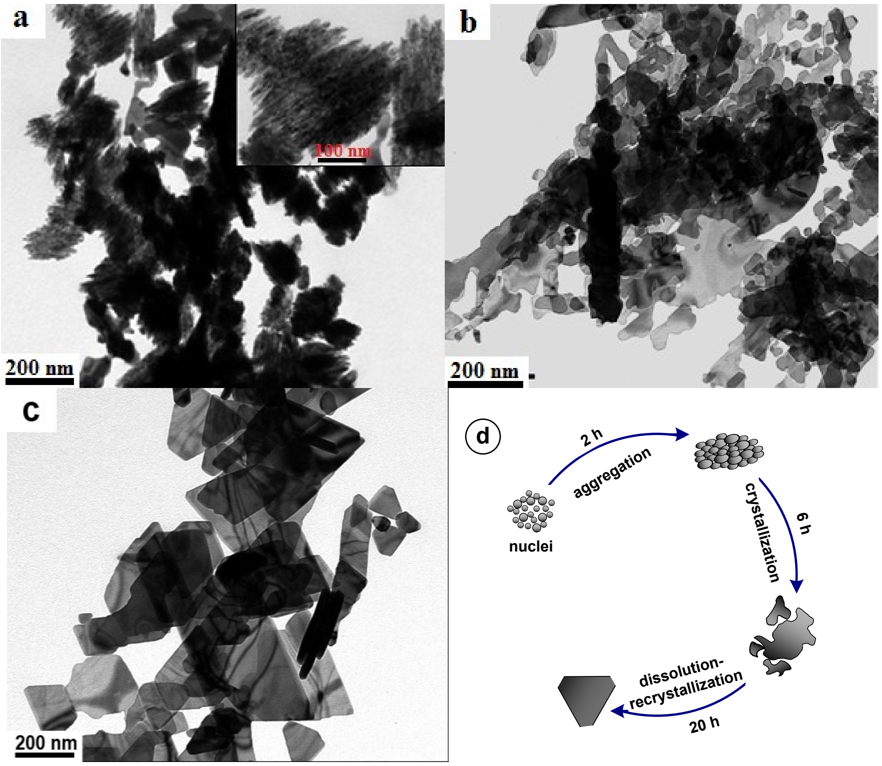

Figure 8.2.10. TEM images of typical $La_2(MoO_4)_3$ nanocrystals hydrothermally synthesized at 180 °C for the different reaction times: (a) 2 h, (b) 6 h, and (c) 20 h. (d) Schematic illustration of the proposed growth mechanism of the $RE_2(MoO_4)_3$ nanosheets.

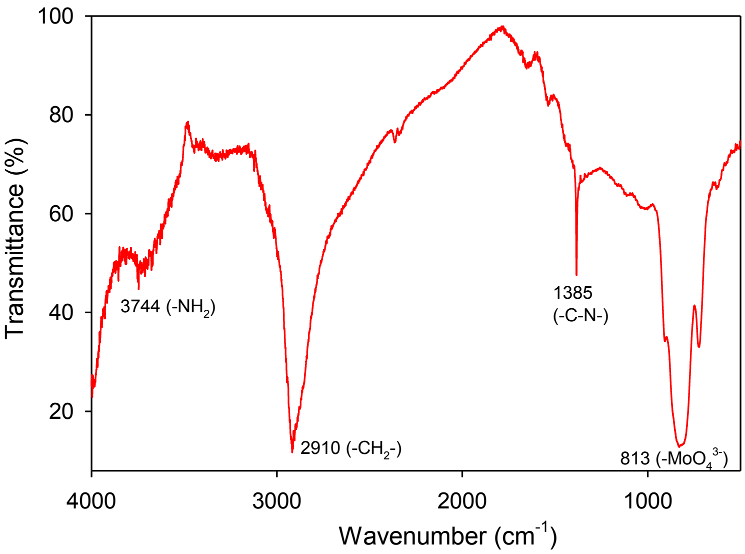

Figure 8.2.11. FTIR spectrum of 6-aminohexanoic acid-capped $La_2(MoO_4)_3$ nanosheets.

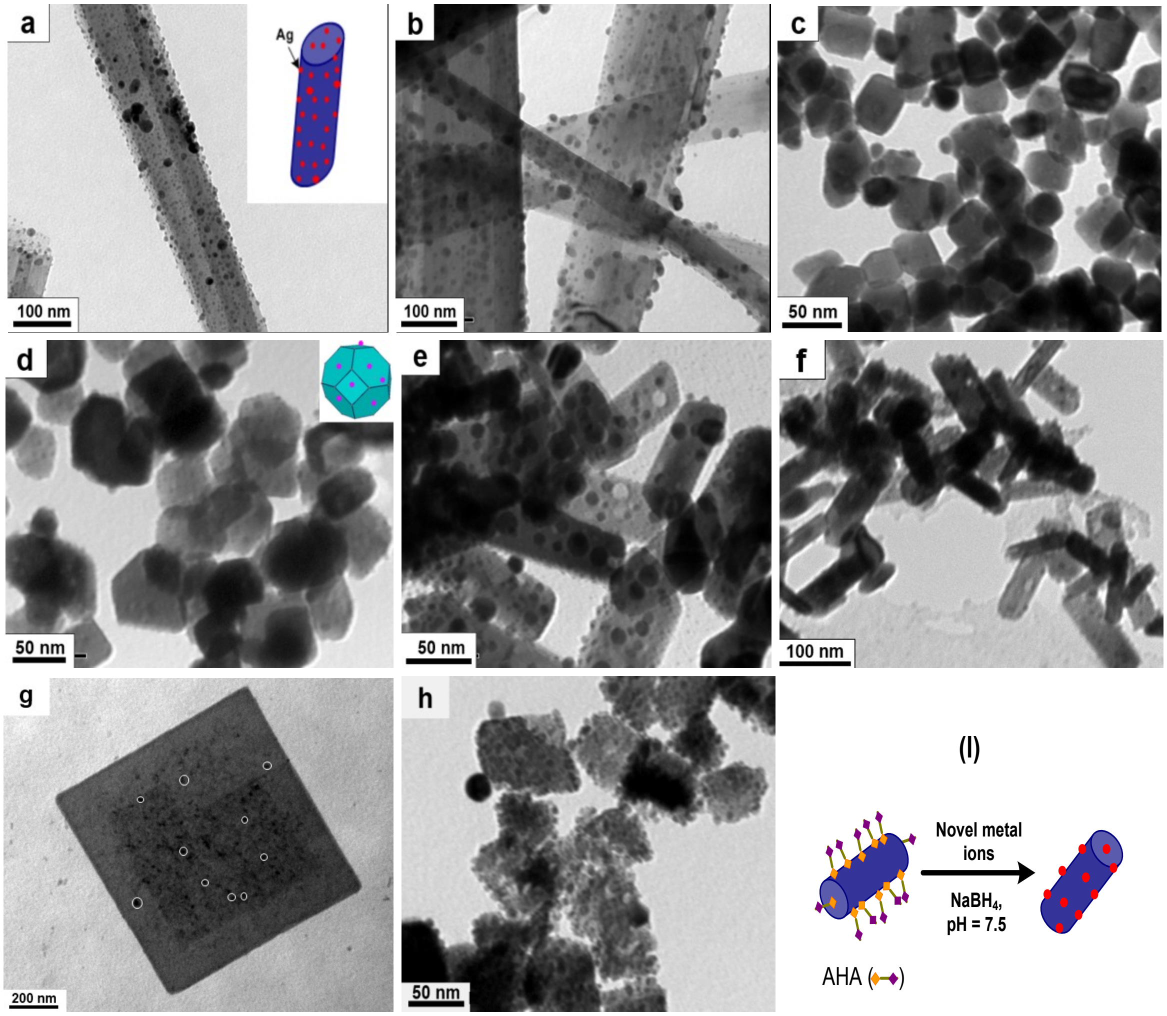

Figure 8.2.12. TEM images of 10.0 wt.% noble-metal/oxide nanohybrid samples: (a) Ag/In_2O_3, (b) Ag/Y_2O_3, (c) Ag/$CoWO_4$, (d) Au/$CoWO_4$, (e) Ag/$MnWO_4$, (f) Au/$MnWO_4$, (g Au/$La_2(MoO_4)_3$, (h) Ag/CeO_2, (l) Scheme of the proposed mechanism of metal precursors deposited on the pre-synthesized oxide nanocrystals for the formation of metal/oxide nanohybrids.

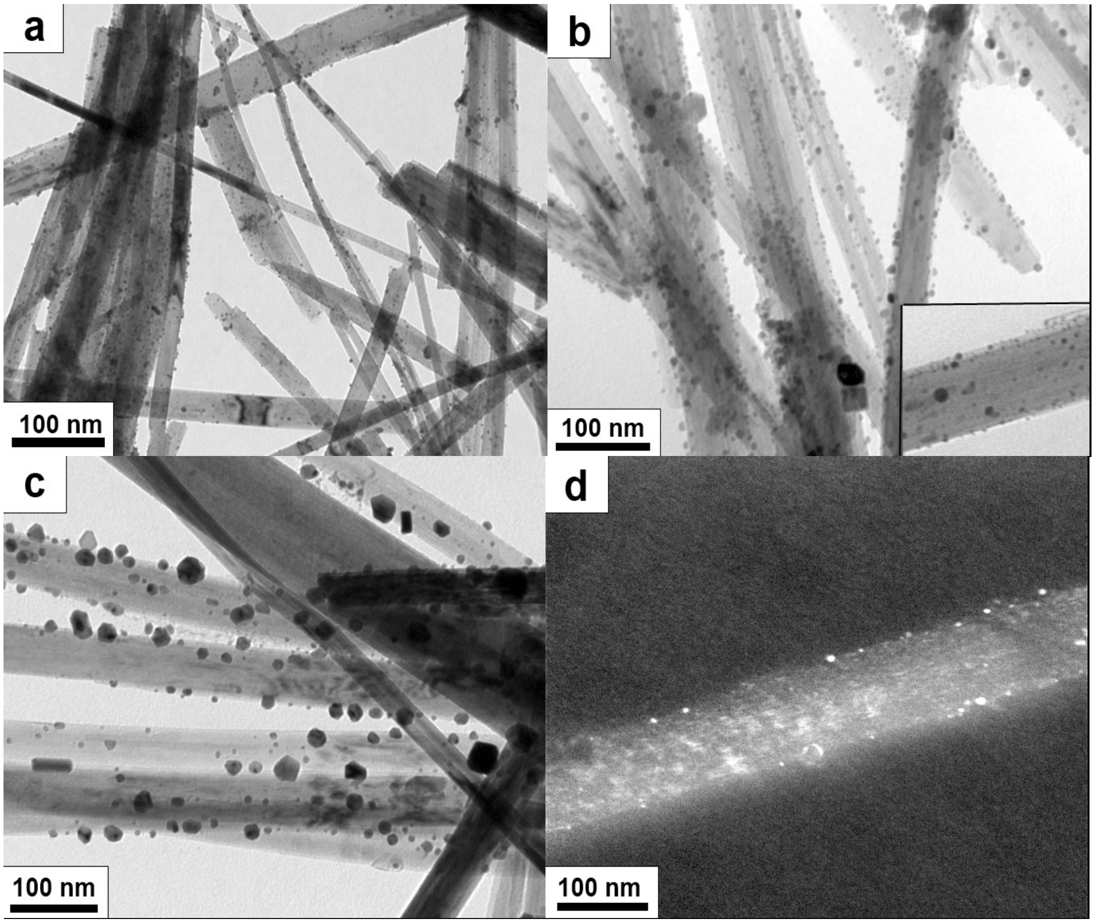

Figure 8.2.13. Effect of Ag ion content (*C, wt.%*) on Ag particle diameters (*d*) in the solid solution. TEM images of the Ag/TiO_2 hybrid nanobelt samples with different Ag contents (*C,* wt.%): (a) *C* = 4.8, *d* = 2-3 nm (b) *C* = 9.5, *d* = 5-7 nm, (c) *C* = 14.6, *d* = 15-20 nm, (d) Dark-field TEM image of a single 9.5 wt.% Ag/TiO_2 nanobelts.

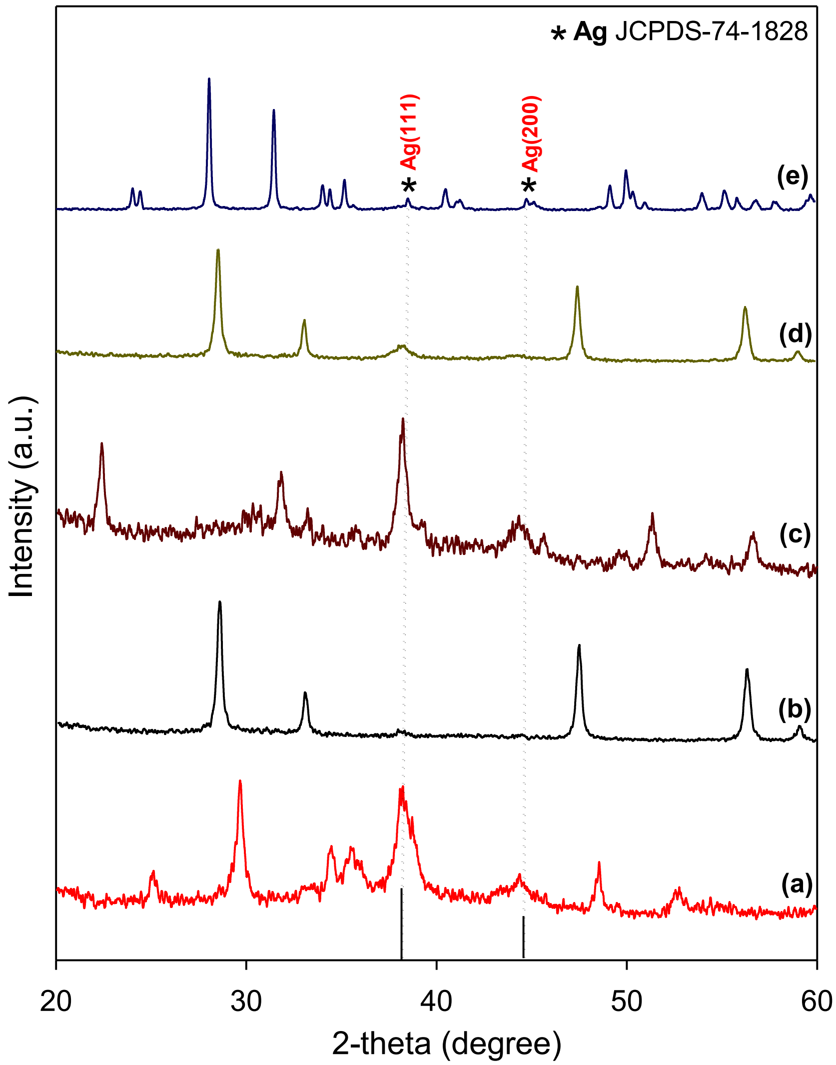

Figure 8.2.14. XRD patterns of the synthesized 10.0 wt.% Ag/oxide hybrid NC samples: (a) Ag/TiO_2 nanobelts, (b) Ag/In_2O_3 nanorods, (c) Ag/Y_2O_3 nanorods, (d) Ag/ZrO_2 nanorods, (e) Ag/CeO_2 nanocubes. The marked with "*" is indexed to deposited face-center-cubic *(fcc)* metallic Ag structure and the other remained peaks are contributed to the corresponding oxide structure.

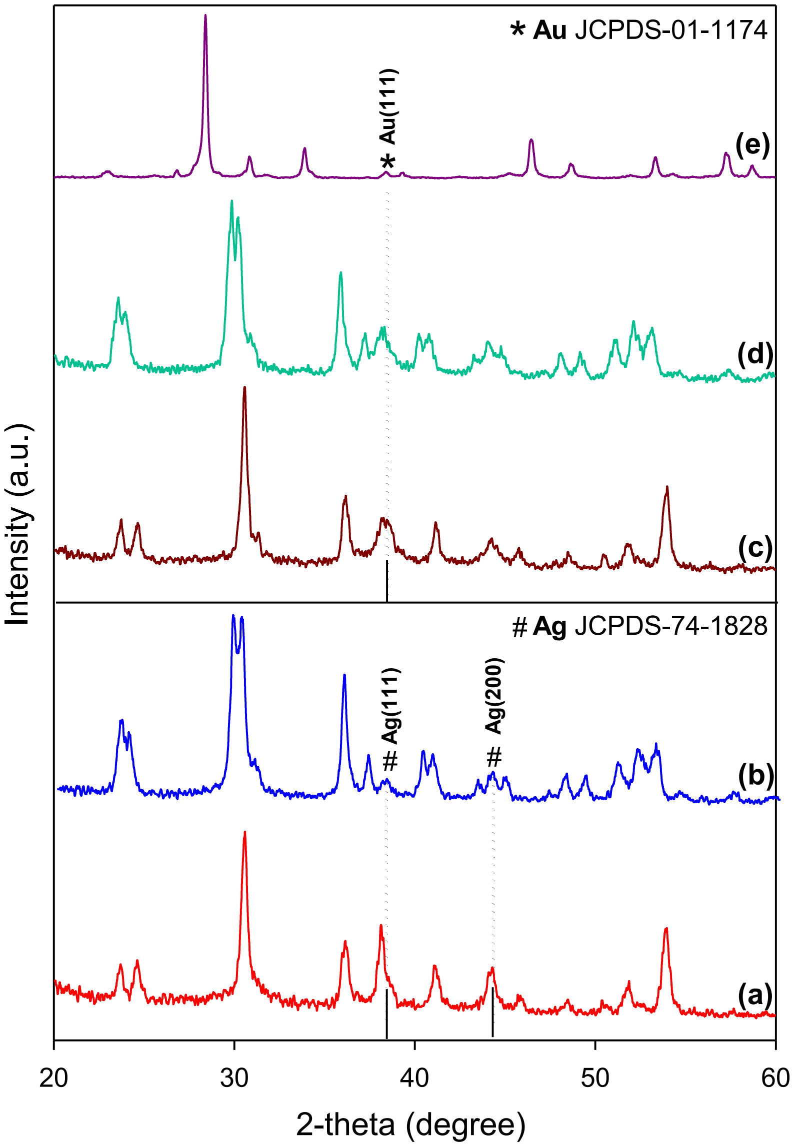

Figure 8.2.15. XRD patterns of the synthesized 10.0 wt.% Ag/mixed oxide and 10.0 wt.% Au/mixed oxide NC samples: (a) Ag/$CoWO_4$, (b) Ag/$MnWO_4$, (c) Au/$CoWO_4$, (d) Au/$MnWO_4$, (e) Au/$La_2(MoO_4)_3$. The marked with "*" and "#" are indexed to deposited face-center-cubic *(fcc)* metallic Ag and Au structures, respectively, and the other remained peaks are contributed to the corresponding mixed oxide structure.

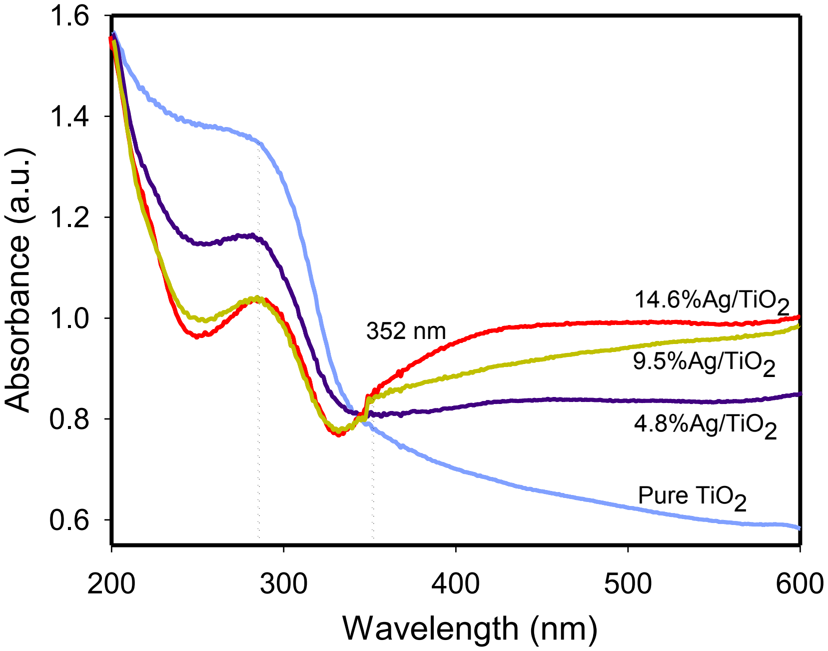

Figure 8.2.16. UV-visible absorption spectra of the as-synthesized Ag/TiO_2 nanohybrids with the different Ag contents.

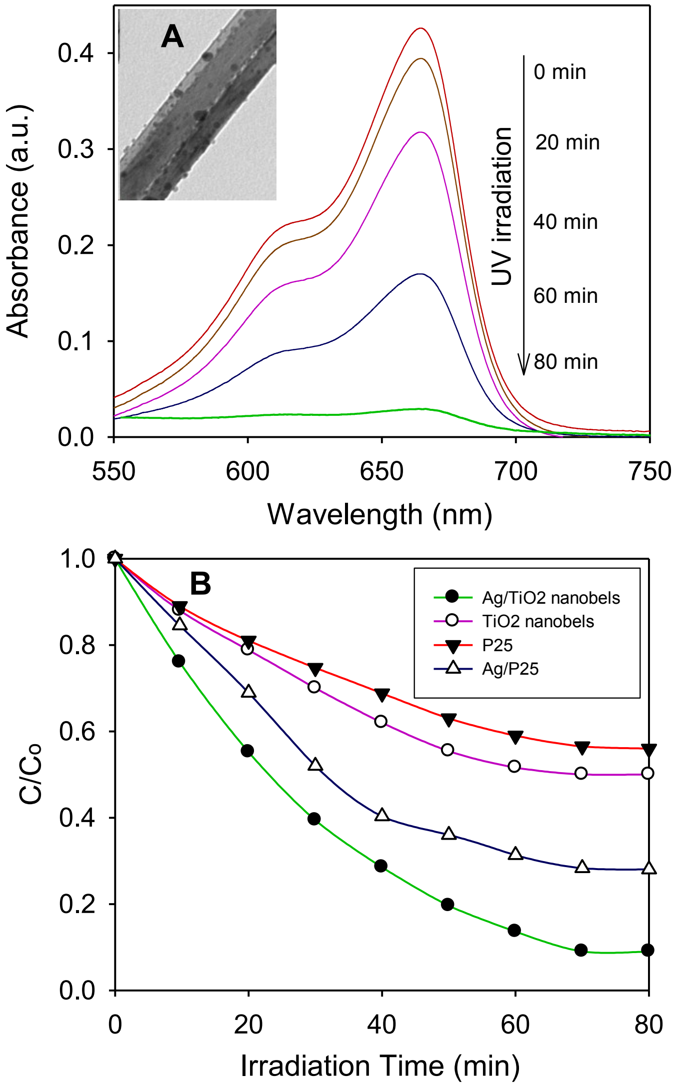

Figure 8.2.17. (A) UV-vis absorption spectra of a methylene blue (MB) solution as a function of irradiation time in the presence of 9.5 wt.% Ag/TiO_2 hybrid NC catalyst and (B) comparison of the MB photodegradation using TiO_2 nanobelts, commercial P25, 9.5 wt.% Ag/TiO_2 hybrid NCs, and 9.5 wt.% Ag/P25 as photocatalysts.

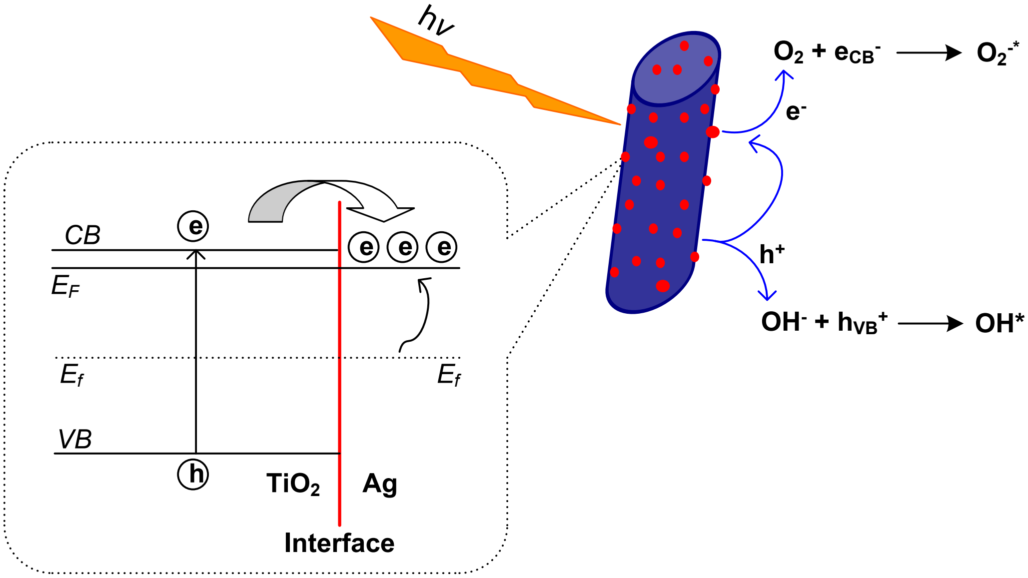

Scheme 8.2.2. Proposed band structure and photocatalytic mechanism for light-induced charge separation in Ag/TiO$_2$ hybrid nanobelts.

Chapter 9 General Conclusions and Recommendations

9.1. General Conclusions

The studies described in this doctoral dissertation allowed drawing four general groups of conclusions concerning the synthesis and characterization of metal oxide, mixed metal oxide, hybrid metal-oxide nanocrystals with controlled size and shape, and catalytic activity of hybrid metal-oxide nanocatalysts, respectively, which can be summarized as follows:

9.1.1. Size- and shape-controlled metal oxide nanocrystals

In this thesis, a series of the monodisperse metal oxide nanocrystals with controlled size and shape were synthesized by using solvo-hydrothermal "two-phase" and "one-phase" approaches.

Different two-phase methods have been developed for the synthesis of two classes of monodisperse metal oxide (rare earth and transition metal) nanocrystals using metal salts as starting precursors. All of the syntheses in this study were carried out in a two-phase water-toluene system by mixing metal sources and capping agents. After solvo-hydrothermal treatment, the capped nanocrystal products were highly dispersed in the toluene phase, and no product was observed in the water phase. The nanocrystal product in the toluene phase was precipitated by adding excess of ethanol and recovered by centrifugation. We have developed three different two-phase pathways. The shape and size of the nanocrystal products can also be controlled by various reaction parameters, including the monomer concentration of metal precursors, type of precursors, and reaction time.

Rare earth oxides (e.g., cerium and samarium) nanocrystals were obtained by the hydrolyzed reaction of the metal nitrate salts in a water-toluene mixture in the presence of capping molecules (fatty acid) and *tert*-butylamine. In the present of *tert*-butylamine as an activation agent, this synthetic route shows the distinct advantage of relatively low temperature compared with the supercritical water method. The products were generated by the hydrolysis of metal nitrate in *tert*-butylamine and followed by dehydrating to oxide nuclei at the interfaces.

Rare earth oxides (e.g., Y, La, Gd, Er) nanocrystals were produced in the two-phase system using the pre-prepared rare earth-oleate complex precursors. The synthetic procedure involves the preparation of rare earth-oleate complexes from the reaction between metal nitrate and potassium oleate in a water-toluene system and followed by the formation of colloidal oxide nanocrystals in the autoclave containing the water-toluene mixture composed of oleylamine/*tert*-butylamine/rare earth-oleate. The formation mechanism of nanocrystals was proposed by the nucleophilic reaction between *tert*-butylamine and carboxyl group of metal-oleate precursor, leading to C-O bond cleavage, the release of a carbonyl group, and then the formation of oxide nuclei at the water-toluene interfaces.

Self-assemblied transition metal oxide (Cr, Co, Mn, Ni) nanocrystals were synthesized in biphasic mixture of (metal ion, ethanol)$_{\text{aqueous}}$/(potassium oleate, oleic acid)$_{\text{toluene}}$. The nanocrystal products were formed by the reduction of ethanol to metal-oleate complex (generated by exchange reaction of metal cation with oleate anion) in the presence of capping fatty acid.

A simple new solvothermal method for the multigram scale synthesis of uniform vanadium oxide nanocrystals using vanadium(V) diperoxo alkylammonium complexes in toluene or toluene/water medium in the presence of aliphatic amine capping agents. The complex precursors were prepared using H_2O_2 solution and commercial bulk V_2O_5 powder as vanadium source instead of expensive organometallic compounds. Monodisperse vanadium oxide NCs with different sizes and shapes including nanospheres, nanocubes, nanorices, and nanorods can be achieved by the control of various reaction parameters, such as water content, types of V(V) diperoxo alkylammonium complexes, and alkyl chain length of capping agents in synthesis mixture.

A new and straightforward approach toward the shape-, size-, and phase-controlled synthesis of ErOOH and Er_2O_3 micro- and nanostructures in high yield, using “one polar phase" system containing erbium nitrate/decanoic acide/ethanol/water at 120-180 °C. The capping products were precipitated at the bottom of a Teflon cup instead of becoming dispersed in the toluene phase as described in two-phase methods. By only tuning the temperature in the reaction system, monoclinic ErOOH and cubic Er_2O_3 phases can be obtained. Furthermore, various particle sizes in the range of thousands to tens of nanometers and a variety of shapes can be achieved simply by varying the synthetic conditions including the concentration of decanoic acid and erbium precursor and the amount of water. The crystalline phase- and particle size-dependent optical properties of these micro/nanomaterials are illustrated.

These synthetic procedures offer several advantages because of the use of inorganic salt precursors, instead of expensive metal alkoxides, nontoxic and inexpensive reagents, and quite mild synthetic conditions. These two-phase and one-phase methods are scalable to multigram using the same conditions used in the milligram ones with phase, size, and shape control.

9.1.2. Size- and shape-controlled mixed metal oxide nanocrystals

A new solvothermal approach for the controllable synthesis of monodisperse and well-crystallized rare earth orthovanadate ($REVO_4$, RE = Sm,Ce) nanocrystals with various shapes from the reaction of $RE(OA)_3$ and $VO_4(TOA)_3$ complexes in toluene in the presence of a capping surfactant (either oleylamine or oleic acid). The $RE(OA)_3$ and $VO_4(TOA)_3$ complex precursors were presynthesized from inexpensive inorganic sources and organic ligands. By varying the reaction parameters, such as reaction temperature, nature and amount of surfactant and metal complex precursor concentration, different morphologies (sphere, cubic, core, rod, wire) of the $SmVO_4$ and $CeVO_4$ nanocrystals can be easily controlled. The XPS results revealed that only one oxidation state of samarium, cerium, and vanadium for each metal (Sm^{3+}, Ce^{3+}, V^{5+}) exists in the mixed $SmVO_4$ and $CeVO_4$ nanocrystals, while two oxidation states for each metal (Sm^{3+}/Sm^{2+}, Ce^{4+}/Ce^{3+}, V^{5+}/V^{4+}) exist in the corresponding single oxide Sm_2O_3, CeO_2, V_2O_5 nanocrystals.

A facile single-step "aqueous-solution" approach for the large-scale synthesis of the single-crystalline $MnWO_4$ nanoparticles and 3D hierarchical mesocrystal microspheres from the hydrothermal aqueous solution reaction containing $Mn(NO_3)_2$ and Na_2WO_4 and capping bifunctional 6-aminohexanoic acid biomolecules. The uniform single-crystalline $MnWO_4$ nanoparticles with bar, rod, square, quasi-sphere, sphere, hexagonal shapes were achieved by tuning the synthesis parameters such as the concentration and the alkyl chain length of amino acids, pH of solution, and reaction temperature. By decreasing the Mn^{2+} and WO_4^{2-} precursor monomer concentration from 0.0150 to 0.0076 M in water medium, rigid $MnWO_4$ mesocrystal hierarchical microspheres were formed from the spontaneous-assembly of primary nanoparticles through the backbone-backbone intermolecular hydrogen-bonding interactions of polypeptide chains. The photoluminescence results indicate that the photoluminescene emission intensity of the $MnWO_4$ nanobars is higher than that of the $MnWO_4$ microspheres indicating the decrease in the luminescence efficiency of the microspheres due to nanobars inside of microspheres.

The synthetic procedure can be extended to the ''green'' synthesis of other nanomaterials. Accordingly, a general method for the hydrothermal high-yield synthesis of many kinds of the highly crystalline metal oxide (e.g., In_2O_3, Y_2O_3, ZrO_2, CeO_2) and mixed oxide nanocrystals (MWO_4, $REVO_4$, $RE_2(MoO_4)_3$, M = Co, Cd, Zn; RE = La, Ce Gd, Nd, Y, Er) with various morphologies including belt, rod, truncated-octahedron, cubic, sphere and sheet. The synthetic procedure was based on the hydrothermal crystallization of inorganic precursors in water medium in the presence of bifunctional 6-aminohexanoic acid (AHA) as a capping agent. Monodisperse oxide nanoparticles were capped by the amino head group of amino acid biomolecules and the uncoordinated carboxylic terminus were oriented outward to provide the water-dispersible nature of the hydrophilic nanoparticles.

As compared to the nonaqueous synthetic routes using hydrophobic organic surfactants such as fatty acids, aliphatic amines, alkyl phosphine oxides, ect, our aqueous-based approach has many advantages including: water is adopted as the continuous solution phase and inorganic salts were used as starting materials; amphiphilic 6-aminohexanoic acid biomolecule is an interesting stabilizer to yield the biocompatible nanocrystal products. Due to the high solubility of the salts in aqueous solution, we could be applicable to synthesize the nanoparticles in scale up by using the high precursor monomer concentrations. This aqueous-based method is thus a promising way in the academic laboratory as well as can be expanded to the industrial scale in a simple way.

In the continuation of the development of a simple two-phase approach of synthesizing uniform-sized nanocrystals, we synthesized undoped and cerium doped $LaCO_3OH$ annular-shaped nanoarchitectures with large specific surface area via the thermolysis of binary source precursor, Ce_xLa_{1-x}(oleate)$_3$ complex (x = 0-20 mol%), in water-toluene system containing *tert*-butylamine/oleylamine. The conversion of $Ce_xLa_{1-x}CO_3OH$ structure to $Ce_xLa_{1-x}(CO_3)O_2$ at 600 ^oC, to $Ce_xLa_{1-x}(OH)_3$ at 800 ^oC, and eventually to $(Ce_xLa_{1-x})_2O_{3-\delta}$ at 900 ^oC were employed. The XRD results reveal that because cerium and lanthanum have the similar ionic radii, the cerium dopant could enter easily into the $LaCO_3OH$ structural lattice. Whereas copper could be unlikely into their lattice due to the large ionic radius difference. The XPS results reveal that only one Ce^{3+} oxidation state is in the as-synthesized $Ce_xLa_{1-x}CO_3OH$ samples with doping level in ranging from 5 to 15 mol%, whereas both 3+ and 4+ ones coexisted in 20 mol%Ce:$LaCO_3OH$. Upon annealing at high temperatures (800-900 ^oC) under air atmosphere, the partial conversion of Ce^{3+} into Ce^{4+} occurring on the surface of mixed cerium-lanthanum hydroxide or oxide was observed. The significant luminescence emission intensity of the as-synthesized $Ce_xLa_{1-x}CO_3OH$ samples was found to increase from 1.5 to 9.0 times with increase in cerium dopant concentration from 5 to 20 mol%.

9.1.3. Size- and shape-controlled hybrid metal@oxide nanocrystals

Using bifunctional hexamethylenediamine surfactant to obtain single-crystalline hydrophilic-surfaced CeO_2 nanocubes in water medium under hydrothermal treatment. The (Cu or Ag)@CeO_2 nanohybrids were prepared by controlled decoration of Cu nanodots with 3-9 nm in diameter on the reactive {100} facets of single-crystalline CeO_2 nanocubes through reducing $Cu(NO_3)_2$ by $NaBH_4$ in aqueous medium.

The obtained 6-aminohexanoic acid (AHA)-capped oxide and mixed nanocrystals were capped by -NH_2 heads of bifunctional AHA molecules and free -COOH groups of other end of AHA molecules were available for further derivativation in polar solvent. As a result, these AHA-capped oxide nanocrystals are excellent support for the preparation of a variety of metal@oxide hybrid nanocrystals, in which noble metal (Ag) particles with the average size of 2-7 nm were deposited on the hydrophilic surface of individual supports.

9.1.4. Catalytic activity of hybrid metal-oxide nanocrystals

Effect of the exposed active {100} facets of single-crystalline CeO_2 nanocubes on the CO oxidation efficiency was illustrated. The hybrid Cu@{100}-faceted CeO_2 nanocubes showed a much higher performance for the CO oxidation conversion as compared to pure CeO_2 materials. Effect of shape of CeO_2 support on the CO oxidation was also found.

The hybrid Ag/TiO_2 nanobelts exhibited a much higher performance for the photocatalytic degradation of MB as compared to Ag/commercial P25.

9.2. Recommendations

The following are some recommendations for future works:

1. Extend the detail study on the nucleation and growth kinetics of the formation of nanocrystals for the different one-phase and two-phase methods. A deeply understanding about the effect of reaction parameters on the nanocrystal formation kinetics will be easily to control the shape and size of inorganic nanocrystals.

2. $MnWO_4$ often exhibits high sensitivity to humidity change, so this property should be measured to the obtained high-crystalline $MnWO_4$ nanocrystals with different shapes.

3. It is well-known that the semiconductor quantum dots have considered the top materials in optical fields because they exhibit the unique luminescence resonance energy transfer properties in highest yield. The recent studies reported that the lanthanide-based materials can also exhibit these unique luminescent properties when their particle size was decreased to ~2-5 nm. This unique luminescent property was also observed in our synthesized $Ce_xLa_{1-x}CO_3OH$ particles with the quantum size of 3-5 nm. In comparison with the luminescent yield of both semiconductor quantum dots and $Ce_xLa_{1-x}CO_3OH$ particles should be systematically studied.

4. Study further the effect of shape and size of metal oxide and mixed oxide nanocrystals on catalytic activity and optical properties.

5. It has known that the rare earth orthovanadate samples are very sensitive for many organic catalytic transformations, particularly $SmVO_4$ nanocrystal sample. So the obtained high-quality $SmVO_4$ nanocatalysts in this thesis work should be tested to the oxidative dehydrogenation of alkanes and compared to bulk $SmVO_4$ references.

6. Study further the effect of particle size of deposited noble metal nanoparticles on oxide nanosupports on catalytic activity for CO oxidation and photocatalysis.

List of Publications during the Thesis as a Ph.D. Candidate

Refereed Publications

1. *Cu Particles on Single-Crystalline CeO_2 Nanocubes as a Synergistic Catalyst for Preferential CO Oxidation*
   Nguyen Thanh-Dinh, Mrabet Driss, Dinh Cao-Thang, Do Trong-On
   Advanced Materials, 2011, Submitted.

2. *A General Procedure to Synthesize Highly Crystalline Metal Oxide and Mixed OxideNanocrystals in Aqueous Medium and Photocatalytic Activity of Metal/Oxide Nanohybrids*
   Nguyen Thanh-Dinh, Dinh Cao-Thang, Do Trong-On
   Nanoscale, 2011, 3, 1861-1873.

3. *Two-Phase Synthesis of Colloidal Annular-Shaped $Ce_xLa_{1-x}CO_3OH$ Nanoarchitectures Assemblied from Small Particles and Their Thermal Conversion to Derived Mixed Oxides*
   Nguyen Thanh-Dinh, Dinh Cao-Thang, Do Trong-On
   Inorganic. Chemistry, 2011, 50, 1309-1320.

4. *Biomolecule-Assisted Route for Shape-Controlled Synthesis of Single-Crystalline $MnWO_4$ Nanoparticles and Spontaneous Assembly of Polypeptide-Stabilized Mesocrystal Microspheres*
   Nguyen Thanh-Dinh, Mrabet Driss, Vu Thi Thuy-Duong, Dinh Cao-Thang, Do Trong-On
   CrystEngComm, 2011, 13, 1450-1460.

5. *A New Route to Size and Population Control of Silver Clusters on Colloidal TiO_2 Nanocrystals*
   Dinh Cao-Thang, **Nguyen Thanh-Dinh**, Kleitz Freddy, Do Trong-On
   ACS Applied Materials & Interfaces, 2011, 3, 2228-2234.

6. *A Novel Single-Step Route Based on Solvothermal Technique to Shape-Controlled Titanium Dioxide Nanocrystals*
   Dinh Cao-Thang, **Nguyen Thanh-Dinh**, Kleitz Freddy, Do Trong-On
   Invited paper to the special issue, *The Canadian Journal of Chemical Engineering*, 2011, in press.

7. *Large-Scale Synthesis of Uniform Silver Orthophosphate Colloidal Nanocrystals Exhibiting High Visible Light Photocatalytic Activity*

Dinh Cao-Thang, **Nguyen Thanh-Dinh**, Kleitz Freddy, Do Trong-On
Chemical Communication, 2011, 47, 7797-7799.

8. *Size- and Shape-Controlled Synthesis of Monodisperse Metal Oxide and Mixed Oxide Nanocrystals*
   Nguyen Thanh-Dinh, Do Trong-On
   In the book entitled: *Nanocrystal*, Chapter 2, Invited Review Article, *InTech Publisher*, 2011, 55-84.

9. *Size- and Shape-Controlled Hybrid Inorganic Nanomaterials and Application for Low-Temperature CO Oxidation*
   Nguyen Thanh-Dinh, Do Trong-On
   In the book entitled: *Controlled Size and Shape of Nanostructured Materials and Their Application*s, Chapter 16, *Pan Stanford Publisher* 2011, 33 pages, in press.

10. *Shape-Controlled Synthesis of Metal Oxide Nanocrystals*
    Dinh Cao-Thang, **Nguyen Thanh-Dinh**, Kleitz Freddy, Do Trong-On
    In the book entitled: *Controlled Size and Shape of Nanostructured Materials and Their Applications*, Chapter 8, *Pan Stanford Publisher*, 2011, in press.

11. *Shape- and Size-Controlled Synthesis of Monoclinic ErOOH and Cubic Er_2O_3 from Micro- to Nanostructures and their Upconversion Luminescence*
    Nguyen Thanh-Dinh, Dinh Cao-Thang, Do Trong-On
    ACS Nano, 2010, 4, 2263-2273.

12. *Shape-Controlled Synthesis of Highly Crystalline Titania Nanocrystals*
    Dinh Cao-Thang, **Nguyen Thanh-Dinh**, Kleitz Freddy, Do Trong-On
    ACS Nano, 2009, 11, 3737-3743.

13. *A Novel Approach for Monodisperse Samarium Orthovanadate Nanocrystals: Controlled Synthesis and Characterization*
    Nguyen Thanh-Dinh, Dinh Cao-Thang, Dinh-Tuyen Nguyen, and Do Trong-On
    Journal of Physical Chemistry C, 2009, 113, 18584-18595.

14. *Monodisperse Samarium and Cerium Orthovanadate Nanocrystals and Metal Oxidation States on the Nanoscrystal Surface*
    Nguyen Thanh-Dinh, Dinh Cao-Thang, Do Trong-On
    Langmuir, 2009, 25, 11142-11148.

15. *General Two-Phase Routes to Synthesize Colloidal Metal Oxide Nanocrystals: Simple Synthesis and Their Ordered Self-Assembly Structure*
    Nguyen Thanh-Dinh, Dinh Cao-Thang, Do Trong-On
    Journal of Physical Chemistry C, 2009, 113, 11204-11214.

16. *Solvo-hydrothermal Approach for Shape-Selective Synthesis of V_2O_5 Nanocrystals and Their Characterization*
    Nguyen Thanh-Dinh, Do Trong-On
    Langmuir, 2009, 25, 5322-5332.

17. *Controlled Self-Assembly of Sm_2O_3 nanocrystals into nanorods: Simple and Large Scale Synthesis using Bulk Sm_2O_3 Powders*
    Nguyen Thanh-Dinh, Mrabet Driss, Do Trong-On

    Journal of Physical Chemistry C, 2008, 112, 15226-15235.

Conference

1. *A Novel Single-Step Route Based on Solvothermal Technique to Shape-Controlled Titanium Oxide Nanocrystals*
   Dinh Cao-Thang, **Nguyen Thanh-Dinh**, Kleitz Freddy, Do Trong-On
   XVIII World Congress of the International Commission of Agricultural and Biosystems Engineering (CIGR), June 13-17, 2010, Quebec City, Canada.

2. *General Two-Phase Routes to Synthesize Colloidal Metal Oxide Nanocrystals: Simple Synthesis and Their Ordered Self-Assembly Structures*
   Nguyen Thanh-Dinh, Dinh Cao-Thang, Do Trong-On
   8th World Congress of Chemical Engineering (WCCE8), August, 2009, Montreal, Quebec, Canada.

3. *Shape-Controlled Synthesis and Oxidation State of Monodisperse Samarium Orthovanadate Nanocrystals*
   Nguyen Thanh-Dinh, Dinh Cao-Thang, Do Trong-On
   8th World Congress of Chemical Engineering (WCCE8), August, 2009, Montreal, Quebec, Canada.

4. *Chemical Routes to Controllable Synthesis of Monodisperse Metal Oxide and Mixed Oxide Nanocrystals*
   Nguyen Thanh-Dinh, Dinh Cao-Thang, Mrabet Driss, Do Trong-On
   Catalysis and Adsorption Conference, August 2009, Hanoi, Viet Nam (*Review).*

5. *Synthesis and Self-Assembly of Uniform Rare Earth Orthovaladate or Molybdate Nanocrystals Using a Solvothermal Approach*
   Nguyen Thanh-Dinh, Mrabet Driss, Do Trong-On
   Particle, May 2008, Orlando, Florida, USA.

6. *Synthesis of Uniform Rare Earth Orthovanadate Nanocrystals Using a Solvothermal Approach*
   Nguyen Thanh-Dinh, Mrabet Driss, Do Trong-On
   ACFAS, May 2008, Quebec City, Canada.